

Doctoral thesis

Doctoral theses at NTNU, 2023:317

Marit Buhaug Folstad

# Slag and its effect on Si and FeSi production

**NTNU**  
Norwegian University of Science and Technology  
Thesis for the Degree of  
Philosophiae Doctor  
Faculty of Natural Sciences  
Department of Materials Science and Engineering



Norwegian University of  
Science and Technology



Marit Buhaug Folstad

# **Slag and its effect on Si and FeSi production**

Thesis for the Degree of Philosophiae Doctor

Trondheim, September 2023

Norwegian University of Science and Technology  
Faculty of Natural Sciences  
Department of Materials Science and Engineering



Norwegian University of  
Science and Technology

**NTNU**

Norwegian University of Science and Technology

Thesis for the Degree of Philosophiae Doctor

Faculty of Natural Sciences

Department of Materials Science and Engineering

© Marit Buhaug Folstad

ISBN 978-82-326-7334-6 (printed ver.)

ISBN 978-82-326-7333-9 (electronic ver.)

ISSN 1503-8181 (printed ver.)

ISSN 2703-8084 (online ver.)

Doctoral theses at NTNU, 2023:317

Printed by NTNU Grafisk senter

## Preface

This thesis has been submitted to the Norwegian University of Science and Technology as a completion of the requirements for the degree of Philosophiae Doctor. The work has been carried out at the Department of Materials Science and Engineering. The thesis is a part of the project “Controlled Tapping”, founded by The Norwegian Ferroalloy Research Association (FFF) and the Norwegian Research Council (NRC) (Project number 267621), where the industry’s overall goal is to minimize uneven tappings and thereby reduce the energy consumption and the risk of hazardous events. The work has been supervised by Professor Merete Tangstad as the main supervisor, and by Senior Research Scientist Eli Ringdalen and Professor Kristian Etienne Einarsrud as co-supervisors.

During the work of this thesis the following scientific papers have been published:

- Folstad M. B., Tangstad M., Ringdalen E., Fredriksli R, and Dalum S., Tapping Procedures in silicon production and the role of female tapping operators, Tapping Conference, 2018 October.14.-17.
- Folstad M. B., Ksiazek M. T. and Tangstad M., Slag in the Tapping Area in a Si Furnace, Silicon for the Chemical and Solar Industry XV, p. 119-127: 2020 June 15.-18.
- Folstad M. B., Ringdalen E., Tveit H. and Tangstad M., Effect of different SiO<sub>2</sub> polymorphs on the reaction between SiO<sub>2</sub> and SiC in Si production, Metallurgical and Materials Transactions B, April 2021, <https://doi.org/10.1007/s11663-020-02053-x>
- Folstad M. B and Tangstad M., SiO<sub>2</sub>-CaO-Al<sub>2</sub>O<sub>3</sub> slags in Si/FeSi furnaces, INFACON XVI 2021 September 27.-29.
- Folstad M. B., Han Y., Wang H. and Tangstad M., Disintegration of six different quartz types during heating to 1600 °C, MDPI Minerals, January 2023, <https://doi.org/10.3390/min13020132>
- M. B. Folstad, Jusnes K. F. and Tangstad M., Investigation of slag and condensate from the charge top in a FeSi75 furnace, TMS, 2023 March 19.-23.



## Abstract

The amount of slag is one of the main differences between different furnaces in silicon (Si) and ferrosilicon (FeSi) production. Slag is primarily formed from impurities in the raw materials, fluxes, and electrodes. Understanding the behaviour of slag and how it reacts in the furnace are important to prevent accumulation of slag, and to optimize a good mass flow. The amount of accumulated slag is believed to be an important factor in the productivity of the furnace. Additionally, knowledge about the slag present in the furnaces is an important step towards identifying the different zones and materials in the furnaces.

Different methods were used to gain knowledge about the slag, and this study is therefore divided into three parts. Part 1 focuses on slag from industrial Si and FeSi furnaces, part 2 investigates the impurities in the quartz, who later contributes to the slag formation in the furnace, and part 3 studies the main action used today for removing accumulated slag from the industrial furnace: dissolving calcium oxide (CaO) in the slag to reduce its viscosity.

Slag in Si and FeSi production has previously not been the focus of research. A significant part of the work has been to identify the slag present in the furnaces, and to investigate the variations between the different zones and furnaces. Slag from different zones in six different Si and FeSi furnaces collected during excavations, tapped slag from three different furnaces and slag from the charge surface of two FeSi furnaces during operation are the basis for the industrial part of this work.

Accumulated slag is typically found along the furnace walls, extending sometimes all the way up to the charge top, and in a thick layer at the furnace bottom, which the metal must pass to exit the tap-hole. Slag towards the furnace walls and up in the furnace will start to solidify as the temperature decreases in the low temperature zone. Too much accumulated slag in the charge area will hinder the raw materials and narrows the reaction route. Accumulated slag at the bottom of the furnace affects the tapping process. Since slag is more viscous than the metal, an accumulation of slag near the tap-hole may hinder the metal flow out of the tap-hole and it can clog to the tap-hole.

Both the accumulated slag and the tapped slag mainly contain  $\text{SiO}_2$ , CaO and  $\text{Al}_2\text{O}_3$ . In the accumulated slag samples, it is found that the slag towards the furnace wall in the higher parts generally has a higher  $\text{SiO}_2$  content compared to the slag accumulated at the furnace bottom. The possible explanation suggested in this study for both the existence of slag in this area, and the increased  $\text{SiO}_2$  content in the slag, is a high crater pressure that pushes the slag towards the furnace walls and upwards.

Furthermore, for the slag next to the tapping channel, the slag above the tapping channel generally has a higher  $\text{SiO}_2$  content compared to the slag below it. This is believed to be due to variations in the densities, where slags with higher  $\text{SiO}_2$  content have lower densities. No significant differences were found in the composition of the slag between different tap-holes within the same furnace. Visually, the zones around the tapping channel appear similar. Next to the Si flow is a bright green layer measuring 5-15 cm in thickness. This

layer mainly consists of  $\text{SiO}_2\text{-CaO-Al}_2\text{O}_3$  slag and smaller silicon carbide (SiC) particles. Following the green layer is a dark grey layer that is mainly  $\text{SiO}_2\text{-CaO-Al}_2\text{O}_3$  slag and larger SiC particles. The green and grey color seem to be dependent on the size of the SiC particles, and not the composition of the slag.

The tapped slags were found to be liquid during tapping at a temperature of  $1800\text{ }^\circ\text{C}$ , except for the solid SiC particles present in the slag. The main difference between the normal tapped slag and the slag reported as high-viscosity slag is the increased amount of  $\text{SiO}_2$  in the slag, and the presence of  $\text{SiO}_2$  and condensates in the samples. These  $\text{SiO}_2$  areas are former quartz which has melted, but not fully dissolved in the slag. The amount of slag, the amount of solid SiC in the liquid slag and the viscosity of the slag are three of the main factors that influence the flow of slag through the tap-hole.

Impurities in quartz will affect both the  $\text{SiO}_2$  properties during heating to elevated temperatures and it affects the composition of the slag in the furnaces. The impurities and the properties in the quartz of six different quartz types suited for Si and FeSi production were studied. It is found that an increased amount of impurities lowers the softening temperature and the melting time. It is also found that  $\text{SiO}_2$  dissolves in the impurities as the temperature increases. Some of the  $\text{SiO}_2$  dissolves in the impurities accumulated in the grain boundaries and cracks, resulting in a separate slag phase with an increased amount of  $\text{SiO}_2$  next to the melted  $\text{SiO}_2$ .

The crack formation in quartz during heating were found to mainly happen at two temperature intervals,  $\sim 300\text{-}600\text{ }^\circ\text{C}$  and  $\sim 1300\text{-}1600\text{ }^\circ\text{C}$ . Cracks formed from  $300\text{ }^\circ\text{C}$  are from an uneven  $\text{SiO}_2$  surface, from activities in form of volume change or color change in the impurity areas, or from fluid inclusion cavities, while cracks occurring from  $1300\text{ }^\circ\text{C}$  is believed to be due to the volume increase and the phase transformations from quartz to cristobalite. The degree of cracking is also found to be different between the different quartz types. No correlation could be found between amounts of cracks and fines formation, nor between the crack formation and the impurity composition.

CaO in form of lime ( $\text{CaCO}_3$ ) is commonly added as a flux in Si and FeSi production to lower the viscosity of the slag, which is beneficial to ensure a good flow of materials through the furnace. The dissolution of CaO in three different compositions of  $\text{SiO}_2\text{-CaO-Al}_2\text{O}_3$  slag, similar to those found in the Si and FeSi furnaces, were investigated at temperatures between  $1500\text{-}1600\text{ }^\circ\text{C}$ . It is found that CaO dissolution into the slag is fast. The initial effect of increasing the CaO content in the slag from 15-21% to 25-30% gives a significant reduction in the viscosity.

During the dissolution process, a boundary layer containing 35-42% CaO formed between the CaO particle and the slag, which corresponded to the phases  $\text{CaO}\cdot\text{Al}_2\text{O}_3\cdot 2\text{SiO}_2$  or  $2\text{CaO}\cdot\text{Al}_2\text{O}_3\cdot\text{SiO}_2$  in this study.

Two models were investigated to determine the dissolution rate of the three slags. In the first model, the CaO particle is assumed to be a smooth shrinking sphere, and the rate controlled by the chemical reaction rate. The second model assumes that the rate is controlled by mass transport and depends on the diffusion rate of CaO through a boundary layer on the surface of the CaO. Both models gave similar results, and a proportional relationship between the rate constants and the viscosities was obtained. The diffusion coefficients were found to be within the range of  $10^{-6}\text{ cm}^2/\text{s}$ .



## Acknowledgement

During this PhD project, I have been fortunate to meet and receive assistance from many excellent individuals whom I would like to acknowledge. First and foremost, I would like to thank my supervisor Professor Merete Tangstad (NTNU) for giving me the opportunity of being one of the first persons to explore the slag in Silicon and Ferrosilicon production in-depth. I am thankful for your guidance and feedback on the work, and for engaging discussions related to slag, quartz, metallurgy, and life itself. Your dedication to your students, and your ability to create an inclusive work environment through gatherings with the SiManTiAl-group are really appreciated. I would also like to thank my co-supervisors Dr. Eli Ringdalen (SINFTEF), who always has a positive mindset for work and social lunches, and Professor Kristian Etienne Einarsrud (NTNU) who is the go-to person for digital problems and understanding when it comes to lack of sleep due to kids.

It has been a pleasure to be a part of the Controlled Tapping project, which included many nice and knowledgeable people. Thanks to Halvard Tveit, Birger Andresen and Lars Klemet Jacobsen for sharing their knowledge and experience from the silicon process. I am also very grateful for both Elkem Thamshavn and Wacker Holla AS, who welcomed me to work there for two months each before the start of this PhD work. That gave me the opportunity to see and to learn about how the process works from an industrial point of view, which have been valuable for the further work. Also, thanks to Haijuan Wang and Han Yu for performing quartz heating experiments at the University of Beijing.

During my time at NTNU there are many people who I had the pleasure of working with who deserve to be acknowledged. Morten Peder Raanes at the EPMA, Sarina Bao and Ingrid Hansen at the wetting lab, Arman Hoseinpur-Kermani, Ivar Andre Ødegård and Berit Vinje Kramer for technical support, and Dmitry Slizovskiy for both technical support and bad jokes. I would also like to mention my former office mates, Karin Fjeldstad Jusnes and Andrea Broggi, and Trygve Storm Aarnes. Our conversations were always interesting, striking a balance between scientific discussions and moments of procrastination. You were all worth sharing my candy with. Throughout the years, I have also had the pleasure of meeting people who have become my friends; Cathrine, Karin, Trine, Kamilla and Benedicte.

I would also like to express my gratitude to my family. My parents and neighbors, Gunnhild and Knut, have always been there for me, supporting me in every way and encouraging me to pursue my dreams.

Finally, I would like to thank my husband Thomas, for his endless patient and support, and for always believing in me. You are the rock in my life. I am so grateful for our sons, Markus (2018) and Paul (2021), who added a bit more duration and complexity to my PhD journey, but I have never once regretted. I love you.



# Contents

Preface.....	I
Abstract.....	III
Acknowledgement.....	V
List of figures.....	XI
List of tables.....	XXIX
Chapter 1: Introduction.....	1
1.1 Silicon and Ferrosilicon Production.....	1
1.2 Goal and thesis outline.....	3
Chapter 2: Slag from industrial furnaces.....	5
2.1 Literature review.....	5
2.1.1 The inner structures of furnaces from excavations.....	5
2.1.2 Stability of oxides in Si and FeSi production.....	12
2.1.3 The SiO <sub>2</sub> -CaO-Al <sub>2</sub> O <sub>3</sub> ternary system.....	13
2.2 Experimental procedure.....	25
2.2.1 Industrial samples.....	25
2.2.2 Collecting slag from industrial furnaces.....	33
2.2.3 Characterization.....	37
2.3 Results.....	39
2.3.1 Accumulated slag.....	39
2.3.2 Tapped slag.....	61
2.3.3 Slag and condensate from the charge surface in FeSi75 furnaces.....	66
Chapter 3: Changes in quartz during heating.....	71
3.1 Literature review.....	71
3.1.1 Quartz in Si and FeSi production.....	71
3.1.2 Impurities in quartz.....	72
3.1.3 Changes in quartz during heating.....	75
3.2 Experimental procedure.....	83
3.2.1 The quartz types.....	83
3.2.2 Quartz heating experiments.....	84
3.2.3 Characterization.....	87
3.3 Results.....	89
3.3.1 Softening and melting of SiO <sub>2</sub> .....	89
3.3.2 Volume expansion during heating.....	92

3.3.3	Impurities behaviour during heating .....	93
3.3.4	Disintegration of quartz during heating .....	105
Chapter 4:	CaO dissolution in SiO <sub>2</sub> -CaO-Al <sub>2</sub> O <sub>3</sub> slag .....	111
4.1	Literature review .....	111
4.1.1	CaO properties .....	111
4.1.2	Theoretical mechanisms of CaO dissolution .....	112
4.1.3	Research on CaO dissolution in slag .....	117
4.2	Experimental procedure .....	125
4.2.1	Materials .....	125
4.2.2	High temperature experiments .....	126
4.2.3	Characterization .....	129
4.3	Results .....	131
4.3.1	Mechanical strength of CaCO <sub>3</sub> and CaO .....	131
4.3.2	Dissolution experiments in graphite tube furnace .....	132
4.3.3	Dissolution experiments in a sessile drop furnace .....	138
Chapter 5:	Discussion .....	153
5.1	Slags in different parts of the furnaces .....	153
5.1.1	More SiO <sub>2</sub> in the higher parts of the furnace .....	155
5.1.2	Alkalis in the slag .....	159
5.1.3	Silicon carbide particles in the slag .....	159
5.1.4	Condensation of SiO gas and CO gas in the furnace .....	163
5.1.5	No differences in slag composition between different tap-holes .....	166
5.1.6	Tapped slag .....	169
5.1.7	Al <sub>2</sub> O <sub>3</sub> phase in slag samples .....	174
5.1.8	Oxynitride found in Furnace B .....	175
5.2	SiO <sub>2</sub> properties affecting the furnace .....	176
5.2.1	Disintegration of SiO <sub>2</sub> .....	176
5.2.2	Softening and melting of SiO <sub>2</sub> .....	182
5.2.3	The effect of impurities and initial slag formation .....	184
5.3	CaO dissolution in SiO <sub>2</sub> -CaO-Al <sub>2</sub> O <sub>3</sub> slags .....	187
5.3.1	The effect of CaO on slag viscosity in Si and FeSi furnaces .....	188
5.3.2	Modelling the dissolution rate of CaO in SiO <sub>2</sub> -CaO-Al <sub>2</sub> O <sub>3</sub> slag .....	192
5.3.3	Effect of temperature .....	200
Chapter 6:	Conclusions and future work .....	203
6.1	Slags in different parts of the furnace .....	203

6.2	Impurities and properties in SiO <sub>2</sub> affecting the Si and FeSi furnaces .....	204
6.3	CaO dissolution in SiO <sub>2</sub> -CaO-Al <sub>2</sub> O <sub>3</sub> slags .....	205
6.4	Future work .....	206
	References .....	209
	Appendix A: Analysis of the industrial samples .....	219
A.1	Excavation of Furnace B .....	219
A.1.1	The beginning of the excavation: behind tap-hole 3 .....	219
A.1.2	Samples including the zones next to the Si tapping channel .....	219
A.1.3	Collected tapped slag samples at the plant from previous tapping .....	233
A.2	Slag samples from five previous Norwegian excavations .....	235
A.3	Tapped slag .....	239
A.4	Samples from the charge surface at Finnfjord AS .....	240
A.4.1	Sample CPR1809 .....	241
A.4.2	Sample CPR0211 .....	243
A.4.3	Sample CPO1101 .....	243
A.4.4	Sample GR1602 .....	249
A.4.5	Sample CPR2502 .....	249
A.4.6	Sample CPR1903 .....	253
	Appendix B: Changes in quartz during heating .....	255
B.1	Trace element behaviour .....	255
	Appendix C: CaO dissolution into SiO <sub>2</sub> -CaO-Al <sub>2</sub> O <sub>3</sub> slag .....	257
C.1	X-ray diffraction .....	257
C.1.1	Heating rate 50 °C/min to 1200 °C and 25°C/min to 1600 °C .....	257
C.1.2	Heating rate 25°C/min to 1200 °C and 15°C/min to 1600 °C .....	262
C.1.3	Heating rate 25°C/min to 1200 °C and 15°C/min to 1600 °C .....	264
C.2	Dissolution experiments in the sessile drop furnace .....	264
C.2.1	Slag 1: 56% SiO <sub>2</sub> – 15% CaO – 29% Al <sub>2</sub> O <sub>3</sub> .....	264
C.2.2	Slag 2: 38% SiO <sub>2</sub> – 20% CaO – 42% Al <sub>2</sub> O <sub>3</sub> .....	267
C.2.3	Slag 3: 56% SiO <sub>2</sub> – 21% CaO – 23% Al <sub>2</sub> O <sub>3</sub> .....	268



## List of figures

- Figure 1 A typical silicon production plant, reprinted from Kero et al. [2]. Raw materials are added at the top of the submerged arc furnace and liquid metal is tapped at the bottom. SiO gas that condense to microsilica (SiO<sub>2</sub>) is a byproduct that is collected and sold as a product. The off-gas leaves the furnace at the top and is captured in an energy recovery unit and dust filters. .... 1
- Figure 2 Simple sketch of the Si furnace and the associated reactions. The red colored reactions are exothermic and happens higher up in the furnace, while the blue colored reactions are endothermic and occurs in the high temperature zone in the furnace. .... 3
- Figure 3 The first figure shows an illustration of the inner structure of a submerged arc furnace, based on several pilot scale experiments [5]. The illustration is based on experiments from the furnace shown in the right illustration, a 40 kW one-phase furnace with 7.5 cm diameter graphite electrode. .... 6
- Figure 4 Overview of zones after excavation of two FeSi furnaces, a) 75 FeSi in Finn fjord, b) 50 FeSi in Elkem Bjølvfossen [8]. .... 7
- Figure 5 Schematic drawings of the zones found in three Si furnaces after excavations; a) Wacker furnace no.1, b) Elkem Thamshavn, c) Wacker furnace no.4 [8]. .... 8
- Figure 6 Overview of zones after excavation at a) Finn fjord [9] and b) Elkem Salten [10] in 2018. .... 9
- Figure 7 The analyzed slag compositions from from Elkem Thamshavn excavation [6], from Elkem Salten excavation [10], from Wacker furnace no.4 [21] and the large red circle is the typical range of normal Siltech slag composition analyzed by Nell et al [19]. .... 10
- Figure 8 The Ellingham diagram for oxides relevant for the silicon smelting [5]. .... 13
- Figure 9 The ternary phase diagram of SiO<sub>2</sub>-CaO-Al<sub>2</sub>O<sub>3</sub> slag system [25]. The red lines mark the liquidus area at 1700 °C. .... 14
- Figure 10 Temperature profile and silicon flow in silicon furnace in a vertical cross section [26]. The model is based on Comsol simulations. .... 15
- Figure 11 Schematic drawing showing the silicate (SiO<sub>4</sub><sup>4-</sup>) network system with blue bridging oxygen and one orange non-bridging oxygen. Cations Ca<sup>2+</sup> and Al<sup>3+</sup> breaks into the network. .... 16
- Figure 12 Isoactivity lines of SiO<sub>2</sub> in stable liquid at 1600 °C from Mao et al. [30]. Their results are compared with the results from Kay and Taylor (1960) and Rein and Chipman (1963). The numbers in the diagram give the activity values. .... 17

Figure 13 To the left in the figure is the isoviscosity curves for the  $\text{SiO}_2\text{-CaO-Al}_2\text{O}_3$  system at 1600 °C [31], and to the right is the viscosity lines for liquid  $\text{Al}_2\text{O}_3\text{-CaO-SiO}_2$  slags at 1500 °C [5]..... 18

Figure 14 Isodensity lines for the  $\text{SiO}_2\text{-CaO-Al}_2\text{O}_3$  system at 1550 °C [25]. ..... 20

Figure 15 Densities in  $\text{g/cm}^3$  for different  $\text{SiO}_2\text{-CaO-Al}_2\text{O}_3$  slag compositions at different temperatures [25]. In the blue circle is two similar compositions measured at 1480 °C and 1727°C and the density decreases by 0.1  $\text{g/cm}^3$ . ..... 20

Figure 16 Isotension curves for  $\text{SiO}_2\text{-CaO-Al}_2\text{O}_3$  melts at 1600 °C [25]...... 22

Figure 17 Interfacial tension between Fe-Si alloys and slags at 1450 °C from Dumay and Cramb [43]. ..... 23

Figure 18 Schematic drawings of the zones found in four excavations; a) Wacker furnace no.1, b) Elkem Thamshavn, c) Wacker furnace no.4 [8] and d) Elkem Salten [10]..... 26

Figure 19 Overview of the samples analyzed. Different colors indicate different furnace. Blue from Furnace B, green from Elkem Salten, orange from Finn fjord, bright grey from Wacker Chemicals furnace no. 1, dark grey from Wacker Chemicals furnace no. 4 and brown from Elkem Thamshavn. Dimensions and the positions of the electrodes are not included in the figure as this varies between the different furnaces. The samples position is based on distance from the tap-hole..... 28

Figure 20 A selection of the analyzed excavation samples. Slag is most often green or grey in the furnace. Picture of T-2 is from Ksiazek [20]. ..... 28

Figure 21 Two of the tapped samples from Finn fjord AS. TPR030122 is tapped during normal conditions, while TPO030322 is reported as high viscosity slag. .... 29

Figure 22 Sample CPR1809a, b, c and CPO1101, S and BK. The charge surface samples were heterogenous, and several samples were analyzed based on visual differences. .... 33

Figure 23 Furnace outside tap-hole 3 before excavation start (left) and after 12 hours of excavation (right). ..... 34

Figure 24 Sample including the Si tapping channel and the zones right next to it..... 34

Figure 25 Equipment used for sampling of tapped slag. The compressed paperboard is designed to be used as a “spoon” to dig out slag from the tap-hole. .... 36

Figure 26 Solidified slag behind the FeSi metal flow in the tapping channel [44]. ..... 36

Figure 27 Photos of Furnace B taken right before excavation start and after the first 12 hours of excavating. The position of tap-hole 3 is marked in both images. .... 39

Figure 28 The top three pictures are taken at the plant and parallels of B-3 after mounted in epoxy. Below are sample B-3.1 and B-3.2 shown with three different magnifications, 40X,



200X and 400X. B-3.1 contains mostly SiC, Al<sub>2</sub>O<sub>3</sub> and a slag phase, in addition to some Si. B-3.2 contains mostly Si/FeSi, SiC and Al<sub>2</sub>O<sub>3</sub>.....42

Figure 29 The top three pictures are taken at the plant and parallels of B-4 after mounted in epoxy. Below are sample B-4.1 and B-4.2 shown with three different magnifications, 40X, 200X and 400X. Both B-4.1 and B-4.2 contain Si/FeSi, SiO<sub>2</sub>-CaO-Al<sub>2</sub>O<sub>3</sub> slag and larger and smaller particles of SiC. ....43

Figure 30 The top three pictures are taken at the plant and parallels of B-7 after mounted in epoxy. Below are sample B-7.1 and B-7.2 shown with three different magnifications, 40X, 200X and 400X. Both B-7.1 and B-7.2 consist of smaller and larger particles of SiC, and SiO<sub>2</sub>-CaO-Al<sub>2</sub>O<sub>3</sub> slag. The slag in B-7.1 has solidified into two separate phases, 80% darker and 20% brighter slag. The white areas in B-7.2 is titanium.....44

Figure 31 The top three pictures are taken at the plant and parallels of B-7 after mounted in epoxy. Below are sample B-7.1 and B-7.2 shown with three different magnifications, 40X, 200X and 400X. Both B-8.1 and B-8.2 contain smaller and larger particles of SiC, SiO<sub>2</sub>-CaO-Al<sub>2</sub>O<sub>3</sub> slag phase and Al<sub>2</sub>O<sub>3</sub>. ....45

Figure 32 The top three pictures are taken at the plant and parallels of B-9 after mounted in epoxy. Below are sample B-9.1 and B-9.2 shown with three different magnifications, 40X, 200X and 400X. Both B-9.1 and B-9.2 contain particles of SiC, SiO<sub>2</sub>-CaO-Al<sub>2</sub>O<sub>3</sub> slag phase, Al<sub>2</sub>O<sub>3</sub> and Si/FeSi. The slag in B-9.1 has solidified into two separate phases, 90% darker and 10% brighter slag. There is also found Al, N, Si and O, shown in the bottom left image. This was not found in any other zones in this furnace. ....46

Figure 33 The top three pictures are taken at the plant and parallels of B-14 after mounted in epoxy. Below are sample B-14.1 and B-14.2 shown with three different magnifications, 40X, 200X and 400X. In B-14.1, there are a lot of small SiC particles in a SiO<sub>2</sub>-CaO-Al<sub>2</sub>O<sub>3</sub> slag phase or a SiO<sub>2</sub> matrix. B-14.2 contains two areas, one with smaller SiC particles and a SiO<sub>2</sub>-CaO-Al<sub>2</sub>O<sub>3</sub> slag phase, and one with larger SiC particles an SiO<sub>2</sub>-CaO-Al<sub>2</sub>O<sub>3</sub> slag. ....47

Figure 34 The top three pictures are taken at the plant and parallels of B-27 after mounted in epoxy. Below are sample B-27.1 and B-27.2 shown with three different magnifications, 40X, 200X and 400X. Both B-27.1 and B-27.2 have two different areas: one with smaller particles of SiC and one with larger SiC particles, both with SiO<sub>2</sub>-CaO-Al<sub>2</sub>O<sub>3</sub> slag and Al<sub>2</sub>O<sub>3</sub>. ....48

Figure 35 Picture during the excavation of Furnace B showing the area around tap-hole 1, and the cut out plate of sample B-48a, visualizing the Si tapping channel and the zones next to it. Marked in orange on the sample are the analyzed areas which corresponds to the number on the EPMA images and the WDS analysis in the next figures and tables. ....51

Figure 36 In the top left image is sample B-48a 1.1 which appears to be condensate. The analyzed grey area is mainly SiO<sub>2</sub> and the white areas are Si. Sample B-48 1.2 consists of a SiO<sub>2</sub> rich slag phase and SiC particles, in addition to some Si and FeSi. Both 2.1 and 2.2 contain mostly SiC and SiO<sub>2</sub>-CaO-Al<sub>2</sub>O<sub>3</sub> slag, and some Si. ....51

Figure 37 B-48a 3.1 and 3.2 consist of larger SiC particles, SiO<sub>2</sub>-CaO-Al<sub>2</sub>O<sub>3</sub> slag and Al<sub>2</sub>O<sub>3</sub>. Some smaller droplets of Si are also present. All parallels from B-48a 4 and 5 are similar as sample B-48 3. The appearance is different due to a different use of contrast on the images. .... 52

Figure 38 The collected earlier tapped slag samples. B-tap 1.1 and 1.2 contain SiO<sub>2</sub>, SiC, SiO<sub>2</sub>-CaO-Al<sub>2</sub>O<sub>3</sub> slag and some Si. B-tap 2.1 and 2.2 contain mostly SiO<sub>2</sub>, and some SiO<sub>2</sub> rich SiO<sub>2</sub>-CaO-Al<sub>2</sub>O<sub>3</sub> slag in sample 2.2. B-tap 3.1 and 3.2 contain SiO<sub>2</sub>-CaO-Al<sub>2</sub>O<sub>3</sub> slag solidified into two phases, some SiC. Sample 3.2 also have some Al<sub>2</sub>O<sub>3</sub>. .... 55

Figure 39 EPMA images with magnification 400X of slag from the higher parts in Si and FeSi furnaces. All samples contain SiC particles and SiO<sub>2</sub>-CaO-Al<sub>2</sub>O<sub>3</sub> slag. F-75 also contain Al<sub>2</sub>O<sub>3</sub>. W<sub>4</sub>-5 and S-37 contain SiO<sub>2</sub> where the grain boundaries are still intact, while the SiO<sub>2</sub> in B-9 has a different look. .... 58

Figure 40 EPMA images with magnification 400X of slag from lower parts in Si and FeSi furnaces. All samples contain SiC particles and SiO<sub>2</sub>-CaO-Al<sub>2</sub>O<sub>3</sub> slag. B-3 also contain some Al<sub>2</sub>O<sub>3</sub>. S-43 and W<sub>4</sub>-20 consist mainly of SiC and only small areas with slag were found here. W<sub>4</sub>-12 also have some SiO<sub>2</sub>. .... 59

Figure 41 EPMA images with magnification 400X of slag from the zones next to tapping channel in Si furnaces. S-43 contain mostly SiC in addition to some SiO<sub>2</sub> and slag. W<sub>1</sub>-114 is mostly SiO<sub>2</sub> with slag in between grain boundaries and cracks, and some SiC particles. W<sub>1</sub>-115 is slag and SiC. .... 59

Figure 42 Picture of the tapping channel from Wacker Chemicals Holla, furnace no.1 [45]. Marked in the picture is also the position of sample W<sub>1</sub>-115. .... 60

Figure 43 EPMA images of normal tapped samples. To the left is from is from Elkem Thamshavn 19-10.26 with magnification 40X, in the middle is Furnace B 20-06.18 with magnification 100X, and to the right. Is from Finnjord AS 20-10.22 with magnification 40X. All samples are mainly slag together with some SiC and Si. Small cracks are in the slag phase from Elkem Bremanger, while small SiC particles are in the slag phase from Elkem Thamshavn. .... 62

Figure 44 The five samples with high viscosity slag from Finnjord AS, Two areas from TPO231120, TPO0102\_T5, TPO230221, two areas from TPO030322 and TPX2022. The high-viscosity slag consists of SiO<sub>2</sub>-rich slag, in addition to some SiC and FeSi. In addition, several samples have SiO<sub>2</sub>, and some have condensate of SiO<sub>2</sub> and Si. Many of the samples are also porous. .... 63

Figure 45 Pictures of charge top samples: CPO1101\_BK.1, CPO1101\_BK.2, CPR1903, CPR1809b and CPO1101\_P.2, that consist of brown, and brown and white condensates. .... 66

Figure 46 EPMA images of CPO1101\_BK.1, CPO1101\_BK.2, CPR1903, CPR1809b and CPO1101\_P.2. The brown condensate consists of SiO<sub>2</sub> matrix with Si spheres. In sample

CPO1101_BK.2 and CPO1101_P.2 are both brown and white condensate, and in the white areas it is also found SiC.....	67
Figure 47 Pictures of charge top samples, slag: CPR1809a, CPO1101_S.1, CPR2502b, CPO1101_P.1, CPO1101_M.1, CPO1101_K.2 and CPO0211.3. Many of the samples were named after visual observation. S: slag, P: porous, M: metallic and K: quartz. ....	68
Figure 48 EPMA images of initial slag formation from SiO <sub>2</sub> : CPR1809a, CPO1101_S.1, CPR2502b, CPO1101_P.1, CPO1101_M.1, CPO1101_K.2 and CPO0211.3. It is found the slag in grain boundaries and cracks in the SiO <sub>2</sub> .....	69
Figure 49 The distribution of trace elements as a function of the boiling temperature of different elements [23]. Slag is also tapped from the furnace and is here included in the metal.....	74
Figure 50 The distribution of trace elements as a function of the boiling temperature of different elements [24]. Slag is also tapped from the furnace and is here included in the metal.....	74
Figure 51 The phase diagram of silica [52]. ....	76
Figure 52 Modelled temperature distribution for selected industrial FeSi and Si furnaces with calculated depth for softening and melting of different quartz sources [69]. ....	78
Figure 53 Fines below 10 mm given in wt% after shock heating at 1500 °C for ten different quartz types [9]. ....	81
Figure 54 Cumulative percentage of different size fractions after 10 minutes shock heating at 1500 °C for 11 quartz types [77]. Fines are defined as particles >10 mm.....	82
Figure 55 Quartz type A, B, C, D, F and G used in this study. ....	83
Figure 56 Schematic overview of the sessile drop furnace. This is a revised figure from Bao et al. [83]. ....	85
Figure 57 Temperature profile for the sessile drop experiments. The argon flow rate was the same 0.1 l/min for all experiments. For the melting experiments, the temperature was held until the SiO <sub>2</sub> samples were completely melted.....	86
Figure 58 The components of the high temperature confocal microscope [84]. ....	87
Figure 59 Picture of the prepared quartz sample before and after a High Temperature Confocal Microscope experiment. ....	87
Figure 60 Images of each quartz type A, B, C, D, F and G at 900 °C, softening temperature, and complete melting.....	90
Figure 61 Overview softening and melting temperatures for quartz A, B, C, D, F and G.....	91

Figure 62 The amount of impurities given in % as a function of the softening temperature (left) and melting time at 1750 °C (right) for quartz A, B, C, D, F and G. .... 91

Figure 63 The amount of Al<sub>2</sub>O<sub>3</sub> given in % as a function of the softening temperature (left) and melting time at 1750 °C (right) for quartz A, B, C, D, F and G. .... 91

Figure 64 The amount of K<sub>2</sub>O given in % as a function of the softening temperature (left) and melting time at 1750 °C (right) in quartz type A, B, C, D, F and G. .... 92

Figure 65 Volume expansion as a function of temperature up to 1750 °C for quartz A, B, C, D, F and G. .... 92

Figure 66 Backscattered images of quartz C; initial, and heated to 1600 °C and 1800 °C, with focus on the impurity areas. .... 95

Figure 67 Backscattered images of quartz D: initial and heated to 1600 °C and 1800 °C, with focus on the impurity areas. .... 96

Figure 68 Backscattered images of quartz F: initial and heated to 1600 °C and 1800 °C, with focus on the impurity areas. .... 97

Figure 69 SEM images and images from high temperature confocal microscope experiments for quartz A, with focus on the impurities. The numbered boxes on the SEM images are related to the area analyzed with EDS in Table 27. .... 98

Figure 70 SEM images and images from high temperature confocal microscope experiments for quartz B, with focus on the impurities. The numbered boxes on the SEM images corresponds to the area analyzed with EDS in Table 27. .... 99

Figure 71 SEM images and images from high temperature confocal microscope experiments for quartz C, with focus on the impurities. The numbered boxes on the SEM images corresponds to the area analyzed with EDS in Table 27. .... 100

Figure 72 SEM images and images from high temperature confocal microscope experiments for quartz D, with focus on the impurities. The numbered boxes on the SEM images corresponds to the area analyzed with EDS in Table 27. .... 101

Figure 73 SEM images and images from high temperature confocal microscope experiments for quartz F, with focus on the impurities. The numbered boxes on the SEM images corresponds to the area analyzed with EDS in Table 27. .... 102

Figure 74 SEM images and images from high temperature confocal microscope experiments for quartz G, with focus on the impurities. The numbered boxes on the SEM images corresponds to the area analyzed with EDS in Table 27. .... 103

Figure 75 Quartz surface during high temperature confocal microscope (HTCM) experiments at temperatures 20 °C, 600 °C, 1200 °C and 1600 °C for A.1 and A.2. The magnification is 275X for both Qz41.1 and Qz41.2. .... 106

Figure 76 Quartz surface during high temperature confocal microscope (HTCM) experiments at temperatures 20 °C, 600 °C, 1200 °C and 1600 °C for B.2 and B.3. The magnification is 1100X for B.2 and 275X for B.3. ....	106
Figure 77 Quartz surface during high temperature confocal microscope (HTCM) experiments at temperatures 20 °C, 600 °C, 1200 °C and 1600 °C for C.1 and C.3. The magnification is 550X for both C.1 and C.3.....	107
Figure 78 Quartz surface during high temperature confocal microscope (HTCM) experiments at temperatures 20 °C, 600 °C, 1200 °C and 1600 °C for D.1, D.2 and D.3. The magnification is 550X for D.1, 275X for D.2 and 550X for D.3. ....	107
Figure 79 Quartz surface during high temperature confocal microscope (HTCM) experiments at temperatures 20 °C, 600 °C, 1200 °C and 1600 °C for F.1, F.2 and F.3. The magnification is 275X for F.1, 550X for F.2 and 550X for F.3.....	108
Figure 80 Quartz surface during high temperature confocal microscope (HTCM) experiments at temperatures 20 °C, 600 °C, 1200 °C and 1600 °C for G.2 and G.3. The magnification is 550X for G.2 and 275X for G.3. ....	108
Figure 81 Summary of the crack formation for all the quartz types after heating to 1600 °C. The amount of cracks is given in mm/mm <sup>2</sup> . ....	109
Figure 82 Schematic illustration of chemical reaction being the rate determining step for CaO dissolution in liquid SiO <sub>2</sub> -CaO-Al <sub>2</sub> O <sub>3</sub> slag.....	113
Figure 83 Schematic illustration of mass transfer kinetic control being the rate determining step for CaO dissolution in liquid SiO <sub>2</sub> -CaO-Al <sub>2</sub> O <sub>3</sub> slag.....	115
Figure 84 Schematic illustration of mass transfer kinetic control being the rate determining step for CaO dissolution in liquid SiO <sub>2</sub> -CaO-Al <sub>2</sub> O <sub>3</sub> slag, given concentration curves with increasing experimental holding time. ....	116
Figure 85 The estimated diffusion coefficient values of Ca diffusion in 40wt% SiO <sub>2</sub> – 40wt% CaO –20wt% Al <sub>2</sub> O <sub>3</sub> from Zhang and Chou. [113], Goto et al. [111] and Ren et al. [114] compared with the measured values from Towers et al. [107], [108], Niwa [109] and Saitô and Maruya [110]. The figure is revised from [114]. ....	123
Figure 86 Picture of the original limestone to the left, and after calcination 1h at 1000 °C to the right. ....	126
Figure 87 A picture of the graphite tube furnace, TF2 (left) and the crucible setup (right). The top right picture is the initial crucible with CaO and SiO <sub>2</sub> -CaO-Al <sub>2</sub> O <sub>3</sub> slag and the bottom right shows the same crucible after heating to 1600 °C. ....	127
Figure 88 Heating profiles for the dissolution experiments in the vertical tube furnace. ....	128
Figure 89 Slag and CaO before sessile drop experiment and slag after dissolution experiment.....	129

Figure 90 EPMA images of horizontal section in the bottom of pure slag and samples heated with heating rate 50 °C/min to 1200 °C and 25°C/min to 1600 °C with 0 minutes (50.0.1) and 60 minutes (50.60.2) holding time. .... 132

Figure 91 Horizontal section of the sample after experiment showing the analysed areas with WDS given in x- and y-direction. .... 132

Figure 92 Results of WDS analysis horizontal section x-direction close to the crucible bottom for the samples with heating rate 50 °C/min to 1200 °C and 25°C/min to 1600 °C. The CaO/slag ratio were 0.1. .... 133

Figure 93 Results of WDS analysis horizontal section y-direction for the samples with heating rate 50 °C/min to 1200 °C and 25°C/min to 1600 °C. .... 133

Figure 94 EPMA image to the left and Ca spatial distribution in the right image for samples with heating rate 50 °C/min to 1200 °C and 25°C/min to 1600 °C with holding times 0-, 10-, 20-, 30-, 40- and 60 minutes. The CaO rich slag phase is found in the bottom of the sample. .... 134

Figure 95 Results of WDS analysis vertical section for the samples with heating rate 50 °C/min to 1200 °C and 25°C/min to 1600 °C. .... 135

Figure 96 Results of WDS analysis vertical section for the samples with heating rate 25°C/min to 1200 °C and 15°C/min to 1600 °C, and heating rate 15°C/min to 1200 °C and 10 °C/min to 1600 °C. .... 136

Figure 97 EPMA image to the left and Ca spatial distribution in the right image for samples with heating rate 25°C/min to 1200 °C and 15°C/min to 1600 °C with holding times 0-, 40- and 60 minutes, and one sample with heating rate 15°C/min to 1200 °C and 10 °C/min to 1600 °C with holding time 40 minutes. The CaO rich slag phase is found in the bottom of the sample. .... 136

Figure 98 CT images of the second parallel heated to 1600 °C with heating rate 50 °C/min up to 1200 °C and 25°C/min up to 1600 °C with 0 minutes holding time. To the left is an image from the top of the sample, and the right image is a vertical cross section in the center of the sample. More CaO in the slag can be observed as the brighter grey color. The darkest grey color is the graphite crucible. .... 137

Figure 99 CT images of sample 50.20, which is heated to 1600 °C with heating rate 50 °C/min up to 1200 °C and 25°C/min up to 1600 °C with 20 minutes holding time. To the left is an image from the top of the sample, and the right image is a vertical cross section in the center of the sample. More CaO in the slag can be observed as the brighter grey color. The darkest grey color is the graphite crucible. .... 137

Figure 100 CT images of sample 50.40, which is heated to 1600 °C with heating rate 50 °C/min up to 1200 °C and 25°C/min up to 1600 °C with 40 minutes holding time. To the left is an image from the top of the sample, and the right image is a vertical cross section

in the center of the sample. More CaO in the slag can be observed as the brighter grey color. The darkest grey color is the graphite crucible. .... 138

Figure 101 Sessile drop experiments with CaO and 56% SiO<sub>2</sub> - 15% CaO - 29% Al<sub>2</sub>O<sub>3</sub> slag heated to 1000 °C, 1400 °C and 1500 °C. .... 138

Figure 102 Images captured during and after experiments of CaO and 56% SiO<sub>2</sub>- 15% CaO-29% Al<sub>2</sub>O<sub>3</sub> slag heated to 1500 °C with 0 minutes holding time. The CaO/slag ratio is 0.40, 0.36 and 0.15 for parallel 1, 2 and 3, respectively. .... 140

Figure 103 Cross-section images and EPMA images of CaO and 56% SiO<sub>2</sub>- 15% CaO-29% Al<sub>2</sub>O<sub>3</sub> slag heated to 1500 °C and with 0 minutes holding time. The CaO/slag ratio is 0.40, 0.36 and 0.15 for parallel 1, 2 and 3, respectively. .... 140

Figure 104 WDS results for the experiments at 1500 °C with CaO and slag 1..... 141

Figure 105 Images captured during and after experiments for the 1500 °C experiments of CaO and slag 1, with 0-, 5- and 10 minutes holding time, and equal CaO/slag ratio of 0.15. .... 142

Figure 106 Cross section images and EPMA images after experiments for the 1500 °C experiments with CaO and Slag 1 with 0-, 5- and 10 minutes holding time, and with equal CaO/slag ratio of 0.15. .... 142

Figure 107 Images captured during the experiment, cross section and EPMA images after experiment for CaO and slag 1 heated to 1550 °C with 0 minutes holding time. .... 143

Figure 108 WDS results for the experiment heated to 1550 °C with CaO and slag 1..... 143

Figure 109 Images captured during and after experiments for the three parallels of CaO and slag 2 at 1500 °C with 10 minutes holding time. The CaO/slag ratio is 0.42, 0.14 and 0.25 for parallel 1, 2 and 3, respectively..... 144

Figure 110 Cross section images and EPMA images after experiments for the three parallels of CaO and slag 2 heated to 1500 °C and with 10 minutes holding time. The CaO/slag ratio is 0.42, 0.14 and 0.25 for parallel 1, 2 and 3, respectively. .... 145

Figure 111 WDS results for the experiments at 1500 °C with CaO and slag 2..... 145

Figure 112 Images during and after experiments of CaO and slag 2 with equal CaO/slag ratio of 0.25 for the 1500 °C experiments with 0-, 5- and 10 minutes holding time. .... 146

Figure 113 Cross section images and EPMA images after experiments of CaO and slag 2 for the experiments with equal CaO/slag ratio of 0.25 for the 1500 °C experiments with 0-, 5- and 10 minutes holding time. .... 146

Figure 114 Images during and after experiments with for the 1550 °C experiments of CaO and slag 2 with 0-, 10- and 20 minutes holding time. The initial slag had composition 38% SiO<sub>2</sub>- 20% CaO-42% Al<sub>2</sub>O<sub>3</sub>..... 147

Figure 115 Cross section images and EPMA images after experiments for the experiments at 1550 °C experiments of CaO and slag 2 with 0-, 10- and 20 minutes holding time. .. 147

Figure 116 WDS results of CaO and slag 2 heated 1550 °C with 0-, 10- and 20 minutes holding time. .... 148

Figure 117 Images during and after experiments for the three parallels of CaO and slag 3 heated to 1500 °C and with 10 minutes holding time. The CaO/slag ratio is 0.50 and 0.41 for parallel 1, and 2, respectively. .... 149

Figure 118 Cross section images and EPMA images after experiments for the three parallels of CaO and slag 3 heated to 1500 °C and with 10 minutes holding time. The CaO/slag ratio is 0.50 and 0.41 for parallel 1, and 2, respectively. .... 149

Figure 119 WDS results for the experiments at 1500 °C with CaO and slag 3. .... 150

Figure 120 Images during and after experiments for CaO and slag 3 with equal CaO/slag ratio 0.41 for the 1500 °C experiments with 0-, 5- and 10 minutes holding time. .... 150

Figure 121 Cross section images and EPMA images after experiments for the experiments of CaO and slag 3 with equal CaO/slag ratio of 0.41 for the 1500 °C experiments with 0-, 5- and 10 minutes holding time. . .... 151

Figure 122 Images during and after experiments with for the 1550 °C experiments of CaO and slag 3 with 0-, 10- and 17 minutes holding time. .... 151

Figure 123 Cross section images and EPMA images after experiments for the experiments at 1550 °C experiments of CaO and slag 3 with 0- and 10 minutes holding time. .... 152

Figure 124 WDS results for the CaO and slag 3 heated to 1550 °C with 0- and 10 minutes holding time. .... 152

Figure 125 Schematic figures illustrating the interior of a Si furnace. Case a) have almost no slag along the furnace walls. Case b) shows an average situation with slag/inactive zone that may affect the furnace operation. Case c) shows an accumulated furnace. Case d) has no slag and SiC in the furnace bottom. The SiC crust is found to vary between different furnaces, ranging from almost zero to the size illustrated in this figure. .... 154

Figure 126 Illustration of a Si furnace including the main zones and approximate temperatures at different positions. The temperatures are based on modelled temperatures from Myrhaug [1]. .... 155

Figure 127 Analyzed accumulated slag samples from six different Norwegian Si and FeSi furnace excavations divided into higher and lower parts of the furnace. .... 156

Figure 128 How the given slag composition will be in the furnace; liquid, liquid+solid, or solid, based on temperatures found from [1]. .... 157



Figure 129 Analyzed slag samples next to the Si tapping channel divided into above or below the channel. All samples are from the Furnace B excavation and are from two different tap-holes. .... 158

Figure 130 Analyzed accumulated slag from Norwegian silicon and ferrosilicon furnace excavations. Samples marked in red are those samples which contain  $Al_2O_3$ ..... 175

Figure 131 EPMA images of B-8.1 and B-27.2 which are collected from a lower and a higher point in the furnace in the Furnace B excavation. .... 160

Figure 132 EPMA image of a tapped slag sample to the left and an accumulated slag sample to the right collected during excavation. Both samples are from furnace B..... 161

Figure 133 The activity of  $SiO_2$  in 50%  $SiO_2$  – 25%  $CaO$  – 25%  $Al_2O_3$  and 70%  $SiO_2$  – 10%  $CaO$  – 20%  $Al_2O_3$  in the temperature interval 1600-2000 °C. The activities are calculated with FactSage 8.1..... 162

Figure 134 The equilibrium constants for reaction 5 and 16 over the temperature interval 1700-1860 °C..... 163

Figure 135 The change in standard Gibbs free energy for reaction 5 and 16 over the temperature interval 1600-2000 °C..... 163

Figure 136 Illustration of where the condensates are likely to be found in the Si and FeSi furnaces. .... 164

Figure 137 Sample CPO1101\_P.2 which is from the charge top at Finn fjord AS. The picture from the left is the mounted sample showing the brown and white condensates, which is shown as areas with  $SiO_2$  and  $SiC$ , and  $SiO_2$  and Si in the right EPMA image. .... 165

Figure 138 Green and white condensate from the zones next to the Si tapping channel from the Furnace B excavation. .... 166

Figure 139 Brown and white condensate from high-viscosity slag from Finn fjord AS. . 166

Figure 140 Images from Furnace B excavation and Wacker Chemicals [21] showing that the Si metal goes through a slag and  $SiC$  layer when exiting the tap-hole. .... 167

Figure 141 Slag from the samples including the zones next to the Si tapping channel for tap-hole 1, 3 and 7 from the Furnace B excavation. The green or the grey color gives if they are from the green or the grey colored layer in the sample..... 168

Figure 142 Slag from the samples including the zones next to the Si tapping channel for tap-hole 1, 3 and 7 from the Furnace B excavation. The tap-holes are separated with different shapes and different shadings of blue. .... 168

Figure 143 The  $SiO_2$  content in the tapped slag samples from Furnace R at Finn fjord AS as a function of the tap-hole they came from. The vertical lines are the standard deviations. .... 169

Figure 144 The composition of all tapped slag samples collected during operation. ....	170
Figure 145 Viscosity versus %SiO <sub>2</sub> at temperature 1600 °C and 1800 °C. The CaO/Al <sub>2</sub> O <sub>3</sub> ratio is kept constant at 2 and 0.25. The viscosities are calculated using FactSage 8.1. .	172
Figure 146 Temperature measured in the ladle compared with the SiO <sub>2</sub> content in the slag collected from the tap-hole. ....	173
Figure 147 The amount of SiO <sub>2</sub> in the slag as a function of furnace load for the tapped slag at Finnfjord AS. ....	174
Figure 148 Stable phases as a function of temperature and N <sub>2</sub> and O <sub>2</sub> relation [35]. ....	176
Figure 149 Illustration of gas permeability in a charge with a low amount of fines (left) and a high amount of fines (right). ....	177
Figure 150 Images from high temperature confocal microscope (HTCM) experiment for B.2 at 20 °C and 300 °C, showing crack formation from impurity areas. ....	179
Figure 151 Images from high temperature confocal microscope (HTCM) experiment for F.2 at 20 °C and 600 °C, showing crack formation from uneven SiO <sub>2</sub> surface. No impurity areas were found in this sample. ....	179
Figure 152 Images from high temperature confocal microscope (HTCM) experiment for A.2 at 300 °C and 600 °C, showing crack formation from cavities from escaped fluid inclusions. ....	180
Figure 153 Images from high temperature confocal microscope (HTCM) experiment for D.2 at 1200 °C and 1600 °C, showing crack formation from expanding grain boundaries. ....	180
Figure 154 Crack formation at 1600 °C and the maximum volume expansion during heating to 1750 °C for quartz A, B, C, D, F and G. ....	181
Figure 155 Crack formation at 1600 °C and fines production from shock heating to 1500 °C [18] for quartz type A, D, F and G. The result from quartz B is from Ringdalen [39]. Fines are defined as particles <10 μm. Crack formation is given in mm/mm <sup>2</sup> , while fines production is given in wt%. ....	182
Figure 156 Softening temperature compared with %FeO with results from Ringdalen and Tangstad [43] and this study. ....	184
Figure 157 Amount of SiO <sub>2</sub> in the impurity areas in the SiO <sub>2</sub> as a function of temperature. The SiO <sub>2</sub> content in the impurities increases with increasing temperature. ....	184
Figure 158 The binary phase diagram of FeO and SiO <sub>2</sub> [50]. ....	185

Figure 159 Initial slag formation in sample CPR1809a.2. Slag accumulates in the grain boundaries and cracks in the SiO<sub>2</sub>, shown as the white phase. An area with slag is also found together with the melted SiO<sub>2</sub>, shown as brighter grey color. .... 186

Figure 160 The observed dissolution of a CaO particle into 56% SiO<sub>2</sub> – 15% CaO – 29% Al<sub>2</sub>O<sub>3</sub> at 1600 °C for different holding times..... 188

Figure 161 Viscosity with increasing %CaO for Slag 1, 2 and 3 at temperature 1600 °C and 1800 °C. The viscosities are calculated using FactSage 8.1. .... 189

Figure 162 The SiO<sub>2</sub>-CaO-Al<sub>2</sub>O<sub>3</sub> ternary phase diagram with 1500 °C liquidus area marked in bright blue. Slag 1, 2 and 3, their dissolution path and the two saturation concentration at the 1500 °C and the CaO phase boundary line are marked with blue, red and green. . 190

Figure 163 The liquidus and solidus temperature with increasing %CaO for Slag 1, 2 and 3. The temperatures are found from the SiO<sub>2</sub>-CaO-Al<sub>2</sub>O<sub>3</sub> ternary phase diagram. .... 191

Figure 164 Cross-section images and EPMA images after experiments with CaO and 56% SiO<sub>2</sub> – 15% CaO – 29% Al<sub>2</sub>O<sub>3</sub> at 1500 °C and 1550 °C with zero minutes holding time. The red lines highlight the boundary layer between the CaO and the slag..... 191

Figure 165 Dissolution curves for slag 1 for the experiments at 1500 °C with 0-, 5- and 10 minutes holding time..... 192

Figure 166 Dissolution curves for slag 2 for the experiments at 1500 °C with 0-, 5- and 10 minutes holding time..... 193

Figure 167 Dissolution curves for slag 3 for the experiments at 1500 °C with 0-, 5- and 10 minutes holding time..... 193

Figure 168 Schematic representation of the shrinking sphere model. The chemical reaction of CaO dissolving into the slag happens at the CaO particle surface and the reaction continuous until the whole CaO particle is consumed..... 194

Figure 169 Modelled dissolution rate curve using the shrinking sphere model and the experimental results for slag 1 at 1500 °C. R gives the correlation error..... 195

Figure 170 Modelled dissolution rate curve using the shrinking sphere model and the experimental results for slag 2 at 1500 °C. R gives the correlation error..... 195

Figure 171 Modelled dissolution rate curve using the shrinking sphere model and the experimental results for slag 3 at 1500 °C. R gives the correlation error..... 196

Figure 172 Schematic representation of dissolution of CaO into SiO<sub>2</sub>-CaO-Al<sub>2</sub>O<sub>3</sub> slag by mass transport control. The process involves transport of ions through a constant thick boundary layer around the CaO particle into the slag..... 196

Figure 173 Modelled dissolution rate curve using mass transport model and the experimental results for slag 1 at 1500 °C. The R<sup>2</sup> number gives the correlation error. . 197

Figure 174 Modelled dissolution rate curve using mass transport model and the experimental results for slag 2 at 1500 °C. The R<sup>2</sup> number gives the correlation error. . 197

Figure 175 Modelled dissolution rate curve using mass transport model and the experimental results for slag 3 at 1500 °C. The R<sup>2</sup> number gives the correlation error. . 198

Figure 176 Schematic illustration of mass transfer kinetic control or chemical reaction being the rate determining step for CaO dissolution in liquid SiO<sub>2</sub>-CaO-Al<sub>2</sub>O<sub>3</sub> slag. The red curve gives the experimental results in this study, which is a mix. .... 199

Figure 177 Upscaled modelled dissolution curves using the mass transport model. 140g CaO are added to 1kg slag. .... 200

Figure 178 EPMA images of cross sections after dissolution experiments of slag 3 and CaO at both 1500 °C and 1550 °C with 0- and 10 minutes holding time. .... 201

Figure 179 Picture of sample B-48b. Marked in orange on the samples are the analyzed areas which corresponds to the number on the EPMA images and the WDS analysis in the next figures and tables. .... 220

Figure 180 EPMA images of sample B-48b 1.1 and -1.2 with three different magnifications; 40X, 200X and 400X. Both samples consist of SiO<sub>2</sub>-CaO-Al<sub>2</sub>O<sub>3</sub> slag, SiC, Al<sub>2</sub>O<sub>3</sub> and some Si. .... 222

Figure 181 EPMA images of sample B-48b 2 and -3 with three different magnifications; 40X, 200X and 400X. Both samples consist of SiO<sub>2</sub>-CaO-Al<sub>2</sub>O<sub>3</sub> slag, SiC and some Si. .... 223

Figure 182 EPMA images of sample B-48b 4 and -4 with three different magnifications; 40X, 200X and 400X. Both samples consist of SiC, SiO<sub>2</sub>-CaO-Al<sub>2</sub>O<sub>3</sub> slag and some Si. .... 224

Figure 183 Sample B-1 and B-2. Marked in orange on the samples are the analyzed areas which corresponds to the number on the EPMA images and the WDS analysis in the next figures and tables. .... 225

Figure 184 EPMA images of sample B-1.1 and -1.2, B-2.1 Area 1 and -2.2 with three different magnifications; 40X, 200X and 400X. All samples consist of SiO<sub>2</sub>-CaO-Al<sub>2</sub>O<sub>3</sub> slag, SiC and some Si. .... 226

Figure 185 EPMA images of sample B-1.3, -2.1 Area 2 and -2.3 with three different magnifications; 40X, 200X and 400X. All samples consist of SiC, SiO<sub>2</sub>-CaO-Al<sub>2</sub>O<sub>3</sub> slag and some Si or FeSi. Sample B-1.3 and -2.3 also have areas with Al<sub>2</sub>O<sub>3</sub>. .... 227

Figure 186 The left picture shows the collected sample at the plant, B-47 from tap-hole 7, and right picture shows the sample crushed into three pieces. The pieces were marked with One, two or three orange dots. .... 229

Figure 187 EPMA images of sample B-47 1.1 and 1.2, with three different magnifications; 40X, 200X and 400X. Both B-47 1.1 and 1.2 consist of  $\text{SiO}_2\text{-CaO-Al}_2\text{O}_3$  slag, SiC,  $\text{Al}_2\text{O}_3$  and some Si. .... 229

Figure 188 EPMA images of sample B-47 2.2, with three different magnifications; 40X, 200X and 400X. The sample consists of mostly  $\text{SiO}_2$ , condensate of  $\text{SiO}_2$  and Si, and condensate of  $\text{SiO}_2$  and SiC. Only a small area with  $\text{SiO}_2\text{-CaO-Al}_2\text{O}_3$  slag with SiC particles around were observed. .... 230

Figure 189 EPMA images of sample B-47 2.1 and 3 with three different magnifications; 40X, 200X and 400X. B-47 2.1 consists of  $\text{SiO}_2\text{-CaO-Al}_2\text{O}_3$  slag, SiC,  $\text{Al}_2\text{O}_3$  and some SiC. Sample B-47 3 consists of the same materials, but with larger SiC particles..... 231

Figure 190 EPMA images of sample B-47 4 and 5 with three different magnifications; 40X, 200X and 400X. Both samples consist of  $\text{SiO}_2\text{-CaO-Al}_2\text{O}_3$  slag, SiC and  $\text{Al}_2\text{O}_3$ . Sample B-47 4 also have some Si. .... 232

Figure 191 EPMA images of sample B-tap 1.1 and 1.2 with three different magnifications; 40X, 200X and 400X. B-tap 1.1 and 1.2 are mainly  $\text{SiO}_2\text{-CaO-Al}_2\text{O}_3$  slag and SiC, and some Si and areas with  $\text{SiO}_2$ . .... 233

Figure 192 EPMA images of sample B-tap 2.1, 2.2, 3.1 and 3.2 with three different magnifications; 40X, 200X and 400X. B-tap 2.1 and 2.2 are  $\text{SiO}_2$ . B-tap 2.2 has a small area with  $\text{SiO}_2$  rich slag. The small white circles are  $\text{SiO}_2$ , which indicates that this is condensate. Both B-tap 3.1 and 3.2 are mainly  $\text{SiO}_2\text{-CaO-Al}_2\text{O}_3$  slag and some SiC. Sample B-tap 3.2 also have some  $\text{Al}_2\text{O}_3$ ..... 234

Figure 193 EPMA images of samples from the higher parts of the furnace, S-37, F-75, W<sub>4</sub>-5 and W<sub>1</sub>-33 with three different magnifications; 40X, 200X and 400X. S-37 consists of  $\text{SiO}_2\text{-CaO-Al}_2\text{O}_3$  slag, SiC and  $\text{SiO}_2$ . F-75 consists of  $\text{SiO}_2\text{-CaO-Al}_2\text{O}_3$  slag, SiC, FeSi and  $\text{Al}_2\text{O}_3$ . W<sub>4</sub>-5 consists of  $\text{SiO}_2\text{-CaO-Al}_2\text{O}_3$  slag, Si and  $\text{SiO}_2$ , and W<sub>1</sub>-33 of SiC,  $\text{SiO}_2\text{-CaO-Al}_2\text{O}_3$  slag and some Si. .... 236

Figure 194 EPMA images of samples from the lower parts of the furnace, F-36, T-2, W<sub>4</sub>-12 and W<sub>4</sub>-20 with three different magnifications; 40X, 200X and 400X. F-36 and T-2 consist of  $\text{SiO}_2\text{-CaO-Al}_2\text{O}_3$  slag and SiC. F-36 also has some FeSi. W<sub>4</sub>-12 and W<sub>4</sub>-20 consist of mostly SiC and some  $\text{SiO}_2\text{-CaO-Al}_2\text{O}_3$  slag. W<sub>4</sub>-12 also has some  $\text{SiO}_2$ . ..... 237

Figure 195 EPMA images of samples from the zone next to the tapping channel, W<sub>1</sub>-114 and -115 with three different magnifications; 40X, 200X and 400X. Both samples consist of  $\text{SiO}_2\text{-CaO-Al}_2\text{O}_3$  slag, SiC and some Si. W<sub>1</sub>-114 also has some  $\text{SiO}_2$ . S-46 consists of mostly SiC and some  $\text{SiO}_2$  and slag of  $\text{SiO}_2$ , MgO, CaO, FeO and  $\text{Al}_2\text{O}_3$ ..... 238

Figure 196 Sample CPR1809a.1 and a.2 with two different magnifications; 40X and 200X. The samples are mostly  $\text{SiO}_2$ , slag and some FeSi. CPR1809a also has some  $\text{Al}_2\text{O}_3$ . The top left picture is taken at the plant and marked with 1 and 2, which corresponds to a.1 and a.2. .... 241

Figure 197 Sample CPR1809b with three different magnifications; 40X, 200X and 400X. The sample is brown condensate, as can be seen in the top left picture taken at the plant. ....242

Figure 198 Sample CPR1809c.1 and c.1 with two different magnifications; 200X and 400X. Both samples are SiO<sub>2</sub> and slag. ....242

Figure 199 Sample CPR0211 1, 2 and 3 with three different magnifications; 40X, 100X and 200X. The top left picture is the whole sample taken from the furnace with marked position of sample 1, 2 and 3. CPR0211.1 is brown condensate of SiO<sub>2</sub> and Si covering quartz and CPR0211.2 is SiO<sub>2</sub> with some SiO<sub>2</sub>+Si in between the grain boundaries and cracks. CPR0211.3 is divided in two areas, marked in the bottom left image. Area 1 is a mix of slag, SiO<sub>2</sub> and FeSi and Area 2 is carbon and slag. The dark grey areas on the EPMA image are some epoxy left from the sample preparation. ....243

Figure 200 Sample CPO1101 S.1 and S.2 with three different magnifications; 40X, 200X and 400X. Both analysis samples from this area is SiO<sub>2</sub> rich slag and brown condensate of SiO<sub>2</sub> and Si. ....244

Figure 201 Sample CPO1101 BK.1 with magnification 1000X and BK.2 with magnifications 40X and 400X. Both samples are brown condensate of SiO<sub>2</sub> and Si. BK.2 have several layers with brown and white condensate. The white condensate is SiO<sub>2</sub> and SiC. ....245

Figure 202 Picture of sample CPO1101 and what appeared to be gas channels where SiO and CO gas have found its way through the hard and compact charge. ....245

Figure 203 Sample CPO1101 M.1 and M.2 with two different magnifications; 40X and 200X. Both samples are mostly SiO<sub>2</sub> and SiO<sub>2</sub> rich slag. Some FeSi was found in M.1, and some brown condensate were found in M.2. ....246

Figure 204 Sample CPO1101 K.1 and K2 with three different magnifications; 40X, 200X and 400X. The top left pictures are taken at the plant. Both samples consist of SiO<sub>2</sub> and its impurities. Some Fe is also found in K.2. ....247

Figure 205 Sample CPO1101 P.1 and P.2 with two different magnifications; 40X and 200X. The top left image is picture of the sample taken at the plant. Sample P.1 is mainly SiO<sub>2</sub> and initial formation of slag. P.2 is layered by brown and white condensate of SiO<sub>2</sub>+Si and SiO<sub>2</sub>+SiC, respectively. ....248

Figure 206 Sample CPO1101\_U with three different magnifications; 40X, 200X and 400X. The sample consists of mainly SiO<sub>2</sub>, a SiO<sub>2</sub> rich slag, and some FeSi particles. A thin layer of FeO is covering the sample. ....248

Figure 207 Sample GR1602 with three different magnifications; 40X, 200X and 400X. The sample consists of mainly SiO<sub>2</sub> and has a thin layer of FeO surrounding the sample. In the sample is also particles of FeSi. ....249

Figure 208 The left picture is the whole sample CPR2502, while the picture in the middle an to the right shows different parts of the sample. ....250

Figure 209 Sample CPR2502k with two different magnifications; 40X and 200X. This was confirmed to be SiO<sub>2</sub>. Some impurity oxides were found in between the grain boundaries and cracks.....250

Figure 210 Sample CPR2502m with three different magnifications; 40X, 200X and 1000X. In the sample was mostly carbon, but also several smaller and larger FeSi areas. Small SiC particles were covering either slag or SiO<sub>2</sub>. ....251

Figure 211 Sample CPR2502y with two different magnifications; 40X and 200X. The sample is mostly SiO<sub>2</sub> and areas with small Si particles in the SiO<sub>2</sub>. ....251

Figure 212 Sample CPR2502 a.1 with two different magnifications; 40X and 200X and a.2 with magnification 40X. Both samples consist of SiO<sub>2</sub> and a SiO<sub>2</sub> rich slag phase, in addition to some particles of FeSi. ....252

Figure 213 Sample CPR2502b with two different magnifications; 40X and 200X. The sample consists of SiO<sub>2</sub> and a SiO<sub>2</sub> rich slag phase, in addition to some particles of FeSi. ....252

Figure 214 Sample CPR1903 with three different magnifications; 40X, 200X and 1000X. The sample consists of SiO<sub>2</sub> with some particles of FeSi. It is found that the matrix is ~96% SiO<sub>2</sub> with traces of mainly Al<sub>2</sub>O<sub>3</sub>, CaO and K<sub>2</sub>O. ....253

Figure 215 Si, Al and Ca elemental mapping on the sample 50.0.1, which is heated with 50 °C/min up to 1200 °C and 25°C/min to 1600 °C with 0 minutes holding time. ....257

Figure 216 Si, Al and Ca elemental mapping on the sample 50.0.2, which is heated with 50 °C/min up to 1200 °C and 25°C/min to 1600 °C with 0 minutes holding time. ....258

Figure 217 Si, Al and Ca elemental mapping on the sample 50.10, which is heated with 50 °C/min up to 1200 °C and 25°C/min to 1600 °C with 10 minutes holding time. ....258

Figure 218 Si, Al and Ca elemental mapping on the sample 50.20, which is heated with 50 °C/min up to 1200 °C and 25°C/min to 1600 °C with 20 minutes holding time. ....259

Figure 219 Si, Al and Ca elemental mapping on the sample 50.30, which is heated with 50 °C/min up to 1200 °C and 25°C/min to 1600 °C with 30 minutes holding time. ....259

Figure 220 Si, Al and Ca elemental mapping on the sample 50.40, which is heated with 50 °C/min up to 1200 °C and 25°C/min to 1600 °C with 40 minutes holding time. ....260

Figure 221 Si, Al and Ca elemental mapping on the sample 50.60.1, which is heated with 50 °C/min up to 1200 °C and 25°C/min to 1600 °C with 60 minutes holding time. ....260

Figure 222 Si, Al and Ca elemental mapping on the sample 50.60.2, which is heated with 50 °C/min up to 1200 °C and 25°C/min to 1600 °C with 60 minutes holding time. ....261

Figure 223 Si, Al and Ca elemental mapping on the sample 25.0, which is heated with 25°C/min up to 1200 °C and 15°C/min to 1600 °C with 0 minutes holding time.....262

Figure 224 Si, Al and Ca elemental mapping on the sample 25.40, which is heated with 25°C/min up to 1200 °C and 15°C/min to 1600 °C with 40 minutes holding time.....263

Figure 225 Si, Al and Ca elemental mapping on the sample 25.60, which is heated with 25°C/min up to 1200 °C and 15°C/min to 1600 °C with 60 minutes holding time.....263

Figure 226 Si, Al and Ca elemental mapping on the sample 15.40, which is heated with 15°C/min up to 1200 °C and 10 °C/min to 1600 °C with 40 minutes holding time.....264

Figure 227 At the top are the images taken during and after experiments for the second parallel of CaO and 56% SiO<sub>2</sub>- 15% CaO-29% Al<sub>2</sub>O<sub>3</sub> slag heated to 1500 °C and with 10 minutes holding time. Below are the cross-section image and the EPMA image after experiment. The initial CaO/slag were 0.36. ....265

Figure 228 At the top are the images taken during and after experiment for the sample of CaO and 56% SiO<sub>2</sub>- 15% CaO-29% Al<sub>2</sub>O<sub>3</sub> slag heated to 1500 °C and with 20 minutes holding time. Below are the cross-section image and the EPMA image after experiment. The initial CaO/slag were 0.30. The camera on the furnace did not work until the end of the experiment and it is therefore not obtained the images during the experiment at 900 °C and right after reached 1500 °C. ....265

Figure 229 At the top are the images taken during and after experiments for the first and second parallel of CaO and 56% SiO<sub>2</sub>- 15% CaO-29% Al<sub>2</sub>O<sub>3</sub> slag heated to 1500 °C and with 30 minutes holding time. Below are the cross-section images and the EPMA images taken after experiment. The initial CaO/slag were 0.46 and 0.38 for the first and second parallel, respectively. ....266

Figure 230 Images taken during and after experiment for the experiment run with slag on a lime substrate. The sample was heated to 1550 °C and held there for 10 minutes.....266

Figure 231 At the top are the images taken during and after experiment for the sample of CaO and 38% SiO<sub>2</sub>- 20% CaO-42% Al<sub>2</sub>O<sub>3</sub> slag heated to 1500 °C and with 20 minutes holding time. Below are the cross-section image and the EPMA images after experiment. The initial CaO/slag were 0.17. ....267

Figure 232 At the top are the images taken during and after experiment for the sample of CaO and 56% SiO<sub>2</sub>- 21% CaO-23% Al<sub>2</sub>O<sub>3</sub> slag heated to 1500 °C and with 20 minutes holding time. Below are the cross-section image and the EPMA images after experiment. The initial CaO/slag were 0.28. ....268



## List of tables

Table 1 Summary of results from industrial excavations. ....	11
Table 2 Furnace and excavation details from the six furnaces summarized.....	27
Table 3 Overview of the excavation samples analyzed and their position area in the furnace. The first letter in the sample ID is the same as the first letter of the plant they are collected from. The different colors are the same as in Figure 19. ....	28
Table 4 Tapped slag samples collected from Elkem Thamshavn, May 2019 to May 2020. Tap-hole number, temperature in the ladle and electrodes position at time of sampling are also included in the table.....	30
Table 5 Tapped slag samples collected from Furnace B in June 2020. Tap-hole number and electrodes position at time of sampling are also included in the table.....	30
Table 6 Samples collected from Finnfjord AS, furnace O and furnace R. The last letter in the labeling indicates which furnace the samples are collected from. The samples are collected from September 2020 to March 2022.....	31
Table 7 Samples collected from the charge top. Sample CPR1809a, CPR1809b, CPR1809c and CPR0211 are also used in another study [44]. ....	32
Table 8 Overview of the samples collected from Furnace B behind tap-hole 3. Lower parts of the furnace is below the electrode tip, while higher parts is above the electrode tip. ...	41
Table 9 Normalized WDS analysis for B-3, B-4, B-7, B-8, B-9, B-14, B-27. Liquidus and solidus temperature are found from the ternary diagram and are given in °C. The viscosity data are calculated from FactSage 8.1, given in Poise.....	49
Table 10 Oxynitride analysis for sample B-9. ....	49
Table 11 Overview of the tap-hole samples collected from taphole 1, 3 and 7. In all samples there were a green zone next to the Si, and next a dark grey zone. Both the green and the grey zone consists of SiO <sub>2</sub> -CaO-Al <sub>2</sub> O <sub>3</sub> slag and SiC.....	50
Table 12 The normalized WDS analysis for B-48 a and b from tap-hole 1, B-1 and B-2 from tap-hole 3, and B-47 from tap-hole 7. The liquidus and solidus temperature are found from the ternary diagram and are given in °C. The viscosity data are calculated from FactSage 8.1, given in Poise. The numbers after the samples name correspond to the marked analyzed number shown in earlier figures and includes slag from both the green and grey zones in all samples. ....	54
Table 13 The normalized WDS analysis for the collected earlier tapped samples B-tap 1 and, B-tap 2 and B-tap 3. The liquidus and solidus temperature are also included in the table, given in °C. Viscosities are calculated using FactSage 8.1 and are given in Poise. ....	56

Table 14 Overview of the excavation samples analyzed and their approximate position area in the furnace. The first letter in the sample ID is related to the first letter in the furnace they are collected from.....	57
Table 15 Normalized WDS results for slag samples. Oxide analysis are given in mass percent. Viscosities are calculated using FactSage 8.1.....	61
Table 16 WDS results for the analyzed slag for the tapped samples collected from Elkem Thamshavn. Oxide analysis are given in mass percent. Viscosities are calculated with FactSage 8.1.....	64
Table 17 WDS results for the analyzed slag for the tapped samples collected from Furnace B. Oxide analysis are given in mass percent. Viscosities are calculated with FactSage 8.1.....	64
Table 18 WDS results for the analyzed slag for the tapped samples collected from Finnfjord AS. Marked with (H) are the high viscosity slags. Oxide analysis are given in mass percent. Viscosities are calculated with FactSage 8.1.....	65
Table 19 Composition of the main slag phases found in the charge surface samples. Compositions are given in wt%.....	70
Table 20 Important factors for selection of quartz in silicon and ferrosilicon production.	72
Table 21 Typical content of trace elements in quartz used for Si and FeSi production [48]. All units except Hg are in ppmw. Some analyses are below detection limit and are marked by <.....	72
Table 22 Average measured volatilities of B, P, K, Fe, Al, Mn, Zn and Pb determined experimentally [51].....	75
Table 23 ICP-MS analysis for quartz A, B, C, D, F and G [9].....	84
Table 24 Heating experiments in the sessile drop furnace. All experiments were run in Argon atmosphere 0.1l/min.....	85
Table 25 High Temperature Confocal Microscope experiments. All experiments were conducted with the same heating rate; 100 °C/min up to 1000 °C and 25°C/min up to 1650 °C.....	87
Table 26 Normalized WDS results for sessile drop experiments for quartz C, D and F. Oxide analysis are given in wt%. Viscosities are calculated using FactSage 8.1.....	94
Table 27 EDS results from the High Temperature Confocal Microscope experiments. The results are used to identify the elements present in the impurities, and to give an indication of the composition.....	104
Table 28 Values of optical basicity for CaO, SiO <sub>2</sub> and Al <sub>2</sub> O <sub>3</sub> [25].....	112

Table 29 Summary of experimental methods and results for CaO dissolution in SiO <sub>2</sub> -CaO-Al <sub>2</sub> O <sub>3</sub> slag.....	118
Table 30 Summary diffusion coefficients from literature.....	119
Table 31 Parameters for model, developed by Ren et al. [114].....	123
Table 32 Chemical analyses and density for industrial lime (CaCO <sub>3</sub> ) from Franzefoss Minerals AS. ....	125
Table 33 SiO <sub>2</sub> -CaO-Al <sub>2</sub> O <sub>3</sub> slags used in the dissolution experiments. The amounts are given in wt% and the viscosities are calculated with FactSage 8.1. ....	126
Table 34 The dissolution experiments, CaO in 56wt% SiO <sub>2</sub> - 15wt% CaO- 29wt% Al <sub>2</sub> O <sub>3</sub> slag. The sample ID gives the heating rate to 1200 °C and the holding time. ....	128
Table 35 Dissolution experiments in sessile drop furnace.....	129
Table 36 The compression tests performed on limestone and CaO, calcined with two different heating rates 5.6°C/min and 1.7°C/min. ....	131
Table 37 Dissolution experiments with CaO and 56% SiO <sub>2</sub> -15% CaO-29% Al <sub>2</sub> O <sub>3</sub> . ....	139
Table 38 Dissolution experiments with CaO and 38% SiO <sub>2</sub> -20% CaO-42% Al <sub>2</sub> O <sub>3</sub> . ....	144
Table 39 Dissolution experiments with CaO and 56% SiO <sub>2</sub> -21% CaO-23% Al <sub>2</sub> O <sub>3</sub> . ....	148
Table 40 The equilibrium constant K and the change in Gibbs free energy ΔG <sup>0</sup> for two SiO <sub>2</sub> -CaO-Al <sub>2</sub> O <sub>3</sub> slag compositions at 1800 °C. The given activities are found with FactSage 8.1, and the equilibrium constant K found with HSC Chemistry. ....	162
Table 41 The lowest and the highest liquidus and solidus temperature found for slag samples in this study. ....	171
Table 42 Calculated viscosities at 1600 °C and 1800 °C using two different viscosity models. The viscosity data are given in Poise. ....	172
Table 43 A summary of the crack formation and mechanism in quartz type A, B, C, D, F and G. ....	178
Table 44 Rate data obtained from shrinking sphere model. k <sub>1</sub> is the rate constant in the dissolution rate equation given in g/s·cm <sup>2</sup> . ....	194
Table 45 Rate data obtained from the mass transport model. k <sub>2</sub> is the rate constant in the dissolution rate equation given in cm/s using the 1500 °C liquidus as the saturation concentration. ....	198
Table 46 Original data from WDS analyses of slag from behind tap-hole 3 from Furnace B excavation. ....	219

Table 47 WDS results for samples collected from B-48a, from the lower parts of tap-hole 1.....220

Table 48 WDS results for samples collected from B-48b, from above tap-hole 1.....220

Table 49 WDS results for sample B-1 and B-2, from above and below tap-hole 3, respectively. ....225

Table 50 WDS results for the slag analyzed in sample B-47, which includes the zones around tap-hole 7. ....228

Table 51 Full WDS results for the collected earlier tapped slag samples B-tap 1, -2 and -3. ....233

Table 52 Full WDS results for the slag in the earlier excavation samples. The first letter in the sample ID refers to the first letter in the furnace they are collected from; Elkem Salten, Finn fjord AS, Wacker Chemicals and Elkem Thamshavn. The oxide compositions are given in wt%. ....235

Table 53 Original WDS results for the analyzed slag for the tapped samples collected from Elkem Thamshavn, furnace no. 2. Oxide analysis are given in mass percent. ....239

Table 54 Original WDS results for the analyzed slag for the tapped samples collected from Furnace B. Oxide analysis are given in mass percent.....239

Table 55 Original WDS results for the analyzed slag for the tapped samples collected from Finn fjord AS. Oxide analysis are given in mass percent. ....240

Table 56 The original WDS results for the impurities found in the quartz C samples....255

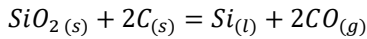
Table 57 The original WDS results for the impurities found in the quartz D samples....255

Table 58 The original WDS results for the impurities found in the quartz F samples. ...255

# Chapter 1: Introduction

## 1.1 Silicon and Ferrosilicon Production

Silicon is one of the most useful elements on earth and is popular due to its semiconductor characteristics and its abundance in form of  $\text{SiO}_2$ . Silicon metalloid is defined as a semi-metal, but in metallurgical production it is referred to as a metal due to its similar production methods to metals like Si- and Mn-alloys. It can be used in a wide range of applications, but the three main uses are as an alloying element in aluminium production, a raw material in silicone production and for further processing to solar cells and semiconductors [1]. Ferrosilicon is normally produced for steel production. The production process for silicon (Si) and ferrosilicon (FeSi) are similar. Both metallurgical Si and FeSi are produced industrially by carbothermic reduction of quartz ( $\text{SiO}_2$ ) in a submerged arc furnace with diameter varying from 5-11m. The overall reaction can be written as in reaction 1, but the actual process is more complex and happens in several steps. Figure 1 illustrates the typical Si production plant.



1

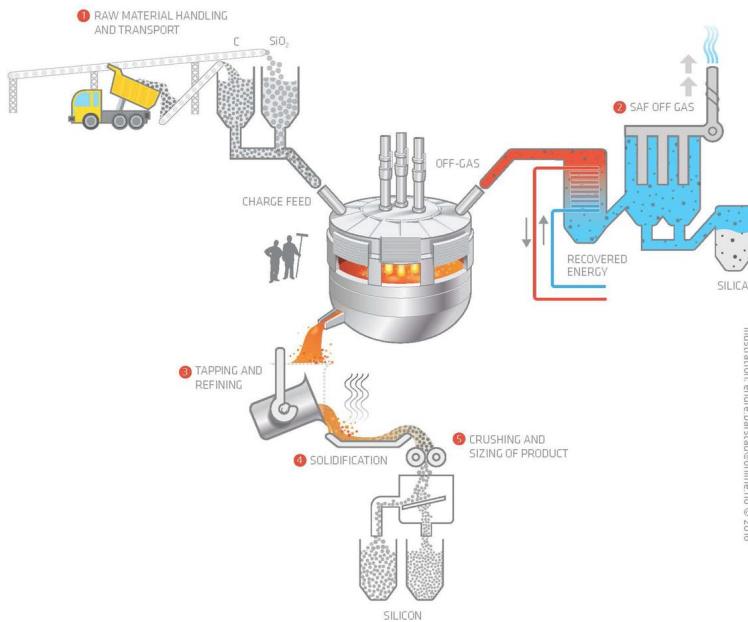
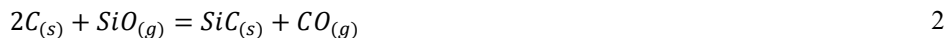


Figure 1 A typical silicon production plant, reprinted from Kero et al. [2]. Raw materials are added at the top of the submerged arc furnace and liquid metal is tapped at the bottom.  $\text{SiO}$  gas that condense to microsilica ( $\text{SiO}_2$ ) is a byproduct that is collected and sold as a product. The off-gas leaves the furnace at the top and is captured in an energy recovery unit and dust filters.

When the raw materials are added to the furnace, they will experience a steep temperature increase as they meet the charge surface that holds a temperature around 1300 °C [1, 2]. The Si and FeSi furnaces are normally divided into a low temperature zone that includes the higher parts of the furnace and along the furnace walls, and a high temperature zone in the lower parts of the furnace around the electrode tip [5]. The boundaries between the zones are diffuse and could shift during operation. The energy to the furnace is supplied by electricity through three carbon electrodes. As the SiO<sub>2</sub> and C descends in the furnace, they react with silicon monoxide (SiO) and carbon monoxide (CO) gas. SiO gas reacts with carbon (C) and forms silicon carbide (SiC) according to reaction 2. The porous carbon material allows diffusion of SiO gas in and CO gas out of the carbon particles, which gives a porous SiC layer covering the carbon material. As the SiC layer becomes thicker the diffusion slows down. SiO gas will also dissociate to Si and SiO<sub>2</sub> according to reaction 3 or react with CO gas to produce SiO<sub>2</sub> and SiC as in reaction 4.



The high temperature zone of the furnace is where most of the electric energy is converted to heat through an electric arc from the electrode tip, and the temperature here will exceed 2000 °C. SiO gas is produced in this high-temperature zone from either SiO<sub>2</sub> and SiC, or SiO<sub>2</sub> and Si, according to reaction 5 and 6. The final Si metal is produced from SiC and SiO gas, as shown in reaction 7. The Si yield and thus also the energy consumption of the process, are determined by the capture of SiO gas in the charge. SiO gas that does not react is lost as microsilica in the off gas.



FeSi production also includes reduction of iron oxides in the low temperature zone of the furnace if oxides are used as raw materials. As the iron oxide pellets mostly contains Fe<sub>2</sub>O<sub>3</sub>, the overall reduction reaction is shown in reaction 8. The submerged arc furnace and the reactions in the Si process are illustrated in Figure 2.



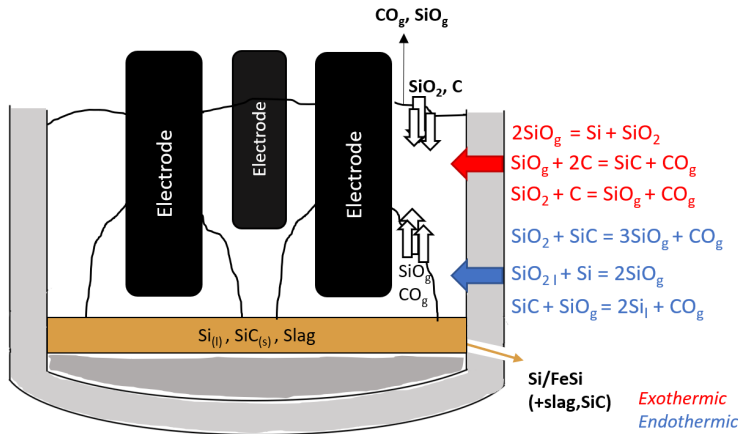


Figure 2 Simple sketch of the Si furnace and the associated reactions. The red colored reactions are exothermic and happens higher up in the furnace, while the blue colored reactions are endothermic and occurs in the high temperature zone in the furnace.

In Si and FeSi furnaces there are several oxide impurities present as slag. Compared to other metallurgical production processes such as manganese and steel, the amount of slag in Si and FeSi production is modest. However, slag will still be formed mainly from the impurities in the raw materials, fluxes, and electrodes. The impurities can either be reduced to their metal components and end up in the metal phase, or they can remain as oxides and form separate slag phases. The amount of accumulated slag is an important factor in the productivity of the furnace, and significant variations have been observed between different furnaces during several furnace excavations over the last fifteen years [6]–[11]. The slag present in the Si and FeSi furnaces mainly consist of  $\text{SiO}_2$ ,  $\text{CaO}$  and  $\text{Al}_2\text{O}_3$ , and different compositions exhibit different properties. Viscosity is one of the most important factors affecting the flow of the slag through the furnace. It is preferable to have a sufficient low viscosity to ensure a good mass flow. Slag mainly composed of  $\text{SiO}_2$  and  $\text{Al}_2\text{O}_3$  are more viscous and can easily accumulate in the furnace.  $\text{Al}_2\text{O}_3$  is a common impurity found in the raw material quartz, as well as the fossil carbon sources. Therefore, calcium oxide ( $\text{CaO}$ ) in form of lime ( $\text{CaCO}_3$ ) is often added as a flux to lower the viscosity of the slag.

## 1.2 Goal and thesis outline

The primary focus in this study is to increase the knowledge about the slag in industrial Si and FeSi furnaces, both the accumulated slag and the tapped slag. When this work started in 2017, the knowledge about slag in industrial Si and FeSi furnaces was limited. The understanding about the slag and how it behaves and reacts in the furnace are important to avoid accumulated slag in the furnaces and to optimize a good flow of materials in the furnaces. It is also an important step towards identifying the different zones and materials in the furnaces. Visual inspections and sampling during operation are not possible in Si and FeSi furnaces, and research based on the materials present and the reported industrial

challenges is highly relevant and valuable on the way of mapping the Si and FeSi furnaces, and to optimize the furnace operation.

It will be used different methods in the process of gaining knowledge about the slag, and this study is therefore divided in three parts. These parts will be described separately in the literature-, experimental methods-, and results chapters, but will be combined in the discussion chapter where the experimental results will be related to the industrial furnace processes.

**Part 1** will focus on slag from industrial Si and FeSi furnaces. Because the literature on slags in these furnaces is limited, a large part of the work will be to try to identify the slag present in the furnaces, and to investigate if there are any variations between the different zones and between the different furnaces. Industrial slag samples from different parts of the furnace will be collected and analyzed. The results from this will help to describe the slag present in the furnace and how it affects the operation and the mechanisms in the industrial furnaces.

**Part 2** will investigate the quartz upon heating to elevated temperatures. The small areas of impurities in the quartz will later contribute to the slag formation in the furnace. This study will look at the impurities behaviour during heating. From heating experiments, it will also be possible to look at the softening and melting properties and the crack formation in the SiO<sub>2</sub>. Six different quartz types suited for Si and FeSi production will be used. The term quartz type is used to describe the raw material quartz, while quartz refers to the silica polymorph.

**Part 3** will study the main action used today for removing the accumulated slag from the industrial furnace: dissolving CaO in the slag to reduce its viscosity. Dissolution experiments of CaO in three different slag compositions will be performed to investigate the dissolution rate and the CaO effect on the viscosity of the slag relevant for the Si and FeSi furnaces.



## Chapter 2: Slag from industrial furnaces

### 2.1 Literature review

Si and FeSi are in principle defined as a slag free process. However, there will still be some oxide impurities present from the raw materials, fluxes and electrodes which will not be reduced. These will form a separate slag phase. Some slag will be tapped together with the final metal, and some will be accumulated in the furnace. The amount of slag accumulated in the furnaces is found to be one of the main differences between different Si and FeSi furnaces during excavations [8].

#### 2.1.1 The inner structures of furnaces from excavations

Due to the high temperature and challenging environment, the interior of the Si and FeSi furnaces is difficult to map. Exactly how the furnaces are inside, how the materials flow and how the electrical current is moving are questions that are still being investigated and debated. The first known comprehensive studies on the furnace inside were performed in the 60s by Zherdev et al. [12], [13], who used electrical probes during operation to observe the areas around the electrode tip. From this, cavities filled with gas produced from the inner zone of the furnace were detected. Gas flowed through the charge material creating gas channels. The cavities existed around the electrode tip above the pool of liquid Si. Further work on the inner structure of the furnace was done by Otani et al. [14], who placed a visual probe into the cavity to study the surroundings of the electrode tip. From this they confirmed that the electrode was surrounded by a cavity, and a bottom deposit of SiC crystals filled with molten Si were observed 5-15 cm below the electrode tip. Otani et al. also observed an electric arc from the electrode to the bottom deposit.

Excavation of pilot scale furnaces after shut-down have also been carried out. Schei and Sandberg [15] and Schei [16] smelted Si and FeSi in a 40 kW single-phase furnace, shown in the right illustration in Figure 3. This furnace was equipped with a 75 mm diameter electrode and bottom contact. It was run with the intention of operating it in the same way as an industrial furnace, but due to small size some modifications were necessary. In an experiment where the SiO and CO gas was cooled with alumina pellets Schei [16] found metal with a high Al content and slag of 86% Al<sub>2</sub>O<sub>3</sub> – 6% SiO<sub>2</sub> at the bottom. A small cavity was found around the electrode, and above the cavity there was a roof of sintered oxidic materials with metal droplets. Schei and Sandberg [15] tapped the furnace right before shut-down. They found, after cooling, partly reacted charge above the cavity, and then porous SiC, partly filled with metal, in the lower parts of the furnace. Based on several pilot scale excavations, Schei et al. [5] made a schematic figure of the inner structure of the industrial Si/FeSi furnace, shown in Figure 3. They found that condensate of Si, SiO<sub>2</sub> and SiC glued the charge together and created a void below the charge as the raw materials were consumed. The cavities surrounded the electrode tip and were surrounded by charge

materials in various states of conversion. A mixture of mainly SiO and CO gas filled the cavity, in addition to some other high temperature gas species. SiC crystals were in the lower part of the cavity walls, with a space between the crystals partly filled with molten Si. They assumed that the SiC crust were sintered together, and that they made the upper part of the deposit firm enough to create a wall. Above the SiC, the materials close to the inner surface of the wall were heated enough to have some reaction, but the materials further behind the surface were rather inactive. The temperature at the top of the furnace was assumed to be in the area of 800-1400 °C [17]. As the gas species ascended into the charge at lower temperatures, a major part of the SiO gas reacted with the carbon materials.

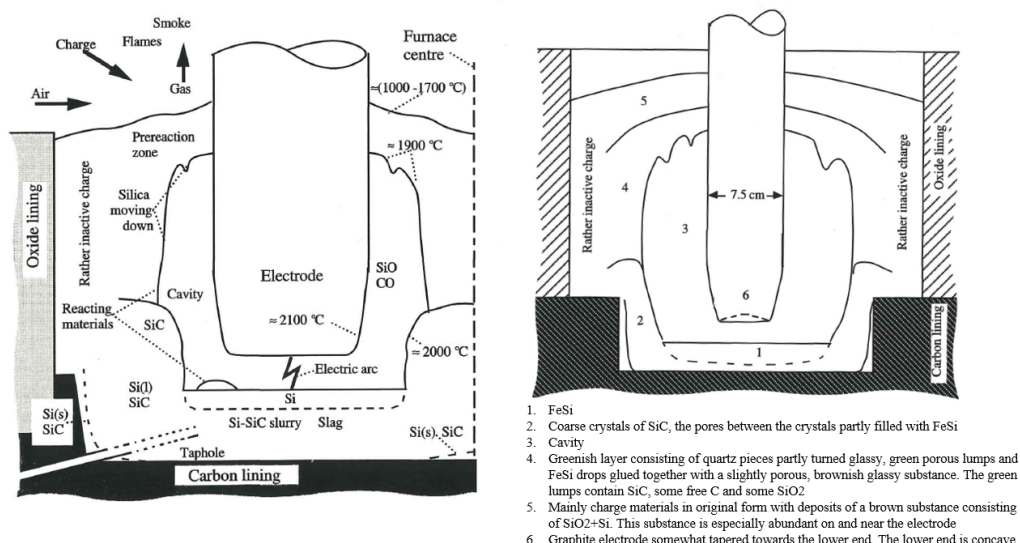


Figure 3 The first figure shows an illustration of the inner structure of a submerged arc furnace, based on several pilot scale experiments [5]. The illustration is based on experiments from the furnace shown in the right illustration, a 40 kW one-phase furnace with 7.5 cm diameter graphite electrode.

It is important to point out that these results are found from a small 40 kW furnace that has only been run for a short time. Many of the zones are similar to those in the industrial furnaces, but some of the results deviates from newer findings from excavations. E.g. the results from Jayakumari [18] found that  $\beta$ -SiC is in the metal bath, while the wall crust is  $\alpha$ -SiC. It is hence not believed that the SiC crystals are sintered together in the metal/slag bath.

Today's industrial furnaces in Norway are operating at typical 30-45 MW, and are only shut down for short periods during maintenance or other unwanted incidents. Excavation of a furnace happens seldom, mainly due to damages that affects the operation, the need for a rebuild or marked situations. Excavations of industrial furnaces the last 15 years have found that the inner structure of a furnace may vary from one furnace to another. The zones inside the furnaces are dependent on the operational history, not only on the raw materials. The first described excavation of an industrial furnace in newer times was done by Tranell et al. [7] in 2009, who excavated a 17.5 MW FeSi75 furnace at Finn fjord. In 2013 Tangstad

et al. [6] described the findings of the excavation of a 40MW Si furnace at Elkem Thamshavn. Ksiazek et al. [8] compared in 2016 the findings from five different Si and FeSi furnace excavation; “Five furnaces, five different stories”. From these five furnaces it was possible to distinguish a few main zones from horizontal cross sections:

- 1) Inactive zone towards the furnace walls that mostly consist of deposited slag and partly melted raw materials. This zone was found in all the excavations.
- 2) Electrode track zone, as the furnace shell is rotating/oscillating.
- 3) Inner zone located in the center of the furnace.

The materials found in these zones, and the size of these zones, were different between the furnaces. Figure 4 and Figure 5 gives a vertical cross section overview of the material zones in the FeSi and Si furnaces in the study, respectively. For the FeSi75 furnace at Finn fjord large cavities were found around the electrode tip surrounded by a SiC crust with gas channels, but no cavities were found in the FeSi50 furnace at Elkem Bjølvefossen and the Si furnace Wacker no. 4, which indicate that they have been very small. For the Si furnaces Wacker no.1 and Elkem Thamshavn, small cavities were found below the electrode tip. One of the main differences between the furnaces was the extent of slag accumulated in the furnaces. In the FeSi50 furnace at Elkem Bjølvefossen, it was found a massive slag layer on the outside of the electrodes all the way up to the charge top, in addition to more than 1m thick slag layer covering the entire bottom. Slag deposited from the bottom lining to the furnace top was also found in all three Si furnaces.

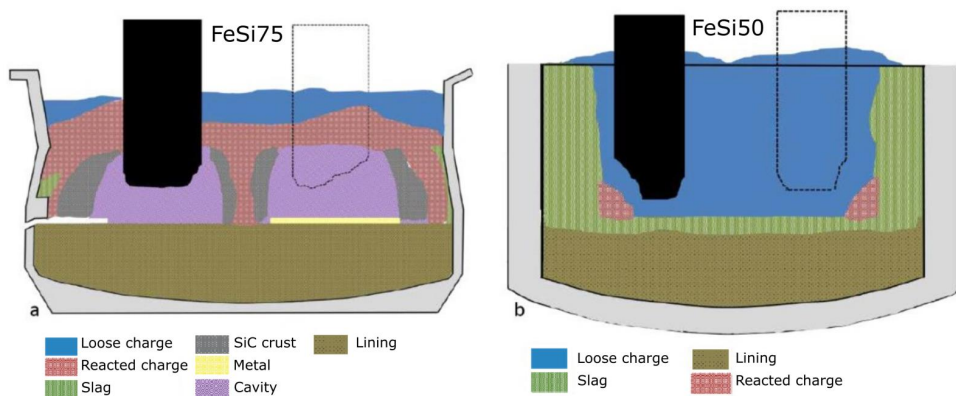


Figure 4 Overview of zones after excavation of two FeSi furnaces, a) FeSi75 in Finn fjord, b) FeSi50 in Elkem Bjølvefossen [8].

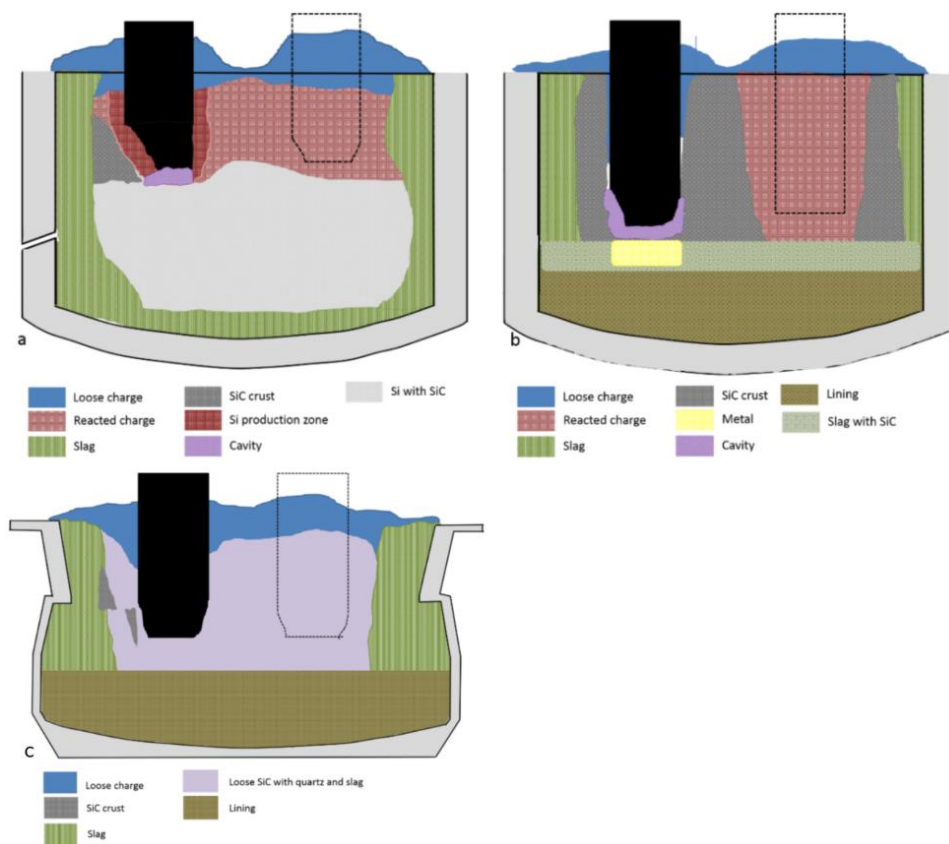


Figure 5 Schematic drawings of the zones found in three Si furnaces after excavations; a) Wacker furnace no.1, b) Elkem Thamshavn, c) Wacker furnace no.4 [8]. Due to lack of time and difficulties in the excavation, the bottom lining is often not prioritized. The lining representation is therefore often based on the furnace drawings from the company, or assumptions. In Wacker furnace no. 1, the lining is left out from the illustration.

Nell and Joubert [19] studied digout samples from a FeSi furnace after a partial sidewall rebuild around two tapholes. They found significant quantities of slag containing SiC and refractory oxide phases between the electrode crater and the tap-hole, and they believed that this was the one of the main reasons causing tapping problems. The slag consisted of the  $\text{SiO}_2\text{-CaO-Al}_2\text{O}_3$  system with an unexpected high content of alumina. It was also commented that the samples were heterogenous in both composition and phase distribution. The alumina content varied as much as 30%.

Two furnace excavations were performed in Norway during 2018. Jusnes [9] described the findings from the excavation of a FeSi75 furnace at Finn fjord and Ksiazek [10] reported the results from the excavation of a 36MW Si furnace at Elkem Salten. A vertical cross section overview of the material zones in the FeSi and Si furnace furnaces is shown in Figure 6. From the figure it can be seen that a large amount of slag was found in the Finn fjord furnace. Loose materials were found around the electrodes and at the charge surface. An area with SiC surrounded the loose materials, and next, towards the outer shell, was a thick layer with slag. Slag was also found in the bottom layer together with the metal.

In the Si furnace at Elkem Salten, condensate of mainly  $\text{SiO}_2$  and  $\text{SiC}$  were found towards the sides of the furnace. In the center of the furnace and up to the charge top, there was a large area with Si metal with  $\text{SiC}$  and a slag mixture. It was believed that this was due to the charging of large amount of metal to the furnace just before it was stopped.

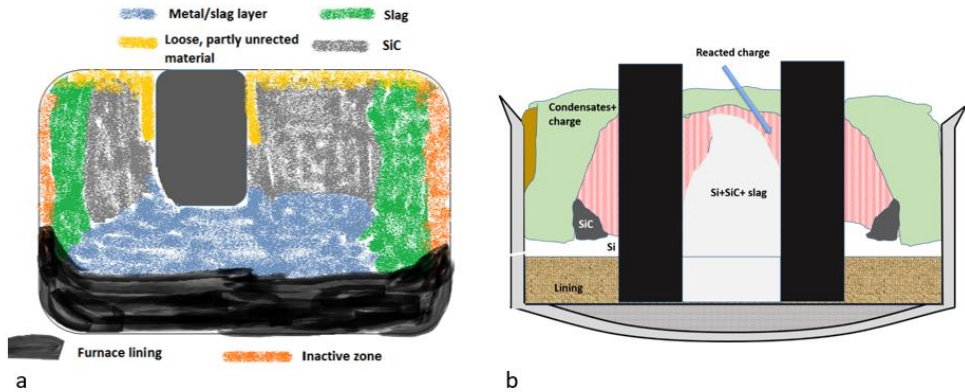


Figure 6 Overview of zones after excavation at a) Finnford [9] and b) Elkem Salten [10] in 2018. Due to lack of time and difficulties in the excavation, the bottom lining is often not prioritized. The lining representation is therefore often based on the furnace drawings from the company, or assumptions.

Slag is found in all industrial excavations from 2009, but its oxide compositions have not been reported in all reports. One slag sample from Elkem Thamshavn from the slag/ $\text{SiC}$  layer at the bottom were analyzed [20], and Bø [21] analyzed several slag samples from the excavation at Wacker Chemicals Holla furnace no.4 in her master thesis. Most of these samples were collected from the inactive layer of the furnace. The slag compositions from Wacker [21], Elkem Thamshavn [20], Elkem Salten [10] and the range of normal Siltech slag compositions [19] are summarized in Figure 7. The slag samples from Wacker consists of  $\sim 30\text{-}55\text{wt}\%$   $\text{SiO}_2$ ,  $\sim 20\text{-}45\text{wt}\%$   $\text{CaO}$  and  $\sim 25\text{-}35\text{wt}\%$   $\text{Al}_2\text{O}_3$ . The typical Siltech slag consists of mainly  $\text{SiO}_2$  and  $\text{Al}_2\text{O}_3$ , while the slag from both Elkem Thamshavn and Salten have a higher  $\text{CaO}$  content around  $45\text{wt}\%$ . A short summary of the slag findings in the excavations from 2009 to 2018 is listed in Table 1.

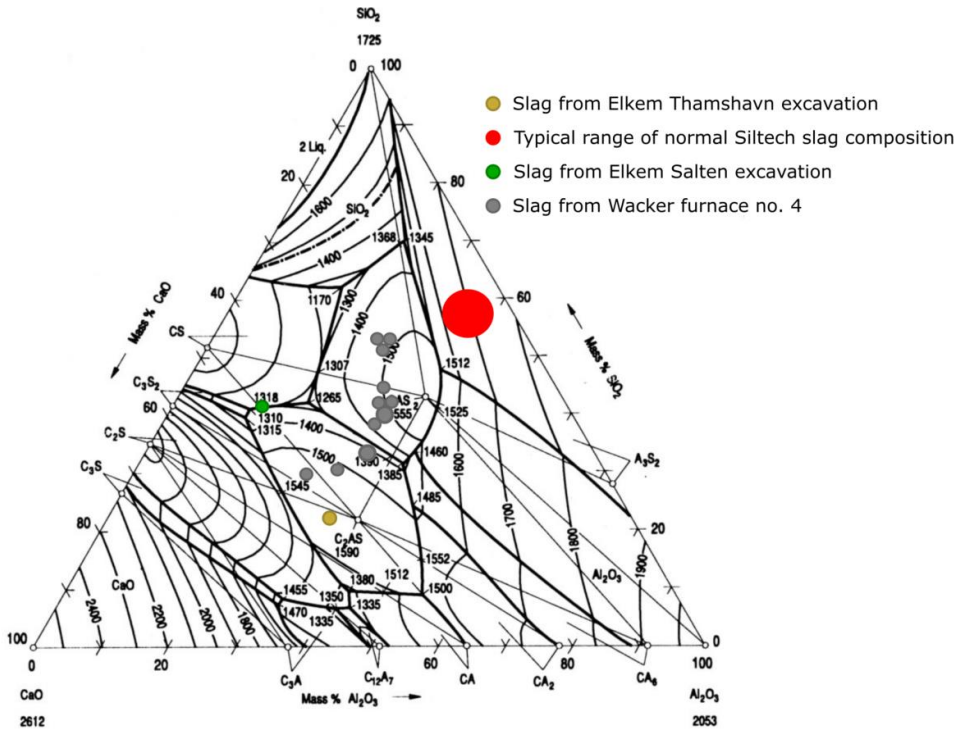


Figure 7 The analyzed slag compositions from from Elkem Thamshavn excavation [6], from Elkem Salten excavation [10], from Wacker furnace no.4 [21] and the large red circle is the typical range of normal Siltech slag composition analyzed by Nell et al [19].

Table 1 Summary of results from industrial excavations.

Excavation	Furnace	Related results		
		Furnace bottom	Outside electrodes	Tap hole area
<b>Finnfjord (2009)</b> [7], [8]	FeSi75	-Only small amounts of slag found near the furnace wall.		
<b>Siltech (2009)</b> [19]	FeSi	-samples collected only from tap hole area		-Significant quantities of slag together with SiC. -Slag rich in alumina
<b>Elkem Thamshavn (2013)</b> [6]	Si	-Slag, mainly anorthite and gehlenite, together with SiC	-condensation layer with mixture of SiO <sub>2</sub> and SiC	-not specified
<b>Wacker Chemicals Holla, no4 (2015)</b> [8], [21]	Si	-green slag with some SiC particles	-green condensation layer of SiC and SiO <sub>2</sub> -thick layer of slag	-not specified
<b>Wacker Chemicals Holla, no1 (2016)</b> [8], [21]	Si furnace	-a thick layer of slag covers the walls of the interior of the furnace		-thick layer of slag
<b>Elkem Bjølvefossen (2016)</b> [8]	FeSi50	-more than 1m high slag layer with some SiC particles	-massive slag layer from bottom to the top of the charge with some SiC particles	-not specified
<b>Finnfjord (2018)</b> [22]	FeSi75	-Metal/slag bath with some SiC particles	Slag layer with SiC	-not specified
<b>Elkem Salten (2018)</b> [10]	Si	-SiC, Si and a slag with dispersed SiO <sub>2</sub> -slag mainly SiO <sub>2</sub> and CaO, with some Al <sub>2</sub> O <sub>3</sub>	-condensation layer with SiO <sub>2</sub> and slag -slag mainly SiO <sub>2</sub> with some CaO and Al <sub>2</sub> O <sub>3</sub>	-SiO <sub>2</sub> with large areas of Si and multiphase slag (Fe, Al, Ca, K, Na, Mg)

## 2.1.2 Stability of oxides in Si and FeSi production

The Ellingham diagram shows the standard Gibbs energy of formation as shown in equation 1, of oxides per mole of oxygen reacted and visualizes the oxides' ability to be reduced.

$$\Delta G^0 = \Delta H^0 + T\Delta S^0 \quad 1$$

Where  $\Delta G^0$  is the change in standard Gibbs free energy,  $\Delta H^0$  is the change of enthalpy for the reaction in J/mole, T is the temperature in K and  $\Delta S^0$  is the change of entropy for the reaction in J/Kmol.

The lower a reaction is in the diagram; the higher energy and temperature is required to reduce the oxide. The Ellingham diagram with the oxides relevant for Si and FeSi production and their stability towards carbon reduction are shown in Figure 8 [5]. For an oxide to be reduced with carbon, the sum of  $\Delta G^0$  for those two reactions need to be zero or less than zero, which happens at temperatures at and above the intersection point between the oxide curve and the carbon curve. For some of the curves, it can be observed a change in the slope of the curves at different temperatures, which is a change in the entropy through either a melting or boiling temperature. This is the case for Ca at  $\sim 1500$  °C. Oxides above  $\text{SiO}_2$  in the diagram, like Fe, Na and Mn are most likely to be reduced to their pure metal state at a lower temperature than needed for reduction of  $\text{SiO}_2$  to Si with C as a reductant. Below  $\text{SiO}_2$  in the diagram are the alkaline earth metal oxides,  $\text{TiO}_2$  and  $\text{Al}_2\text{O}_3$ , which require a lower oxygen potential than  $\text{SiO}_2$  to react and form metal in its standard state. The intersection of  $\text{SiO}_2$ , CaO and  $\text{Al}_2\text{O}_3$  with the CO curve is at 1550 °C, 2100 °C and 2040 °C, respectively. For CaO and  $\text{Al}_2\text{O}_3$  this happens at a higher temperature than shown in the diagram in Figure 8. This means that CaO and  $\text{Al}_2\text{O}_3$  are more stable oxides than  $\text{SiO}_2$  and are likely to end up in the slag phase. It should be noted that this is only valid when all the components are in their reference state, and in most metallurgical processes that is not the case. Both the metal phase and the slag phase contain several different components. Myrhaug and Tveit [23] and Kamfjord [24] have made overviews of where the impurity elements in the Si and FeSi furnace are likely to be found in the various mass flows. These are discussed further in the literature review in chapter 3.1.2: Impurities in quartz.



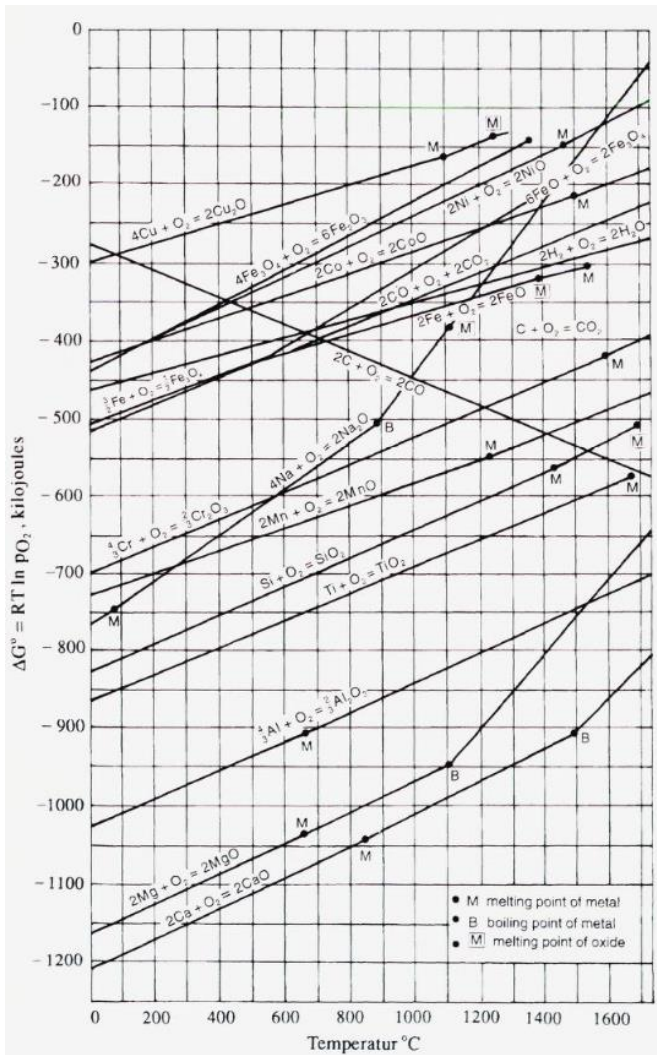


Figure 8 The Ellingham diagram for oxides relevant for the silicon smelting [5].

### 2.1.3 The SiO<sub>2</sub>-CaO-Al<sub>2</sub>O<sub>3</sub> ternary system

It is found that the slag in Si and FeSi production mainly consists of the SiO<sub>2</sub>-CaO-Al<sub>2</sub>O<sub>3</sub> system. The ternary phase diagram of the SiO<sub>2</sub>-CaO-Al<sub>2</sub>O<sub>3</sub> system is shown in Figure 9 [25], which provides a fundamental foundation for understanding the industrial behavior of this slag system. The diagram shows the liquidus isotherms, the boundaries between coexisting phases and the tie-lines between coexisting phases below solidus temperature. Melting of slag does not happen at a single temperature, and a slag system may contain both liquid matter and solid particles. It is therefore pertinent to refer to a liquidus temperature, which is the lowest temperature where the system is completely liquid, and a

solidus temperature which gives the highest temperature that the system is completely solid. For many metallurgical processes, the liquidus temperature of the slag is one of the most important properties as it is essential to maintain a liquid slag. The slag inside the Si and FeSi furnaces will experience different temperatures depending on where it is found in the furnace. Based on COMSOL simulations, Myrhaug [26] made a conceptual model of the temperature profile and Si flow in the Si furnace, shown in Figure 10. He also found temperatures  $>1700\text{ }^{\circ}\text{C}$  for the tapped Si. From the liquidus isotherms in the ternary diagram it can be found that a wide compositional range is liquid with temperatures around and above  $1700\text{-}1800\text{ }^{\circ}\text{C}$ , as shown in Figure 9 [5], [27]. This means that the slag that exits the tap-hole is most likely in liquid state. Accumulated slag found in the higher parts in the furnace, where the temperature is lower, might experience precipitation of solid particles as the temperature becomes lower than the liquidus temperature of that composition. As described above, the composition of the slag accumulated in the furnace varies, both between different furnaces and within the same furnace, and will depend on the input of materials in the furnace and how the furnace is operated. Thermo-physical properties of the slag such as viscosity, density, and surface tension are important to optimize the high temperature process.

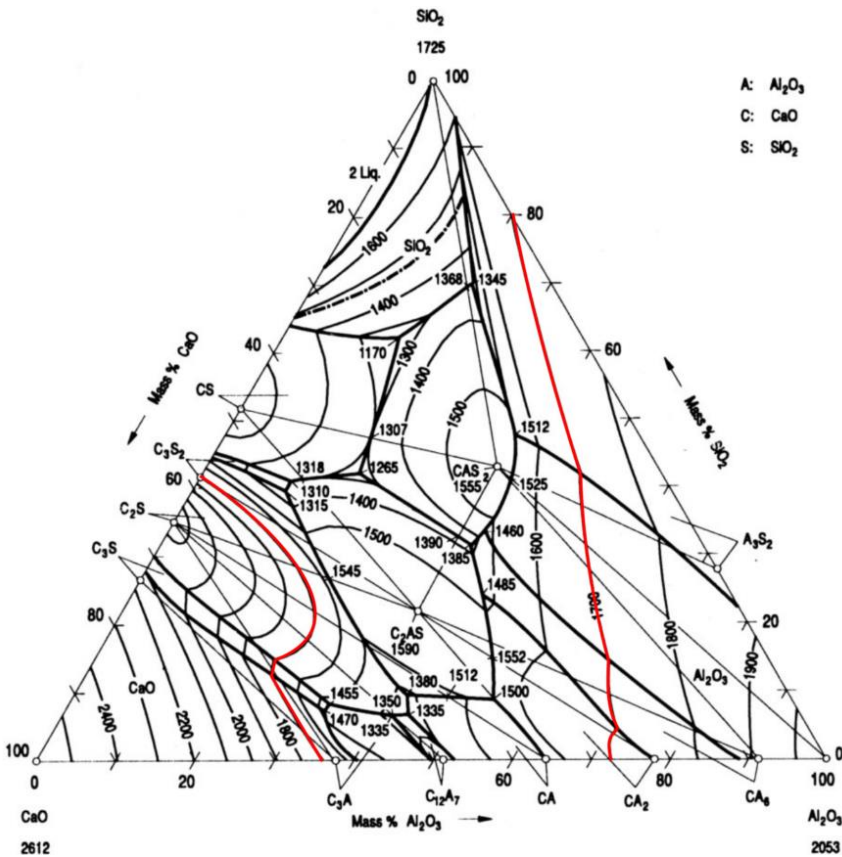


Figure 9 The ternary phase diagram of the  $\text{SiO}_2\text{-CaO-Al}_2\text{O}_3$  slag system [25]. The red lines mark the liquidus area at  $1700\text{ }^{\circ}\text{C}$ .

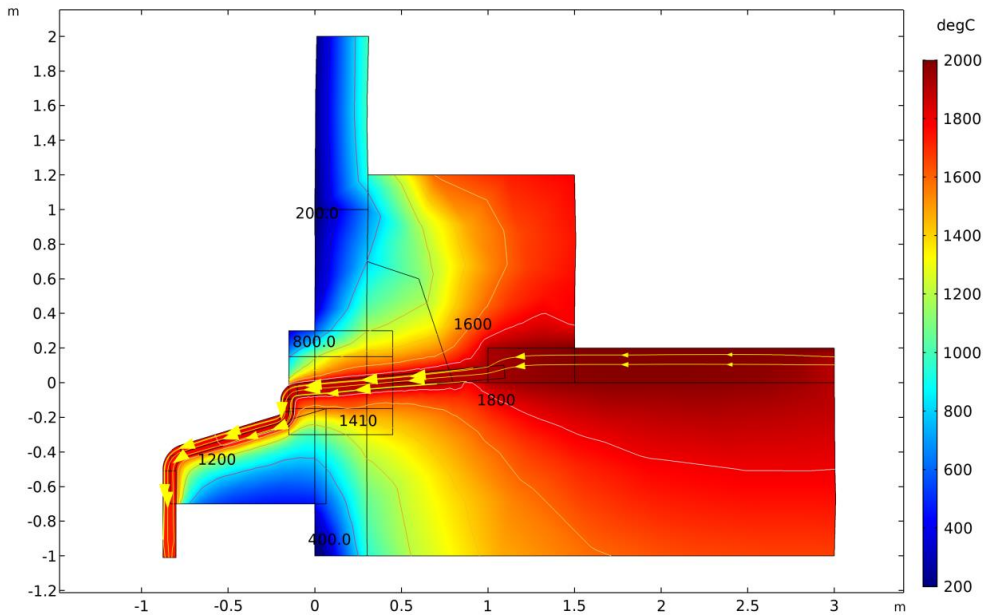


Figure 10 Temperature profile and silicon flow in silicon furnace in a vertical cross section [26]. The model is based on COMSOL simulations.

### 2.1.3.1 The structure of silica melts

The building block for slags that contains silica is the  $\text{SiO}_2$ , with a centrally placed  $\text{Si}^{4+}$  ion surrounded by  $4\text{O}^{2-}$  ions in the frame of a tetrahedron. The bonds within the tetrahedron are covalent. In pure  $\text{SiO}_2$ , each divalent  $\text{O}^{2-}$  connects to two  $\text{Si}^{4+}$  tetrahedral, which gives a nearly perfect three-dimensional polymerized network structure, shown in Figure 11. The slag is of ionic nature, and the oxides can be categorized depending on their ability to form simple or complex bonds [28].  $\text{SiO}_2$  is the most important acidic oxide, forming  $\text{SiO}_4^{4-}$  as in reaction 9, and is referred to as a network former.  $\text{CaO}$  is a basic oxide and will form simple cations,  $\text{Ca}^{2+}$  as in reaction 10 that will break up some of the  $\text{Si}^{4+}-\text{O}^{2-}$  bonds and replace them with ionic  $\text{Ca}^{2+}$  bonded to two  $\text{O}^-$  bonds.  $\text{CaO}$  is therefore referred to as a network breaker.  $\text{Al}_2\text{O}_3$  is an amphoteric oxide, which means that it can both have basic and acidic behavior, depending on the composition of the slag. In a silicate system, alumina forms  $\text{Al}^{3+}$  ions as in reaction 10 that balances the free oxygen ions and combine with free oxygen ions to form  $\text{AlO}_4^{5-}$  ions, as in reaction 11.  $\text{Al}^{3+}$  is more stable in an acidic region, while  $\text{AlO}_4^{5-}$  in a basic region, and the relation between  $\text{Al}^{3+}$  and  $\text{AlO}_4^{5-}$  ions will depend on the slag basicity. The ionic radii are related to the charge of an element, and generally cations in lower oxidation state are larger [25]. The metal-oxygen bonding in the oxides in lower oxidation states, like alkali and alkali earth metals, will be more ionic and hence they will be more basic than oxides of higher valence. Therefore, metal oxides with higher oxidation state, as  $\text{Al}_2\text{O}_3$ , are known as amphoteric, neutral. They behave like a basic oxide

in an acidic environment and as an acidic oxide in a basic environment. If  $Al_2O_3$  is added to the silicate network,  $Al^{3+}$  ions can be absorbed into the silicate structure. Thus, addition of  $Al_2O_3$  acts principally as network formers, but when large amounts are added to the slag the  $Al^{3+}$  ions can also act as network breakers. As there are different types of bonds between the  $Ca^{2+}$ -oxygen (ionic) and within the tetrahedron (covalent), silicate slags thermophysical properties are therefore very dependent upon the level of polymerization in the slag.

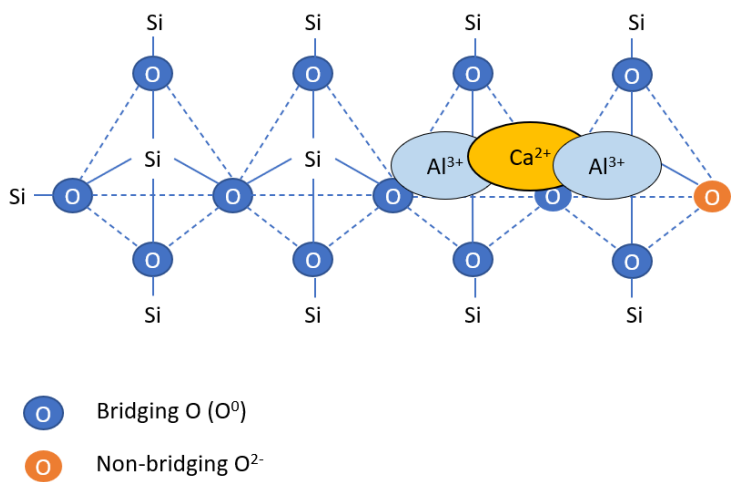


Figure 11 Schematic drawing showing the silicate ( $SiO_4^{4-}$ ) network system with blue bridging oxygen and one orange non-bridging oxygen. Cations  $Ca^{2+}$  and  $Al^{3+}$  breaks into the network.

The amount of the different components in the slag will also have an influence on how the oxygen ions bond to the system. Oxygen ions in the slag can be classified as either bridging oxygen (BO) or non-bridging oxygen (NBO). A bridging oxygen is bonded to two silicon ions, whereas a non-bridging oxygen is bonded to only one silicon ion. The amount of NBO in a slag system, also explained by the O/Si ratio, gives an idea of the extent of depolymerization in the slag [29]. An increasing value of O/Si ratio and hence a higher number of NBO in a slag system breaks up the silicate structure into smaller units. The smaller units will have higher mobility, which affects the overall structure and behavior of the slag.

Even though silicate melts are ionic, their thermodynamic properties must be described by their neutral oxides. The oxide components activities are the most common used. The  $SiO_2$  activities within the liquid region of the  $SiO_2$ - $CaO$ - $Al_2O_3$  system at  $1600^\circ C$  are shown in

Figure 12. Mao et al. [30] compares their results with earlier results from Kay and Taylor (1960) and Rein and Chipman (1963). The numbers in the diagram gives the activity values.

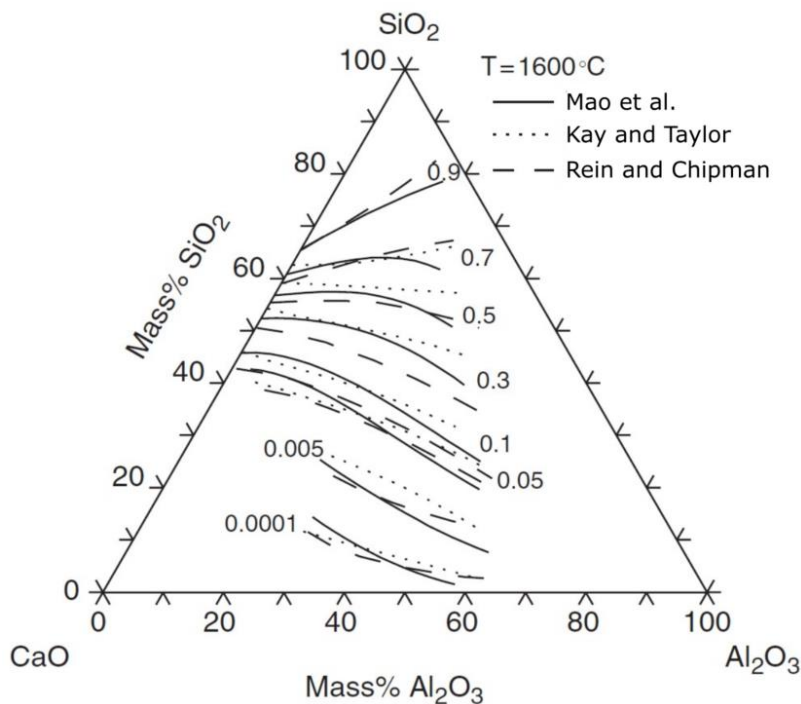


Figure 12 Isoactivity lines of  $\text{SiO}_2$  in stable liquid at 1600 °C from Mao et al. [30]. Their results are compared with the results from Kay and Taylor (1960) and Rein and Chipman (1963). The numbers in the diagram give the activity values.

### 2.1.3.2 Viscosity

The viscosity of the slag is defined as the resistance to flow of one layer of molecules over another and is related to the silicate structures [28]. The longer silicate network structure (smaller O/Si ratio), the more difficult the ability to flow. Basic oxides that break up the silicate structure into smaller units will decrease the viscosity. The viscosity of molten slags is hence dependent on the composition and temperature. The viscosity of the slag is one of the most important factors affecting the fluid flow in the furnace and is hence an important process variable. It is preferable to have a lower viscosity to ensure a good flow out of the furnace. The basicity is the ratio between the basic and the acidic oxides in a slag system and gives a measure of the polymerization and hence also of the viscosity. In the  $\text{SiO}_2$ - $\text{CaO}$ - $\text{Al}_2\text{O}_3$  system, the basicity, B can be defined as in equation 2.

$$B = \frac{\%CaO}{\%SiO_2 + \%Al_2O_3}$$

2

The network breaker  $\text{Ca}^{2+}$  breaks down the silicate chains and decrease the viscosity of the melt, while the network former  $\text{SiO}_4^-$  increases the viscosity. Slag of mainly  $\text{SiO}_2$  and  $\text{Al}_2\text{O}_3$  are sticky and more viscous and will more easily clog the furnace. The isoviscosity curves for the  $\text{SiO}_2$ - $\text{CaO}$ - $\text{Al}_2\text{O}_3$  system at  $1600^\circ\text{C}$  is shown in the left diagram in Figure 13. It can be seen that the amphoteric oxide  $\text{Al}_2\text{O}_3$  acts as a network former, increases the viscosity, when it is added to a basic slag. The effect increases with increasing basicity. The variation in viscosity within the liquid range of the system  $\text{Al}_2\text{O}_3 - \text{CaO} - \text{SiO}_2$  at  $1500^\circ\text{C}$  is shown in the right diagram in Figure 13. From this diagram, it can be seen that the contours are running nearly parallel to constant B, and that it is an escalation in the rate of viscosity at  $B < 0.15$ . It is important to note that the basicity model is valid only for a completely molten slag. Presence of any solid particles in the slag melt increases the viscosity considerably.

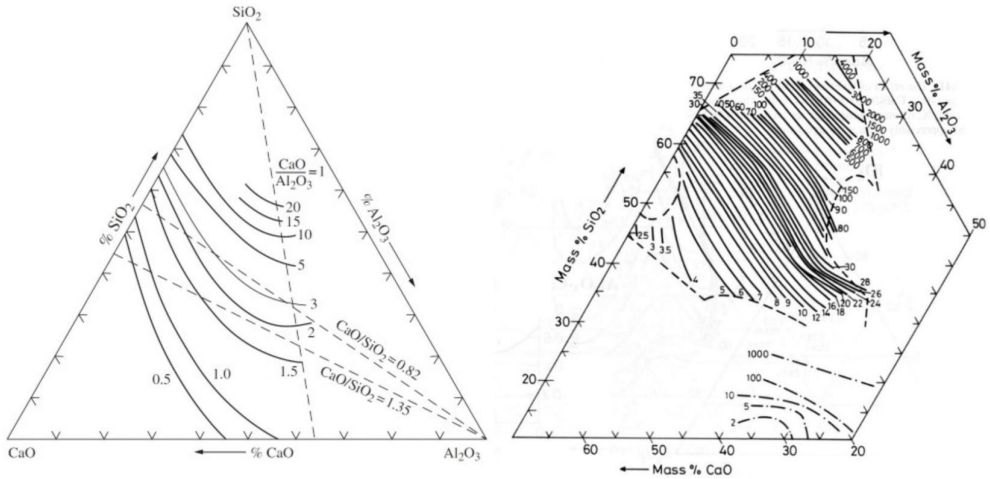


Figure 13 To the left in the figure is the isoviscosity curves for the  $\text{SiO}_2$ - $\text{CaO}$ - $\text{Al}_2\text{O}_3$  system at  $1600^\circ\text{C}$  [31], and to the right is the viscosity lines for liquid  $\text{Al}_2\text{O}_3$ - $\text{CaO}$ - $\text{SiO}_2$  slags at  $1500^\circ\text{C}$  [5].

The viscosity,  $\eta$  is also dependent on the temperature. In liquids, the viscosity decreases with increasing temperature and can be expressed by the Arrhenius equation as in equation 3 [28].

$$\eta = A \exp\left(\frac{E_\eta}{RT}\right) \quad 3$$

Where A is the frequency or pre-exponential factor,  $E_\eta$  is the activation energy for viscous flow of the slag, R is the universal gas constant and T is the temperature. There is no negative sign in front of  $E_\eta$  since the equation is derived from viscosity and not from a rate. Increasing temperature will loosen the network structure, and hence decrease the viscosity. Since the viscosity is also dependent on the structure, both the preexponential factor and the activation energy will be dependent and vary with the composition.  $E_\eta$  expresses the

difficulty of moving the chain from one position to another, which gives that acidic slag systems with longer chains have higher activation energies than basic slags with smaller chains. Viscosity-temperature data are usually presented in the form  $\ln \eta$  as a function of  $1/T$ , but for silicates this usually gives some curvature. In many cases it is found to give a better fit using the Weyman-Frenkel kinetic theory of liquids [32], given in equation 4. This equation accounts for the temperature dependency of the activation energy.

$$\eta = A_w T \exp\left(\frac{E_w}{RT}\right) \quad 4$$

Many researchers have tried to develop models to estimate viscosities of slag. The models are usually based on the composition and temperature dependency in various forms, e.g. [33]–[38]. The performance of the different models varies depending on the range of viscosity they cover. The estimated values from the models are expected to have uncertainties of ca  $\pm 25\%$ , which are in the same size range as the experimental uncertainties. The FactSage model for viscosity of liquid melts also relates the viscosity to the structure of the solution. The structure is calculated using the Modified Quasichemical Model. This model expresses the energy of pair formation as a function of composition for a multicomponent system [39], and the parameters are fitted to the experimental data for selected ternary oxide system. The “Melt viscosity database” is based upon measurements made above liquidus temperature or a bit below the liquidus for supercooled liquids.

### 2.1.3.3 Density

The density of the slag is defined as mass per unit volume and gives information on how the materials will distribute. The density is important in the lower parts of the furnace, in the silicon/slag bath and in the refining process, where it is important to have a sufficient metal-slag separation. Pure silicon at 1500-1900 °C has a density of  $\sim 2.4\text{-}2.5 \text{ g/cm}^3$  [40]. At temperatures below 1500 °C, most  $\text{SiO}_2\text{-CaO-Al}_2\text{O}_3$  slag are denser than liquid silicon. At temperatures  $>1500 \text{ °C}$ , which is the case in the lower parts of the Si and FeSi furnaces, the slag is in the same density area as silicon. This can be seen in the isodensity lines at 1550 °C for the  $\text{SiO}_2\text{-CaO-Al}_2\text{O}_3$  ternary system in Figure 14. The density decreases with increasing amount of  $\text{SiO}_2$  from  $2.66 \text{ g/cm}^3$  at 50wt%  $\text{SiO}_2$  to  $2.30$  at 70wt%  $\text{SiO}_2$ . Figure 15 shows density data from Slag Atlas [25] at different temperatures. In the blue circle are two similar compositions measured at 1480 °C and 1727°C and the density decreases by  $0.1 \text{ g/cm}^3$ . When the temperature increases, objects expand and become larger and therefore the density decreases. The density of the slag with the same composition further down in the furnace is hence lower than higher up in the furnace.

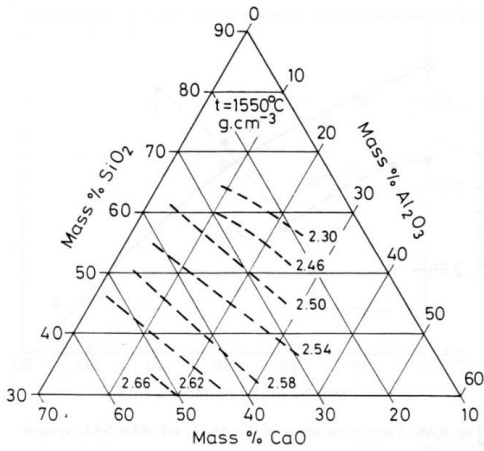


Figure 14 Isodensity lines for the  $\text{SiO}_2\text{-CaO-Al}_2\text{O}_3$  system at 1550 °C [25].

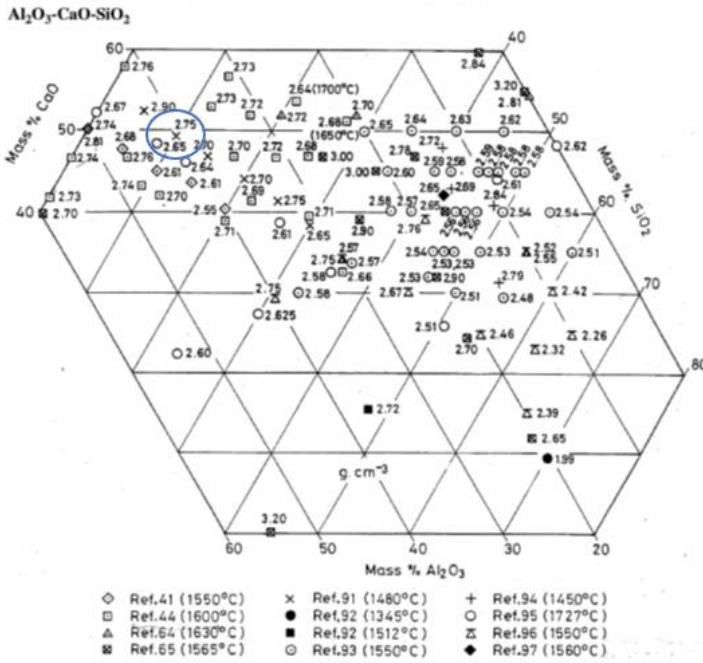


Figure 15 Densities in  $\text{g/cm}^3$  for different  $\text{SiO}_2\text{-CaO-Al}_2\text{O}_3$  slag compositions at different temperatures [25]. In the blue circle is two similar compositions measured at 1480 °C and 1727 °C and the density decreases by  $0.1 \text{ g/cm}^3$ .

As for the viscosity measurements, there are also technical difficulties and a high cost for doing experimental density measurements. It is therefore a high motivation for developing an accurate model for density calculations. Since the density is proportional to the reciprocal volume, most of the models are based on different ways to represent the molar volume. A short summary of many models were presented by Xin et al. [41], who also



developed a density model that calculated the molar volume of the slag according to molar volume of pure components and excess molar volume of the slag, as in equation 5. Compared with the viscosity models, the density models have small deviations from 0.12-5%. However, in all the density models it was a problem with including the composition dependence of the partial molar volume, which for Xin et al. were tried to account for with adding the excess molar volume to the equation.

$$V_m = \sum X_i V_i(T) + V^{EX} \quad 5$$

Where  $V_m$  is the molar volume of the slag,  $X_i$  is the mole fraction of component  $i$ ,  $V_i$  is the partial molar volume of component  $i$ ,  $T$  is the temperature and  $V^{EX}$  is the temperature-independent excess molar volume of the slag.

The density,  $\rho$  of molten slag could then be calculated from equation 6.

$$\rho = \frac{\sum X_i M_i}{V_m} \quad 6$$

Where  $M_i$  is the molar mass of component  $i$ .

#### 2.1.3.4 Surface tension and interfacial tension

The slag formed in the silicon furnaces is often found together with SiC and/or metal. An interface is a dividing plane of two contacting phases. High temperature reactions as slag-metal and slag-SiC take place at or through these interfaces. Interfacial properties are important thermodynamic properties which affect reaction kinetics, nucleation and formation of suspensions of solid particles or liquid droplets in molten slags. The surface or interfacial tension is defined as reversible work that is required to create a unit area of the surface at constant temperature, volume and chemical potentials [42], given in equation 7. If not otherwise stated, they are recorded at equilibrium conditions.

$$\gamma = \left( \frac{\partial G}{\partial A} \right)_{n,P,T} \quad 7$$

Where  $\gamma$  is the surface or interfacial tension given in mN/m,  $n$  is the number of phases,  $P$  is the pressure and  $T$  is the temperature.

Figure 16 shows the surface tensions for  $\text{SiO}_2$ -CaO- $\text{Al}_2\text{O}_3$  slags at 1600 °C [25], which represent the trend for these slags based on a large amount of collected data. This shows that the surface tension decreases with increasing  $\text{SiO}_2$  content up to 40wt%. In addition, it is found that the surface tension of liquids decreases with increasing temperatures. Silicate melts rich in  $\text{SiO}_2$  have a high degree of polymerization, which gives structural changes in

the melt caused by dissociation and formation of smaller anionic groups at higher temperatures. The extent depends on the composition of the slag and it is therefore difficult to look at the dependence on temperature without taking into account the chemical nature for these SiO<sub>2</sub>-rich compositions [5]. The interfacial tension also depends on the chemical nature of the phases. The less energy is required, the more chemically similar the phases are.

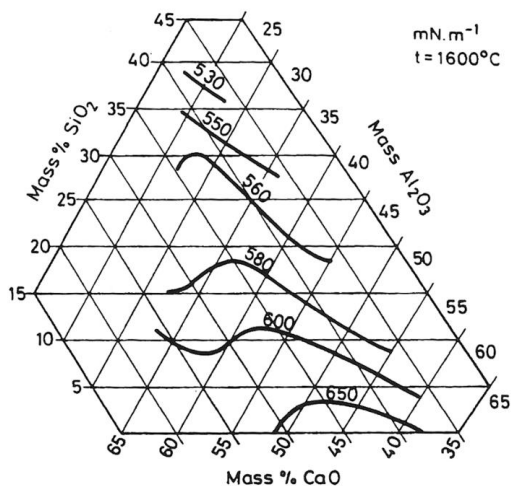


Figure 16 Isotension curves for SiO<sub>2</sub>- CaO-Al<sub>2</sub>O<sub>3</sub> melts at 1600 °C [25].

Dumay and Cramb [43] investigated the interfacial tension at 1450 °C between Fe-Si-alloys and two different SiO<sub>2</sub>-CaO-Al<sub>2</sub>O<sub>3</sub> slags.

- Slag 1: 36% SiO<sub>2</sub>-46% CaO-18% Al<sub>2</sub>O<sub>3</sub>
- Slag 2: 42% SiO<sub>2</sub>-42% CaO-16% Al<sub>2</sub>O<sub>3</sub>.

Their results are summarized in Figure 17 and are based on assumption that the two phases are in equilibrium. From this, the surface tension decreases with increasing Si content in the FeSi alloy.

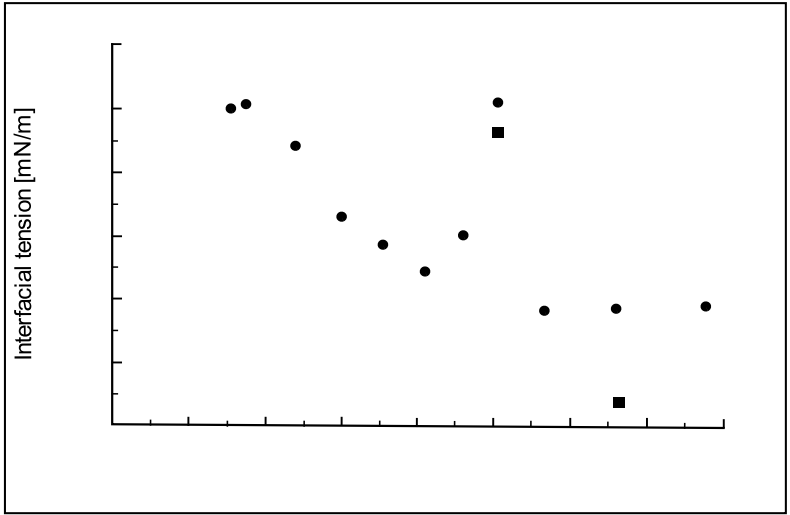


Figure 17 Interfacial tension between Fe-Si alloys and slags at 1450 °C from Dumay and Cramb [43].



## 2.2 Experimental procedure

When this work started in 2017, the knowledge about slag in industrial Si and FeSi furnaces was limited. Over the past 15 years, several excavations of industrial Si and FeSi furnaces have been conducted, and samples analyzed to increase the knowledge of the zones and materials within the furnaces. Previously, slag has not been the focus, but it is found that the amount of slag is one of the main differences between the different furnaces. Numerous industrial slag samples, accumulated slag from previous excavations, and slag from charge surface and tapped slag during operation have been collected. The primary objective has been to identify the types of slag present in the furnace and determine if there are any variations within different zones and among different furnaces.

### 2.2.1 Industrial samples

#### 2.2.1.1 *Accumulated slag*

Slag samples from five previous industrial excavations, four Si furnaces and one FeSi75 furnace, were selected for this study. The selection of samples was based on notes and reports written by the current excavation team [8]–[10], [20], [21]. Figure 18 illustrates schematic drawings of zones identified in four of the excavations; a) Wacker furnace no.1, b) Elkem Thamshavn, c) Wacker furnace no.4 and d) Elkem Salten. In all four cases, substantial amounts of slag were observed, both along the furnace walls, all the way up to the charge, and a layer covering the furnace bottom. Furthermore, the author was present during the Furnace B excavation in August 2019, which involved a Si-producing furnace. During this excavation, slag samples were collected from both higher and lower parts of the furnace as the excavator progressed deeper in the furnace. Additionally, samples were obtained from the Si tapping stream and adjacent slag layers. Table 2 summarizes important details of the furnaces and their respective excavations. According to the Elkem Salten report [10], it was mentioned that visually, Elkem Salten furnace 2 is similar to Wacker Chemicals furnace no. 1. The author of the report, Michal Ksiazek, was present during both excavations, as well as during the Elkem Thamshavn and Wacker Chemicals furnace no. 4 excavations.



Table 2 Furnace and excavation details from the six furnaces summarized.

Furnace excavation	Year of excavation	Production	Furnace and excavation details
Elkem Thamshavn, no2	2013	Si	-40MW -4.5m high from the shell to the top of the charge, 11.3m diameter - <u>not</u> burned down before shut-down -electrodes cut before excavation start
Wacker Chemicals Holla, no4	2015	Si	-33MW -~4m high, 8.5m inner diameter - <u>not</u> burned down before shut-down -electrodes cut before excavation start
Wacker Chemicals Holla, no1	2016	Si	-13MW -~3m high, 5m inner diameter -not burned down before shut-down -stopped with electrodes down in operating position
Elkem Salten	2018	Si	-36MW -5m high, 11m outer diameter -burned down -electrodes moved down to position 60cm after shut-down -when compared with other excavated Si-furnaces, Salten was most similar to Wacker 1 furnace [10]
Finnfjord	2018	FeSi75	-30MW -4.7m high, 8.8m inner diameter - <u>not</u> burned down before shut-down -only two tap-holes in use last period before shut-down, and the furnace was therefore oscillating instead of rotating
Furnace B	2019	Si	-40MW -4m high, 10m inner diameter -burned down before shut-down -tap-hole 7 last tapped

The approximate position where the slag samples were collected is shown in Figure 19. All samples from Furnace B are collected behind the same tap-hole no.3. The dimensions and electrode position are not included in the figure as these varies between the different furnaces. Different colors represent different furnaces. Table 3 lists the samples collected, divided in the three main areas of the furnaces: higher parts, lower parts and the tap-hole area of the furnaces. The borderline between the higher and lower parts of the furnace is the electrode tip. Pictures of a selection of the slag samples can be seen in Figure 20.

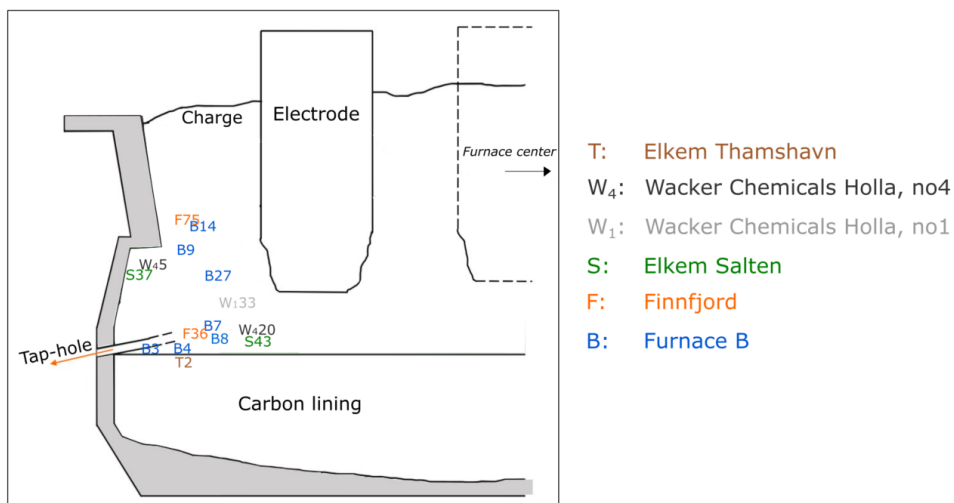


Figure 19 Overview of the samples analyzed. Different colors indicate different furnace. Dimensions and the positions of the electrodes are not included in the figure as this varies between the different furnaces. The samples position is based on distance from the tap-hole.

Table 3 Overview of the excavation samples analyzed and their position area in the furnace. The first letter in the sample ID is the same as the first letter of the plant they are collected from. The different colors are the same as in Figure 19.

Zone in the furnace	Sample ID
Higher parts	B-9, B-14, B-27, S-37, F-75, W1-33, W4-5
Lower parts	B-3, B-4, B-7, B-8, F-36, S-43, T-2
Tap-hole area	B-1, B-2, B-47, B-48a, B-48b, S-46, W1-114, W1-115, W4-20

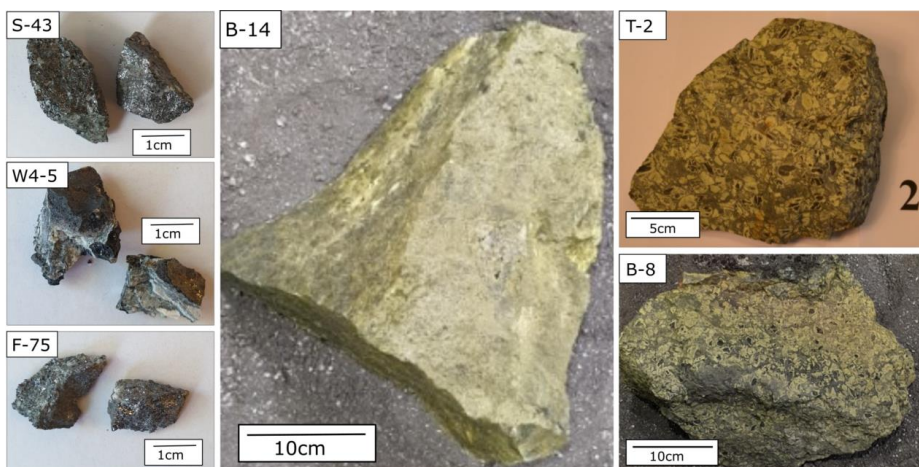


Figure 20 A selection of the analyzed excavation samples. Slag is most often green or grey in the furnace. Picture of T-2 is from Książek [20].



### 2.2.1.2 Tapped slag

Slag is also tapped together with the metal, and the properties of this slag will therefore have a great impact on the drainage of the furnace. In this study, tapped slag samples were obtained from two Si furnaces and two FeSi75 furnaces (located within the same plant). Regular sampling was conducted over a one-year period from furnace no.2 at Elkem Thamshavn. Additionally, three samples were collected from Furnace B in June 2020, approximately ten months after the excavation. An overview of dates, tap-hole, temperature in the ladle and electrodes position at time of sampling for the tapped slag samples from Elkem Thamshavn and Furnace B are listed in Table 4 and Table 5, respectively. Temperature measurements were carried out at various positions in the runner of the same furnace at Elkem Thamshavn, 6-12 months prior to the tapped slag sampling. These measurements revealed temperatures ranging from 1714-1830 °C [27], indicating that the temperature in the ladle is 100-300 °C lower than in the runner, approximately 1500-1600 °C. It should be noted that the temperature in the ladle can vary depending on the sampling time and method. As the ladle is filled with molten metal from the tap-hole, its temperature increases. Additionally, the temperature distribution within the ladle is not necessarily homogenous, but will be lower at the top. The temperature in the ladle for the samples from Furnace B was not measured. The electrode position indicates the vertical position of the electrode, measured from the electrode holder, and has a maximum value of 150 cm. The position gives the highest point for power supply and ideally, this correlates with the electrode tip position. Samples of tapped slag were also collected from two furnaces at Finnfjord, both of which run on the same type of raw materials. Most of the samples were obtained from furnace O, with some additional samples from furnace R. Both furnace O and R produce FeSi75 and have a maximum power of 42 MW and 45 MW respectively. It is worth noting that furnace R experienced maintenance issues during this period, leading to load and rotation variations. The samples from Finnfjord AS also include five high-viscosity slags. This is slag that is reported by the tapping operators as slag that clogs the tap-hole and makes tapping process difficult. Example of normal tapping slag and high viscosity slag can be observed in Figure 21. All samples obtained from Finnfjord AS are listed in Table 6.

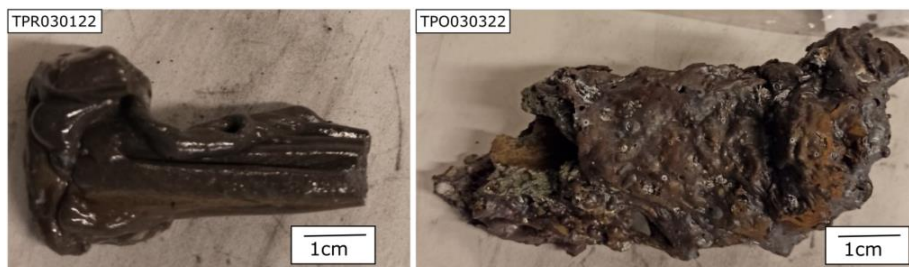


Figure 21 Two of the tapped samples from Finnfjord AS. TPR030122 is tapped during normal conditions, while TPO030322 is reported as high viscosity slag.

Table 4 Tapped slag samples collected from Elkem Thamshavn, May 2019 to May 2020. Tap-hole number, temperature in the ladle and electrodes position at time of sampling are also included in the table.

Date	Tap-hole no.	Temperature in ladle	Electrode pos.	Metal in ladle	
				%Ca	%Al
19-05.24	4	1480°C	*	0.542	0.683
19-06.05	2	1500°C	1: 86cm 2: 58cm 3: 68cm	0.469	0.651
19-08.18	5	1565°C	1: 70cm 2: 89cm 3: 47cm	0.589	0.651
19-10.26	7	-	-	-	-
19-12.03	3	1520°C	1: 83cm 2: 123cm 3: 99cm	0.335	0.548
19-12.04	3	1540°C	1: 30cm 2: 102cm 3: 84cm	0.506	0.704
19-12.07	4	1550°C	1: 81cm 2: 110cm 3: 82cm	0.778	0.884
19-12.09	5	1590°C	1: 114cm 2: 95cm 3: 59cm	0.484	0.700
20-01.10	7	1630°C	1: 75cm 2: 90cm 3: 91cm	0.627	0.757
20-02.07	5	1630°C	1: 52cm 2: 61cm 3: 56cm	0.514	0.655
20-05.05	2	1600°C	1: 59cm 2: 113cm 3: 105cm	0.268	0.453

Table 5 Tapped slag samples collected from Furnace B in June 2020. Tap-hole number and electrodes position at time of sampling are also included in the table.

Date	Tap-hole no.	Electrode pos.
20-06.09	5	1: 72.4cm 2: 82cm 3: 96cm
20-06.18	6	1: 105cm 2: 92cm 3: 100cm
20-06.19	6	1: 106cm 2: 89cm 3: 115cm

Table 6 Samples collected from Finnford AS, furnace O and furnace R. The last letter in the labeling indicates which furnace the samples are collected from. The samples are collected from September 2020 to March 2022.

Sample	Furnace power [MW]	Position	Rotation
TPR1709a	36	Tap-hole 2	Yes
TPR1809a	38	Tap-hole 3	Yes
TPR1809c	37	Tap-hole 3	Yes
TPR1909a	38	Tap-hole 3	Yes
TPR2209a	31	Tap-hole 3	No
TPR2309a	34	Tap-hole 3	Only 2 hours ahead
TPR2309b	34	Tap-hole 3	No
TPR2210a	30	Tap-hole 6	Yes
TPR2710	37	Tap-hole 7	Yes
TPR2810	35	Tap-hole 7	Yes
TPR0411	34	Tap-hole 1	Yes
TPR1311	24	Tap-hole 2	No

Sample	Furnace power [MW]	Position	Comments
TPO2209	40	Tap-hole 6	
TPO2210a	35	Tap-hole 4	
TPO1311	44	Tap-hole 1	
TPO2311	32	Tap-hole 5	High-viscosity slag
TPO1701a	44	Tap-hole 3	Rotation
TPO1701b	44	Tap-hole 3	Rotation
TPO1701c	44	Tap-hole 3	Rotation
TPO2601	44	Tap-hole 1	Rotation
TPO2302	41		High-viscosity slag
TPR3101	33	Tap-hole 4	
TPR0102.T3	23	Tap-hole 3*	No rotation
TPR0102.T5	23	Tap-hole 5	High-viscosity slag
TPR1202	33	Tap-hole 6	
TPR1402	32	Tap-hole 6	
TPR1802	27		
TPR0903	32	Tap-hole 7	
TPR1703N	19		
TPR27421	21	Tap-hole 5	
TPR261121	34	Tap hole 7	
TPX2022			High-viscosity slag, unknown furnace
TPR030122	35	Tap-hole 3	
TPO030322	32	Tap-hole 1	High-viscosity slag

\*Not the active tap-hole

### 2.2.1.3 Charge surface samples

Samples were also collected from the charge surface of Finnjord furnace O and R. The identification of materials present at the charge surface is valuable to help explain the furnace operation. When the operation is in good condition, only heated raw materials will be present at the charge top. When deviation from this situation occur, the materials may give knowledge on reactions in the furnace. The distribution of raw materials within the charge significantly affects the furnace operation. Sampling during operation, or short operational stops, can be related to the furnace condition during operation, and are in addition more economic, efficient and exact compared to samples taken during furnace excavations. The furnaces have a maximum power of 42 MW and 45 MW, respectively. The sampling was done in a period of 6 months. An overview of the samples is listed in Table 7. Some of the samples have also been used in another study by Jusnes et al. [44]. Most of the samples were large and heterogenous, as depicted in Figure 22, and were divided into multiple pieces. Different areas were selected for sampling. Many of the samples were classified based on visual observations, such as S for slag, P for porous, M for metallic, and K for quartz.

*Table 7 Samples collected from the charge top. Sample CPR1809a, CPR1809b, CPR1809c and CPR0211 are also used in another study [44].*

Sample		Comment
CPR1809a	Same time of sampling, different location	Charge top, unknown position
CPR1809b		Viscous matter between two electrodes
CPR1809c		0.5m from crust edge
CPR0211		Viscous matter
CPO1101		Large sample. Viscous and hard charge surface. Divided into S (slag), BK (brown condensate), M (metallic), K (quartz), P (porous), U (unknown)
GR1602		Viscous matter, glued together
CPR2502		Large sample. Divided into k (quartz), m (metallic), y (edge), a, b
CPR1903		Large areas with brown condensate

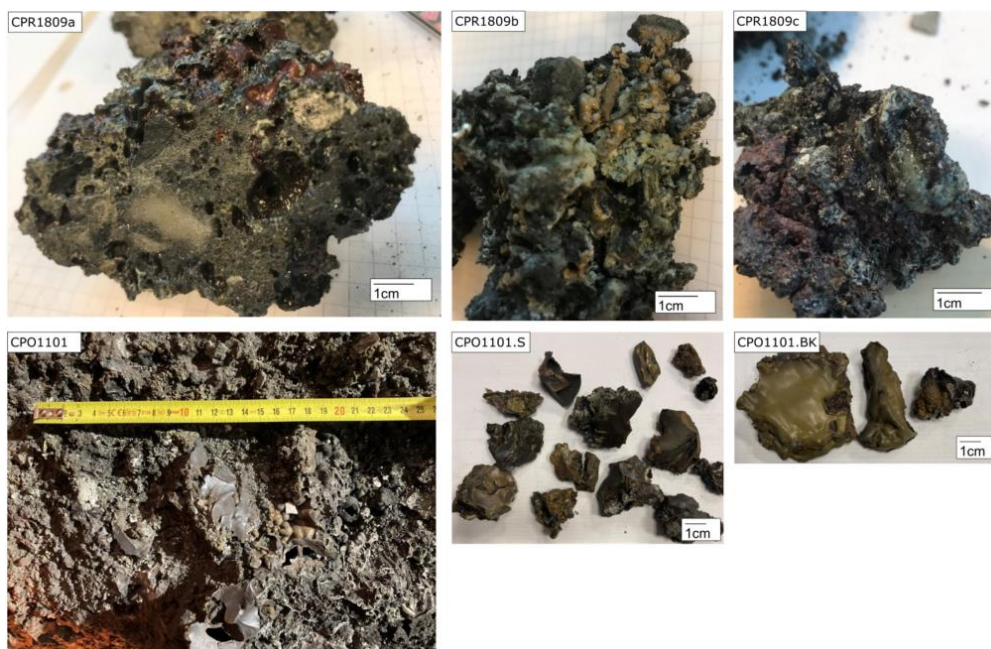


Figure 22 Sample CPR1809a, b, c and CPO1101, S and BK. The charge surface samples were heterogenous, and several samples were analyzed based on visual differences.

## 2.2.2 Collecting slag from industrial furnaces

### 2.2.2.1 Excavation of Furnace B

Samples obtained from furnace excavations play a vital role in mapping the zones and understanding the Si and FeSi processes since it is not possible with sampling inside the furnace during operation. The author was present during excavation of Furnace B. The sampling process during the excavation was carried out in collaboration with plant employees and a hired company responsible for the physical excavation. Communication was carried out through the use of walkie talkies, enabling continuous sample collection as the excavator progressed. The excavator collected samples after instructions from the metallurgists. The position of the samples is approximate, as it is not possible to physically enter the furnace and mark the exact positions due to health, safety, and environmental (HSE) restrictions. The positions are therefore based on images captured just before collecting the specific sample. Furnace and excavation details can be seen in Table 2. The furnace was opened from the side, outside tap-hole 3 and samples were collected continuously. In Figure 23 is picture at the start of the excavation and after 12 hours of excavation. Most of the sampling were done within the first 48 hours of the excavation. All collected samples were numbered, pictured, and stored for further investigation. Among the samples were several lumps obtained from different tap-holes, including zones around the Si tapping channel, as shown in Figure 24. One of these lumps was sent to Nidaros Domkirkes Restaureringsarbeider, where a cut-out plate was created, framed, and displayed

on the wall. The author organized the transportation of the sample and provided instructions during the cutting process. After the cutting, Dr. Michael Ksiazek and the author mounted the plate in cement and framed the plate.

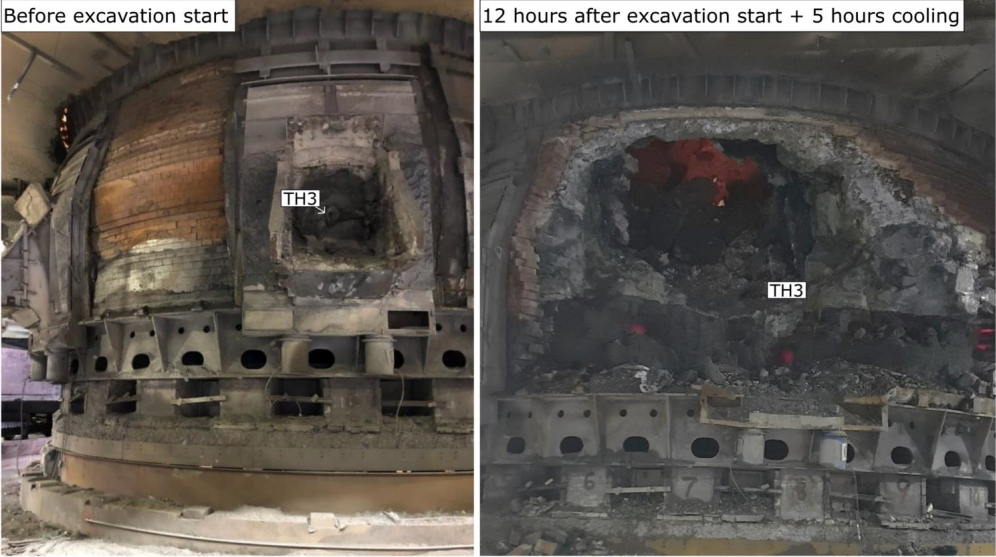


Figure 23 Furnace outside tap-hole 3 before excavation start (left) and after 12 hours of excavation (right).

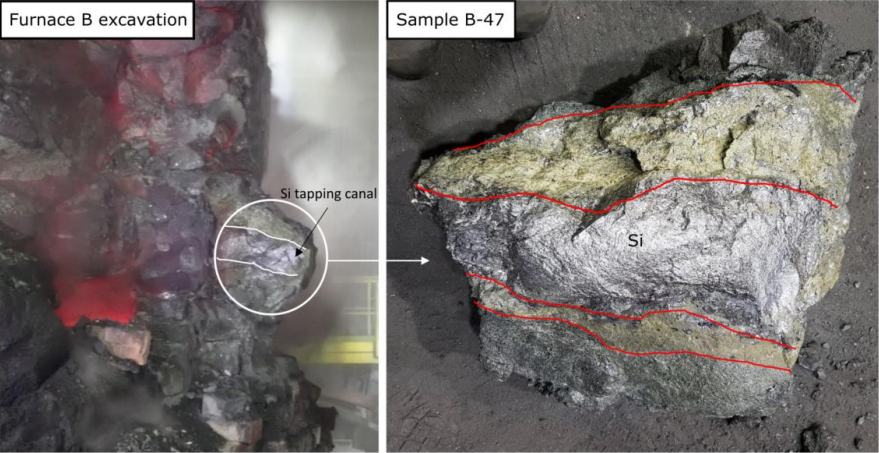


Figure 24 Sample including the Si tapping channel and the zones right next to it.

### *2.2.2.2 Slag from previous Si and FeSi excavations*

In the recent years, several excavations of Norwegian Si and FeSi furnaces have been conducted, with a metallurgical team from NTNU frequently present to collect samples for analysis. The objective for the sampling is to increase the knowledge of the zones and materials in the furnaces. Although slag has not been the focus of previous studies, reports indicate that several slag samples have been collected. The author has therefore retrieved samples from 5 previous Si and FeSi excavations from the archive. These excavations include Elkem Thamshavn in 2013, Wacker Chemicals Holla no2 in 2015, Wacker Chemicals Holla no 4 in 2016, Elkem Salten in 2018 and Finnfjord AS in 2018. The author has specially selected and gathered some of the reported slag samples for further analysis.

### *2.2.2.3 Tapped slag*

For the tapped slag samples from Elkem Thamshavn and Furnace B, a sampling technique using compressed paperboard was employed, as shown in Figure 25. The design was created in collaboration with employees at Elkem Thamshavn. The paperboard is attached to a steel rod, which can be utilized in the multitool tapping platform. It is designed to be used as a “spoon” to extract slag coming out from the tap-hole. Paperboard is used to avoid contamination of metals that affect the composition analysis. Due to the limited lifespan of the paperboard before it is burned, the sampling needed to be effective and new equipment was required before each sampling. To obtain slag with composition without any contamination it is important to find the optimal time for sampling. Tappers must regularly use equipment to maintain good drainage from the furnace, and some of them may affect the slag composition. For instance, blowing of oxygen through either aluminum or iron lances will consume the lances and result in higher Al- and Fe content in the slag. Therefore, sampling is conducted when the slag flows naturally from the tap-hole, rather than immediately after the use of other metals near the tap-hole. The author did the organizing before sampling and was present at the plant during the sampling of the first five samples, and the sample collected in January 2020. It was the same tapping operator, Sissel Mjøen, who collected the seven last samples and did the temperature measurements in the ladle and metal analysis with XRF. Information regarding the electrode tip position, metal analysis and tap-hole number were noted after instructions from the author.



Figure 25 Equipment used for sampling of tapped slag. The compressed paperboard is designed to be used as a “spoon” to dig out slag from the tap-hole.

At Finn fjord AS, slag samples were collected during or right after tapping using a carbon cup. At this time, a stream of slag often drips behind the flow of FeSi metal, as depicted in Figure 26. If the slag was not dripping, it was carefully knocked off and collected. Due to the distance of over 1000 km between Finn fjord AS and Gløshaugen NTNU, communication was carried out online. Dr. Karin F. Jusnes organized the sampling at Finn fjord AS and the author and held periodic meetings with Dr. Jusnes to ensure effective communication and ensure proper exchange and handling of information, and to make agreements before the next samplings.

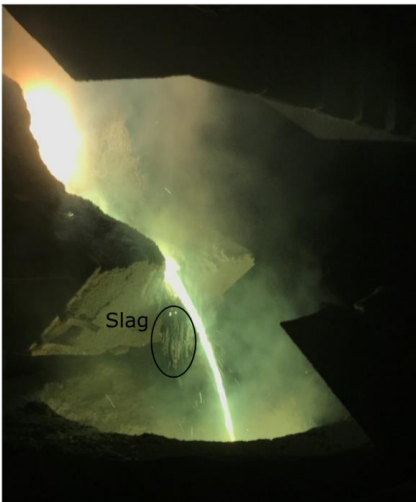


Figure 26 Solidified slag behind the FeSi metal flow in the tapping channel [44].



#### 2.2.2.4 Charge surface samples

Samples from two different FeSi75 furnaces, O and R, were collected from the charge surface. The samples were dragged out of the furnace with a stoking car by furnace operators when the furnace operation was reduced or during a planned maintenance stop.

### 2.2.3 Characterization

#### 2.2.3.1 Electron probe micro-analysis

Electron probe micro-analysis (EPMA), JEOL JXA 8500 was used to investigate all industrial slag samples. EPMA images were captured at magnifications of 40X, 200X and 400X. Higher magnifications are used for some of the samples to show finer details. Representative areas were chosen for images and for further analysis. To quantify the different elements in the samples, the oxide compositions were found using wavelength-dispersive X-ray spectrometer (WDS). The composition of the samples can be determined through either spot analysis or defocused area analysis. The last case gives the average composition within the selected area, typically 1 mm<sup>2</sup>. In some samples, the presence of small SiC particles made the oxide analyses challenging due to contamination. Most of the samples were analyzed using spot-analysis, but in cases where the areas were too small to separate different phases, defocused area analyses were conducted.

The results are considered as reliable if the total column mass percent in the analysis falls within the range of 97-103. All samples were solid when analyzed, while they were most likely in liquid state during operation. Due to precipitation of phases during solidification some slag may appear as heterogenous. In those situations, an estimation of the distribution between the different phases is performed through visual observation of the structure. The lever rule is used to calculate the liquid slag composition based on the percentage distribution of each solidified phase, as shown for SiO<sub>2</sub> in SiO<sub>2</sub>-CaO-Al<sub>2</sub>O<sub>3</sub> slag in equation 8.

$$\%SiO_2 = \sum_{i=1}^n \frac{(\%SiO_2)_i}{(\%SiO_2 + \%CaO + \%Al_2O_3)_i} * (\%phase)_i \quad 8$$



## 2.3 Results

### 2.3.1 Accumulated slag

#### 2.3.1.1 Excavation of Furnace B

In August 2019, an excavation of an Elkem Si furnace was conducted due to damage in the bottom lining. The furnace had an inner diameter of 10m and 4m height. The excavation was carried out by opening the furnace outside tap-hole 3, and most of the samples in this study were collected behind this tap-hole. Photos of the furnace before excavation start and after the first 12 hours of excavating can be seen in Figure 27. The main focus of the investigation was to examine the slag in different zones of the furnace. Therefore, only samples believed to be slag were further investigated. However, other samples containing such as  $\text{SiO}_2$ ,  $\text{SiC}$  and condensate were also collected and stored.

The furnace was burned down before shut-down, and a lot of slag is therefore expected to have escaped the furnace during this process. This means that during operation, there may have been more slag with different compositions around the last tapped tap-hole area. Tap-hole 7 (sample B-47) was the last tapped tap-hole before shut-down, but no visual differences were observed compared to the other tap-holes.



Figure 27 Photos of Furnace B taken right before excavation start and after the first 12 hours of excavating. The position of tap-hole 3 is marked in both images.

#### 2.3.1.1.1 The beginning of the excavation: behind tap-hole 3

During the excavation, the first samples were collected outside tap-hole 3. At this point, it was assumed the zones were approximately the same as when the furnace stopped. However, as the excavation progressed and materials were moved around, it became difficult to determine the exact original positions of most of the collected materials. An approximate range of  $\pm 1\text{m}$  must be taken into account when considering the positions of the materials.

In this study, seven samples from behind tap-hole 3 were analyzed: B-3, 4, 7, 8, 9, 14 and 27. Table 8 provides an overview of the samples, including a short description and references to their figures. The approximate position of the samples in the furnace are marked in Figure 19 in section 2.2.1.1 Accumulated slag. All of the samples primarily consisted of  $\text{SiO}_2\text{-Al}_2\text{O}_3\text{-CaO}$  slag and  $\text{SiC}$ . Some of the samples also contained areas with  $\text{Al}_2\text{O}_3$  and some small droplets of Si and/or FeSi.

Table 8 Overview of the samples collected from Furnace B behind tap-hole 3. Lower parts of the furnace is below the electrode tip, while higher parts is above the electrode tip.

Sample	Figure	Description	
Lower parts of furnace	B-3	Figure 28	One of the first samples collected right below tap-hole 3. Two smaller areas were analyzed and are marked in the photo from the plant. B-3.1 contains both smaller and larger particles of SiC, SiO <sub>2</sub> -CaO-Al <sub>2</sub> O <sub>3</sub> slag, in addition to some Al <sub>2</sub> O <sub>3</sub> and Si. In sample B-3.2 it is mostly Si, SiC and Al <sub>2</sub> O <sub>3</sub> . No SiO <sub>2</sub> -CaO-Al <sub>2</sub> O <sub>3</sub> slag phase were found in this sample.
	B-4	Figure 29	Collected near the furnace bottom. Both B-4.1 and B-4.2 are similar and contains Si/FeSi, SiO <sub>2</sub> -CaO-Al <sub>2</sub> O <sub>3</sub> slag, and larger and smaller particles of SiC.
	B-7	Figure 30	Collected approximately 1 m to the left side of tap-hole 3. Both B-7.1 and B-7.2 consist of larger and smaller particles of SiC together with SiO <sub>2</sub> -CaO-Al <sub>2</sub> O <sub>3</sub> slag. Sample B-7.2 also have some small particles containing Ti. In sample B-7.1 the slag has solidified into two separate phases, ~80% darker colored and ~20% white colored.
	B-8	Figure 31	Collected from the lower part of the furnace. Both B-8.1 and B-8.2 contain larger and smaller particles of SiC, SiO <sub>2</sub> -CaO-Al <sub>2</sub> O <sub>3</sub> slag and larger areas with Al <sub>2</sub> O <sub>3</sub> .
Higher parts of furnace	B-9	Figure 32	Was collected higher up in the furnace, approximately 1 m above tap-hole 3. Both B-9.1 and B-9.2 consist of SiC, SiO <sub>2</sub> -CaO-Al <sub>2</sub> O <sub>3</sub> slag, Al <sub>2</sub> O <sub>3</sub> and some Si/FeSi. In addition, there was a small area with particles containing Al, N, Si and O. This was not found in any other samples in the furnace.
	B-14	Figure 33	Collected from above tap-hole 3, approximate 1 m to the right from sample B-9. Both parallels consist of a SiO <sub>2</sub> rich slag phase (~ 80 %), smaller and larger particles of SiC, and some Si droplets. Sample B-14.1 also contains SiO <sub>2</sub> .
	B-27	Figure 34	Collected from approximately 0.5 m above and 0.5 m to the right side of tap-hole 3. The sample has a similar look as sample B-8, which is collected from approximately 1 m below the same tap-hole. The samples consist of smaller and larger particles of SiC, a SiO <sub>2</sub> -CaO-Al <sub>2</sub> O <sub>3</sub> slag phase and Al <sub>2</sub> O <sub>3</sub> . B-27 also look similar as B-8 in the EPMA images.

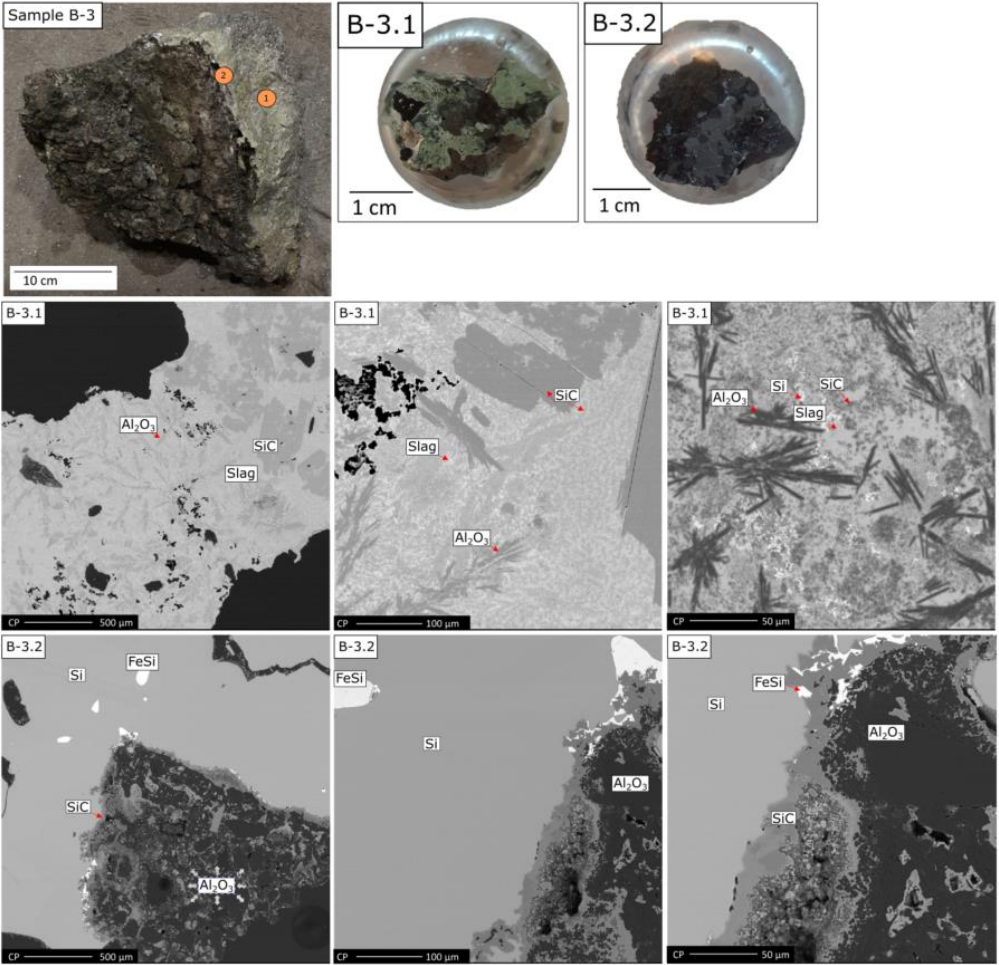


Figure 28 The top three pictures are taken at the plant and parallels of B-3 after mounted in epoxy. Below are sample B-3.1 and B-3.2 shown with three different magnifications, 40X, 200X and 400X. B-3.1 contains mostly SiC,  $Al_2O_3$  and a slag phase, in addition to some Si. B-3.2 contains mostly Si/FeSi, SiC and  $Al_2O_3$ .

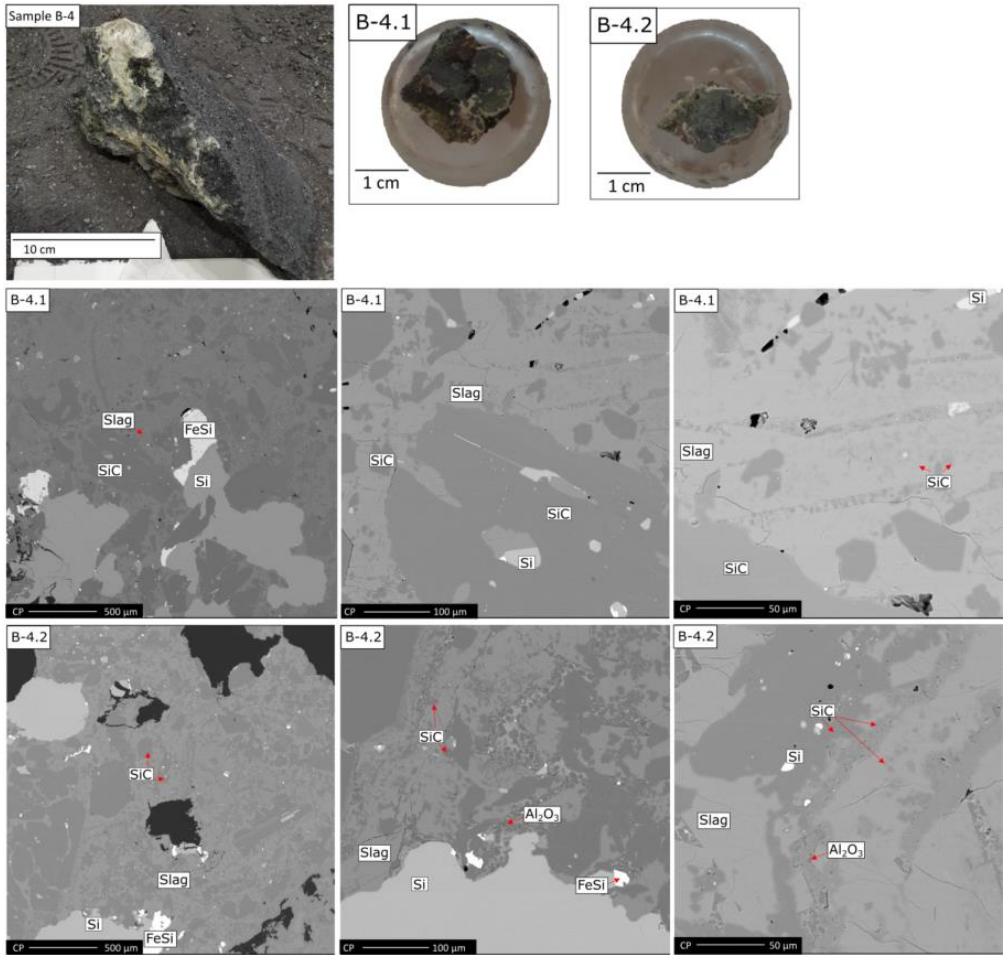


Figure 29 The top three pictures are taken at the plant and parallels of B-4 after mounted in epoxy. Below are sample B-4.1 and B-4.2 shown with three different magnifications, 40X, 200X and 400X. Both B-4.1 and B-4.2 contain Si/FeSi, SiO<sub>2</sub>-CaO-Al<sub>2</sub>O<sub>3</sub> slag and larger and smaller particles of SiC.

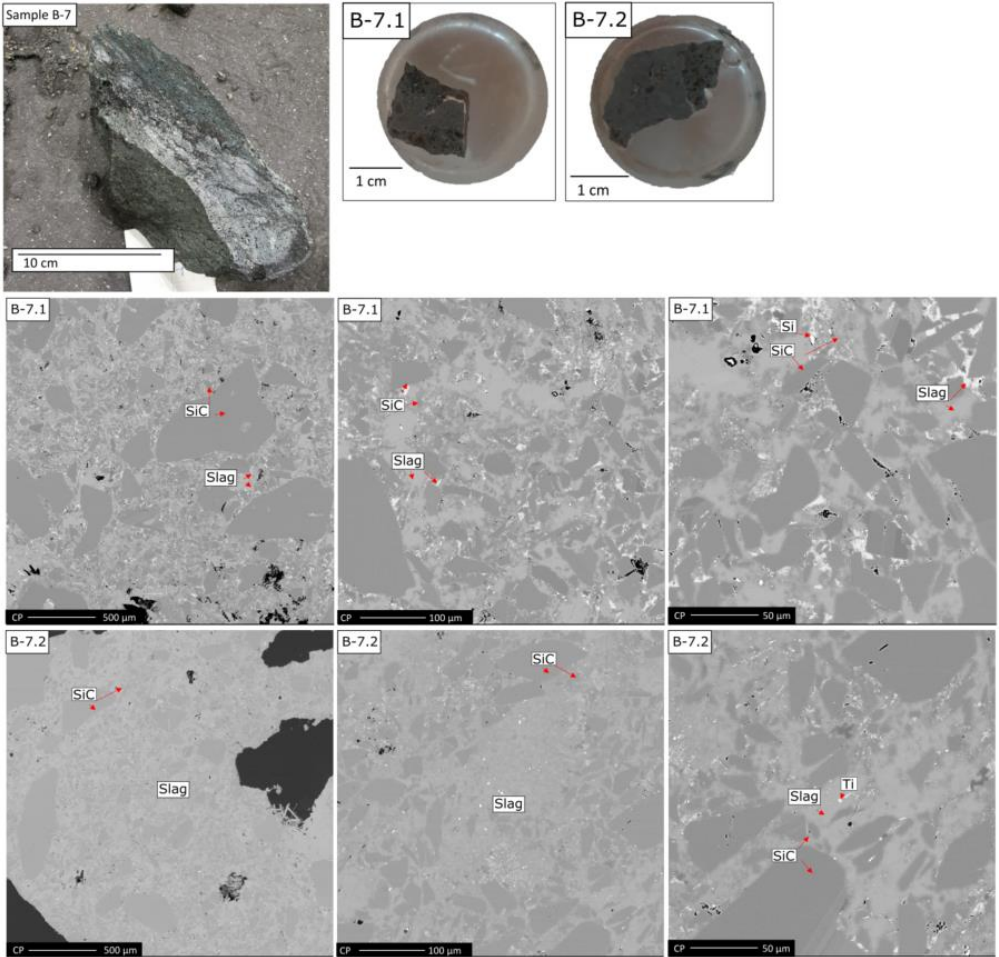


Figure 30 The top three pictures are taken at the plant and parallels of B-7 after mounted in epoxy. Below are sample B-7.1 and B-7.2 shown with three different magnifications, 40X, 200X and 400X. Both B-7.1 and B-7.2 consist of smaller and larger particles of SiC, and  $\text{SiO}_2\text{-CaO-Al}_2\text{O}_3$  slag. The slag in B-7.1 has solidified into two separate phases, 80% darker and 20% brighter slag. The white areas in B-7.2 is titanium.



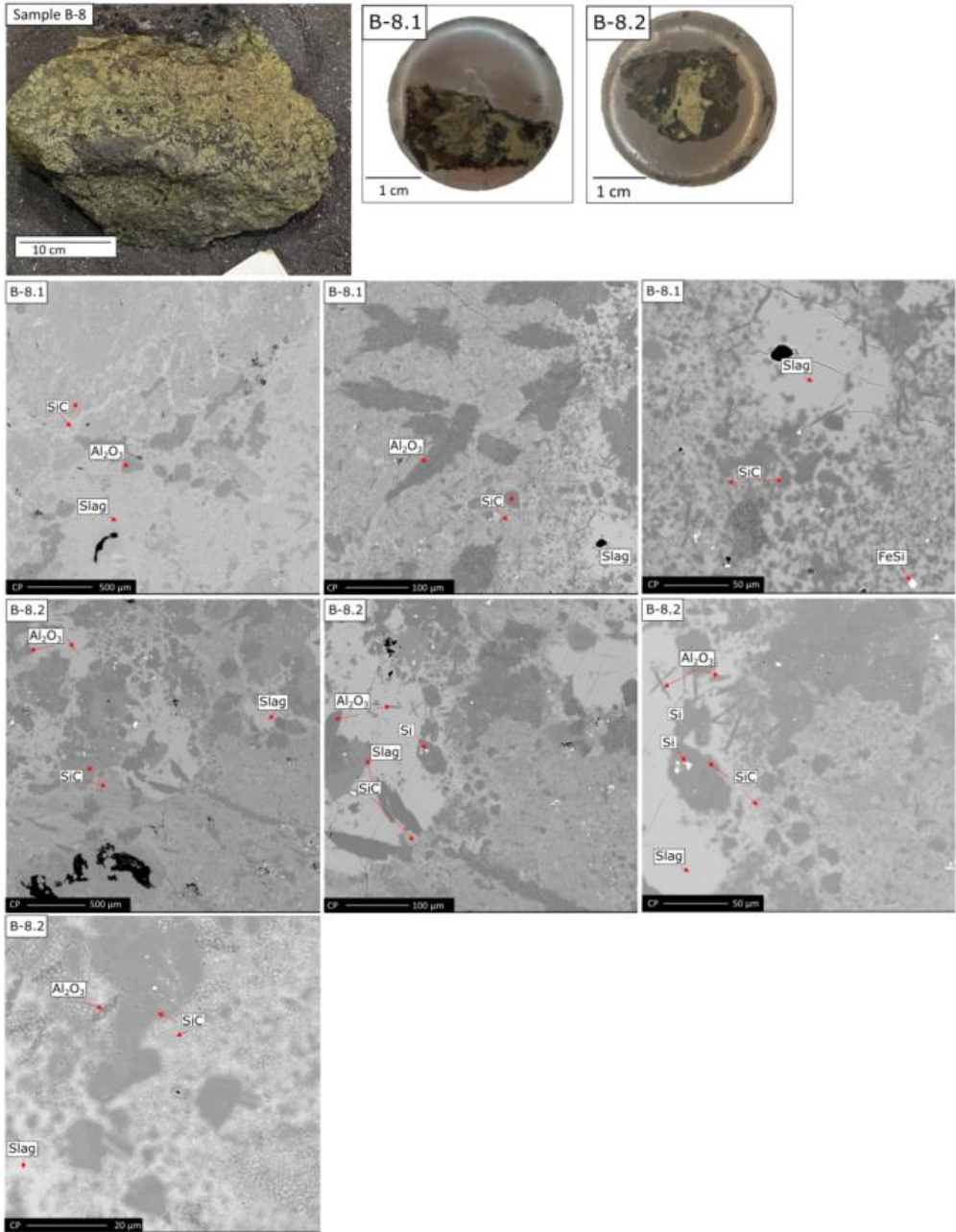


Figure 31 The top three pictures are taken at the plant and parallels of B-7 after mounted in epoxy. Below are sample B-7.1 and B-7.2 shown with three different magnifications, 40X, 200X and 400X. Both B-8.1 and B-8.2 contain smaller and larger particles of SiC, SiO<sub>2</sub>-CaO-Al<sub>2</sub>O<sub>3</sub> slag phase and Al<sub>2</sub>O<sub>3</sub>.

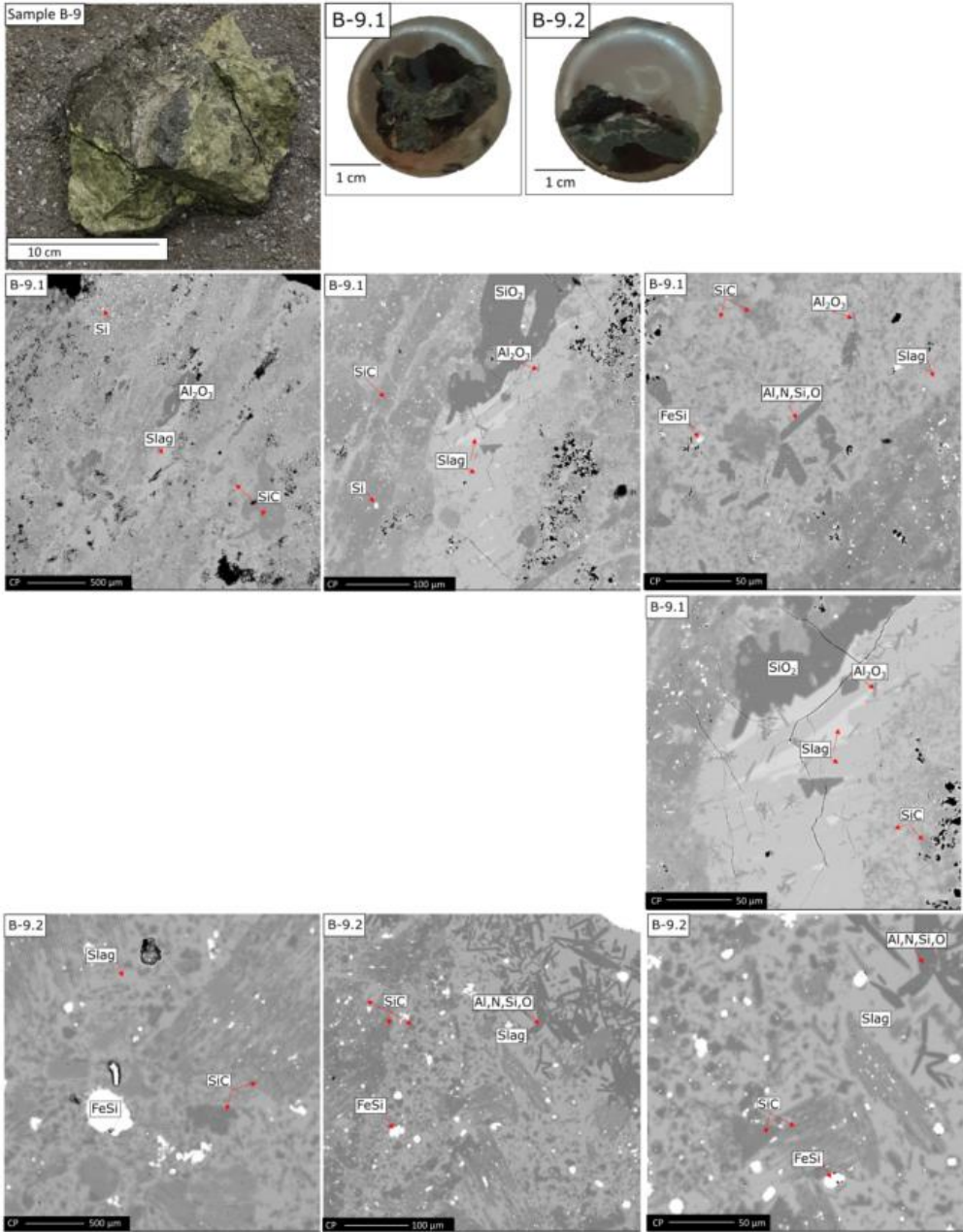


Figure 32 The top three pictures are taken at the plant and parallels of B-9 after mounted in epoxy. Below are sample B-9.1 and B-9.2 shown with three different magnifications, 40X, 200X and 400X. Both B-9.1 and B-9.2 contain particles of SiC, SiO<sub>2</sub>-CaO-Al<sub>2</sub>O<sub>3</sub> slag phase, Al<sub>2</sub>O<sub>3</sub> and Si/FeSi. The slag in B-9.1 has solidified into two separate phases, 90% darker and 10% brighter slag. There is also found Al, N, Si and O, shown in the bottom left image. This was not found in any other zones in this furnace.

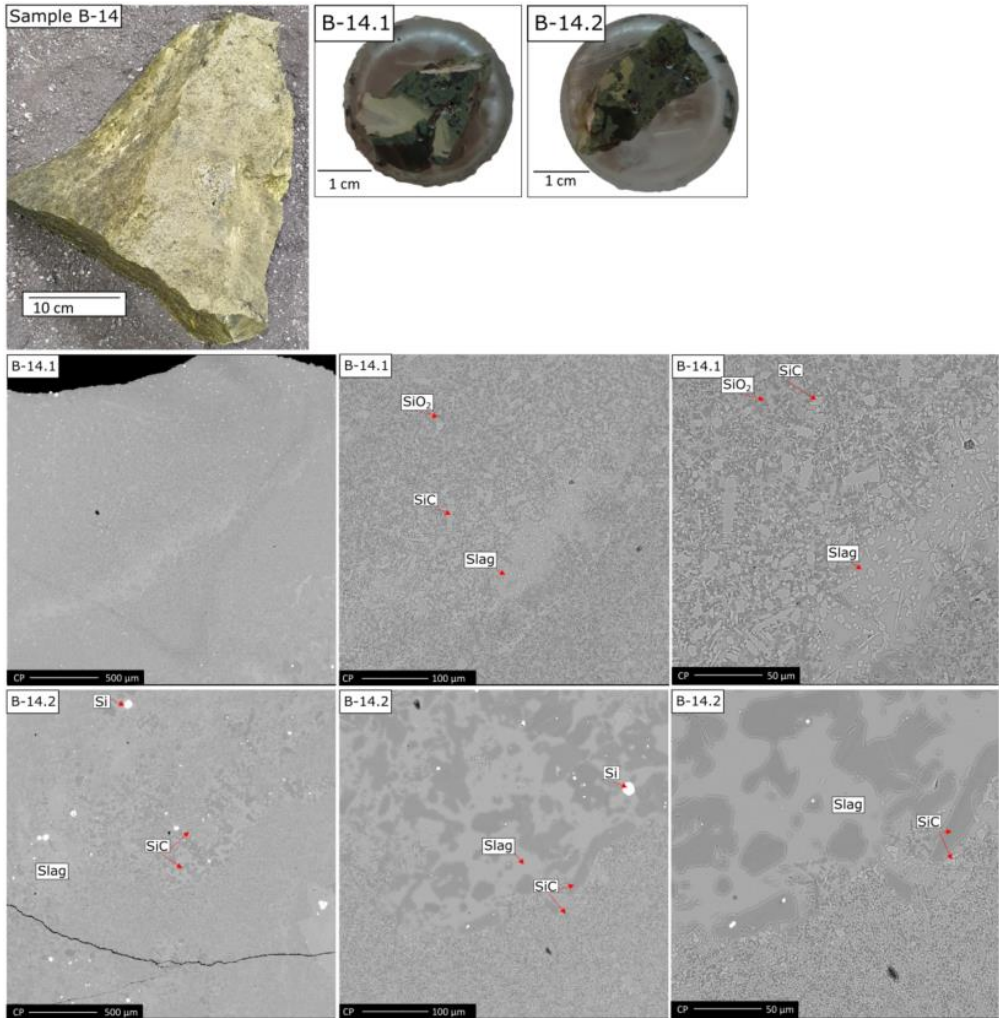


Figure 33 The top three pictures are taken at the plant and parallels of B-14 after mounted in epoxy. Below are sample B-14.1 and B-14.2 shown with three different magnifications, 40X, 200X and 400X. In B-14.1, there are a lot of small SiC particles in a  $\text{SiO}_2\text{-CaO-Al}_2\text{O}_3$  slag phase or a  $\text{SiO}_2$  matrix. B-14.2 contains two areas, one with smaller SiC particles and a  $\text{SiO}_2\text{-CaO-Al}_2\text{O}_3$  slag phase, and one with larger SiC particles an  $\text{SiO}_2\text{-CaO-Al}_2\text{O}_3$  slag.

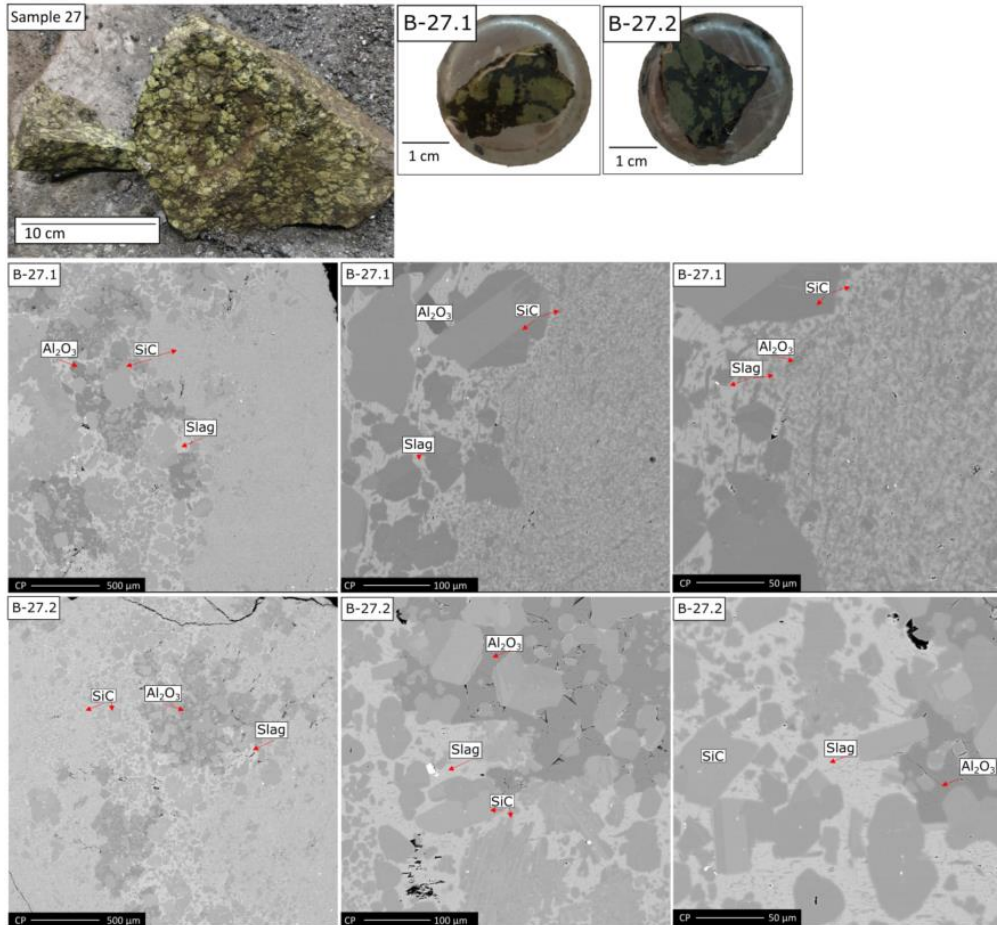


Figure 34 The top three pictures are taken at the plant and parallels of B-27 after mounted in epoxy. Below are sample B-27.1 and B-27.2 shown with three different magnifications, 40X, 200X and 400X. Both B-27.1 and B-27.2 have two different areas: one with smaller particles of SiC and one with larger SiC particles, both with SiO<sub>2</sub>-CaO-Al<sub>2</sub>O<sub>3</sub> slag and Al<sub>2</sub>O<sub>3</sub>.

Table 9 provides the normalized results of the WDS analysis conducted on all areas with slag. Since elements other than SiO<sub>2</sub>, CaO and Al<sub>2</sub>O<sub>3</sub> make up less than 1 mass percent, it is assumed that SiO<sub>2</sub>-CaO-Al<sub>2</sub>O<sub>3</sub> ≈ 100%. The table also includes the liquidus and solidus temperature, confirming that the slag is liquid at temperatures above 1540 °C. The original WDS data for the samples from behind tap-hole 3 can be found in Table 46 in Appendix A.

The general trend is that slag from the higher, inactive parts of the furnace has a higher SiO<sub>2</sub> content. Sample B-9, B-14 and B-27, which were collected higher up in the furnace, also contain smaller amounts of K<sub>2</sub>O and/or MgO. This is most likely from the impurities in the raw materials. It can also be noticed higher viscosity values for most of the slag in the higher parts of the furnace both at 1600 °C and 1800 °C.

Additionally, in sample B-9, areas containing oxynitride were found. The element analysis for these areas are listed in Table 10. Oxynitride was not found in any of the other samples from the Furnace B excavation, and the author have not found any mention of this in reports from previous Norwegian Si and FeSi excavations.

Table 9 Normalized WDS analysis for B-3, B-4, B-7, B-8, B-9, B-14, B-27. Liquidus and solidus temperature are found from the ternary diagram and are given in °C. The viscosity data are calculated from FactSage 8.1, given in Poise.

Sample	Oxide analysis					T <sub>liquidus</sub> [°C]	T <sub>solidus</sub> [°C]	Viscosity [Poise]	
	SiO <sub>2</sub>	CaO	Al <sub>2</sub> O <sub>3</sub>	K <sub>2</sub> O	MgO			1600°C	1800°C
B-3.1	37	26	37			1490	1265	17	4
B-4.1	44	21	35			1540	1170	39	8
B-4.2	44	21	35			1540	1170	39	8
B-7.1	34	37	29			1440	1265	5	2
B-7.2	44	21	35			1540	1170	39	8
B-8.1	46	21	33			1530	1170	44	9
B-8.2	45	21	34			1530	1170	41	8
B-9.1	49	17	33		1	1540	1512	69	12
B-9.2	67	10	23			1500	1512	519	67
B-14.1	85	2	9		4	1520	1170	5260	557
B14.2	79	4	13	3	1	1450	1170	2274	249
B27.1	49	19	32			1530	1512	63	12
B27.2	51	17	32			1520	1512	86	15

Table 10 Oxynitride analysis for sample B-9.

Sample	Solidified phase	Al	N	Si	O	Total
B-9.1	Oxynitride	1.1	28.1	50.3	15.4	95.0
B-9.2	Oxynitride	0.7	27.0	51.1	16.1	94.9

### 2.3.1.1.2 Samples next to the Si tapping channel

Five samples were collected from three different tap-holes, which included parts of the tapping channel together with the adjacent zones. While the other samples were from different parts in the furnace behind tap-hole 3, these have known position next to the tap-hole. These samples are B-48a and B-48b from tap-hole 1, B-1 and B-2 from tap-hole 3, and B-47 from tap-hole 7. Visually, the zones around all the tap-holes appeared similar. Closest to the Si channel is an approximately 5-15 cm thick green layer, followed by a dark grey layer.

Unfortunately, one of the samples from tap-hole 3 (B-2) and the sample from tap-hole 7 (B-47), were crushed into smaller pieces at the plant due to a misunderstanding with the excavators. Consequently, the analyzed samples were chosen based on their colors.

This result chapter includes EPMA images from sample B-48a, both from the green and grey zones. Table 11 lists an overview of all collected tap-hole samples, and a short

description. All pictures from the plant and all EPMA images are included in Appendix A and are referenced to in the table.

*Table 11 Overview of the tap-hole samples collected from taphole 1, 3 and 7. In all samples there were a green zone next to the Si, and next a dark grey zone. Both the green and the grey zone consists of SiO<sub>2</sub>-CaO-Al<sub>2</sub>O<sub>3</sub> slag and SiC.*

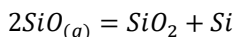
Tap-hole no.	Sample	Figure	Description
1	B-48a	Figure 35, Figure 36, Figure 37	From the upper part of the Si tapping channel. A cross section plate that shows the zones next to the Si canal was made from this sample.
	B-48b	Figure 180 Figure 181 Figure 182	From the lower part of the Si canal
3	B-1	Figure 184	From below the tap-hole. B-2 was unfortunately crushed into smaller pieces by the excavators. The analyzed areas are therefore chosen based on colors.
	B-2	Figure 185	
7	B-47	Figure 188 Figure 189 Figure 190	This sample did originally contain the zones from both above and below the Si tapping channel. Unfortunately, this sample was crushed into smaller pieces by the excavators. The analyzed areas are therefore chosen based on colors.

A cross section plate was made from sample B-48a (tap-hole 1), which includes the zones adjacent to the Si tapping channel. Figure 35 displays, with the left image showing the tap-hole during the excavation of Furnace B, and the right image showing the cut-out plate of B-48a that visualizes the typical look of the zones around the Si tapping channel. The analyzed areas are marked in orange on the plate, corresponding to the numbers in Figure 36 and Figure 37.

Figure 36 shows the EPMA images from the green zone next to the Si tapping channel. Sample B-48a 1 is from the layer closest to the Si canal and closest to the tap-hole. The first parallel consists of mainly SiO<sub>2</sub>, and the white areas are Si. This is most probably from condensed SiO gas as in reaction 3. The second parallel contains SiC particles, and SiO<sub>2</sub>-CaO-Al<sub>2</sub>O<sub>3</sub> slag that has solidified into two phases.

B-48a 2 is also from the layer closest to the Si channel, but from deeper in the furnace. Both parallels contain SiC particles, SiO<sub>2</sub>-CaO-Al<sub>2</sub>O<sub>3</sub> slag and some smaller Si droplets.

EPMA images from the grey zone are shown in Figure 37. B-48 3, 4 and 5 are large particles of SiC, SiO<sub>2</sub>-CaO-Al<sub>2</sub>O<sub>3</sub> slag and Al<sub>2</sub>O<sub>3</sub>. The samples from the grey area have larger SiC particles compared to those in the green zone.



3

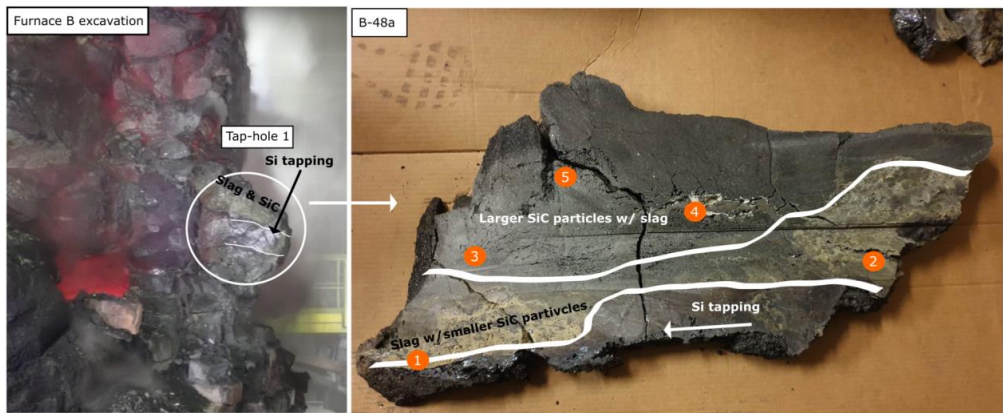


Figure 35 Picture during the excavation of Furnace B showing the area around tap-hole 1, and the cut out plate of sample B-48a, visualizing the Si tapping channel and the zones next to it. Marked in orange on the sample are the analyzed areas which corresponds to the number on the EPMA images and the WDS analysis in the next figures and tables.

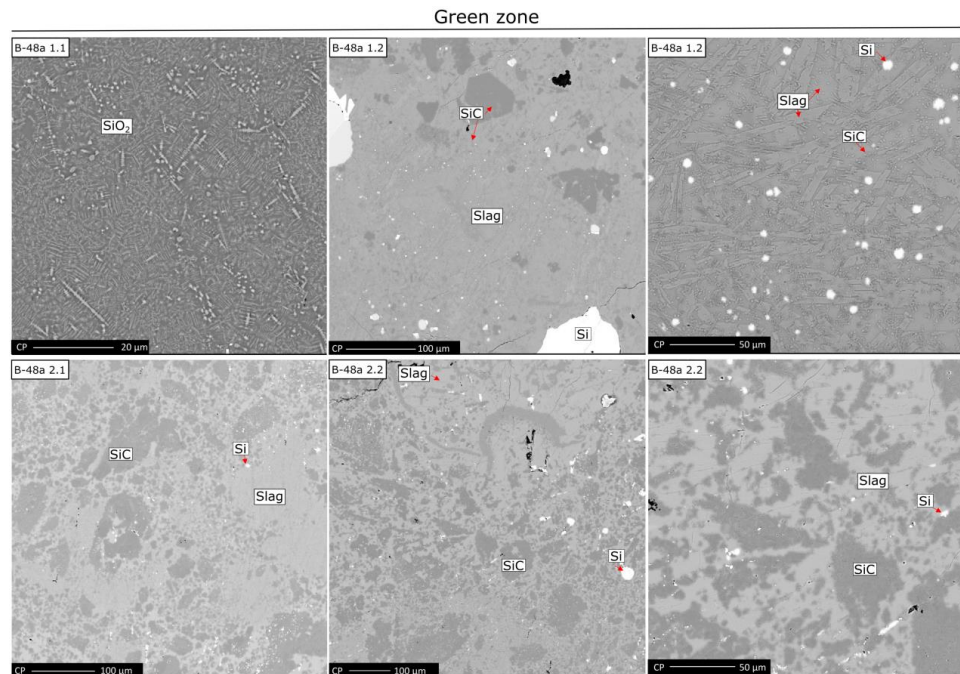


Figure 36 In the top left image is sample B-48a 1.1 which appears to be condensate. The analyzed grey area is mainly  $\text{SiO}_2$  and the white areas are Si. Sample B-48 1.2 consists of a  $\text{SiO}_2$ -rich slag phase and SiC particles, in addition to some Si and FeSi. Both 2.1 and 2.2 contain mostly SiC and  $\text{SiO}_2$ -CaO- $\text{Al}_2\text{O}_3$  slag, and some Si.

## Grey zone

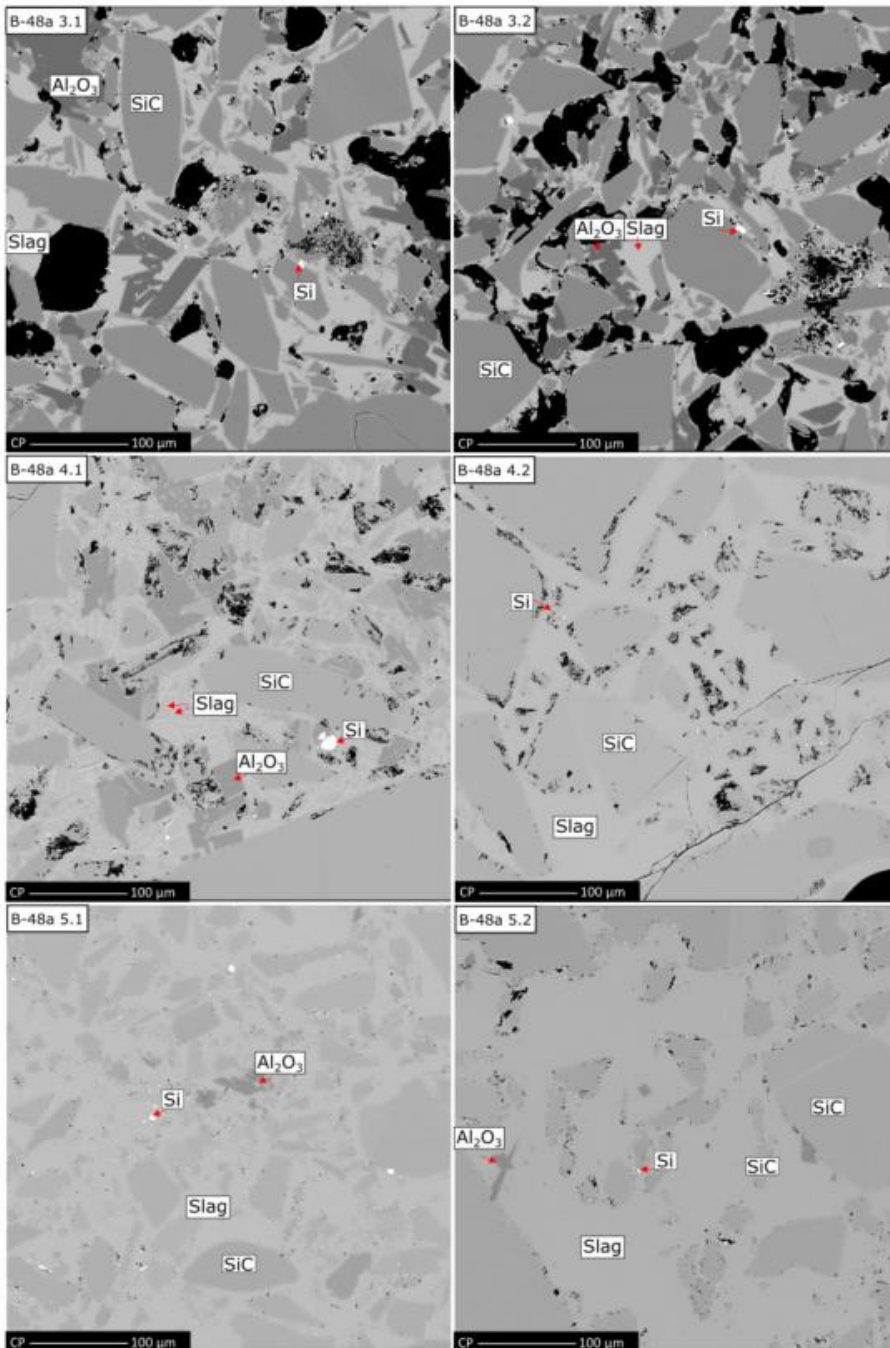


Figure 37 B-48a 3.1 and 3.2 consist of larger SiC particles, SiO<sub>2</sub>-CaO-Al<sub>2</sub>O<sub>3</sub> slag and Al<sub>2</sub>O<sub>3</sub>. Some smaller droplets of Si are also present. All parallels from B-48a 4 and 5 are similar as sample B-48 3. The appearance is different due to a different use of contrast on the images.



The normalized WDS results conducted on the samples adjacent to the tapping channel are listed in Table 12. The table also includes the liquidus and solidus temperature, which confirm that the slag is liquid at temperatures above 1550 °C. The SiO<sub>2</sub> content varies from 17wt% to 81wt%, but 85% of the samples are within 30-70wt%. There is no significant difference between the slag composition in the green zone and the dark grey zone. The CaO/Al<sub>2</sub>O<sub>3</sub> ratio is approximately the same, ~1/1 for almost all analyzed slag. The viscosity of the slag next to the tapping channel ranges from 1 to 2346 Poise. The original WDS data can be found in Table 47, Table 48, Table 49 and Table 50 in Appendix A.

For tap-hole 1 and 3, the samples were collected from above (B-48a) and below (B-48b and B-2) the Si tapping channel. Generally, a higher SiO<sub>2</sub> content is found above the Si channel.

Tap-hole 7 (B-47) was the last tapped tap-hole before shut-down. Although the furnace was burned down before shut-down, no visual differences or significant compositional differences were found in the slag compared to tap-hole 1 and 3. Burning down the furnace may result in larger amount of slag and/or other accumulated matter in the furnace area around the last tapped tap-hole, but this was not found in this study.

Table 12 The normalized WDS analysis for B-48 a and b from tap-hole 1, B-1 and B-2 from tap-hole 3, and B-47 from tap-hole 7. The liquidus and solidus temperature are found from the ternary diagram and are given in °C. The viscosity data are calculated from FactSage 8.1, given in Poise. The numbers after the samples name correspond to the marked analyzed number shown in earlier figures and includes slag from both the green and grey zones in all samples.

Sample	From zone	Oxide analysis				T <sub>liquidus</sub> [°C]	T <sub>solidus</sub> [°C]	Viscosity [Poise]	
		SiO <sub>2</sub>	CaO	Al <sub>2</sub> O <sub>3</sub>	K <sub>2</sub> O			1600°C	1800°C
48a 1.2	Green	63	15	22		1400	1170	226	36
48a 2.1	Green	46	21	33		1530	1170	44	8
48a 2.2	Green	46	21	33		1530	1170	44	8
48a 3.1	Grey	42	22	36		1540	1170	32	7
48a 3.2	Grey	43	23	34		1540	1170	30	6
48a 4.1	Grey	56	15	29		1490	1170	144	23
48a 4.2	Grey	66	9	25		1650	1512		62
48a 5.1	Grey	68	8	24		1650	1512		75
48a 5.2	Grey	68	8	24		1650	1512		75
48b1.1	Green	36	31	33		1390	1265	10	3
48b1.2	Grey	37	30	33		1400	1265	11	3
48b2	Grey	30	35	35		1470	1265	6	2
48b3	Grey	36	29	35		1420	1265	12	3
48b4	Grey	35	30	35		1390	1265	10	3
48b5	Grey	69	18	13		1400	1170	176	34
1.1	Green	34	30	36		1380	1265	10	3
1.2	Green	27	35	38		1500	1385	5	2
1.3	Grey	33	32	35		1400	1265	8	2
2.1	Green	17	33	50		1550	1485	5	1
2.2	Green	37	28	35		1450	1265	14	3
2.3	Grey	56	15	29		1480	1345	144	23
47 1.1	Green	45	19	36		1550	1512	49	9
47 1.2	Green	53	16	31		1510	1512	107	18
47 2.1	A1: grey	72	12	16		1400	1170	604	87
	A2: grey	66	14	20		1350	1170	310	48
47 2.2	Grey	81	4	11	4	1500	1170	9597	861
47.3	Grey	36	29	35		1430	1265	12	3
47.4	Grey	37	29	34		1430	1265	12	3
47.5	Grey	47	22	31		1530	1170	41	8

### 2.3.1.1.3 Tapped slag from previous tapping

In Si and FeSi production, all tapped metal and slag end up in the same ladle and are later separated. At Elkem Plant B, the slag is stored in a separate pile outside. This pile is emptied approximately every sixth weeks. During a break in the excavation process, three visually different samples were collected from the slag pile. These samples were brought back and analyzed to compare with the samples from inside the furnace.

The EPMA images for all tapped slag samples can be seen in Figure 38. B-tap 1.1 and 1.2 consist of SiC and SiO<sub>2</sub>-CaO-Al<sub>2</sub>O<sub>3</sub> slag, along with some Si. The slag has solidified into two separate phases. The darker area is SiO<sub>2</sub> together with some Si. B-tap 2 is visually slightly darker than B-tap 1. Both parallels contain mostly SiO<sub>2</sub> and some Si. Sample 2.1 does not contain any slag, while sample 2.2 has a small area with SiO<sub>2</sub>-CaO-Al<sub>2</sub>O<sub>3</sub> slag. B-tap 3.1 and 3.2 both contain mostly slag and some SiC. Sample 3.1 also have areas with Al<sub>2</sub>O<sub>3</sub>.

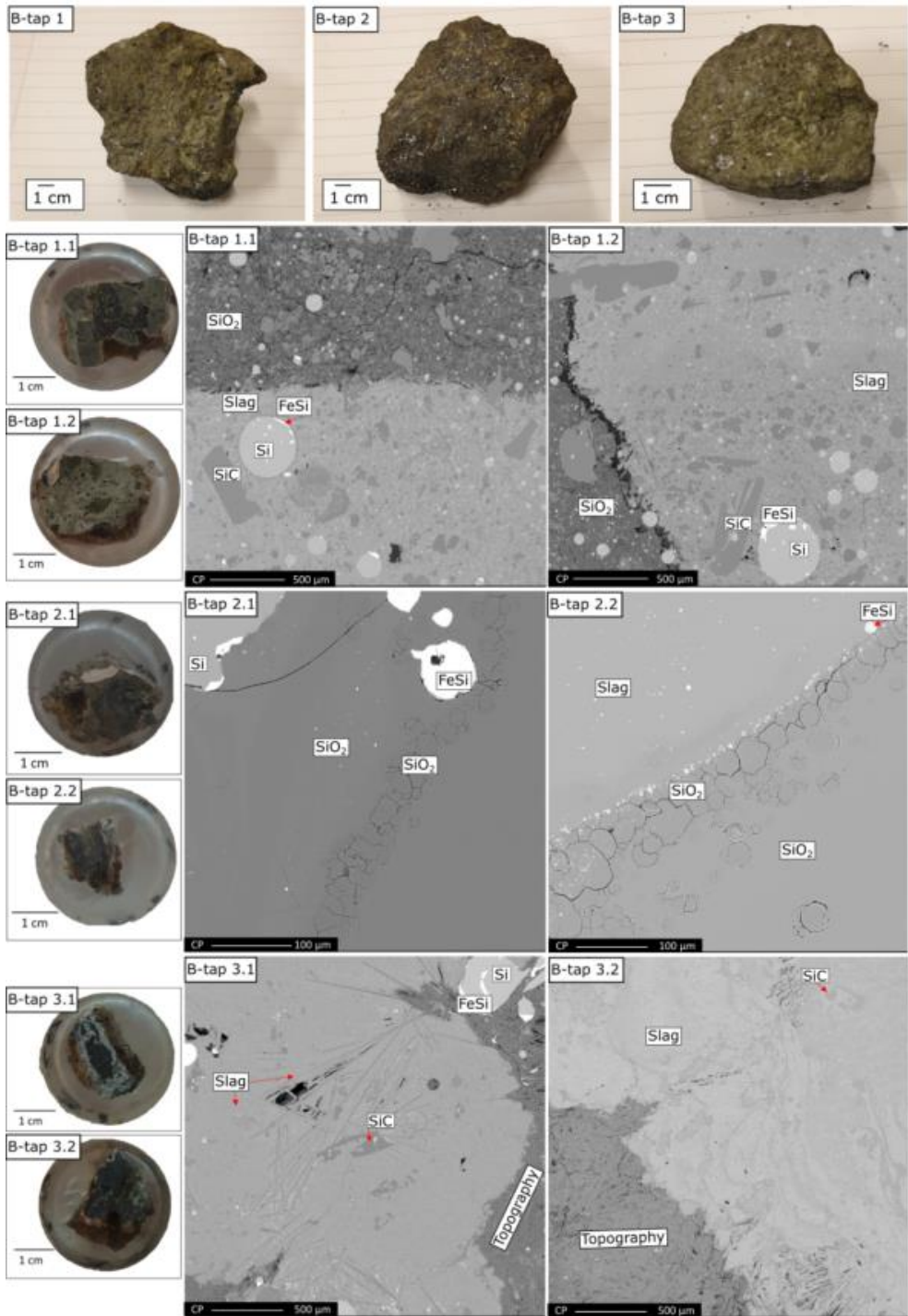


Figure 38 The collected earlier tapped slag samples. B-tap 1.1 and 1.2 contain  $\text{SiO}_2$ , SiC,  $\text{SiO}_2\text{-CaO-Al}_2\text{O}_3$  slag and some Si. B-tap 2.1 and 2.2 contain mostly  $\text{SiO}_2$ , and some  $\text{SiO}_2$  rich  $\text{SiO}_2\text{-CaO-Al}_2\text{O}_3$  slag in sample 2.2. B-tap 3.1 and 3.2 contain  $\text{SiO}_2\text{-CaO-Al}_2\text{O}_3$  slag solidified into two phases, some SiC. Sample 3.2 also have some  $\text{Al}_2\text{O}_3$ .

Table 13 presents the normalized WDS results for the previous tapped samples. The original data can be found in Table 51 in Appendix A. The analysis of the darkest areas for Btapp-3.1 (EPMA image at the bottom left in Figure 38) is valuable only for indicating the phases present, not the percentage distribution. This is due to topography, which makes the analysis uncertain. The result is therefore not used in the table for normalized data, but it shows that the slag consists of SiO<sub>2</sub>, CaO and Al<sub>2</sub>O<sub>3</sub>, which is consistent with the other slag samples.

The table also includes the liquidus and solidus temperature, which confirms that the slag is liquid with tapping temperatures around 1700-1800 °C. In B-tap 2, both parallels consist mostly of SiO<sub>2</sub>, with a smaller area of SiO<sub>2</sub> rich slag observed in sample 2.2. The viscosity data indicates this slag is very viscous.

The slags from sample Btapp-1 and 3 are within the same area as for many of the accumulated slag samples from Furnace B, and consist of an approximately 1-1-1 ratio of SiO<sub>2</sub>-CaO-Al<sub>2</sub>O<sub>3</sub>. At 1800 °C all slags are < 7 Poise, which gives that this is normal tapped slag.

*Table 13 The normalized WDS analysis for the collected earlier tapped samples B-tap 1 and, B-tap 2 and B-tap 3. The liquidus and solidus temperature are also included in the table, given in °C. Viscosities are calculated using FactSage 8.1 and are given in Poise.*

Sample				T <sub>liquidus</sub>	T <sub>solidus</sub>	Viscosity [Poise]	
	SiO <sub>2</sub>	CaO	Al <sub>2</sub> O <sub>3</sub>	[°C]	[°C]	1600°C	1800°C
Btapp-1.1	33	32	36	1400	1265	8.2	2.2
Btapp-1.2	41	28	31	1490	1265	15.6	3.8
Btapp-2.1	-	-	-	-	-	-	-
Btapp-2.2	78	6	16	1500	1512	2209.0	230.6
Btapp-3.1	38	27	35	1500	1265	16.0	3.8
Btapp-3.2	41	22	37	1550	1385	30.5	6.2

### 2.3.1.2 Slag samples from five previous excavations of Norwegian Si and FeSi furnaces

Several excavations have been conducted in Norwegian Si and FeSi industrial furnaces during the last years. In this study, samples from five of these are analyzed and compared. The slags samples were categorized based on their origin: higher parts in the inactive zone, lower parts close to the furnace bottom, or near the tapping channel. Table 14 lists the collected samples, categorized into these three main areas. The first letter in the sample ID corresponds to the first letter in the furnace they were collected from. The approximate positions of the samples in the furnace can also be seen in Figure 19 in section 2.2.1.1 Accumulated slag. It is important to note that the given position is based on reports and notes from other researchers as the author was not present during these excavations.

EPMA images of the samples from the higher parts and the lower parts in the furnace can be seen in Figure 39 and Figure 40, respectively. Detailed images at different magnification can be found in Appendix A.

Most of the slag are found together with SiC, but the size and amount vary. Melted, or partly melted, SiO<sub>2</sub> is often found in the inactive zones of the furnaces. In W<sub>4</sub>-12, W<sub>4</sub>-20 and S-43, most of the samples are SiC. There were only small areas with slag, and some SiO<sub>2</sub> for W<sub>4</sub>-12. Those are shown in the images, but are not a large part of the samples. Sample T-2 is from the slag/SiC layer and is the same sample that were mentioned and analyzed earlier [20]. The images from this study are similar with those in the excavation report. This sample contains mainly smaller SiC particles and SiO<sub>2</sub>-CaO-Al<sub>2</sub>O<sub>3</sub> slag, which has solidified into two phases. S-46 was collected from the outer edge of a tap-hole and consist of mainly SiC and SiO<sub>2</sub>. Here it was only found a small area with slag.

Two samples from Wacker Chemicals furnace no 1 are from the zones next to the tapping channel. The EPMA images can be seen in Figure 41. Figure 42, shows a picture of the tapping channel in Wacker Holla furnace no. 1 with marked sample position of W<sub>1</sub>-115. Here is also a green layer of slag next to the Si tapping channel, followed by a dark grey area. W<sub>1</sub>-115 consists of slag and SiC, similar as in the green zone in Furnace B. W<sub>1</sub>-114 is mostly SiO<sub>2</sub> with slag in between grain boundaries and cracks, and some SiC particles.

*Table 14 Overview of the excavation samples analyzed and their approximate position area in the furnace. The first letter in the sample ID is related to the first letter in the furnace they are collected from.*

Sample ID	Approximate position in the furnace	
Higher parts in the furnace	S-37	near the furnace wall, between two tap-holes
	F-75	approximately 1.5m above tap-hole
	W <sub>4</sub> -5	above the tap-hole close to the electrode, from the beginning of the excavation.
Lower parts of the furnace	F-36	in the slag/metal bath in the furnace bottom
	S-43	1.8m above the flat furnace bottom, close to the electrode
	T-2	slag/SiC layer at the bottom of the furnace
	W <sub>1</sub> -33	slag layer below the electrode.
	W <sub>4</sub> -12	big lump from the bottom side of the electrode
	W <sub>4</sub> -20	behind the tap-hole, deeper in the furnace
	S-46	the outer edge of a tap-hole
Next to tapping channel	W <sub>1</sub> -114,	next to the Si tapping channel
	W <sub>1</sub> -115	

## Higher parts of Si and FeSi furnaces

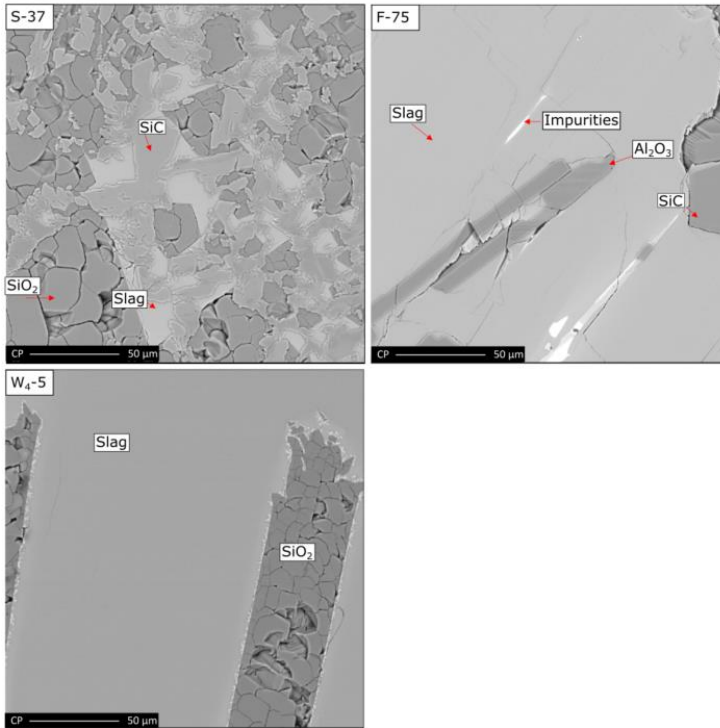


Figure 39 EPMA images with magnification 400X of slag from the higher parts in Si and FeSi furnaces. All samples contain SiC particles and SiO<sub>2</sub>-CaO-Al<sub>2</sub>O<sub>3</sub> slag. F-75 also contain Al<sub>2</sub>O<sub>3</sub>. W<sub>4</sub>-5 and S-37 contain SiO<sub>2</sub> where the grain boundaries are still intact, while the SiO<sub>2</sub> in B-9 has a different look.

## Lower parts of Si and FeSi furnaces

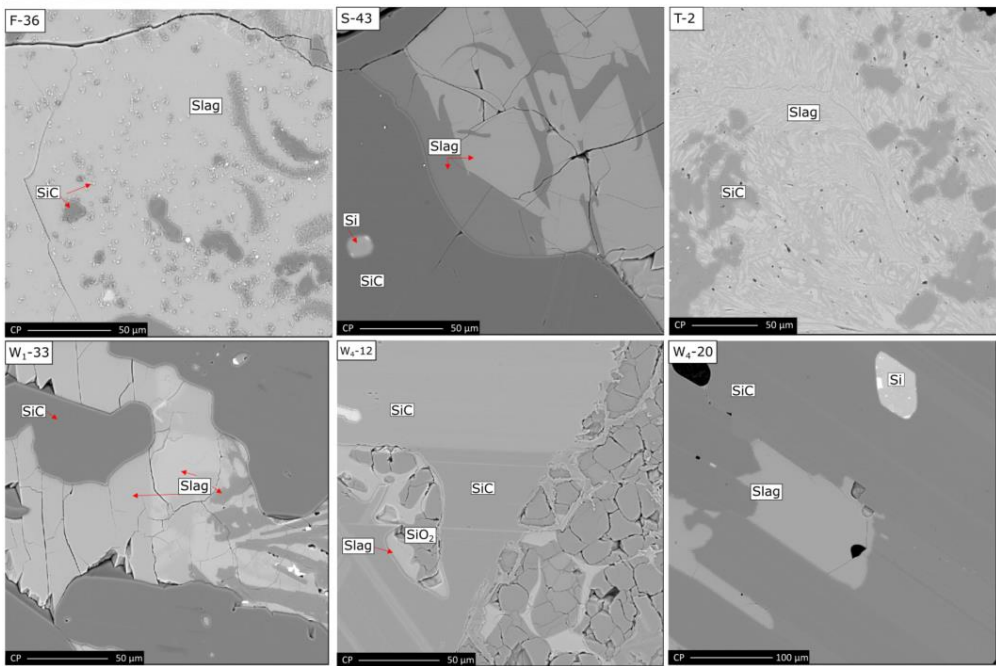


Figure 40 EPMA images with magnification 400X of slag from lower parts in Si and FeSi furnaces. All samples contain SiC particles and SiO<sub>2</sub>-CaO-Al<sub>2</sub>O<sub>3</sub> slag. B-3 also contain some Al<sub>2</sub>O<sub>3</sub>. S-43 and W4-20 consist mainly of SiC and only small areas with slag were found here. W4-12 also have some SiO<sub>2</sub>.

## Zones next to tapping canal of Si furnaces

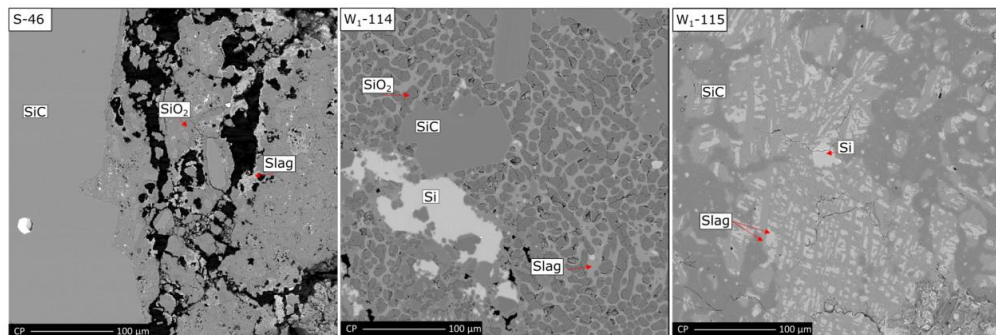
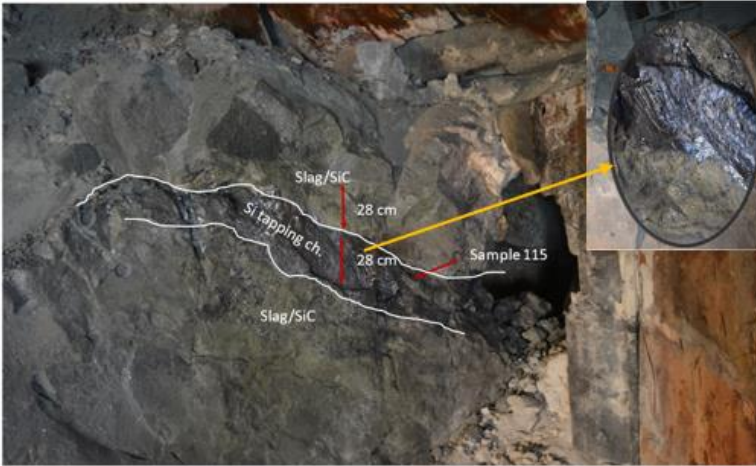


Figure 41 EPMA images with magnification 400X of slag from the zones next to tapping channel in Si furnaces. S-43 contain mostly SiC in addition to some SiO<sub>2</sub> and slag. W1-114 is mostly SiO<sub>2</sub> with slag in between grain boundaries and cracks, and some SiC particles. W1-115 is slag and SiC.



Wacker no1 2016

Figure 42 Picture of the tapping channel from Wacker Chemicals Holla, furnace no.1 [45]. Marked in the picture is also the position of sample  $W_1-115$ .

Table 15 provides the normalized WDS results for the slag samples obtained from previous excavations. Generally, there is a higher content of  $\text{SiO}_2$ ,  $>50\text{wt}\%$ , in the slag collected from higher parts in the furnace, except for sample F-75. The  $\text{CaO}/\text{Al}_2\text{O}_3$  ratio varies between 0.4-1.8. Furthermore, it is also found a higher content of other elements than  $\text{SiO}_2$ ,  $\text{CaO}$  and  $\text{Al}_2\text{O}_3$  in the samples collected higher up in the furnace, such as  $\text{K}_2\text{O}$ ,  $\text{MgO}$  and  $\text{Na}_2\text{O}_3$ . The slag in  $W_4-5$  contains multiple oxides. From the notes of the present excavator from NTNU it says that it is collected in the very beginning of the excavation, while it is placed deeper in the furnace on the sample map in the report [21]. The table also presents the liquidus and solidus temperatures of the slag. Some of these samples have liquidus temperature close to and above the assumed furnace temperature in the inactive zone, as seen in the case of F-75. The viscosity of the slag is generally high in the higher parts of the furnace.

In the lower part of the furnace, 80% of the slag have  $\text{SiO}_2$  content  $<50\text{wt}\%$ . The  $\text{CaO}/\text{Al}_2\text{O}_3$  ratio ranges from 0.6 to 4.4. The composition variations are also smaller in the lower parts of the furnace. Three of the samples from the lower parts of the furnace have a higher  $\text{SiO}_2$  content, S-43,  $W_4-12$  and  $W_4-20$ . These samples are mainly SiC, with smaller areas of slag “encapsulated”, and are believed to be from the SiC crust area. The liquidus temperature for all the slags in the lower parts of the furnace are  $< 1540\text{ }^\circ\text{C}$ , which confirms liquid slag in the high-temperature zone. The viscosities at  $1800\text{ }^\circ\text{C}$  are  $< 8$  Poise for all the slag from the lower parts of the furnace.

The position for sample  $W_1-115$  is above the tapping channel and confirms a higher content of  $\text{SiO}_2$ , similar as found for the samples close to the tapping channel in Furnace B. The slag in between the  $\text{SiO}_2$  in sample  $W_1-114$  has similar composition as in  $W_1-115$ . The liquidus temperatures confirm liquid slag with a tapping temperature around  $1700-1800\text{ }^\circ\text{C}$



[27], [46]. The viscosities at 1800 °C for W<sub>1</sub>-114 and 115 are 23 and 32 Poise, respectively, which corresponds to the viscosity of maple syrup.

Table 15 Normalized WDS results for slag samples. Oxide analysis are given in mass percent. Viscosities are calculated using FactSage 8.1.

	Sample ID	Oxide analysis					T <sub>liquidus</sub> [°C]	T <sub>solidus</sub> [°C]	Viscosity [Poise]	
		SiO <sub>2</sub>	CaO	Al <sub>2</sub> O <sub>3</sub>	K <sub>2</sub> O	MgO			1600°C	1800°C
Higher parts in the furnace	S-37	66	19	12	2	1	1390	1170	101	22
	F-75	45	20	35			1550	1170	46	9
	W4-5	57%SiO <sub>2</sub> - 5%CaO - 21%Al <sub>2</sub> O <sub>3</sub> - 1%K <sub>2</sub> O - 3%MgO - 11%FeO - 2%Na <sub>2</sub> O <sub>3</sub>							77	16
Lower parts in the furnace	S-43	62	31	7			1350	1170	16	5
	F-36	34	38	28			1430	1265	4	1
	T-2	39	30	31			1420	1265	12	3
	W1-33	35	38	27			1440	1265	4	1
	W <sub>4</sub> -12	43	33	24			1380	1265	9	2
	(In SiO <sub>2</sub> ) W <sub>4</sub> -20	76	15	10			1490	1170	415	75
Next to tapping channel	S-46	52%SiO <sub>2</sub> - 20%CaO - 3%Al <sub>2</sub> O <sub>3</sub> - 9%FeO - 16%MgO							2	1
	W <sub>1</sub> -114	63	19	18			1320	1170	119	23
	W <sub>1</sub> -115	63	16	21			1390	1170	195	32

### 2.3.2 Tapped slag

As mentioned earlier, slag is tapped together with the metal, and samples of tapped slag give valuable information about the slag present in the furnace. In this study, tapped slag samples were obtained from two Si furnaces and two FeSi75 furnaces. A total of 11 samples were collected from furnace no. 2 at Elkem Thamshavn over a one-year period from May 2019 to May 2020. Additionally, three samples were collected from Furnace B in June 2020, approximately ten months after the excavation. Furthermore, 34 samples were collected from two FeSi furnaces at Finnfjord, furnace O and R, from September 2020 to March 2022. The time intervals between the collected samples ranged from a couple of months to several samples a day.

Figure 43 shows three typical images of the normal tapped slag samples, one from each plant. All samples have presence of SiC and some metal along with the slag. In some samples from Finnfjord AS, small amounts of carbon were also observed, which is assumed originate from the tap-hole clay. The oxide composition, liquidus and solidus temperature, as well as the viscosities at 1600 °C and 1800 °C for the tapped slag at Elkem Thamshavn, Furnace B and Finnfjord AS, are presented in Table 16, Table 17 and Table 18, respectively. The original WDS analysis can be found in Table 53, Table 54 and Table 55 in Appendix A. Assuming a tapping temperature range around 1700-1900 °C, the liquidus temperatures confirm liquid slag for all collected samples.

The SiO<sub>2</sub> content in the slag from Elkem Thamshavn ranges from 40-70wt% and the viscosity values ranges from 1-34 Poise. The CaO/Al<sub>2</sub>O<sub>3</sub> ratio is approximately 1.6. The

slags with higher SiO<sub>2</sub> content have higher viscosity values, and some of the slag found in this study could potentially cause accumulation. However, this was not reported, which could be that there were limited amounts of slag present by the tap-hole during sampling time of this slag.

The slags from Furnace B have a lower CaO/Al<sub>2</sub>O<sub>3</sub> ~0.6, and also a lower SiO<sub>2</sub> content, 30-50wt%. The samples from Furnace B have a higher Al<sub>2</sub>O<sub>3</sub> content compared with Elkem Thamshavn and Finnjord AS. This was expected, as this furnace generally has a higher Al content than the average Norwegian Si plants.

The slag collected during normal tapping conditions at Finnjord AS has a CaO/Al<sub>2</sub>O<sub>3</sub> ratio around 0.9, and SiO<sub>2</sub> content ranging from 32wt% to 44wt%. Traces of Na<sub>2</sub>O, MgO and/or BaO were also detected in several of the samples. At Elkem Thamshavn and Furnace B, only normal tapping conditions were reported at sampling times. However, at Finnjord AS, 5 out of 34 samples were reported as high-viscosity slag, which means that there were challenging tapping conditions with slag clogging the tap-hole and poor drainage at the sampling time. For the high-viscosity slag, the CaO/Al<sub>2</sub>O<sub>3</sub> ratio is both lower ~0.4 and higher ~1.6 compared to the normal tapped slag. However, these samples have a significant higher SiO<sub>2</sub> content in the slag. Figure 44 shows EPMA images of the high-viscosity slag. In addition to a SiO<sub>2</sub>-rich slag phase, areas of SiO<sub>2</sub> are often present. These SiO<sub>2</sub> areas are former quartz which has melted, but not fully dissolved in the slag. These will later be referred to as SiO<sub>2</sub> areas. Softened and molten SiO<sub>2</sub> are known to be very viscous and are not ideal to have in the tapping area. Iron oxide (FeO) is also found in some of the high-viscosity slags. This is due to use of blowing oxygen through iron lances, which is normal procedure during difficult tapping conditions.

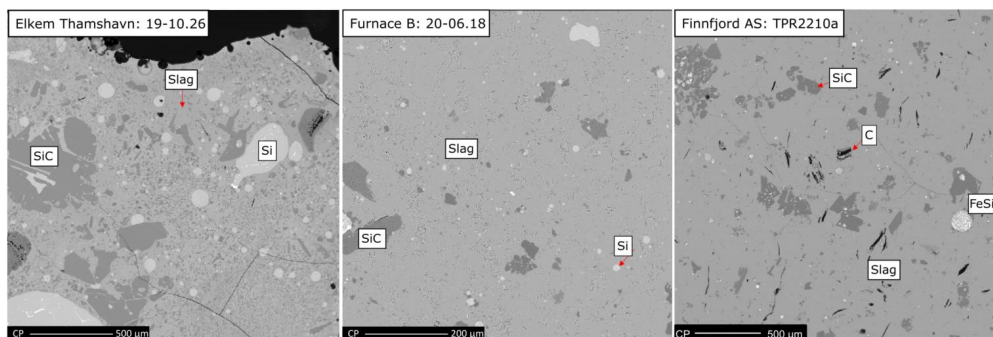


Figure 43 EPMA images of normal tapped samples. To the left is from is from Elkem Thamshavn 19-10.26 with magnification 40X, in the middle is Furnace B 20-06.18 with magnification 100X, and to the right. Is from Finnjord AS 20-10.22 with magnification 40X. All samples are mainly slag together with some SiC and Si. Small cracks are in the slag phase from Elkem Bremanger, while small SiC particles are in the slag phase from Elkem Thamshavn.

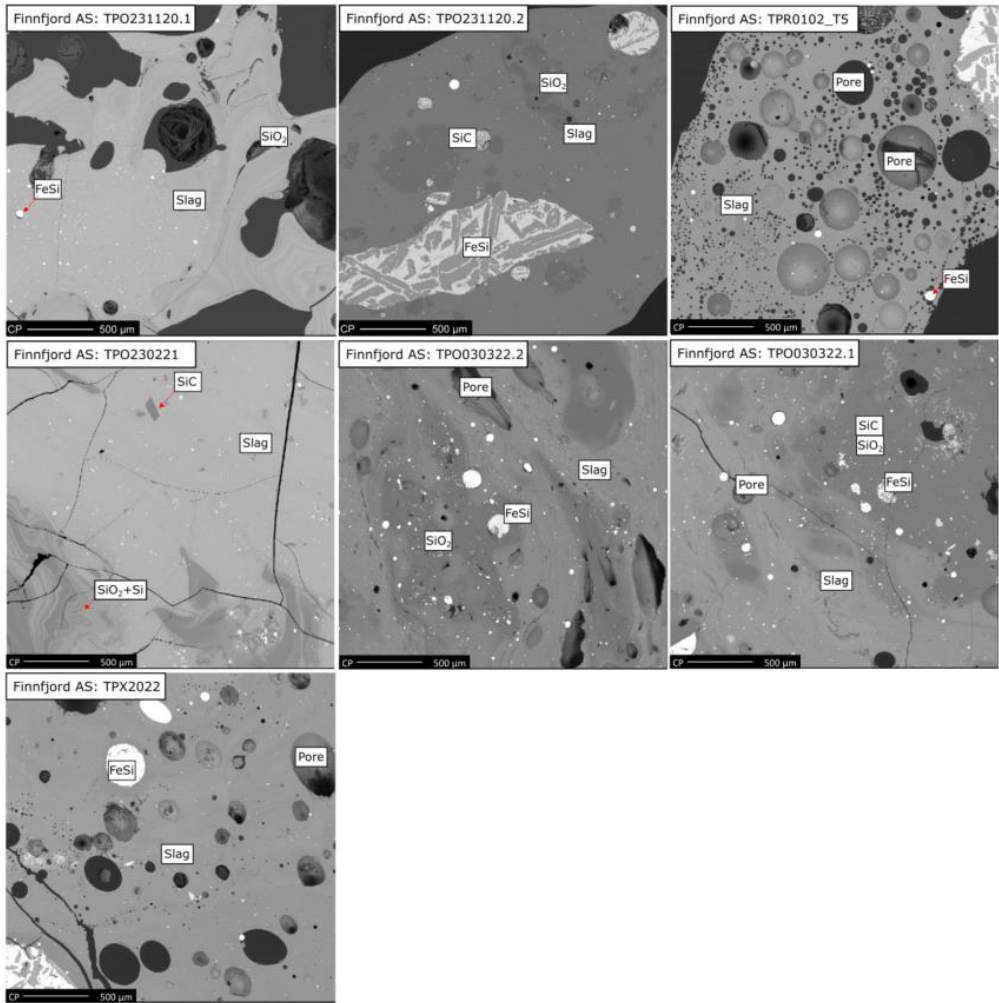


Figure 44 The five samples with high viscosity slag from Finnjord AS, Two areas from TPO231120, TPO0102\_T5, TPO230221, two areas from TPO030322 and TPX2022. The high-viscosity slag consists of SiO<sub>2</sub>-rich slag, in addition to some SiC and FeSi. In addition, several samples have SiO<sub>2</sub>, and some have condensate of SiO<sub>2</sub> and Si. Many of the samples are porous.

Table 16 WDS results for the analyzed slag for the tapped samples collected from Elkem Thamshavn. Oxide analysis are given in mass percent. Viscosities are calculated with FactSage 8.1.

Date	Tap-hole no.	Oxide analysis					T <sub>liquidus</sub> [°C]	T <sub>solidus</sub> [°C]	Viscosity [Poise]	
		SiO <sub>2</sub>	CaO	Al <sub>2</sub> O <sub>3</sub>	Na <sub>2</sub> O	MgO			1600°C	1800°C
19.05.24	1	4	67	21	9	3	1400	1170	83	20
	2		53	27	20		1350	1170	24	6
19.06.05	1	2	39	34	27		1350	1265	7	2
	2		46	31	23		1390	1265	12	3
19.08.18	1	5	46	41	13		1350	1265	4	1
	2		46	33	21		1370	1265	9	3
19.10.26	1	7	54	29	17		1300	1170	18	5
	2		63	25	12		1300	1170	42	11
19.12.03	1	3	53	26	21		1400	1170	28	7
	2		52	25	23		1400	1170	32	7
19.12.04	1	3	59	25	16		1200	1170	38	9
	2		58	27	15		1200	1170	27	7
19.12.07	1	4	59	28	14		1200	1170	24	6
	2		50	30	20		1380	1170	15	4
19.12.09	1	5	55	26	19		1390	1170	30	7
	2		56	28	17		1390	1170	23	6
20.01.10	1	7	42	36	23		1300	1265	6	2
	2		69	15	13	3	1390	1170	150	30
20.02.07	1	5	53	31	16		1300	1170	13	4
	2		49	28	23		1410	1170	19	5
20.05.05	1	2	45	23	29	3	1500	1170	28	6
	2		54	20	19	7	1350	1170	50	6

Table 17 WDS results for the analyzed slag for the tapped samples collected from Furnace B. Oxide analysis are given in mass percent. Viscosities are calculated with FactSage 8.1.

Date	Tap-hole no.	Oxide analysis				T <sub>liquidus</sub> [°C]	T <sub>solidus</sub> [°C]	Viscosity [Poise]		
		SiO <sub>2</sub>	CaO	Al <sub>2</sub> O <sub>3</sub>	Na <sub>2</sub> O			1600 °C	1800 °C	
20.06.09	1	5	40	22	35	3	1510	1265	26	6
	2		50	19	31		1520	1170	67	12
20.06.18	1	6	30	27	43		1510	1385	12	3
	2		31	26	43				13	3
20.06.19	1	6	46	20	34		1550	1170	48	9
	2		34	25	41		1510	1385	17	4

Table 18 WDS results for the analyzed slag for the tapped samples collected from Finnjord AS. Marked with (H) are the high viscosity slags. Oxide analysis are given in mass percent. Viscosities are calculated with FactSage 8.1.

Sample ID	Tap-hole	Oxide analysis					T <sub>liq</sub>	T <sub>sol</sub>	Viscosity [Poise]	
		SiO <sub>2</sub>	CaO	Al <sub>2</sub> O <sub>3</sub>	MgO	BaO	[°C]	[°C]	1600°C	1800°C
TPR170920a	2	33	28	38		1	1370	1385	11	2
TPR180920a	3	37	27	35		1	1460	1385	16	3
TPR180920c	3	35	24	39	1	1	1490	1385	21	5
TPR190920a	3	36	26	37		1	1495	1385	17	4
TPR220920a	3	37	27	36			1490	1265	16	4
TPR230920a	3	37	24	37	1	1	1500	1385	16	4
TPR230920b	3	37	25	36	1	1	1500	1265	17	4
TPR221020a	6	34	29	38	1	1	1490	1460	17	4
TPR271020	7	34	34	31		1	1450	1265	13	3
TPR281020	7	37	28	33	1	1	1450	1265	13	3
TPR041120	1	39	28	31	1	1	1460	1265	13	3
TPR131120	2	36	28	34	1	1	1450	1265	12	3
TPO220920	6	34	31	35			1350	1265	9	2
TPO221020a	4	42	23	33	1	1	1540	1265	32	7
TPO131120	1	35	31	33		1	1390	1265	10	3
TPO231120.1 (H)	5	71	8	21	1		1550	1512	897	106
TPO231120.2		56	12	30	1	1	1550	1512	180	27
TPO170121a	3	35	33	32			1400	1265	8	2
TPO170121b	3	35	32	33			1400	1265	8	2
TPO170121c	3	35	33	32			1400	1265	8	2
TPO260121	1	37	32	31			1410	1265	9	2
TPO230221 (H)		56	27	17			1300	1170	26	7
TPR310121	4	36	36	28			1400	1265	6	2
TPR010221.T3	3*	42	35	23			1340	1265	7	2
TPR010221.T5 (H)	6	64% SiO <sub>2</sub> – 6% CaO – 11% Al <sub>2</sub> O <sub>3</sub> – 9% FeO							49	12
TPR120221	6	35	35	30			1410	1265	6	2
TPR140221	6	32	36	32			1480	1265	5	2
TPR180221		37	34	29			1390	1265	7	2
TPR090321	7	35	37	28			1440	1265	5	2
TPR170321N		40	29	31			1460	1265	13	3
TPR27421	5	35	30	35			1390	1265	10	3
TPR261121	7	33	37	30			1420	1265	5	2
TPX2022 (H)		66% SiO <sub>2</sub> – 12% CaO – 20% Al <sub>2</sub> O <sub>3</sub> – 2% FeO							317	48
TPR030122	3	38	27	36			1500	1265	16	4
TPO030322.1 (H)	1	74% SiO <sub>2</sub> – 1% CaO – 3% Al <sub>2</sub> O <sub>3</sub> – 22% FeO							259	52
TPO030322.2 (H)		80% SiO <sub>2</sub> – 1% CaO – 3% Al <sub>2</sub> O <sub>3</sub> – 16% FeO							1144	180

\*Not the active tap-hole

### 2.3.3 Slag and condensate from the charge surface in FeSi75 furnaces

The raw materials will experience a steep temperature increase as they meet the charge surface that holds a temperature around 1300 °C [3], [4]. During normal conditions, it is only expected to find lumpy materials that have not reacted with each other on the charge top. When deviation from this situation occur, the materials from the charge top can give knowledge on the reactions in the furnace. In this study, partly melted samples from the charge surface are analyzed. Some of the samples were collected during troubling conditions and are referred to as viscous and “glued” together. In this chapter, the main focus will be on condensates and slag formation from SiO<sub>2</sub>. All EPMA images from the charge surface can be seen in Figure 196-214 in Appendix A.

#### 2.3.3.1 Brown and white condensates

In many samples, areas of SiO<sub>2</sub> were covered with a thin layer of brown condensate, and in some cases brown and white condensate, as shown in Figure 45. EPMA images of the same samples are shown in Figure 46. The brown condensate consists of a SiO<sub>2</sub> matrix with small Si spheres from condensation reaction 3, which is the same as Broggi [47] found in his samples. For the samples with both white and brown condensate, the white area is SiO<sub>2</sub> and SiC from condensation reaction 4.

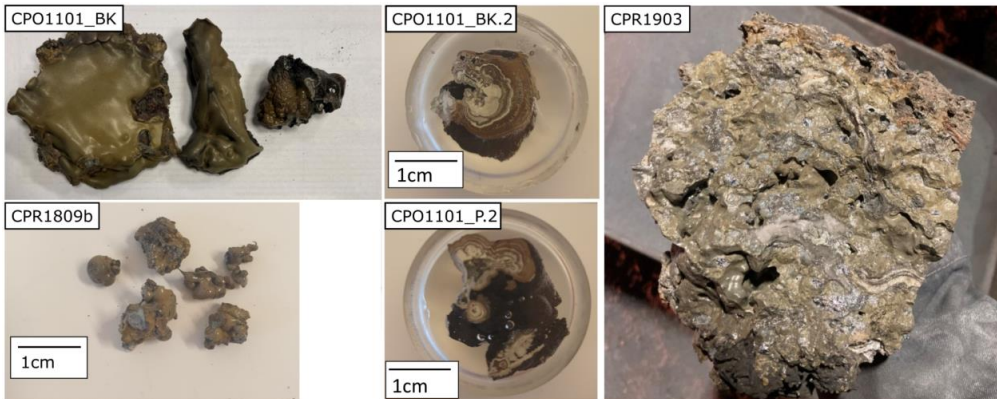


Figure 45 Pictures of charge top samples: CPO1101\_BK.1, CPO1101\_BK.2, CPR1903, CPR1809b and CPO1101\_P.2, that consist of brown, and brown and white condensates.

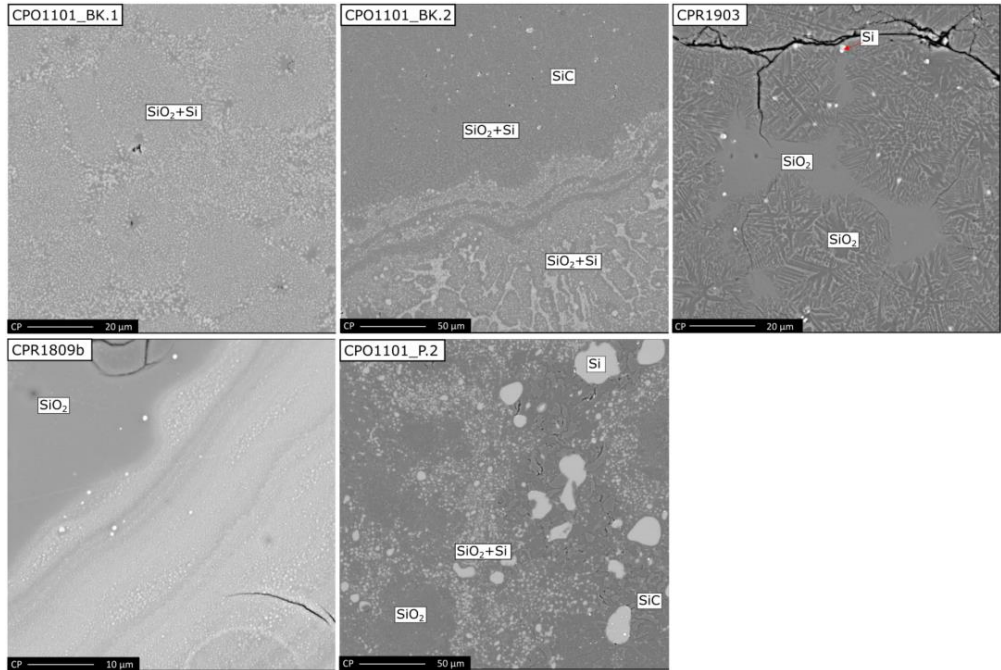


Figure 46 EPMA images of CPO1101\_BK.1, CPO1101\_BK.2, CPR1903, CPR1809b and CPO1101\_P.2. The brown condensate consists of  $\text{SiO}_2$  matrix with Si spheres. In sample CPO1101\_BK.2 and CPO1101\_P.2 are both brown and white condensate, and in the white areas it is also found SiC.

### 2.3.3.2 Slag formation from $\text{SiO}_2$

As mentioned earlier, it is expected to find accumulated oxide impurities in the form of slag in Si and FeSi furnaces. The raw materials used contain varying amounts of impurities. As the temperature increases downwards in the furnace, the impurity oxides less noble than Si will be reduced from the  $\text{SiO}_2$ . In this study, the borderline between slag and  $\text{SiO}_2$  is defined as 90wt%  $\text{SiO}_2$ . Initial slag formation was observed in several of the charge surface samples. Figure 47 and Figure 48 show pictures and EPMA images of samples containing  $\text{SiO}_2$  and slag. Initially, slag accumulates at the grain boundaries and in the cracks in the  $\text{SiO}_2$ . As the  $\text{SiO}_2$  melts, a bright grey slag phase can be found next to the melted  $\text{SiO}_2$ .  $\text{SiO}_2$ -rich slag can also be seen as the brighter grey-colored phase within the  $\text{SiO}_2$  matrix.

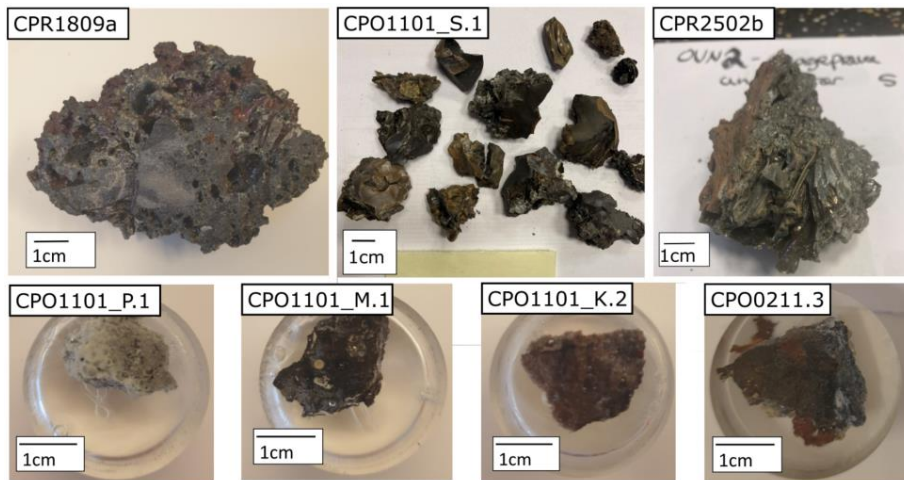


Figure 47 Pictures of charge top samples, slag: CPR1809a, CPO1101\_S.1, CPR2502b, CPO1101\_P.1, CPO1101\_M.1, CPO1101\_K.2 and CPO0211.3. Many of the samples were named after visual observation. S: slag, P: porous, M: metallic and K: quartz.



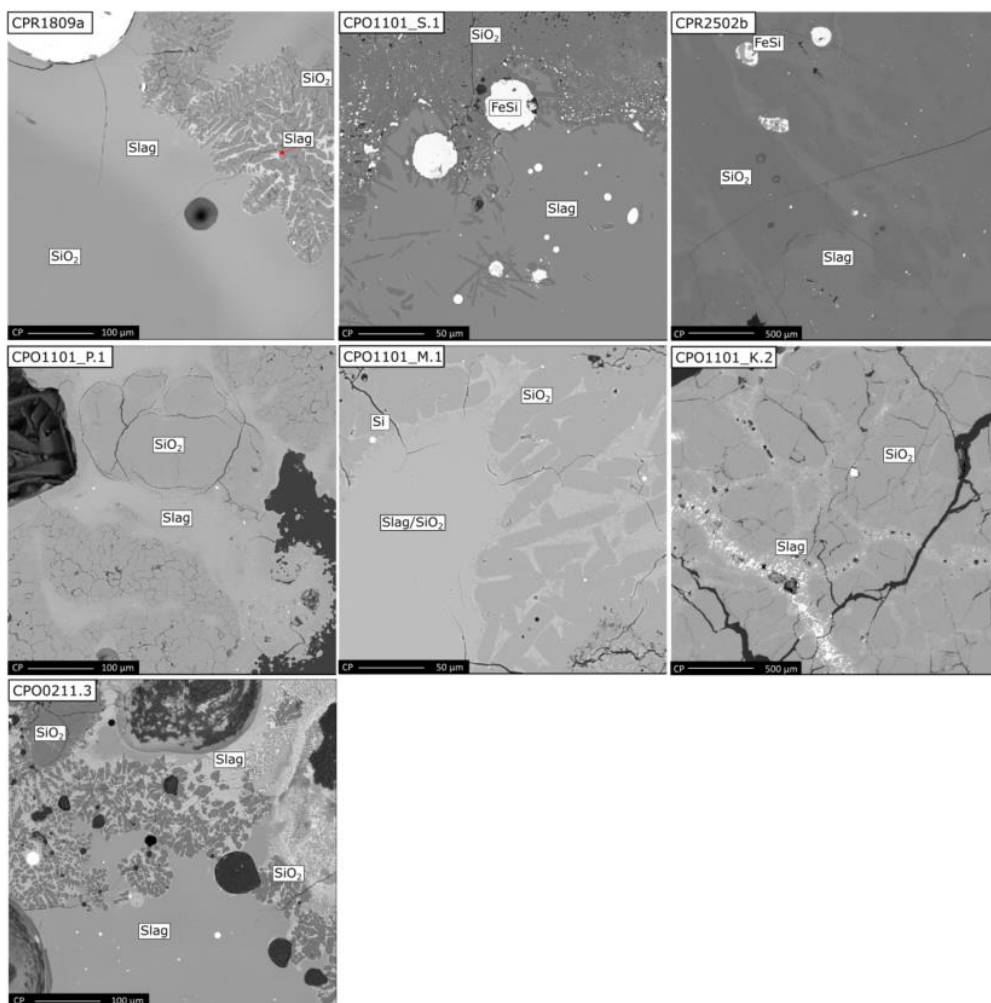


Figure 48 EPMA images of initial slag formation from  $\text{SiO}_2$ : CPR1809a, CPO1101\_S.1, CPR2502b, CPO1101\_P.1, CPO1101\_M.1, CPO1101\_K.2 and CPO0211.3. It is found the slag in grain boundaries and cracks in the  $\text{SiO}_2$ .

Table 19 lists the compositions for the slags found in the charge surface samples in this study. The slag mostly contains  $\text{SiO}_2$  in addition to  $\text{FeO}$ ,  $\text{Al}_2\text{O}_3$  and traces of alkali oxides Na, K, Mn, Mg and Ca, which are common impurities in the  $\text{SiO}_2$ . The existence of  $\text{FeO}$  in the slag probably comes from iron oxide pellets that are added together with the raw materials. As the temperature increases, the alkali oxides and the  $\text{FeO}$  will be reduced from the slag. By summarizing the basic oxides and fitting the slag system into the  $\text{SiO}_2$ - $\text{FeO}$ - $\text{Al}_2\text{O}_3$  or  $\text{SiO}_2$ - $\text{CaO}$ - $\text{Al}_2\text{O}_3$  system the liquidus temperatures can be found, given in the right column in Table 19. The liquidus temperatures give an indication of the charge surface temperature. It can be noticed that the slags in the grain boundaries and cracks in the  $\text{SiO}_2$  have a liquidus temperature around the expected charge surface temperature around 1300 °C. An increased  $\text{SiO}_2$  content to > 80 wt% increases the liquidus temperature considerably to >1600 °C. Softened/melted  $\text{SiO}_2$  and  $\text{SiO}_2$  rich slag around its liquidus temperature are

viscous, which gives a sticky and compact charge surface. Several of the samples were reported as viscous during sampling.

Table 19 Composition of the main slag phases found in the charge surface samples. Compositions are given in wt%.

Sample	SiO <sub>2</sub>	Na <sub>2</sub> O	K <sub>2</sub> O	MgO	CaO	FeO	Al <sub>2</sub> O <sub>3</sub>	TiO <sub>2</sub>	T <sub>sol.</sub>	T <sub>liq.</sub>
CPR1809a.1.1	64	0.3	0.4	0.4	1.7	11.7	21.1	0.4	1365	1490
CPR1809a.1.2	54	0.1	0.1	0.7	2.9	24	18	0.6	1200	1350
(in between SiO <sub>2</sub> )										
CPR1809a.2.1	84	0.1	0.4	0.3	1.6	8	5.7	0.1	1465	1610
CPR1809a.2.2	51	0.2	0.5	1.1	5.1	24	18	0.2	1200	1310
(in between SiO <sub>2</sub> )										
CPR1809c.1.1	83	0.4	0.9	0.2	0.7	10.3	4	0.2	1465	1640
CPR1809c.1.2	43	0.2	0.3	0.1	2.4	43	9.6	0.4	1200	1250
(in between SiO <sub>2</sub> )										
CPR1809c.2.1	87	0.5	1.7	0.7	0.6	5.5	3.4	0.1	1465	1620
CPR1809c.2.2	73	0.8	2.2	1.7	1.6	15	6.1	0	1465	1650
(in between SiO <sub>2</sub> )										
CPR0211.3.1	72	1.0	2.4	2.0	1.2	21	0.4	0	1190	1690
CPR0211.3.2	50	0.5	2.2	3.2	1.4	42	0.6	0	1465	1560
(in between SiO <sub>2</sub> )										
CPO1101.S1	80	2.3	7.3	1.6	1.2	5.5	2.6	0	1465	1660
CPO1101.S2	86.2	1.7	6.0	6.0	0	0	0	0	1465	1700
CPO1101.M1	85.3	1.9	2.9	2.5	2.3	0.1	1.7	SO <sub>3</sub> : 2.5		
CPO1101.M2*	80.9	2.7	3.8	3.7	1.0	0.4	0.4	SO <sub>3</sub> : 15.0		
CPO1101.P1	79.1	0	9.3	0	0	0.2	11.4	0	1170	1500
CPO1101.U	83.2	1.7	5.8	1.5	1.9	2.0	3.5	0.4	1512	1650
CPR2502m	55	0	0	2	11	0	32	0	1170	1570
CPR2502b	81	0	0	0	6	0	13	0	1170	1480
CPR2502a1	81	0	0	0	6	0	13	0	1170	1480
CPR2502a2	86	0	0	0	5	0	9	0	1170	1550

\* Analysis are only valid to know which oxides are in the sample, not the amount.

## Chapter 3: Changes in quartz during heating

### 3.1 Literature review

Quartz is one of the raw materials in Si and FeSi production, and its high temperature properties are an important factor when studying the furnace operation. The quartz impurities have an influence on both the composition of the final metal product and the slag, and hence the slag accumulation in the furnace. Its softening and melting properties, and crack formation will affect the charge properties and the reaction zones in the furnace. To ensure a good furnace operation it is important to have raw materials with optimal properties suited for the production.

#### 3.1.1 Quartz in Si and FeSi production

Quartz is a mineral that consists of mainly SiO<sub>2</sub>, around 99%. Several types of quartz can be used for Si and FeSi production, and how the quartz behaves at elevated temperatures is an important factor when selecting quartz for production. SiO<sub>2</sub> can react in both solid and liquid form with either liquid Si or SiC to produce SiO gas, as can be seen in reaction 5 and 6, respectively. It is preferable that these reactions happen in the lower, high temperature parts of the furnace. The metal producing reaction with SiO gas and SiC forming CO gas and Si, reaction 7, requires a temperature above 1811°C in addition to a SiO partial pressure >0.67bar. This is believed to happen around the electric arc below the electrodes.



Schei et al. [5] divided the requirements for selection of the raw material quartz into three categories. They are listed together with a short summary of their impact in Table 20.

Table 20 Important factors for selection of quartz in silicon and ferrosilicon production.

Important factor	Affects	Consequence
Impurity content	Final Si/FeSi product Slag production	-Elements more noble than Si will be reduced into the Si product and may be difficult to remove afterwards. -Impurities will also have an influence of the components and the composition in the slag that are produced in the furnace.
Size fraction and degradation properties	The charge properties	It is preferable with size fraction 10-150 mm. Too much fines present will affect the gas flow in the charge.
Melting properties	Reaction zones	It is important that the quartz does not melt too high up in the furnace to ensure that reaction 5 and 6 happens in the high temperature zone.

### 3.1.2 Impurities in quartz

Quartz can carry impurities in three different forms: structural impurities, fluid inclusions and minerals (solid inclusion). Structural impurities are interstitial or substitutional point defects in the lattice structure, and are the most common impurity form in quartz due to its open structure [48]. Impurities in the quartz will affect the properties upon heating to elevated temperatures. Typical impurities and their content in quartz used for Si and FeSi production are given in Table 21. From this, Al, Fe, Ca, K, Mn, S and Ti are the most common impurity elements in the quartz.

Table 21 Typical content of trace elements in quartz used for Si and FeSi production [48]. All units except Hg are in ppmw. Some analyses are below detection limit and are marked by <.

Element	Amount [ppmw]	Element	Amount [ppmw]	Element	Amount [ppmw]
Al	300-3200	Fe	100-1500	Sb	<0.1-0.9
As	<1-3	Hg	<5-10 ppbm	Se	<2-5.2
B	<10-45	K	<75-1700	Sn	<0.5-2.2
Ba	0.5-25	Mg	20-140	Sr	<0.5-12
Be	<0.5-0.6	Mn	3-600	Ti	20-200
Bi	<0.5	Mo	<2-8	V	<1-4
Ca	<75-160	Na	50-170	W	<0.5-640
Cd	<0.1-1.5	Ni	<1-9	Zn	<1-3
Co	<1-200	P	<50-170	Zr	<0.5-3.3
Cr	3-25	Pb	<1-9		
Cu	1-3	S	<5-1400		

All impurities in the Si and FeSi furnace are either from the raw materials, the electrodes or in the added fluxes. The impurity content in the quartz is therefore an important factor in the operational process and the final Si and FeSi product. Impurities in the quartz will follow the same path in the furnace as the SiO<sub>2</sub>. Volatile elements escape with the off-gas, while some will follow the SiO<sub>2</sub>. Bernardis [49] investigated Fe, Ti and Ca from SiO<sub>2</sub> and C during carbothermic reduction. She found that the impurities in the silica melt tend to cluster along solid-liquid interfaces between crystalline and molten silica. At higher temperatures, impurities were located along liquid-gas interfaces between silica and gaseous inclusions. She also found that Fe reduces late in the reduction process. It was suggested that the silica melt would hinder the gases present in the furnace and hence minimizing Fe reduction.

The impurities in the producing furnace will either be in the liquid metal, in the microsilica, in the off gas, in the condensate or form a separate slag phase. Myrhaug and Tveit [23] found that the distribution of impurities in the metal, off-gas and slag was mainly determined by the boiling temperature of the different elements. They made an overview of where the impurity elements are likely to be found in the various mass flows of the furnace, shown in Figure 49. Kamfjord [24] made a similar investigation of the element distribution and the boiling point of each element, shown in Figure 50. In the figure from Kamfjord, slag is included in the “metal” group, and coarse particles included in the “silica fume” group. Some slag will also be tapped from the furnace with the liquid Si. These two figures are in general quite similar. The major differences are found for the elements P, S, As, Se, Sb and Mn. From the figures, it appears as more than 80% of the Si, 70% Al and 60% Ca, which are the main oxide components in the slag that are tapped out from the furnace, go to the final metal product. It should be mentioned that these two models both consider the elements in their pure state, and both Myrhaug and Tveit, and Kamfjord believed that deviations in the model could be due to formation of oxides, sulfides or other chemical compounds that changes the boiling point. It should also be mentioned that the recoveries will be different for FeSi production.

## Distribution of trace elements

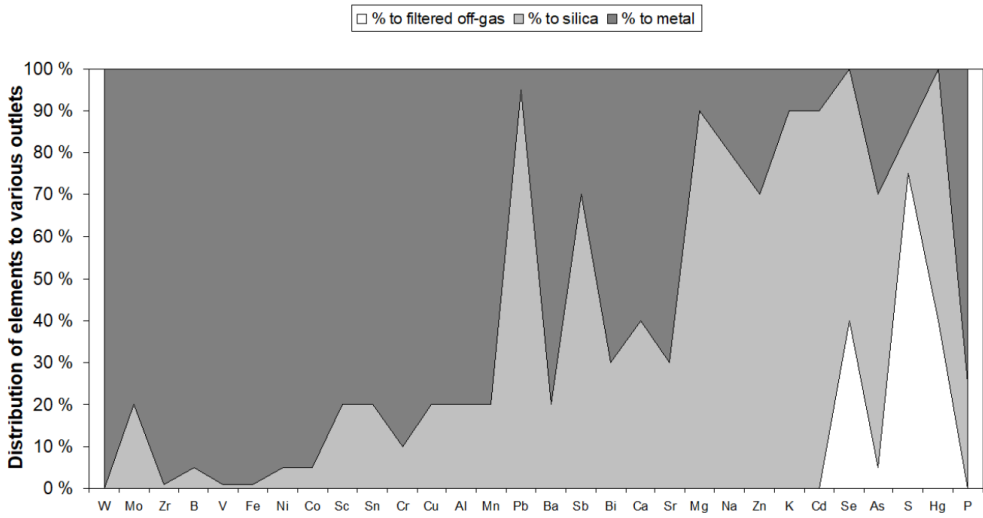


Figure 49 The distribution of trace elements as a function of the boiling temperature of different elements [23]. Slag is also tapped from the furnace and is here included in the metal.

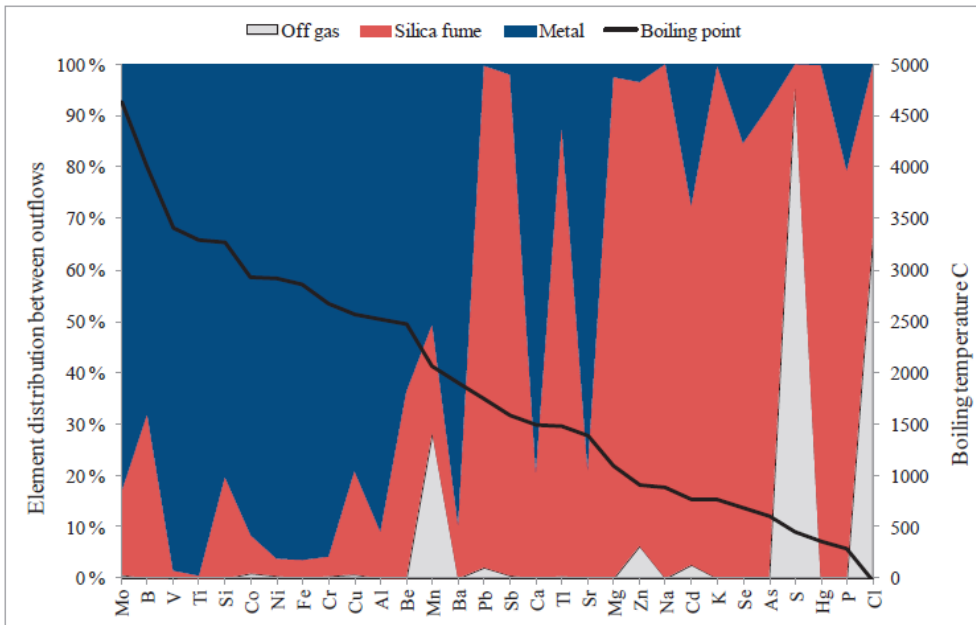


Figure 50 The distribution of trace elements as a function of the boiling temperature of different elements [24]. Slag is also tapped from the furnace and is here included in the metal.

Dal Martello et al [50] examined the behaviour of trace elements in hydrothermal quartz and quartzite in reaction with Si or SiC. Pellets or lumps of SiO<sub>2</sub>, SiC and Si were heated to 1650 °C and 1850 °C in high purity graphite crucibles under Argon gas flow. The phases present in the reacted charge and the collected condensates were analyzed after the experiments. They found that Muscovite, which is a common mineral phase in the quartz, formed two immiscible liquids during melting of quartz. One Al-rich melt placed at the core of the mineral, and one SiO<sub>2</sub>-rich melt at the mineral boundaries. During heating in reducing atmosphere to temperatures above 1650 °C, B, Mn, Zn and Pb were removed from the SiO<sub>2</sub>. With presence of silicon, Mn, Fe, Al, Zn and B diffused from SiO<sub>2</sub> into the silicon. In the second part of their work [51] it was investigated which volatile impurities that went into to the gas phase and the conditions which enhance gaseous compound's formation. They found that each impurity element in the initial quartz entered the gas phase during SiO<sub>2</sub> reduction to some degree. The average measured volatilities of B, P, K, Fe, Al, Mn, Zn and Pb are shown in Table 22. Fe and Al showed limited volatility compared to the other elements. It was also found that fluid inclusions enhance the distribution of the contaminants to the gas phase.

Table 22 Average measured volatilities of B, P, K, Fe, Al, Mn, Zn and Pb determined experimentally [51].

B	P	K	Fe	Al	Mn	Zn	Pb
11%	25%	26%	4%	1%	38%	10%	36%

### 3.1.3 Changes in quartz during heating

The quartz properties will undergo several changes during heating. Those who are most relevant for the Si and FeSi furnaces are the degradation properties and the properties that might affect the reaction rates, such as structural changes due to phase transformations and melting. These changes may be different between the different quartz types, and it is therefore important to compare knowledge on the properties of several quartz types before selecting the most suitable quartz as a raw material for production.

#### 3.1.3.1 Polymorphs of silica

The simplest building block of SiO<sub>2</sub> is the Si atom surrounded by four oxygen atoms. To have the correct 2:1 ratio, the Si atoms are shared with neighboring oxygen atoms, making a tetrahedra. When SiO<sub>2</sub> is heated, it changes into different SiO<sub>2</sub> polymorphs, which means that these tetrahedrons changes and can be arranged in numerous ways. The phase diagram of silica with the most common polymorphs are shown in Figure 51.

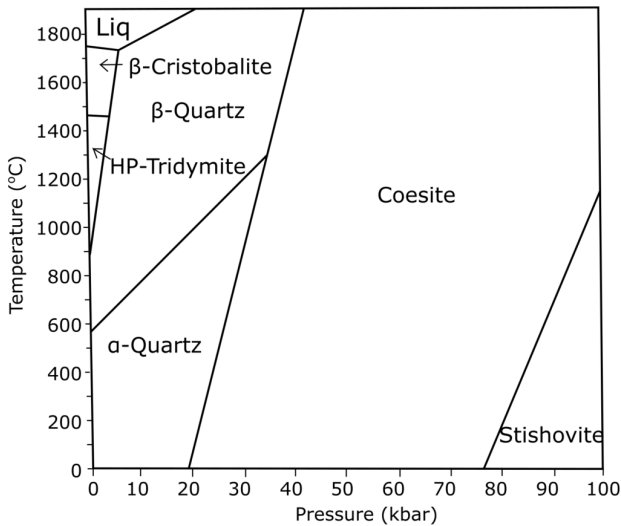


Figure 51 The phase diagram of silica [52].

$\alpha$ -quartz is the low temperature form and the predominant phase of  $\text{SiO}_2$ . Quartz transforms to  $\beta$ -quartz at  $573^\circ\text{C}$ . This transformation is a displacive transition, which means that it flips the Si-O-Si bonds to a tilted  $\text{SiO}_2$  tetrahedra. No bonds are broken, which means that this transformation has a smaller energy barrier to happen. Low  $\alpha$ -quartz has a trigonal crystal structure, while  $\beta$ -quartz has a hexagonal crystal form. The densities in  $\alpha$ -quartz and  $\beta$ -quartz are similar with  $2.65 \text{ g/cm}^3$  and  $2.53 \text{ g/cm}^3$ , respectively [53]. When  $\beta$ -quartz is cooled down, the framework changes to a denser  $\alpha$ -quartz configuration [54]. According to the phase diagram,  $\beta$ -quartz will transform to tridymite around  $870^\circ\text{C}$ . However, several researchers have suggested that this phase needs addition of certain impurity elements to be stable [55], [56]. Sodium and aluminium stabilize the structure of tridymite. It is therefore debated if tridymite is a pure phase of its own or just an impurity derived structure. The next transformation is to  $\beta$ -cristobalite around  $1470^\circ\text{C}$ , but this phase has also been detected already at  $1000^\circ\text{C}$  [57]. The transformation is reconstructive, which means that it breaks up Si-O bonds and rearrange the atoms positions. As this is a more comprehensive transformation, it is also slower than the displacive transformations. While quartz has a closely packed spiral form, cristobalite in the high temperature form has a more open structure where oxygen atoms are arranged in a cubic structure with repeating three-layer stacking sequence. The open structure gives a low density of  $2.20 \text{ g/cm}^3$  [54]. Different densities means that during the transformation from quartz to cristobalite, the volume will increase. The theoretical volume increase is about 17%, but experimental studies have found that some quartz types may increase their volume up to 44% [58], [59].

The  $\beta$ -quartz to  $\beta$ -cristobalite transformation is also found to go through an amorphous intermediate phase [60]–[63]. Amorphous silica has no long-range, periodic atomic structure. The short-range order is commonly specified by stating that each Si atom is surrounded almost tetrahedrally by four oxygen atoms, while each oxygen atom bridges between two Si atoms at the same distance. Amorphous silica has a density range of 2.0–



2.20 g/cm<sup>3</sup>. The most common coordination of the network structure in amorphous silica is the 6-membered ring, but other forms can also be present. A random network hypothesis allows several forms of coordination [64]. While tridymite and cristobalite has a void space of 51.7% and 48.4%, respectively, amorphous silica has a void space of 57% [65]. Presser and Nickel [66] therefore believed that gas diffusion is faster in amorphous materials compared to crystalline phases.

### 3.1.3.2 *Softening and melting properties*

As mentioned earlier, the softening and melting properties of the SiO<sub>2</sub> have a great impact on where SiO<sub>2</sub> reacts with either Si or SiC in the furnace, and hence for the reaction zones in the furnace. Before SiO<sub>2</sub> melts it will soften, which is described by Ringdalen et al [67] as when the shape of the quartz sample has lost its sharp edges. The softening and melting of quartz will affect the mass flow in the furnace [11], [68]. Pure SiO<sub>2</sub> melts around 1720 °C, but for industrial quartz sources exposed to conditions as in industrial furnaces, there are found softening and melting temperatures between 1600-1800 °C [59]. It is preferable to have high softening and melting temperatures so that melting of SiO<sub>2</sub> happens as deep in the furnace as possible. Softened SiO<sub>2</sub> is very viscous and if SiO<sub>2</sub> starts to soften at a higher position in the furnace, it might cause a more compact charge which again decrease the gas permeability.

Nordnes [69] created a temperature profile for a FeSi production furnace with different zones for heating, softening and melting of quartz, shown in Figure 52. This was done based on calculated temperature data obtained from Elkem, and the zones were created based on her experiments on softening and melting temperatures for three different quartz types. For two of the quartz types, it was observed a large softening zone. This could mean that the quartz uses longer time to melt. It was suggested that charge materials that were glued together by softened and melted quartz in the charge area would become electrically conductive and alter electrical paths in the furnace. This would in worst case reduce the power in the arc.

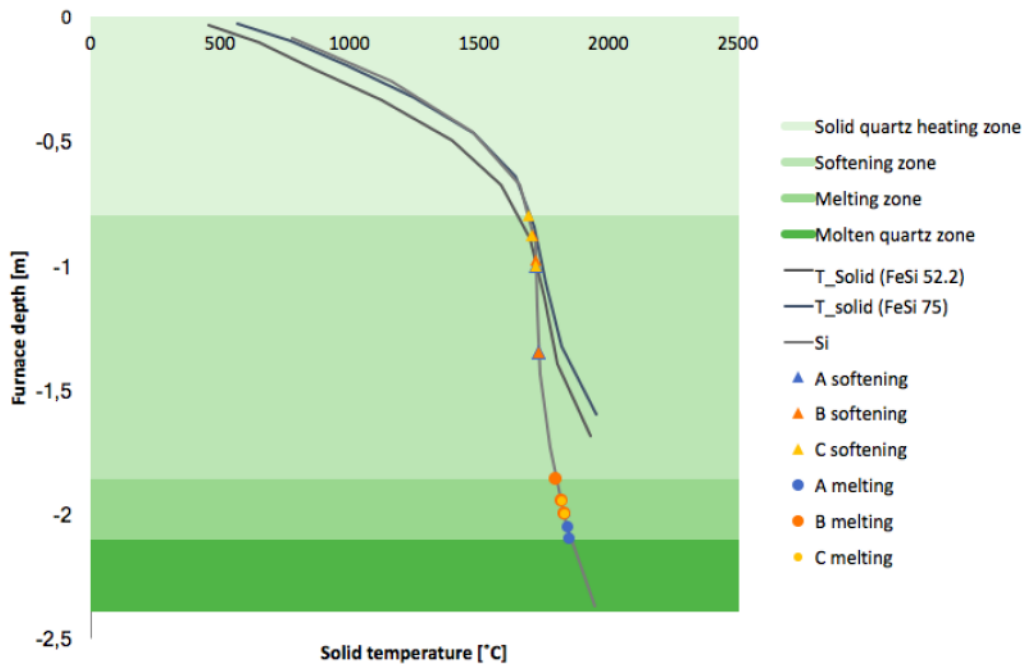


Figure 52 Modelled temperature distribution for selected industrial FeSi and Si furnaces with calculated depth for softening and melting of different quartz sources [69].

The border line between softened and melted quartz may also be diffuse and the exact determination of temperature/time depends on the eye of the operator. Jusnes [70] presented some criteria to determine the difference:

- Melted particles have more round shape than softened.
- Melted particles have adjusted themselves to the surroundings, softened have not.
- Melted particles may have melted together, forming larger particles. If there still exists a boundary between the particles, they are softened.

A number of recent studies have been performed on softening and melting temperatures of quartz [58], [67], [70]–[72]. These show that there are variations in the softening and melting temperatures between different quartz types. It was also found that the heating rate affects the softening and melting temperature. A slower heating rate gives lower softening and melting temperatures, which means that melting of  $\text{SiO}_2$  takes time. Nordnes [69] believed that this was due to the high viscosity of the  $\text{SiO}_2$  at its melting point, and a change in the shape is therefore difficult to observe.

Impurities in the quartz can affect the softening and melting temperature. The effect will depend on the impurity, but contaminants are expected to give lower softening and melting temperatures. Contaminants will break up the  $\text{SiO}_2$  network structure and create bindings between dislocation cores, which will decrease the system energy and thus lower the melting temperature [73]. It has also been suggested that impurities will catalyze the

movement on the crystal- liquid interface, when the crystal is covalently bonded [74]. In addition, type and amount of fluid inclusions can influence the melting behaviour of SiO<sub>2</sub> [75].

Ringdalen and Tangstad [58] found no clear correlation between observed softening temperatures and content of Al<sub>2</sub>O<sub>3</sub> or alkalis in the quartz, but found that softening temperature decreased with increasing content of FeO in their work. Nordnes [69] also studied the effect of impurities on the melting rate of quartz in her work. She found a that the rate of melting increased with increasing impurity concentration.

### 3.1.3.3 *Disintegration of quartz*

When quartz is added to the furnace, it will experience a steep temperature increase from room temperature to the charge top temperature around 1300 °C [3], [4]. The temperature on the charge surface can be higher than in the charge [76], and is most probably due to exothermic combustion of SiO and CO gas. The shock heating might cause the quartz to disintegrate, and this can again have a negative effect on the furnace operation. Too many fine particles in the charge will agglomerate or melt together and may hinder an even flow of materials and gases [5], [77]. Course particles ensures a good charge permeability and enables the ascending gas to interact and react with the carbon materials. Clogging of the furnace leads to creation of gas channels and can cause small outbursts of gas. The gas channels have less interaction with the descending raw materials and more SiO gas will escape the furnace, decreasing the total Si yield. A good permeability of the charge mixture requires raw materials with a good size distribution, giving more space around the raw materials and enables an even gas flow. Ideal lump size for the quartz used in Si and FeSi furnaces are 10-150 mm [78], and fine particles are defined as materials below 10 mm.

Several studies [9], [77]–[79] have shown that different quartz types will disintegrate differently, but the reason for this is not clear. Mechanical handling before heating and thermal strength during heating could both be contributors to production of fines upon shock heating. There are three main factors which contributes to the crack formation in SiO<sub>2</sub> [80]: 1) low density high temperature silica polymorphs, 2) presence of fluid inclusions and 3) mineral inclusions at the grain boundaries.

- 1) When quartz is heated, it will transform into different SiO<sub>2</sub> polymorphs. As earlier described in 3.1.3.1: Polymorphs of silica, this will cause a volume change due to different densities in the different phases. Crack formation occurs when grains expand differently in different directions and induce stress in the crystal group [78].
- 2) The internal partial pressure of fluid inclusions in the quartz will increase with increasing temperature until they escape the SiO<sub>2</sub>, normally in the temperature range from 200-600 °C. The fluid inclusions in the quartz mainly consists of water or water+CO<sub>2</sub>. Water inclusions have a higher internal pressure and will decrepitate at a lower temperature than water+CO<sub>2</sub>. With increasing internal pressure, cracks

will develop in the SiO<sub>2</sub> and enable degassing of water and CO<sub>2</sub> from the inclusions [81].

- 3) Mineral inclusions in the quartz are most often present at the grain boundaries. Typical impurities in the quartz are muscovite (KAl<sub>2</sub>(Si<sub>3</sub>Al)O<sub>10</sub>(OH,F)<sub>2</sub>) and feldspar (KAlSi<sub>3</sub>O<sub>8</sub> – NaAlSi<sub>3</sub>O<sub>8</sub> - CaAl<sub>2</sub>Si<sub>2</sub>O<sub>8</sub>). These minerals have a lower melting temperature than SiO<sub>2</sub> and heating can therefore lead to crack formation.

To investigate the extent of disintegration for different quartz types, shock heating experiments have been performed. Jusnes [9] studied the degree of disintegration for ten different quartz types used in Si and FeSi production. This was done by inserting a ~200 g sample in a preheated carbon crucible at 1500 °C for 10 minutes. Her results can be seen in Figure 53, which shows the amount of fines below 10 mm after shock heating. Large variations were found between the different quartz types, from around 5 wt% up to 85 wt%. CT-scans were performed on some of the samples to measure the crack area before and after heating, and it was found a correlation between measured cracks and amount of fines produced during shock heating. By FT-IR, it was found that the quartz with larger grain sizes created more fines than the quartz with smaller grains. It was also found that the quartz containing more impurities of muscovite, produced the least amount of fines. It was suggested that the layered structure of muscovite would absorb some of the tension created during shock heating. The phase transformation from quartz to amorphous phase and to cristobalite happens around 1300 °C and 1470 °C, respectively [54], and it was believed that the volume increase during this transformation would cause disintegration in the SiO<sub>2</sub> [79]. Jusnes did not find any correlation between the amount of amorphous phase and cristobalite, and the amount of fines after shock heating.

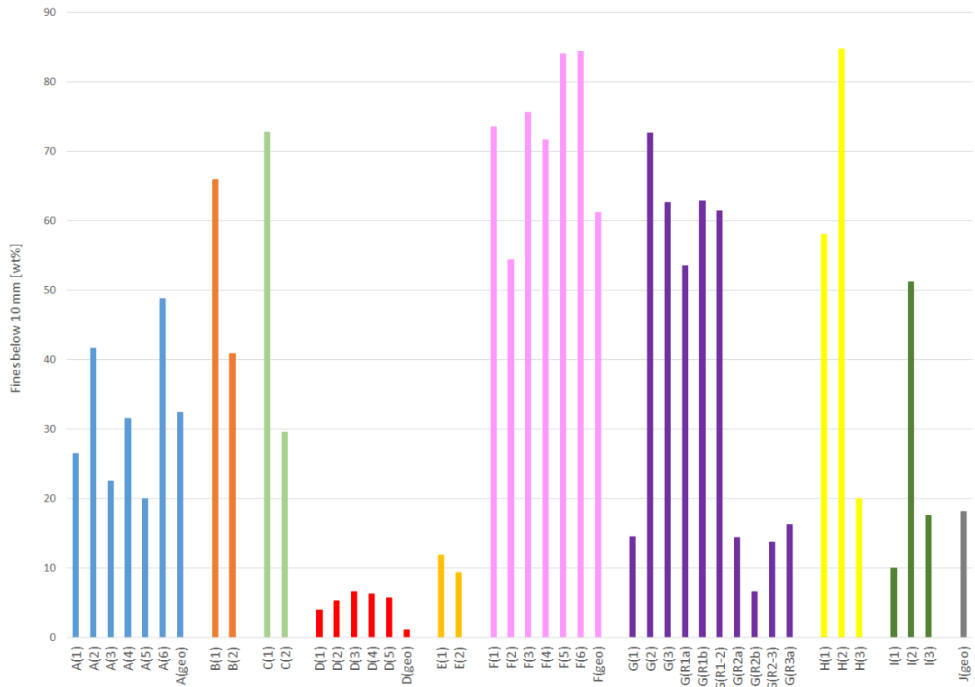


Figure 53 Fines below 10 mm given in wt% after shock heating at 1500 °C for ten different quartz types [9].

The same method for shock heating of quartz at 1500 °C was also earlier used by Ringdalen [77]. Her results were combined with the work of Paulsen and Bakken. Figure 54 shows the cumulative percentage of the different size fractions. Similar to the results from Jusnes [9], it can also here be observed large variations between the different quartz types. The amount of fines varied from 10% to 87%.

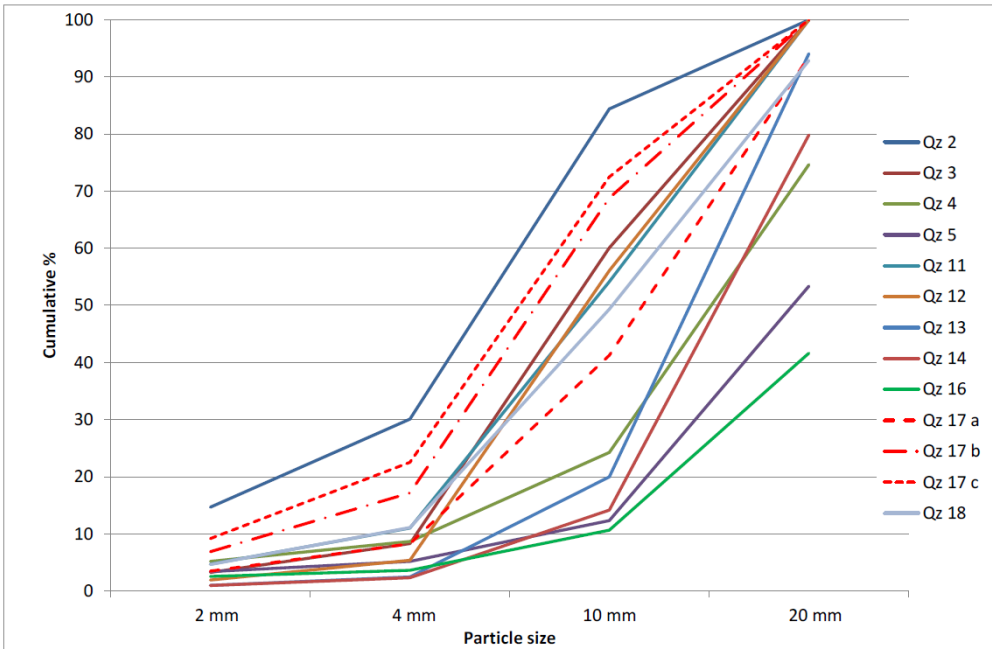


Figure 54 Cumulative percentage of different size fractions after 10 minutes shock heating at 1500 °C for 11 quartz types [77]. Fines are defined as particles <10 mm.

Aasly et al. [82] studied fines generation for six different quartz types after shock heating to 1300 °C. They also found that the amount of fines produced varied between the different quartz types. In addition, samples were compared before and after heating by microscopic methods. Fluorescent epoxy filling micro cracks, grain boundaries and cavities in the samples were visualized in polarized light microscopy. From this, it could be seen that heating of the samples opened the grain boundaries in most samples, leading to micro cracks. In addition, a network of micro cracks was observed in the fluid inclusion planes as a result of fluid inclusion decrepitations. This was not in agreement with the results from Birkeland and Carstens, cited by Aasly [82], which concluded that the fluid inclusion were not important for the crack generation in quartz.

## 3.2 Experimental procedure

To ensure a raw material quartz with optimal properties suited for the production, more knowledge about the different quartz types, its impurities and how it behaves at elevated temperatures are important. The behaviour at high temperature has a great impact on the initial reacting process in the higher parts of the furnace, and hence also the further production of Si. Slag originates mainly from the impurities in the quartz. Heating experiments were performed to study the impurities behavior, the melting properties, and the crack formation during heating up to softening and melting temperatures. The main goal in this investigation is to study the impurities behaviour in the quartz during heating and to verify earlier experiments on quartz disintegration and melting properties with comparable results.

### 3.2.1 The quartz types

Six different quartz types were used for the quartz experiments, shown in Figure 55. The quartz names are anonymized and are labelled with a letter, quartz A, B, C, D, F and G. The quartz types were chosen based on the expected amount of impurities and expected degree of degradation during heating. Table 23 lists the general ICP-MS analysis, which gives the initial chemical composition. It is important to note that when working with natural materials, inhomogeneity must be expected, and variations may therefore occur. The analysis will still provide an indication of the degree of impurities in the quartz. Quartz B, C and D have the highest degree of impurities ~1%, while quartz A, F and G contain ~99.9% SiO<sub>2</sub>. The pseudonym for quartz type A, D, F and G are the same quartz as used in Jusnes [9] doctoral thesis. Quartz B and C are Qz8 and Qz35, respectively.

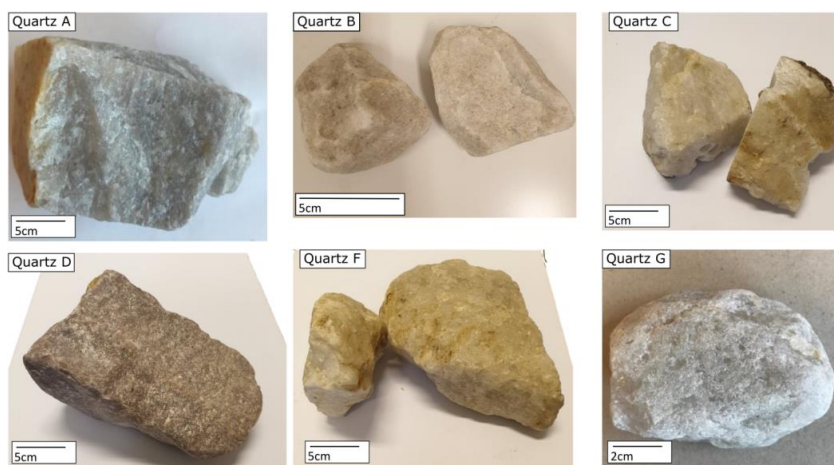


Figure 55 Quartz type A, B, C, D, F and G used in this study. °C

Table 23 ICP-MS analysis for quartz A, B, C, D, F and G [9].

Quartz type	% Al <sub>2</sub> O <sub>3</sub>	%K <sub>2</sub> O	%FeO/Fe <sub>2</sub> O <sub>3</sub>	%CaO	%MnO
Quartz A	0.020	0.002	0.003	0.0004	~0.4 ppm
Quartz B	0.613	0.154	0.0771	0.0084	0.9 ppm
Quartz C	1.19	0.180	0.09	0.09	0.140
Quartz D	0.492	0.075	0.314	0.005	<0.1 ppm
Quartz F	0.017	0.005	0.003	0.001	~1 ppm
Quartz G	0.015	0.002	0.003	0.004	~0.4 ppm

## 3.2.2 Quartz heating experiments

### 3.2.2.1 Sessile drop furnace

Heating experiments with quartz were conducted in a sessile drop furnace. A schematic overview of the furnace is shown in Figure 56. The furnace consists of a horizontally oriented enclosed chamber where the sample is placed, with graphite heat elements. Surrounding the heater are graphite radiation shields, and a water-cooling system is connected to remove heat from the components during heating. The temperature is measured with a B-type thermocouple measures, which has a limited of 1800 °C. However, the furnace can be operated at a maximum temperature of 2400 °C. An additional temperature control is provided by a pyrometer. Regular calibrations with Fe are performed to ensure accurate temperature measurements.

Quartz cylinders measuring 2-3 mm in height and 4 mm in diameter were placed on a 3 mm high graphite substrate with a diameter of 10 mm (made from ISO88 (Tanso)). These components were then positioned on the sample holder and inserted into the inner chamber of the furnace. The furnace operates in a reducing atmosphere. Prior to heating and purging the process gas, it is necessary to establish vacuum conditions. This is obtained by using a vacuum pump to evacuate gas from the chamber until a sufficient vacuum level of 10<sup>-1</sup> mbar is reached. The addition of gas is controlled by mass flow controllers. For the experiments in this study, argon gas with a flow rate of 0.1 l/min is used as process gas. Argon is an inert gas that does not react with the quartz samples or the graphite substrate. The same heating profile, as shown in Figure 57, is used for all experiments. A firewire digital video camera equipped with a telecentric lens is mounted in the front of a window on the heater, allowing continuous observations and recording of images from the furnace during the heating experiments.



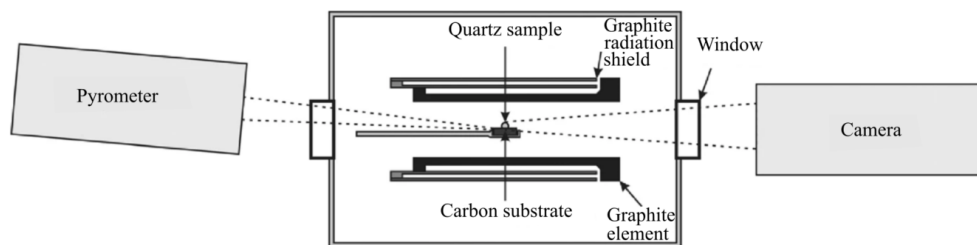


Figure 56 Schematic overview of the sessile drop furnace. This is a revised figure from Bao et al. [83].

Softening and melting experiments to 1750 °C were conducted in the sessile drop furnace. This temperature is just above the theoretical melting temperature of pure SiO<sub>2</sub>, which is around 1720 °C. To ensure reproducible results, three repetitions were performed for each quartz type. After the temperature reached 1750 °C, it was held until the SiO<sub>2</sub> samples were completely melted.

Furthermore, heating experiments were carried out to investigate the behaviour of the impurities in the quartz during heating to elevated temperatures. Samples of quartz C, D and F were heated to 1600 °C and 1800 °C, which are slightly below and above the theoretical melting temperature of pure SiO<sub>2</sub>. An overview of all the quartz sessile drop experiments is listed in Table 24, and the heating profiles are shown in Figure 57.

Table 24 Heating experiments in the sessile drop furnace. All experiments were run in Argon atmosphere 0.1l/min.

Quartz type	Softening and melting exp. [#] 1750°C	Impurities behaviour [#]		
		Initial	1600°C	1800°C
Quartz A	3			
Quartz B	3			
Quartz C	3	1	2	2
Quartz D	3	1	2	2
Quartz F	3	1	2	2
Quartz G	3			

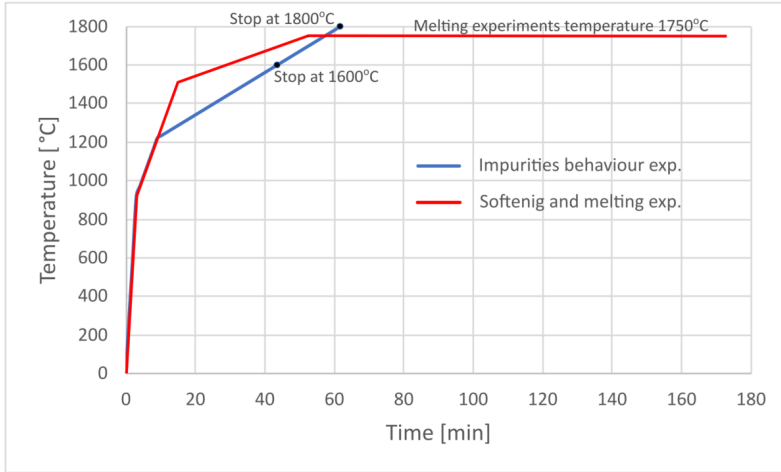


Figure 57 Temperature profile for the sessile drop experiments. The argon flow rate was the same 0.1 l/min for all experiments. For the melting experiments, the temperature was held until the SiO<sub>2</sub> samples were completely melted.

### 3.2.2.2 High temperature confocal microscope experiments

To study the behavior of SiO<sub>2</sub> during heating, a high temperature confocal microscope (HTCM) was used. This equipment possesses the function of metallographic analysis and laser confocal real-time analysis. In total 18 experiments were conducted, and an overview is listed in Table 25. The quartz samples were sent to Beijing and the experiments were performed at the University of Science and Technology Beijing. The sample surface is observed and monitored from room temperature and up to 1600 °C [84]. Continuous information about the surface structure, crack occurrence, the impurities behavior and other phenomena during heating are obtained, and this gives valuable information about the quartz behavior at different temperatures. The HTCM consists of a laser confocal microscope, type VL2000DX, and a high temperature heating furnace, type SVF17SP [85]. Figure 58 shows an overview of the basic components of the HTCM. Quartz cubes with lengths of 5.5×5.5 mm and a height of 3.5 mm are placed in an alumina crucible with a diameter of 8 mm, and then placed in the microscope. Pictures of the sample before and after a HTCM experiment are shown in Figure 59. Next, the samples are heated with a heating rate 100 °C/min up to 1000 °C, and 25 °C/min up to 1650 °C in argon atmosphere. The beam from the light is first focused on the surface of the sample. The reflecting light source on the surface of the sample returns along the original light path, and it focuses again through the semi-reflected and semi-transmitted light in the middle. The pinhole effect enables the light to image on the photoreceptor and the image information with high resolution and contrast can be obtained.

Table 25 High Temperature Confocal Microscope experiments. All experiments were conducted with the same heating rate; 100 °C/min up to 1000 °C and 25 °C/min up to 1650 °C.

Quartz	Repetitions
Quartz A	3
Quartz B	3
Quartz C	3
Quartz D	3
Quartz F	3
Quartz G	3

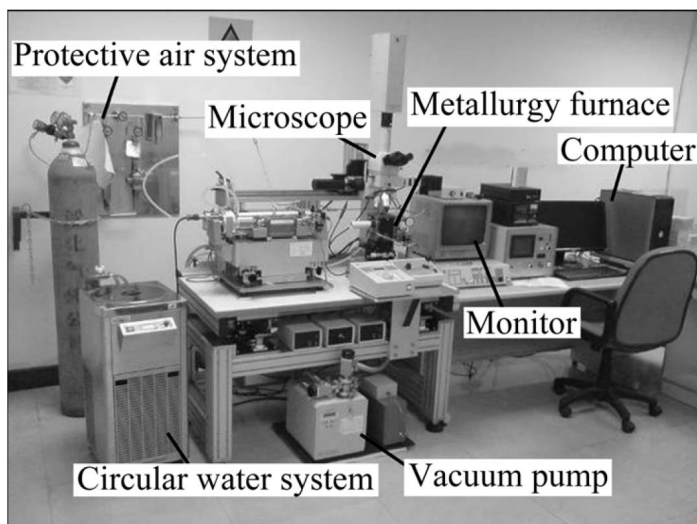


Figure 58 The components of the high temperature confocal microscope [84].

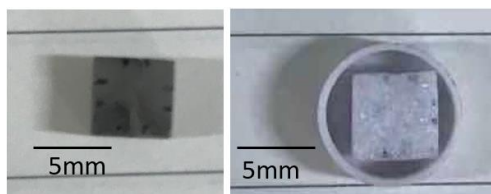


Figure 59 Picture of the prepared quartz sample before and after a High Temperature Confocal Microscope experiment.

### 3.2.3 Characterization

#### 3.2.3.1 Electron probe micro-analysis

EPMA, JEOL JXA 8500 was used to investigate the quartz samples after the sessile drop furnace experiments. Representative areas were chosen for imaging and for further analysis with WDS. The equipment and experimental work are the same as for the industrial samples and are described in section 2.2.3.1.

### *3.2.3.2 Field emission scanning electron microscope*

To study the surface of the quartz surface before and after the HTCМ experiments, a field emission scanning electron microscopy (FESEM), JSM-6701F, at the University of Science and Technology Beijing was used. Secondary imaging mode was applied for these samples. The equipment is attached with a NS7 type X-ray energy spectrometer (EDS) which allows for semi-quantitative microchemical analysis of the sample. EDS was used to analyze the impurity areas in the quartz samples both before and after the HTCМ experiments.

### 3.3 Results

When quartz is added as a raw material to the Si/FeSi furnace, it will experience a steep temperature increase from room temperature to the charge top temperature around 1300 °C [3], [4], [76]. How the SiO<sub>2</sub> and its impurities behave at elevated temperature are hence important for the furnace operation, and different quartz types have been found to behave differently [9], [58], [59], [77]. Six types of quartz used for Si and FeSi production are therefore used in this study for comparison.

#### 3.3.1 Softening and melting of SiO<sub>2</sub>

Images of the different quartz types at softening and melting point are shown in Figure 60. The softening temperatures and the melting times for the different quartz types are summarized in Figure 61. It can be seen that there are significant differences between the different quartz types. Quartz B and C have the lowest softening temperatures, ranging from around 1670 °C to 1700 °C, and shorter melting times. Quartz G has the highest softening temperature at 1745 °C and takes approximately 80 minutes at 1750 °C to melt completely. The lower softening temperatures and melting times were expected for quartz B and C, as these two quartz types have higher impurity contents. Figure 62 presents graphs illustrating the relationship between impurities content in the quartz and the softening temperature on the left, and melting time at 1750 °C on the right. Generally, a higher impurity content correlates with lower softening temperatures and shorter melting times. However, Quartz D has one of the highest impurity content, but also has a higher softening temperature and a longer melting time than Quartz B and C. Figure 63 and Figure 64 show the same graphs, this time focusing on the amount of Al<sub>2</sub>O<sub>3</sub> and K<sub>2</sub>O as a function of the softening temperatures and melting times, respectively. The melting times increases with decreasing amount of both Al<sub>2</sub>O<sub>3</sub> and K<sub>2</sub>O. In addition to Al<sub>2</sub>O<sub>3</sub> and K<sub>2</sub>O, Quartz D also contains 0.314% FeO/Fe<sub>2</sub>O<sub>3</sub>, while quartz B and C have iron oxides contents of 0.08% and 0.09%, respectively. Based on this, it appears that Al<sub>2</sub>O<sub>3</sub> and K<sub>2</sub>O impurities have more influence on the softening and melting properties than FeO/Fe<sub>2</sub>O<sub>3</sub>.

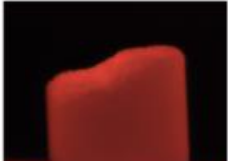


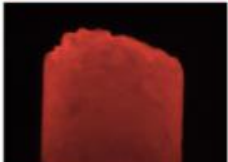
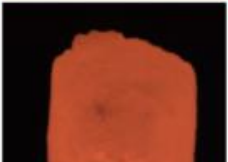

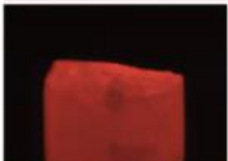





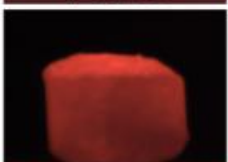
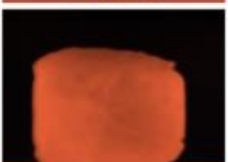




Quartz type	Initial	Softening	Complete melting
A.1	 T=900°C	 T=1730°C	 T=1750°C
B.3	 T=900°C	 T=1675°C	 T=1750°C
C.1	 T=900°C	 T=1695°C	 T=1750°C
D.3	 T=900°C	 T=1735°C	 T=1750°C
F.1	 T=900°C	 T=1720°C	 T=1750°C
G.3	 T=900°C	 T=1745°C	 T=1750°C

Figure 60 Images of each quartz type A, B, C, D, F and G at 900 °C, softening temperature, and complete melting.

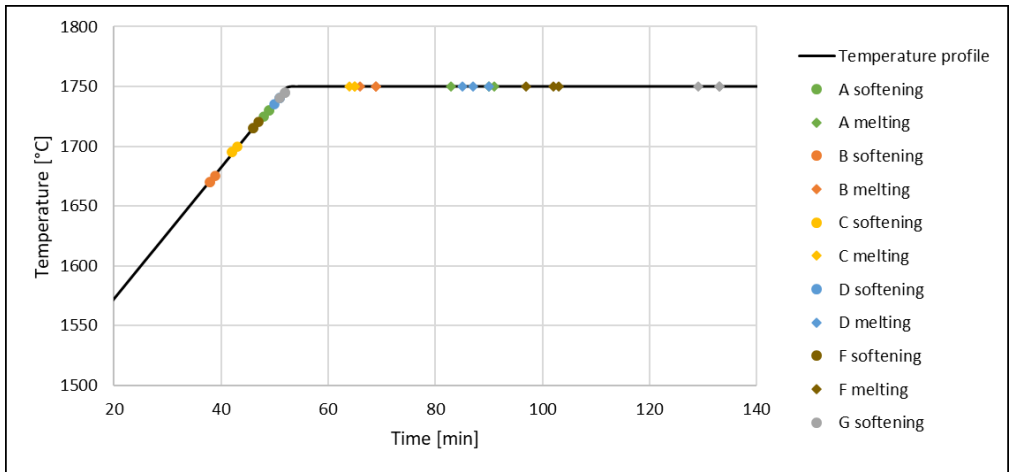


Figure 61 Overview softening and melting temperatures for quartz A, B, C, D, F and G.

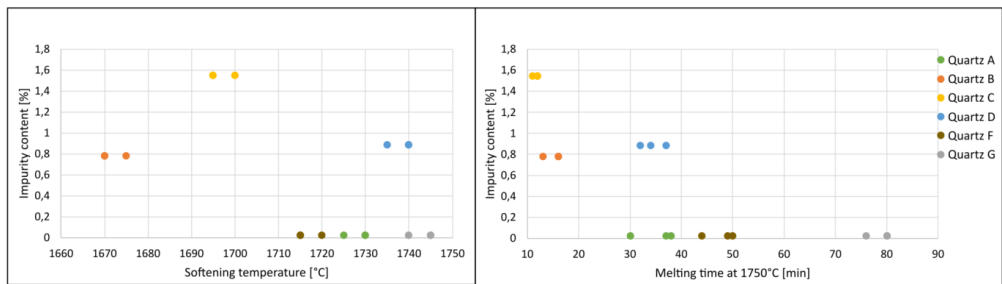


Figure 62 The total amount of impurities given in % as a function of the softening temperature (left) and melting time at 1750 °C (right) for quartz A, B, C, D, F and G.

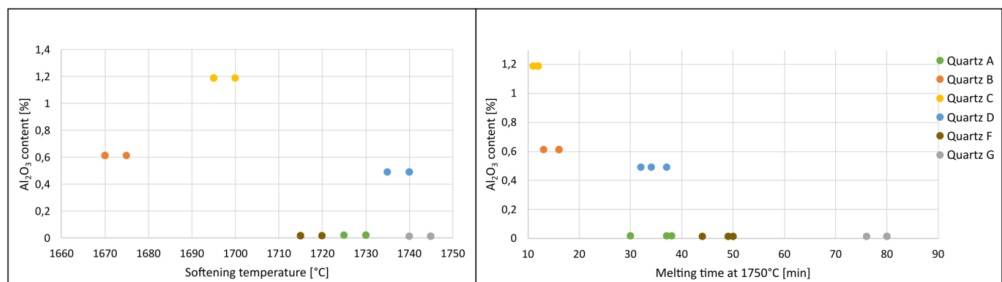


Figure 63 The amount of Al<sub>2</sub>O<sub>3</sub> given in % as a function of the softening temperature (left) and melting time at 1750 °C (right) for quartz A, B, C, D, F and G.

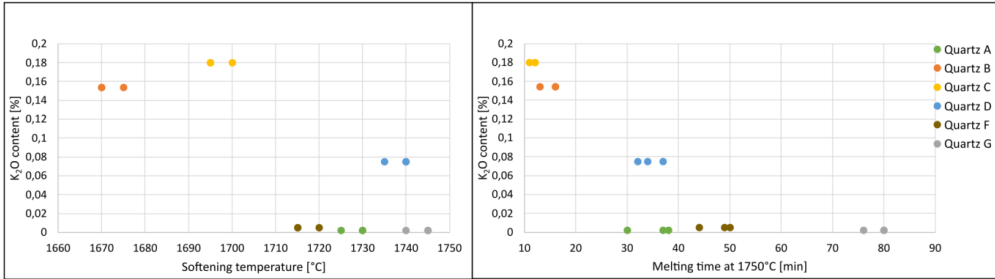


Figure 64 The amount of  $K_2O$  given in % as a function of the softening temperature (left) and melting time at 1750 °C (right) in quartz type A, B, C, D, F and G.

### 3.3.2 Volume expansion during heating

The volume expansion for the experiments in the sessile drop furnace was measured using ImageJ through a custom-made software that analysis the experiments video. Figure 65 illustrates the results, showing the volume expansion as a function of temperature up to 1750 °C. For all the quartz types, the volume increased with increasing temperature. The measurements showed volume expansion from 5% and up to 31%. Most of the samples have a linear increase up 1500 °C, followed by a steeper volume increase. The transformation from  $\alpha$ -quartz to  $\beta$ -cristobalite happens from around 1470 °C, which is expected to cause a volume increase due to different densities of quartz and cristobalite polymorphs. The maximum volume was found in the temperature interval 1600-1700 °C. The decrease in volume after 1700 °C is most likely that the melting of the  $SiO_2$  has started. Quartz B was the quartz type that in this study had the smallest volume expansion. All three parallels increased less than 8%. Quartz G experienced the largest volume increase where two of the samples increased to around 30%, while the third increased with around 19%.

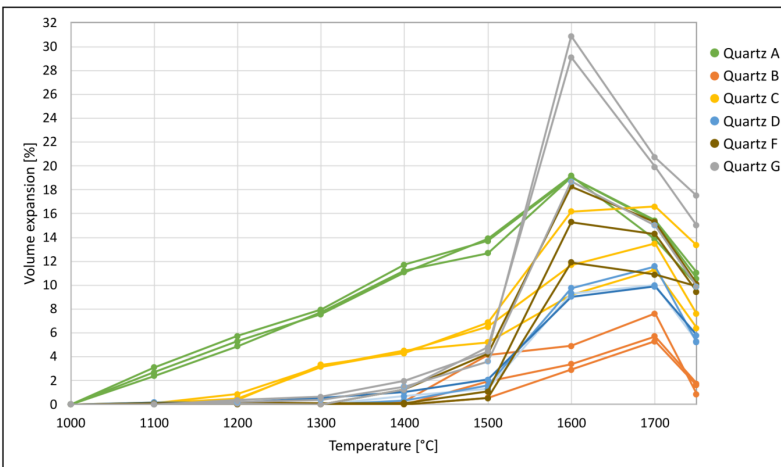


Figure 65 Volume expansion as a function of temperature up to 1750 °C for quartz A, B, C, D, F and G.



### 3.3.3 Impurities behaviour during heating

#### 3.3.3.1 Heating experiments from sessile drop furnace

Quartz type C, D and F were heated to 1600 °C and 1800 °C in the sessile drop furnace and the impurities in the SiO<sub>2</sub> were studied. Based on the ICP-MS analysis presented in Table 23 in section 3.2.1. The quartz types, it was expected that quartz C and D would contain more impurities compared to quartz F. Backscattered images focusing on the impurities are shown in Figure 66, Figure 67 and Figure 68. The normalized WDS results are presented in Table 26, while the original results can be found in Table 56, Table 57 and Table 58 in Appendix B. Generally, the amount of SiO<sub>2</sub> in the impurity areas increases with increasing temperature. It should be noted that these analysis are performed on different samples. It is therefore not the development of the same impurity areas that were analyzed. These results are still used to see the trend, that amount of SiO<sub>2</sub> in the impurities increases with increasing temperature. It is also worth noting that the viscosities for many of the impurity compositions are very high.

For quartz C, the impurities mainly consisted of SiO<sub>2</sub>, Al<sub>2</sub>O<sub>3</sub> and K<sub>2</sub>O. In the initial sample and the samples heated to 1600 °C, the SiO<sub>2</sub> content was approximately 50% and 70%, respectively. In the sample heated to 1800 °C, the impurity areas consisted of 88% SiO<sub>2</sub>.

In the case of quartz D, the impurities primarily contained SiO<sub>2</sub>, FeO and Al<sub>2</sub>O<sub>3</sub>. In the initial sample, the impurities contained around 60% FeO. In one of the quartz D samples heated to 1600 °C, two different impurity areas were found: one white colored and one bright grey, with SiO<sub>2</sub> content of 61% and 83%, respectively. The other sample had areas with 92% SiO<sub>2</sub>. In the two samples heated to 1800 °C, the SiO<sub>2</sub> was melted. There were some brighter areas in both samples, both consisting of >93% SiO<sub>2</sub>. A SiO<sub>2</sub> content ~90-95% could be attributed to SiO<sub>2</sub> contamination in the analysis due to a thin impurity area.

No impurities were found in the quartz F samples heated to 1600 °C and 1800 °C. Although brighter areas can be observed on the EPMA images, the WDS results indicates that this is 99% SiO<sub>2</sub>. The initial quartz F contained one impurity “spot” consisting of SiO<sub>2</sub>, K<sub>2</sub>O and Al<sub>2</sub>O<sub>3</sub>. From the ICP-MS analysis, it was determined that quartz F is 99.9% SiO<sub>2</sub>, and impurity areas are therefore seldomly found.

Table 26 Normalized WDS results for sessile drop experiments for quartz C, D and F. Oxide analysis are given in wt%. Viscosities are calculated using FactSage 8.1.

Quartz Type		SiO <sub>2</sub>	Al <sub>2</sub> O <sub>3</sub>	FeO	K <sub>2</sub> O	MgO	MnO	TiO <sub>2</sub>	Viscosity [Poise]	
									1600°C	1800°C
C <sub>initial</sub>	1	50.4	35.9	2.1	10.3	1.3			1.8·10 <sup>2</sup>	3.1·10
	2	52.8	33.7	1.5	9.3	1.4		1.3	2.1·10 <sup>2</sup>	5.6·10
C <sub>1600°C (1)</sub>		70.3	23.1		6.7				2.3·10 <sup>3</sup>	1.0·10 <sup>3</sup>
C <sub>1600°C (2)</sub>		66.9	23.4		9.7				4.3·10 <sup>3</sup>	1.7·10 <sup>2</sup>
C <sub>1800°C (2)</sub>		87.6	7.4		1.7	1.3	2.1		4.4·10 <sup>4</sup>	4.4·10 <sup>4</sup>
D <sub>initial</sub>		22.6	14.0	59.7	3.7				3.0·10 <sup>-1</sup>	8.0·10 <sup>-2</sup>
D <sub>1600°C (1)</sub>		91.8	4.7	3.5					7.0·10 <sup>4</sup>	4.8·10 <sup>3</sup>
D <sub>1600°C (2)</sub>	white	60.9	13.8	23.0	2.3				9.6·10	2.7·10
		grey	83.3	9.7	4.9	2.1			1.1·10 <sup>4</sup>	8.3·10 <sup>3</sup>
D <sub>1800°C (1)</sub>		93.2	1.6	2.9				2.2	2.0·10 <sup>5</sup>	1.2·10 <sup>5</sup>
D <sub>1800°C (2)</sub>		95.0	2.4	1.3				1.3	9.2·10 <sup>5</sup>	8.1·10 <sup>5</sup>
F <sub>initial</sub>		57.2	31.5	2.3	9.0				4.0·10 <sup>2</sup>	9.1·10
F <sub>1600°C (1)</sub>		99.9								
F <sub>1600°C (2)</sub>		99.9								
F <sub>1800°C (1)</sub>		99.9								
F <sub>1800°C (2)</sub>		99.8								

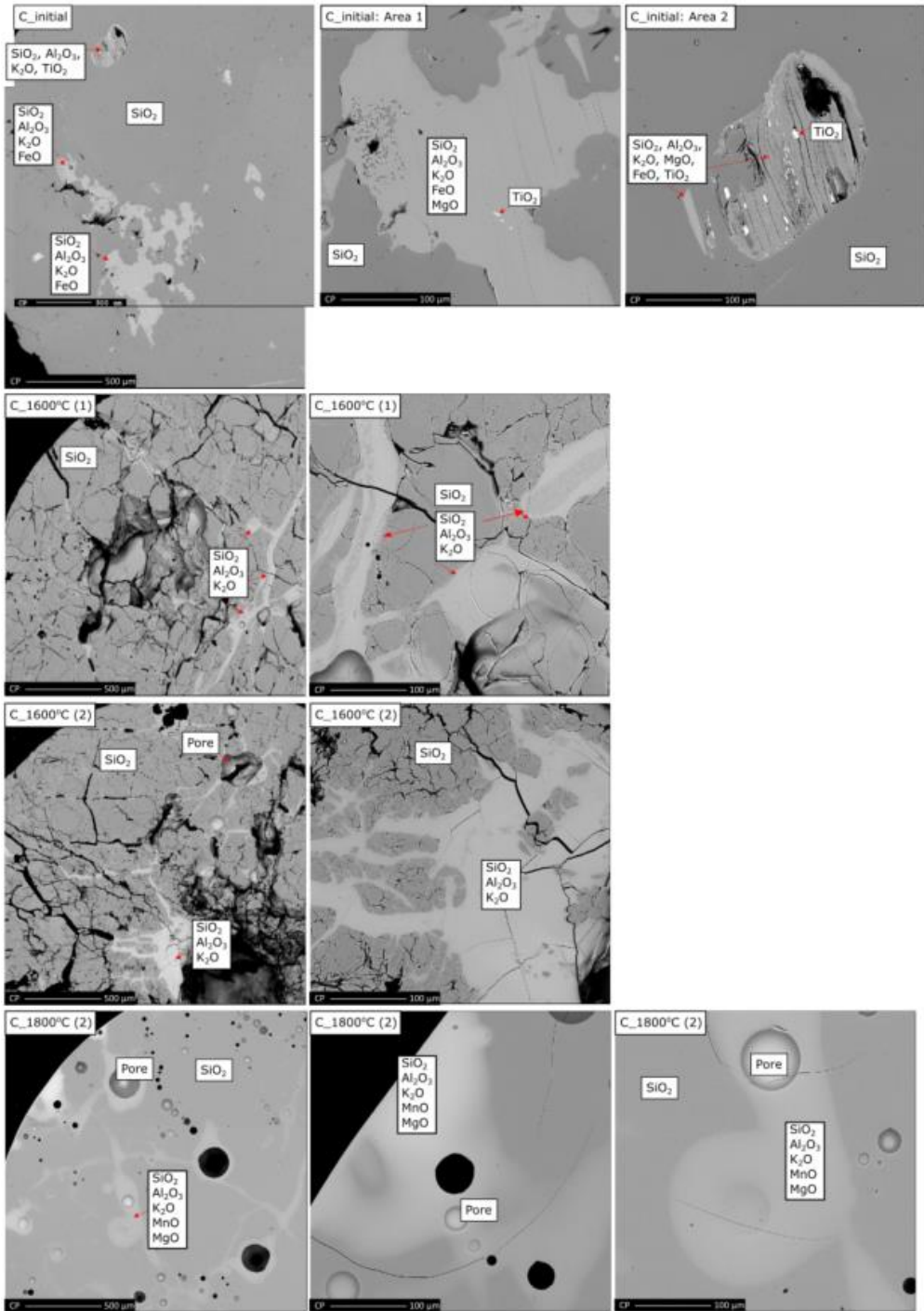


Figure 66 Backscattered images of quartz C; initial, and heated to 1600 °C and 1800 °C, with focus on the impurity areas.

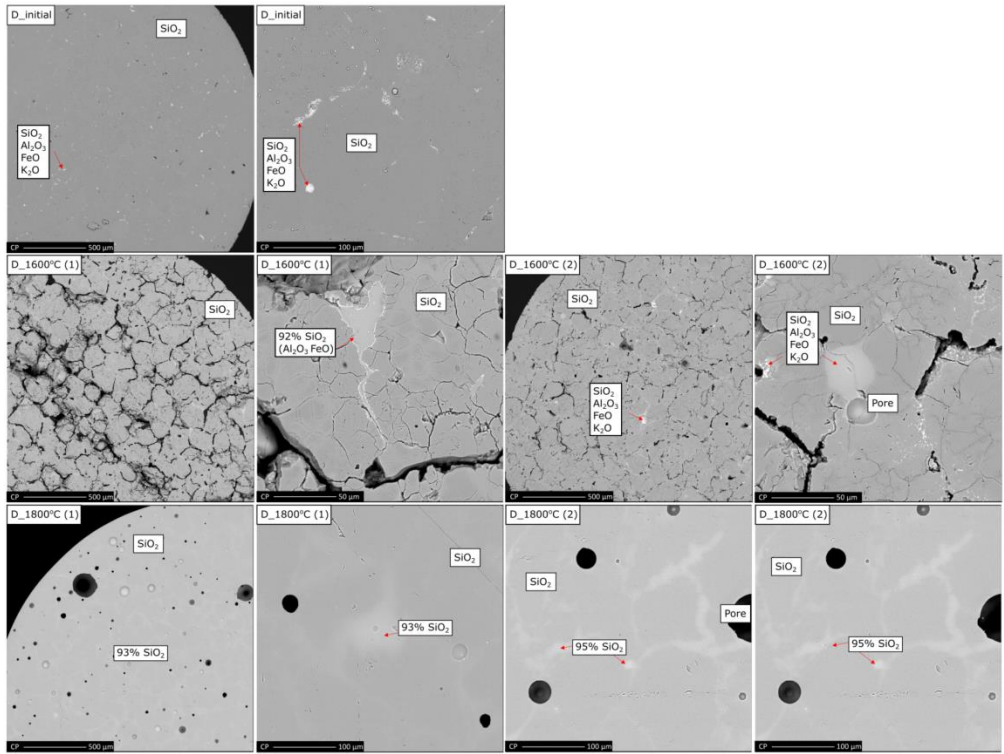


Figure 67 Backscattered images of quartz D: initial and heated to 1600 °C and 1800 °C, with focus on the impurity areas.

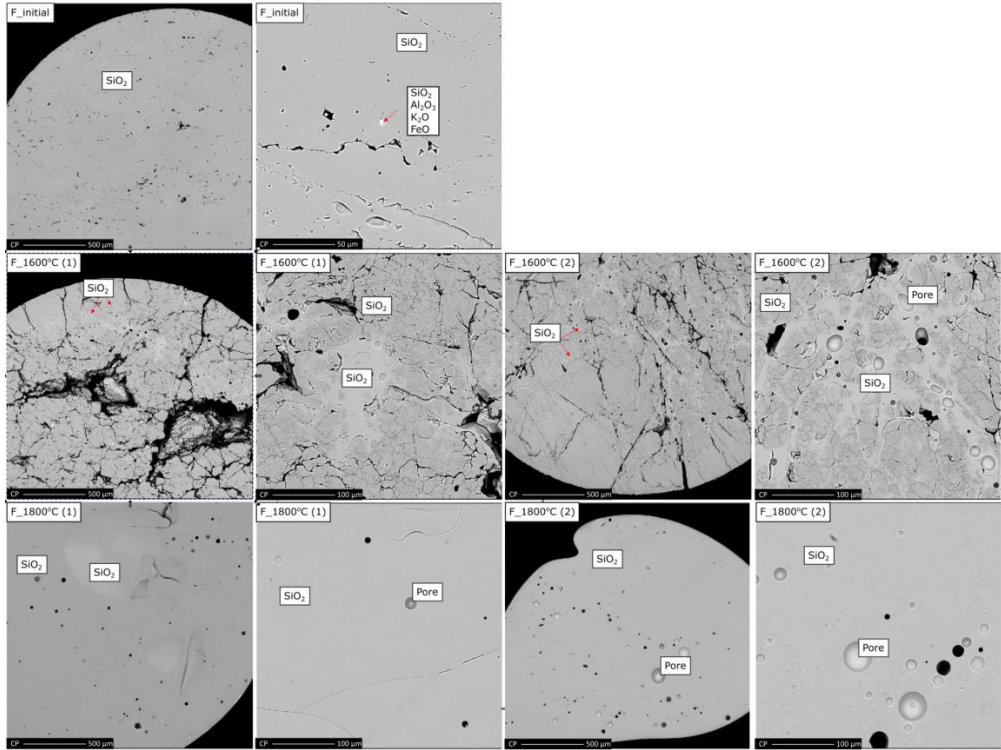


Figure 68 Backscattered images of quartz F: initial and heated to 1600 °C and 1800 °C, with focus on the impurity areas.

### 3.3.3.2 Heating experiments from HTCM

Samples of all quartz types, A, B, C, D, F and G were studied in HTCM during heating up to 1600 °C. Specially, samples containing areas with impurities were selected as the behaviour of these impurities was one of the focus areas in this study. Prior to and after the HTCM experiments, the samples were also studied in FESEM. The FESEM images, along with the HTCM images, for quartz A, B, C, D, F and G are presented in Figure 69, Figure 70, Figure 71, Figure 72, Figure 73 and Figure 74, respectively.

During heating in the HTCM, it was observed that certain impurity areas expanded, as seen in B.1, B.3, C.2, which contained SiO<sub>2</sub> and Al<sub>2</sub>O<sub>3</sub>, or SiO<sub>2</sub>, Al<sub>2</sub>O<sub>3</sub>, FeO and TiO<sub>2</sub>. However, other impurities with the same oxides did not experience similar expansion, and it can therefore not be concluded any consistent trend. Some of the impurities underwent a color change, as observed in C.1, C.3, D.1 and D.3, all containing ZrO<sub>2</sub>. This color change is likely due to the phase transformations in ZrO<sub>2</sub> from monoclinic structure to tetragonal structure. The temperature of this transformation is dependent on both the grain size and the stress in the ZrO<sub>2</sub>, but is typically around 1200 °C [86]. Many impurities also induce cracking, which will be the focus in the next subchapter. The impurity area in A.1 remained visually unchanged, but in general, the trend was that the impurities triggered activity in form of cracking in the SiO<sub>2</sub>, expansion, or color change during heating.

EDS analysis were performed on many of the impurities, and the numbered boxes on the FESEM images corresponds to the area analyzed, given in Table 27. EDS analysis are used to identify the elements present and provides an indication of their distribution. It should also be noted that there is a high risk of SiO<sub>2</sub> contamination from the SiO<sub>2</sub> matrix during these analysis, as many of the impurities are very small. For many of the samples, the analysis revealed a similar trend as for the samples run in the sessile drop furnace: an increased SiO<sub>2</sub> content in the impurities after heating. However, in some areas, different additional oxides were detected in the EDS analysis conducted after the HTCM experiment compared to the initial sample. This may be due to a slight shift in the EDS analyzer, meaning that it is not the exact same spot that was analyzed. This further indicates that some of the impurity areas are very heterogenous.

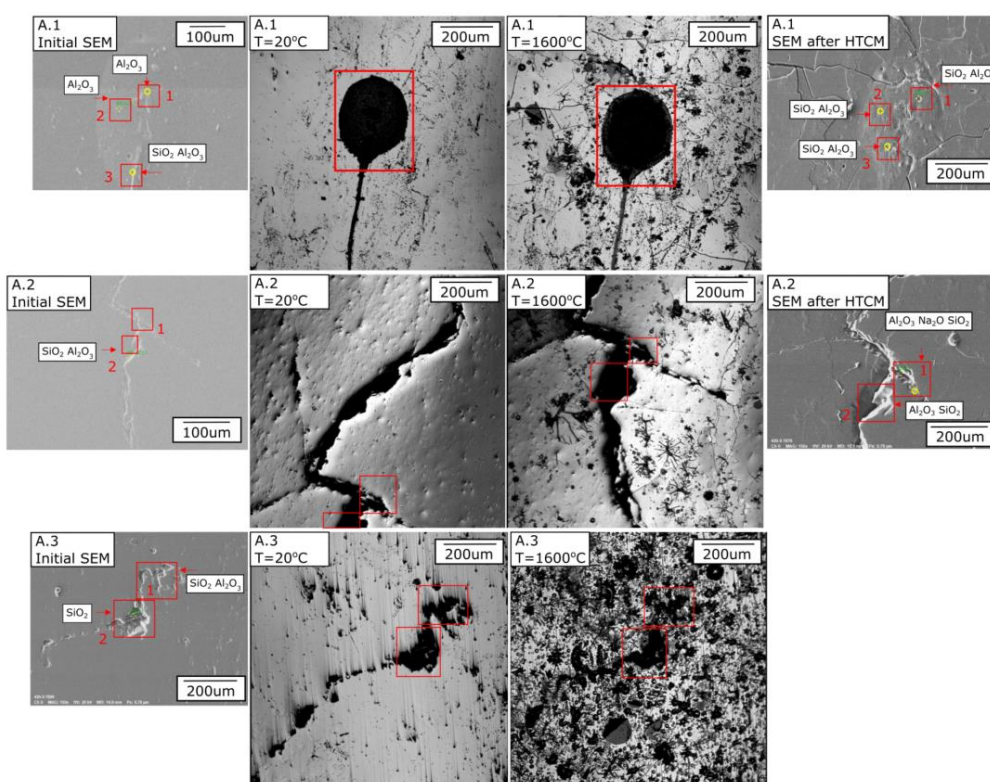


Figure 69 SEM images and images from high temperature confocal microscope experiments for quartz A, with focus on the impurities. The numbered boxes on the SEM images are related to the area analyzed with EDS in Table 27.

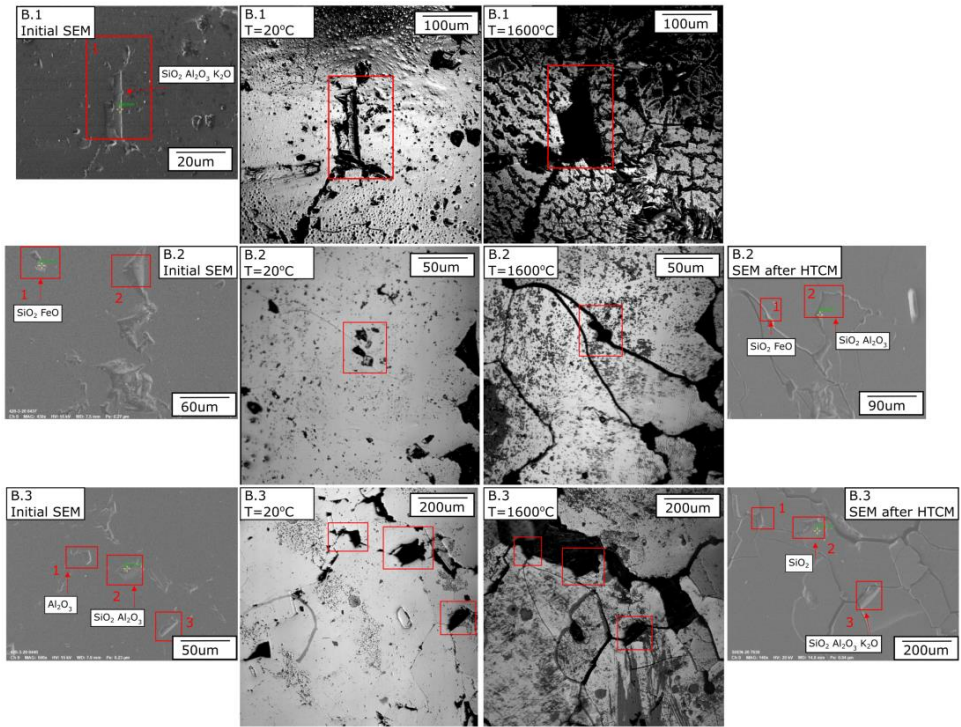


Figure 70 SEM images and images from high temperature confocal microscope experiments for quartz B, with focus on the impurities. The numbered boxes on the SEM images corresponds to the area analyzed with EDS in Table 27.

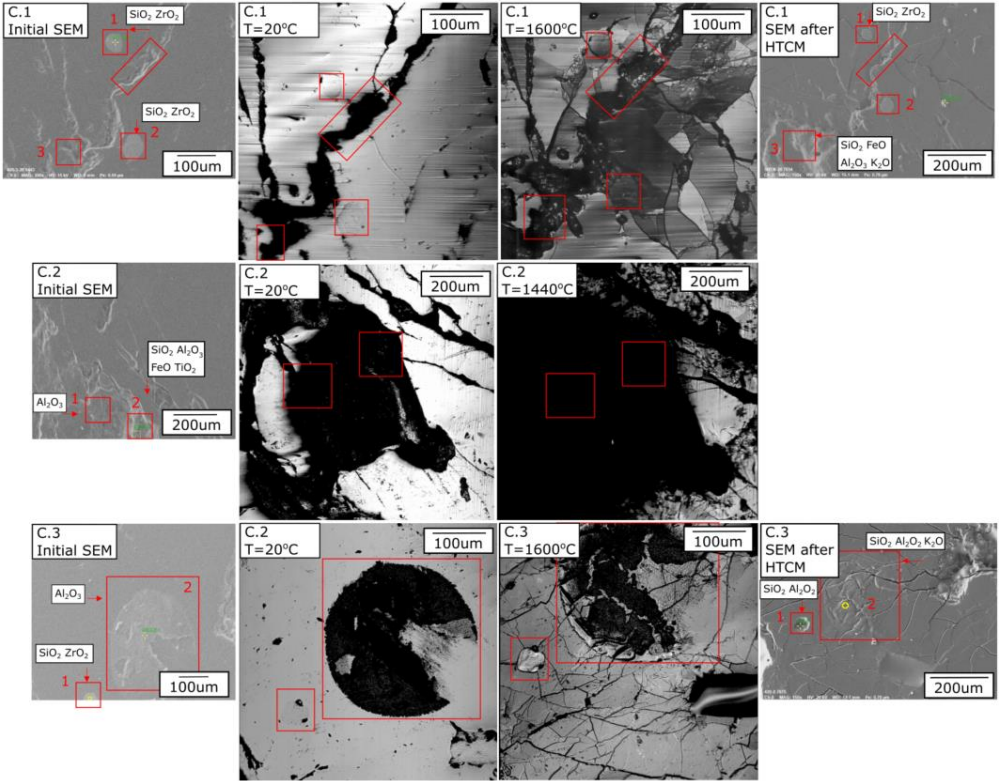


Figure 71 SEM images and images from high temperature confocal microscope experiments for quartz C, with focus on the impurities. The numbered boxes on the SEM images corresponds to the area analyzed with EDS in Table 27.



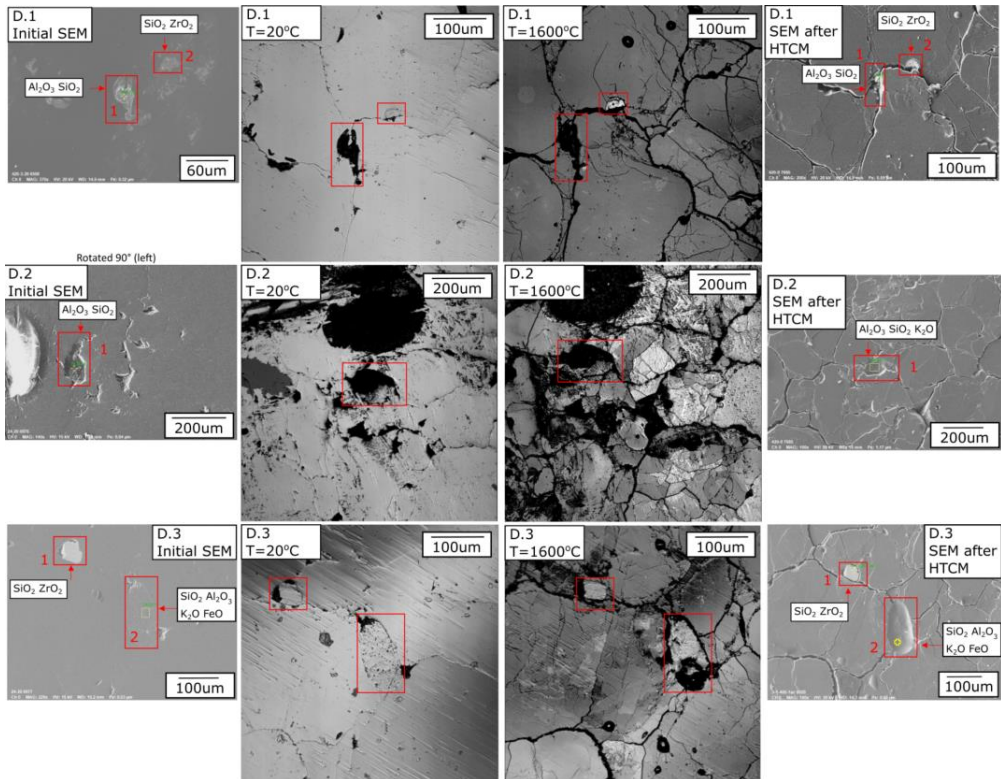


Figure 72 SEM images and images from high temperature confocal microscope experiments for quartz D, with focus on the impurities. The numbered boxes on the SEM images corresponds to the area analyzed with EDS in Table 27.

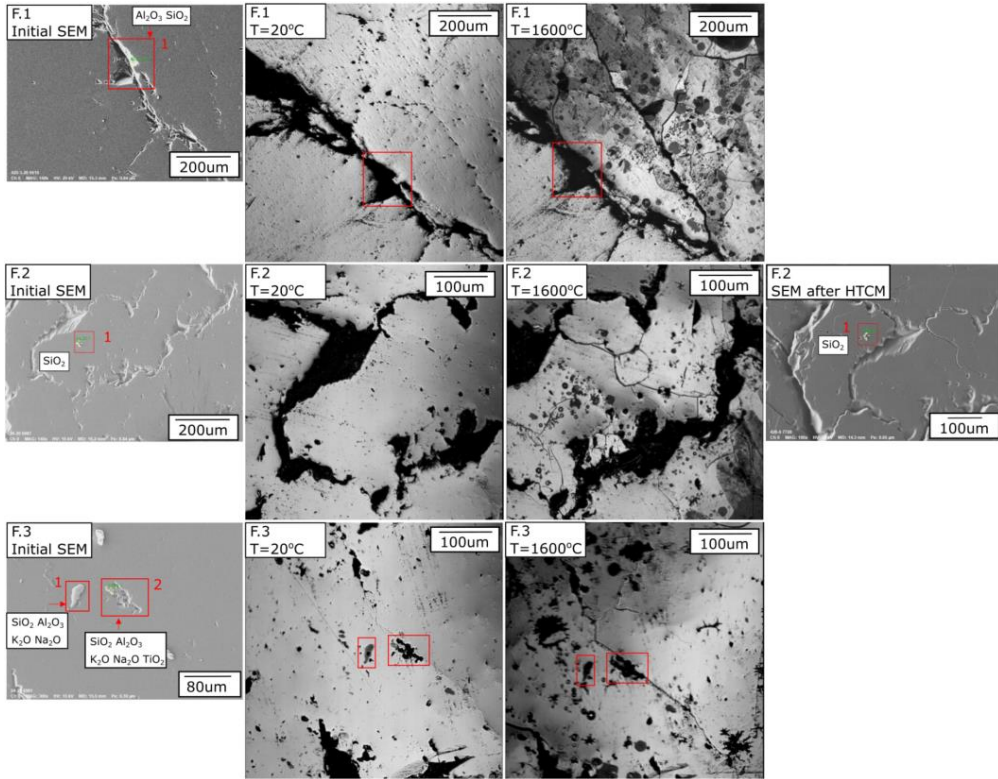


Figure 73 SEM images and images from high temperature confocal microscope experiments for quartz F, with focus on the impurities. The numbered boxes on the SEM images corresponds to the area analyzed with EDS in Table 27.

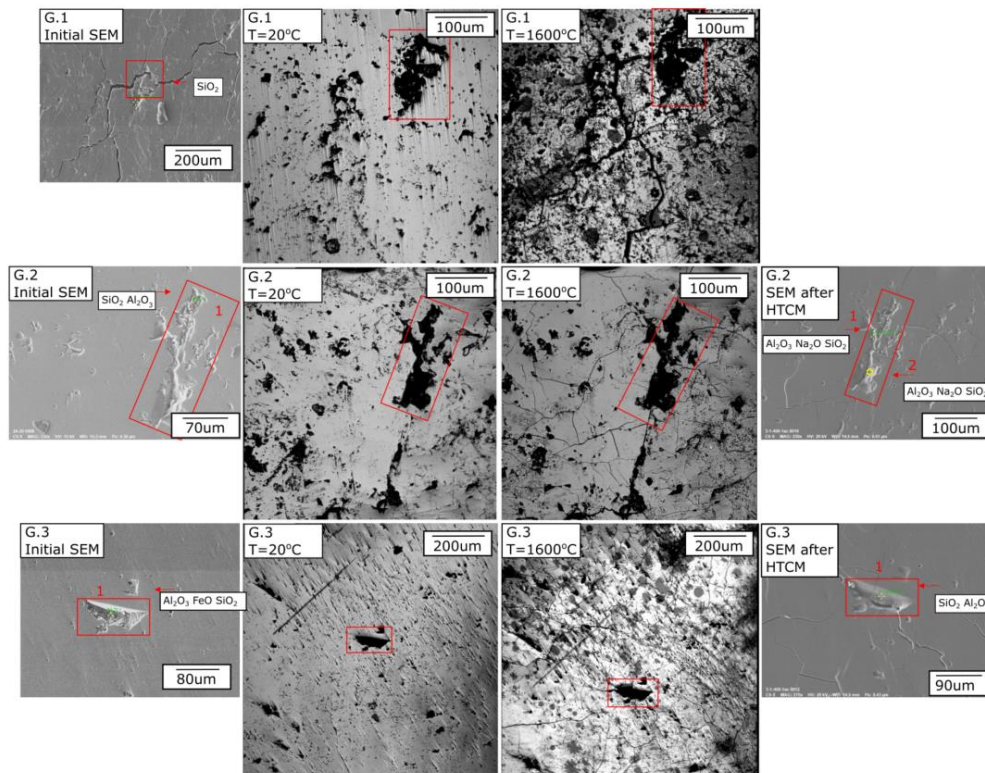


Figure 74 SEM images and images from high temperature confocal microscope experiments for quartz G, with focus on the impurities. The numbered boxes on the SEM images corresponds to the area analyzed with EDS in Table 27.

Table 27 EDS results from the High Temperature Confocal Microscope experiments. The results are used to identify the elements present in the impurities, and to give an indication of the composition.

Quartz	Initial sample			After HTCM exp.		
	Area 1	Area 2	Area 3	Area 1	Area 2	Area 3
A	1	Al <sub>2</sub> O <sub>3</sub>	Al <sub>2</sub> O <sub>3</sub>	52% SiO <sub>2</sub> 48% Al <sub>2</sub> O <sub>3</sub>	65% SiO <sub>2</sub> 35% Al <sub>2</sub> O <sub>3</sub>	97% SiO <sub>2</sub> 3% Al <sub>2</sub> O <sub>3</sub>
	2	<i>Not analyzed</i>	69% SiO <sub>2</sub> 31% Al <sub>2</sub> O <sub>3</sub>		63% SiO <sub>2</sub> 36% Al <sub>2</sub> O <sub>3</sub> 1% Na <sub>2</sub> O	90% SiO <sub>2</sub> 10% Al <sub>2</sub> O <sub>3</sub>
	3	99% SiO <sub>2</sub> 1% Al <sub>2</sub> O <sub>3</sub>	SiO <sub>2</sub>		*	
B	1	47% SiO <sub>2</sub> 40% Al <sub>2</sub> O <sub>3</sub> 13% K <sub>2</sub> O			*	
	2	50% SiO <sub>2</sub> 50% FeO	<i>Not analyzed</i>	73% SiO <sub>2</sub> 27% FeO	98% SiO <sub>2</sub> 2% Al <sub>2</sub> O <sub>3</sub>	
	3	Al <sub>2</sub> O <sub>3</sub>	60% SiO <sub>2</sub> 40% Al <sub>2</sub> O <sub>3</sub>	<i>Not analyzed</i>	<i>Not analyzed</i>	SiO <sub>2</sub> 81% SiO <sub>2</sub> 14% Al <sub>2</sub> O <sub>3</sub> 5% K <sub>2</sub> O
C	1	67% ZrO <sub>2</sub> 33% SiO <sub>2</sub>	71% ZrO <sub>2</sub> 29% SiO <sub>2</sub>	<i>Not analyzed</i>	63% SiO <sub>2</sub> 37% ZrO <sub>2</sub>	<i>Not analyzed</i> 51% SiO <sub>2</sub> 35% Al <sub>2</sub> O <sub>3</sub> 12% K <sub>2</sub> O 2% FeO
	2	Al <sub>2</sub> O <sub>3</sub>	41% Al <sub>2</sub> O <sub>3</sub> 34% FeO 19% SiO <sub>2</sub> 6% TiO <sub>2</sub>		*	
	3	74% ZrO <sub>2</sub> 26% SiO <sub>2</sub>	Al <sub>2</sub> O <sub>3</sub>		99% SiO <sub>2</sub> 1% Al <sub>2</sub> O <sub>3</sub>	51% Al <sub>2</sub> O <sub>3</sub> 43% SiO <sub>2</sub> 5% K <sub>2</sub> O
D	1	78% SiO <sub>2</sub> 22% Al <sub>2</sub> O <sub>3</sub>	63% SiO <sub>2</sub> 37% ZrO <sub>2</sub>		71% Al <sub>2</sub> O <sub>3</sub> 29% SiO <sub>2</sub>	69% SiO <sub>2</sub> 31% ZrO <sub>2</sub>
	2	97% SiO <sub>2</sub> 3% Al <sub>2</sub> O <sub>3</sub>			81% SiO <sub>2</sub> 17% Al <sub>2</sub> O <sub>3</sub> 1% K <sub>2</sub> O	
	3	53% SiO <sub>2</sub> 47% ZrO <sub>2</sub>	85% SiO <sub>2</sub> 9% Al <sub>2</sub> O <sub>3</sub> 4% K <sub>2</sub> O 2% FeO		60% SiO <sub>2</sub> 40% ZrO <sub>2</sub>	63% SiO <sub>2</sub> 27% Al <sub>2</sub> O <sub>3</sub> 5% FeO 4% K <sub>2</sub> O
F	1	93% SiO <sub>2</sub> 7% Al <sub>2</sub> O <sub>3</sub>			*	
	2	<i>No impurities found</i>				
	3	64% SiO <sub>2</sub> 21% Al <sub>2</sub> O <sub>3</sub> 14% K <sub>2</sub> O 1% Na <sub>2</sub> O	58% SiO <sub>2</sub> 31% TiO <sub>2</sub> 7% Al <sub>2</sub> O <sub>3</sub> 3% K <sub>2</sub> O 1% Na <sub>2</sub> O		*	
G	1	<i>No impurities found</i>				
	2	81% Al <sub>2</sub> O <sub>3</sub> 19% SiO <sub>2</sub>	<i>Not analyzed</i>		84% SiO <sub>2</sub> 15% Al <sub>2</sub> O <sub>3</sub> 1% Na <sub>2</sub> O	53% SiO <sub>2</sub> 46% Al <sub>2</sub> O <sub>3</sub> 1% Na <sub>2</sub> O
	3	46% FeO 39% Al <sub>2</sub> O <sub>3</sub> 15% SiO <sub>2</sub>			64% Al <sub>2</sub> O <sub>3</sub> 35% SiO <sub>2</sub> 1% Na <sub>2</sub> O	

\*Sample too fragile for FESEM

### 3.3.4 Disintegration of quartz during heating

The shock heating experienced when quartz is added to the Si/FeSi furnace may cause disintegration of SiO<sub>2</sub>. The figures below show images from the HTCM experiments taken at 20 °C, 600 °C, 1200 °C and 1600 °C for all the quartz types. For some of the samples, the carbon coating loosened, showing as black and shiny spots on the surface. For those experiments it was impossible to quantify the crack formation, and those images are not included in this report. It should also be noted that different magnifications are sometimes used at different parallels in the same quartz type.

Figure 75 shows images from the HTCM experiments for quartz A. In A.1, the black, prominent impurity is identified as Al<sub>2</sub>O<sub>3</sub>. During heating, it is observed that the extension of the impurity circle appears to detach from the surface and move towards the left. Most of the cracks seem to form between 1200-1600 °C. The second parallel A.2, there is also a significant impurity area consisting of Al<sub>2</sub>O<sub>3</sub> with some Na<sub>2</sub>O. This impurity area experiences a small volume increase. The crack formation is less than for A.1, but some cracks can be observed in the middle of the image. Most cracks developed before 600 °C.

The images from the HTCM experiments for Quartz B are shown in Figure 76. For both parallels B.2 and B.3, cracks are formed from expanded impurity areas, and they continue between the impurities. The impurities in these samples consist of Al<sub>2</sub>O<sub>3</sub> and FeO for B.2, and Al<sub>2</sub>O<sub>3</sub> and K<sub>2</sub>O for B.3. Most of the cracks form before 600 °C.

Figure 77 shows the images from HTCM experiments for quartz C. In both C.1 and C.3, the cracks form mainly between 1200-1600 °C. Also, black dots can be observed from 600 °C. These are believed to be fluid inclusion that escapes the SiO<sub>2</sub> surface.

Figure 78 shows all three parallels of the HTCM experiments for Quartz D. In D.1 it can also be seen that the impurities are at the SiO<sub>2</sub> grain boundaries. These are more visible during heating, and it can also be seen some crack formation from the grain boundaries.

HTCM images for all three parallels of Quartz F are shown in Figure 79. Quartz F is 99.9% quartz, and only small impurity areas were found. It is also only small amounts of cracks developed during heating. In the second parallel, no impurities were found. The crack formation is here from an uneven SiO<sub>2</sub> surface. For F.1 and F.3, the cracks develop from the impurities before 600 °C. Some crack formation is also observed after 1200 °C.

Figure 80 shows the HTCM images during the quartz G experiments. For both parallels, the crack formation is observed from the impurity areas between 1200 °C and 1600 °C.

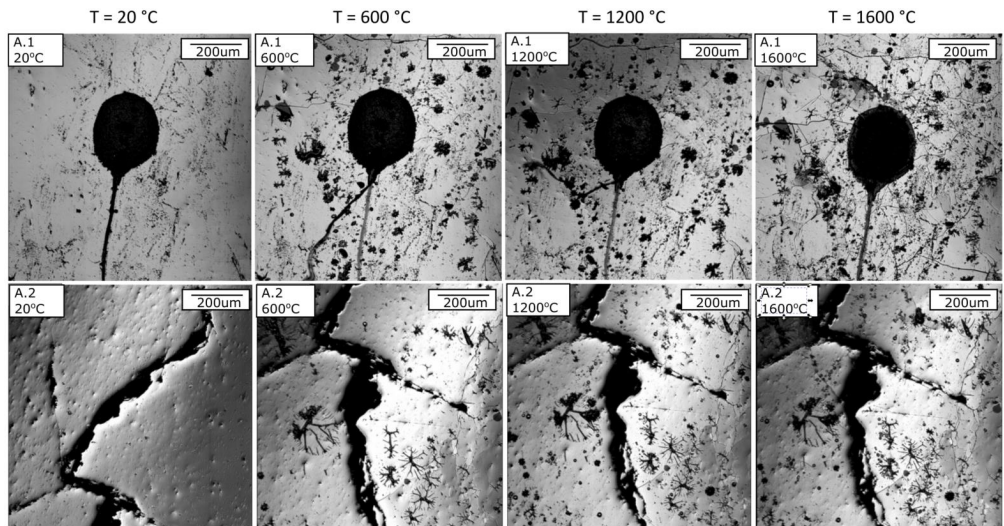


Figure 75 Quartz surface during high temperature confocal microscope (HTCM) experiments at temperatures 20 °C, 600 °C, 1200 °C and 1600 °C for A.1 and A.2. The magnification is 275X for both Qz41.1 and Qz41.2.

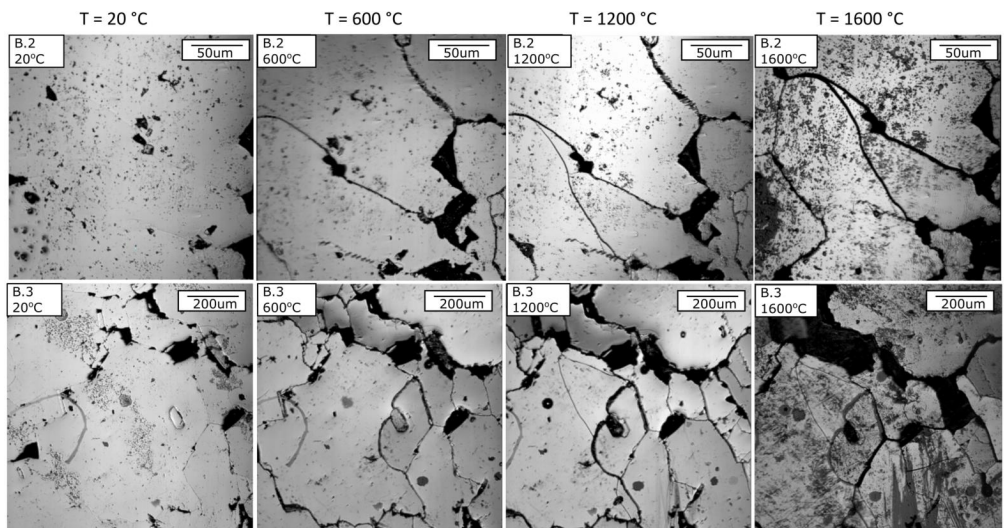


Figure 76 Quartz surface during high temperature confocal microscope (HTCM) experiments at temperatures 20 °C, 600 °C, 1200 °C and 1600 °C for B.2 and B.3. The magnification is 1100X for B.2 and 275X for B.3.

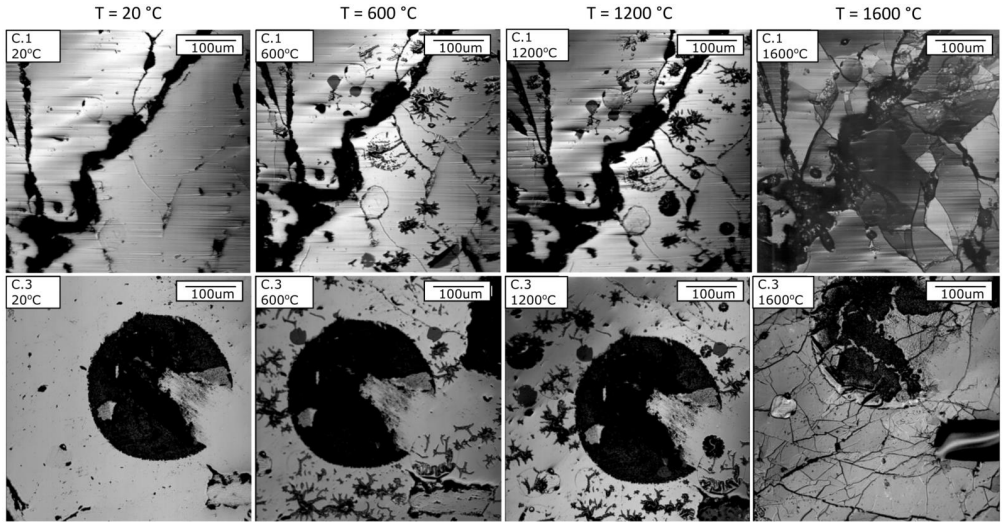


Figure 77 Quartz surface during high temperature confocal microscope (HTCM) experiments at temperatures 20 °C, 600 °C, 1200 °C and 1600 °C for C.1 and C.3. The magnification is 550X for both C.1 and C.3.

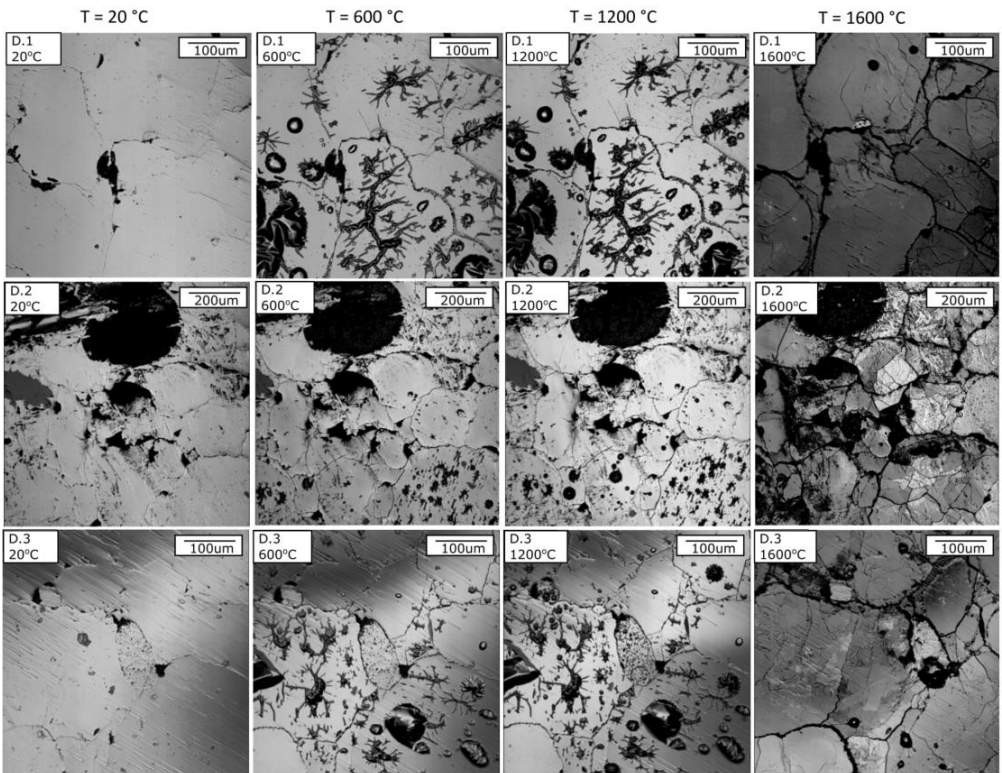


Figure 78 Quartz surface during high temperature confocal microscope (HTCM) experiments at temperatures 20 °C, 600 °C, 1200 °C and 1600 °C for D.1, D.2 and D.3. The magnification is 550X for D.1, 275X for D.2 and 550X for D.3.

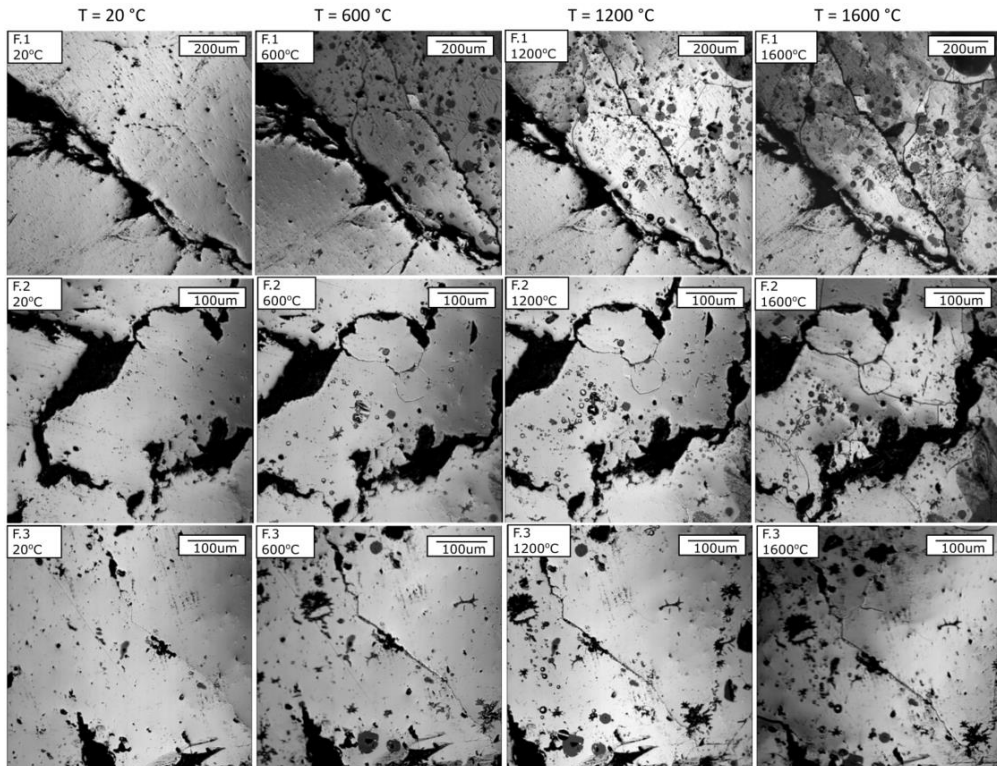


Figure 79 Quartz surface during high temperature confocal microscope (HTCM) experiments at temperatures 20 °C, 600 °C, 1200 °C and 1600 °C for F.1, F.2 and F.3. The magnification is 275X for F.1, 550X for F.2 and 550X for F.3.

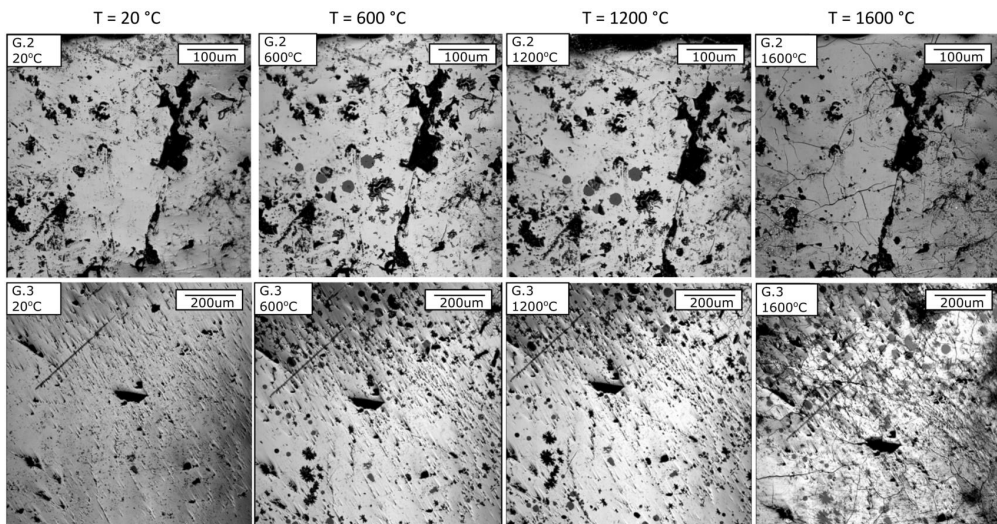


Figure 80 Quartz surface during high temperature confocal microscope (HTCM) experiments at temperatures 20 °C, 600 °C, 1200 °C and 1600 °C for G.2 and G.3. The magnification is 550X for G.2 and 275X for G.3.



The quantification of crack formation during heating is summarized in Figure 81. The different quartz sources have earlier shown different behaviour upon heating [9] and it can also be observed large differences between the different quartz types in this study. Quartz C, D and G have the highest crack formation,  $>10 \text{ mm/mm}^2$ , while quartz A and F forms less cracks,  $< 8 \text{ mm/mm}^2$ . Furthermore, it is found variations within the same quartz type, which can be explained by natural differences in the samples heated, e.g., impurities, grain size, damages in the  $\text{SiO}_2$  surface and other textural properties. The crack formation for A.1 and A.2 are  $12.2 \text{ mm/mm}^2$  and  $4.7 \text{ mm/mm}^2$ , respectively. From the initial HTCM images, it can be seen that A.2 has a more uniform surface. More damages in the  $\text{SiO}_2$  surface are more prone to the stress which causes microcracks. Most of the cracks in A.1 form at temperatures  $>1300 \text{ }^\circ\text{C}$ , at which the phase transformation from quartz to cristobalite happens. Additionally, quartz A contains two domains with different grain size. Domain 1 has medium to coarse grained quartz in the mm and  $\mu\text{m}$  scale, while the grains in the second domain are stretched and deformed: 10-200  $\mu\text{m}$  thick and a few mm long [11]. However, since these two samples are from the same stone, grain size differences are not likely to be the reason for different degree of cracking.

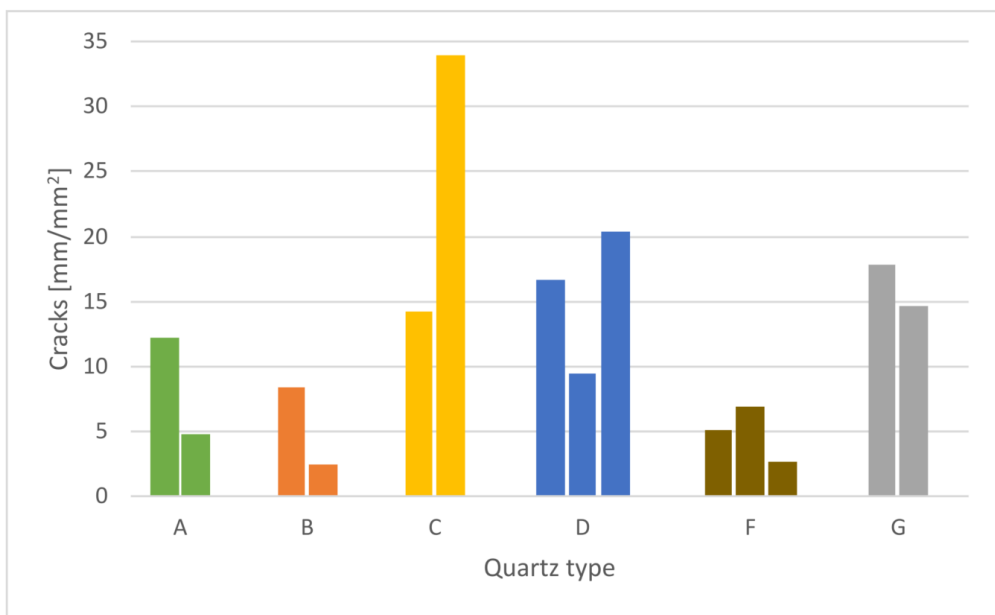


Figure 81 Summary of the crack formation for all the quartz types after heating to 1600 °C. The amount of cracks is given in  $\text{mm/mm}^2$ .



## Chapter 4: CaO dissolution in SiO<sub>2</sub>-CaO-Al<sub>2</sub>O<sub>3</sub> slag

### 4.1 Literature review

CaO, in the form of CaCO<sub>3</sub>, is often added as a flux in Si and FeSi production. Its purpose is to reduce the viscosity of the slag and thereby prevent accumulation. Too much accumulated slag is negative for the furnace operation. CaCO<sub>3</sub> is also added to the metal during the refining process to ensure sufficient Ca relative to Al and a suitable viscosity for optimal slag/metal separation. Therefore, the dissolution rate of CaO into SiO<sub>2</sub>-CaO-Al<sub>2</sub>O<sub>3</sub> slag plays an important role on the slag properties in the furnace and it is of interest to investigate the kinetics of this process.

#### 4.1.1 CaO properties

CaO is one of the light alkaline-earth oxides. At normal conditions, CaO is of ionic nature and crystalizes into the cubic rock salt (NaCl) structure. In the simplest model, solid state CaO is formed by highly ionic bindings between Ca<sup>2+</sup> cations and O<sup>2-</sup> anions. Because of the basic catalytic activity of the CaO surfaces, CaO is a popular chemical compound. It is the cheapest, most widely used alkali in the world [87]. It is a paramagnetic insulator material with a wide bandgap of 6.25 eV [88], but it also has properties typical of a semiconductor with a high dielectric constant of 11.95 [89]. CaO is a caustic crystal that reacts with atmospheric CO<sub>2</sub> to form calcium carbonate, as in reaction 13. It is therefore unstable at room temperature conditions.



CaO is considered to be a basic oxide in slags, which means that Ca<sup>2+</sup> ions will break up some of the Si<sup>4+</sup>-O<sup>-</sup> bonds in the SiO<sub>4</sub><sup>4-</sup> network system. A thorough description of the slag network system can be read in section 2.1.3.1: the structure of silica melts. A measure of the electron donor power of different ions relative to that of CaO is the optical basicity ( $\Lambda$ ) [90]. The shift in frequency of the absorption band observed in the UV region of the spectrum can be related to the basicity of a slag. This is a useful measurement to differentiate between different cations on the structure, and it can also be used to measure the depolymerization of the melt. The values for optical basicity for CaO, SiO<sub>2</sub> and Al<sub>2</sub>O<sub>3</sub> are given in Table 28. Optical basicity equation for a multicomponent slag is given in equation 9 [28].

$$\Lambda = \frac{\sum_i X_i m_i \Lambda_i}{\sum_i X_i m_i} \quad 9$$

Table 28 Experimental values of optical basicity ( $\Lambda$ ) for CaO, SiO<sub>2</sub> and Al<sub>2</sub>O<sub>3</sub> from measurements of UV shift [25].

	CaO	SiO <sub>2</sub>	Al <sub>2</sub> O <sub>3</sub>
$\Lambda$	1.0	0.48	0.605

Natalie and Evans [91] studied the relationship between lime properties and the rate of dissolution in molten SiO<sub>2</sub>-CaO-FeO<sub>x</sub> slags. They found that pretreatment of lime had significant effect on the reactivity result. Soft burned lime gave larger pores and a higher porosity, which also increased the reactivity. The rate of dissolution was found to be directly dependent on the pore surface area. They suggested that the dissolution of CaO happens in the pores by penetration of slag into the CaO. Maruoka et al. [92] and Kitamura [93] studied the possibility of CaO where a core of CaCO<sub>3</sub> remained and suggested that the increased porosity with CO<sub>2</sub> formation inside the pores and slag penetration may break the 2CaO:SiO<sub>2</sub> layer formed on the lime surface and hence increase the diffusion rate.

Vieira et al. [94] studied the effect of the lime particle size, and the lime calcination level 80% and 100% on the dissolution into SiO<sub>2</sub>-CaO-FeO slags. They found that smaller particle sizes, that favor a larger area of specific contact of the particle with the slag, gave higher dissolution rates. And similar as Natalie and Evans [91] they found that the lowest level of calcination gave the highest dissolution rates. They also found that an increased ratio between FeO and SiO<sub>2</sub> in the slag, which increases the basicity, decreased the dissolution rate. This was explained with the decrease in the percentage of CaO saturation as a consequence of an increase in the lime activity. From this, they concluded that the lime-slag contact area and percentage of CaO saturation had a more significant impact on the dissolution rate than the basicity of the slag. The effect of a reduced amount of lime dissolved in slag with increasing lime particle size is also confirmed by [93], [95], [96].

## 4.1.2 Theoretical mechanisms of CaO dissolution

The rate of a reaction is defined as the amount of product formed per time unit and is dependent on several properties, as mentioned in the previous subchapter. The reaction can either be controlled by the rate of the chemical reaction or by mass transfer. In the following subchapters, both mechanisms are described in relation to CaO dissolution in SiO<sub>2</sub>-CaO-Al<sub>2</sub>O<sub>3</sub> slag.

### 4.1.2.1 Chemical reaction control: Shrinking sphere model

The first case assumes that the dissolution is controlled by the rate of chemical reaction. The shrinking sphere model [97], [98] describes the concentration of the dissolved CaO as a function of time and it assumes that the rate of reaction depends only on the surface area of the CaO. The dissolving CaO is regarded as a shrinking smooth sphere. The rate of CaO dissolution in SiO<sub>2</sub>-CaO-Al<sub>2</sub>O<sub>3</sub> slag is proportional to its surface area and the model

assumes that the mass transport is fast relative to the surface chemical reaction. This gives the equation of the rate is as in equation 10.

$$R = kA \quad 10$$

Where R is the rate of dissolution, k is the rate constant, and A is the surface area of the CaO. The mechanism of CaO concentration as a function of distance from CaO/interface is illustrated in Figure 82.

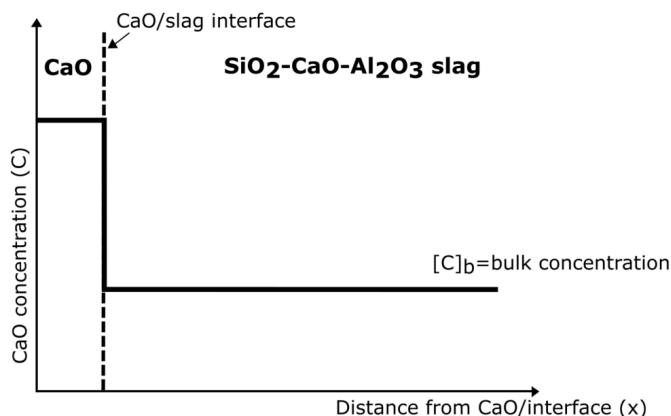


Figure 82 Schematic illustration of chemical reaction being the rate determining step for CaO dissolution in liquid SiO<sub>2</sub>-CaO-Al<sub>2</sub>O<sub>3</sub> slag.

It is assumed that the particle of CaO added together with the slag is a smooth sphere with an initial radius  $r_0$ . The initial surface area of the total CaO added is then as in equation 11.

$$A_0 = \frac{3M_0}{r_0\rho} \quad 11$$

Where  $A_0$  is the initial surface area of the total amount of CaO added,  $M_0$  is the initial mass of added CaO and  $\rho$  is the CaO particle density.

The surface area of CaO decreases as the mass of the undissolved CaO decreases by the relationship given by equation 12.

$$A = A_0 \left( \frac{M}{M_0} \right)^{\frac{2}{3}} \quad 12$$

Where  $A$  is the surface area of the CaO at time  $t$  and  $M$  is the mass of CaO remaining undissolved at time  $t$ .

The mass of undissolved CaO can be related to the concentration of CaO in the slag by the relationship given in equation 13.

$$M = M_0 - (C - C_i)V \quad 13$$

Where  $C_i$  is the initial CaO concentration in the slag,  $C$  is the CaO concentration in the slag at time  $t$  and  $V$  is the volume of the slag.

In order to simplify the equations,  $\Delta C$  is defined as  $\Delta C = C - C_i$ . An expression for the CaO dissolution rate as in equation 14 can then be obtained by using the shrinking sphere model.

$$R = \frac{dC}{dt}V = kA_0 \left(1 - \frac{V}{M_0} \Delta C\right)^{\frac{2}{3}} \quad 14$$

By rearranging equation 14, integrating with respect to concentration and time, and obtain the integration constant from initial conditions  $t=0$  and  $\Delta C=0$ , an expression for time as a function of the CaO concentration is obtained as in equation 15.

$$t = \frac{3M_0}{A_0k} \left[ \left(\frac{V}{M_0} \Delta C - 1\right)^{\frac{1}{3}} + 1 \right] \quad 15$$

And to give the concentration of CaO,  $\Delta C$ , equation 15 can be rearranged to equation 16 [98].

$$\Delta C = \frac{M_0}{V} \left[ 1 + \left(\frac{A_0k}{3M_0} t - 1\right)^3 \right] \quad 16$$

#### 4.1.2.2 Mass transport control

The second mechanism assumes that the rate of dissolution is mass transfer controlled and includes the influence of concentration difference of CaO between the CaO and the slag. Dissolved CaO diffuses into the bulk of the slag. The higher the solubility of CaO in the slag, the larger the driving force to dissolve in the slag. The dissolution rate may then be given by a first order reaction as shown in equation 17.

$$\frac{dC}{dt} = k_2 A (C_{\text{saturated}} - C)$$

Where  $k$  is the rate constant,  $A$  is the interfacial contact area,  $C_{\text{saturated}}$  is the saturated/equilibrium concentration of CaO in the slag and  $C$  is the concentration of CaO in the slag at time  $t$ .

It is assumed that diffusion is one dimensional through a boundary layer with constant thickness, and that this boundary layer is not affected by the particle size. This mechanism, illustrated with CaO concentration as a function of distance from CaO/interface is shown in Figure 83.

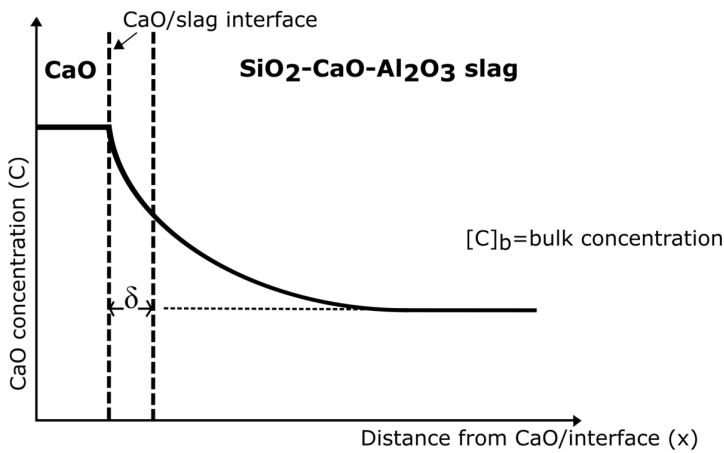


Figure 83 Schematic illustration of mass transfer kinetic control being the rate determining step for CaO dissolution in liquid SiO<sub>2</sub>-CaO-Al<sub>2</sub>O<sub>3</sub> slag.

With the assumption of excess CaO, CaO will dissolve into the slag until the saturated concentration is reached. This is illustrated in Figure 84, which shows the concentration curves in the sample with increasing time  $t_1$  to  $t_4$ .

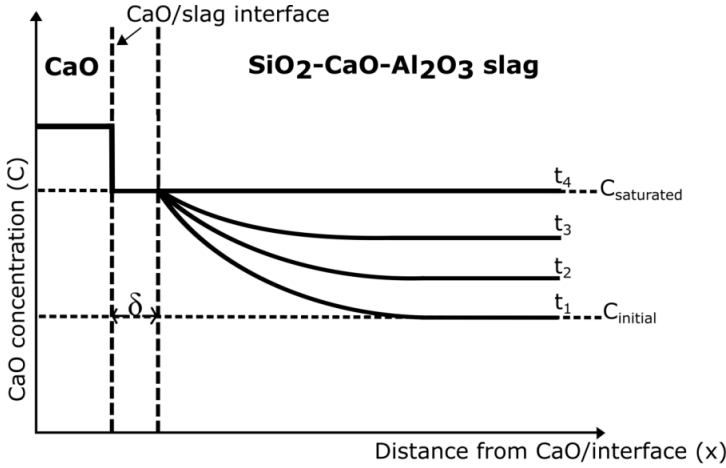


Figure 84 Schematic illustration of mass transfer kinetic control being the rate determining step for CaO dissolution in liquid  $\text{SiO}_2\text{-CaO-Al}_2\text{O}_3$  slag, given concentration curves with increasing experimental holding time.

With the same relations as in chapter 4.1.2.1, the rate equation can be written as in equation 18 [97].

$$R = \frac{dC}{dt}V = k_2A(C_{sat} - C) = k_2A_0 \left(1 - \frac{V}{M_0} \Delta C\right)^{\frac{2}{3}} (\Delta C_{sat} - \Delta C) \quad 18$$

Where  $\Delta C$  is the concentration at time  $t$  minus the initial concentration and  $\Delta C_{saturated}$  is the saturation concentration of CaO dissolved in a  $\text{SiO}_2\text{-CaO-Al}_2\text{O}_3$  slag with a specific composition minus,  $C_{sat}$  the initial concentration,  $C_i$ , given in equations 19 and 20.

$$\Delta C = C - C_i \quad 19$$

$$\Delta C_{sat} = C_{sat} - C_i \quad 20$$

The diffusion coefficient of a solute in a melt is a fundamental constant required to characterize mass-transport rates. The diffusion coefficient describes how easy a particle can move through a given volume. It is a physical constant dependent on molecule size and other properties of the diffusing substance and the medium it is moving through, in addition to temperature and pressure.

If it is assumed that the composition of the liquid slag phase is constant, the diffusion coefficient would also be constant. On the particle surface is a local equilibrium condition established, where the slag is saturated with CaO. The diffusion coefficient could then be found from the boundary layer thickness,  $\delta$  and the rate constant, given by equation 21 [97].

$$k_2 = \frac{D}{\delta} \quad 21$$



### 4.1.3 Research on CaO dissolution in slag

The literature available on CaO dissolution in  $\text{SiO}_2\text{-CaO-Al}_2\text{O}_3$  slag is related to the steel industry. The progress of slag-metal reactions in basic oxygen and electric furnaces is strongly influenced by the CaO content, and accordingly also by the dissolution rate of CaO into slag. It is also believed that this dissolution rate would have an influence on the blast furnace condition and its productivity. Thus, a lot of research has been conducted on this dissolution reaction, with slag compositions similar to those in steel production, which is around 40wt%  $\text{SiO}_2$  – 40wt%  $\text{CaO}$  – 20wt%  $\text{Al}_2\text{O}_3$ . This CaO content is slightly higher than the slag in Si and FeSi production.

The experimental techniques used to study lime dissolution in  $\text{SiO}_2\text{-CaO-Al}_2\text{O}_3$  slag have been divided into four types:

- 1) static conditions
- 2) using rotating rod/disc
- 3) increased or forced convection
- 4) direct observation

The experimental techniques and a short summary of the results are summarized in Table 29.

Table 29 Summary of experimental methods and results for CaO dissolution in SiO<sub>2</sub>-CaO-Al<sub>2</sub>O<sub>3</sub> slag.

Experimental condition	Description and references	Findings
Static conditions	Heated slag with a piece of lime [99]–[101], placing lime in preheated liquid slag [102]	2CaO·SiO <sub>2</sub> or 3CaO·SiO <sub>2</sub> boundary layer at the lime-slag interface act as kinetic barrier for lime dissolution. Dissolution rate increased with decreasing slag basicity.
Rotating rod/disc	Rotating a lime disc/cylinder in molten slag [103], [104]	Mass transfer in the slag is the limiting step of lime dissolution
Forced convection	Stirring slag using sapphire disc, Eccentrically stirring the molten slag (containing a lime cube) using sapphire disc [102], argon gas bubbling in slag via an iron tube [105]	Increased mass transfer in slag
Direct observation	Observation of lime particle dissolution in slag using HT-CLSM [106]	Lime dissolution influenced by temperature and slag chemistry. Slag penetrates along cracks in CaO and enhance lime dissolution

From the experimental research it is found that the mass transfer in the slag is the rate determining step for the CaO dissolution in SiO<sub>2</sub> – CaO – Al<sub>2</sub>O<sub>3</sub> slag. A number of researchers have also deduced the diffusivity from dissolution rate data [107]–[112], [104], [113], [114]. A short summary with the diffusion coefficients together with the respective slag composition and temperature are listed in Table 30.

Table 30 Summary diffusion coefficients from literature.

Authors	Slag composition			Temperature [°C]	D [cm <sup>2</sup> /s]	E <sub>a</sub> [kcal]	Comment
	SiO <sub>2</sub>	CaO	Al <sub>2</sub> O <sub>3</sub> [wt%]				
Towers et al. [107] (1953)	40	40	20	1450	1.3·10 <sup>-6</sup>	70±20	Radioactive Tracer Technique, Ca <sup>45</sup>
Towers and Chipman [108] (1957)	40	39	21	1430	1·10 <sup>-6</sup>		Radioactive Tracer Technique, Ca <sup>45</sup>
Niwa [109] (1957)	40	40	20	1350	3.3·10 <sup>-7</sup>	70±20	Radioactive Tracer Technique, Ca <sup>45</sup>
				1400	6.2·10 <sup>-7</sup>		
				1450	1.3·10 <sup>-7</sup>		
	39	43	18	1350	5.2·10 <sup>-7</sup>	30±15	
				1400	6.4·10 <sup>-7</sup>		
				1450	9.5·10 <sup>-7</sup>		
Saitô and Maruya [110] (1958)	41	40	19	1350	3.2·10 <sup>-7</sup>	50±20	Semi-infinite medium, Ca <sup>45</sup>
				1395	3.9·10 <sup>-7</sup>		
				1440	10·10 <sup>-7</sup>		
				1440	8·10 <sup>-7</sup>		
				1510	10·10 <sup>-7</sup>		
				1510	10·10 <sup>-7</sup>		
	37	43	20	1440	8·10 <sup>-7</sup>		
				1510	10·10 <sup>-7</sup>		
				1510	10·10 <sup>-7</sup>		
	39	49	12	1440	11.5·10 <sup>-7</sup>		
				1510	17·10 <sup>-7</sup>		
				1510	17·10 <sup>-7</sup>		
36	45	19	1510	8.5·10 <sup>-7</sup>			
			1530	9.9·10 <sup>-7</sup>			
			1440	3.8·10 <sup>-7</sup>			
			1485	7.1·10 <sup>-7</sup>			
			1510	8.4·10 <sup>-7</sup>			
			1530	10.3·10 <sup>-7</sup>			
34	46	20	1440	3.8·10 <sup>-7</sup>			
			1485	7.1·10 <sup>-7</sup>			
			1510	8.4·10 <sup>-7</sup>			
			1530	10.3·10 <sup>-7</sup>			
			1575	13.0·10 <sup>-7</sup>			
			1575	13.0·10 <sup>-7</sup>			
Goto et al. [111] (1977)	40	40	20	1400	9.2·10 <sup>-7</sup>		Calculated values from Nernst-Einstein relation
				1450	1.6·10 <sup>-6</sup>		
				1500	2.6·10 <sup>-6</sup>		
				1500	2.6·10 <sup>-6</sup>		
Liang et al. [112] (1996)	60	30	10	1500	7.41·10 <sup>-7</sup>		Isotope tracer method, Ca <sup>40</sup> and Ca <sup>42</sup>
					5.18·10 <sup>-7</sup>		
					3.3·10 <sup>-7</sup>		
					4.78·10 <sup>-7</sup>		
					7.12·10 <sup>-7</sup>		
					3.66·10 <sup>-7</sup>		
					4.5·10 <sup>-7</sup>		
					9.32·10 <sup>-7</sup>		
					1.34·10 <sup>-6</sup>		
Amini et al. [104] (2006)	8	50	42	1500-1600	In the range 10 <sup>-5</sup> -10 <sup>-4</sup>	55	Calculated from forced convection dissolution rate data using known mass-transfer correlations

Authors	Slag composition			Temperature [°C]	D [cm <sup>2</sup> /s]	Comment
	SiO <sub>2</sub>	CaO [wt%]	Al <sub>2</sub> O <sub>3</sub>			
Zhang and Chou [113] (2011)	40	40	20	1350	9.0·10 <sup>-7</sup>	Calculated values from Nernst-Einstein relation
				1400	1.3·10 <sup>-7</sup>	
				1450	1.9·10 <sup>-7</sup>	
				1500	2.8·10 <sup>-7</sup>	
Ren et al. [114] (2013)	25	46	29	1350	3.74·10 <sup>-7</sup>	Model from relation between diffusion activation energy and optical basicity
				1395	6.13·10 <sup>-7</sup>	
				1440	9.8·10 <sup>-7</sup>	
	27	49	24	1440	8.80·10 <sup>-7</sup>	
				1510	18.90·10 <sup>-7</sup>	
				1350	3.14·10 <sup>-7</sup>	
	45	45	10	1400	5.72·10 <sup>-7</sup>	
				1450	10.6·10 <sup>-7</sup>	
				1350	8.39·10 <sup>-7</sup>	
	44	47	9	1400	11.43·10 <sup>-7</sup>	
1450				15.28·10 <sup>-7</sup>		
1350				2.64·10 <sup>-7</sup>		
1500				16.67·10 <sup>-7</sup>		
25	49	26	1350	2.64·10 <sup>-7</sup>		
			1500	16.67·10 <sup>-7</sup>		
				1540	25.88·10 <sup>-7</sup>	

\*Low value of diffusion coefficient most likely due to solid phase in the slag

\*\* Accuracy is somewhat reduced

The chemical and physical properties in the slag are important factors when describing the rate of dissolution reactions in oxides. The earliest calculations on the diffusion coefficient used its relationship with the electrical conductivity. The electrical conductivity studies have shown that the molten slag is ionic in nature. Herasymenko [115] proposed already in 1938 the theory that liquid slags consisted of cations, anions and anion complexes. Under the external electrical field, the different ions have different mobilities. The ions with smaller charge and small radius generally have a significant role in the transport process. From the similar micro-mechanism between the diffusion and ionic electrical conduction, it was assumed that there was a relationship between the diffusion coefficient and the ionic conductivity.

The first studies on the diffusion process of the Ca ion into SiO<sub>2</sub>-CaO-Al<sub>2</sub>O<sub>3</sub> slag were done by using the radioactive tracer technique and the capillary method [107]–[109]. In this technique, the diffusion ion Ca<sup>2+</sup> is replaced with its isotope Ca<sup>45</sup> and the diffusion process would then be tracer diffusion. It is assumed to give the same results as in self-diffusion since tracer diffusivity is considered to be equivalent to self-diffusivity in liquids [25]. The results suggested that the diffusion coefficient for Ca diffusion in ~40wt% SiO<sub>2</sub> – 40wt% CaO – 20wt% Al<sub>2</sub>O<sub>3</sub> is in the range of 10<sup>-7</sup>–10<sup>-6</sup> cm<sup>2</sup>/s in the temperature range of 1350–1550 °C. Saitô and Maruya [110] used the semi-infinite medium method in the temperature range 1350-1600 °C to measure the self-diffusion coefficients of calcium in several compositions of molten SiO<sub>2</sub>-CaO-Al<sub>2</sub>O<sub>3</sub> slags. As Towers et al. and Niwa, the radioactive calcium Ca<sup>45</sup> were used. From the experiments the concentration-penetration curve of Ca<sup>45</sup> was obtained and Fick's second law of diffusion were used to calculate the diffusion coefficient. The diffusion coefficients were found to be in the order of 10<sup>-6</sup>~10<sup>-7</sup> cm<sup>2</sup>/s.

Goto et al. [111] calculated diffusion coefficients for 40wt% SiO<sub>2</sub> – 40wt% CaO –20wt% Al<sub>2</sub>O<sub>3</sub> slag in the temperature interval 1350-1500 °C based on Nernst-Einstein relation, as given in equation 22. This equation can be used when there is only one ion dominating in the transport process.

$$\sigma = \frac{n_i(z_i e)^2}{kTf t_i} D_i^{tr} \quad 22$$

Where  $\sigma$  is the conductivity in A/V\*cm,  $D_i^{tr}$  is the tracer diffusivity of an ionic species  $i$  in cm<sup>2</sup>/s,  $n_i$ ,  $z_i$  and  $t_i$  are the concentration, valency, and transference number the ionic species  $i$ , respectively.  $e$  is the unit charge  $1.6 \cdot 10^{-19}$  A s,  $k$  is the Boltzmann constant  $1.38 \cdot 10^{-23}$  V A s/K,  $T$  is the absolute temperature and  $f$  the correlation factor of successive jumps of the tracer [116], [117]. It was also assumed that  $f$  and the transference number of Ca<sup>2+</sup> would be unity. The purpose was to examine its validity on multi-component oxide slags. For this, they compared with experimental data from Towers et al. [107], [108], Niwa [109] and Saitô and Maruya [110]. Zhang and Chou [113] used the same method to estimate the diffusion coefficient of calcium ions in the same slag in the same temperature interval 1350-1500 °C. They also used the relation between the calcium ion concentration and diffusivities to calculate the diffusion coefficient, as in equation 23.

$$D_{eff} = \frac{\kappa RT}{C_{Ca^{2+}} + Z_{Ca^{2+}}^2 F^2} \quad 23$$

Where  $D_{eff}$  is the apparent diffusion coefficient in cm/s,  $\kappa$  is the ionic conductivity in  $\Omega/cm$ ,  $C_{Ca^{2+}}$  is the concentration of the mobile Ca<sup>2+</sup> ion in mol/cm<sup>3</sup>,  $Z_{Ca^{2+}}$  is the valence of the ion and  $F$  is the Faraday constant 96 485 C/mol.

For both Goto et al. and Zhang and Chou, the calculated results were larger than the experimental values. Zhang and Chou suggested that the deviation was that interactions among different ions are omitted in the Nernst-Einstein relation. A stricter relation between the ionic conductivity and the diffusion coefficient, which considers the transport coefficients of Ca<sup>2+</sup>, Si<sup>4+</sup>, Al<sup>3+</sup> and O<sup>2-</sup> in SiO<sub>2</sub>-CaO-Al<sub>2</sub>O<sub>3</sub> liquid slag, were proposed for further work, as in equation 24.

$$\kappa = F^2 \left( \frac{4C_{Ca^{2+}}}{RT} D_{eff} + 8L_{12} + 6L_{13} - 4L_{10} \right) \quad 24$$

Where  $L_{12}$ ,  $L_{13}$  and  $L_{10}$  are the transport coefficient in mol/J s. Suffix 1, 2, 3, 0 means Ca<sup>2+</sup>, Si<sup>4+</sup>, Al<sup>3+</sup>, O<sup>2-</sup> in SiO<sub>2</sub>-CaO-Al<sub>2</sub>O<sub>3</sub> liquid slag.

Liang et al. [112] measured the diffusion coefficient of Ca<sup>40</sup> and Ca<sup>42</sup> at 1500 °C and 1GPa for several slag compositions using the isotope tracer method. Their results for 40wt% SiO<sub>2</sub> – 40wt% CaO –20wt% Al<sub>2</sub>O<sub>3</sub> are similar as the results from Towers and Chipman [108]. They also found that the self-diffusion coefficient increased with decreasing viscosity of

the slag, i.e., with decreasing SiO<sub>2</sub> and Al<sub>2</sub>O<sub>3</sub> content in the slag. However, they did not obey the Stokes-Einstein equation 25 or the Eyring equation 26.

$$D = \frac{kT}{6\pi\eta a} \quad 25$$

$$D = \frac{kT}{\lambda\eta} \quad 26$$

Where k is the Boltzmann constant, T is the absolute temperature, η is the viscosity, a is the radius of the sphere, and λ is the particle's mean jump distance.

The Eyring equation has often been used to relate melt viscosities with diffusion coefficients [25]. Eyring et al. [118] suggested that the driving force for diffusion resulted from the concentration gradient of diffusion ions, and that the standard free energy changed with the jumping distance. The structure and physical properties of molten slags may then change with the increasing content of CaO, which again changes the jumping distance of Ca ion and the value of the diffusion activation energy. Self-diffusion coefficients of alkali and alkaline earth elements in molten silicates, however, did not follow this simple relation, which was also supported by [119]–[121].

The diffusion coefficient is strongly influenced by the viscosity of the slag. The viscosity will affect the mass transfer of ions between the CaO and slag interface, and through the liquid slag. The viscosity in SiO<sub>2</sub>-CaO-Al<sub>2</sub>O<sub>3</sub> slag is earlier described thoroughly in subchapter 2.1.3.2: Viscosity. The viscosity of a slag depends on composition and temperature. Dogan et al. [95] found that with increased slag density, which in their case decreased the viscosity, the diffusivity of slag in SiO<sub>2</sub>-CaO-FeO also increased. This gives that the slag structure is an important factor for the diffusion of CaO in slag.

Ren et al. [114] developed a model for estimating the diffusion coefficient related to the structure of the slag instead of viscosity and electrical conductivity. The structure of the slag is often described by optical basicity, free oxygen, bridging oxygen, non-bridging oxygen and the ratio of non-bridging oxygen to tetrahedral cations. The optical basicity was used to both describe the structure of the slag and to estimate its physical properties. They used equation 27 from Mills [35] for optical basicity that accounts for the cations required for the charge balance of AlO<sub>4</sub><sup>5-</sup>. The valence of Al<sup>3+</sup> is lower than Si<sup>4+</sup>, so Ca<sup>2+</sup> is needed to keep the charge balance and forming [½Ca(AlO<sub>4</sub>)]<sup>4-</sup>.

$$\Lambda^{corr} = \frac{1.0(\chi_{CaO} - \chi_{Al_2O_3}) + 0.6 \cdot 3\chi_{Al_2O_3} + 0.48 \cdot 2\chi_{SiO_2}}{(\chi_{CaO} - \chi_{Al_2O_3}) + 3\chi_{Al_2O_3} + 2\chi_{SiO_2}} \quad 27$$

Where Λ<sup>corr</sup> is the corrected optical basicity, x<sub>i</sub> is the mole fraction of each component, and the coefficients 1.0, 0.6 and 0.48 are the optical basicities of CaO, Al<sub>2</sub>O<sub>3</sub> and SiO<sub>2</sub>, respectively.

Next, they plotted  $\Lambda^{corr}$  as a function of  $B=E/R$ , and found the approximate relation as in equation 28.  $R$  is the universal gas constant  $8.314 \text{ J/K mol}$ .

$$B = a\Lambda^{corr3} + b\Lambda^{corr2} + c\Lambda^{corr} + d \quad 28$$

The constants  $a$ ,  $b$ ,  $c$  and  $d$  were optimized for using the same experimental data as Goto et al. [111] and Zhang and Chou [113], shown in Table 31. Figure 85 shows the comparison between the measured diffusion coefficients for  $\text{Ca}^{2+}$  in for 40wt%  $\text{SiO}_2$  – 40wt%  $\text{CaO}$  – 20wt%  $\text{Al}_2\text{O}_3$  slag [107]–[110] with the calculated values from Goto et al. [111], Zhang and Chou [113] and Ren et al. [114]. In the model from Ren et al., there was an increasing function relationship between the logarithm of pre-exponential factor and the diffusion activation energy calculated by optical basicity. With increasing polymerization degree of molten slag, the diffusion coefficient of calcium ions decreases. They explained that a decreasing concentration of free  $\text{Ca}^{2+}$  and weaker mobility of these calcium ions in  $[\text{1/2Ca}(\text{AlO}_4)]^{4-}$  resulted in a lower diffusion coefficient because of the charge balance in the  $\text{CaO}$ – $\text{Al}_2\text{O}_3$ – $\text{SiO}_2$  slag.

Table 31 Parameters for model, developed by Ren et al. [114].

a	b	c	d
$1.7565 \cdot 10^9$	$-3.2773 \cdot 10^9$	$2.037 \cdot 10^9$	$-4.2172 \cdot 10^8$

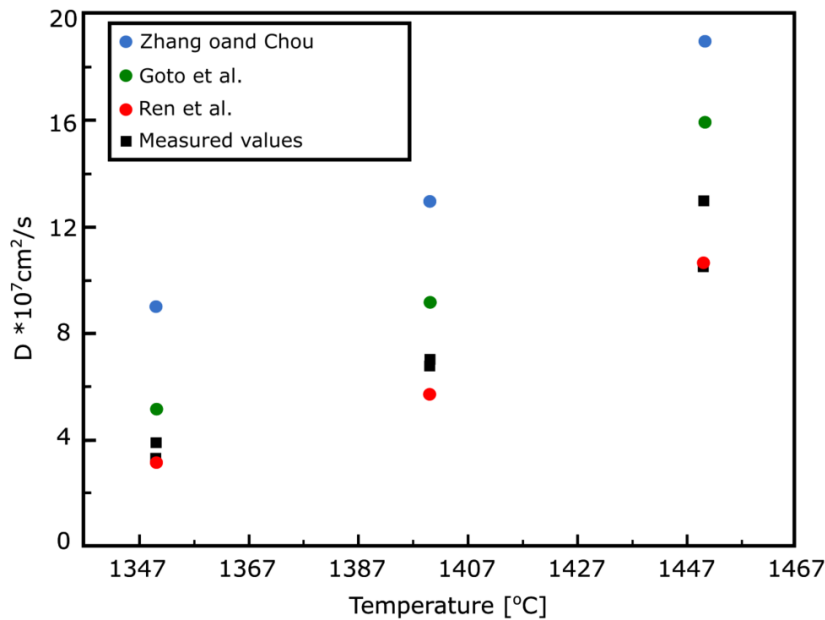


Figure 85 The estimated diffusion coefficient values of Ca diffusion in 40wt%  $\text{SiO}_2$  – 40wt%  $\text{CaO}$  – 20wt%  $\text{Al}_2\text{O}_3$  from Zhang and Chou. [113], Goto et al. [111] and Ren et al. [114] compared with the measured values from Towers et al. [107], [108], Niwa [109] and Saitô and Maruya [110]. The figure is revised from [114].

Amini et al. [104] calculated the diffusivity of lime in 8wt% SiO<sub>2</sub>- 50wt% CaO- 42wt% Al<sub>2</sub>O<sub>3</sub> slag from experimental results on dissolution rate in the temperature interval 1500-1600 °C. A rotating disc was used during the dissolution rate experiments, and calculated the diffusion coefficient via the total mass flux, as given in equation 29.

$$j_{total} = j_{disk} + j_{cylinder}$$

$$\kappa_{total}A_{total}\Delta C = \kappa_{disk}A_{disk}\Delta C + \kappa_{cylinder}A_{cylinder}\Delta C \quad 29$$

By using Levich equation [122] relates the mass-transfer coefficient to the angular velocity of the disk and the physical properties of the liquid phase, and a derived modified correlation analysis of dissolution of rotating cylinders in various molten metallic systems from Kosaka and Minowa [123], the diffusion coefficient could be calculated from 30.

$$k_{total} = D^{\frac{2}{3}}(A\omega^{\frac{1}{2}} + B\omega^{\frac{3}{4}}) \quad 30$$

Where D is the chemical diffusivity in cm<sup>2</sup>/s,  $\omega$  the angular velocity of the disk in rad/s, and A and B are constants including the density of the slag, the radius of rotating sample and the depth of the immersion of the sample in the melt.

They found that the diffusion coefficient was in the range of 10<sup>-4</sup> cm<sup>2</sup>/s. As the diffusion coefficient was calculated from dissolution data under forced convection, it is expected to give a higher value than for self-diffusion. They also looked at the effect of adding 5wt% SiO<sub>2</sub> to the slag, which decreased the CaO diffusivity.



## 4.2 Experimental procedure

The aim of these experiments is to study the dissolution rate of CaO in SiO<sub>2</sub>-CaO-Al<sub>2</sub>O<sub>3</sub> slag. Many Si and FeSi plants add calcium in form of lime together with the raw materials to ensure sufficient low viscosity of the slag.

### 4.2.1 Materials

#### 4.2.1.1 Industrial lime

Industrial lime was supplied by Franzefoss Minerals AS. Product data are listed in Table 32.

Table 32 Chemical analyses and density for industrial lime (CaCO<sub>3</sub>) from Franzefoss Minerals AS.

Parameter	Method	Result	Parameter	Method	Result
CaO	WD-XRF	>54%	Hg	ICP-AES	0,0053 ppm
MgO		0,4%	As		n.d.
SiO <sub>2</sub>		0,2%	Pb		n.d.
Al <sub>2</sub> O <sub>3</sub>		0,1%	Cd		n.d.
Fe <sub>2</sub> O <sub>3</sub>		<0,12%	Al		60 ppm
Na <sub>2</sub> O		0,01%	B		<20 ppm
K <sub>2</sub> O		0,02%	Fe		364 ppm
MnO		0,005%	Ni		<2 ppm
P <sub>2</sub> O <sub>5</sub>		0,005%	Na		2 ppm
TiO <sub>2</sub>		0,01%	Cu		6 ppm
Density	Pycnometer	2.7kg/dm <sup>3</sup>	Mn		45 ppm
			Cr		<2 ppm

#### 4.2.1.2 SiO<sub>2</sub>-CaO-Al<sub>2</sub>O<sub>3</sub> slag

Based on slag compositions found in the industrial samples, a master SiO<sub>2</sub>-CaO-Al<sub>2</sub>O<sub>3</sub> slag was made. It is beneficial to have a similar slag composition as in the Si and FeSi furnaces so that experimental results can be compared with the industrial production. Powder of SiO<sub>2</sub>, limestone and Al<sub>2</sub>O<sub>3</sub> with weight ratio 2:1:1 was mixed and melted in an induction furnace. To ensure a homogenous slag phase, the slag mix were remelted three times up to 1800 °C. This was well above the expected liquidus temperature for this mix. The composition in the final slag mix is given in Table 33, referred to as “Slag 1”. Additionally, two other slags from Kristiansen [124] were used. Table 33 presents the compositions of all three slag compositions along with their respective liquidus and solidus temperature.

Table 33 SiO<sub>2</sub>-CaO-Al<sub>2</sub>O<sub>3</sub> slags used in the dissolution experiments. The amounts are given in wt% and the viscosities are calculated with FactSage 8.1.

Slag	SiO <sub>2</sub>	CaO	Al <sub>2</sub> O <sub>3</sub>	T <sub>liquidus</sub>	T <sub>solidus</sub>	Viscosity [Poise]	
	[wt%]	[wt%]	[wt%]	[°C]	[°C]	1500°C	1550°C
1	56	15	29	1490	1170	456	250
2	38	20	42	1550	1385	-	48
3	56	21	23	1420	1170	180	108

## 4.2.2 High temperature experiments

### 4.2.2.1 Calcination of limestones

At elevated temperatures, limestone decomposes to CaO. It is assumed that CaO reacts with the slag in the industrial furnace, and CaO will hence be used in these experiments. To prepare the CaO for the dissolution experiments, limestones from Franzfoss were calcined in a muffle furnace. Calcination is decomposition of carbonate ores, which in this case is to drive off the carbon dioxide according to reaction 14. This reaction occurs at 900 °C to 1050 °C.



Cracks may form during heating, and a slow heating rate is used to ensure no damage in the final CaO. Different heating rates were tested and 5.6°C/min was found suitable for these experiments. The limestones were calcined at 1000 °C for 1 hour. The CaO were then stored in a desiccator to avoid reactions with the humidity or atmospheric CO<sub>2</sub> before the dissolution experiments. Pictures of limestone and CaO before and after calcination is shown in Figure 86.



Figure 86 Picture of the original limestone to the left, and after calcination 1h at 1000 °C to the right.

Compression tests were performed on the original limestones, and on CaO heated with two different heating rates: 5.6 °C/min and 1.7 °C/min. The objective was to investigate whether varying heating rates influence the strength of the material. Prior to the calcination and

tests, the limestones were cut into 2cm cubes to ensure consistent contact area and volume of the stones. The compression tests were carried out using an MTS 880, which is a servo hydraulic universal testing machine. The MTS 793 software was used to download the force results data.

#### 4.2.2.2 Dissolution experiments in graphite tube furnace

The first dissolution experiments were conducted using a graphite tube furnace under an inert gas atmosphere. A picture of the furnace is shown to the left in Figure 87. This furnace has a maximum temperature of 1700 °C and is equipped with a resistant graphite element for heat supply. The furnace temperature is controlled by a B-type thermocouple, and additionally, a C-type thermocouple is placed right above the sample. ~1-3 g CaO and ~25-30 g of slag 1 were placed in a graphite crucible with a 40 mm diameter and 55 mm height, as shown in the top right picture in Figure 87. The crucible is placed in the reaction chamber in the furnace. A vacuum pump evacuates the gas from the furnace before it is filled with argon process gas. All experiments were run in argon atmosphere with a gas flow rate of ~2.5 dm<sup>3</sup>/min. Several pilot heating sequences were conducted to find the correct temperature settings. The samples were heated with three different heating rates up to 1600 °C, which is well above the liquidus temperature of slag 1 of 1490 °C, and different holding times were used as shown in Figure 88. An overview of all the experiments is listed in Table 34.



Figure 87 A picture of the graphite tube furnace, TF2 (left) and the crucible setup (right). The top right picture is the initial crucible with CaO and SiO<sub>2</sub>-CaO-Al<sub>2</sub>O<sub>3</sub> slag and the bottom right shows the same crucible after heating to 1600 °C.

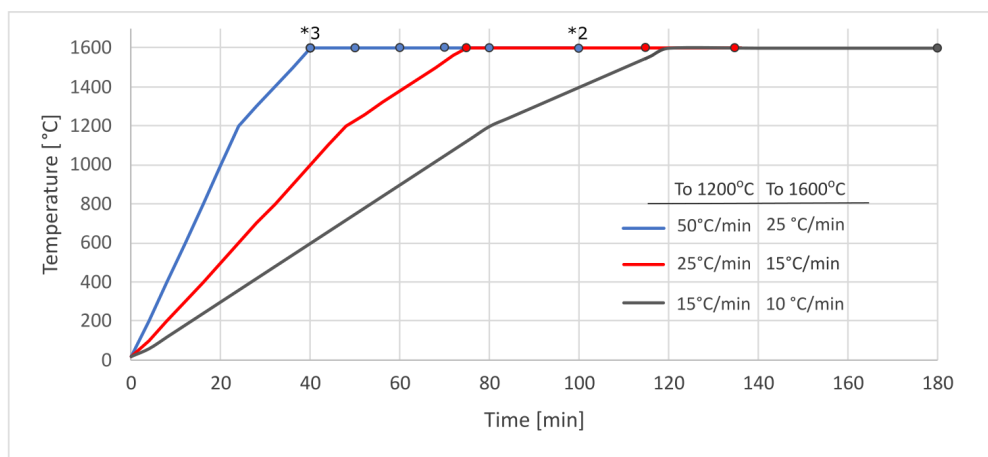


Figure 88 Heating profiles for the dissolution experiments in the vertical tube furnace.

Table 34 The dissolution experiments, CaO in 56wt% SiO<sub>2</sub>- 15wt% CaO- 29wt% Al<sub>2</sub>O<sub>3</sub> slag. The sample ID gives the heating rate to 1200 °C and the holding time.

Sample ID	Heating rate [°C/min]		Holding time [min]	Mass [g]		
	To 1200°C	1200-1600°C		CaO	Slag	CaO/slag
Pure slag	50	25	0	-	25.30	
50-0.1	50	25	0	2.30	23.0	0,10
50-0.2	50	25	0	2.19	25.93	0,08
50-0.3	50	25	0	3.72	32.86	0,11
50-10	50	25	10	3.00	28.17	0,11
50-20	50	25	20	2.21	22.43	0,10
50-30	50	25	30	2.75	28.30	0,10
50-40	50	25	40	2.43	29.56	0,08
50-60.1	50	25	60	1.93	27.57	0,07
50-60.2	50	25	60	1.85	27.47	0,07
25-0	25	15	0	1.20	24.03	0,05
25-40	25	15	40	2.17	27.32	0,08
25-60	25	15	60	2.34	27.36	0,09
15-40	15	10	40	3.06	31.95	0,10

#### 4.2.2.3 Dissolution experiments in the sessile drop furnace

In total 29 dissolution experiments were conducted in the sessile drop furnace. This is the same furnace as used for the quartz heating experiments and a thorough description of the furnace can be found in subchapter 3.2.2.1. Approximately 0.2 to 0.3 g of slag and 0.04 to 0.07 g of CaO with physical contact were placed on a 3 mm high graphite substrate with 10 mm diameter. Initially, two experiments with slag 1 and CaO were heated to 1600 °C. During the experiments, it was observed that the dissolution reaction accelerated in the temperature interval 1450-1500 °C. Based on this, it was decided to run experiments at 1500 °C and 1550 °C. An overview of the experiments is listed in Table 35. Pictures of the

slag and CaO prior to experiment and the slag after experiment can be seen in Figure 89. Additionally, three experiments with slag 1 and CaO were heated to 1000 °C, 1200 °C and 1400 °C to illustrate the visual changes during heating. It was also attempted to do experiments with slag on a lime substrate. However, due to fast dissolution and pulverization of excess CaO during cooling, the samples could not be analyzed after the experiments.

Table 35 Dissolution experiments in sessile drop furnace.

	Slag composition			T <sub>liq</sub> [°C]	Experiments at 1500°C					Experiments at 1550°C		
	SiO <sub>2</sub>	CaO	Al <sub>2</sub> O <sub>3</sub>		0	5	10	20	30	0	10	20
	[wt%]				[min]					[min]		
1	56	15	29	1490	3	1	2	1	2	1		
2	38	20	42	1550	1	1	3	1		1	1	1
3	56	21	23	1420	1	1	2	1		1	1	(17min)

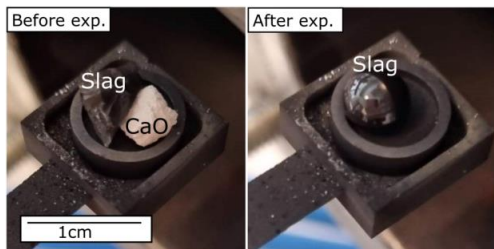


Figure 89 Slag and CaO before sessile drop experiment and slag after dissolution experiment.

## 4.2.3 Characterization

### 4.2.3.1 Computed tomography (CT-imaging)

X-ray computed tomography (CT) was performed on three samples from the graphite tube furnace experiments; 50-0, 50-20 and 50-40, to have a 3D view of the distribution of CaO in the SiO<sub>2</sub>-CaO-Al<sub>2</sub>O<sub>3</sub> slag. The scans were performed with a Nikon XT H 225 ST Instrument. The instrument uses x-rays to measure the loss of flux intensity through the sample. From this, it is made a three-dimensional representation of the scanned sample, and different slag compositions and CaO are separated by different intensities, which is due to different atomic mass in Si (28g/mol), Ca (40g/mol) and Al (26g/mol). However, the difference between these components is small, which may result in small shading differences in the final CT images. The instrument was run with 175kV and 86μA, and each sample was scanned for about an hour. The software ImageJ was used to optimize color and contrast on the resulting CT images.

#### 4.2.3.2 *Electron probe micro-analysis*

EPMA, JEOL JXA 8500 was used to investigate the CaO and slag after both the graphite tube furnace experiments and the sessile drop furnace experiments. The equipment and experimental work are the same as earlier described in section 2.2.3.1: Electron probe micro-analysis (EPMA).

Si, Al and Ca elemental mapping were also performed on selected samples from the graphite tube furnace experiments to see the spatial distribution of the different oxides in the slag.

## 4.3 Results

Understanding the mechanism and rate of CaO dissolution in SiO<sub>2</sub> – CaO – Al<sub>2</sub>O<sub>3</sub> slag is important in Si and FeSi production, as it is currently the main action used for removing accumulated slag in the furnaces. The available literature on this reaction primarily focuses on the steel industry, but this study aims to provide results more specific for the Si and FeSi production.

### 4.3.1 Mechanical strength of CaCO<sub>3</sub> and CaO

To investigate how easily the lime would fracture before it reaches the slag in the furnace, the compression strength was measured. The compression strength of limestone and calcined CaO heated with two different heating rates up to calcination temperature 1000 °C were done in an MTS 880 servo hydraulic universal testing machine. The results are listed in Table 36, and the mass before and after calcination is also included in the table. More force is needed to induce cracks in the limestones than in the CaO, as expected. For the CaO heated with two different heating rates, the strength is similar. It was therefore also assumed that the heating rate up to calcination temperature of 1000 °C had no effect on how easily it fractured in the later dissolution experiments.

Table 36 The compression tests performed on limestone and CaO, calcined with two different heating rates 5.6 °C/min and 1.7 °C/min.

Sample		Mass		w.l.	Force	Area	Strength	Ave.	Std.
		Initial	CaO						
		[g]	[g]	[%]	[N]	[mm <sup>2</sup> ]	[N/mm <sup>2</sup> ]		
Original limestone	1	24.9	-	-	20 260	40	507		
	2	26.5	-	-	25 718	40	643		
	3	22.9	-	-	26 213	40	655		
	4	24.0	-	-	33 046	40	826	658	131
Calcined at 1000°C with heating rate 5.6°C/min	1	22.7	12.7	43.9	7 985	40	200		
	2	25.9	14.6	43.8	9 415	40	235		
	3	22.6	12.7	43.9	8 953	40	224	220	18
	4	25.4	14.3	43.7	-	-	-		
Calcined at 1000°C with heating rate 1.7°C/min	1	25.7	14.5	43.7	8 029	40	201		
	2	26.2	14.7	43.8	8 377	40	209		
	3	23.0	12.9	43.7	8 566	40	214		
	4	26.0	14.7		7 022	40	176	200	17

### 4.3.2 Dissolution experiments in graphite tube furnace

The first dissolution experiments were performed in a graphite tube furnace placing CaO in the bottom of a graphite crucible together with slag 1, with CaO/slag ratio of 0.1. Fourteen experiments were performed, and after the experiments, a Dremel was used to remove the graphite crucible from the sample. The bottom of the samples was first imaged. Initial slag, and two of the samples heated with the fastest heating rate, 50 °C/min to 1200 °C and 25°C/min to 1600 °C, with 0- (50.0.1) and 60 minutes (50.60.2) holding time are shown in Figure 90. WDS analyses across the samples as shown in Figure 91 were also performed on all samples. The results are graphed in Figure 92 and Figure 93. No CaO were found in any of the samples, which means that the dissolution is fast. A brighter color with more CaO in the slag could be found in the samples with shortest holding times, seen as peaks in the graphs. From 10 minutes to 60 minutes holding time, the CaO concentration in the bottom slag decreases.

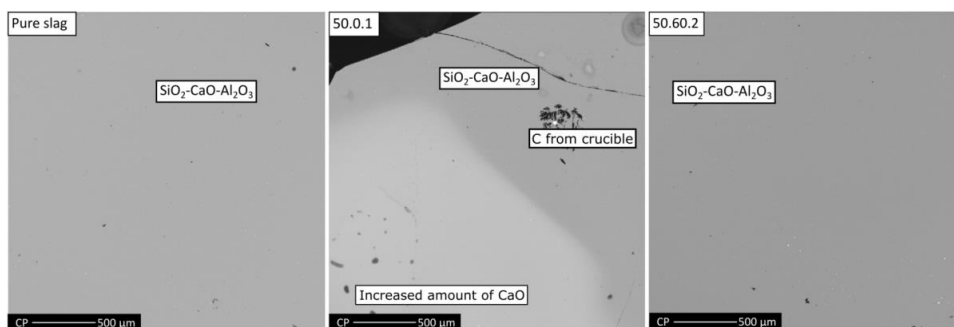


Figure 90 EPMA images of horizontal section in the bottom of pure slag and samples heated with heating rate 50 °C/min to 1200 °C and 25°C/min to 1600 °C with 0 minutes (50.0.1) and 60 minutes (50.60.2) holding time.

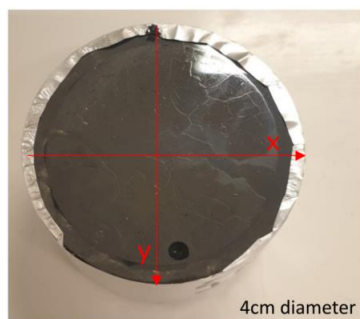


Figure 91 Horizontal section of the sample after experiment showing the analysed areas with WDS given in x- and y-direction.



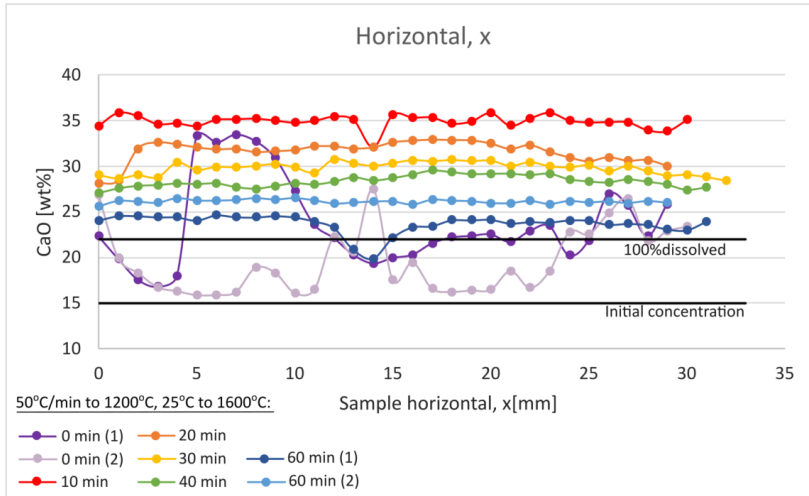


Figure 92 Results of WDS analysis horizontal section, x-direction close to the crucible bottom for the samples with heating rate 50 °C/min to 1200 °C and 25 °C/min to 1600 °C. The CaO/slag ratio was 0.1.

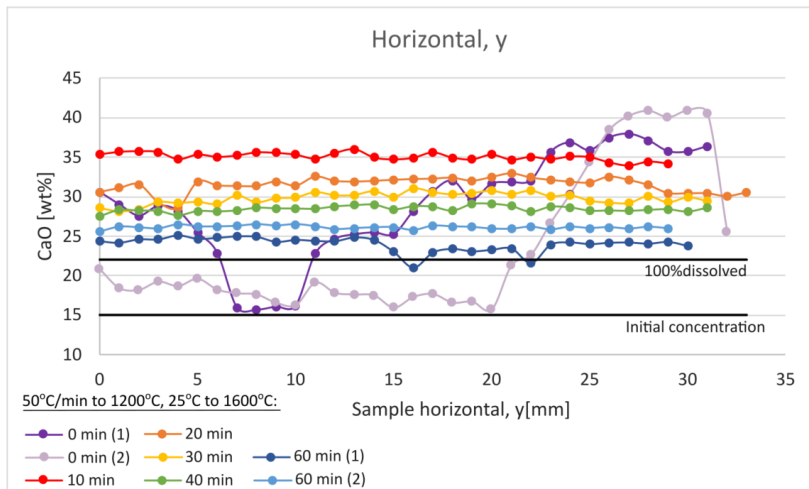


Figure 93 Results of WDS analysis horizontal section, y-direction for the samples with heating rate 50 °C/min to 1200 °C and 25 °C/min to 1600 °C. The CaO/slag ratio was 0.1.

Next, the samples were cut in two to study the vertical section with EPMA. X-ray diffractions (XRD) with Si, Al and Ca elemental mapping were also conducted to see the spatial distribution of the different oxides in the slag. The EPMA images together with the spatial distribution of Ca for the samples with fastest heating rate are shown in Figure 94. The complete XRD images are shown in Figure 215-222 in Appendix C. These images confirm a small concentration gradient, also after 60 minutes holding time. From this, it appears as the dissolution is very fast in the beginning before it slows down after around 20 minutes.

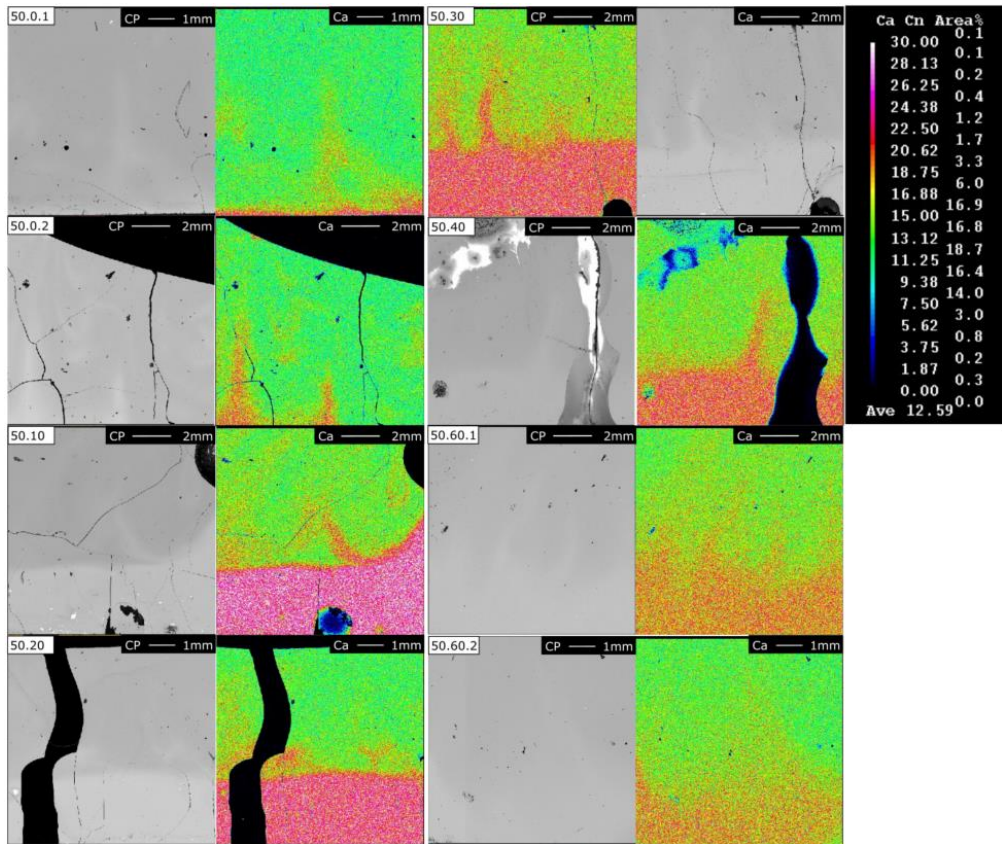


Figure 94 EPMA image to the left and Ca spatial distribution in the right image for samples with heating rate 50 °C/min to 1200 °C and 25 °C/min to 1600 °C with holding times 0-, 10-, 20-, 30-, 40- and 60 minutes. The CaO rich slag phase is found in the bottom of the sample.

This is also confirmed by the WDS analysis for the vertical samples, given in Figure 95. For every sample, three lines are analyzed from bottom to top. The slope of the curves decreases from 10 minutes to 60 minutes. For the 0-minute experiments, most of the samples are slag close to the initial concentration. This is believed to be due to the small lumps of CaO. In the horizontal section, it was also found concentration differences in the 0-minute experiments and based on this, it is believed that the initial CaO lump decomposes into smaller lumps before it dissolves in the slag. The analysis will hence depend on the analyzed area includes one of these lumps.

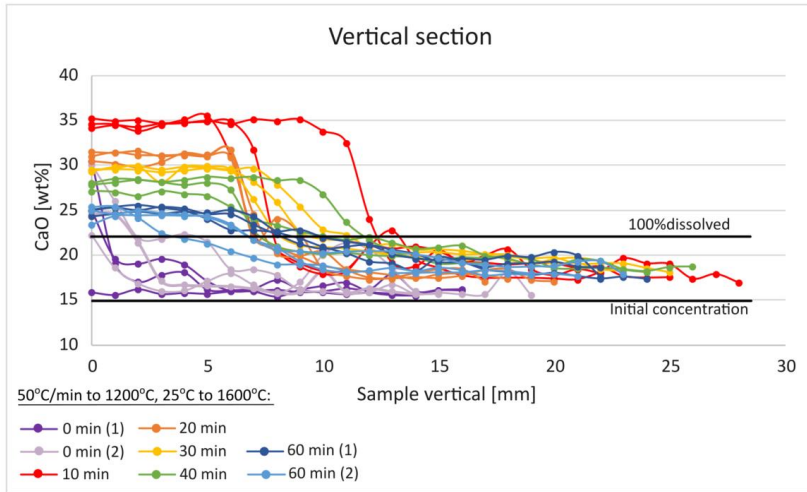


Figure 95 Results of WDS analysis vertical section for the samples with heating rate 50 °C/min to 1200 °C and 25 °C/min to 1600 °C. The CaO/slag ratio was 0.1.

No effect of heating rate up to 1600 °C was found. The composition results for the samples with slower heating rates are shown in Figure 96. Figure 97 displays the EPMA images together with the spatial distribution of Ca. It is not observed any differences in the slag structure for the different heating rates, and it is found that the curves are similar with similar slopes. The bottom slag in the 15+10 °C/min experiment has a higher CaO concentration, ~28-29%, compared to the 50+25 °C/min and 25+15 °C/min experiments, ~26-28% CaO. The solidus temperature for the heated slag is 1170 °C, and a slower heating rate facilitates more time in the temperature range 1200-1600 °C, which would expect some more reaction for the slowest heating rate. This was not observed in this study, and it is believed that the dissolution rate is slow before the liquidus temperature of the slag at 1490 °C. The concentration difference could also be explained by the location of the cross section in the sample. All samples are cut right in the middle, but the CaO rich slag phase is not symmetrical in the sample, which can be seen previous images and analysis.

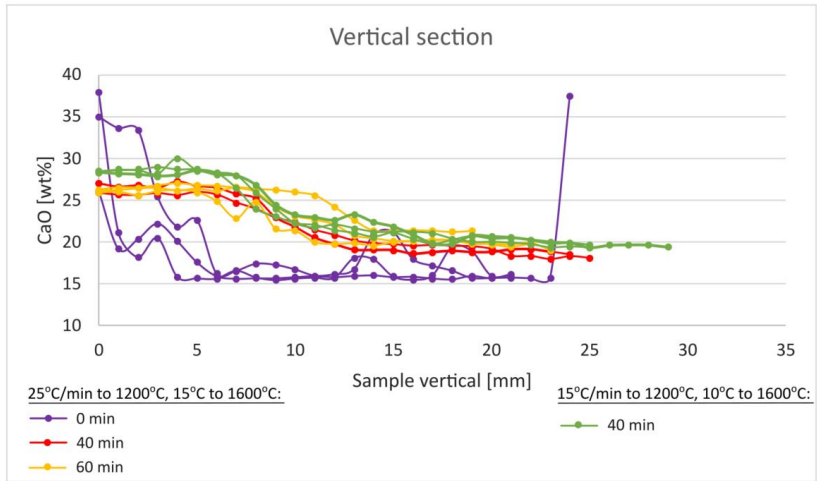


Figure 96 Results of WDS analysis vertical section for the samples with heating rate 25 °C/min to 1200 °C and 15 °C/min to 1600 °C, and heating rate 15 °C/min to 1200 °C and 10 °C/min to 1600 °C. The CaO/slag ratio was 0.1.

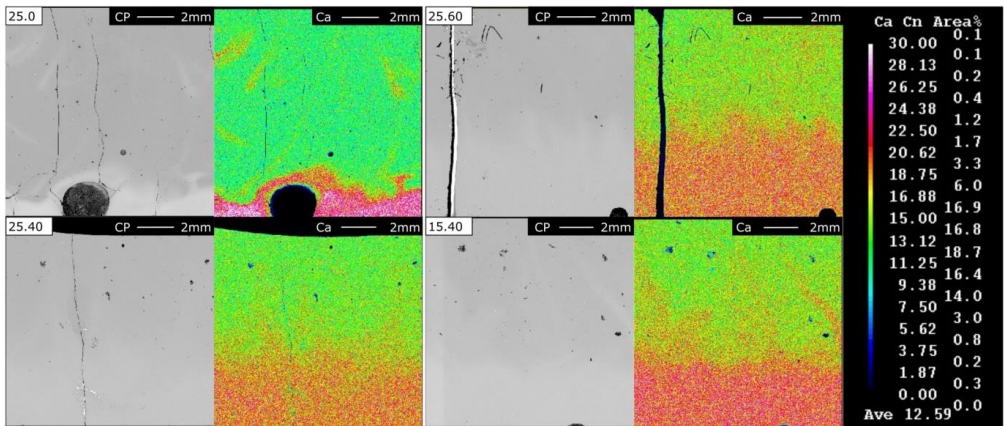


Figure 97 EPMA image to the left and Ca spatial distribution in the right image for samples with heating rate 25 °C/min to 1200 °C and 15 °C/min to 1600 °C with holding times 0-, 40- and 60 minutes, and one sample with heating rate 15 °C/min to 1200 °C and 10 °C/min to 1600 °C with holding time 40 minutes. The CaO rich slag phase is found in the bottom of the sample.

#### 4.3.2.1 CT-imaging

Three of the samples with the fastest heating rates from the graphite tube furnace experiments were analyzed with CT: 0 minutes holding time in Figure 98, 40 minutes holding time in Figure 99, and 60 minutes holding time in Figure 100. These images confirm the observations from EPMA. CaO forms a CaO rich slag phase at the bottom of the sample before it dissolves into the slag. It can also be observed footprints of CaO rich slag further up in the sample. This indicates that the CaO disintegrates before liquidus

temperature of the slag at 1490 °C and to some degree spread in the slag. This might also be due to convection due to the difference of density between the CaO and the slag. This creates a circulating flow of some of the CaO or CaO rich SiO<sub>2</sub>-CaO-Al<sub>2</sub>O<sub>3</sub> slag.

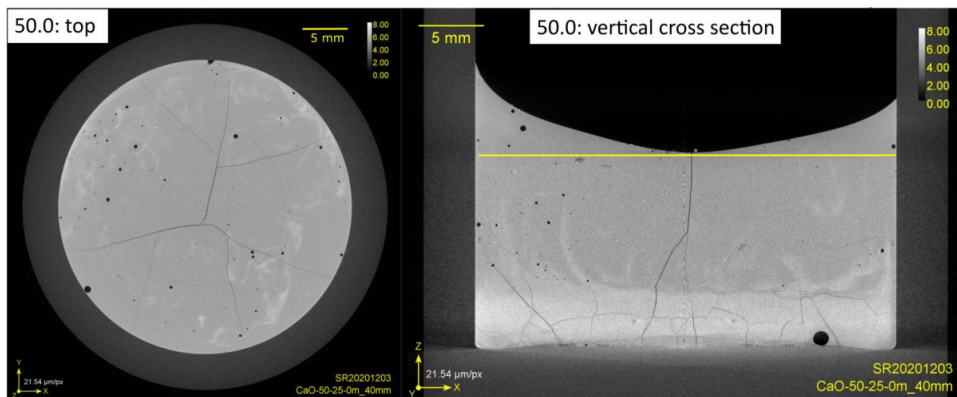


Figure 98 CT images of the second parallel heated to 1600 °C with heating rate 50 °C/min up to 1200 °C and 25 °C/min up to 1600 °C with 0 minutes holding time. To the left is an image from the top of the sample, and the right image is a vertical cross section in the center of the sample. The yellow line in the vertical section marks the height of the horizontal image. More CaO in the slag can be observed as the brighter grey color. The darkest grey color is the graphite crucible.

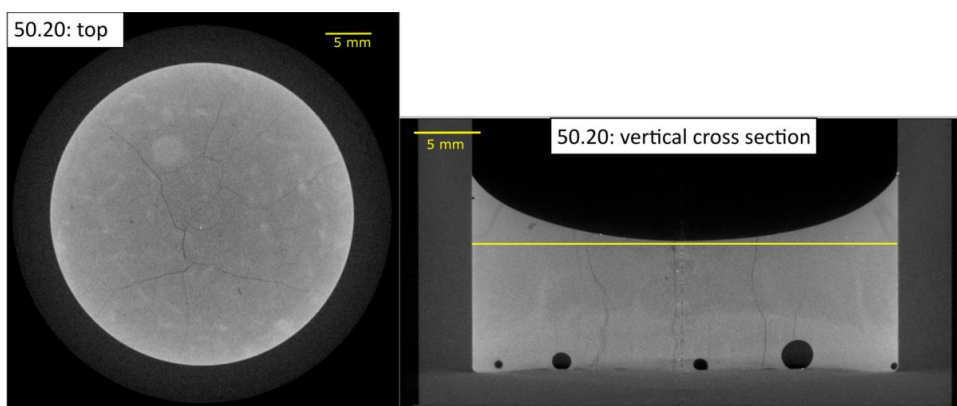


Figure 99 CT images of sample 50.20, which is heated to 1600 °C with heating rate 50 °C/min up to 1200 °C and 25 °C/min up to 1600 °C with 20 minutes holding time. To the left is an image from the top of the sample, and the right image is a vertical cross section in the center of the sample. The yellow line in the vertical section marks the height of the horizontal image. More CaO in the slag can be observed as the brighter grey color. The darkest grey color is the graphite crucible.

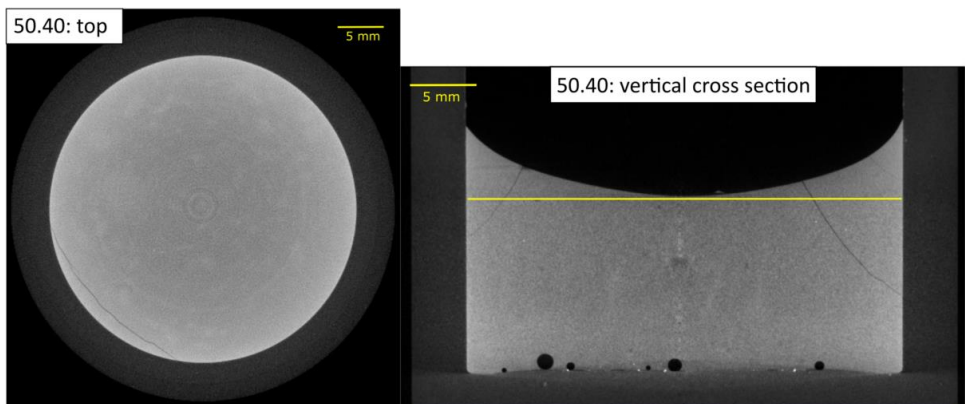


Figure 100 CT images of sample 50.40, which is heated to 1600 °C with heating rate 50 °C/min up to 1200 °C and 25°C/min up to 1600 °C with 40 minutes holding time. To the left is an image from the top of the sample, and the right image is a vertical cross section in the center of the sample. The yellow line in the vertical section marks the height of the horizontal image. More CaO in the slag can be observed as the brighter grey color. The darkest grey color is the graphite crucible.

### 4.3.3 Dissolution experiments in a sessile drop furnace

Based on the previous graphite tube furnace experiments, it was decided to do small-scale experiments. Experiments with CaO and slag 1 were first heated and stopped at different temperatures up to 1500 °C. The images after these experiments are shown in Figure 101. It was observed that the dissolution accelerates at approximately 1400 °C, and at 1500 °C, the slag has encapsulated the CaO. Dissolution experiments in the sessile drop furnace were conducted with different holding times at 1500 °C up to 30 minutes, and at 1550 °C up to 20 minutes. SiO<sub>2</sub>-CaO-Al<sub>2</sub>O<sub>3</sub> slag with three different compositions are used as shown in Table 33. The CaO content ranges from 15-21%. Slag 3 has the lowest liquidus temperature, while for slag 2 many of the experiments were run below the liquidus temperature.

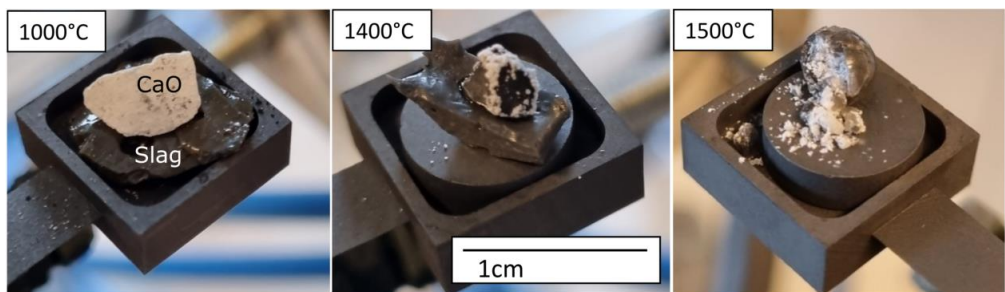


Figure 101 Sessile drop experiments with CaO and 56% SiO<sub>2</sub> - 15% CaO - 29% Al<sub>2</sub>O<sub>3</sub> slag heated to 1000 °C, 1400 °C and 1500 °C.

Table 33 The three master slags used for the dissolution experiments in sessile drop furnace. The viscosities are calculated with FactSage 8.1.

Slag	SiO <sub>2</sub>	CaO	Al <sub>2</sub> O <sub>3</sub>	T <sub>liquidus</sub>	T <sub>solidus</sub>	Viscosity [Poise]	
	[wt%]	[wt%]	[wt%]	[°C]	[°C]	1500°C	1550°C
1	56	15	29	1490	1170	456	250
2	38	20	42	1550	1385	-	48
3	56	21	23	1420	1170	180	108

#### 4.3.3.1 Slag 1: 56% SiO<sub>2</sub> – 15% CaO – 29% Al<sub>2</sub>O<sub>3</sub>

An overview of all the dissolution experiments with slag 1 is shown in Table 37. It was also attempted to do experiments with excess of CaO to see the effect on the dissolution rate. However, because the materials decriptated in room atmosphere it was not possible to do any analysis of the materials after the materials were cooled down.

Table 37 Dissolution experiments with CaO and 56% SiO<sub>2</sub>-15% CaO-29% Al<sub>2</sub>O<sub>3</sub>.

Temp [°C]	Holding time [min]		CaO/slag ratio	%CaO at 100% dissolved [wt%]
1500	0	#1	0.40	39
	0	#2	0.36	38
	0	#3	0.15	26
	5		0.15	26
	10	#1	0.15	26
	10	#2	0.36	37
	20		0.30	35
	30	#1	0.46	42
	30	#2	0.38	39
	1550	0		0.20

Three parallels with heating up to 1500 °C and 0 minutes holding time were performed, with different CaO/slag ratio of 0.40, 0.36 and 0.15. The images captured during the experiments are shown in Figure 103, and EPMA images after the experiments in Figure 105. For all three experiments it can be observed disintegrated CaO in the slag matrix. For the first and third parallel, it is found a concentration differences in the slag, as can be seen as a brighter color of the slag next to the CaO. In the second parallel, this is also observed in a small area at the bottom of the sample. Generally, the thickness of the slag in this sample is very thin.

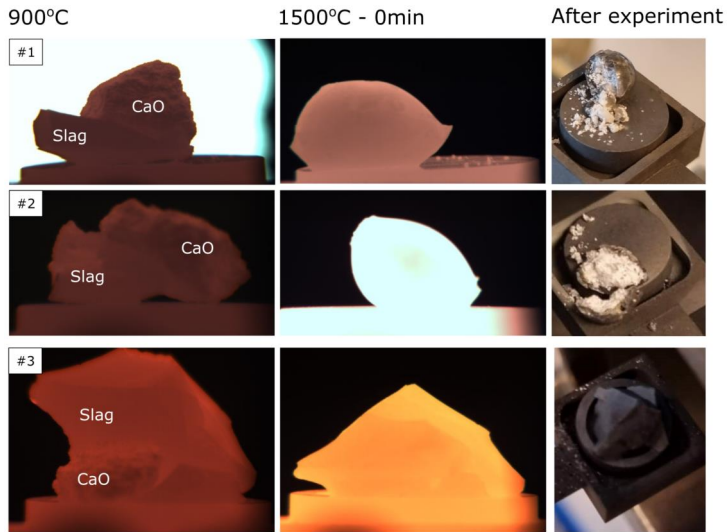


Figure 102 Images captured during and after experiments of CaO and 56% SiO<sub>2</sub>- 15% CaO-29% Al<sub>2</sub>O<sub>3</sub> slag heated to 1500 °C with 0 minutes holding time. The CaO/slag ratio is 0.40, 0.36 and 0.15 for parallel 1, 2 and 3, respectively.

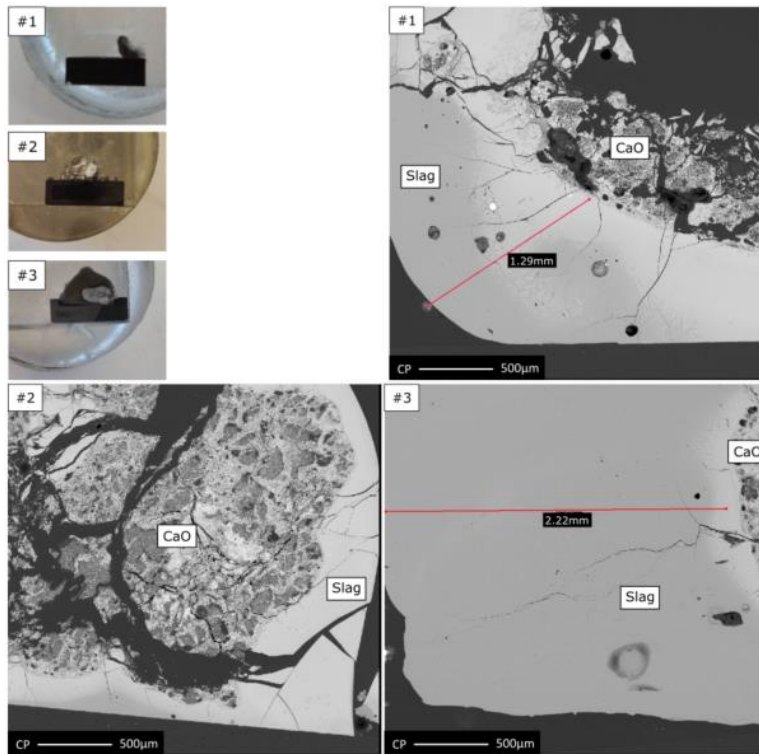


Figure 103 Cross-section images and EPMA images of CaO and 56% SiO<sub>2</sub>- 15% CaO-29% Al<sub>2</sub>O<sub>3</sub> slag heated to 1500 °C and with 0 minutes holding time. The CaO/slag ratio is 0.40, 0.36 and 0.15 for parallel 1, 2 and 3, respectively.



WDS line analysis were conducted on all samples after the experiments, and the results are graphed in Figure 104. A concentration gradient was observed in all experiments at 0 minutes, 5 minutes and 10 minutes holding time. Additionally, the CaO appeared to be dissolved after approximately 20 minutes at 1500 °C. In cases where CaO formed a CaO-rich slag phase, it is assumed that the CaO/slag interface is located at the point with the highest CaO concentration. For many of the experiments, analysis could be performed on both sides of the CaO particle, which are labeled as “left” or “right” on the graph. The CaO/slag ratio varies across the experiments, so the graph does not include the 100% dissolved concentrations.

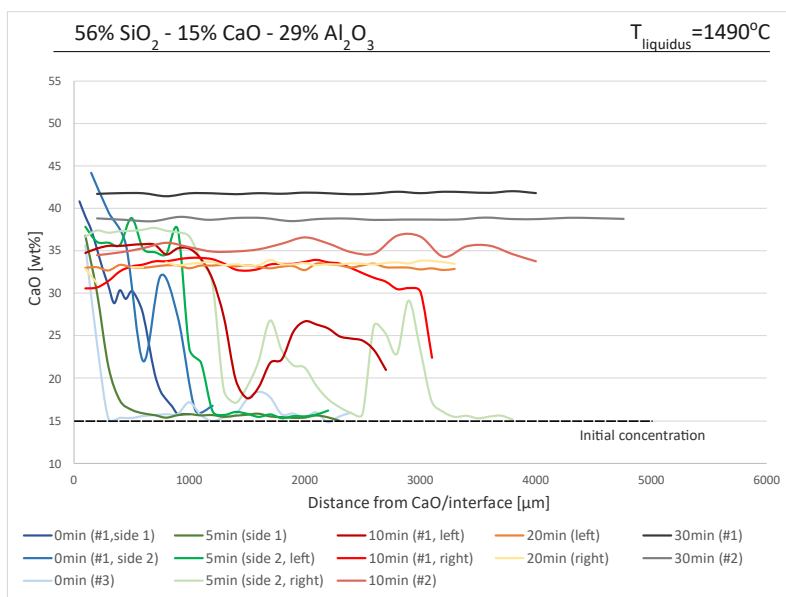


Figure 104 WDS results for the experiments at 1500 °C with CaO and slag I.

Experiments were conducted at 1500 °C with holding times 0, 5 and 10 minutes, using a CaO/slag ratio of 0.15. The images captured during the experiments are shown in Figure 105, while the EPMA images after the experiments can be seen in Figure 106. The red line is the analyzed line. In the 5-minute experiment, both sides of the cut sample were analyzed. On one side, disintegrated CaO can be observed, while the other side includes only a CaO rich slag, indicating a very small CaO particle at this point. No CaO was found after 10 minutes.

It can be observed that the 0- and 5-minute experiments are not fully liquid, despite the experimental temperature being above the liquidus temperature of 1490 °C. This may be due to small temperature differences. The furnace thermocouple was changed between the 0- and 5-minute and the 10-minute experiments. Calibrations were performed for both thermocouples, but small variations may still occur. As 1500 °C is close to the liquidus temperature, even minor deviations might be visible in the experiments.

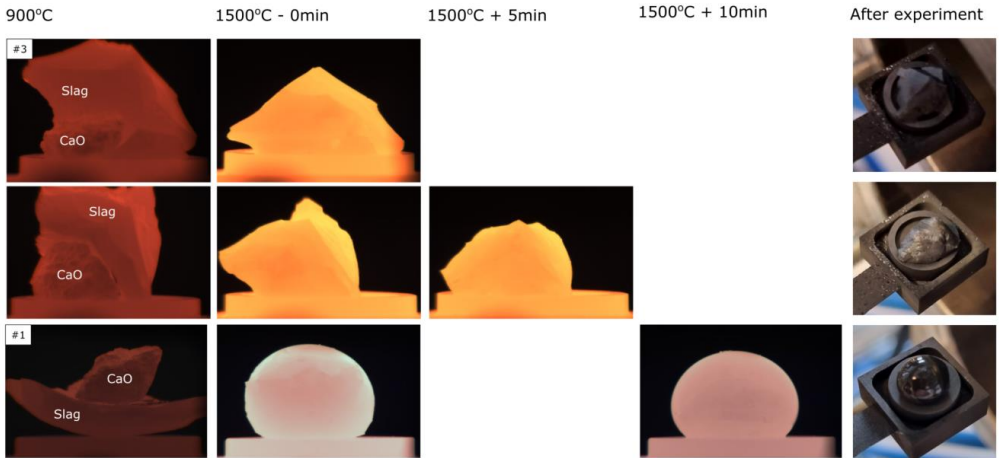


Figure 105 Images captured during and after experiments for the 1500 °C experiments of CaO and slag 1, with 0-, 5- and 10 minutes holding time, and CaO/slag ratio of 0.15.

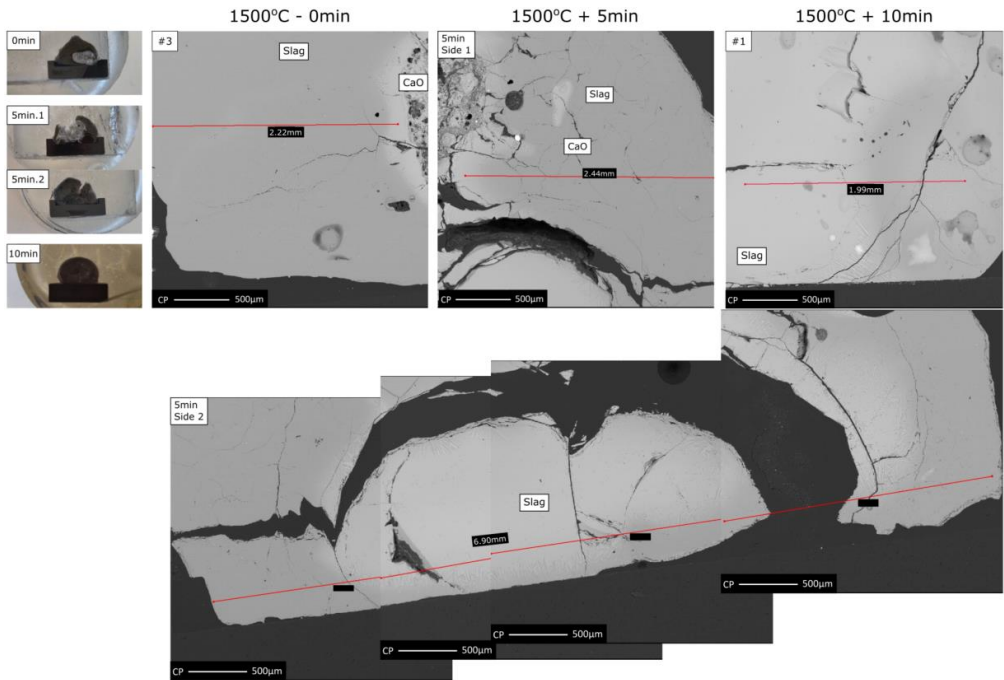


Figure 106 Cross section images and EPMA images after experiments for the 1500 °C experiments with CaO and Slag 1 with 0-, 5- and 10 minutes holding time, and with CaO/slag ratio of 0.15.

One experiment was conducted at 1550 °C with 0 minutes holding time. The images captured during the experiment, the cross-section image and the EPMA image after the experiment are shown in Figure 107. The red line is the analyzed line, and the corresponding results are graphed in Figure 108. The results are similar to those of the 1500 °C - 0 minutes experiment, wherein disintegrated CaO and slag with the initial composition, with a CaO rich boundary layer in between.

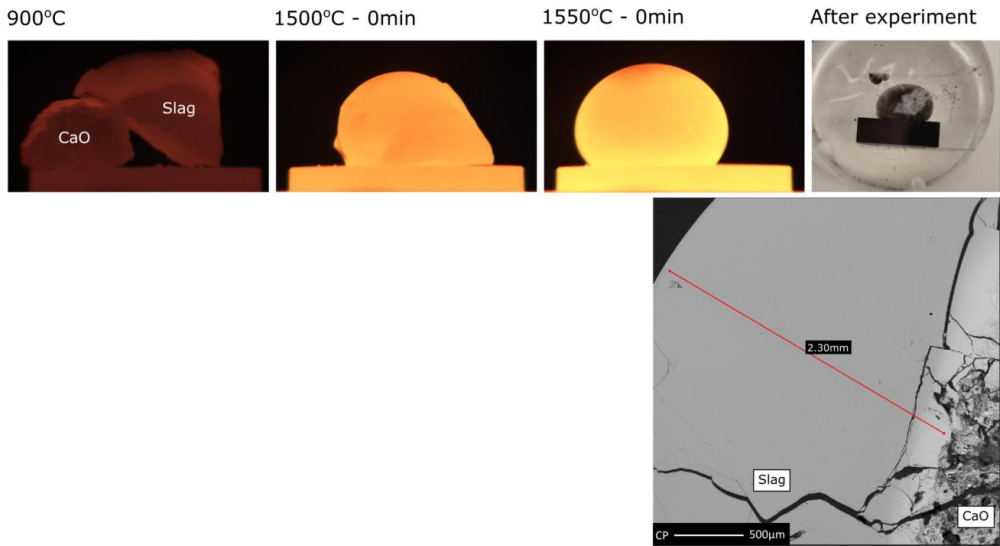


Figure 107 Images captured during the experiment, cross section and EPMA images after experiment for CaO and slag 1 heated to 1550 °C with 0 minutes holding time.

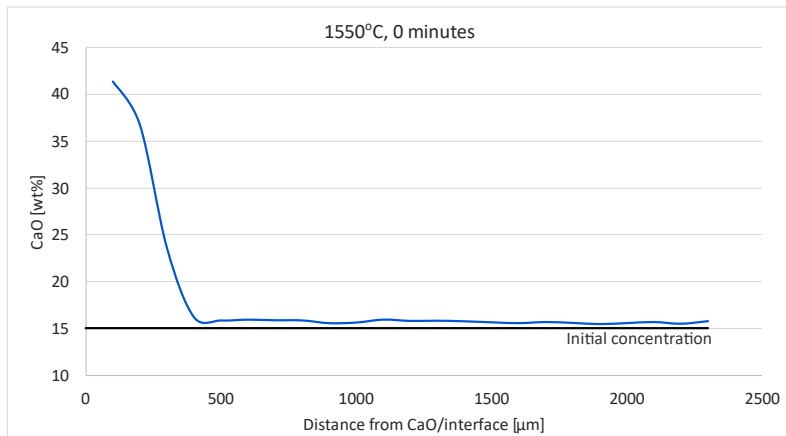


Figure 108 WDS results for the experiment heated to 1550 °C with CaO and slag 1.

#### 4.3.3.2 Slag 2: 38% SiO<sub>2</sub> – 20% CaO – 42% Al<sub>2</sub>O<sub>3</sub>

An overview of the experiments conducted with slag 2 is shown in Table 38. The liquidus temperature of slag 2 is 1550 °C, which is above the experimental temperature of 1500 °C.

Table 38 Dissolution experiments with CaO and 38% SiO<sub>2</sub>-20% CaO-42% Al<sub>2</sub>O<sub>3</sub>.

Temp [°C]	Holding time [min]	CaO/slag ratio	%CaO at 100% dissolved [wt%]
1500	0	0.25	36
	5	0.25	36
	10	#1 0.42	44
	10	#2 0.14	30
	10	#3 0.25	36
	20	0.17	31
1550	0	0.33	40
	10	0.41	43
	20	0.27	37

Three parallels with holding time 10 minutes at 1500 °C were performed, with CaO/slag ratios of 0.42, 0.14 and 0.25. The images captured during the experiments are shown in Figure 109, and EPMA images after the experiments are displayed in Figure 110. For the first and third parallel with the CaO/slag ratio of 0.42 and 0.25, there is still CaO left after 10 minutes at 1500 °C. For parallel 2 with lower CaO/slag ratio, there is only a CaO rich slag phase, seen as the brighter color in the EPMA image.

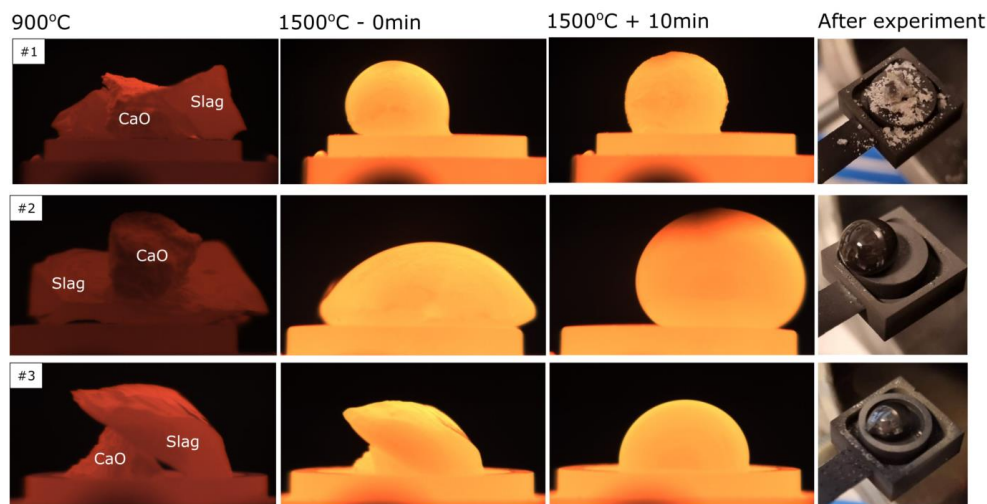


Figure 109 Images captured during and after experiments for the three parallels of CaO and slag 2 at 1500 °C with 10 minutes holding time. The CaO/slag ratio is 0.42, 0.14 and 0.25 for parallel 1, 2 and 3, respectively.

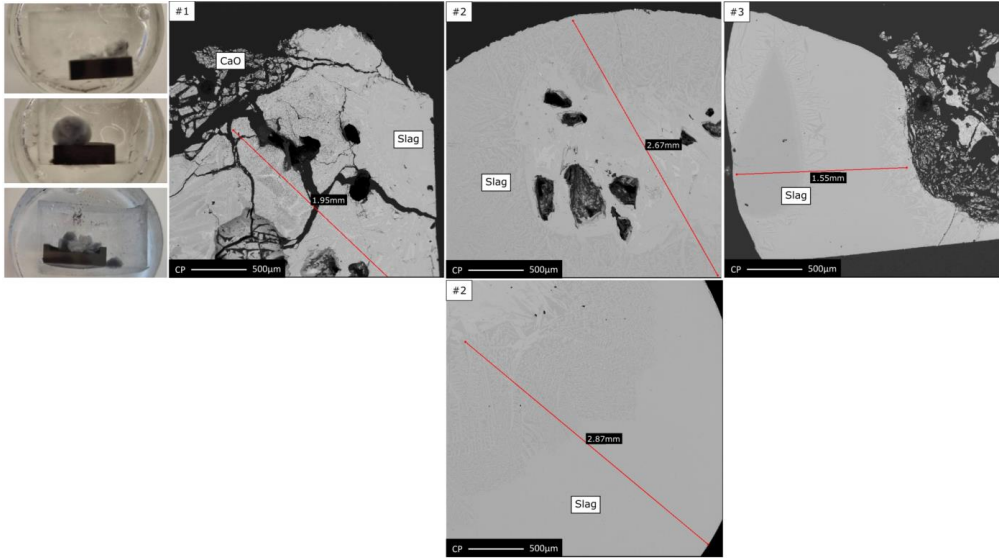


Figure 110 Cross section images and EPMA images after experiments for the three parallels of CaO and slag 2 heated to 1500 °C and with 10 minutes holding time. The CaO/slag ratio is 0.42, 0.14 and 0.25 for parallel 1, 2 and 3, respectively.

The analyzed results for the 1500 °C experiments are shown in Figure 111. From the 10-minute experiments curves, the CaO concentration showed several small peaks. From the EPMA images it can also be observed that the brighter slag does not appear glassy, but have crystallized. This is believed to have happened during solidification. Smaller CaO peaks can also be observed in the 20 minutes sample, and towards the end of the sample the concentration is close to equilibrium concentration, which is concentration with 100% dissolved CaO.

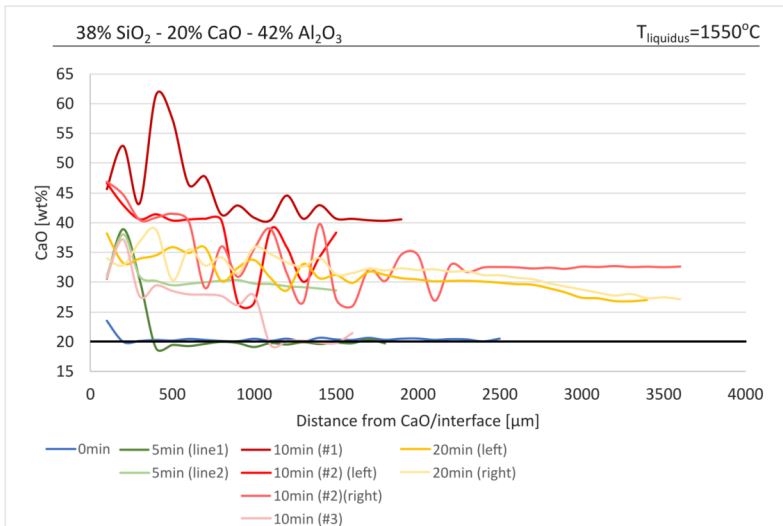


Figure 111 WDS results for the experiments at 1500 °C with CaO and slag 2.

Experiments with CaO/slag ratio of 0.25 were conducted at 1500 °C with 0-, 5- and 10 minutes holding times. The images captured during the experiments are shown in Figure 112, and EPMA images after the experiments in Figure 113. After all experiments, there are still remaining CaO.

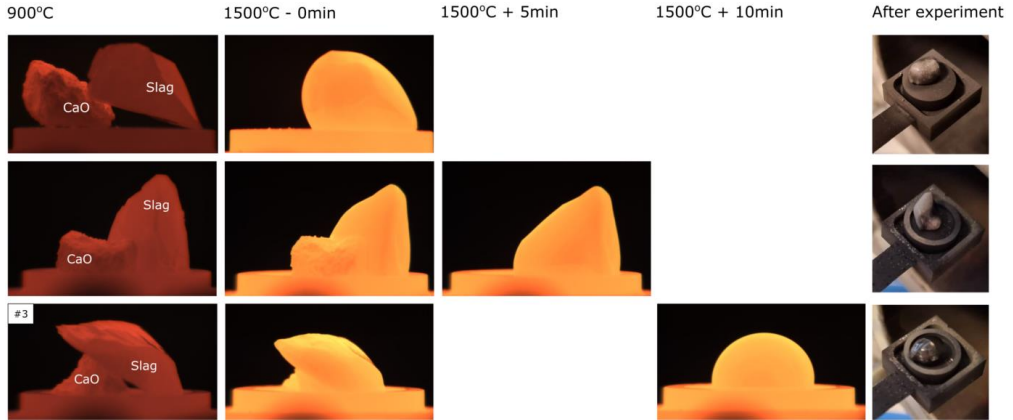


Figure 112 Images during and after experiments of CaO and slag 2 with CaO/slag ratio of 0.25 for the 1500 °C experiments with 0-, 5- and 10 minutes holding time.

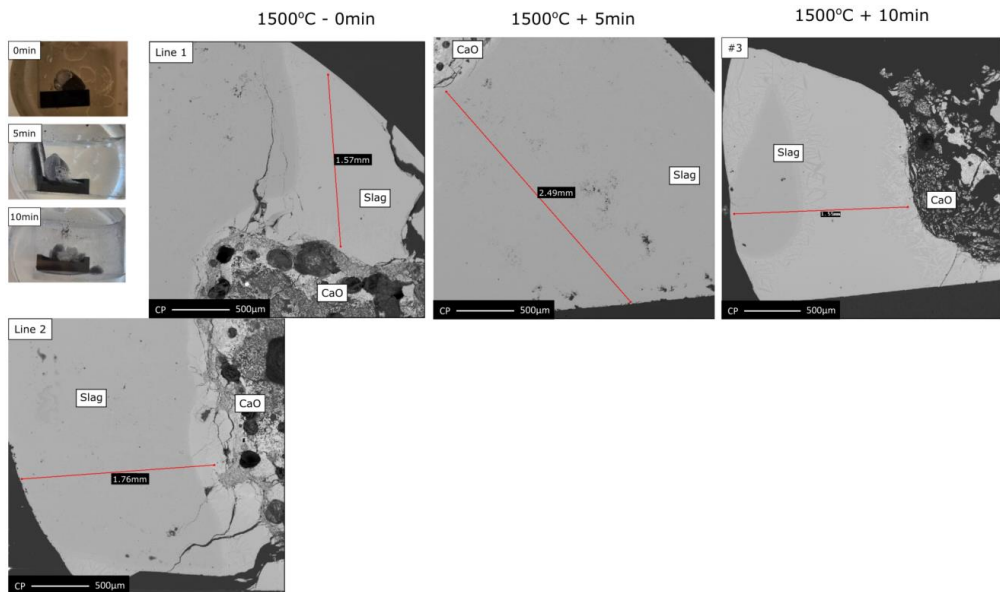


Figure 113 Cross section images and EPMA images after experiments of CaO and slag 2 for the experiments with CaO/slag ratio of 0.25 for the 1500 °C experiments with 0-, 5- and 10 minutes holding time.

Furthermore, three experiments were conducted at 1550 °C with holding times 0-, 10- and 20 minutes. Figure 114 and Figure 115 shows the images captured during the experiments and the EPMA images after the experiments, respectively. In the EPMA image at 0 minutes, some remaining CaO can be observed in the bottom right corner. In the 10-minute experiment, a black area is seen at the bottom, but this is epoxy. The analysis curves in Figure 116 show that the CaO is dissolved at both 10- and 20 minutes.

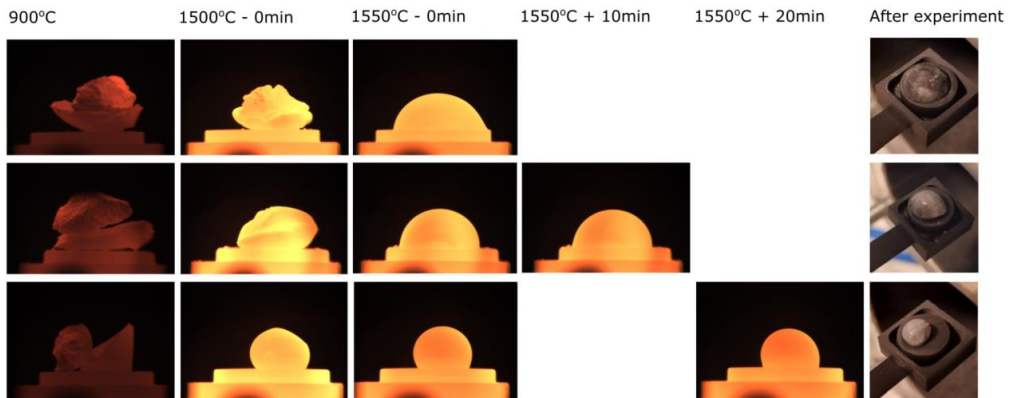


Figure 114 Images during and after experiments with for the 1550 °C experiments of CaO and slag 2 with 0-, 10- and 20 minutes holding time. The initial slag had composition 38% SiO<sub>2</sub>- 20% CaO-42% Al<sub>2</sub>O<sub>3</sub>.

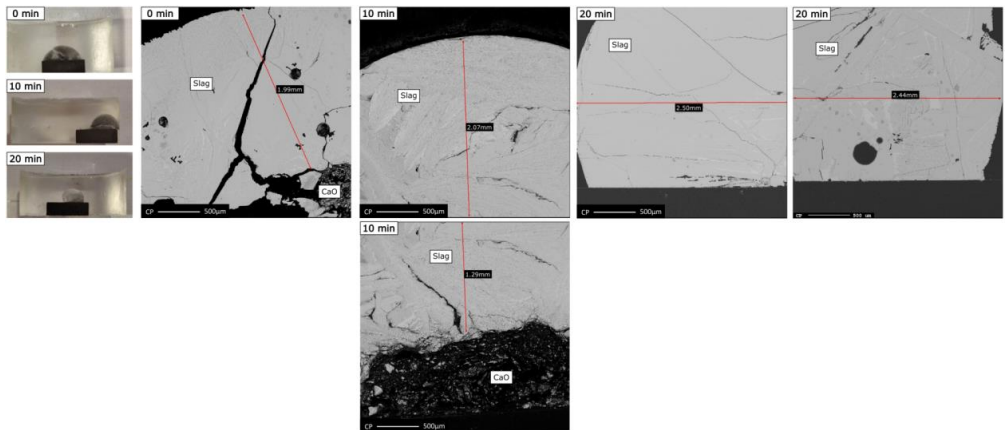


Figure 115 Cross section images and EPMA images after experiments for the experiments at 1550 °C experiments of CaO and slag 2 with 0-, 10- and 20 minutes holding time.

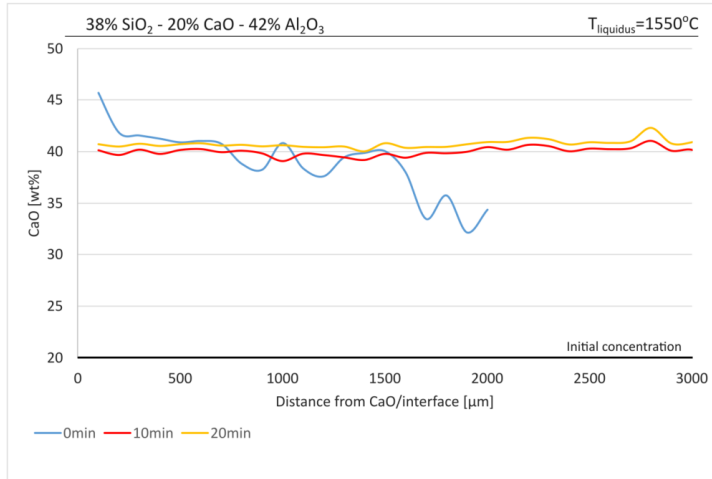


Figure 116 WDS results of CaO and slag 2 heated 1550 °C with 0-, 10- and 20 minutes holding time.

#### 4.3.3.3 Slag 3: 56% SiO<sub>2</sub> – 21% CaO – 23% Al<sub>2</sub>O<sub>3</sub>

An overview of all the dissolution experiments with slag 3 is shown in Table 39. The liquidus temperature for slag 2 is 1420 °C, which is the lowest in this study.

Table 39 Dissolution experiments with CaO and 56% SiO<sub>2</sub>-21% CaO-23% Al<sub>2</sub>O<sub>3</sub>.

Temp [°C]	Holding time [min]	CaO/slag ratio	CaO conc. if 100% dissolved [wt%]
1500	0	0.41	44
	5	0.41	44
	10	#1 0.50	47
	10	#2 0.41	44
	20	0.28	38
1550	0	0.36	42
	10	0.2	34
	17	0.15	31

Two parallel experiments were conducted at 1500 °C with a holding time of 10 minutes, with CaO/slag ratios of 0.50 and 0.41. The images captured during the experiments are presented in Figure 117, while the EPMA images after the experiments are shown in Figure 118. In both parallels, undissolved CaO can be observed. Figure 119 displays the analyzed results. In the second 10-minute parallel, there are two analyzed lines, labeled “line 1” and “line 2”. Both lines appear homogenous on the EPMA images. In the first line is a concentration gradient ranging from 41-36%, whereas in line 2, the concentration ranges from 37-35%. This indicates that there are differences within the same sample. After 20



minutes, the concentrations are close to the concentration of 100% dissolution, which in this case is 38%.

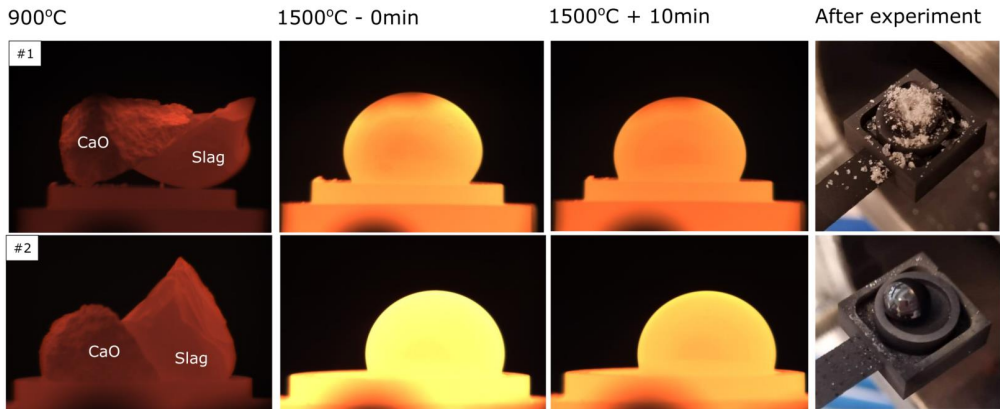


Figure 117 Images during and after experiments for the three parallels of CaO and slag 3 heated to 1500 °C and with 10 minutes holding time. The CaO/slag ratio is 0.50 and 0.41 for parallel 1, and 2, respectively.

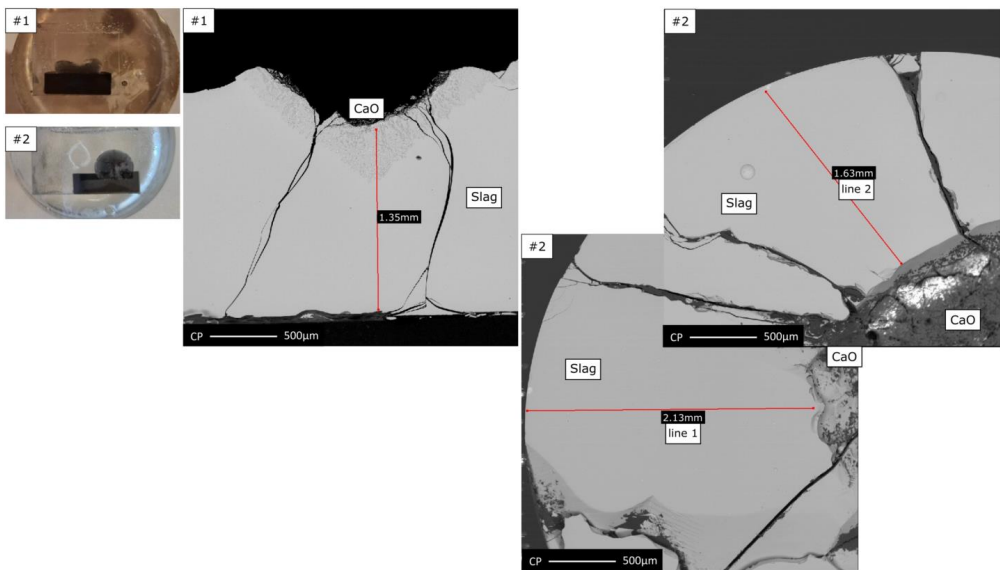


Figure 118 Cross section images and EPMA images after experiments for the three parallels of CaO and slag 3 heated to 1500 °C and with 10 minutes holding time. The CaO/slag ratio is 0.50 and 0.41 for parallel 1, and 2, respectively.

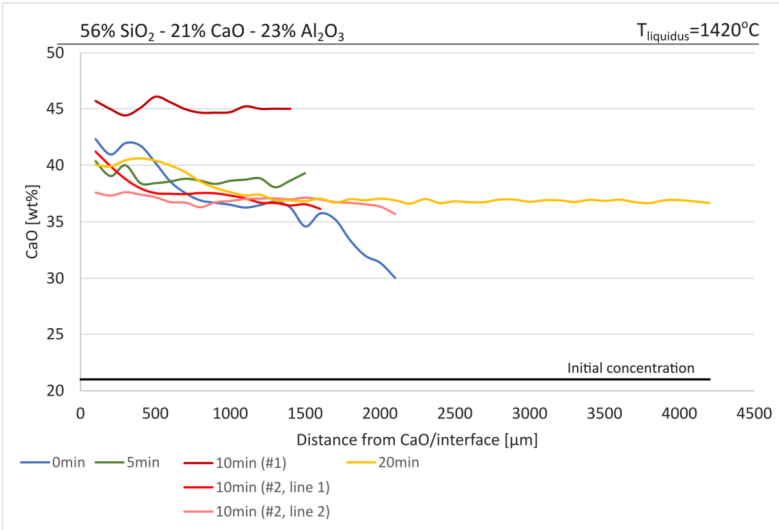


Figure 119 WDS results for the experiments at 1500 °C with CaO and slag 3.

Experiments with a CaO/slag ratio of 0.41 were conducted at 1500 °C with holding times 0-, 5- and 10 minutes. The images captured during the experiments are shown in Figure 120, and EPMA images after the experiments in Figure 121. Undissolved CaO are observed for all the experiments. Slag 3 has the lowest liquidus temperature of 1420 °C, but also the highest CaO/slag ratio. Reaction between the slag and CaO was observed during the experiments at a lower temperature for slag 3, around 1300 °C, compared to 1350 °C for slag 1 and 1400 °C for slag 2.

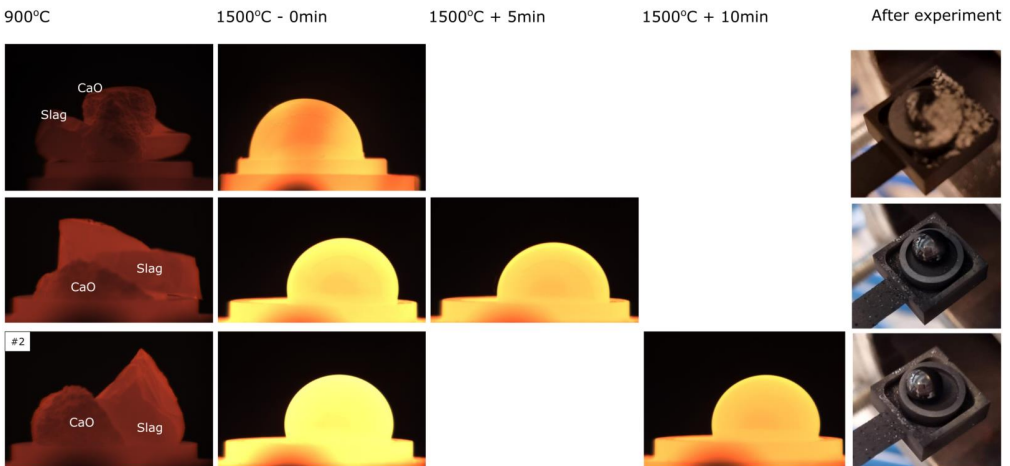


Figure 120 Images during and after experiments for CaO and slag 3 with CaO/slag ratio 0.41 for the 1500 °C experiments with 0-, 5- and 10 minutes holding time.

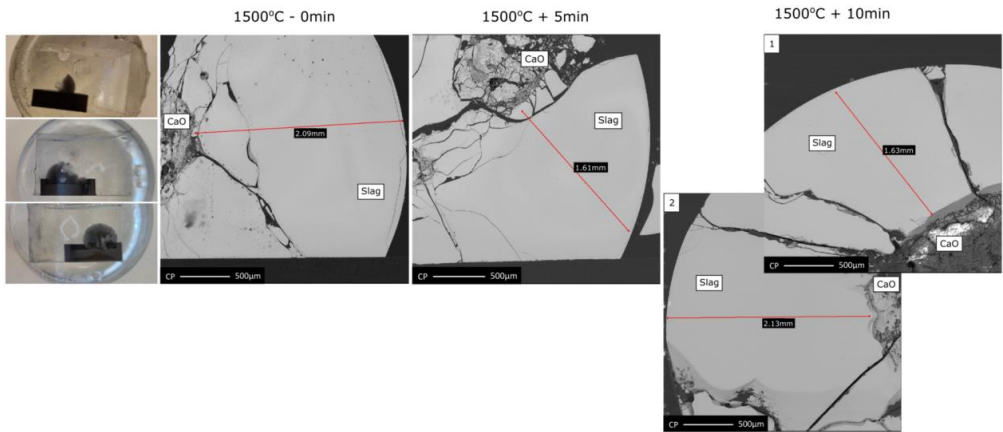


Figure 121 Cross section images and EPMA images after experiments for the experiments of CaO and slag 3 with CaO/slag ratio of 0.41 for the 1500 °C experiments with 0-, 5- and 10 minutes holding time.

Three experiments were also performed at 1550 °C with holding times 0-, 10- and 17 minutes. Figure 122 and Figure 123 show the images captured during the experiments and the EPMA images after the experiments, respectively. The analyzed results are shown in Figure 124. After 10 minutes, the CaO concentration curve is ~34% throughout the sample. The CaO particle is fully dissolved. It was intended to have 20 minutes holding time, but the sample rolled of the carbon substrate after 17 minutes. It was therefore not possible to do EPMA and WDS on this sample.

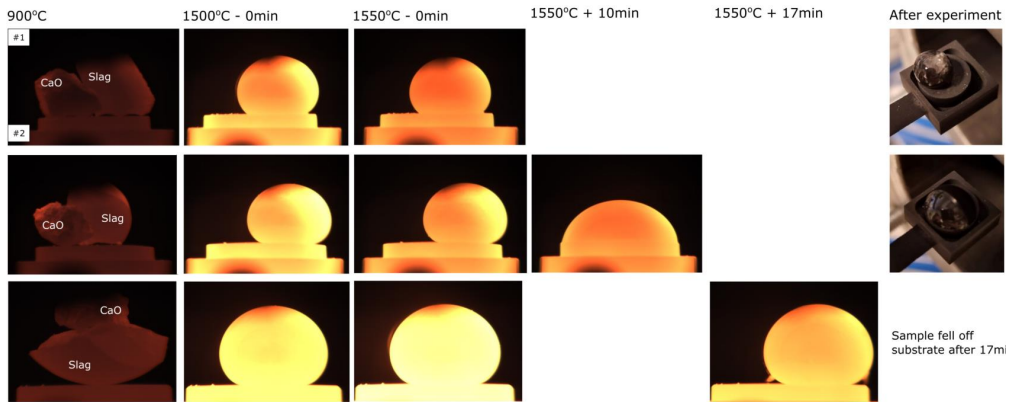


Figure 122 Images during and after experiments with for the 1550 °C experiments of CaO and slag 3 with 0-, 10- and 17 minutes holding time.

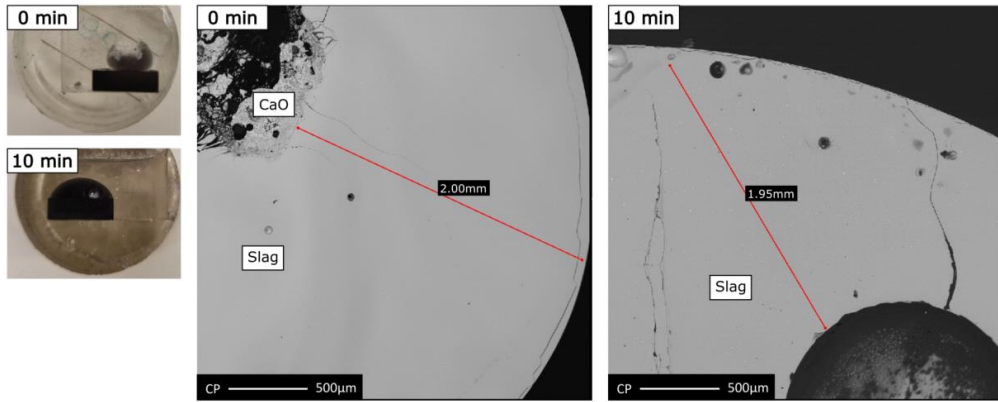


Figure 123 Cross section images and EPMA images after experiments for the experiments at 1550 °C experiments of CaO and slag 3 with 0- and 10 minutes holding time.

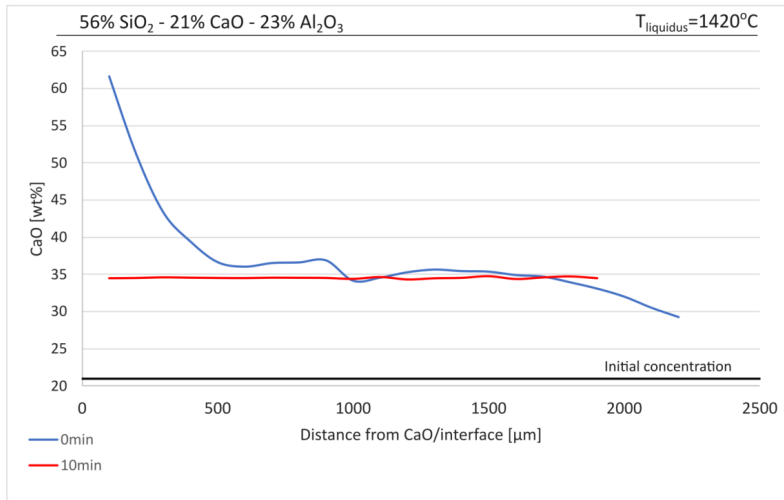


Figure 124 WDS results for the CaO and slag 3 heated to 1550 °C with 0- and 10 minutes holding time.

## Chapter 5: Discussion

The previous chapters presented the results obtained from the industrial samples, from the quartz experiments and from CaO dissolution in  $\text{SiO}_2\text{-CaO-Al}_2\text{O}_3$  slags. The industrial samples included slag samples from excavations, tapped slag and materials from the charge surface from Si and FeSi furnaces. The literature review summarized previous findings on slag from excavations in both industrial furnaces and pilot scale experiments in a 50kW furnace. The second part of this study focused on impurities in the quartz behaviour during heating, in addition to  $\text{SiO}_2$  disintegration upon heating and softening and melting experiments for different quartz types. The last part looked at the dissolution of CaO in three different compositions of  $\text{SiO}_2\text{-CaO-Al}_2\text{O}_3$  slags. The experimental results from this research will be discussed and compared with earlier research. The focus will be on how the results affect the Si and FeSi furnace operation. Slag in different zones will be described, and various factors that affects the slag and its effect on the furnace operation and the tapping conditions will be discussed. Condensates are also found in different parts of the furnace and an evaluation of these are included in this subchapter. The next section looks at how different quartz behaves when they experience a steep temperature increase similar as when they are added as a raw material to the furnace, and an evaluation of the findings from the charge surface. From the CaO dissolution experiments, it will be evaluated its effect on the slag viscosity and the mechanism in the dissolution. Further, the experimental results will be used to model the dissolution rates for the slag compositions in this study.

### 5.1 Slags in different parts of the furnace

In this research, slag from different zones in six different Si and FeSi furnaces have been analyzed. Furthermore, tapped slag samples from three different furnaces and slag from the charge top of two FeSi furnaces during operation are obtained. These results are used to describe different features of the slag in the different zones of the furnace.

From Norwegian excavations of industrial Si and FeSi furnaces, it is found that the extent of slag varies between different furnaces. In comparison to other metallurgical production processes, such as manganese and steel, the amount of slag in Si and FeSi production is modest. However, in recent years there has been an increased focus on the effect of the slag on the production process. Accumulated slag is typically found along the furnace walls, sometimes all the way up to the charge top, and in a thick layer at the furnace bottom, which the metal must pass to exit the tap-hole. Figure 125 summarizes four different cases illustrating different amount of slag. The exact geometry will depend on the operational history of the furnace.

In case **a**, there is almost no slag present along the furnace wall, allowing sufficient space for the raw materials to descend and react throughout the furnace. Case **b** represent a more average situation, where the presence of slag may affect the furnace operation. Slag in the higher parts of the furnace along the furnace walls will start to solidify as the temperature

decreases in the low temperature zone. Too much accumulated slag in the charge area will hinder the raw materials and narrows the reaction route. Case **c** illustrates an accumulated situation with very little room for the reacting materials to descend.

Accumulated slag at the bottom of the furnace will affect the tapping process, which plays an important role in the Si and FeSi production. To obtain an optimal production yield, it is essential to have good draining of the furnace. If Si is accumulated over time, it might react with C or SiO<sub>2</sub> and hence decrease the Si-yield. Slag is more viscous than the metal, and accumulated slag in the tap-hole area might hinder the metal flow to the tap-hole and/or clog to the tap-hole walls. The following use of tapping tools and equipment to maintain good drainage may also influence the quality of the melt. In Si and FeSi production, it is one tap-hole open at the time for the materials to exit. The tappers must work their way through the slag layer to the metal bath. Since slag is more viscous than the metal, it might clog the tap-hole and it is necessary to take actions such as blowing oxygen through Al or Fe lances, or stoking the tap-hole with soaked wooden poles to keep the tap-hole and runner “clean”. During tapping, some slag will also be tapped together with the metal. From the industry, it is referred to both normal, viscous and solidified lumps of slag that exit the tap-holes. The last case **d** shows a furnace with no slag in the bottom layer.

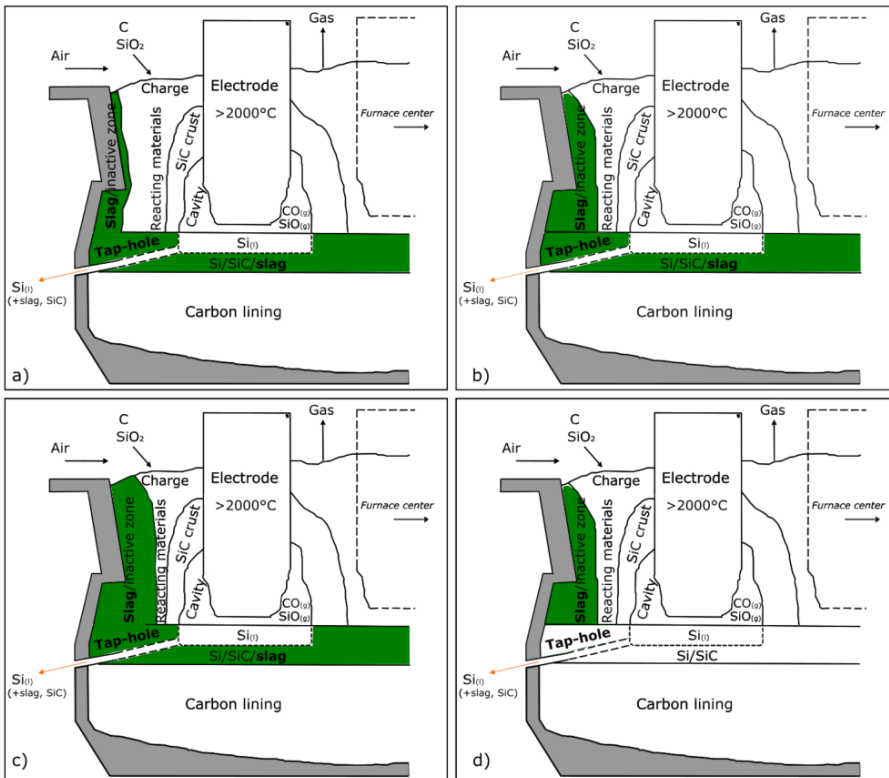


Figure 125 Schematic figures illustrating the interior of a Si furnace. Case a) have almost no slag along the furnace walls. Case b) shows an average situation with slag/inactive zone that may affect the furnace operation. Case c) shows an accumulated furnace. Case d) has SiC, but no slag in the furnace bottom. The SiC crust is found to vary between different furnaces, ranging from almost zero to the size illustrated in this figure.

As mentioned earlier, Si and FeSi furnaces are divided in a low temperature and a high temperature zone. This is a simplification. Inside the furnace there are several temperature gradients. Figure 126 shows an illustration of a Si furnace, including the main zones and approximate temperatures at different positions. The figure is based on modelled temperatures from Myrhaug [26]. The highest temperatures can be found right below the electrodes, by the arc. Below the cavity is the metal bath, which inside the furnace holds a temperature around 1900-2000 °C. With increasing distance from the arc, upwards in the furnace and towards the furnace lining, the temperature decreases. Above the tap-hole and in the slag/inactive zone, the temperature ranges from around 1000 °C to 1500 °C. The slag in the furnace will therefore experience different temperatures, depending on where it is located.

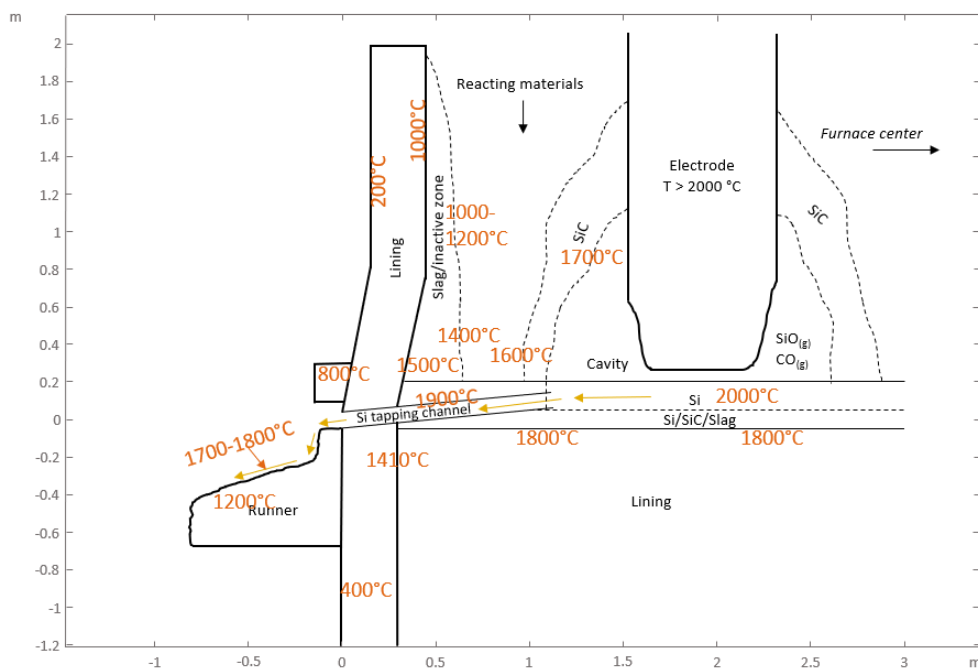


Figure 126 Illustration of a Si furnace including the main zones and approximate temperatures at different positions. The temperatures are based on modelled temperatures from Myrhaug [26].

### 5.1.1 More SiO<sub>2</sub> in the higher parts of the furnace

It is found that the samples higher up in the furnace, above the electrode tip level and close to the furnace wall in the inactive zone, generally contain more SiO<sub>2</sub> compared to the lower parts of the furnace close to the tapping channel and in the Si/SiC/slag bath. This can be seen in the SiO<sub>2</sub>-CaO-Al<sub>2</sub>O<sub>3</sub> ternary diagram in Figure 127, which includes all the accumulated slag samples. The CaO/Al<sub>2</sub>O<sub>3</sub> ratio is approximately the same within the same furnace. The samples from Furnace B contain a higher amount of Al<sub>2</sub>O<sub>3</sub>. This was expected, as Furnace B generally has a higher Al content compared to the average Norwegian Si

plant. The samples collected higher up in the inactive zone have a  $\text{SiO}_2$  content  $>50\%$ , whereas samples below the electrode tip level generally have  $\text{SiO}_2$  content below  $50\%$ . Among the different samples from Furnace B, marked with blue color in the figure, it can be observed that the composition variations are lower in the lower parts of the furnace. Two samples from the lower parts have a higher  $\text{SiO}_2$  content, S-43 and W<sub>4</sub>-20. In addition, the slag found in between the  $\text{SiO}_2$  in W<sub>4</sub>-12 has a  $\text{SiO}_2$  concentration of  $76\%$ . However, these three samples are collected from deeper in the furnace and the samples contain mainly  $\text{SiC}$ . In the EPMA images it was found larger areas with  $\text{SiC}$  with slag in the  $\text{SiC}$  pores, which suggests that the samples are from the  $\text{SiC}$  crust area.

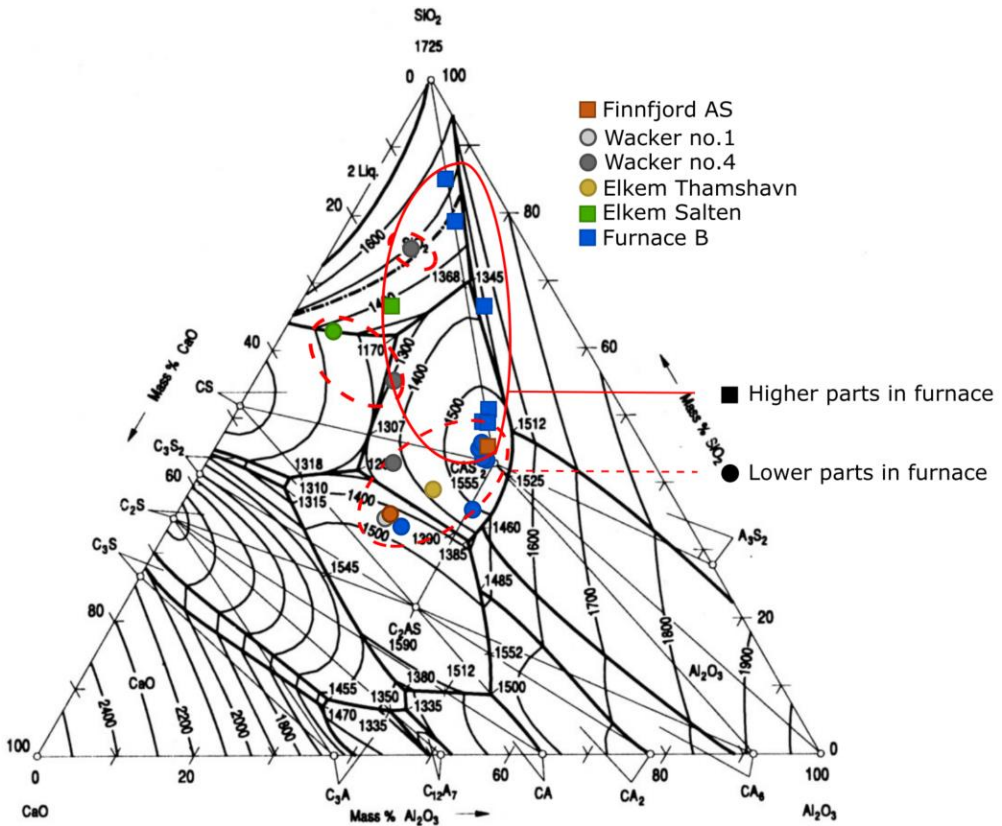


Figure 127 Analyzed accumulated slag samples from six different Norwegian Si and FeSi furnace excavations divided into higher and lower parts of the furnace.

The existence of slag higher up in the inactive zone could be explained by slag being pushed towards the furnace walls and upwards from the lower parts. An increased amount of  $\text{SiO}_2$  in the slag in the higher parts would then be due to dissolution of descending quartz in the ascending  $\text{SiO}_2$ - $\text{CaO}$ - $\text{Al}_2\text{O}_3$  slag. A 24 MW Si furnace adds materials in the order of  $1 \text{ l/s}$ , which gives a  $\text{SiO}$  and  $\text{CO}$  gas volume in the crater in the order of  $10 \text{ m}^3/\text{s}$  [125]. A significant production of process gas in the lower parts of the furnace and a dense charge



area, result in a higher pressure in the crater compared to the external pressure. The pressure in the crater was measured at Icelandic Alloy plant in Iceland [126] and at Elkem Thamshavn furnace 2 in an internal Elkem report mentioned in [125]. They both found the crater pressure to be between 2-19 kPa. This high pressure may hence be an important source for pressing the slag from the bottom to the lining, and up to the charge top. Kadkhodabeigi [127] modelled the effect of the crater pressure on the melt flow pattern in the furnace bottom and found that a high crater pressure pushes the melt towards the furnace walls. This model does not include slag in the melt, which has a higher viscosity than the metal. However, the findings of slag higher up in the furnace in the inactive zone indicate a sufficient high crater pressure to move the slag in the same way as the metal to the furnace wall and upwards.

Slag and a higher content of  $\text{SiO}_2$  in the slag in the higher parts of the inactive zone could also suggest that slag is formed in the higher parts of the furnace. Since quartz is added as a raw material at the top of the furnace, it is likely to have a higher content of  $\text{SiO}_2$  in the slag phase at the start of the reaction path. As the temperature increases further,  $\text{SiO}_2$  will be reduced from the slag. The reduction reaction of  $\text{SiO}_2$  from  $\text{SiO}_2$ -CaO- $\text{Al}_2\text{O}_3$  slag is strongly dependent on temperature [128], [129]. Increasing temperature increases the  $\text{SiO}_2$  reduction rate, and lower amounts of  $\text{SiO}_2$  in the slag phase further down in the furnace is therefore expected. However, this requires sufficient high temperatures in the higher parts to form slag. The liquidus temperatures for the slag found in the higher parts in the furnace ranges from 1390-1550 °C, with an average of ~1500 °C. The charge surface temperature is assumed to be around 1300 °C [3], [4], but next to the wall it is expected lower temperatures, around 1000-1200 °C, as seen in Figure 126. Figure 128 shows an example of how a slag would be in the furnace based on temperatures found from [26]. The temperature increases downwards in the furnace, but the high liquidus temperature of the slag suggests a higher temperature in the charge than expected. Heating of materials, including the core of the lumps, takes time. The gas temperature is 1000-1400 °C, but it might be that the materials are only heated at the surface when they enter the lower, high temperature part of the furnace.

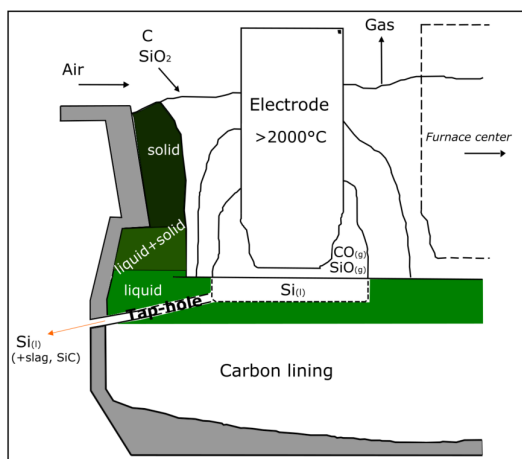


Figure 128 How the given slag composition will be in the furnace; liquid, liquid+solid, or solid, based on temperatures found from [26].

A similar trend was observed for the slag next to the tapping channel, with an increased  $\text{SiO}_2$  content in the slag above the tapping channel compared to below, as can be seen in Figure 129. These samples are from the Furnace B excavation and are from two different tap-holes. The slag above the Si has a higher  $\text{SiO}_2$  content than below. The  $\text{CaO}/\text{Al}_2\text{O}_3$  ratio is approximately the same. The slags from above the tapping channel are marked with the dark blue color and have a  $\text{SiO}_2$  content  $>50\%$ . The higher content of  $\text{SiO}_2$  could be explained by the density. Increasing amount of  $\text{SiO}_2$  decreases the density in the slag [25]. A higher  $\text{SiO}_2$  content above the tapping channel is therefore expected due to the lower density. At  $1550\text{ }^\circ\text{C}$ , the difference from 30-65%  $\text{SiO}_2$  is  $2.66\text{-}2.30\text{ g/cm}^3$ . Pure silicon has a density of  $\sim 2.4\text{-}2.5\text{ g/cm}^3$  at  $1500\text{-}1900\text{ }^\circ\text{C}$  [40], which is in the same density area as this slag.

Another factor could be the viscosity. Increasing amount of  $\text{SiO}_2$  in the slag also increases the viscosity, which means that the slag above the tapping channel is more viscous than below. Additionally, a lower temperature in this zone would suggest a viscous slag in the inactive zone of the furnace. The liquidus temperature for some of the slags in the inactive zone are higher than the expected temperature in that area, around  $1000\text{-}1500\text{ }^\circ\text{C}$  [26], and the slag system may therefore only be partly liquid. Higher viscosity is more resistance to flow, and it is likely to have the high viscosity slag at the top.

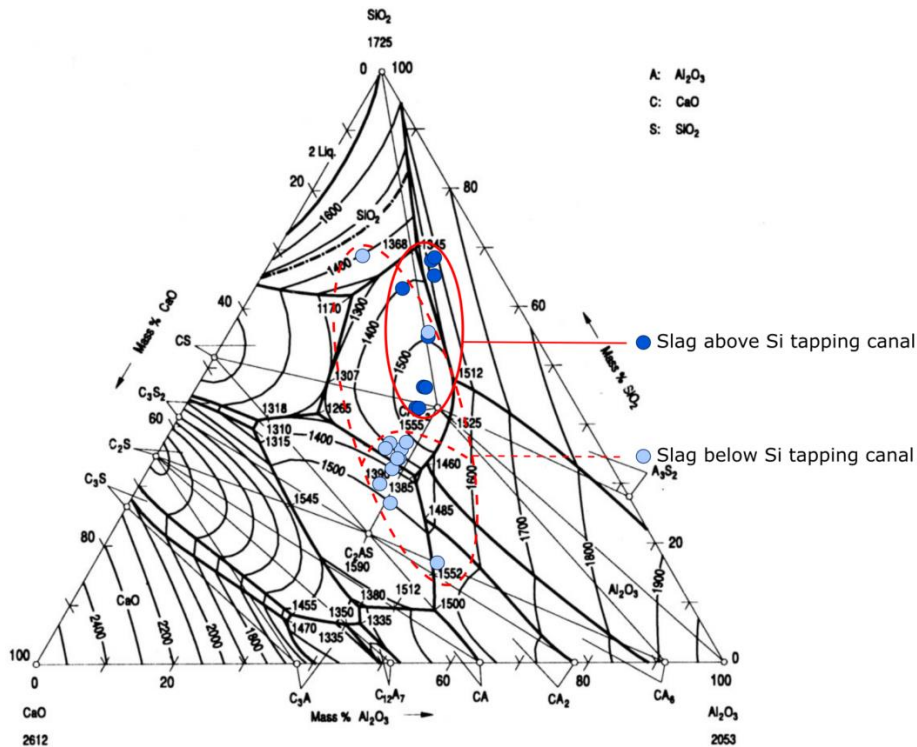


Figure 129 Analyzed slag samples next to the Si tapping channel divided into above or below the channel. All samples are from the Furnace B excavation and are from two different tap-holes.

### 5.1.2 Alkalis in the slag

In addition to SiO<sub>2</sub>, FeO and Al<sub>2</sub>O<sub>3</sub>, most of the slag from the charge surface have alkali and alkaline earth oxide content >5%. This was also found in some of the samples from the inactive zones. Potassium (K), magnesium (Mg) sodium (Na) are expected as impurities in the quartz with 75-1700 ppmw, 20-140 ppmw and 50-170 ppmw, respectively [48]. Their stability decreases with increasing temperature due to the low melting and boiling point of their metal. The boiling temperatures of K, Mg and Na are 760 °C, 1090 °C and 880 °C, respectively. These are therefore expected to leave the furnace in the off-gas system when reduced. However, oxides of K, Mg and Na are also found in some of the excavation samples, in addition to SiO<sub>2</sub>, CaO and Al<sub>2</sub>O<sub>3</sub>. Additionally, traces of Na<sub>2</sub>O, MgO or BaO were found in several of the tapped slag samples. Hoover et al. [130] similarly found both slag and condensates containing K<sub>2</sub>O and Na<sub>2</sub>O during the excavation of a 160 kW pilot scale Si furnace that had operated continuously for approximately 80 hours. This suggests that Si and FeSi furnaces have alkali circulations, which is also discussed in Mn-ferroalloy furnaces and blast furnaces.

K<sub>2</sub>O, MgO and Na<sub>2</sub>O may be reduced with carbon and form their respective gas phases according to reaction 15, 16 and 17.



The alkali vapors are then carried upwards along with the other process gases. In the higher parts of the furnace, these vapors can either leave as gases in the off-gas system or condense onto the charge materials before descending again in the furnace. During excavations, the materials in the furnace are cooled down with water. The water dissolves the alkalis and hence only traces of potassium, magnesium and sodium in the furnace would be found in the slag during excavations. Most of the slag samples do not contain these oxides, and it is therefore still an open question whether alkali circulation is an important feature.

### 5.1.3 Silicon carbide particles in the slag

In all slag samples in this study, including the accumulated slag from excavations and the tapped slag, SiC was found together with the slag. SiC is in solid form until 2730 °C, which means that it will be solid in Si and FeSi furnaces. No analyses were performed on the SiC in this study, and this subchapter is based on visual observations. It is not found a clear trend with more or less SiC in the higher or lower parts of the furnace, as seen in the two EPMA images in Figure 130. The left image is a sample from the lower part in the furnace,

while the right image is from the inactive zone. The distribution of SiC is similar in those two images.

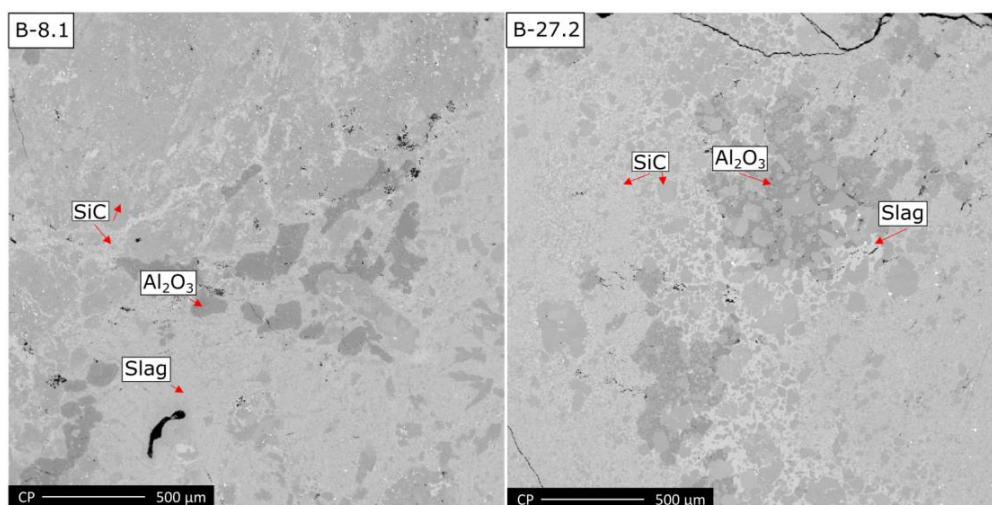


Figure 130 EPMA images of B-8.1 and B-27.2 which are collected from a lower and a higher point in the furnace in the Furnace B excavation.

SiC is found both as smaller particles ranging from ~10-200μm, and in larger areas. In the last case it is often more SiC than slag in the samples and look similar to the SiC crusts. Accumulation of SiC have earlier also been reported from several Norwegian excavations [6]–[8]. At the Elkem Thamshavn excavation in 2013 [6], the SiC deposits were present from about 0.5m below the charge top and all the way down to the electrode tip position, which were about 2.5m in height. In the SiC crust, there are gas channels for ascending gases in the furnace.

It is observed significantly more SiC in the accumulated slag compared with the tapped slag, including the high-viscosity slag. This can be seen in Figure 131, which is two typical EPMA images of an accumulated sample to the left and a tapped sample to the right. The carbon content in the charge mix and properties of the selected carbon will have an influence on the Si yield [131]. If too much carbon is added to the furnace, a large amount will react with SiO gas to form SiC. Accumulated SiC might increase the electrical conductivity of the materials in the high-temperature zone. Additionally, with an increased amount of solid SiC in the slag, the viscosity will also increase considerably and not be easily drained during tapping. Hence the slag would more easily accumulate in the furnace.

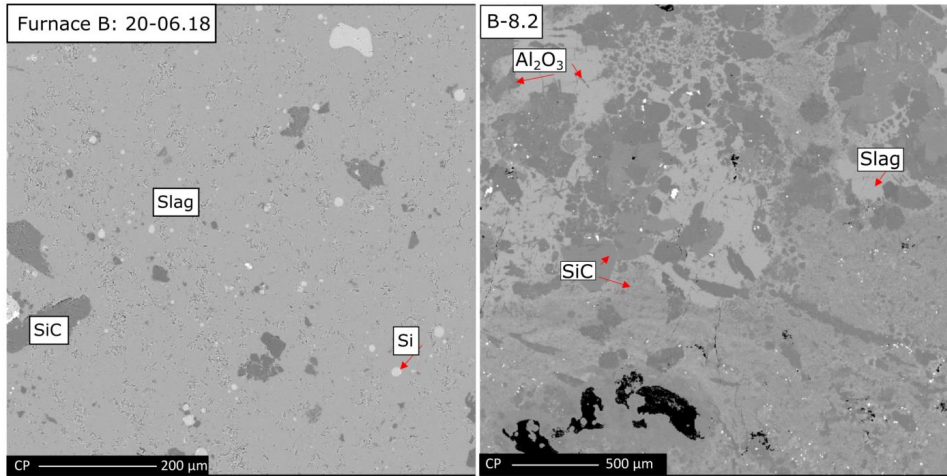


Figure 131 EPMA image of a tapped slag sample to the left and an accumulated slag sample to the right collected during excavation. Both samples are from furnace B.

SiO<sub>2</sub>-CaO-Al<sub>2</sub>O<sub>3</sub> slag and SiC wet each other well and by looking at the activity of the SiO<sub>2</sub> in the slag, it is possible to look at the stability of SiO<sub>2</sub> in the slag and how easy it will be reduced with SiC to produce CO gas and either SiO gas or Si through reaction 6 and 18, respectively. Reaction 6 will preferably happen in the high temperature zone of the furnace to form SiO gas for the metal forming reaction with CO gas. The reaction between SiO<sub>2</sub> and SiC to form Si and CO gas is not one of the main reactions in the Si or FeSi furnaces, but the reversed reaction of Si spheres reacting with surrounding CO gas has been proposed as an option related to the SiO<sub>2</sub>-SiC condensate in the furnace [68].



The stability of SiO<sub>2</sub> over the temperature range 1600-2000 °C for two slag compositions,

50% SiO<sub>2</sub> – 25% CaO – 25% Al<sub>2</sub>O<sub>3</sub>

70% SiO<sub>2</sub> – 10% CaO – 20% Al<sub>2</sub>O<sub>3</sub>

is graphed in Figure 132. With 50% SiO<sub>2</sub>, the activity will increase with 0.02 from 1600 °C to 2000 °C, and 0.1 for the slag with 70% SiO<sub>2</sub>. The reaction quotient, Q, compared to the equilibrium constant K, can be used to determine the progression of the given reactions. Q can be calculated from the activities and partial pressures. The activity of SiC and Si are equal to 1 since they are in their reference state. The total gas pressure in the furnace is equal to the atmospheric pressure, and a normal first approximation is to assume that CO and SiO are the only gas species in the system. This gives p<sub>SiO</sub>+p<sub>CO</sub> = 1 bar. In this case, the partial pressures of SiO and CO in reaction 6 are assumed to be 0.67 bar and 0.33 bar, respectively. The partial pressure of CO is set to 1 bar for reaction 18. This is because the

reaction happens in the slag sample where there is no available SiO gas. Q for reaction 6 and 18 for this given case for the two slag compositions are then as listed in Table 40. The equilibrium constants, K for the reactions in the temperature interval 1700-1860 °C are shown in Figure 133. From this it can be seen that  $Q < K$  for reaction 6 at around 1820 °C for 70% SiO<sub>2</sub> and 1860 °C for 50% SiO<sub>2</sub>, which means that SiO<sub>2</sub> in the slag will react with SiC to form SiO and CO gas from these temperatures. For Reaction 18, neither slags will react with SiC to form Si and CO gas before 1900 °C.

Figure 134 shows the change in Gibbs free energy for the two reactions in the temperature interval 1600-2000 °C, and from this it can be seen that reaction 6 is in equilibrium at around 1860 °C and reaction 18 around 1900 °C, when all species are in their standard state.

Table 40 The equilibrium constant K and the change in Gibbs free energy  $\Delta G^0$  for two SiO<sub>2</sub>-CaO-Al<sub>2</sub>O<sub>3</sub> slag compositions at 1800 °C. The given activities are found with FactSage 8.1, and the equilibrium constant K found with HSC Chemistry.

Slag composition	$2SiO_2 + SiC = 3SiO_{(g)} + 2CO_g$		$SiO_2 + 2SiC = 3Si + 2CO_{(g)}$
	$a_{SiO_2}$	$Q_{SiO}$	$Q_{Si}$
50% SiO <sub>2</sub> – 25% CaO – 25% Al <sub>2</sub> O <sub>3</sub>	0,34	0.86	1.08
70% SiO <sub>2</sub> – 10% CaO – 20% Al <sub>2</sub> O <sub>3</sub>	0,77	0.17	1.29

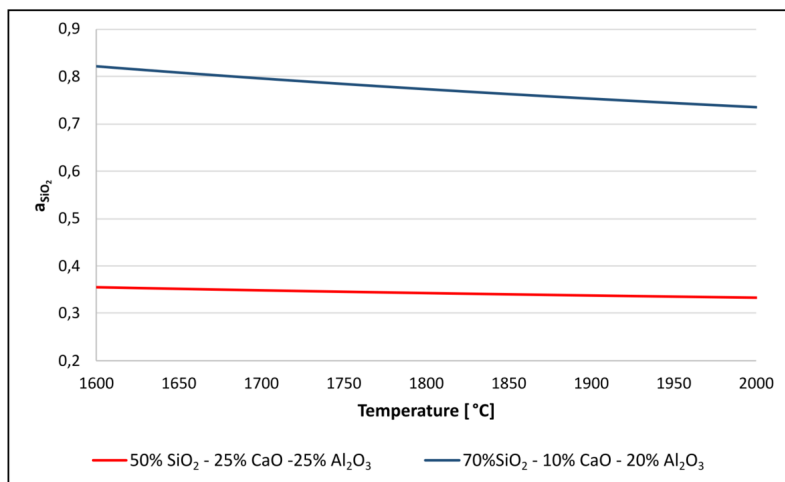


Figure 132 The activity of SiO<sub>2</sub> in 50% SiO<sub>2</sub> – 25% CaO – 25% Al<sub>2</sub>O<sub>3</sub> and 70% SiO<sub>2</sub> – 10% CaO – 20% Al<sub>2</sub>O<sub>3</sub> in the temperature interval 1600-2000 °C. The activities are calculated with FactSage 8.1.

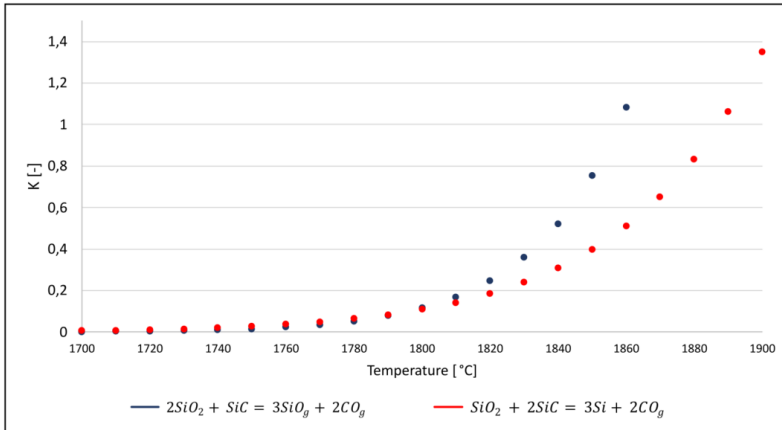


Figure 133 The equilibrium constants for reaction 6 and 18 over the temperature interval 1700-1860 °C.

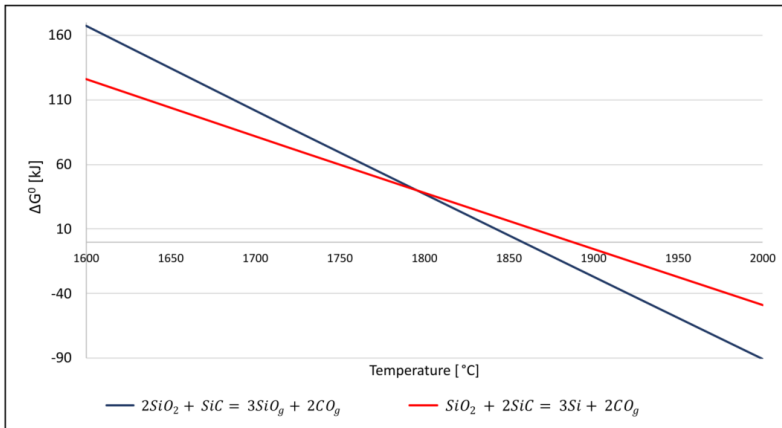


Figure 134 The change in standard Gibbs free energy for reaction 6 and 18 over the temperature interval 1600-2000 °C.

#### 5.1.4 Condensation of SiO gas and CO gas in the furnace

In Si and FeSi furnaces, there are mainly two types of condensates: brown and white. These are generated from the gas mixture of mainly CO and SiO according to reaction 3 and 4, respectively. SiO and CO gas are created in the high temperature zone and ascend to the low temperature zone. Condensates will stick firmly to any raw material and create a crust. The crust in the charge area is referred to as the stoking crust. Too much condensate in the charge might reduce the charge permeability. The condensate can clog the charge and result in peaks of high pressure in the furnace, which again could cause gassing through the tap-hole [132]. Figure 135 shows where the condensates are likely to be found in the furnace, and are based on previous results from several Norwegian Si and FeSi furnace excavations [6]–[10], [21].

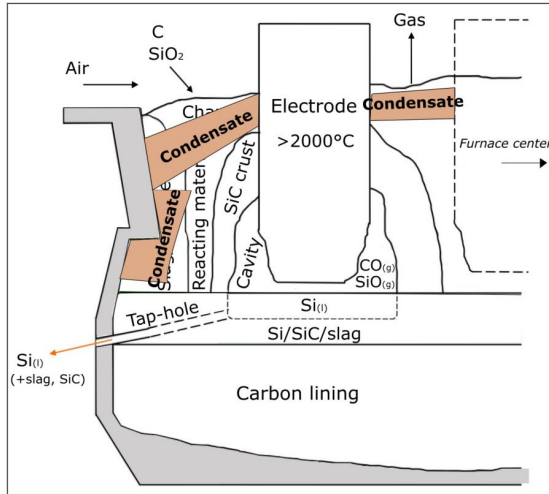


Figure 135 Illustration of where the condensates are likely to be found in the Si and FeSi furnaces.

White-green condensate of  $\text{SiO}_2$  and  $\text{SiC}$  together with a  $\text{SiO}_2$  rich slag was found in sample B-14.1, which is from the higher, inactive part of the furnace. Condensates were also found in the charge top samples from Finnfold AS. Most of the condensates here were brown and covering  $\text{SiO}_2$ , but some of the samples also included some white condensate. Brown and white stripes of condensate were observed, which were observed as different areas with  $\text{SiO}_2+\text{Si}$  and  $\text{SiO}_2+\text{SiC}$  in the EPMA images, as highlighted in Figure 136. Areas with Si spheres embedded in the  $\text{SiO}_2$  matrix are from the brown-colored area, while the white area is  $\text{SiO}_2$  and  $\text{SiC}$  from condensation reaction 4. Materials from the charge area have earlier been analyzed during excavations [6]–[8], [11], and it is found glassy condensates with white, brown, and in some cases green color that are covering and holding together partly melted raw materials. Broggi [47] characterized the product of reaction 3 and found that the brown condensate consists of a mixture of Si spheres embedded in a  $\text{SiO}_2$  matrix, which is the same as found in this study. He also found that this condensate generates in the temperature interval from 1400 °C to 1780 °C. The expected charge surface temperature is around 1300 °C [3], [4]. The white condensate consists of a  $\text{SiO}_2$  matrix with  $\text{SiC}$ .



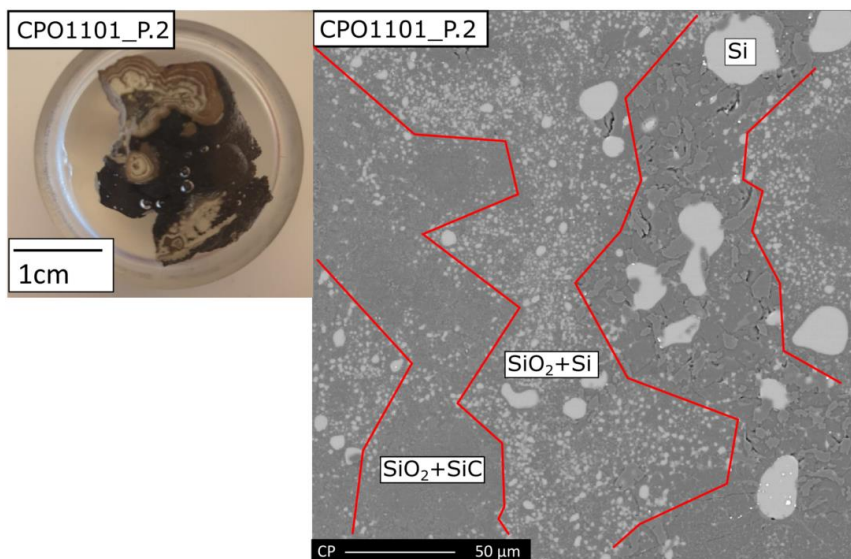


Figure 136 Sample CPO1101\_P.2 which is from the charge top at Finnfjord AS. The picture from the left is the mounted sample showing the brown and white condensates, which is shown as areas with SiO<sub>2</sub> and SiC, and SiO<sub>2</sub> and Si in the right EPMA image.

Condensates were also found in some of the samples in the tapping channel, and in some of the high-viscosity tap slag from Finnfjord, shown in Figure 137 and Figure 138, respectively. Here, both brown and white condensates were found. From equilibrium calculations and temperature measurements, Broggi [47] found that the brown Si-SiO<sub>2</sub> condensate develops from 1400-1780 °C with SiO partial pressures of 0.58-0.99. White SiO<sub>2</sub>-SiC condensates is produced in the temperature range 920-1800 °C and p<sub>SiO</sub> ranging from 0.53-0.99. This means that condensates are not expected to be found in the tapping area where the temperature is ~1900 °C during production [26]. In the case of excavation samples, the condensate might have formed during cooling after shut-down.

However, this is not possible for the tapped slag samples, which were collected during production. A possible reason is that the slag has descended from the slag above the tapping area, in the layer along the furnace wall. In this zone the temperature is around 1300-1500 °C [26].

Another option is that the condensates were formed when the tap-hole was closed. During this time, the temperature might be lower and condensate could form close to the tap-hole. When the tap-hole is opened for tapping, it will be tapped out together with the slag and SiC.

A third option is that the temperature during tapping were lower than expected, which may occur. The temperature in the tapping area during normal operation is expected to be >1800 °C when the tap-hole is open [27], [46]. Tapping operators have reported “cold” conditions and then actions to increase the temperature must be done. These samples were collected during challenging conditions, and the slag were reported as high-viscosity slag. A lower tapping temperature could be a likely explanation of the condensate formation.

The first option is that the slags were exposed to SiO gas at the end of the runner, where the temperature is sufficiently low for SiO to condense.

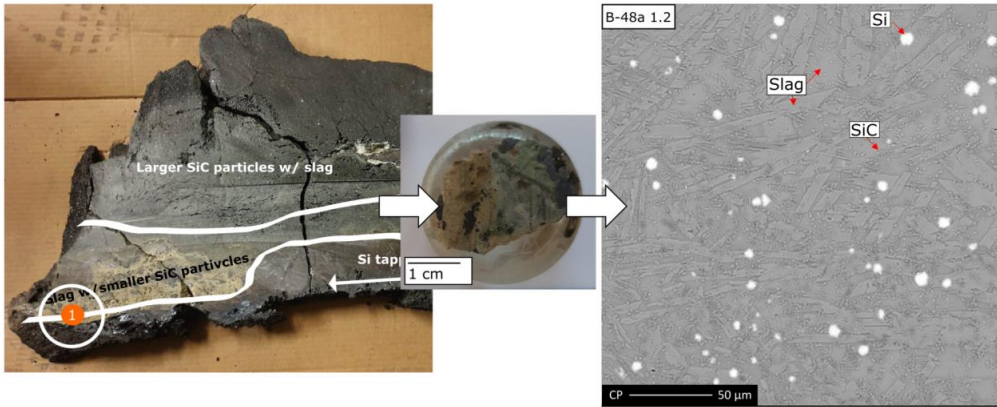


Figure 137 Green and white condensate from the zones next to the Si tapping channel from the Furnace B excavation.

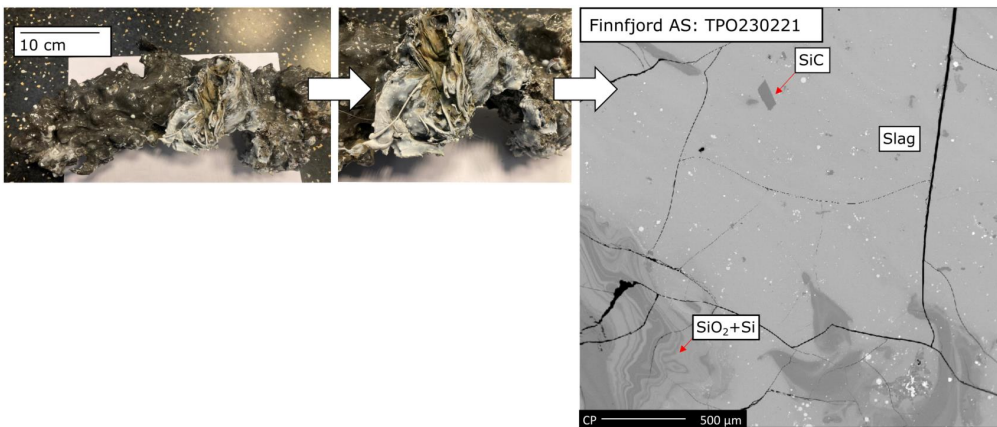


Figure 138 Brown and white condensate from high-viscosity slag from Finnford AS.

### 5.1.5 No differences in slag composition between different tap-holes

Five samples from three different tap-holes were obtained from the Furnace B excavation which included parts of the tapping channel together with the adjacent zones. It is found that the tapping channel goes through a thick layer of slag, which is the same as Ksiazek found [11]. This is shown for three different tap-holes in Figure 139. Visually, the zones around all the tap-holes appear similar. Next to the Si is a 5-15 cm bright green layer which consists of mainly  $\text{SiO}_2\text{-CaO-Al}_2\text{O}_3$  slag and smaller SiC particles. Next is a dark grey layer

which is mainly  $\text{SiO}_2\text{-CaO-Al}_2\text{O}_3$  slag and larger SiC particles. In both layers there are also some samples with Si and/or  $\text{Al}_2\text{O}_3$ .

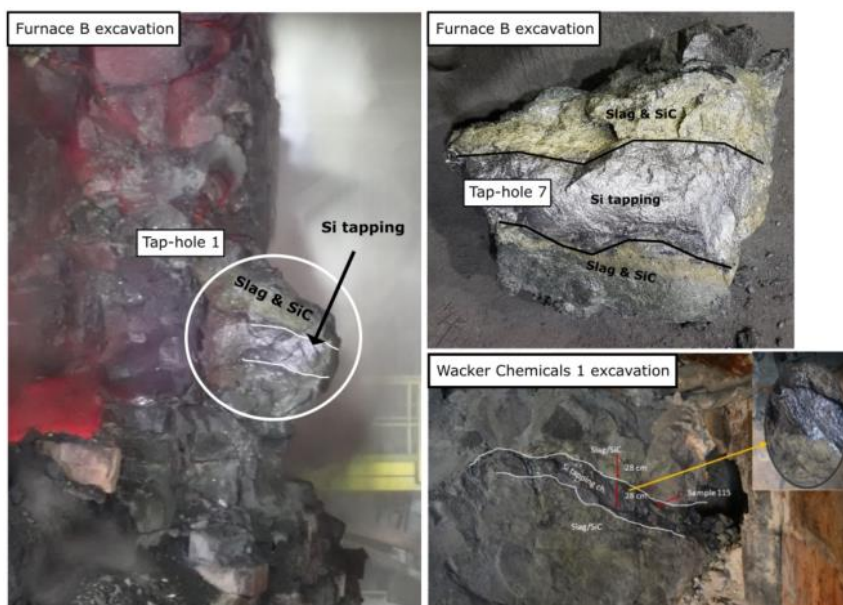


Figure 139 Images from Furnace B excavation and Wacker Chemicals [11] showing that the Si metal goes through a slag and SiC layer when exiting the tap-hole.

Figure 140 shows the oxide analysis for the tap-hole samples, grouped by whether they are from the grey or green colored area. No significant difference was found between the slag in the green and grey layers. Previous suggestions indicate that slag with green color contains more  $\text{Al}_2\text{O}_3$  [5], but this was not the case in this study. In this study, it appears as the color is more dependent on the amount and size of the SiC particles. Figure 141 shows the analyzed slag from all three tap-holes plotted in the  $\text{SiO}_2\text{-CaO-Al}_2\text{O}_3$  ternary diagram. Different shapes and shades of blue separate the different tap-holes and the slags within the same tap-hole are circled in the diagram. ~90% of the samples are within 30-70%  $\text{SiO}_2$ .

The furnace was burned down before shut-down, which may result in larger amounts of slag and other accumulated matter around this area. Tap-hole 7 (B-47) was the last tapped tap-hole, but it was not observed any visual differences, and it is not found any differences between the slag composition in tap-hole 7 compared to tap-hole 1 and 3.

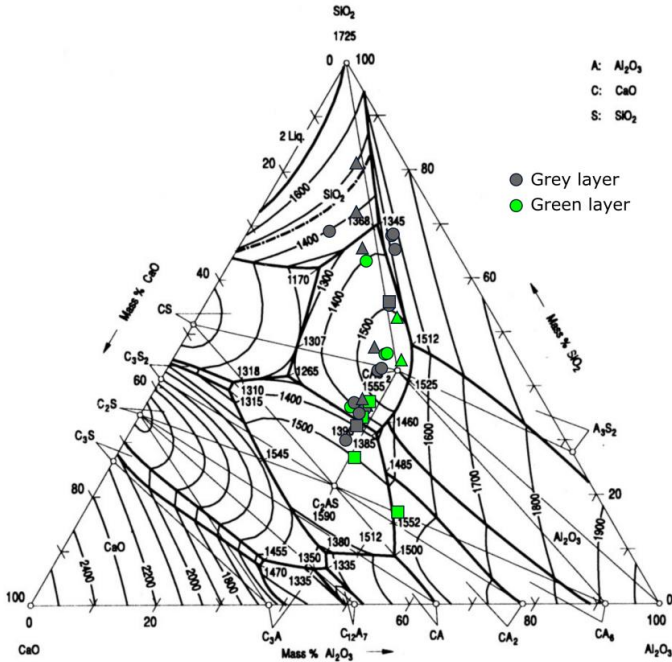


Figure 140 Slag from the samples including the zones next to the Si tapping channel for tap-hole 1, 3 and 7 from the Furnace B excavation. The green or the grey color gives if they are from the green or the grey colored layer in the sample.

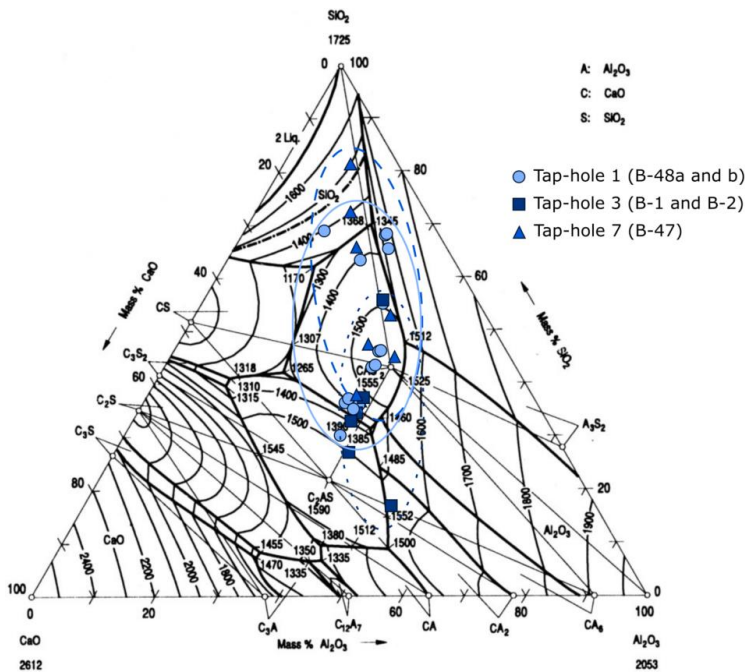


Figure 141 Slag from the samples including the zones next to the Si tapping channel for tap-hole 1, 3 and 7 from the Furnace B excavation. The tap-holes are separated with different shapes and different shadings of blue.

In order to find any potential differences in the slag composition of tapped slag samples from different tap holes, the SiO<sub>2</sub> content as a function of tap-hole were plotted in Figure 142 for the samples from Furnace R at Finnfjord AS. The standard deviation calculations only consider the normal tapped slags. For tap-hole 1, 4 and 5, only one slag sample from each tap-hole were obtained, with SiO<sub>2</sub> content 40%, 36% and 35%, respectively. For tap-hole 2, 3, 6 and 7 the average concentrations were 35%, 38%, 34% and 35%. For the tap-holes including several samples, it can also be seen that the standard deviations overlap between the tap-holes. This supports that there are no significant differences between the different tap-holes.

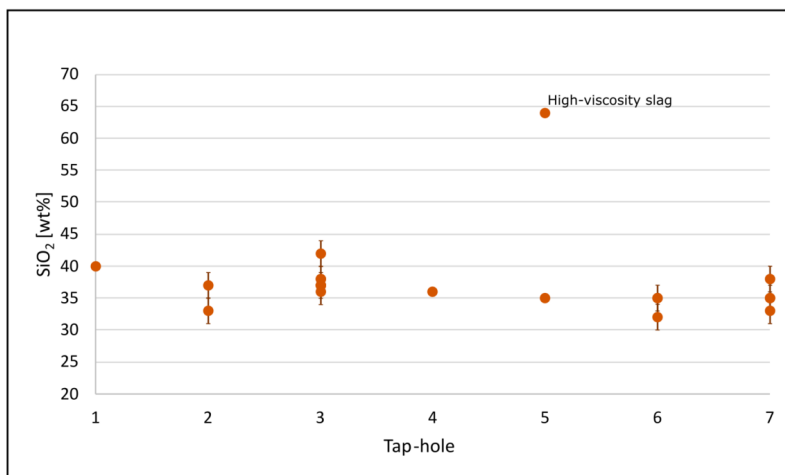


Figure 142 The SiO<sub>2</sub> content in the tapped slag samples from Furnace R at Finnfjord AS as a function of the tap-hole they came from. The vertical lines are the standard deviations.

### 5.1.6 Tapped slag

This study includes tapped slag samples from four different Si and FeSi furnaces, from three different plants: furnace no. 2 at Elkem Thamshavn, Elkem Furnace B and two furnaces at Finnfjord AS. The slag compositions for all the tapped samples are plotted in the SiO<sub>2</sub>-CaO-Al<sub>2</sub>O<sub>3</sub> phase diagram in Figure 143.

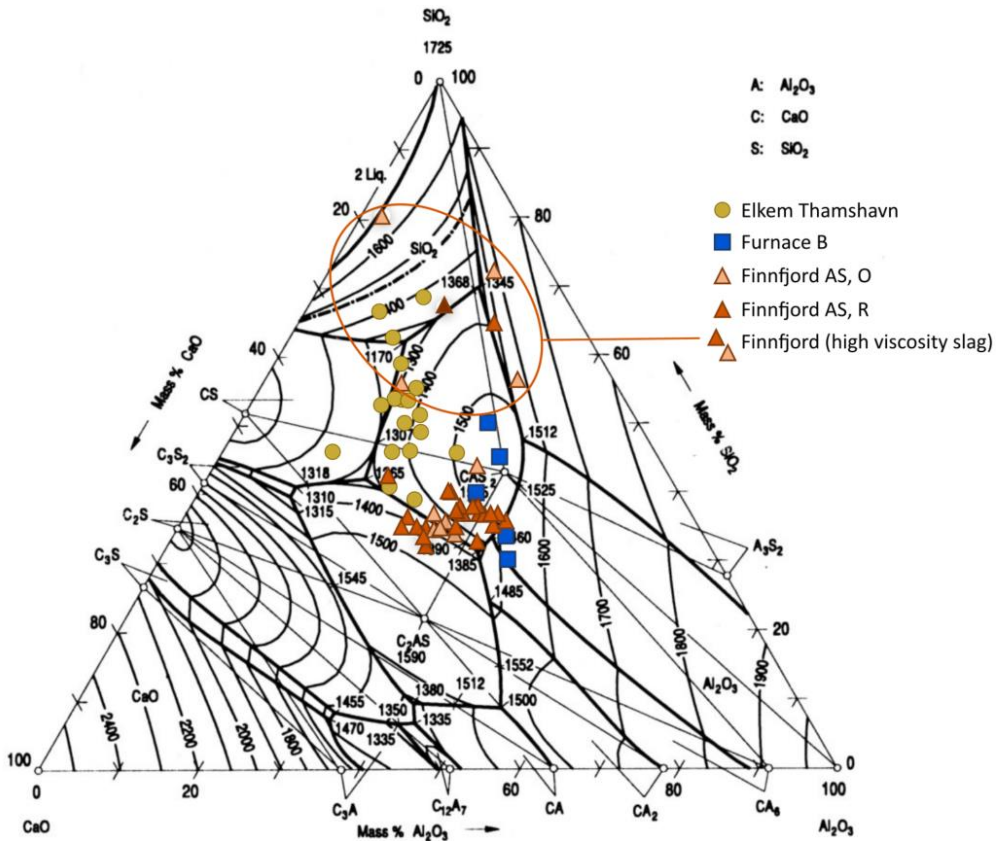


Figure 143 The composition of all tapped slag samples collected during operation.

The main difference between the normal tapped slag and the slag reported as high-viscosity slag is the increased amount of  $\text{SiO}_2$  in the slag, and the presence of  $\text{SiO}_2$  areas and condensates in the samples. Areas of  $\text{SiO}_2$  and condensates were also found in some of the previously tapped slag, collected during the Furnace B excavation. As earlier mentioned in chapter 5.1.4 Condensation of  $\text{SiO}$  gas and  $\text{CO}$  gas in the furnace, the condensates might be from the slag layer above the tapping area. Presence of  $\text{SiO}_2$  areas might be from quartz “falling” down into the metal flow. A high amount of  $\text{SiO}_2$  in the high-viscosity slag also suggests presence of solid  $\text{SiO}_2$  which dissolves in the slag. Kristiansen [124], [133] modelled the dissolution rate of three different  $\text{SiO}_2$ - $\text{CaO}$ - $\text{Al}_2\text{O}_3$  slags in  $\text{SiO}_2$  at  $1500^\circ\text{C}$  and  $1550^\circ\text{C}$ . For slag with initial  $\text{SiO}_2$  content of 38%, 50% and 62%, he found that the dissolution rate constants,  $k$  were in the range of  $10^{-3}$  g/s for 38% and 50%  $\text{SiO}_2$  and  $10^{-4}$  g/s for the slag with 62%  $\text{SiO}_2$  at  $1550^\circ\text{C}$ . Additionally, he found that the  $\text{SiO}_2$  concentration experienced a rapid increase up to 75-80%. This suggests that the presence of small particles of solid  $\text{SiO}_2$  next to normal tapping slag with  $\text{SiO}_2$  concentrations of 30-40% would rapidly increase the  $\text{SiO}_2$  concentration to similar concentrations as found in the high-viscosity slag. It is likely that this high-viscosity slag has formed in the lower part of the furnace. If it was formed in the higher parts, the high viscosities of these slags suggests that the flow down through the furnace would be very slow.

The amount of slag, the amount of solid SiC in the liquid slag and the viscosity of the slag are three of the main factors that influences the flow of slag through the tap-hole. The viscosity is a measure of how easy the melt will flow. The liquidus temperature data for the collected slag samples are listed in Table 41. The metal that is tapped from the furnace was earlier assumed to hold a temperature around 1500-1600 °C [5], which were based on the temperatures measured in the ladle. However, temperature measurements from 2018 in the runner at Finnfjord AS and 2019 in the runner at Elkem Thamshavn have found temperatures around 1700-1900 °C [27], [46]. This confirms that all collected slag samples in the tapping area in this study are liquid during tapping. This is also the case for all slag next to the tapping channel from the Furnace B excavation. The liquidus temperatures ranges from 1170 °C to 1550 °C. With assumption of ~1800 °C tapping temperature, the viscosities range from 1-34 Poise for the reported normal tapping slag, and from 12-180 Poise for the slag that is reported as high-viscosity slag. Some of the slag samples collected at Elkem Thamshavn have viscosities that are in the same range as the slag reported as high-viscosity slag at Finnfjord AS. At Elkem Thamshavn, tapped slag was only collected during normal tapping conditions. This could be because the amount of slag during sampling time at Thamshavn was too small to have a negative effect in the same way as it was reported at Finnfjord for the high-viscosity slag, or that the tapping temperature was higher.

Table 41 The lowest and the highest liquidus and solidus temperature found for slag samples in this study.

Zone in the furnace	T <sub>liquidus</sub> [°C]	T <sub>solidus</sub> [°C]
Higher parts of furnace	1390–1550	1170–1512
Lower parts of furnace	1310–1540	1170–1265
Tap-hole area	1310–1650	1170–1512
Tapped slag (Thamshavn)	1200–1500	1170–1265
Tapped slag (Furnace B)	1510–1550	1170–1385
Tapped slag (Finnfjord)	1350-1550	1170-1512

From the viscosity data it can be noted that samples with a higher SiO<sub>2</sub> content have higher viscosities. Figure 144 gives the viscosity in a logarithmic scale for a fixed CaO/Al<sub>2</sub>O<sub>3</sub> ratio of 0.25 and 2 at 1600 °C and 1800 °C, with increasing amount of SiO<sub>2</sub>. The viscosity areas in the SiO<sub>2</sub>-CaO-Al<sub>2</sub>O<sub>3</sub> ternary phase diagram in Figure 143 are shown as blue and red arrows. The graph confirms increasing viscosity with increasing amount of SiO<sub>2</sub>, and the effect increases with higher concentrations of SiO<sub>2</sub>. The difference is significant, also at 1800 °C. Also, presence of any solid particles in the sample would increase the viscosity further. This is not accounted for in the viscosity calculations in FactSage, and this means that the viscosity numbers for the different samples are higher than what is given in the figure in the cases where solid SiC is found together with the slag. However, it is not observed an increased amount of SiC in the reported high-viscosity slags, and this indicates that the main factor influencing the slag in the tapping area is the concentration of SiO<sub>2</sub> in the slag. Small variations have a great influence. A significant amount of slag with an increased SiO<sub>2</sub> content would easier accumulate next to the tap-hole and clog the tap-hole, which would hinder the metal drainage.

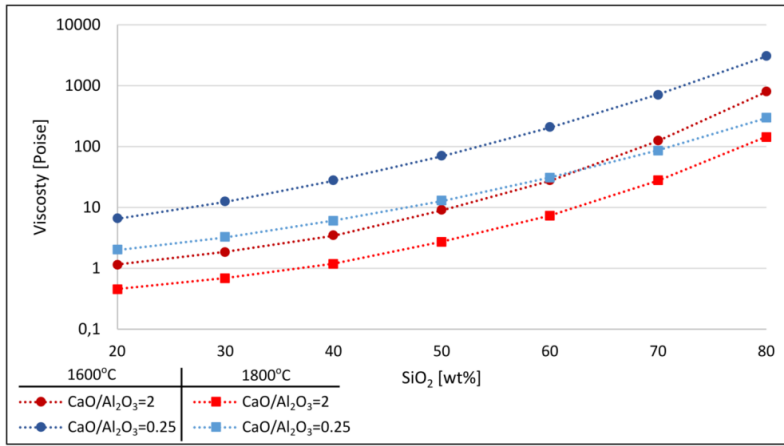


Figure 144 Viscosity versus %SiO<sub>2</sub> at temperature 1600 °C and 1800 °C. The CaO/Al<sub>2</sub>O<sub>3</sub> ratio is kept constant at 2 and 0.25. The viscosities are calculated using FactSage 8.1.

### 5.1.6.1 Evaluation of the viscosity data

The viscosity data are calculated with Factsage 8.1, which relates the viscosity to the structure of the solution. The structure is calculated using the Modified Quasichemical Model. Several researchers have tried to develop models to estimate viscosities of slag, and these are usually based on the composition and temperature dependency in various forms [33]–[38]. Table 42 lists the viscosity data for four of the tapped slag compositions using two different viscosity models: FactSage 8.1 and Tang et al. [38]. The last model uses the modified Vogel-Fulcher-Tammann (VFT) formalism and the Mauro equation. The viscosity results from the models are in the same size range, but the difference increases with increasing viscosity. This shows that different models give different results. The estimated values from viscosity models are expected to have uncertainties up to  $\pm 25\%$ . The viscosity data in this study are mainly used to give an estimate of how the slag behaved in the tap-hole area. It can be seen that the viscosity data for the slags that are reported as high-viscosity slag have significantly higher values than for the normal slag.

Table 42 Calculated viscosities at 1600 °C and 1800 °C using two different viscosity models. The viscosity data are given in Poise.

SiO <sub>2</sub>	CaO [wt%]	Al <sub>2</sub> O <sub>3</sub>	Factsage 8.1		Tang et al. [38]	
			1600°C	1800°C	1600°C	1800°C
70	21	9	105	24	157	36
55	27	18	25	6	33	10
39	34	27	7	2	9	3
46	31	23	12	3	7	3



### 5.1.6.2 The effect of temperature and furnace load

From the curves showing the effect of increasing SiO<sub>2</sub> concentration in the SiO<sub>2</sub>-CaO-Al<sub>2</sub>O<sub>3</sub> slag in Figure 144, it can also be noticed the effect of temperature. Normal tapping temperature is around 1800-1900 °C [27], [46], but deviations may occur. The temperature in the ladle at sampling time were measured for most of the samples collected at Elkem Thamshavn. The temperature is measured by dipping a thermocouple connected to a lance in the ladle, approximately 10-20 cm below the metal level. This temperature will not be the same as in the runner, but it might indicate if there are variations in the tapping temperature. Figure 145 shows the measured temperature in the ladle as a function of the SiO<sub>2</sub> content in the slag. The trendline shows a small decrease in SiO<sub>2</sub> concentration in the slag with increasing temperature. However, the difference is <5%. The correlation coefficient, R<sup>2</sup>, which is a number between 0 and 1, is the statistical measure of how much of the variation is explained by the model parameters. In this case, R<sup>2</sup> 0.0066, which means that the temperature changes in the ladle only explain a very small fraction of the change in SiO<sub>2</sub> content in the slag at sampling time. Nor any correlation was found between the measured temperature and the CaO or Al<sub>2</sub>O<sub>3</sub> concentration in the slag. The tapping temperature is believed to mostly have an influence on the viscosity of the slag during the process of draining the furnace. Decreasing the temperature increases the viscosity significantly. A lower temperature of the tapped metal will also have an influence on the refining and the casting process. The melting temperature of silicon is 1410 °C. With temperatures close to this the metal could solidify and create a crust at the top of the ladle.

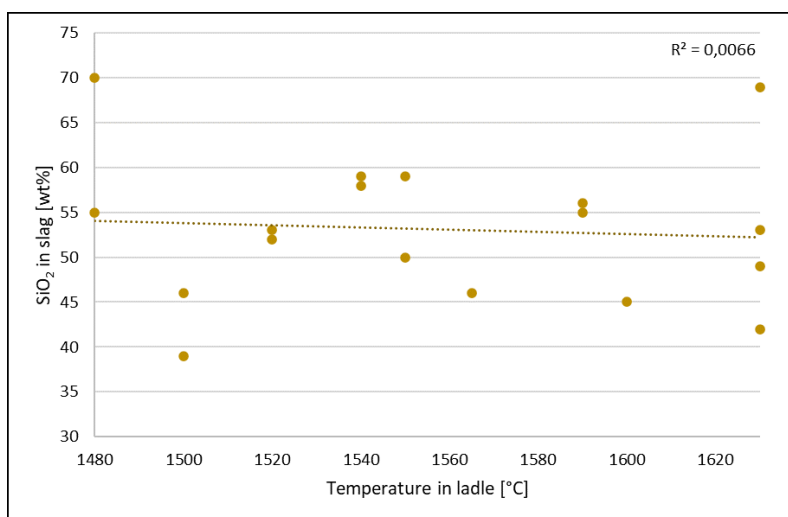


Figure 145 Temperature measured in the ladle compared with the SiO<sub>2</sub> content in the slag collected from the tap-hole.

The furnace power gives how much energy is supplied to the furnace. Typically, more power is applied to the furnace to increase the furnace temperature and to increase the

production. The furnace power given in MW for the tapped slag samples from Finnford AS at the sampling time and the amount of SiO<sub>2</sub> in the slag samples can be seen in Figure 146. There is an indication that a higher load has a lower SiO<sub>2</sub> content in the slag. An increased temperature in the furnace as a result of more energy supplied to the system could affect the reduction of SiO<sub>2</sub> from SiO<sub>2</sub>-CaO-Al<sub>2</sub>O<sub>3</sub> slag, which is strongly dependent on temperature [128], [129]. Increasing temperature increases the SiO<sub>2</sub> reduction rate and lower amounts of SiO<sub>2</sub> in the slag phase.

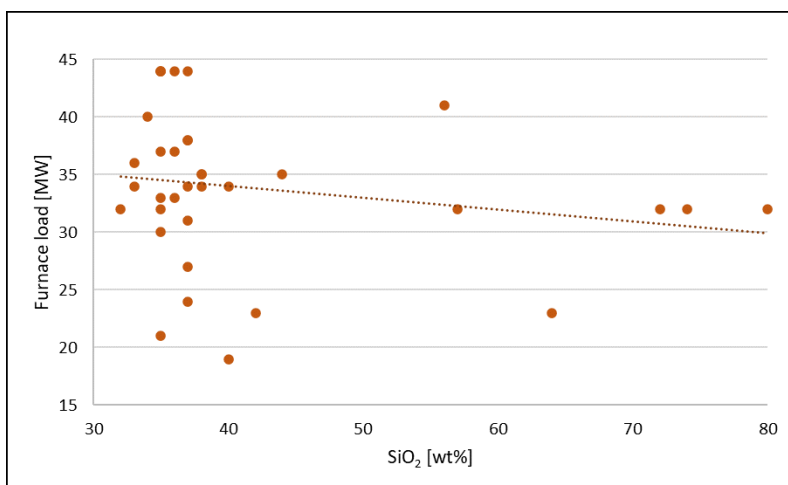


Figure 146 The amount of SiO<sub>2</sub> in the slag as a function of furnace load for the tapped slag at Finnford AS.

### 5.1.7 Al<sub>2</sub>O<sub>3</sub> phase in slag samples

In many of the accumulated slag samples, it was found an Al<sub>2</sub>O<sub>3</sub> phase together with SiO<sub>2</sub>-CaO-Al<sub>2</sub>O<sub>3</sub> slag and SiC, both in the higher and the lower parts of the furnace. Pure Al<sub>2</sub>O<sub>3</sub> is not added to the furnace, but Al<sub>2</sub>O<sub>3</sub> is an expected impurity in the raw materials. Oxides of aluminium are the most common impurity in quartz, often in form of muscovite (KAl<sub>2</sub>(Si<sub>3</sub>Al)O<sub>10</sub>(OH,F)<sub>2</sub>) or feldspar (KAlSi<sub>3</sub>O<sub>8</sub> – NaAlSi<sub>3</sub>O<sub>8</sub> – CaAl<sub>2</sub>Si<sub>2</sub>O<sub>8</sub>). Al<sub>2</sub>O<sub>3</sub> requires higher energy and temperature than SiO<sub>2</sub> to be reduced, and for Al<sub>2</sub>O<sub>3</sub> to be reduced with carbon, a temperature above ~2040 °C is needed. In a Si or FeSi furnace, that is only the case below the electrode next to the arc. Al<sub>2</sub>O<sub>3</sub> is therefore expected to be found in the slag phase. Figure 147 shows an overview of all the analyzed accumulated slag from the six excavations. The samples which contain a pure Al<sub>2</sub>O<sub>3</sub> phase are marked in red. For many of the samples the SiO<sub>2</sub>-CaO-Al<sub>2</sub>O<sub>3</sub> slag is close to the Al<sub>2</sub>O<sub>3</sub> boundary line. This means that Al<sub>2</sub>O<sub>3</sub> most likely has precipitated during solidification. However, for some of the slag samples next to the tapping channel, there is not likely to have any precipitation. For those samples it is believed that the Al<sub>2</sub>O<sub>3</sub> is from the tap-hole clay.

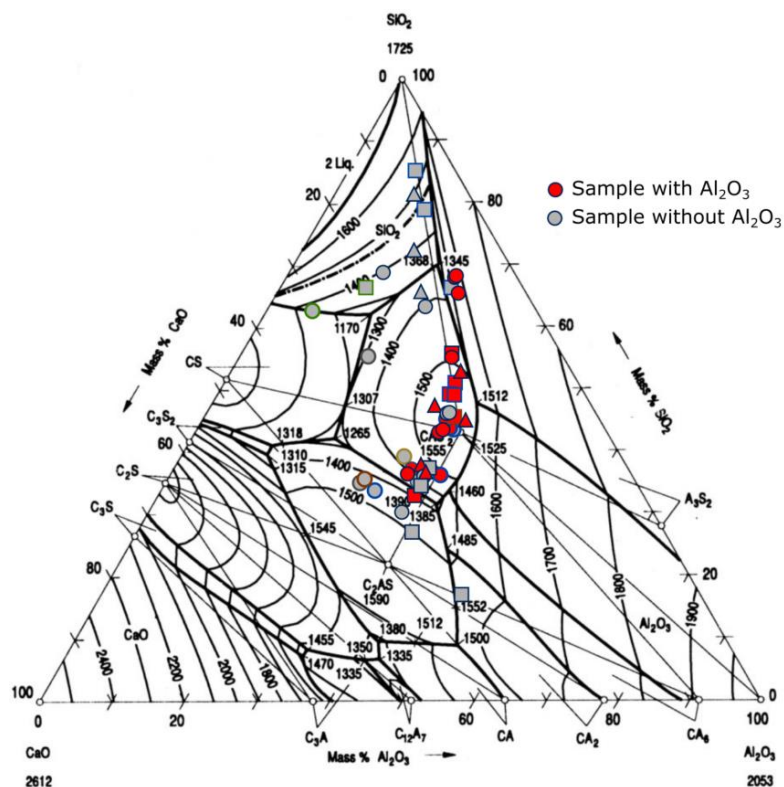


Figure 147 Analyzed accumulated slag from Norwegian silicon and ferrosilicon furnace excavations. Samples marked in red are those samples which contain  $Al_2O_3$ .

### 5.1.8 Oxynitride found in Furnace B

In both parallels of sample B-9 from the excavation of Furnace B, it was found areas with oxynitride. Oxynitride is formed when Si fines are heated and react with both the oxygen and nitrogen in the air. However, it is not expected inside the furnace where the gas atmosphere is mainly SiO gas and CO gas. B-9 was from the higher parts of the furnace and approximately 1-2 m from the furnace wall. Nitrogen gas ( $N_2$ ) could originate from the impurities in the carbon materials. However, for oxynitride to be the stable phase, the  $N_2$  partial pressure must be several magnitudes higher than  $p_{O_2}$ . This can be seen in Figure 148, which shows the stable phases of oxynitrides [134] for temperatures up to  $\sim 1700$  °C. It is also possible that  $N_2$  gas in air enters the furnace through the furnace wall due to thermal buoyancy. The oxygen in this air reacts with C or Si. At a point,  $p_{N_2}$  is sufficiently higher than  $p_{O_2}$  in this air so that the nitrogen reacts with the Si. This can only happen in areas where there is no overpressure of SiO gas and CO gas. However, it is also likely that the oxynitride was formed during the excavation, where the samples were exposed to air during cooling. A similar effect is seen during casting. When Si metal is tapped from Furnace B, it is casted directly in molds. The molds are then sprinkled with Si fines. Oxynitride is often found in between the cast Si and the Si fines.

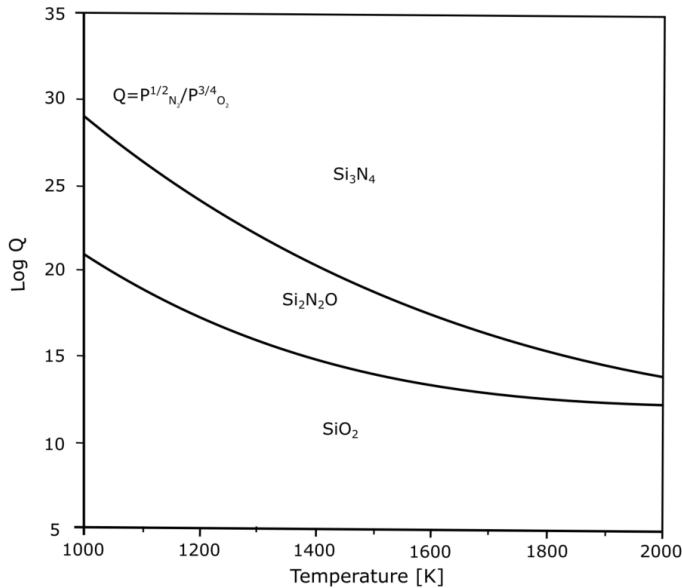


Figure 148 Stable phases as a function of temperature and  $N_2$  and  $O_2$  relation [134].

## 5.2 $SiO_2$ properties affecting the furnace

### 5.2.1 Disintegration of $SiO_2$

As mentioned previously, quartz experiences a steep temperature increase when it is added to the charge surface, which during normal operation holds a temperature around 1300 °C [3], [4], [76]. The shock heating might cause the  $SiO_2$  to disintegrate, and this might have a negative effect on the operation. Too much fine particles in the charge will clog the furnace and hinder an even flow of materials and gases[5], [59], as shown in the right illustration in Figure 149. Clogging of the furnace decreases the gas permeability and leads to creation of gas channels that can cause small outbursts of gas. Gas in the channels has less interaction with the descending raw materials and more SiO gas escapes the furnace. It is preferable to have a charge with a good permeability so that all raw materials meet the ascending SiO and CO gas. A good permeability of the charge mixture requires raw materials with a good

size distribution, giving more space around the raw materials and enables an even gas flow. This is illustrated to the left in Figure 149.

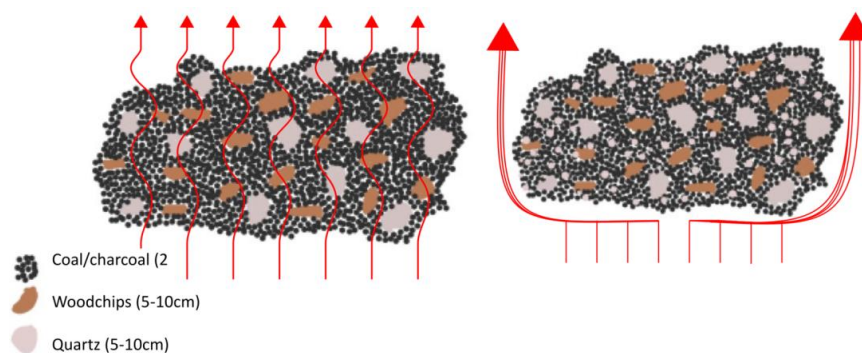


Figure 149 Illustration of gas permeability in a charge with a low amount of fines (left) and a high amount of fines (right).

Crack formation is the first start of fines formation. In this study it is found that crack formation in the quartz mainly happens at two temperature intervals,  $\sim 300\text{-}600\text{ }^{\circ}\text{C}$  and  $\sim 1300\text{-}1600\text{ }^{\circ}\text{C}$ . This is similar with what Aasly [82] found in his work where he also found two main temperature intervals for crack formation,  $\sim 180\text{-}573\text{ }^{\circ}\text{C}$  and from  $\sim 1200\text{ }^{\circ}\text{C}$ . A summary of the crack formation and the mechanism in this study is shown in Table 43. It should also be mentioned that the degree of cracking is found to be different between the different quartz types, which is also confirmed by several other researchers [9], [77]–[79].

Table 43 A summary of the crack formation and mechanism in quartz type A, B, C, D, F and G.

Quartz type	Crack formation [mm/mm <sup>2</sup> ]	300-600°C	1300-1600°C
A	12.2 and 5.2	Crack formation from fluid inclusions.	Crack formation due to volume change: expanding cracks and new formation of cracks from fluid inclusions and cracks from impurities.
B	8.4 and 2.4	Crack formation from volume change in impurity areas.	Crack formation due to volume change: cracks initiating both from existing cracks and from impurities with changing color on the HTCM image.
C	14.2 and 34	Crack formation from fluid inclusions.	Crack formation due to volume change: cracks initiating both from existing cracks and from impurities with changing color on the HTCM images.
D	16.7, 9.4 and 20.4	Crack formation from impurities. In the D.2 there was no crack formation before 1300°C.	Crack formation due to volume change. Cracks initiates from impurities with changing color on the HTCM images and expanding grain boundaries.
F	5.1, 6.9 and 2.6	Crack formation due to uneven SiO <sub>2</sub> surface. In F.3 it was also crack formation due to volume change in impurities	Existing cracks expand due to volume change
G	17.8 and 14.6	No crack formation	Crack formation due to volume change. Cracks initiates from impurities.

The crack formation from 300 °C is in most cases from an uneven SiO<sub>2</sub> surface, from volume changes in the impurity areas or from fluid inclusion cavities, illustrated in Figure 150, Figure 151 and Figure 152, respectively. The uneven surface is most likely from the cutting process. If the cut is close to or at the edge of an impurity area or a fluid inclusion, this would result in an uneven or damaged SiO<sub>2</sub> surface. A damaged SiO<sub>2</sub> surface is prone for more damage, as cracking, during heating. Also, changes in the molecular structure of the impurities during heating, e.g., phase transformations, can induce cracking. Most of the

impurities in this study contain  $\text{Al}_2\text{O}_3$ , which were found to induce different degree of cracking.

Escape of fluid from fluid inclusions were also observed for several of the quartz samples from 300 °C. With increasing temperature, the internal partial pressure of the fluid inclusions in the quartz will increase until they escape the  $\text{SiO}_2$ , which contributes to fracture. It was observed small black “dots” that appeared on the surface and cracks that induced from these. The relation between cracking from 300-400 °C and fluid inclusions were discussed already in the 1960’s by Birkeland and Carstens in an internal report, referred to by Aasly [135]. Aasly also found in his work [82] the importance of fluid inclusions, who believed that the low temperature interval below 573°C could be significant for the thermal properties of the quartz. Martinsen, also referred to by Aasly [135], studied the fluid inclusions for quartz which were classified with “good” or “bad” thermal properties and found it reasonable that the fluid inclusion composition in the quartz has an influence on the quartz quality as a raw material for the Si and FeSi process.

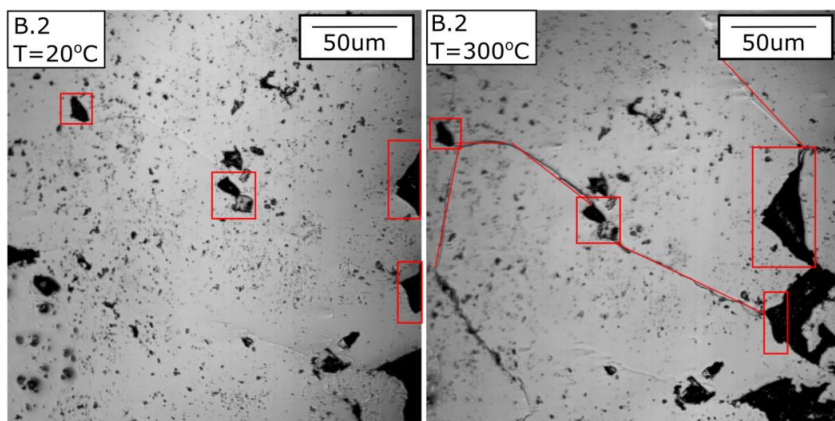


Figure 150 Images from high temperature confocal microscope (HTCM) experiment for B.2 at 20 °C and 300 °C, showing crack formation from impurity areas.

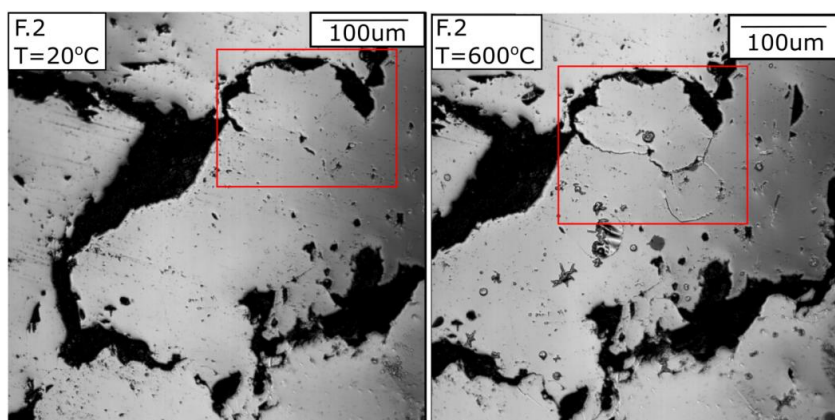


Figure 151 Images from high temperature confocal microscope (HTCM) experiment for F.2 at 20 °C and 600 °C, showing crack formation from uneven  $\text{SiO}_2$  surface. No impurity areas were found in this sample.

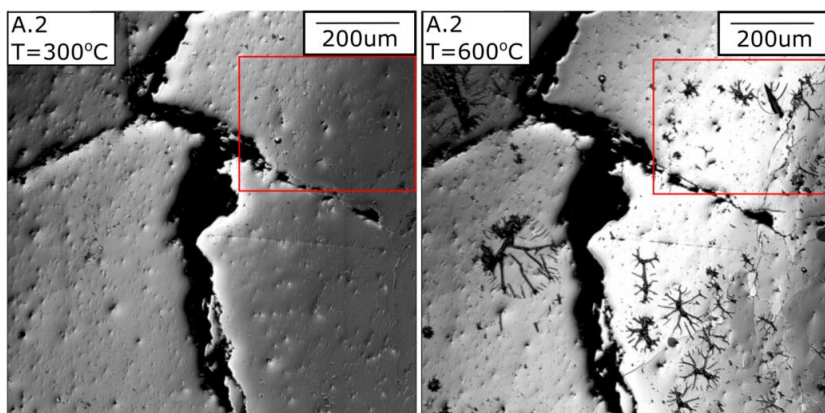


Figure 152 Images from high temperature confocal microscope (HTCM) experiment for A.2 at 300 °C and 600 °C, showing crack formation from cavities from escaped fluid inclusions.

Cracks occurring from  $\sim 1300$  °C is believed to be due to the  $\text{SiO}_2$  phase transformation from quartz to cristobalite. Cristobalite has a lower density than quartz and the volume will increase as more quartz transforms to cristobalite. The grains will then expand and induce stress that causes microcracks, as illustrated in Figure 153. The volume increase also causes more tension in the existing cracks, leading to more crack formation. Gemeinert, referred to by Aasly [135], observed in his experiments that the properties of the fluid inclusions increased the speed of the  $\beta$ -quartz  $\rightarrow$   $\beta$ -cristobalite phase transformation. A faster phase transformation would expect to also cause a faster volume increase. In this study it was also found that the crack formation from fluid inclusions further developed from  $\sim 1300$  °C. The volume increase as an important parameter for disintegration of  $\text{SiO}_2$  were also proposed by Ringdalen [77]. A volume increase was observed during heating up to 1750 °C for all the quartz types in this study.

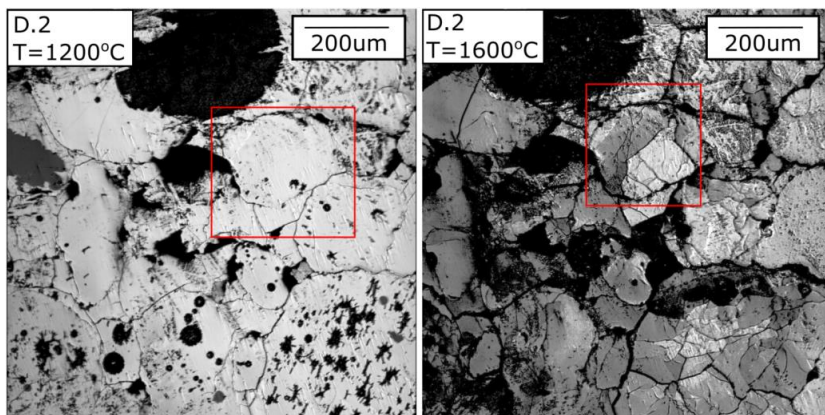


Figure 153 Images from high temperature confocal microscope (HTCM) experiment for D.2 at 1200 °C and 1600 °C, showing crack formation from expanding grain boundaries.



Figure 154 compares the degree of cracking with the maximum volume increase. The maximum volume increase varied from 5% to 31% in this study, which is similar with Ringdalen's [59] results. An increased volume expansion is expected to cause more disintegration. This is also the main trend and shows that the phase transformation from quartz to cristobalite have a great influence on the crack formation in the quartz. However, neither Jusnes [9] or Ringdalen and Tangstad [58] could find any correlation between the amount of cristobalite and the amount of fines formed during heating. A volume increase around 22% is expected to be due to the phase transformation to cristobalite, and the higher results for some of the quartz types suggests that there are more factors that affects the volume expansion during heating. It was found that Quartz G and A have the largest volume increase, and it is also found that most of the crack formation for these developed after 1300 °C. This was also the case for quartz C and D. Quartz B has both a low degree of crack formation and the lowest volume expansion. For quartz F, most of the cracks occurred before 1200 °C, even with a volume expansion of ~12-18% at 1600-1700 °C. This could most likely be due to larger grain boundaries in the F quartz, which is found to be both in the range 70-130µm and  $\geq 1\text{cm}$  [9]. In the smaller samples heated in this study, it could be that the cube only contained one set of grains.

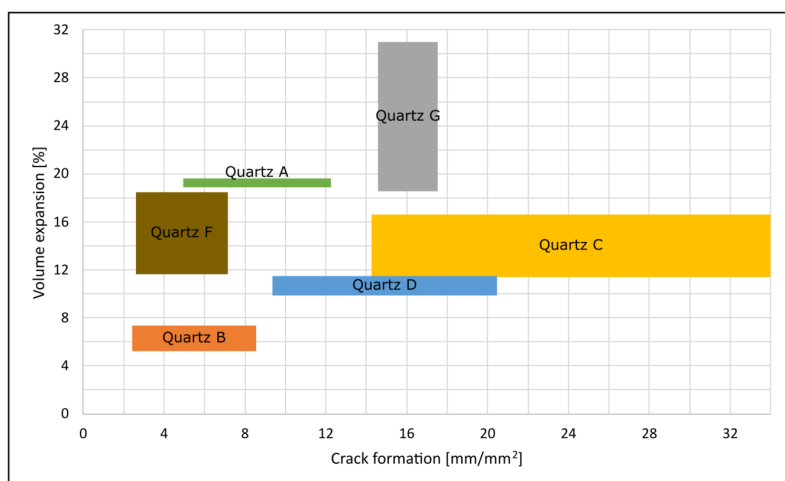


Figure 154 Crack formation at 1600 °C and the maximum volume expansion during heating to 1750 °C for quartz A, B, C, D, F and G.

Figure 155 compares the amount of cracks produced during heating to 1600 °C in this study with amount of fines produced from shock heating to 1500 °C from Jusnes [9] and Ringdalen [77]. Jusnes investigated the fines formation for quartz A, D, F and G and Ringdalen for quartz B after shock heating to 1500 °C. Fines were defined as material below 10 mm. The following descriptions of the nature of the quartz are found from Elkem reports referred to by Jusnes [9]. From Figure 155 it can be noticed that quartz D, which has a high degree of cracking, has the lowest wt% of fines produced. Quartz F has the highest formation of fines, but the lowest formation of cracks. This is believed to be due to the different nature of these two quartz types. Quartz D has more impurities on the grain

boundaries. These melts and binds the grains together and will also absorb a lot of the stress from the SiO<sub>2</sub> volume increase. Less fines will then be produced, even with a higher degree of crack formation. Quartz F has larger grain boundaries and the impurities have therefore no binding effect in the SiO<sub>2</sub> matrix. It should also be mentioned the internal variations in fines formation for Quartz G. Quartz G has three regimes where the grain sizes, the degree of recrystallization and the temperature experienced are different. Regime 1 produced the largest amount of fines, while regime 2 and 3 produced less [9]. The fines formation of quartz type G is therefore divided in two areas in the figure. It is not known which regime the samples in this study are from. Quartz B has a low degree of both fines and cracks. Ringdalen [77] could not find the main causes for disintegration of quartz, but suggested fluid inclusions, impurities in the quartz and volume changes as possible parameters. Jusnes [9] investigated the effect of initial microcracks in the quartz and found that an increasing amount of initial cracks gave an increased number of fines. Aasly [82] found the same trend after shock heating of six quartz types up to 1300 °C, which is before the α-quartz → β-cristobalite transformation. This suggests that the initial microcracks have a larger effect on the fines production than the crack formation during heating. It is not possible to find a correlation between amount of cracks and fines formation based on these results, and further work is needed to clarify.

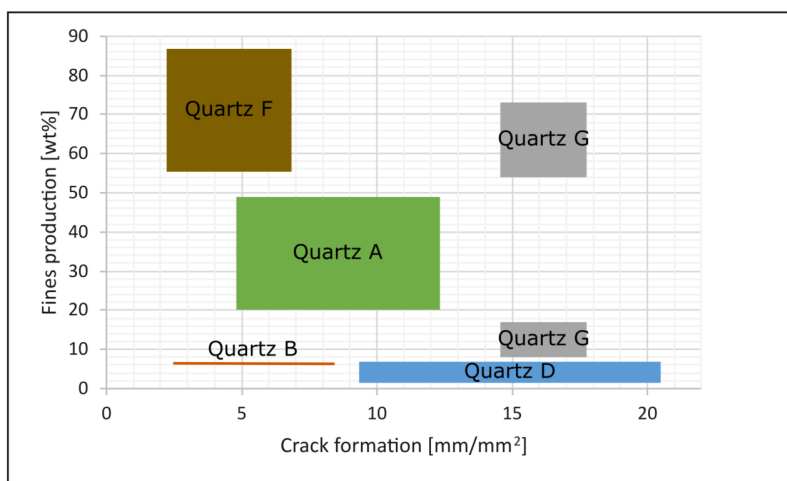
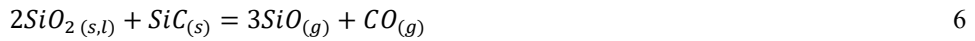


Figure 155 Crack formation at 1600 °C and fines production from shock heating to 1500 °C [9] for quartz type A, D, F and G. The result from quartz B is from Ringdalen [77]. Fines are defined as particles <10 mm. Crack formation is given in mm/mm<sup>2</sup>, while fines production is given in wt%.

### 5.2.2 Softening and melting of SiO<sub>2</sub>

Deciding the softening and melting temperature for quartz is a semi-quantitative method. Softening of quartz is defined as when the shape has lost its sharp edges [67], i.e. the temperature at which the SiO<sub>2</sub> starts to melt. This study shows that different quartz types have different softening temperature and melting time, which is also found in earlier heating

experiments [59], [70], [71]. Increasing heating rate also increases the softening and melting temperature [71], which gives that melting of quartz takes time or that the melting is influenced by the heat transfer rate. The melting properties influences where SiO<sub>2</sub> melts in the furnace. It is important that the SiO<sub>2</sub> have sufficient long melting time to ensure that its reactions with Si, reaction 5, and SiC, reaction 6, happen in the high temperature zone.



The general trend in this study is that a higher impurity content gives a shorter melting time, which is in agreement with Nordnes' results [69]. Contaminants may break up the SiO<sub>2</sub> network system and create bindings between dislocated cores. Quartz B, C and D, which have the most impurities in this study, melts before quartz A, F and G. For the softening results it is found lower softening temperatures for quartz B and C, but quartz D has one of the highest softening temperatures. Quartz C has a higher total impurity content around 1.6% than quartz B around 0.8%, but it is found the lowest softening temperature for quartz B. The same trends are found when comparing the amount of Al<sub>2</sub>O<sub>3</sub> or K<sub>2</sub>O, which is the most common impurity oxides in this study, with the softening temperature and melting time. From the ICP-MS analysis it can be seen that quartz D also contains 0.314% FeO/Fe<sub>2</sub>O<sub>3</sub>, in addition to Al<sub>2</sub>O<sub>3</sub> and K<sub>2</sub>O. The iron oxides content for quartz B and C are 0.08 and 0.09, respectively. Ringdalen and Tangstad [58] suggested that the softening temperature decreased with increasing FeO/Fe<sub>2</sub>O<sub>3</sub> content. This is not confirmed in this study. The results from their study compared to this study are shown in Figure 156. Their main correlation is seen for quartz with FeO content up to ~0.120%, which is ~1/3 of the iron oxide content in quartz D. Ringdalen and Tangstad did not find any clear correlation between the observed softening temperatures and the content of Al<sub>2</sub>O<sub>3</sub> or alkalis in the quartz. It is also not known if their results include experiments with different heating rates. In the later years it is found that increasing heating rate also increases the softening temperature and melting time [70]–[72], which is also mentioned by Ringdalen and Tangstad in their paper. Different heating rates would then affect the results when comparing the impurity content with the softening temperature and melting time.

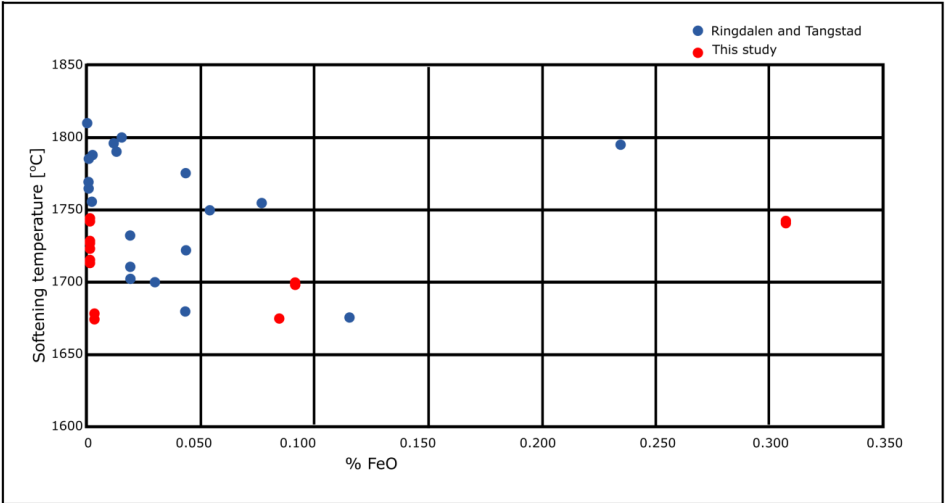


Figure 156 Softening temperature compared with %FeO with results from Ringdalen and Tangstad [58] and this study.

### 5.2.3 The effect of impurities and initial slag formation

Impurities that enter the Si furnace embedded in the quartz will follow the same path as the quartz. The impurities effect on SiO<sub>2</sub> upon heating is hence an important factor when studying the behaviour of SiO<sub>2</sub> in the furnace. It is found that the SiO<sub>2</sub> dissolves in the impurities with increasing temperature, as can be seen in Figure 157. For the quartz samples in this study, it is found that the impurities consist of mostly Al<sub>2</sub>O<sub>3</sub> and K<sub>2</sub>O, and FeO for quartz D. This is consistent with the ICP-MS analysis. The results from this study indicate that SiO<sub>2</sub> dissolve in the impurities as the temperature increases.

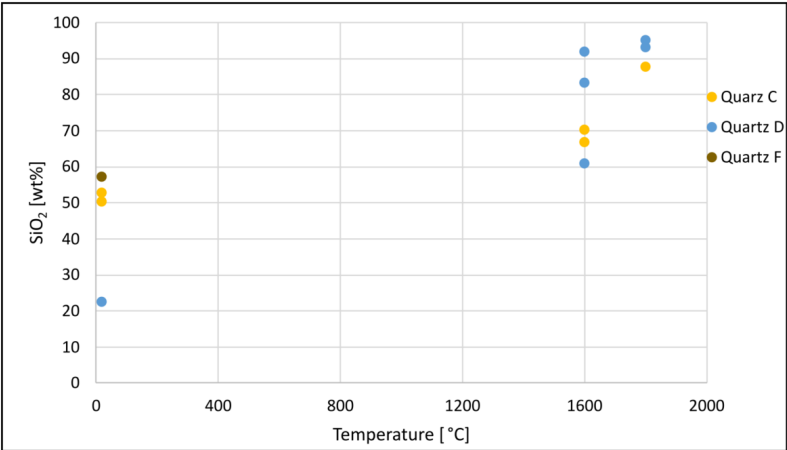


Figure 157 Amount of SiO<sub>2</sub> in the impurity areas in the SiO<sub>2</sub> as a function of temperature. The SiO<sub>2</sub> content in the impurities increases with increasing temperature.

The impurities in the  $\text{SiO}_2$  will contribute to the slag formation in Si and FeSi furnaces. In several of the charge surface samples from Finnjord AS, it was found slag together with the  $\text{SiO}_2$ . During normal conditions, the charge surface temperature is around 1300 °C [3], [4], and it is expected to only contain heated raw materials and some melting of the impurities inside the raw materials. Slag formation in this area might indicate a higher temperature than expected. The slag at the charge surface mostly contains  $\text{SiO}_2$  in addition to FeO,  $\text{Al}_2\text{O}_3$  and traces of alkali oxides Na, K, Mn, Mg and Ca, which are common impurities in the  $\text{SiO}_2$ . The existence of iron is expected since iron oxide pellets are added together with the raw materials. Saadieh [136] did small scale experiments to simulate FeSi production with experimental temperatures 1850 °C and 1900 °C. He found in his experiments that the iron ore pellets were reduced at the top of his crucible, and that the iron reduces to its metal component long before  $\text{SiO}_2$  and FeO dissolves with each other. Findings of FeO in the slag indicates that the temperature increase in the furnace is sufficient fast so that melting happens before the iron oxide reduces to its metal component. Figure 158 shows the binary phase diagram of the FeO- $\text{SiO}_2$  system. The solidus temperature is just below 1200 °C, which is below the expected charge surface temperature ~1300 °C. The liquidus temperature gives an indication of the charge surface temperature. The FeO content in the slags in this study ranges from 5-43 wt%, which corresponds to 4-39 mole%. From the phase diagram it can be seen that FeO- $\text{SiO}_2$  slag with FeO > 39 mole% is all liquid at approximately 1400 °C.

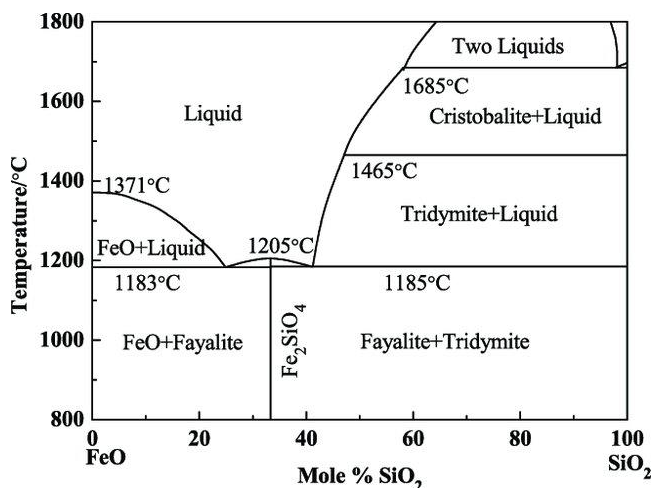


Figure 158 The binary phase diagram of FeO and  $\text{SiO}_2$  [137].

One of the main observations from the charge surface samples is that slag initiates from the grain boundaries and the cracks in the  $\text{SiO}_2$ , and it is also often a  $\text{SiO}_2$  rich slag next to the melted  $\text{SiO}_2$ . This is shown in Figure 159.  $\text{SiO}_2$  is not expected to melt before ~1700 °C, but impurities may lower the melting temperature and time [13, 14]. However, melted or partly melted  $\text{SiO}_2$  indicates a temperature <1600 °C. Since melting of  $\text{SiO}_2$  takes time, the

SiO<sub>2</sub>-rich slag is most probably the initial formation of slag from SiO<sub>2</sub> areas with increased content of impurities.

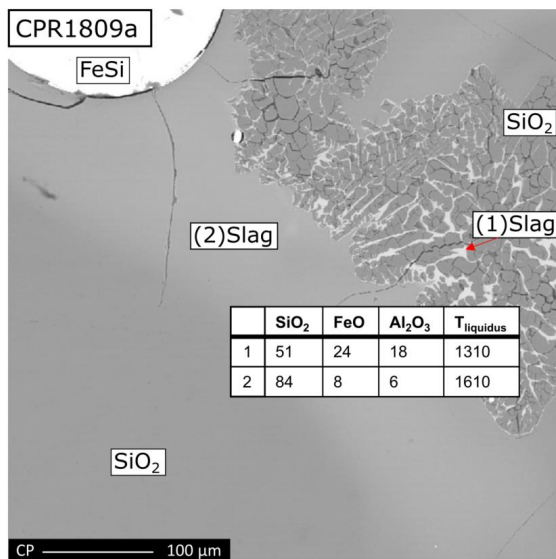


Figure 159 Initial slag formation in sample CPR1809a.2. Slag accumulates in the grain boundaries and cracks in the SiO<sub>2</sub>, shown as white color. An area with slag is also found together with the melted SiO<sub>2</sub>, shown as brighter grey color.

The SiO<sub>2</sub> content in the slag inside the grain boundaries and cracks in the SiO<sub>2</sub> are lower than the slag phase next to the SiO<sub>2</sub>, which can be seen in Figure 159. It can also be noticed that the slags in the grain boundaries/cracks in the SiO<sub>2</sub> have liquidus temperatures around the expected charge surface temperature. The increased SiO<sub>2</sub> content in the slag next to the SiO<sub>2</sub> also increases the liquidus temperature considerably to >1600 °C. The existence of this slag composition in the charge surface means either the slag has been pushed upwards from deeper in the furnace, or that the charge surface temperature is sufficient high to produce this slag composition. This is described thoroughly in section 5.1.1 More SiO<sub>2</sub> in the higher parts of the furnace. Softened/melted SiO<sub>2</sub> and SiO<sub>2</sub> rich slag around its liquidus temperature are viscous, which gives a sticky and compact charge surface. Several of the samples were reported as viscous during sampling.

Droplets of FeSi were also observed in several of the charge surface samples, which can be seen to the top left in Figure 159. This also substantiates either that materials have been pushed upwards from deeper in the furnace, or that the charge surface temperature is higher than expected. A too high temperature in the charge might have a negative effect on the furnace conditions. The high temperature might come from gas outburst from deeper in the furnace, which is caused by an increased pressure in the lower parts of the furnace [138]. The main outlet for the process gas is the charge, and the increased temperature in the charge might be from hot ascending process gas with sufficient energy to melt the materials in the charge. If the pressure build-up in the crater is too high, it will be released by blows

of gas through the charge mixture. This will most likely bring some materials from the lower part of the furnace up to the charge surface.

### 5.3 CaO dissolution in SiO<sub>2</sub>-CaO-Al<sub>2</sub>O<sub>3</sub> slags

CaO in form CaCO<sub>3</sub> is often added as a flux in Si and FeSi production. CaO lowers the viscosity of the slag, which is beneficial to ensure a good flow of materials through the furnace. The compositions, the liquidus and solidus temperatures, and the viscosities at 1500 °C and 1550 °C for slag 1, 2 and 3, used in this study, are listed in Table 33. These are slags with typical CaO content found in the higher, inactive parts of the furnace. The solidus temperatures are 1170 °C and 1385 °C, and it is observed that the slag encapsulates the CaO particle during heating around 1300-1400 °C for the slag compositions used in this study. Some slag was also observed on the CaO particle already at 1000 °C for slag 1. This means that dissolution of CaO into the accumulated slag in the Si and FeSi furnaces may also happen if slag is present in the inactive zones, where the temperature is above the solidus temperature of the slag.

*Table 33 SiO<sub>2</sub>-CaO-Al<sub>2</sub>O<sub>3</sub> slags used in the dissolution experiments. The amounts are given in wt% and the viscosities are calculated with FactSage 8.1.*

Slag	SiO <sub>2</sub>	CaO	Al <sub>2</sub> O <sub>3</sub>	T <sub>liquidus</sub>	T <sub>solidus</sub>	Viscosity [Poise]	
	[wt%]	[wt%]	[wt%]	[°C]	[°C]	1500°C	1550°C
1	56	15	29	1490	1170	456	250
2	38	20	42	1550	1385	-	48
3	56	21	23	1420	1170	180	108

The observed dissolution of a CaO particle into slag 1 at 1600 °C for different holding times are illustrated in Figure 160. The initial CaO particle disintegrates between 1400-1500 °C, and dissolve. As the temperature reaches 1600 °C, there are CaO footprints in the slag. This was observed both in the CT images and as peaks of CaO in the oxide analysis in the bottom layer close to the crucible. It was also observed a layer with a brighter color in the EPMA images, surrounding the CaO particle, in the 1500 °C experiments in this study. After 10 minutes at 1600 °C, a CaO rich slag forms as a bottom layer in the crucible, with CaO concentration around 35%. The CaO concentration near the crucible bottom decreases with increasing holding time at 1600 °C up to 60 minutes. After 60 minutes at 1600 °C, only a small concentration gradient is measured in the vertical section of the slag, and the CaO concentration in the bottom slag near the crucible is close to 100% dissolution of the CaO. These observations indicate that the CaO dissolution into slag 1 is fast.

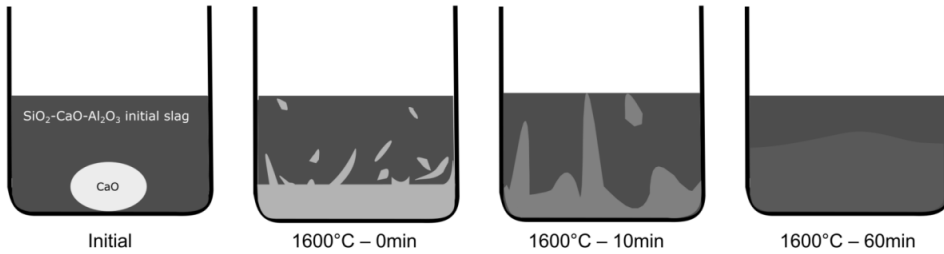
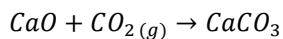


Figure 160 The observed dissolution of a CaO particle into 56% SiO<sub>2</sub>– 15% CaO – 29% Al<sub>2</sub>O<sub>3</sub> at 1600 °C for different holding times.

### 5.3.1 The effect of CaO on slag viscosity in the Si and FeSi furnaces

The main purpose of adding CaO to Si and FeSi furnaces is to lower the viscosity of the accumulated slag in the furnace. Too much accumulated slag is negative for the operation and a sufficient low viscosity is important to ensure a stable flow of materials through the furnace. However, with increasing amount of CaO added to the furnace, more SiO<sub>2</sub> will enter the slag phase and hence decrease the Si yield. It is therefore beneficial to add the least amount of CaO that would decrease the slag viscosity sufficient to have a stable flow of materials through the furnace. The viscosities as a function of increasing CaO concentration for the slags used in this study can be seen in Figure 161. The initial CaO concentration for slag 1, 2 and 3 is 15%, 20% and 21%, respectively, and it can be observed a great initial effect of dissolving more CaO into the slag systems. For slag 1 at 1600 °C the viscosity decreases to 1/12 of its initial value by increasing the CaO concentration to 30%. From 30-35% CaO, the viscosities decrease is smaller. The accumulated slag analyzed in this research have found CaO concentrations varying from ~10-30% in the higher, inactive parts of the furnace, which are similar with slag 1, 2 and 3. The dissolution reaction between CaO and SiO<sub>2</sub>-CaO-Al<sub>2</sub>O<sub>3</sub> slag were in this study found to start between 1300-1400 °C. When lime (CaCO<sub>3</sub>) is added together with the raw materials at the charge top where the temperature is around 1300 °C [3], [4] it will calcine to CaO according to reaction 19. It was found in the compression tests that the mechanical strength of the CaO is considerably lower than the initial CaCO<sub>3</sub>. The heating rate up to calcined temperature had no effect on how easily it fractured in the later dissolution experiments.



19



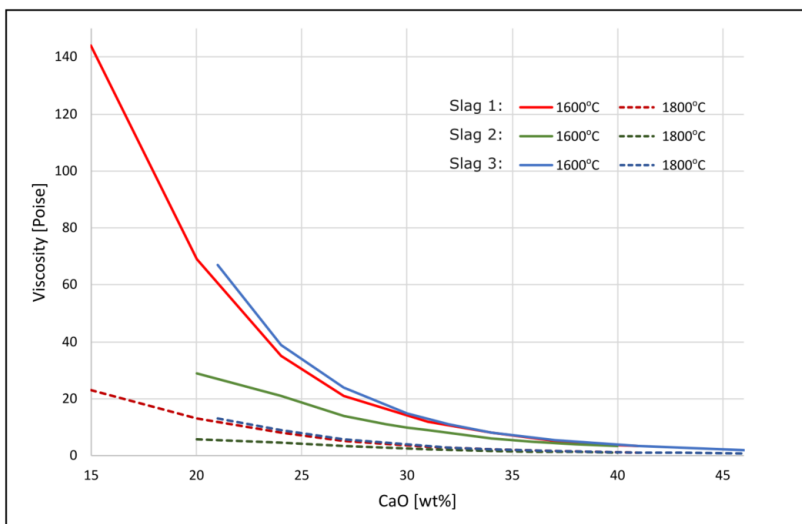


Figure 161 Viscosity with increasing %CaO for Slag 1, 2 and 3 at temperature 1600 °C and 1800 °C. The viscosities are calculated using FactSage 8.1.

In the Si and FeSi furnaces, the CaO is expected to disintegrate and dissolve in any slag close by. With increasing temperature, the dissolution rate also increases. The viscosity of the SiO<sub>2</sub>-rich slag is therefore expected to decrease rapidly in contact with the CaO. The CaO concentration in the slag collected in the lower parts of the furnace is ~20-40%, and for the tapped slag ~15-40% at the Elkem Thamshavn, ~20-30% at the Furnace B, and ~20-40% for the normal slag at Finnfjord AS. During the sampling period at Finnfjord AS, there were certain periods lime was added together with the raw materials: 10<sup>th</sup> to 25<sup>th</sup> of February 2021, 19<sup>th</sup> to 27<sup>th</sup> of March 2021 and 15<sup>th</sup> of November to 5<sup>th</sup> of December 2021. These additions resulted in a generally higher CaO content around 35-37% for the slag collected the 12<sup>th</sup> and 14<sup>th</sup> of February 2021, the 9<sup>th</sup> of March 2021, and the 26<sup>th</sup> of November 2021. From the viscosity curves in Figure 161, it can be seen that by increasing the CaO concentration from 20-21% to 35-40%, the viscosity reduces from 13 Poise to 1 Poise for slag 1 and 3 at 1800 °C. In the lower parts of the furnace, where the temperature is around 2000 °C, the change in viscosity and its effect on the accumulated slag would be less significant. However, there may be situations where the temperature in the tapping area might be lower than normal. In these situations, the CaO concentration has a great effect on the viscosity, and a sufficient high level can prevent challenging conditions for the tapping operators.

The rate of dissolution of CaO into the SiO<sub>2</sub>-CaO-Al<sub>2</sub>O<sub>3</sub> slag is expected to be directly related to the saturation concentration. The further from saturation, the larger driving force for the solid CaO to dissolve in the slag. The saturation concentration for this dissolution reaction is the phase boundary line for the CaO phase in the SiO<sub>2</sub>-CaO-Al<sub>2</sub>O<sub>3</sub> ternary diagram, as shown in Figure 162. For slag 1, 2 and 3, the CaO boundary line is 69%, 66% and 70% CaO, respectively. However, the dissolution rate is also influenced by the temperature. In the oxide system, there are a liquidus and a solidus temperature, which means that there are temperature intervals where both liquid and solid phases will be present

in the system. This will also affect the dissolution rate. If the liquidus temperature falls below the experimental temperature during the dissolution path, solid particles will start to precipitate, and the dissolution rate also decreases due to higher viscosity. Figure 163 shows the liquidus and solidus temperatures for slag 1, 2 and 3 with increasing amount of CaO in the slag. The effect of the liquidus temperature is also seen in this study. Slag 2 has similar initial CaO concentration as slag 3, but significantly higher liquidus temperatures compared to slag 1 and 3. Slag 2 start to melt at 1385°C, while slag 1 and 3 begin at 1170 °C. The experimental temperatures at 1500 °C and 1550 °C are close to the initial liquidus temperatures. As more CaO dissolves into the slags, the liquidus temperature decreases for slag 1, 2 and 3, and are below 1500 °C until 39% CaO for slag 2, and until the  $2\text{CaO}\cdot\text{SiO}_2$  phase boundary line at 49% CaO for slag 1 and 3, marked in Figure 162. With a further increase of the CaO concentration from 39% for slag 2 and from 49% for slag 1 and 3, the liquidus temperatures also increases. This is expected to slow down the dissolution rate considerably. Görnerup and Wijk [139] did experiments to determine the saturation lines for  $\text{CaO}$ ,  $2\text{CaO}\cdot\text{SiO}_2$  and  $3\text{CaO}\cdot\text{SiO}_2$  in the  $\text{SiO}_2\text{-CaO-Al}_2\text{O}_3$  system at 1600 °C and 1700 °C. Slag mixtures close to saturation in contact with its saturation phase were heated until its liquidus temperatures and run until equilibrium, which at 1600 °C-1700 °C was around 6 hours. With lower experimental temperatures in this study, the time until equilibrium is expected to further increase.

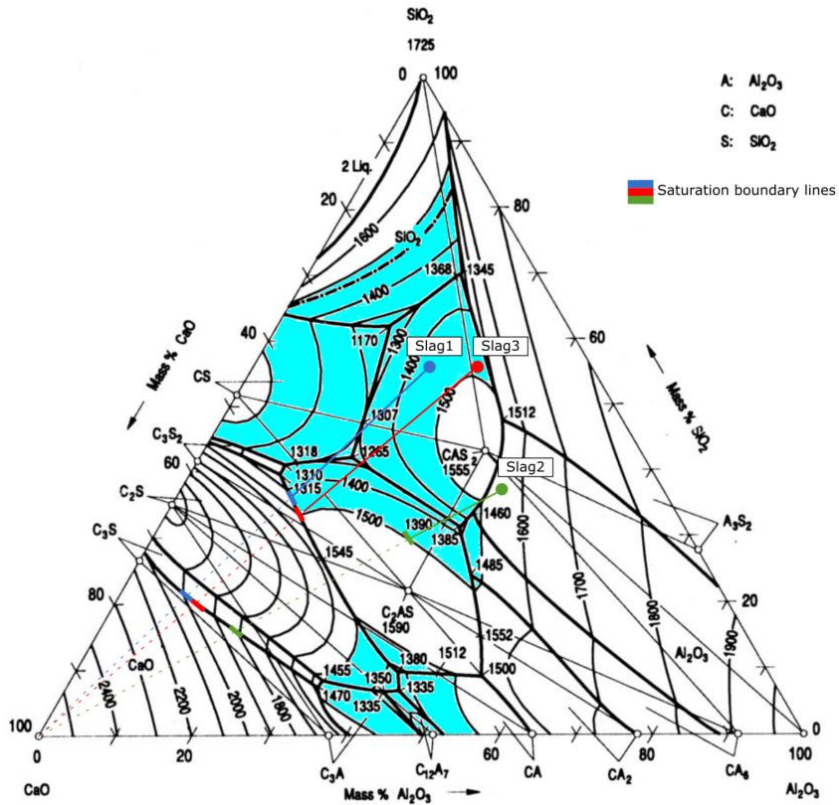


Figure 162 The  $\text{SiO}_2\text{-CaO-Al}_2\text{O}_3$  ternary phase diagram with 1500 °C liquidus area marked in bright blue. Slag 1, 2 and 3, their dissolution path and the two saturation concentration at the 1500 °C and the CaO phase boundary line are marked with blue, red and green.

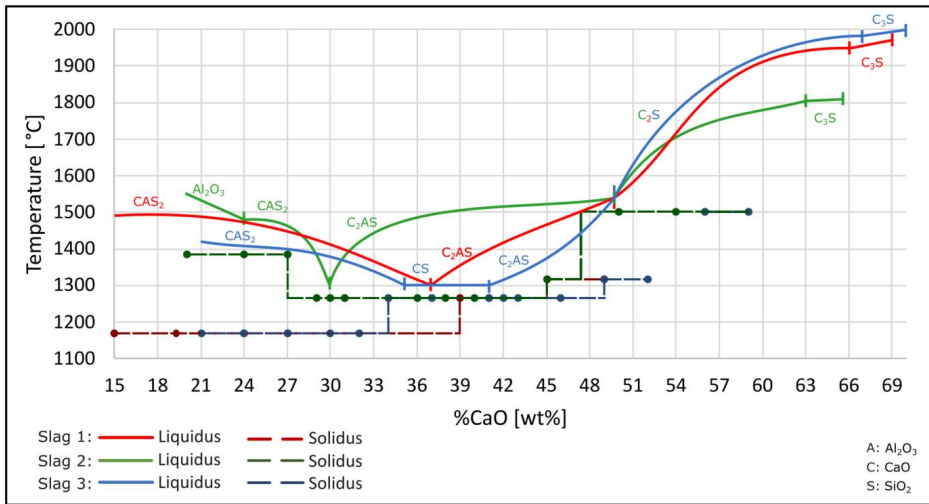


Figure 163 The liquidus and solidus temperature with increasing %CaO for Slag 1, 2 and 3. The temperatures are found from the  $\text{SiO}_2\text{-CaO-Al}_2\text{O}_3$  ternary phase diagram.

Also, in this study it was observed a layer with brighter color on the EPMA images around the CaO particle for both the 1500 °C and 1550 °C experiments, as are highlighted between the red lines in Figure 164. A  $2\text{CaO}\cdot\text{SiO}_2$  or  $3\text{CaO}\cdot\text{SiO}_2$  boundary layer next to the slag at the CaO-slag interface has earlier been found by several researchers [99]–[102]. However, the CaO concentration in these layers are between 35–42%, which is close to the 1500 °C liquidus line for slag 2 and somewhat lower than the  $2\text{CaO}\cdot\text{SiO}_2$  phase boundary line. The boundary layers are in this study is the  $\text{CaO}\cdot\text{Al}_2\text{O}_3\cdot 2\text{SiO}_2$  for slag 1 and  $2\text{CaO}\cdot\text{Al}_2\text{O}_3\cdot\text{SiO}_2$  for slag 2 and 3.

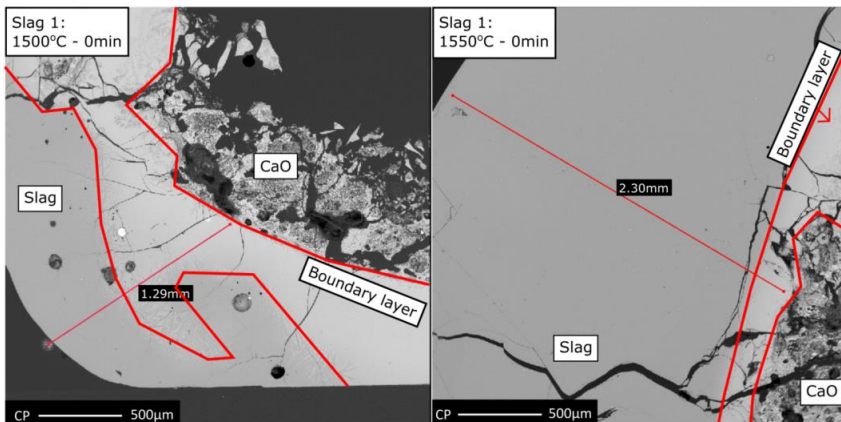


Figure 164 Cross-section images and EPMA images after experiments with CaO and slag 1 at 1500 °C (left) and 1550 °C (right) with zero minutes holding time. The red lines highlight the boundary layer between the CaO and the slag.

### 5.3.2 Modelling the dissolution rate of CaO in SiO<sub>2</sub>-CaO-Al<sub>2</sub>O<sub>3</sub> slag

This subchapter shows two models for the dissolution rates of CaO in slag 1, 2 and 3. The rate of a reaction gives the degree of conversion per unit time, and gives knowledge about the effect of adding CaCO<sub>3</sub> together with the raw materials in the Si and FeSi furnaces. In the first model, the CaO particle is assumed to be a shrinking smooth sphere and the rate controlled by the rate of chemical reaction. The second model assumes that the rate is controlled by the mass transport and depends on the diffusion rate of CaO through a boundary layer at the surface of the CaO. The basis for the models is the experimental dissolution curves shown in Figure 165, Figure 166 and Figure 167. The %CaO from outside the boundary layer are calculated by using the average slag concentrations, which are shown as the black, flat lines in the figures. The dissolution of CaO in SiO<sub>2</sub>-CaO-Al<sub>2</sub>O<sub>3</sub> slags has been studied by a wide range of researchers, i.e. [93], [99]–[104], [106] and it is found that the mass transfer in the slag is the rate determining step. Ions of Ca<sup>2+</sup> and O<sup>2-</sup> transfer through a 2CaO·SiO<sub>2</sub> or 3CaO·SiO<sub>2</sub> boundary layer next to slag at the CaO-slag interface. As the %CaO is not equal to the saturation CaO at the surface of the CaO particle, this is not the case here.

Most of the existing literature data on the dissolution rates and diffusivities are mostly related to the steel industry and includes CaO concentrations around 40%. The initial CaO content in the slag in Si and FeSi furnaces before addition of lime is expected to be lower, around 10-20%, which would increase the driving force of CaO mass transfer in the slag and hence increase the reaction rate.

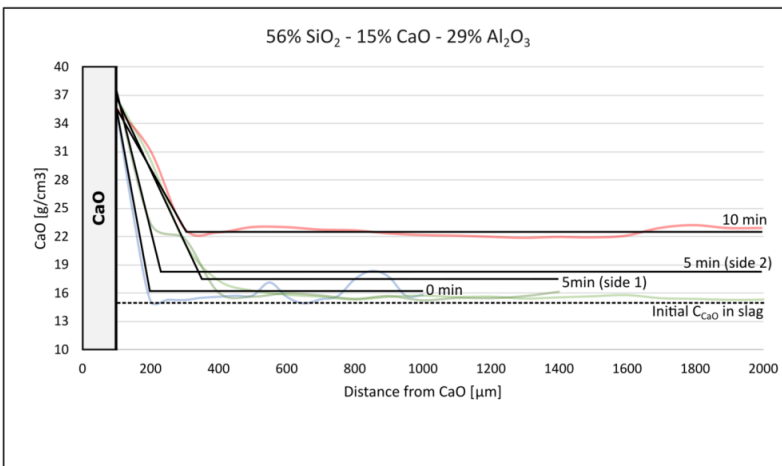


Figure 165 Dissolution curves for slag 1 for the experiments at 1500 °C with 0-, 5- and 10 minutes holding time.

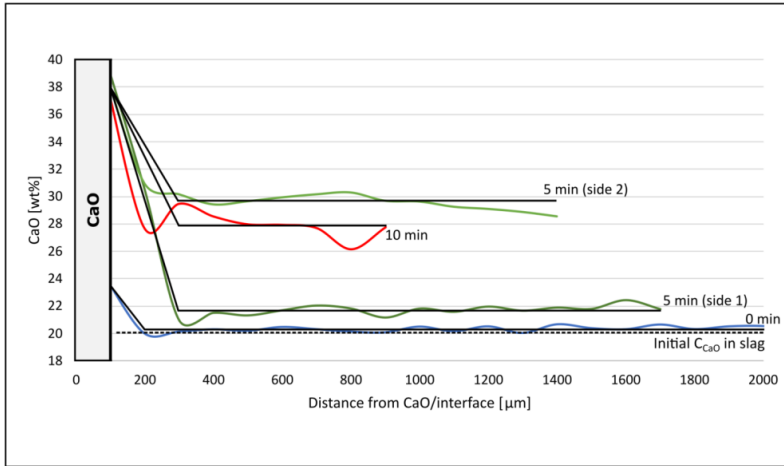


Figure 166 Dissolution curves for slag 2 for the experiments at 1500 °C with 0-, 5- and 10 minutes holding time.

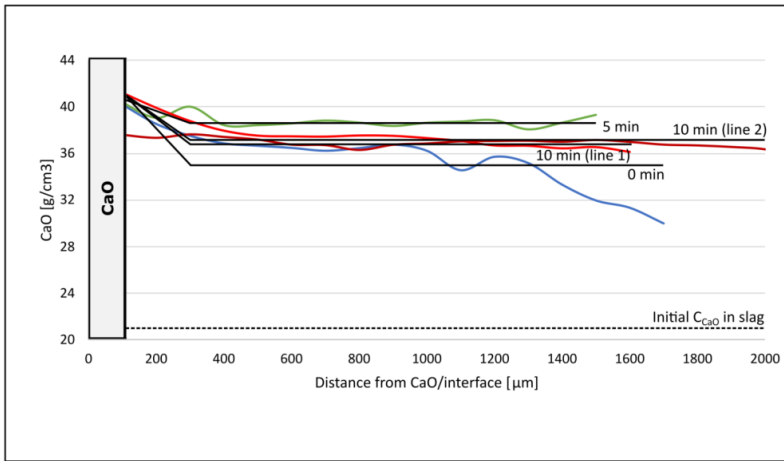


Figure 167 Dissolution curves for slag 3 for the experiments at 1500 °C with 0-, 5- and 10 minutes holding time.

### 5.3.2.1 Dissolution rate controlled by chemical reaction – shrinking sphere model

The shrinking sphere model describes the solid sphere CaO being consumed by dissolution into the liquid SiO<sub>2</sub>-CaO-Al<sub>2</sub>O<sub>3</sub> slag. A simple illustration of the process is shown in Figure 168. The rate depends on the rate of the surface reaction involving the breaking of the CaO network and is proportional to the CaO surface area. The dissolution rate expression is then as in equation 14 [98].

$$R = \frac{dC}{dt} V = k_1 A_0 \left(1 - \frac{V}{M_0} \Delta C\right)^{\frac{2}{3}} \quad 14$$

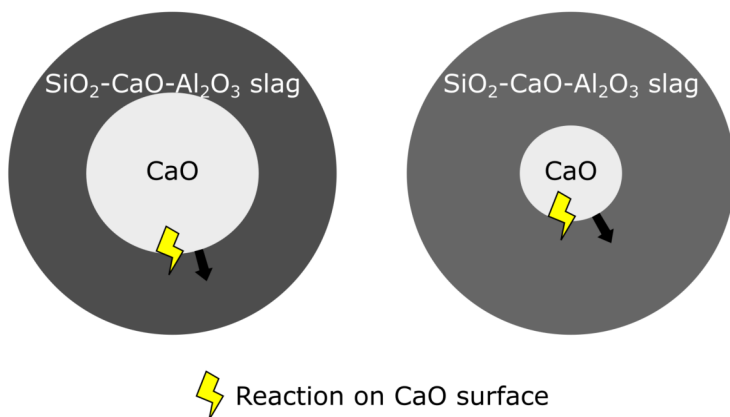


Figure 168 Schematic representation of the shrinking sphere model. The chemical reaction of CaO dissolving into the slag happens at the CaO particle surface and the reaction continues until the whole CaO particle is consumed.

The modelled dissolution rates using the shrinking sphere model together with the experimental results at 1500 °C for slag 1, 2 and 3 are shown in Figure 169, Figure 170 and Figure 171, respectively. The modelled rate equation is fitted to the experimental data by using the Solver function in Excel, to obtain an optimal value of the rate constant,  $k_1$ . The rate data which were found to be the best fit from this model are listed in Table 44. The rate constants are in the order  $10^{-5}$ - $10^{-4}$  g/s·cm<sup>2</sup>. Slag 3 is found to have the highest dissolution rate constant and slag 2 the lowest.

Table 44 Rate data obtained from shrinking sphere model.  $k_1$  is the rate constant in the dissolution rate equation given in g/s·cm<sup>2</sup>.

Slag (SiO <sub>2</sub> -CaO-Al <sub>2</sub> O <sub>3</sub> ) [wt%]	$k_1$ [g/s·cm <sup>2</sup> ]
1: 56-15-29	$1.2 \cdot 10^{-4}$
2: 38-20-42	$9.0 \cdot 10^{-5}$
3: 56-21-23	$2.9 \cdot 10^{-4}$

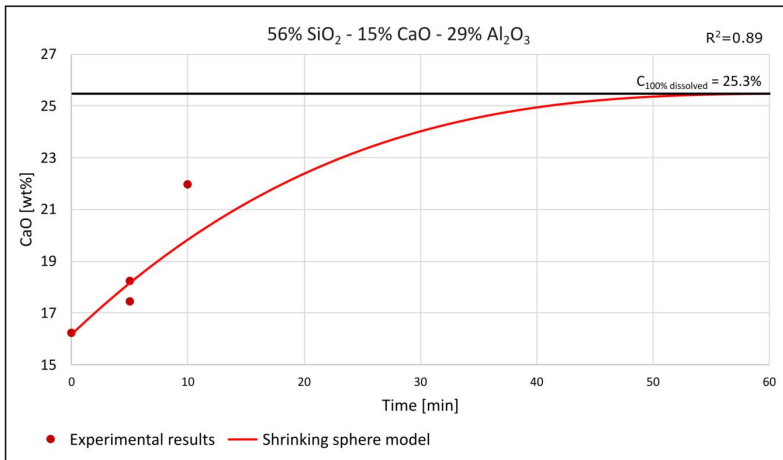


Figure 169 Modelled dissolution rate curve using the shrinking sphere model and the experimental results for slag 1 at 1500 °C. R gives the correlation error.

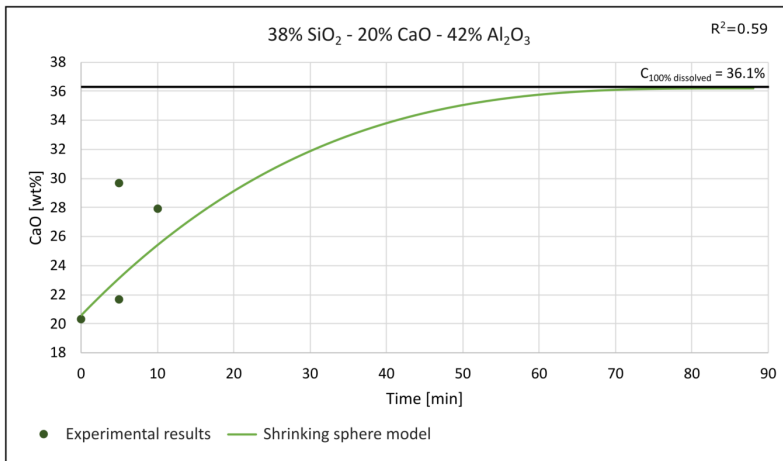


Figure 170 Modelled dissolution rate curve using the shrinking sphere model and the experimental results for slag 2 at 1500 °C. R gives the correlation error.

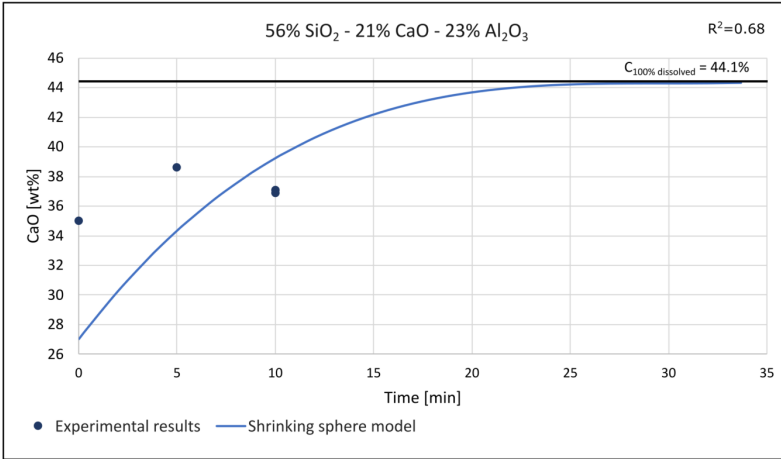


Figure 171 Modelled dissolution rate curve using the shrinking sphere model and the experimental results for slag 3 at 1500 °C.  $R$  gives the correlation error.

### 5.3.2.2 Dissolution rate controlled by mass transfer of CaO

In addition to the rate constant and the surface area, the second model takes into account the diffusion of dissolved CaO away from the solid CaO into the slag. A simple illustration of the process is shown in Figure 172. It is assumed that the diffusion is one dimensional through a constant thick boundary layer, which is also constant with respect to the CaO particle size. The driving force for this diffusion is the concentration difference in dissolved CaO between that at the surface of the CaO, which is the saturated concentration, and that of the bulk of the SiO<sub>2</sub>-CaO-Al<sub>2</sub>O<sub>3</sub> slag. The dissolution rate can then be expressed as in equation 18 [97].

$$R = \frac{dc}{dt} V = k_2 A (C_{sat} - C) = k_2 A_0 \left(1 - \frac{V}{M_0} \Delta C\right)^{\frac{2}{3}} (\Delta C_{sat} - \Delta C) \quad 18$$

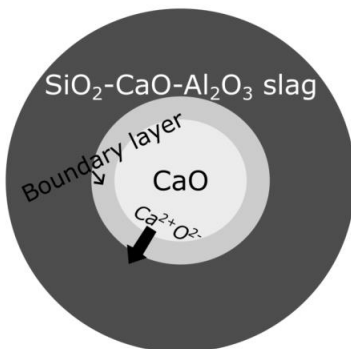


Figure 172 Schematic representation of dissolution of CaO into SiO<sub>2</sub>-CaO-Al<sub>2</sub>O<sub>3</sub> slag by mass transport control. The process involves transport of ions through a constant thick boundary layer around the CaO particle into the slag.



Equation 18 is solved numerically in MATLAB R2022a using the ode45 method. Ode45 uses the Runge-Kutta method to find the solution, which is an effective and widely used method for solving the initial-value problems of differential equations [140]. The modelled dissolution curves for slag 1, 2 and 3 together with the experimental results at 1500 °C can be seen in Figure 173, Figure 174 and Figure 175, respectively. The rate data which were found to be the best fit from this model are presented in Table 45. Similar as for the shrinking sphere,  $R_{\text{slag 1}} > R_{\text{slag 3}} > R_{\text{slag 2}}$ .

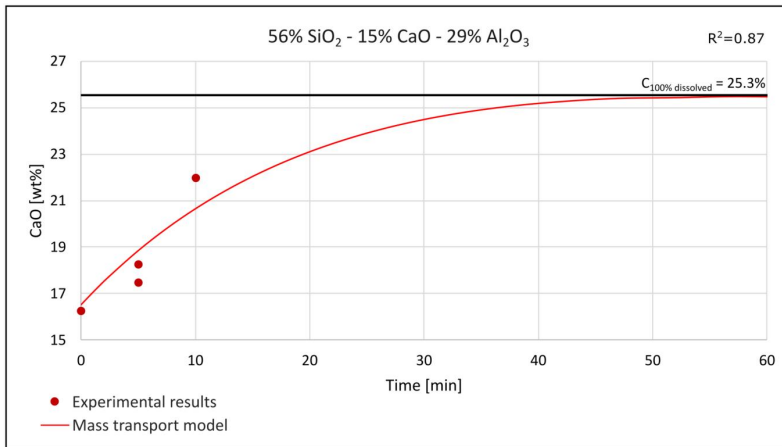


Figure 173 Modelled dissolution rate curve using mass transport model and the experimental results for slag 1 at 1500 °C. The R<sup>2</sup> number gives the correlation error.

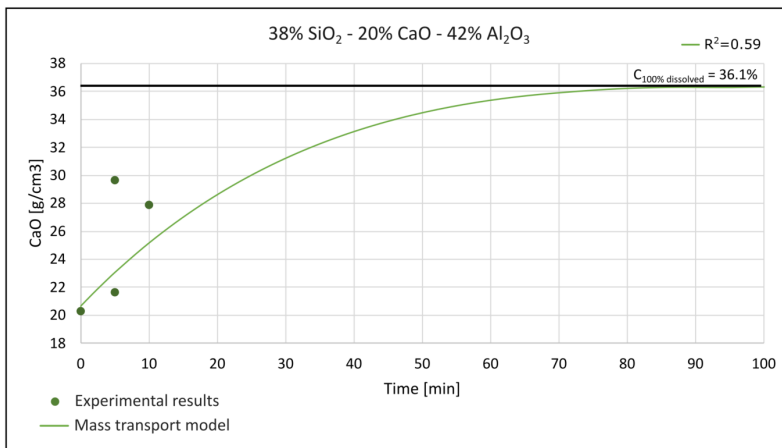


Figure 174 Modelled dissolution rate curve using mass transport model and the experimental results for slag 2 at 1500 °C. The R<sup>2</sup> number gives the correlation error.

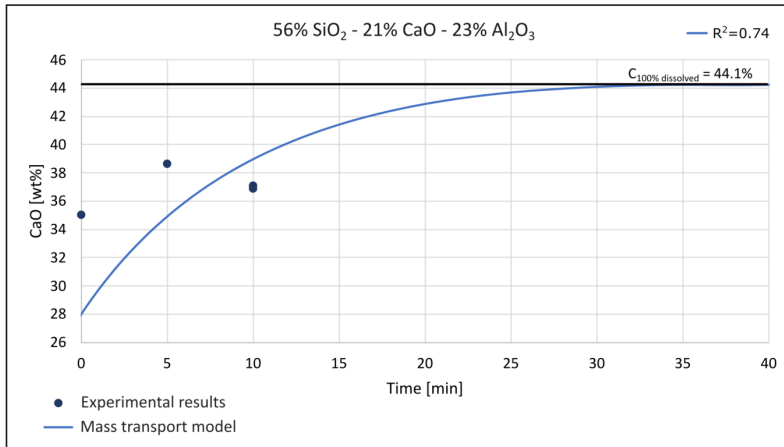


Figure 175 Modelled dissolution rate curve using mass transport model and the experimental results for slag 3 at 1500 °C. The  $R^2$  number gives the correlation error.

Table 45 Rate data obtained from the mass transport model.  $k_2$  is the rate constant in the dissolution rate equation given in cm/s using the 1500 °C liquidus as the saturation concentration.

Slag	$k_2$ [cm/s]	D [cm <sup>2</sup> /s]
1	$5.5 \cdot 10^{-5}$	$1.7 \cdot 10^{-6}$
2	$4.0 \cdot 10^{-5}$	$1.2 \cdot 10^{-6}$
3	$1.4 \cdot 10^{-4}$	$4.2 \cdot 10^{-6}$

The diffusion coefficient, D describes the amount of CaO that diffuses per time unit and can be found from relationship between the rate data and the boundary layer thickness,  $\delta$  through equation 21 [97]. The boundary layer in this case is the CaO·Al<sub>2</sub>O<sub>3</sub>·2SiO<sub>2</sub> for slag 1 and 2CaO·Al<sub>2</sub>O<sub>3</sub>·SiO<sub>2</sub> for slag 2 and 3 layers, which is found outside the remaining CaO particle. The boundary layer thickness is assumed to be constant 0.3 mm for all three slags.

$$k_2 = \frac{D}{\delta} \quad 21$$

The diffusion constants for the three slag compositions are presented in Table 45 together with the rate data. They are found to be in the order of  $10^{-6}$  cm<sup>2</sup>/s, which is somewhat higher than literature data for similar slags. Liang et al. [112] used the isotope tracer method and found the diffusion coefficients for 65% SiO<sub>2</sub> – 20% CaO – 15% Al<sub>2</sub>O<sub>3</sub> to be  $3.3 \cdot 10^{-7}$  cm<sup>2</sup>/s and for 60% SiO<sub>2</sub> – 20% CaO – 20% Al<sub>2</sub>O<sub>3</sub> to be  $3.66 \cdot 10^{-7}$  cm<sup>2</sup>/s at 1500 °C. In these experiments, the diffusion coefficient for slag 3, which has the most similar composition 56% SiO<sub>2</sub> – 21% CaO – 23% Al<sub>2</sub>O<sub>3</sub>, is found to be  $5.7 \cdot 10^{-6}$  cm<sup>2</sup>/s. For the most studied composition 40% SiO<sub>2</sub> – 40% CaO – 20% Al<sub>2</sub>O<sub>3</sub>, the diffusion coefficients at 1500 °C are  $1.34 \cdot 10^{-6}$  cm<sup>2</sup>/s [112] and  $2.6 \cdot 10^{-6}$  cm<sup>2</sup>/s [111]. The last case is calculated from the Nernst-Einstein relation. At lower temperatures it is found to vary between  $1.6 \cdot 10^{-6}$ – $1.3 \cdot 10^{-7}$  cm<sup>2</sup>/s

[107]–[111], [113]. This slag composition is on the same dissolution path as for slag 1, 56% SiO<sub>2</sub> – 15% CaO – 29% Al<sub>2</sub>O<sub>3</sub>, where the diffusion coefficient was found to be in the same order, at 10<sup>-6</sup> cm<sup>2</sup>/s.

The diffusion coefficient is often found to be proportional with the viscosity,  $\eta$ , as derived from both Stokes-Einstein [25] and Eyring [118] equations for diffusivity. The calculated viscosities for slag 1, 2 and 3 at 1500 °C using FactSage 8.1 are 456 Poise, 82 Poise and 180 Poise, respectively. However, this model does not consider solid particles in the slag. The liquidus temperature of slag 2 is 1550 °C, which means that presence of solid particles in the melt increases the viscosity considerably. It is therefore assumed that slag 2 has the highest viscosity, and hence  $\eta_{\text{slag2}} > \eta_{\text{slag1}} > \eta_{\text{slag3}}$ . This is consistent with  $k_{\text{slag3}} > k_{\text{slag1}} > k_{\text{slag2}}$ .

### 5.3.2.3 Evaluation of the dissolution mechanisms

Theoretically, a reaction can be controlled by the rate of the chemical reaction, by mass transfer or a mix of both factors. From the experimental dissolution curves presented earlier, it is found that in this study, the dissolution process is a mix, as illustrated in Figure 176. Models based on either chemical or mass transfer control will therefore have some deviation from the actual dissolution rate curves. However, both models show similar results, and it is therefore assumed that the models are an acceptable approximation.

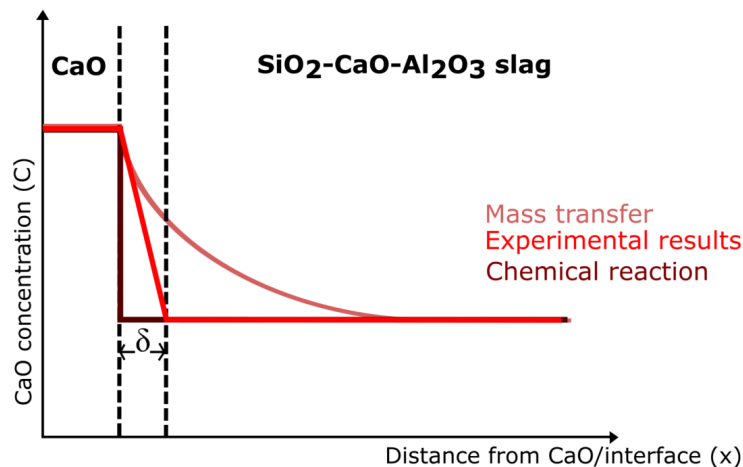


Figure 176 Schematic illustration of mass transfer kinetic control or chemical reaction being the rate determining step for CaO dissolution in liquid SiO<sub>2</sub>-CaO-Al<sub>2</sub>O<sub>3</sub> slag. The red curve gives the experimental results in this study, which is a mix.

Both models for the dissolution rates found similar curves for dissolution. However, the models are based on small amounts of CaO and slag, <5 g, whereas in Si and FeSi production, CaCO<sub>3</sub> is added as lumps with sizes up to 2-3 cm radius. Figure 177 presents upscaled modelled results using the mass transport model, where 250 g of CaO is added to

1 kg of slag. The results show that slag 3 uses 10 h, slag 1 uses 15 h, and slag 2 uses 30 h until the CaO lump is dissolved. In the industrial furnace, it is assumed the particles will remain in the furnace for around 8-12 h, which means that particles of this size will not dissolve completely at 1500 °C for slag 1 and 3. However, it is likely that the CaO will disintegrate into smaller particles in the furnace, as observed through the poor mechanical strength of CaO in compression strength tests and the disintegration of the CaO during heating in the graphite tube furnace. With smaller particle sizes, the CaO will dissolve faster in the slag. CaO is rarely found during excavations. Therefore, it is likely that the CaCO<sub>3</sub> added to the furnace at an early stage will calcine and disintegrate to smaller fractions. These smaller fractions of CaO will then likely have sufficient time in the furnace to dissolve completely.

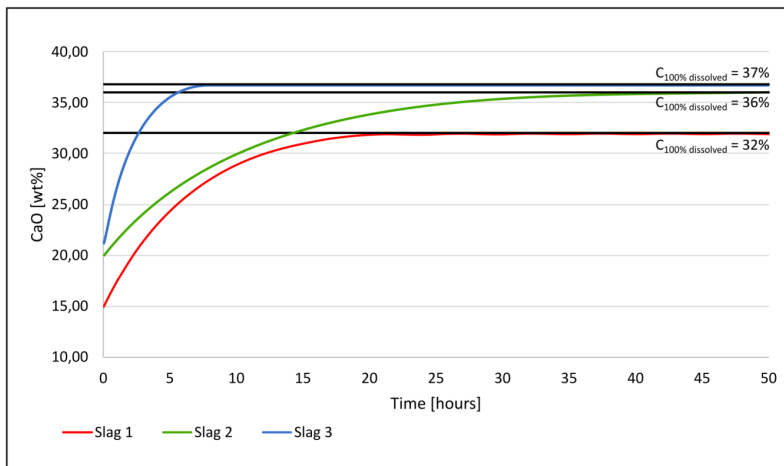


Figure 177 Upscaled modelled dissolution curves using the mass transport model. 250 g CaO are added to 1 kg slag.

### 5.3.3 Effect of temperature

The temperature dependence for the dissolution of CaO into SiO<sub>2</sub>-CaO-Al<sub>2</sub>O<sub>3</sub> slag is assumed to be expressed by the Arrhenius equation as in equation 31.

$$D = D_0 \exp\left(\frac{E_a}{RT}\right) \quad 31$$

Where D is the diffusivity, D<sub>0</sub> is a constant for the given solute and is independent of temperature, E<sub>a</sub> is the activation energy, R is the universal gas constant and T is the temperature.

From this expression, an increased temperature is expected to increase the diffusivity and hence also the dissolution rate. Increased dissolution was observed in this study for all three

slag compositions for the experiments in the sessile drop furnace at 1500 °C and 1550 °C. Figure 178 compares the EPMA images of cross sections after dissolution experiments of slag 3 and CaO at both 1500 °C and 1550 °C with 0- and 10 minutes holding time. At 1500 °C there is still remaining CaO and a concentration gradient through the boundary layer for both the 0 minutes and 10 minutes experiments, which is the two top images in the figure. At 1550 °C – 0 minutes, both the measured oxide compositions and the EPMA images are similar with the 1500 °C – 0 minutes experiment. However, after 10 minutes at 1550 °C there is no remaining CaO nor a concentration gradient in the final slag solution. A pore can be observed down to the right in the EPMA image, the bottom right image in the figure. This is assumed to be gas trapped during the melting process. The final slag composition also confirms a homogenous slag and that the CaO particle has dissolved 100%.

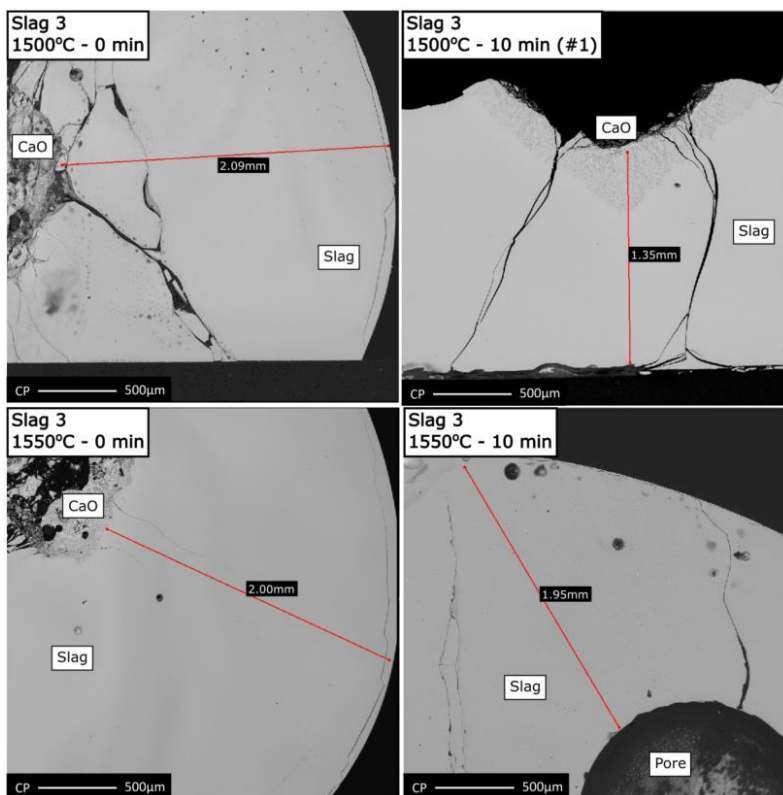


Figure 178 EPMA images of cross section after dissolution experiments of slag 3 and CaO at both 1500 °C and 1550 °C with 0- and 10 minutes holding time.



## Chapter 6: Conclusions and future work

The main focus of this study has been to increase the knowledge about the slag in the Si and FeSi furnaces. This has been done by looking at and analyzing a number of different slag samples collected from different parts of the industrial furnaces during excavations. In addition, several samples are collected from tapping slag and from the charge surface during operation. The behaviour of the impurities in the quartz, which contributes to the slag formation in the furnace, the SiO<sub>2</sub> disintegration and the melting behaviour of SiO<sub>2</sub> have been studied for six different quartz types in both a sessile drop furnace and in a high temperature confocal microscope (HTCM). In addition, the dissolution of CaO in SiO<sub>2</sub>-CaO-Al<sub>2</sub>O<sub>3</sub> slag has been investigated through experiments in both a graphite tube furnace and a sessile drop furnace, and the results characterized with EPMA, WDS, elemental mapping and CT.

### 6.1 Slags in different parts of the furnace

Slag from different zones in six different Si and FeSi furnaces collected during excavations, tapped slag from three different furnaces and slag from the charge surface of two FeSi furnaces during operation are the basis for these conclusions. It is found that slag accumulates typically along the furnace walls, sometimes all the way up to the charge top, and in a thick layer at the furnace bottom, together with the metal and SiC. The slag mainly consists of SiO<sub>2</sub>, CaO and Al<sub>2</sub>O<sub>3</sub>. In the accumulated slag samples, it is found that the slag towards the furnace wall in the higher parts generally has a higher SiO<sub>2</sub> content than the slag accumulated at the furnace bottom. The CaO/Al<sub>2</sub>O<sub>3</sub> relation is approximately the same for all slags within the same furnace. The possible explanations for the existent of slag and the increased SiO<sub>2</sub> content in the slag suggested in this study are either by a high crater pressure that pushes the slag towards the furnace walls and then upwards, or by a higher temperature in the inactive zone than expected.

It is also found that the metal tapping channel passes through a thick layer of slag before it enters the tap-hole. Additionally, the slag above the tapping channel in this area has a higher SiO<sub>2</sub> content compared to the slag below it. This difference is believed to be due to varying densities, where slags with higher SiO<sub>2</sub> content have lower densities, or it may be influenced by the higher viscosity of the slag with an increased SiO<sub>2</sub> content. No difference in slag composition were found between the different tap-holes in the same furnace. Visually, the zones around the tap-holes look similar. Next to the metallic Si is 5-15 cm bright green layer which consists of mainly SiO<sub>2</sub>-CaO-Al<sub>2</sub>O<sub>3</sub> slag and smaller SiC particles, and then a dark grey layer that is mainly SiO<sub>2</sub>-CaO-Al<sub>2</sub>O<sub>3</sub> slag and larger SiC particles. The green and grey color seem to be dependent on the size of the SiC particles, and not the composition of the slag.

In almost all the accumulated slag samples and the tapped slag samples, it was found presence of SiC particles. Significantly higher amounts of SiC were observed in the

accumulated slag compared with the tapped slag, including the high-viscosity slag. The increased amount of SiC in the accumulated slag increases the viscosity considerably, making it more difficult to drain during tapping. Furthermore, at sufficient high temperatures, the SiO<sub>2</sub> in the slag may also react with the SiC and form SiO and CO gas, or CO gas and Si.

Most of the slag from the charge surface have alkali and alkaline earth oxide content >5%, and traces of these were also found in some of the samples from the inactive zone and in the tapped slag samples. This indicates that silicon and ferrosilicon furnaces have alkali circulations.

All of the tapped slag were found to be liquid during tapping at a temperature of 1800 °C, with solid SiC particles. The main difference between the normal tapped slag and the slag reported as high-viscosity slag is the increased amount of SiO<sub>2</sub> in the slag, and the presence of SiO<sub>2</sub> and condensates in the samples. The amount of slag, the amount of solid SiC in the liquid slag and the viscosity of the slag are three of the main factors that influences the flow of slag through the tap-hole.

Brown condensates formed from SiO gas and white condensates from SiO and CO gas were found in one sample from the higher, inactive part of the furnace and in the charge top samples, where it is expected to find condensates. However, condensates were also found in some of the samples close to the tapping channel and in several of the tapped slag samples reported as high-viscosity slag, where the temperature is believed to be too high for condensation formation. This is therefore believed to be slag that has descended from above the tapping area in layer along the furnace wall, where the temperature is lower.

## **6.2 Impurities and properties in SiO<sub>2</sub> affecting the Si and FeSi furnaces**

The impurity behaviour and the properties of six different quartz types; A, B, C, D, F and G, suited for Si and FeSi production were studied during heating to 1600 °C, 1750 °C and 1800 °C. It is found that an increased amount of impurities in the quartz lowers the softening and melting temperature. It is also found that SiO<sub>2</sub> dissolves in the impurities as the temperature increases. The impurities in the SiO<sub>2</sub> will contribute to the slag formation in Si and FeSi furnaces. In several of the charge surface samples from Finnfjord AS it was found slag together with the SiO<sub>2</sub>. Some of the SiO<sub>2</sub> dissolves in the impurities accumulated in the grain boundaries and cracks and forms a separate slag phase with an increased amount of SiO<sub>2</sub> next to the melted SiO<sub>2</sub>. This slag phase has a higher liquidus temperature than the expected charge surface temperature.

The disintegration of SiO<sub>2</sub> were studied and it is found that crack formation mainly happens at two temperature intervals, ~300-600 °C and ~1300-1600 °C. The degree of cracking is also found to be different between the different quartz types. The crack formation from 300 °C is from an uneven SiO<sub>2</sub> surface, from activity in form of volume change or color change in the impurity areas, or from fluid inclusion cavities, while the cracks occurring from 1300 °C is believed to be due to the volume increase and the phase transformations from quartz



to cristobalite. When comparing the crack formation with the fines formation [9], no trend could be found. This supports that there are more factors than cracking which contributes to the fines formation. No correlation could be found between the impurity composition and the crack formation. Most of the impurities in this study contain  $\text{Al}_2\text{O}_3$ , which were found to induce different degree of cracking.

### 6.3 CaO dissolution in $\text{SiO}_2$ -CaO- $\text{Al}_2\text{O}_3$ slags

The dissolution of CaO in three different compositions of  $\text{SiO}_2$ -CaO- $\text{Al}_2\text{O}_3$  slag similar as in the Si and FeSi furnaces were investigated through experiments up to 1600 °C.

Slag 1: 56%  $\text{SiO}_2$  – 15% CaO – 29%  $\text{Al}_2\text{O}_3$

Slag 2: 38%  $\text{SiO}_2$  – 20% CaO – 42%  $\text{Al}_2\text{O}_3$

Slag 3: 56%  $\text{SiO}_2$  – 21% CaO – 23%  $\text{Al}_2\text{O}_3$

It is found that the initial CaO disintegrate during heating before it dissolves in the slag. The dissolution reaction between CaO and the slag in this study were found to start between 1300-1400 °C. During the dissolution process, a boundary layer with 35-42% CaO is formed between the CaO particle and the slag, which for slag 1 correspond to  $\text{CaO}\cdot\text{Al}_2\text{O}_3\cdot 2\text{SiO}_2$ , and  $2\text{CaO}\cdot\text{Al}_2\text{O}_3\cdot\text{SiO}_2$  for slag 2 and 3. This is different from earlier research [99]–[102], which has found a  $2\text{CaO}\cdot\text{SiO}_2$  or  $3\text{CaO}\cdot\text{SiO}_2$  boundary layer next to the slag at the CaO-slag interface.

It is also found that the initial effect of increasing the CaO content in the slag from 15-21% to 25-30% gives a significant reduction in the viscosity.

Two models for the dissolution rate for the three slags in this study were made. In the first model, the CaO particle is assumed to be a smooth shrinking sphere, and the rate controlled by the rate of chemical reaction. The second model assumes that the rate is controlled by the mass transport and depends on the diffusion rate of CaO through a boundary layer at the surface of the CaO. In both models it was found that  $k_{\text{slag } 3} > k_{\text{slag } 1} > k_{\text{slag } 2}$ , which is consistent with the proportional relationship with viscosities. The diffusion coefficients are found to be in the range of  $10^{-6} \text{ cm}^2/\text{s}$ .

Based on the model, it is found that particles of 250g CaO added to 1kg slag would use 15h to dissolve in slag 1, 30h in slag 2 and 10h in slag 3. In the industrial furnace, it is assumed the particles will remain in the furnace for approximately 8-12h, which implies that particles of this size will not fully dissolve at 1500 °C for slag 1 and 3. However, it is likely that the  $\text{CaCO}_3$  added to the furnace at an early stage will calcine and disintegrate into smaller fractions. Smaller fractions of CaO will then most likely have sufficient time in the furnace to dissolve completely.

## 6.4 Future work

To further investigate and gain knowledge about the slag and how it affects the Si and FeSi furnace operation, one could look at the following topics:

- Alkalis and alkaline earth metal have been found in the slag, both in the inactive zone and to some extent in the tapped slag samples. Na, K, Mn, Mg and BaO are all common impurities in the quartz. Previously, it was assumed that these would leave with the off-gas. The discovery of alkalis and alkaline earth metal in the slag raises questions about whether there are alkali circulations in the furnace, which has also been discussed in Mn-ferroalloy furnaces and blast furnaces. However, there are still several samples that have been found without any content of these, so further research is needed to answer this.
- The discovery of slag in the higher, inactive zone of the furnace and on the charge surface is not expected, and further research is necessary to determine the cause of this. In this study, a high pressure in the crater has been proposed as the most likely cause, pushing the slag towards the furnace walls and then upwards. Simulations on how different crater pressures affect the mass flow, including the slag, in the furnace would be interesting. This would help determine if it is possible to generate enough pressure to push the slag all the way to the charge top. Another possible option that has been suggested includes formation of slag in the inactive zone. However, this assumes that the temperature in the inactive zone is sufficient high to facilitate slag formation. If so, more research is needed to identify the reason(s) that causes the elevated temperatures.
- Slag is almost always found together with SiC particles in the industrial slag samples. Solid particles of SiC in the liquid slag would increase the viscosity considerably and the slag would easier accumulate. More research on how SiC and slag behave and react at elevated temperature would give more answers on the mechanisms in the furnace.
- It is found that slag initiates from grain boundaries and cracks in the SiO<sub>2</sub>, and there is often a slag phase next to the SiO<sub>2</sub>. This slag often contains FeO and other typical impurities from the quartz. For further research, it would be interesting to investigate the subsequent formation of slag. There is a higher amount of slag found than what the impurities in the quartz suggest. More research with SiO<sub>2</sub> together with K<sub>2</sub>O, Al<sub>2</sub>O<sub>3</sub>, CaO and/or other typical impurities at higher temperatures, with focus on slag formation and how the slag behaves next to the SiO<sub>2</sub>, could be interesting.
- It is found that the dissolution of CaO into SiO<sub>2</sub>-CaO-Al<sub>2</sub>O<sub>3</sub> slags with CaO concentrations from 15-21% is fast. The existing literature today on CaO dissolution is related to the steel industry. For further research customized for the Si and FeSi production it is suggested to do more experiments to confirm the results

in this study, and to further test for more slag compositions similar to those in the Si and FeSi furnaces.

- It is also found that the dissolution rate of CaO in the  $\text{SiO}_2\text{-CaO-Al}_2\text{O}_3$  slag is controlled by both chemical reaction and mass transport. For further modelling of the dissolution rate, a model that considers both these mechanisms should be developed.



## References

- [1] “Silicon metalloid | What is silicon?,” *Elkem.com*. <https://www.elkem.com/products/silicon/silicon-metalloid/> (accessed Jun. 20, 2023).
- [2] I. Kero, S. Grådahl, and G. Tranell, “Airborne Emissions from Si/FeSi Production,” 2016, doi: 10.1007/s11837-016-2149-x.
- [3] S. T. Johansen, H. Tveit, S. Grådahl, A. Valderhaug, and J. Å. Byberg, “Environmental aspects of Ferro-Silicon furnace operations - an investigation of waste gas dynamics,” presented at the INFACON VIII, Beijing, 1998.
- [4] M. Ksiazek, S. Grådahl, E. A. Rotevant, and B. Wittgens, “Capturing and Condensation of SiO Gas From Industrial Si Furnace,” in *Advances in Molten Slags, Fluxes, and Salts: Proceedings of the 10th International Conference on Molten Slags, Fluxes, and Salts*, John Wiley & Sons, 2016, pp. 1153–1160.
- [5] A. Schei, J. Kr. Tuset, and H. Tveit, *Production of High Silicon Alloy*. Trondheim: Tapir, 1998.
- [6] M. Tangstad, M. Ksiazek, and J. E. Andersen, “Zones and Materials in the Si Furnace,” *Silicon Chem. Sol. Ind. XII*, 2014.
- [7] G. Tranell, M. Andersson, E. Ringdalen, O. Ostrovski, and J. J. Steinmo, “REACTION ZONES IN A FeSi75 FURNACE – RESULTS FROM AN INDUSTRIAL EXCAVATION,” p. 8, 2010.
- [8] M. Ksiazek, M. Tangstad, and E. Ringdalen, “Five furnaces five different stories,” *Silicon Chem. Sol. Ind. XIII*, pp. 33–42, 2013.
- [9] K. F. Jusnes, “Phase transformations and thermal degradation in industrial quartz,” Thesis for the degree of Philosophiae Doctor, Norwegian University of Science and Technology, Department of Materials Science and Engineering, Department of Materials Science and Engineering, Trondheim, 2020.
- [10] M. Ksiazek, “Report: Excavation of Si furnace at Elkem Salten,” Trondheim, SINTEF report 2018:00692, 2018.
- [11] M. Ksiazek, M. Tangstad, and E. Ringdalen, “The rapid Si-furnace excavation - an unique chance to investigate the interior of the furnace,” presented at the INFACON XV, Cape Town, 2018.
- [12] I. T. Zherdev, D. P. Moskovtsev, and I. I. Polyakov, “Dimensions of the gas spaces in ferrosilicon furnaces,” *Stal*, vol. 8, pp. 716–717, 1965.
- [13] I. T. Zherdev, I. I. Polyakov, V. E. Semenov, I. I. Barashkin, D. P. Moskovtsev, and E. S. Yas’kov, “Critical rate for rotation for ferrosilicon furnace baths,” *Stal*, pp. 406–408, 1968.
- [14] Y. Otani, M. Saito, K. Usui, and N. Chino, “The inner structure of the submerged arc furnace,” presented at the The International Congress on electro-heat, Brighton, 1968.
- [15] A. Schei and O. Sandberg, “Back reactions during production of silicon metal in a submerged arc electric furnace,” *Sel. Top. High Temp. Chem.*, pp. 145–155, 1966.
- [16] A. Schei, “on the Chemistry of Ferrosilicon Production,” *Tidsskr. Kjemi Bergves. Metall.*, vol. 27, no. 8–9, pp. 152–158, 1967.
- [17] M. Tangstad, *Ferrosilicon and Silicon Technology, in Handbook of Ferroalloys*. Butterworth-Heinemann, 2013.
- [18] S. Jayakumari, “Formation and characterization of  $\beta$ - and  $\alpha$ -Silicon Carbide produced during Silicon/Ferrosilicon process,” Doctoral thesis, NTNU, 2020. Accessed: May 08, 2023. [Online]. Available: <https://ntnuopen.ntnu.no/ntnu-xmlui/handle/11250/2678922>

- [19] J. Nell and C. Joubert, "Phase Chemistry of Digout Samples from a Ferrosilicon Furnace," *INFACON XIII*, pp. 265–272, 2013.
- [20] M. Ksiazek, "An industrial Si furnace excavation – results and observations," Thamshavn, SINTEF Report, 2013.
- [21] S. M. Bø, "Phases and Zones in the Silicon Furnace," Master Thesis, Norwegian University of Science and Technology, Department of Materials Science and Engineering, 2016.
- [22] K. F. Jusnes, "SINTEF Report: Excavation of a FeSi75 furnace at Finnjord," 2018.
- [23] E. Myrhaug and H. Tveit, "Material Balances of Trace Elements in the Ferrosilicon and Silicon Processes," *Electr. Furn. Conf.*, vol. 58, pp. 591–606, 2000.
- [24] N. E. Kamfjord, "Mass and energy Balances of the Silicon Process," Thesis for the degree of Philosophiae Doctor, Norwegian University of Science and Technology, Department of Materials Science and Engineering, Trondheim, 2012.
- [25] V. D. Eisenhüttenleute, *Slag Atlas*. Verlag Stahleisen, 1995.
- [26] E. Myrhaug, "KPN CONTROLLED TAPPING, Examples of conceptual models based on simplified comsol simulations," Industrial presentation from Elkem, KPN Controlled Tapping Meeting 05.03.2020 regarding Conceptual Models, NTNU, 2020.
- [27] T. Werner, "As-tapped liquid silicon temperatures.docx," Norwegian University of Science and Technology, Department of Materials Science and Engineering, 2019.
- [28] K. C. Mills, M. Hayashi, L. Wang, and T. Watanabe, "The Structure and Properties of Silicate Slags," in *Treatise on Process Metallurgy*, Elsevier, 2014, pp. 149–286. doi: 10.1016/B978-0-08-096986-2.00008-4.
- [29] S. Jaiker, "Effect of Oxygen to Silicon Ratio on the Viscosity of Metallurgical Slags," *ISIJ Int.*, vol. 45, pp. 1014–1018, 2005.
- [30] H. Mao, M. Hillert, M. Selleby, and B. Sundman, "Thermodynamic assessment of the CaO-Al<sub>2</sub>O<sub>3</sub>-SiO<sub>2</sub> system," *J. Am. Ceram. Soc. - J AMER CERAM SOC*, vol. 89, pp. 298–308, Jan. 2006, doi: 10.1111/j.1551-2916.2005.00698.x.
- [31] L. Coudurier, D. W. Hopkins, and I. Wilkomirsky, *Fundamentals of metallurgical processes*, vol. 27. Pergamon Press, 1985.
- [32] G. Urbain and M. Boiret, "Viscosities of liquid silicates," *Ironmak. Steelmak.*, vol. 17, no. 4, pp. 255–260, 1990.
- [33] G. Urbain, "Viscosity estimation of slags," *Steel Res.*, vol. 58, no. 3, pp. 111–116, 1987, doi: 10.1002/srin.198701513.
- [34] R. Zhang, Y. Min, Y. Wang, X. Zhao, J. X. Jia, and C. J. Liu, "Viscosity Estimation of Multicomponent Slags of the CaO–SiO<sub>2</sub>–Al<sub>2</sub>O<sub>3</sub>–Fe<sub>x</sub>O System Based on Microstructure Analysis," *Energy Fuels*, vol. 34, no. 7, pp. 8129–8138, Jul. 2020, doi: 10.1021/acs.energyfuels.0c00926.
- [35] K. C. Mills and S. Sridhar, "Viscosities of ironmaking and steelmaking slags," *Ironmak. Steelmak.*, vol. 26, pp. 262–268, 1999.
- [36] G.-H. Zhang, K.-C. Chou, and K. Mills, "Modelling Viscosities of CaO–MgO–Al<sub>2</sub>O<sub>3</sub>–SiO<sub>2</sub> Molten Slags," *ISIJ Int.*, vol. 52, no. 3, pp. 355–362, 2012, doi: 10.2355/isijinternational.52.355.
- [37] K. Tang, S. Gouttebroze, X. Ma, and C. van der Eijk, "Representation of the Multiphysical Properties of SiO<sub>2</sub>-Al<sub>2</sub>O<sub>3</sub>-CaO Slags by Deep Neural Networks," in *Proceedings of the 16th International Ferro-Alloys Congress*, Trondheim, 2021.
- [38] K. Tang, C. van der Eijk, Q. Du, S. Gouttebroze, and J. Safarian, "Rheological Properties of Ternary SiO<sub>2</sub>-CaO-Al<sub>2</sub>O<sub>3</sub> Silicate System," in *The 11th Molten Slags, Fluxes and Salts*, 2020.

- [39] A. D. Pelton and P. Chartrand, "The modified quasi-chemical model: Part II. Multicomponent solutions," *Metall. Mater. Trans. A*, vol. 32, no. 6, pp. 1355–1360, Jun. 2001, doi: 10.1007/s11661-001-0226-3.
- [40] M. J. Assael, I. J. Armyra, J. Brillo, S. V. Stankus, J. Wu, and W. A. Wakeham, "Reference Data for the Density and Viscosity of Liquid Cadmium, Cobalt, Gallium, Indium, Mercury, Silicon, Thallium, and Zinc," *J. Phys. Chem. Ref. Data*, vol. 41, no. 3, p. 033101, Sep. 2012, doi: 10.1063/1.4729873.
- [41] J. Xin, L. Gan, L. Jiao, and C. Lai, "Accurate Density Calculation for Molten Slags in SiO<sub>2</sub>–Al<sub>2</sub>O<sub>3</sub>–CaO–MgO Systems," *ISIJ Int.*, vol. 57, no. 8, pp. 1340–1349, 2017, doi: 10.2355/isijinternational.ISIJINT-2017-070.
- [42] J. S. Vermaak, C. W. Mays, and D. Kuhlmann-Wilsdorf, "On surface stress and surface tension," *Surf. Sci.*, vol. 12, no. 2, pp. 128–133, 1968, doi: 10.1016/0039-6028(68)90118-0.
- [43] C. Dumay and A. W. Cramb, "Density and interfacial tension of liquid Fe-Si alloys," *Metall. Mater. Trans. B*, vol. 26, no. 1, pp. 173–176, Feb. 1995, doi: 10.1007/BF02648989.
- [44] K. F. Jusnes, R. Hjelmseth, M. B. Folstad, N. S. Ditlefsen, and M. Tangstad, "Investigation of slag compositions and possible relation to furnace operation of a FeSi75 furnace," presented at the INFACON, Trondheim, To be published 2021.
- [45] M. Ksiazek, "Knowledge from excavation Si-furnaces," presented at the Controlled Tapping Autumn meeting, Trondheim, 2018.
- [46] M. Ksiazek *et al.*, "Metal temperature measurements during tapping of fesi industrial furnace.," presented at the Furnace Tapping, Southern African Institute of Mining and Metallurgy, Kruger National Park: The Southern African Institute Of Mining And Metallurgy, 2018, p. 12.
- [47] A. Broggi, M. Tangstad, and E. Ringdalen, "Characterization of a Si-SiO<sub>2</sub> Mixture Generated from SiO(g) and CO(g)," *Metall. Mater. Trans. B*, vol. 50, no. 6, pp. 2667–2680, Dec. 2019, doi: 10.1007/s11663-019-01678-x.
- [48] E. Myrhaug, "Non-fossil reduction materials in the silicon process: properties and behavior," Thesis for the degree of Philosophiae Doctor, Norwegian University of Science and Technology, Department of Materials Science and Engineering, Trondheim, 2003.
- [49] S. Bernardis, "Engineering impurity behavior on the micron-scale in metallurgical-grade silicon production," Thesis, Massachusetts Institute of Technology, 2012. Accessed: Oct. 21, 2020. [Online]. Available: <https://dspace.mit.edu/handle/1721.1/101457>
- [50] E. D. Martello *et al.*, "Trace Elements in the Si Furnace. Part I: Behavior of Impurities in Quartz During Reduction," *Metall. Mater. Trans. B*, vol. 44, no. 2, p. 233, 2013.
- [51] E. Dal Martello *et al.*, "Trace Elements in the Si Furnace-Part II: Analysis of Condensate in Carbothermal Reduction of Quartz," *Metall. Mater. Trans. B*, vol. 44, no. 2, pp. 244–251, 2012.
- [52] C. Klein and C. S. Hurlbut, "Mineral Stability Diagrams," in *Manual of mineralogy*, 21st ed. New York: Wiley, 1993.
- [53] W. Pabst and E. Gregorová, "Elastic properties of silica polymorphs – a review," *J. Ceram.-Silikáty*, pp. 167–184, 2013.
- [54] P. J. Heaney, C. T. Prewitt, and G. V. Gibbs, *Silica: Physical Behaviour, Geochemistry and Materials Application*, vol. 29. Mineralogical Society of America, 1994.
- [55] S. J. Stevens, R. J. Hand, and J. H. Sharp, "Polymorphism of silica," *J. Mater. Sci.*, vol. 32, no. 11, pp. 2929–2935, Jun. 1997, doi: 10.1023/A:1018636920023.

- [56] A. C. D. Chaklader, "Effect of Trace Al<sub>2</sub>O<sub>3</sub> on Transformation of Quartz to Cristobalite," *J. Am. Ceram. Soc.*, vol. 44, no. 4, pp. 175–180, 1961.
- [57] D. L. Lakshtanov, S. V. Sinogeikin, and J. D. Bass, "High-temperature phase transitions and elasticity of silica polymorphs," *Phys. Chem. Miner.*, vol. 34, no. 1, pp. 11–22, Jan. 2007, doi: 10.1007/s00269-006-0113-y.
- [58] E. Ringdalen and M. Tangstad, "Softening and Melting of SiO<sub>2</sub>, an Important Parameter for Reactions with Quartz in Si Production," in *Advances in Molten Slags, Fluxes, and Salts: Proceedings of the 10th International Conference on Molten Slags, Fluxes and Salts 2016*, R. G. Reddy, P. Chaubal, P. C. Pistorius, and U. Pal, Eds., Cham: Springer International Publishing, 2016, pp. 43–51. doi: 10.1007/978-3-319-48769-4\_4.
- [59] E. Ringdalen, "Changes in Quartz During Heating and the Possible Effects on Si Production," *JOM*, vol. 67, no. 2, pp. 484–492, Feb. 2015, doi: 10.1007/s11837-014-1149-y.
- [60] A. C. D. Chaklader and A. L. Roberts, "Transformation of Quartz to Cristobalite," *J. Am. Ceram. Soc.*, vol. 44, no. 1, pp. 35–41, 1961, doi: 10.1111/j.1151-2916.1961.tb15344.x.
- [61] H. Schneider, A. Majdic, and R. Vasudevan, "Kinetics of the Quartz-Cristobalite Transformation in Refractory-Grade Silica Materials," *Mater. Sci. Forum*, vol. 7, pp. 91–102, 1986, doi: 10.4028/www.scientific.net/MSF.7.91.
- [62] C. S. Marians and L. W. Hobbs, "Network properties of crystalline polymorphs of silica," *J. Non-Cryst. Solids*, vol. 124, no. 2, pp. 242–253, Oct. 1990, doi: 10.1016/0022-3093(90)90269-R.
- [63] M. E. Kjelstadli, "Kinetics and Mechanism of Phase Transformations from Quartz to Cristobalite," Master Thesis, Norwegian University of Science and Technology, 2016. Accessed: Feb. 07, 2020. [Online]. Available: <https://ntnuopen.ntnu.no/ntnu-xmlui/handle/11250/2406964>
- [64] F. L. Galeener, "Current Models for Amorphous SiO<sub>2</sub>," in *The Physics and Technology of Amorphous SiO<sub>2</sub>*, R. A. B. Devine, Ed., Boston, MA: Springer US, 1988, pp. 1–13. doi: 10.1007/978-1-4613-1031-0\_1.
- [65] M. A. Lamkin, F. L. Riley, and R. J. Fordham, "Oxygen mobility in silicon dioxide and silicate glasses: a review," *J. Eur. Ceram. Soc.*, vol. 10, no. 5, pp. 347–367, Jan. 1992, doi: 10.1016/0955-2219(92)90010-B.
- [66] V. Presser and K. G. Nickel, "Silica on Silicon Carbide," *Crit. Rev. Solid State Mater. Sci.*, vol. 33, no. 1, pp. 1–99, Feb. 2008, doi: 10.1080/10408430701718914.
- [67] E. Ringdalen, D. Adisty, and L. Kolbeinsen, "Quartz-Cristobalite Transformation and Its Effect on Reactions in Si Production: Initial Studies," in *Celebrating the Megascale*, P. J. Mackey, E. J. Grimsey, R. T. Jones, and G. A. Brooks, Eds., Cham: Springer International Publishing, 2016, pp. 225–236. doi: 10.1007/978-3-319-48234-7\_19.
- [68] A. Broggi, M. Tangstad, and E. Ringdalen, "Characterization of a Si-SiO<sub>2</sub> mixture generated from SiO and CO," *Metall. Mater. Trans. B Process Metall. Mater. Process. Sci.*, pp. 2667–2770, 2019, doi: 10.1007/s11663-019-01678-x.
- [69] E. Nordnes, "Softening and Melting Properties of Quartz," Master Thesis, Norwegian University of Science and Technology, Department of Materials Science and Engineering, Trondheim, 2019.
- [70] K. F. Jusnes, "Parameters Affecting Softening and Melting of Quartz," Master Thesis, Norwegian University of Science and Technology, Department of Materials Science and Engineering, Trondheim, 2016. Accessed: Apr. 16, 2019. [Online]. Available: <https://ntnuopen.ntnu.no/ntnu-xmlui/handle/11250/2406976>



- [71] E. Ringdalen, H. Tveit, S. Bao, and E. Nordnes, “Melting properties of quartz and their effect on industrial Si and FeSi production,” presented at the Non-ferrous Metals and Minerals, Krasnoyarsk, 2019.
- [72] N. G. Ainslie, J. D. Mackenzie, and D. Turnbull, “Melting kinetics of quartz and cristobalite,” *J. Phys. Chem.*, vol. 65, no. 10, pp. 1718–1724, 1961, doi: 10.1021/j100827a012.
- [73] D. Kuhlmann-Wilsdorf, “Theory of Melting,” *Phys. Rev.*, vol. 140, no. 5A, pp. A1599–A1610, Nov. 1965, doi: 10.1103/PhysRev.140.A1599.
- [74] D. Turnbull and M. H. Cohen, “Concerning Reconstructive Transformation and Formation of Glass,” *J. Chem. Phys.*, vol. 29, no. 5, pp. 1049–1054, Nov. 1958, doi: 10.1063/1.1744654.
- [75] J. Götze, “Classification, Mineralogy and Industrial Potential of SiO<sub>2</sub> Minerals and Rocks,” in *Quartz: Deposits, Mineralogy and Analytics*, J. Götze and R. Möckel, Eds., in Springer Geology. Berlin, Heidelberg: Springer, 2012, pp. 1–27. doi: 10.1007/978-3-642-22161-3\_1.
- [76] M. Ksiazek *et al.*, “Industrial measurements of the gas and temperature in Si and FeSi production process,” presented at the INFACON XVI, Trondheim, 2021.
- [77] E. Ringdalen, “Quartz Properties in the Silicon Production,” in *Silicon for the Chemical and Solar Industry XII*, Trondheim, 2014.
- [78] K. Aasly, “Properties and behavior of quartz for the silicon process,” Thesis for the degree of Philosophiae Doctor, Norwegian University of Technology and Science, Department of Materials Science and Engineering, 2008. Accessed: Feb. 07, 2020. [Online]. Available: <https://ntnuopen.ntnu.no/ntnu-xmlui/handle/11250/235844>
- [79] K. Aasly and V. Dosaj, “Assessment of production performance of quartz in the Si-furnace,” in *Silicon for the Chemical and Solar Industry XIII*, Kristiansand, 2016.
- [80] E. Dal Martello, “Impurity distribution and reduction behaviour of quartz in the production of high purity silicon,” Norges teknisk-naturvitenskapelige universitet, Fakultet for naturvitenskap og teknologi, Institutt for materialteknologi, 2012. Accessed: Jan. 12, 2021. [Online]. Available: <https://ntnuopen.ntnu.no/ntnu-xmlui/handle/11250/249045>
- [81] M. Gemeinert, M. Gaber, I. Hager, M. Willfahrt, and D. Bortschuloun, “On correlation of gas-liquid-inclusion’s properties and melting behaviour of different genetic quartzes for production of transparent fused silica,” *Neues Jahrb. Für Mineral. Abh.*, vol. 165, pp. 19–27, 1992.
- [82] K. Aasly, T. Malvik, and E. H. Myrhaug, “Advanced methods to characterize thermal properties of quartz,” presented at the INFACON XI, New Dehli, India, 2007, pp. 381–392.
- [83] S. Bao *et al.*, “Investigation of Two Immiscible Liquids Wetting at Elevated Temperature: Interaction Between Liquid FeMn Alloy and Liquid Slag,” *Metall. Mater. Trans. B*, vol. 52, no. 5, pp. 2847–2858, Oct. 2021, doi: 10.1007/s11663-021-02222-6.
- [84] Z. Miao, A. Shan, W. Wang, J. Lu, W. Xu, and H. Song, “Solidification process of conventional superalloy by confocal scanning laser microscope,” *Trans. Nonferrous Met. Soc. China*, vol. 21, no. 2, pp. 236–242, 2011.
- [85] “VL2000DX-SVF17SP | Laser microscopes | Lasertec Corporation.” <https://www.lasertec.co.jp/en/products/microscope/laser/vl2000dx.html> (accessed Dec. 15, 2020).
- [86] D. Vollath, F. D. Fischer, M. Hagelstein, and D. V. Szabo’, “Phases and phase transformations in nanocrystalline ZrO<sub>2</sub>,” *J. Nanoparticle Res.*, vol. 8, pp. 1003–1016, 2006, doi: DOI 10.1007/s11051-006-9116-3.

- [87] “British Lime Association (BLA) part of the Mineral Products Association (MPA).” [https://britishlime.org/education/the\\_importance\\_of\\_lime.php](https://britishlime.org/education/the_importance_of_lime.php) (accessed May 01, 2023).
- [88] D. K. Nguyen, V. V. On, D. M. Hoat, J. F. Rivas-Silva, and G. H. Cocoltzi, “Structural, electronic, magnetic and optical properties of CaO induced by oxygen incorporation effects: A first-principles study,” *Phys. Lett. A*, vol. 397, p. 127241, May 2021, doi: 10.1016/j.physleta.2021.127241.
- [89] M. A. Subramanian, R. D. Shannon, B. H. T. Chai, M. M. Abraham, and M. C. Wintersgill, “Dielectric constants of BeO, MgO, and CaO using the two-terminal method,” *Phys. Chem. Miner.*, vol. 16, no. 8, pp. 741–746, Nov. 1989, doi: 10.1007/BF00209695.
- [90] T. Nakamura, Y. Ueda, and J. M. Toguri, “New development in optical basicity,” *Nippon Kinzoku Gakkaishi Journal Jpn. Inst. Met.*, vol. 50, no. 5, pp. 456–461, May 1986.
- [91] C. A. Natalie and Ewans, “Influence of Lime Properties on Rate of Dissolution in CaO-SiO<sub>2</sub>-FeO Slags,” *Ironmak. Steelmak.*, vol. 6, pp. 101–109, 1979.
- [92] N. Maruoka, A. Ito, M. Hayasaka, S. Kitamura, and H. Nogami, “Enhancement of Quicklime Dissolution in Steelmaking Slags by Utilizing Residual CO<sub>2</sub> from Quicklime,” *ISIJ Int.*, vol. 57, no. 10, pp. 1677–1683, 2017, doi: 10.2355/isijinternational.ISIJINT-2017-103.
- [93] S. Kitamura, “Dissolution Behavior of Lime into Steelmaking Slag,” *ISIJ Int.*, vol. 57, no. 10, pp. 1670–1676, 2017, doi: 10.2355/isijinternational.ISIJINT-2017-109.
- [94] L. Vieira, H. Oliveira, V. Telles, E. Junca, E. Vieira, and J. Oliveira, “Influence of lime particle and slag properties on lime dissolution in BOF converter,” *J. Mater. Res. Technol.*, vol. 9, pp. 14878–14886, Nov. 2020, doi: 10.1016/j.jmrt.2020.10.058.
- [95] N. Dogan, G. A. Brooks, and M. A. Rhamdhani, “Kinetics of Flux Dissolution in Oxygen Steelmaking,” *ISIJ Int.*, vol. 49, no. 10, pp. 1474–1482, 2009, doi: 10.2355/isijinternational.49.1474.
- [96] T. Deng, J. Gran, and D. Sichen, “Dissolution of Lime in Synthetic ‘FeO’-SiO<sub>2</sub> and CaO-‘FeO’-SiO<sub>2</sub> Slags,” *Steel Res. Int.*, vol. 81, no. 5, pp. 347–355, 2010, doi: 10.1002/srin.201000017.
- [97] R. G. Haverkamp, B. J. Welch, and J. B. Metson, “Models of Alumina Dissolution in Cryolite,” *ECS Proc. Vol.*, vol. 1992–16, no. 1, pp. 646–659, 1992, doi: 10.1149/199216.0646PV.
- [98] A. Marabi, G. Mayor, A. Burbidge, R. Wallach, and I. S. Saguy, “Assessing dissolution kinetics of powders by a single particle approach,” *Chem. Eng. J.*, vol. 139, no. 1, pp. 118–127, May 2008, doi: 10.1016/j.cej.2007.07.081.
- [99] S. Amini, M. Brungs, and O. Ostrovski, “Dissolution of Dense Lime in Molten Slags under Static Conditions,” *ISIJ Int.*, vol. 47, no. 1, pp. 32–37, 2007, doi: 10.2355/isijinternational.47.32.
- [100] D. Sato, R. Kubota, A. Nishimoto, M. Kubota, and H. Matsuda, “Kinetic Study on Dissolution of CaO Particle into CaO-SiO<sub>2</sub>-Al<sub>2</sub>O<sub>3</sub> Molten Slag from Simulated Municipal Solid Wastes Melting,” *J. Chem. Eng. Jpn.*, vol. 50, no. 4, pp. 324–331, 2017.
- [101] H. Kimura, T. Yanagase, F. Noguchi, and Y. Ueda, “Studies on the Mechanism of CaO Dissolution into Slag Melts,” *J. Jpn. Inst. Met.*, vol. 38, pp. 226–232, 1974.
- [102] A. R. Cooper Jr. and W. D. Kingery, “Dissolution in Ceramic Systems: I, Molecular Diffusion, Natural Convection, and Forced Convection Studies of Sapphire Dissolution in Calcium Aluminum Silicate,” *J. Am. Ceram. Soc.*, vol. 47, no. 1, pp. 37–43, 1964, doi: 10.1111/j.1151-2916.1964.tb14638.x.

- [103] M. Matsushima, S. Yadoomaru, K. Mori, and Y. Kawai, "A Fundamental Study on the Dissolution Rate of Solid Lime into Liquid Slag," *Trans. Iron Steel Inst. Jpn.*, vol. 17, no. 8, pp. 442–449, Aug. 1977, doi: 10.2355/isijinternational1966.17.442.
- [104] S. H. Amini, M. P. Brungs, O. Ostrovski, and S. Jahanshani, "Effects of additives and temperature on dissolution rate and diffusivity of lime in Al<sub>2</sub>O<sub>3</sub>-CaO-SiO<sub>2</sub> based slags," *Metall. Mater. Trans. B*, vol. 37, no. 5, pp. 773–780, Oct. 2006, doi: 10.1007/s11663-006-0059-y.
- [105] S. Kitamura, "Dissolution Behavior of Lime into Steelmaking Slag," *ISIJ Int.*, vol. 57, no. 10, pp. 1670–1676, 2017, doi: 10.2355/isijinternational.ISIJINT-2017-109.
- [106] X. Guo, Z. H. I. Sun, J. Van Dyck, M. Guo, and B. Blanpain, "In Situ Observation on Lime Dissolution in Molten Metallurgical Slags – Kinetic Aspects," *Ind. Eng. Chem. Res.*, vol. 53, no. 15, pp. 6325–6333, Apr. 2014, doi: 10.1021/ie500070h.
- [107] H. Towers, M. Paris, and J. Chipman, "Diffusion of Calcium Ion in Liquid Slag," *JOM*, vol. 5, no. 11, pp. 1455–1458, Nov. 1953, doi: 10.1007/BF03397634.
- [108] H. Towers and J. Chipman, "Diffusion of Calcium and Silicon in a Lime-Alumina-Silica Slag," *JOM*, vol. 9, no. 6, pp. 769–773, Jun. 1957, doi: 10.1007/BF03377932.
- [109] K. Niwa, "A study on the Diffusion of Calcium Ion in Molten Lime-Silica-Alumina slags by Using a Radioactive Tracer Technique," *J. Jpn. Inst. Met. Mater.*, vol. 21, pp. 304–308, 1957.
- [110] T. Saitō and K. Maruya, "Diffusion of Calcium in Liquid Slags," *Res. Inst. Miner. Dress. Metall.*, vol. 10A, pp. 306–314, 1958.
- [111] K. S. Goto, M. Sasabe, and M. Kawakami, "Relation between Tracer Diffusivity and Electrical Conductivity on Multi-component Oxide Slags at 900° to 1600°C," *Trans. Iron Steel Inst. Jpn.*, vol. 17, pp. 212–214, 1977.
- [112] Y. Liang, F. M. Richter, A. M. Davis, and B. E. Watson, "Diffusion in silicate melts: I. Self diffusion in CaO-Al<sub>2</sub>O<sub>3</sub>-SiO<sub>2</sub> at 1500°C and 1 GPa," *Geochim. Cosmochim. Acta*, vol. 60, no. 22, pp. 4353–4367, 1996, doi: 10.1016/S0016-7037(96)00288-8.
- [113] G. Zhang and K. Chou, "Diffusion Coefficient of Calcium Ion in CaO-Al<sub>2</sub>O<sub>3</sub>-SiO<sub>2</sub> Melts," *J. Iron Steel Res.*, vol. 18, no. 3, pp. 13–16, 2011.
- [114] Z. S. Ren, X. H. Hu, and K. C. Chou, "Model for diffusion coefficient estimation of calcium ions in CaO-Al<sub>2</sub>O<sub>3</sub>-SiO<sub>2</sub> slags," *Ironmak. Steelmak.*, vol. 40, no. 8, pp. 625–629, Nov. 2013, doi: 10.1179/1743281212Y.0000000090.
- [115] P. Herasymenko, "ELECTROCHEMICAL THEORY OF SLAG-METAL EQUILIBRIA. PART 1.-REACTIONS OF MANGANESE AND SILICON IN ACID OPEN-HEART FURNACE."
- [116] J. Bardeen and C. Herring, *Imperfections in Nearly Perfect Crystals*. New York: John Wiley & Sons, 1952. Accessed: May 03, 2023. [Online]. Available: <https://onlinelibrary.wiley.com/doi/abs/10.1107/S0365110X53000429>
- [117] K. Compaan and Y. Haven, "Correlation factors for diffusion in solids," *Trans. Faraday Soc.*, vol. 52, pp. 786–780, 1956.
- [118] S. Glasstone, K. J. Laidler, and H. Eyring, *The theory of rate processes : the kinetics of chemical reactions, viscosity, diffusion and electrochemical phenomena*. New York: McGraw-Hill Book Company, 1941.
- [119] A. W. Hofmann, "Diffusion in natural silicate melts: A critical review," in *Physics of Magmatic Processes*, New Jersey: Princeton Univ. Press, 1980, pp. 385–417.
- [120] C. A. Angell, P. A. Cheeseman, and S. Tamaddon, "Pressure Enhancement of Ion Mobilities in Liquid Silicates from Computer Simulation Studies to 800 Kilobars," *Science*, vol. 218, no. 4575, pp. 885–887, 1982.

- [121] E. B. Watson, "Calcium diffusion in a simple silicate melt to 30 kbar," *Geochim. Cosmochim. Acta*, vol. 43, no. 3, pp. 313–322, Mar. 1979, doi: 10.1016/0016-7037(79)90197-2.
- [122] V. G. Levich, *Physicochemical hydrodynamics*. in Prentice-Hall international series in the physical and chemical engineering sciences. Englewood Cliffs, N.J.: Prentice-Hall, 1962.
- [123] Kosaka M. and Minowa S., "Mass-Transfer from Solid Metal Cylinder into Liquid Metal," *Tetsu--Hagane*, vol. 52, no. 12, pp. 1748–1762, 1966, doi: 10.2355/tetsutohagane1955.52.12\_1748.
- [124] S. Kristiansen, "Dissolution rate and wettability of SiO<sub>2</sub>–CaO–Al<sub>2</sub>O<sub>3</sub> slag on quartz," Project work, Norwegian University of Science and Technology, Department of Materials Science and Engineering, Trondheim, 2022.
- [125] H. Tveit, V. Andersen, K. H. Berget, and R. Jensen, "The tapping process in silicon production," p. 10, 2014.
- [126] H. T. Ingason, J. Halfdanarson, and J. A. Bakken, "HOLLOW ELECTRODES IN THE PRODUCTION OF FESI75," presented at the INFACON 7, Trondheim: FFF, 1995.
- [127] M. Kadkhodabeigi, "Modeling of Tapping Processes in Submerged Arc Furnaces," Thesis for the degree of Philosophiae Doctor, Norwegian University of Science and Technology, Department of Materials Science and Engineering, Trondheim, 2011.
- [128] J. Fulton and J. Chipman, "Kinetic Factors in the Reduction of Silica from Blast-Furnace Type Slags," *Trans. Am. Inst. Min. Metall. Eng.*, vol. 215, pp. 888–891, 1959.
- [129] H. Sun, K. Mori, and R. D. Pehlke, "Reduction Rate of SiO<sub>2</sub> in Slag by Carbon-Saturated Iron," *Metall. Trans. B*, p. 8.
- [130] H. Hoover, "Excavation of 160 KW Pilot Scale Si Furnace," *Asp. Min. Miner. Sci.*, vol. 9, no. 2, May 2022, doi: 10.31031/AMMS.2022.09.000707.
- [131] A. Valderhaug, "Modelling and control of submerged-arc ferrosilicon furnaces," Dr. ing. thesis, The Norwegian Institute of Technology, Department of Engineering Cybernetics, Trondheim, 1992.
- [132] E. Ringdalen, K. E. Einarsrud, and A. Nordhus, "Gas Flow and Pressure Drop in Charge Material in Silicon Production," *JOM*, vol. 74, no. 11, pp. 3971–3979, Nov. 2022, doi: 10.1007/s11837-022-05431-9.
- [133] S. Kristiansen, "Dissolution Rate and Wettability of SiO<sub>2</sub>-CaO-Al<sub>2</sub>O<sub>3</sub> Slags on Quartz," Master Thesis, Norwegian University of Science and Technology, Department of Materials Science and Engineering, Trondheim, 2023.
- [134] H. Du, R. E. Tressler, and K. E. Spear, "Thermodynamics of the Si-N-O System and Kinetic Modeling of Oxidation of Si<sub>3</sub>N<sub>4</sub>," *J. Electrochem. Soc.*, vol. 136, no. 11, p. 3210, Nov. 1989, doi: 10.1149/1.2096427.
- [135] K. Aasly, T. Malvik, and E. H. Myrhaug, "A review of previous work on important properties of quartz for FeSi and Si metal production," in *Innovations in Ferro Alloy Industry*, New Delhi, India: The Indian Ferro Alloy Producers' Association, 2007, pp. 393–401.
- [136] R. Saadieh, "Elkem University Presentation," Kristiansand, 2017.
- [137] Y. Luo, D. Zhu, X. Zhou, B. Shi, and F. Zhang, "Coproduct of DRI Powder and Semi-coke from Siderite Ore and Low Rank Coal by Excessive Coal-based Direct Reduction in Rotary Kiln," *ISIJ Int.*, vol. 56, Nov. 2015, doi: 10.2355/isijinternational.ISIJINT-2015-390.
- [138] H. Tveit, "The Silicon Process and the Safety," in *Production of High Silicon Alloys*, Trondheim: to be published.

- [139] M. Görnerup and O. Wijk, “Liquidus Relationships in the CaO-corner of the Ternary System CaO-Al<sub>2</sub>O<sub>3</sub>-SiO<sub>2</sub>,” *ISIJ Int.*, vol. 36, no. 12, pp. 1465–1470, 1996, doi: 10.2355/isijinternational.36.1465.
- [140] W. H. Press, S. A. Teukolsky, W. T. Vetterling, and B. P. Flannery, *Numerical Recipes in C++: The Art of Scientific Computing*, 2nd edition. Cambridge, UK ; New York: Cambridge University Press, 2002.



## Appendix A: Analysis of the industrial samples

### A.1 Excavation of Furnace B

#### A.1.1 The beginning of the excavation: behind tap-hole 3

The excavation dig-out started outside tap-hole 3. Table 46 lists the full WDS analysis for the samples B-3, -4, -7, -8, 9-, -14 and -27. The oxide analysis are given in wt%.

Table 46 Original data from WDS analyses of slag from behind tap-hole 3 from Furnace B excavation.

Sample	Distribution	SiO <sub>2</sub>	Na <sub>2</sub> O	K <sub>2</sub> O	MnO	MgO	CaO	FeO	Al <sub>2</sub> O <sub>3</sub>	TiO <sub>2</sub>	BaO	Total
B-3.1		37.0	0.02	0.1	0.02	0.3	25.3	0.01	36.1	0.03	0.4	99.1
B-4.1		45.0	0	0.1	0	0.2	21.7	0.01	35.9	0.02	0.1	103.0
B-4.2		44.9	0.02	0.01	0.02	0.1	21.7	0.04	26.0	0.02	0.05	102.9
B-7.1	Bright, 20%	32.9	0.01	0.02	0	0.04	42.2	0.04	27.5	0.01	0.03	102.8
	Dark, 80%	45.1	0.01	0	0	0.01	22.0	0.03	35.8	0	0.1	102.9
B-7.2		45.0	0.01	0.01	0	0.1	21.9	0.01	35.7	0.03	0.1	102.8
B-8.1		47.0	0.02	0.02	0	0.1	21.5	0.01	33.9	0.01	0.01	102.6
B-8.2		46.2	0.01	0.02	0.01	0.1	21.7	0.01	34.6	0.04	0.04	102.8
B-9.1	Bright, 10%	62.5	0.1	0.6	0.05	2.4	9.0	0.1	23.1	0.1	1.5	99.4
	Dark, 90%	46.5	0.04	0.01	0	0.1	18.7	0.02	34.2	0	0.1	99.6
B-9.2		65.9	0.1	0.3	0.01	0.2	9.5	0.01	22.3	0.03	0.3	98.7
B-14.1		83.8	0.1	4.1	0	0.5	1.5	0.02	8.8	0.01	0	98.9
B14.2		78.2	0.2	2.8	0.02	1.3	3.8	0.03	13.4	0.01	0	98.9
B27.1	w/small SiC	48.8	0	0.1	0	0.4	18.6	0.01	31.6	0.01	0.05	99.6
	w/large SiC	47.0	0.03	0.1	0.01	0.4	18.7	0.01	32.0	0.03	0.04	98.3
B27.2		51.4	0.05	0.3	0.01	2.0	16.9	0.03	32.2	0.02	0.1	103.1

#### A.1.2 Samples including the zones next to the Si tapping channel

##### A.1.2.1 Tap-hole 1

Two samples from tap-hole 1 were collected, sample 48a from the upper part, and 48b from the lower part. Sample B-48a is described in section 2.3.1.1.2 Samples next to the Si tapping channel. The full WDS analysis for the samples from B-48a are listed in Table 47. The WDS results for the slag in sample B-48b are presented in

Table 48. Picture of B-48b is in Figure 179. Marked in orange on the samples are the analyzed areas which corresponds to the number on the EPMA images and the full WDS analysis in the next figures and tables. Five samples were analyzed.

B-48b 1.1, -1.2, -2 and -3 were from the green color zone closest to the Si canal. EPMA images of the samples are in Figure 180 and Figure 181. They all consist of SiO<sub>2</sub>-CaO-Al<sub>2</sub>O<sub>3</sub> slag, SiC and some Si. Sample B48a 1.1 and -1.2 also have some Al<sub>2</sub>O<sub>3</sub>.

Sample B-48b 4 and -5 are from the grey colored zone. EPMA images are shown in Figure 182. The samples are mainly larger areas with SiC, SiO<sub>2</sub>-CaO-Al<sub>2</sub>O<sub>3</sub> slag and smaller droplets of Si.

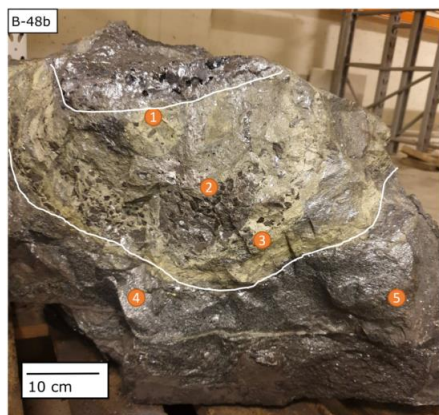


Figure 179 Picture of sample B-48b. Marked in orange on the samples are the analyzed areas which corresponds to the number on the EPMA images and the WDS analysis in the next figures and tables.

Table 47 WDS results for samples collected from B-48a, from the lower parts of tap-hole 1.

Sample	Distribution	SiO <sub>2</sub>	Na <sub>2</sub> O	K <sub>2</sub> O	MnO	MgO	CaO	FeO	Al <sub>2</sub> O <sub>3</sub>	TiO <sub>2</sub>	BaO	Total
B-48a 1.2	Top	52.0	0.2	0.2	0	0.3	19.0	0.04	31.4	0	0.01	103.2
	matrix	71.9	0.1	2.9	0.01	2.2	10.8	0	11.8	0.02	0.4	100.2
B-48a 2.1		46.1	0.03	0.01	0.01	0.1	21.3	0.03	33.4	0.02	0.1	101.9
B-48a 2.2		46.8	0.03	0.02	0.01	0.2	20.7	0	33.7	0	0.05	101.6
B-48a 3.1		47.5	0.1	0.1	0.02	0.03	20.5	0.02	32.8	0.04	0	101.1
B-48a 3.2		60.3	0.2	0.5	0.01	0.6	12.2	0	26.4	0.03	0.03	100.2
B-48a 4.1		41.9	0.1	0.1	0.01	0.3	22.3	0.1	36.2	0.03	0.03	100.9
B-48a 4.2		63.4	0.3	1.9	0	1.3	8.5	0.03	24.5	0.01	0.03	99.9
B-48a 5.1		65.3	0.7	2.4	0.01	0.1	7.9	0.04	23.4	0.01	0.03	99.9
B-48a 5.2		65.1	0.9	2.2	0.01	0.1	7.7	0.01	23.6	0.02	0	99.6

Table 48 WDS results for samples collected from B-48b, from above tap-hole 1.



Sample	Distribution	SiO <sub>2</sub>	Na <sub>2</sub> O	K <sub>2</sub> O	MnO	MgO	CaO	FeO	Al <sub>2</sub> O <sub>3</sub>	TiO <sub>2</sub>	BaO	Total
B-48b1.1	Bright 50%	31.1	0.03	0.1	0.01	0.2	43.0	0	31.9	0	0.07	106.3
	Dark, 50%	43.6	0.01	0.1	0	0.1	21.1	0.01	36.0	0.02	0.2	101.2
B-48b1.2	Bright 50%	29.1	0.02	0.02	0.01	0.2	43.2	0.01	32.0	0.01	0.03	104.7
	Dark, 50%	47.3	0.01	0.05	0.01	0.1	20.2	0.02	36.5	0.01	0.2	104.4
B-48b2	Bright 70%	24.9	0.01	0.01	0.01	0.04	43.2	0.03	35.0	0	0.02	103.2
	Dark 30%	42.4	0.02	0.1	0	0.1	21.1	0.03	37.1	0	0.4	101.2
B-48b3	Bright 40%	24.9	0.04	0.01	0	0.1	42.7	0.1	34.2	0.01	0.3	102.1
	Dark 60%	44.3	0.01	0	0.01	0.01	21.0	0.01	35.4	0.02	0.1	100.9
B-48b4	Bright 50%	26.1	0.1	0.02	0.02	0.04	40.6	0.04	33.1	0.01	0.03	100.0
	Dark 50%	42.6	0.01	0.02	0.02	0.05	20.0	0.05	36.0	0	0.1	98.9
B-48b5	Bright 90%	70.1	0.04	2.5	0	1.2	13.4	0.02	10.7	0.04	1.2	99.2
	Dark 10%	51.0	0.04	0.1	0	0.04	19.6	0.02	28.8	0	0.01	99.4

Green zone

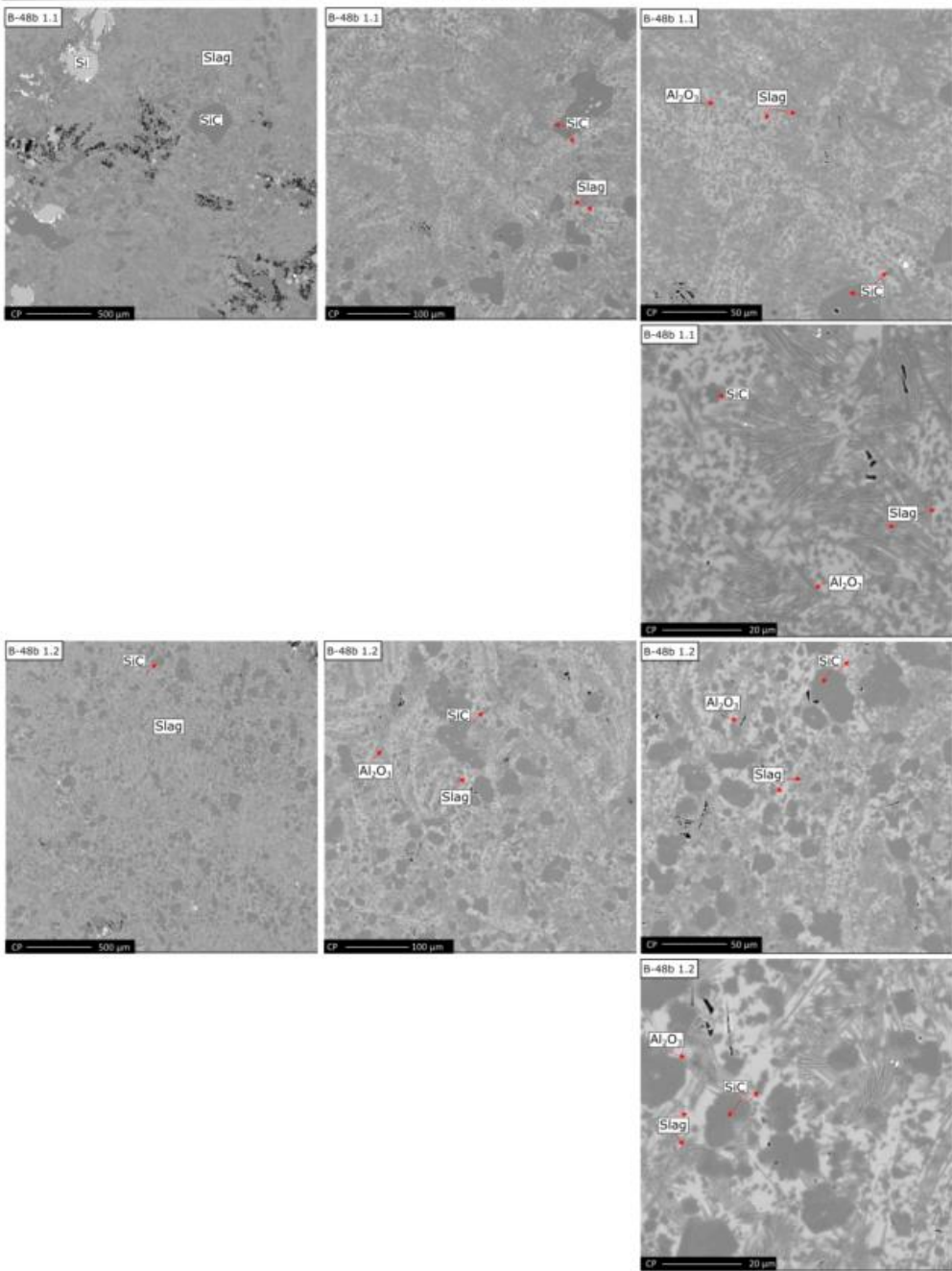


Figure 180 EPMA images of sample B-48b 1.1 and -1.2 with three different magnifications; 40X, 200X and 400X. Both samples consist of SiO<sub>2</sub>-CaO-Al<sub>2</sub>O<sub>3</sub> slag, SiC, Al<sub>2</sub>O<sub>3</sub> and some Si.

Green zone

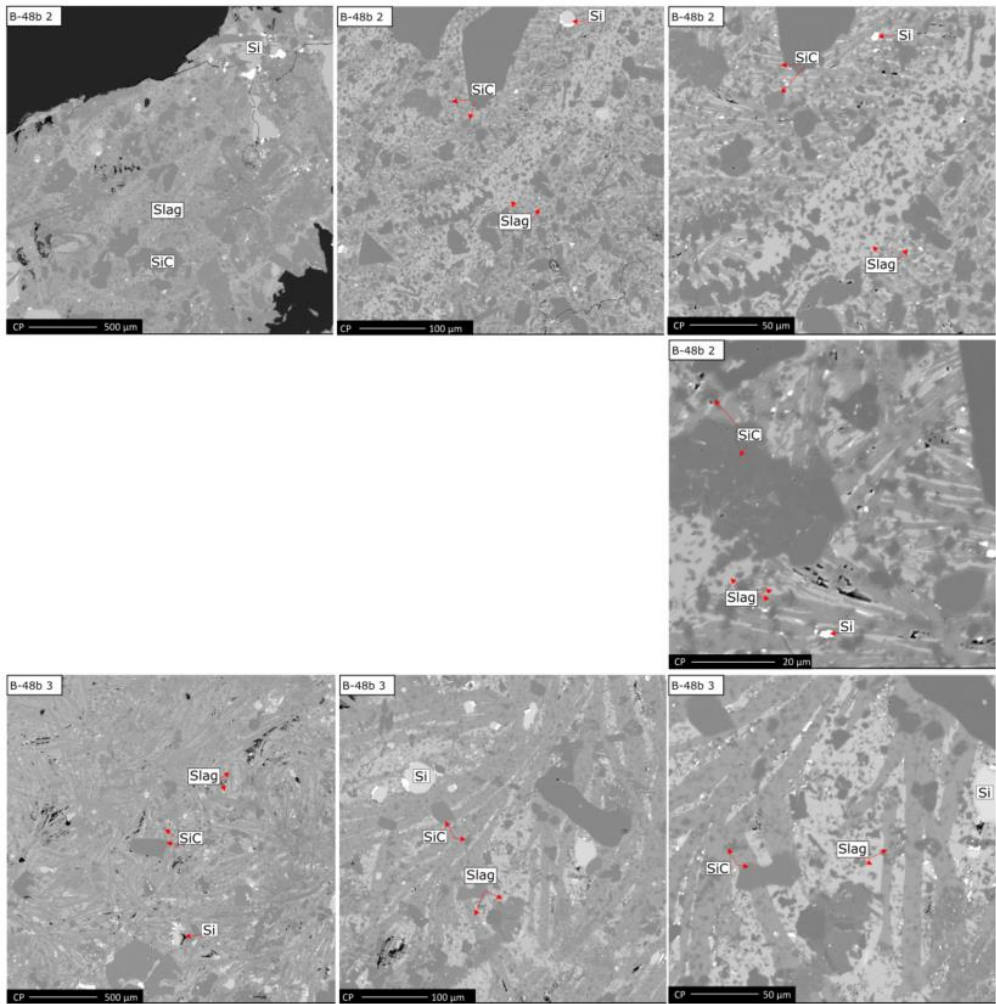


Figure 181 EPMA images of sample B-48b 2 and -3 with three different magnifications; 40X, 200X and 400X. Both samples consist of  $\text{SiO}_2\text{-CaO-Al}_2\text{O}_3$  slag, SiC and some Si.

### Grey zone

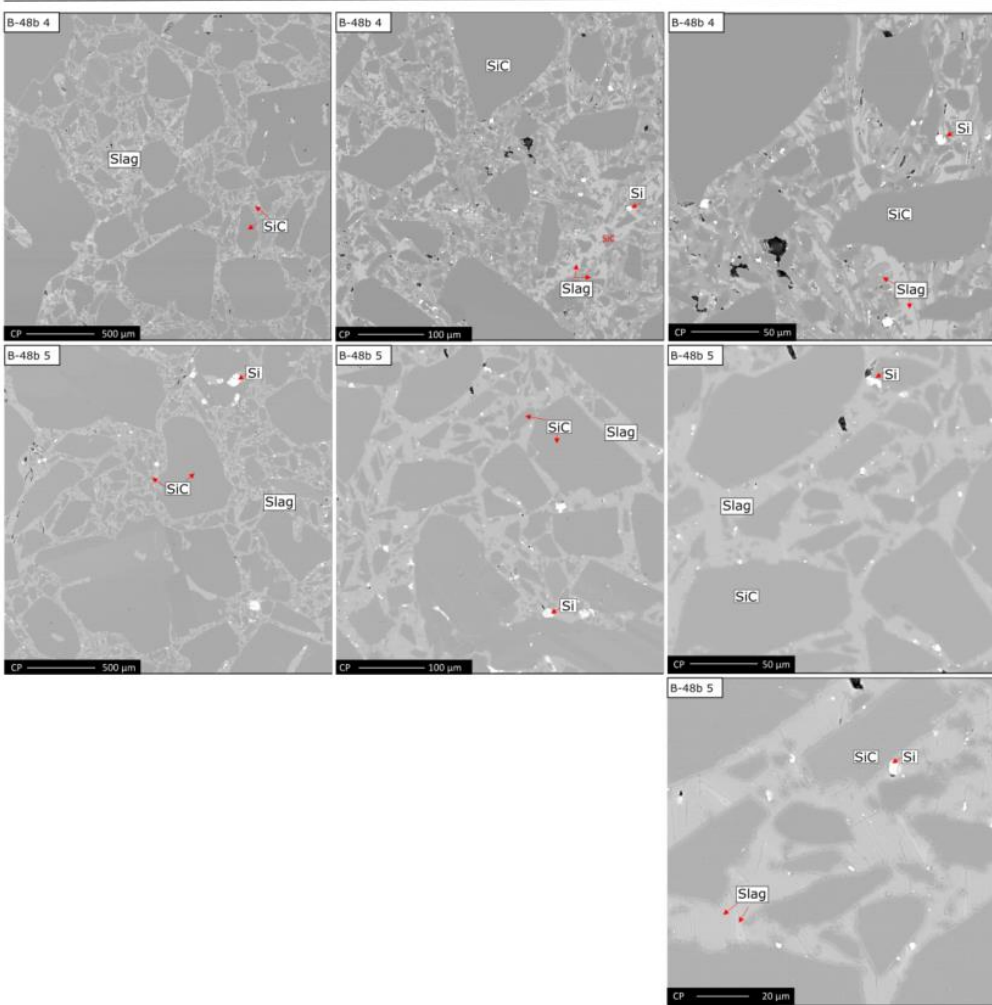


Figure 182 EPMA images of sample B-48b 4 and -4 with three different magnifications; 40X, 200X and 400X. Both samples consist of SiC, SiO<sub>2</sub>-CaO-Al<sub>2</sub>O<sub>3</sub> slag and some Si.

#### A.1.2.2 Tap-hole 3

Sample B-1 and B-2 were collected from tap-hole 3. The full WDS results for the slag in sample B-1 and B-2 are presented in Table 49. Figure 183 shows pictures of B-1 and B-2 taken at the plant. Marked in orange are the analyzed areas which correspond to the number on the EPMA images and the WDS analysis in the next figures and tables. B-2 was unfortunately crushed into smaller pieces by the excavators by a misunderstanding. The analyzed samples are therefore chosen based on colors. The black colored layer seen to the left in B-2 is clogging paste.

B-1 and B-2 are both from below the tapping channel. B-1 1 and -2, and B-2 2 are from the green zone. All three samples consist of  $\text{SiO}_2\text{-CaO-Al}_2\text{O}_3$  slag, SiC and some Si. Sample B-2.1 are taken in the transition between the green and the grey zone and contains both. Area 1 is from the green area and Area 2, as can be seen in the third line in Figure 185. Both Area 1 and 2 consist of  $\text{SiO}_2\text{-CaO-Al}_2\text{O}_3$  slag, SiC and some Si, but the difference is the size of the SiC particles.

B-1 3 and B-2 3 are from the grey colored zone and are in Figure 185. In addition to  $\text{SiO}_2\text{-CaO-Al}_2\text{O}_3$  slag, SiC and Si, those two also have some  $\text{Al}_2\text{O}_3$ .

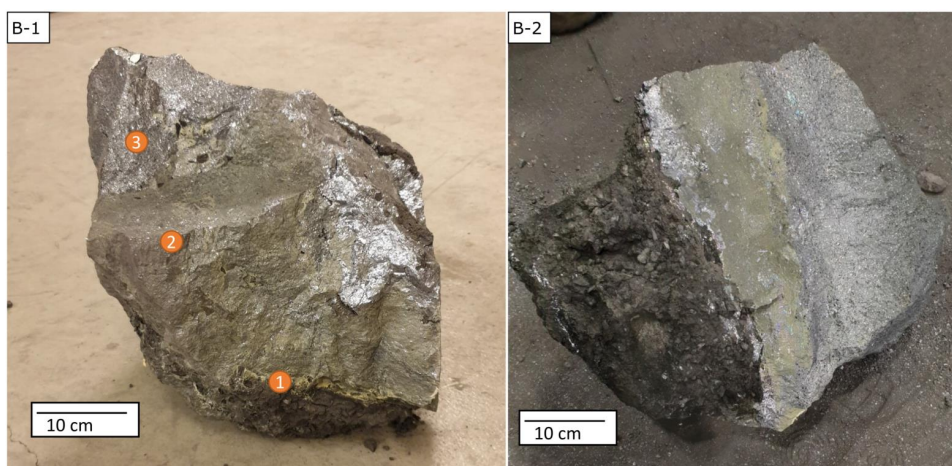


Figure 183 Sample B-1 and B-2. Marked in orange on the samples are the analyzed areas which corresponds to the number on the EPMA images and the WDS analysis in the next figures and tables.

Table 49 WDS results for sample B-1 and B-2, from above and below tap-hole 3, respectively.

Sample	Distribution	$\text{SiO}_2$	$\text{Na}_2\text{O}$	$\text{K}_2\text{O}$	$\text{MnO}$	$\text{MgO}$	$\text{CaO}$	$\text{FeO}$	$\text{Al}_2\text{O}_3$	$\text{TiO}_2$	$\text{BaO}$	Total
B-1.1		34.3	0.1	0.1	0	0.4	30.0	0.03	36.0	0.01	0.4	101.2
B-1.2	Bright 70%	24.1	0.01	0.01	0	0.4	43.3	0.01	36.0	0.01	0.1	102.9
	Dark 30%	36.7	0	0.1	0.03	0.1	18.3	0.01	45.1	0.04	0.7	101.1
B-1.3	Bright 60%	24.2	0.03	0.01	0.1	0.05	40.6	0.03	34.0	0.01	0.1	99.0
	Dark 40%	42.6	0.02	0.03	0.01	0.3	19.8	0.02	34.9	0.01	0.3	97.7
B-2.1	Bright 60%	25.0	0	0.02	0	0.04	41.6	0.03	33.6	0	0.03	100.3
	Dark 40%	4.0	0.01	0	0	0.02	21.9	0.02	72.1	0.02	0	98.1
B-2.2	Bright 40%	26.2	0.01	0.02	0	0.2	40.8	0.02	34.1	0.01	0.1	101.5
	Dark 60%	44.0	0	0.01	0.01	0.01	19.8	0.03	34.6	0.01	0.1	98.5
B-2.3	Bright 40%	52.2	0.5	0.2	0.01	0.1	17.5	0.04	29.9	0	0.03	100.6
	Dark 60%	57.8	1.0	0.6	0.01	0.4	12.6	0.02	27.1	0.03	0.03	99.6

Green zone

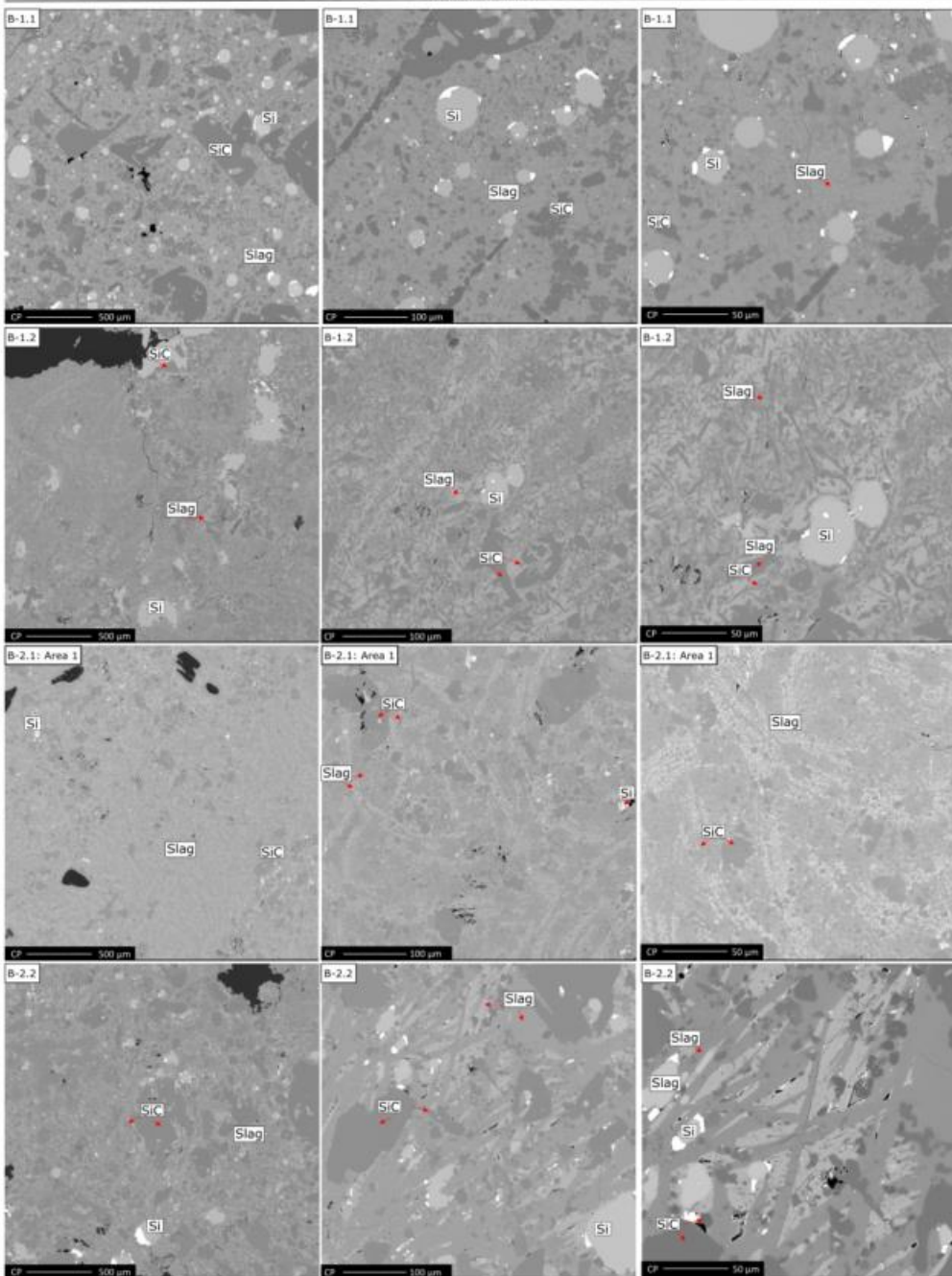


Figure 184 EPMA images of sample B-1.1 and -1.2, B-2.1 Area 1 and -2.2 with three different magnifications; 40X, 200X and 400X. All samples consist of  $\text{SiO}_2\text{-CaO-Al}_2\text{O}_3$  slag, SiC and some Si.

Grey zone

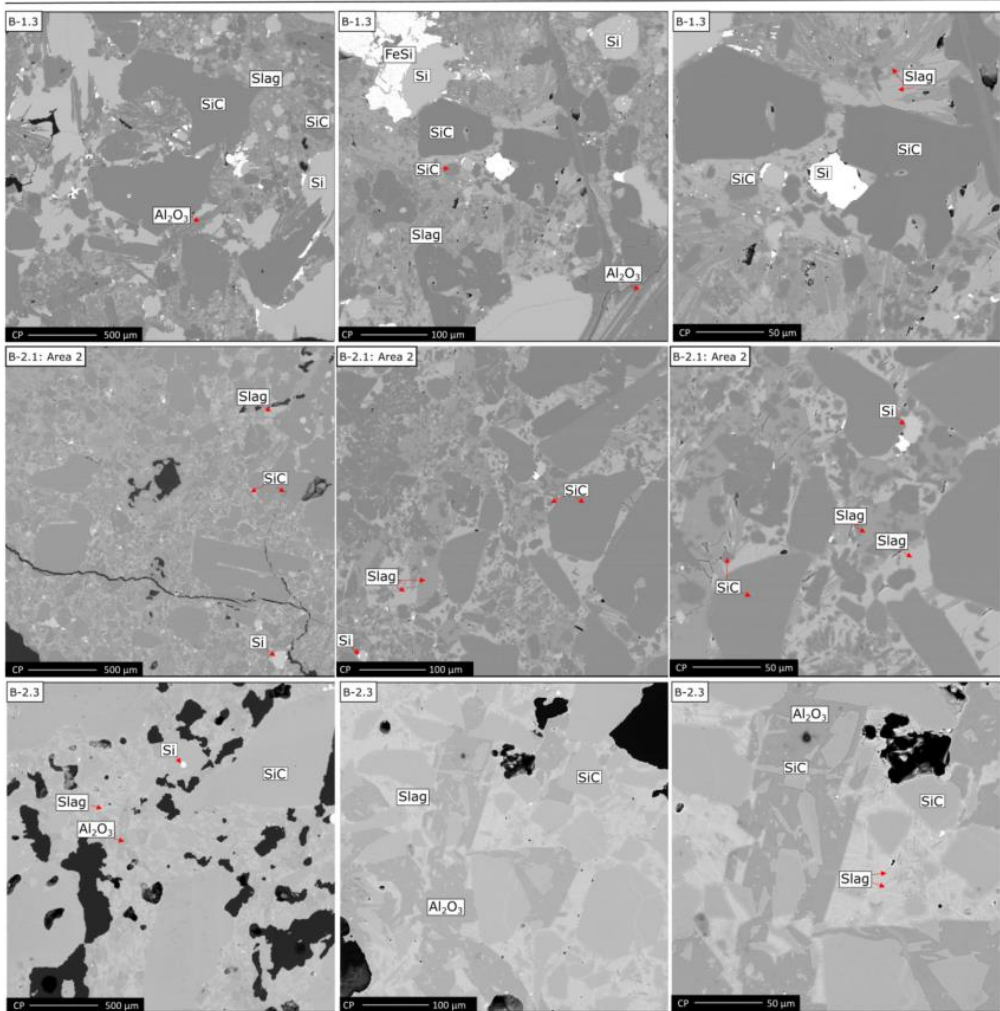


Figure 185 EPMA images of sample B-1.3, -2.1 Area 2 and -2.3 with three different magnifications; 40X, 200X and 400X. All samples consist of SiC, SiO<sub>2</sub>-CaO-Al<sub>2</sub>O<sub>3</sub> slag and some Si or FeSi. Sample B-1.3 and -2.3 also have areas with Al<sub>2</sub>O<sub>3</sub>.

### A.1.2.3. Tap-hole 7

Sample 47 includes the Si tapping channel and the zones around from tap-hole 7, as seen in Figure 186. Unfortunately, this sample was crushed into three pieces. The following analyzed samples are collected from the three pieces. It is not possible to place an exact position on the original sample picture, and analyzed samples are therefore based on visual colors. Table 50 lists the full WDS results for the analyzed slag in B-47.

Sample B-47 1.1 and 1.2 is collected from the green zone from the piece marked with one dot. EPMA images are shown in Figure 187. Both samples contain mostly SiO<sub>2</sub>-CaO-Al<sub>2</sub>O<sub>3</sub> slag and SiC particles in addition to some areas with Al<sub>2</sub>O<sub>3</sub> and Si.

Sample B-47 2.1 and 2.2 is from the grey colored area from the piece marked with one dot and are shown in Figure 189 and Figure 188, respectively. In sample B-47 2.1 small SiC particles are covering large areas of the sample, and SiO<sub>2</sub>-CaO-Al<sub>2</sub>O<sub>3</sub> slag have solidified into several phases. Larger areas with Si were also observed. Sample B-47 2.2 is taken right next to -2.1, but this sample is condensates of both Si and SiO<sub>2</sub>, and SiC and SiO<sub>2</sub>.

B-47.3 and -4 are from the grey colored zone in the piece marked with two dots, and B-47 5 is from the grey colored zone in the piece marked with three dots. They can be seen in Figure 189 and Figure 190. The samples are similar with larger SiC particles, SiO<sub>2</sub>-CaO-Al<sub>2</sub>O<sub>3</sub> slag, Al<sub>2</sub>O<sub>3</sub> and some Si.

Table 50 WDS results for the slag analyzed in sample B-47, which includes the zones around tap-hole 7.

Sample	Distribution	SiO <sub>2</sub>	Na <sub>2</sub> O	K <sub>2</sub> O	MnO	MgO	CaO	FeO	Al <sub>2</sub> O <sub>3</sub>	TiO <sub>2</sub>	BaO	Total
B-47 1.1		44.4	0.05	0.01	0	0.3	19.0	0.01	35.2	0	0.1	98.7
B-47 1.2	Bright 80%	47.6	0.1	0.03	0.02	0.1	18.1	0.1	33.2	0	0.1	99.2
	Dark 20%	72.9	0.1	0.7	0.01	1.3	5.9	0.4	17.9	0.04	0.7	99.6
B-47 2.1:	Bright 30%	71.1	0.1	4.5	0	0.7	7.5	0.1	15.5	0	0.2	99.7
	Grey 50%	70.0	0.1	2.2	0.01	0.7	9.6	0.01	17.2	0.02	0.2	100.2
A1	Dark 20%	72.5	0.2	0.2	0.03	0.7	9.5	0	16.4	0	0.1	00.6
	Bright 40%	76.5	0.4	4.6	0.3	1.0	6.6	0	11.9	0.02	0.4	101.0
A2	Dark 60%	57.1	0.1	1.4	0.03	0.4	13.7	0.01	25.8	0	0.1	98.7
	B-47 2.2	82.4	0.1	4.3	0.02	0.5	4.0	0.01	10.7	0.01	0.1	102.2
B-47.3		35.3	0.1	0.4	0.1	0.2	28.0	0	34.7	0.02	0.2	98.5
B-47.4	Bright 50%	28.9	0	0	0.03	0.03	38.6	0	31.7	0.01	0.02	99.3
	Dark 50%	44.0	0	0.1	0.02	0	19.7	0.03	36.1	0	0.4	98.9
B-47.5		47.5	0.5	0.4	0.01	0.5	22.5	0.02	31.1	0	0.03	102.2





Figure 186 The left picture shows the collected sample at the plant, B-47 from tap-hole 7, and right picture shows the sample crushed into three pieces. The pieces were marked with One, two or three orange dots.

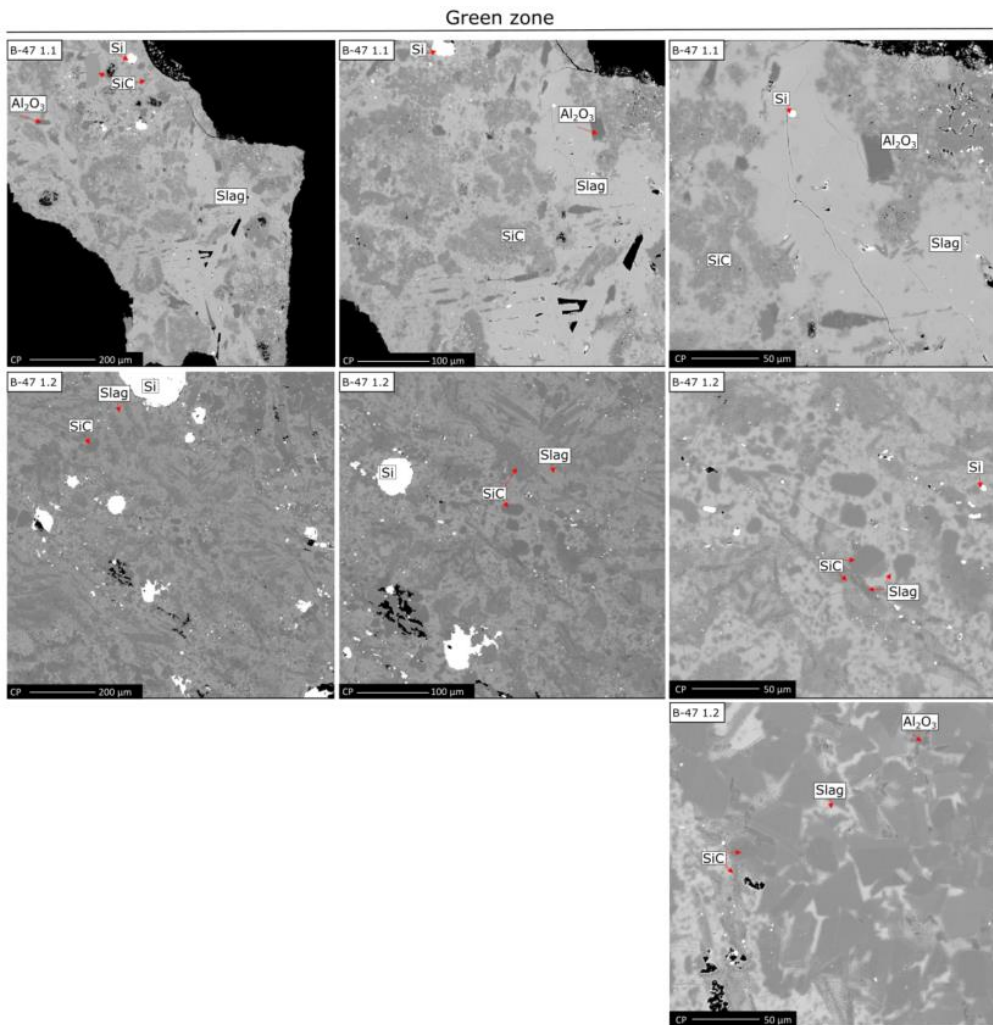


Figure 187 EPMA images of sample B-47 1.1 and 1.2, with three different magnifications; 40X, 200X and 400X. Both B-47 1.1 and 1.2 consist of  $\text{SiO}_2$ -CaO- $\text{Al}_2\text{O}_3$  slag, SiC,  $\text{Al}_2\text{O}_3$  and some Si.

### Condensate

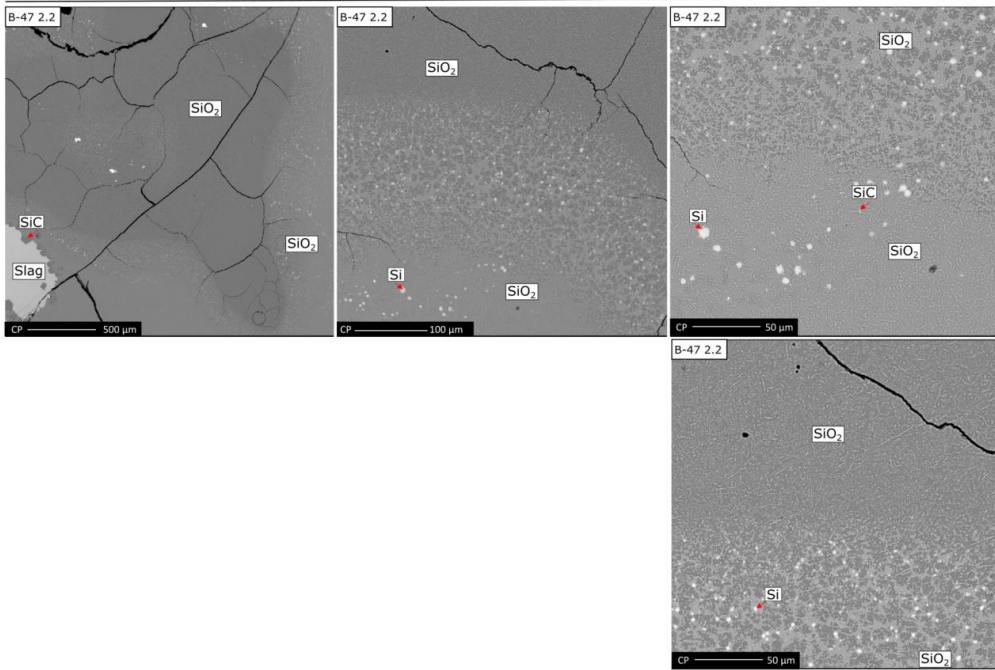


Figure 188 EPMA images of sample B-47 2.2, with three different magnifications; 40X, 200X and 400X. The sample consists of mostly SiO<sub>2</sub>, condensate of SiO<sub>2</sub> and Si, and condensate of SiO<sub>2</sub> and SiC. Only a small area with SiO<sub>2</sub>-CaO-Al<sub>2</sub>O<sub>3</sub> slag with SiC particles around were observed.

Grey zone

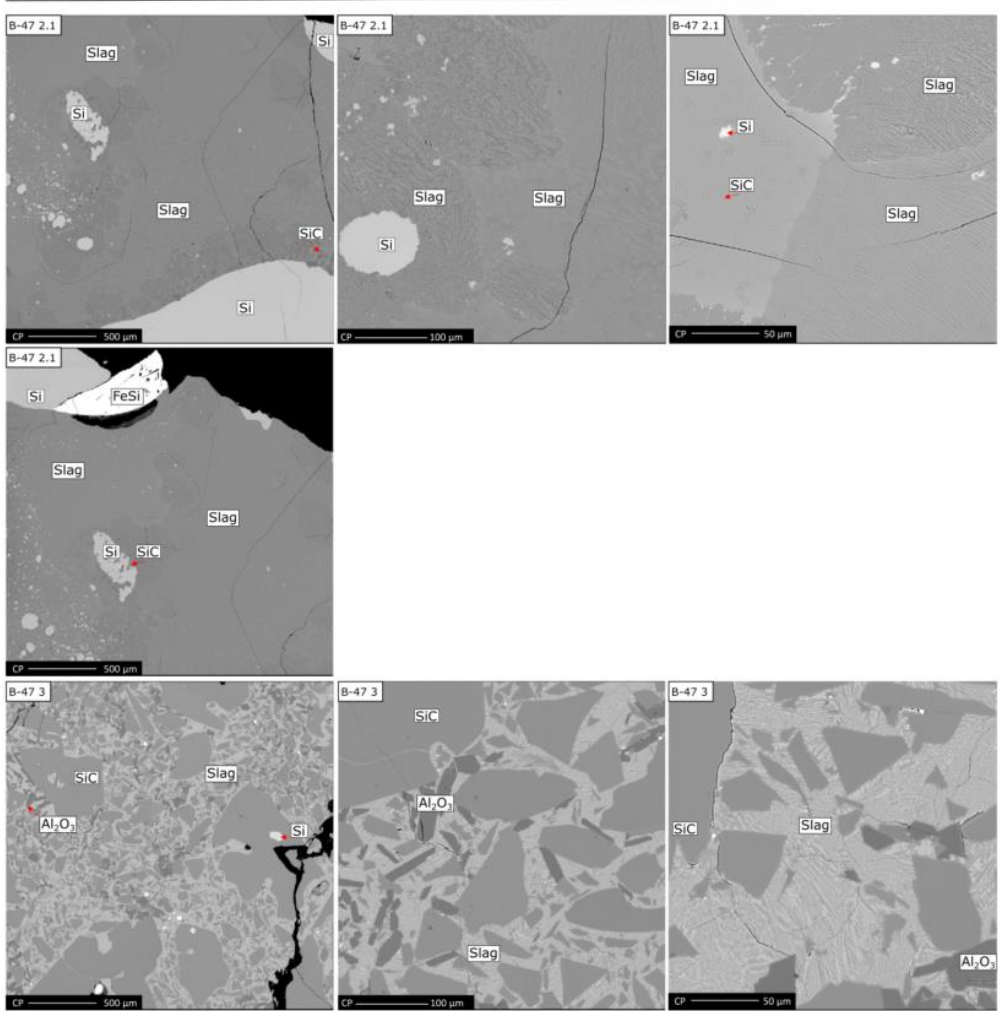


Figure 189 EPMA images of sample B-47 2.1 and 3 with three different magnifications; 40X, 200X and 400X. B-47 2.1 consists of SiO<sub>2</sub>-CaO-Al<sub>2</sub>O<sub>3</sub> slag, SiC, Al<sub>2</sub>O<sub>3</sub> and some SiC. Sample B-47 3 consists of the same materials, but with larger SiC particles.

Grey zone

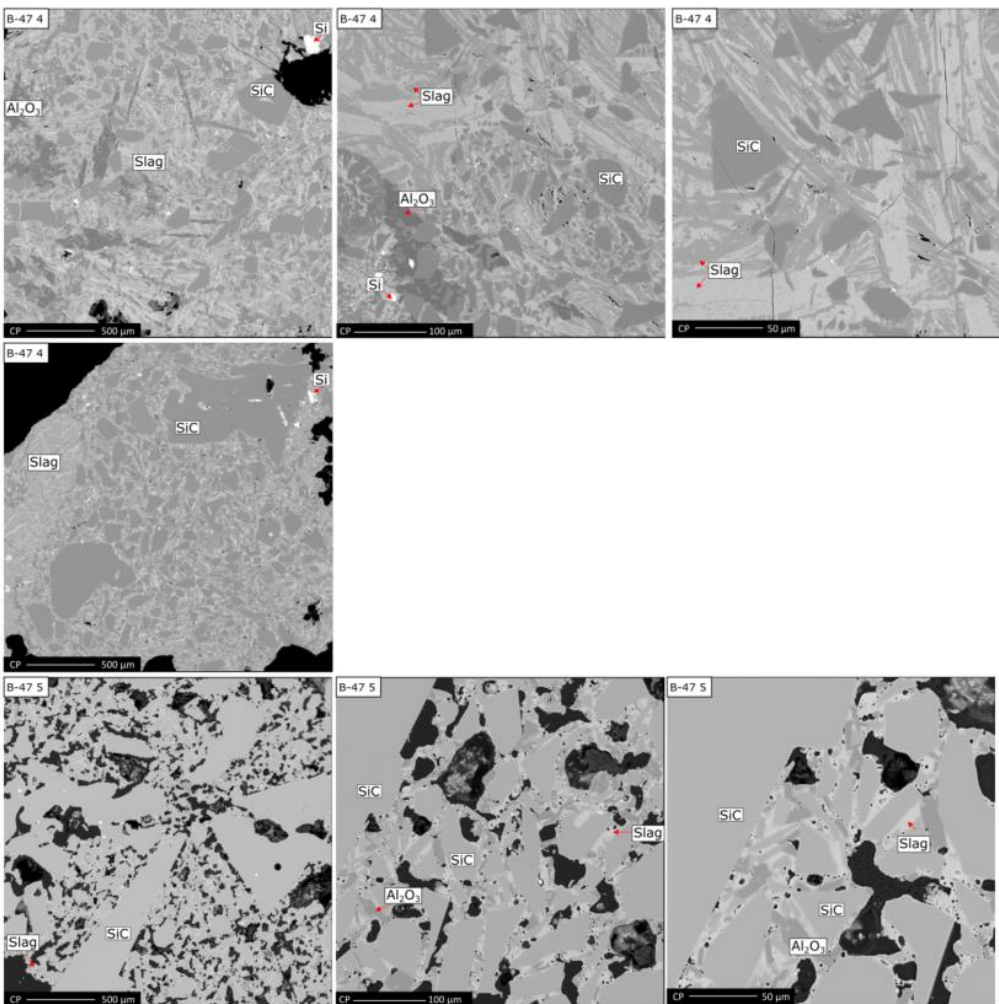


Figure 190 EPMA images of sample B-47.4 and 5 with three different magnifications; 40X, 200X and 400X. Both samples consist of  $\text{SiO}_2\text{-CaO-Al}_2\text{O}_3$  slag, SiC and  $\text{Al}_2\text{O}_3$ . Sample B-47.4 also have some Si.

### A.1.3 Collected tapped slag samples at the plant from previous tapping

At Furnace B, all metal and slag are tapped into the same ladle and separated in a later step. The slag is stored in a pile outside the plant and three visually different slag samples, B-tap 1, -2 and -3, were collected for further analysis. Table 51 lists the full WDS analysis for the tapped slag samples. Figure 191 and Figure 192 shows the EPMA images with three different magnifications: 40X, 200X and 400X.

B-tap 1.1 and 1.2 consist of SiC and SiO<sub>2</sub>-CaO-Al<sub>2</sub>O<sub>3</sub> slag, in addition to some Si. The slag has solidified into two separate phases. The darker area is SiO<sub>2</sub> together with some Si.

Both parallels of B-tap 2 contain mostly SiO<sub>2</sub> and some Si. Sample 2.1 does not contain any slag, but sample 2.2 has a small area with SiO<sub>2</sub>-CaO-Al<sub>2</sub>O<sub>3</sub> slag.

B-tap 3.1 and 3.2 both contain mostly slag and some SiC. Sample 3.1 also have areas with Al<sub>2</sub>O<sub>3</sub>.

Table 51 Full WDS results for the collected earlier tapped slag samples B-tap 1, -2 and -3.

Sample	Distribution	SiO <sub>2</sub>	Na <sub>2</sub> O	K <sub>2</sub> O	MnO	MgO	CaO	FeO	Al <sub>2</sub> O <sub>3</sub>	TiO <sub>2</sub>	BaO	Total
B-tap 1.1	Bright, 50%	24.1	0.01	0.01	0	0.1	42.3	0.04	34.6	0.02	0.01	101.2
	Dark, 50%	40.8	0.01	0.03	0.01	0.1	21.1	0.02	37.6	0.1	0.6	100.3
B-tap 1.2	Bright, 50%	44.7	0.02	0.2	0	0.6	28.3	0	26.6	0.1	1.8	102.4
	Dark, 50%	37.1	0	0.2	0	0.2	27.6	0.02	37.3	0.02	0.3	102.7
B-tap 2.1						SiO <sub>2</sub>						
B-tap 2.2		75.9	2.1	2.1	0	0.7	5.3	0	15.8	0.01	0.1	100.2
B-tap 3.1	Bright, 50%	32.2	0.1	0.4	0.01	1.1	33.8	0.03	33.7	0.02	0.6	101.9
	Dark, 50%	42.9	0	0.02	0.01	0.04	22.0	0	35.7	0.02	0.1	100.9
B-tap 3.2		40.9	0.02	0.1	0	0.4	22.4	0.02	36.5	0.02	0.3	100.7

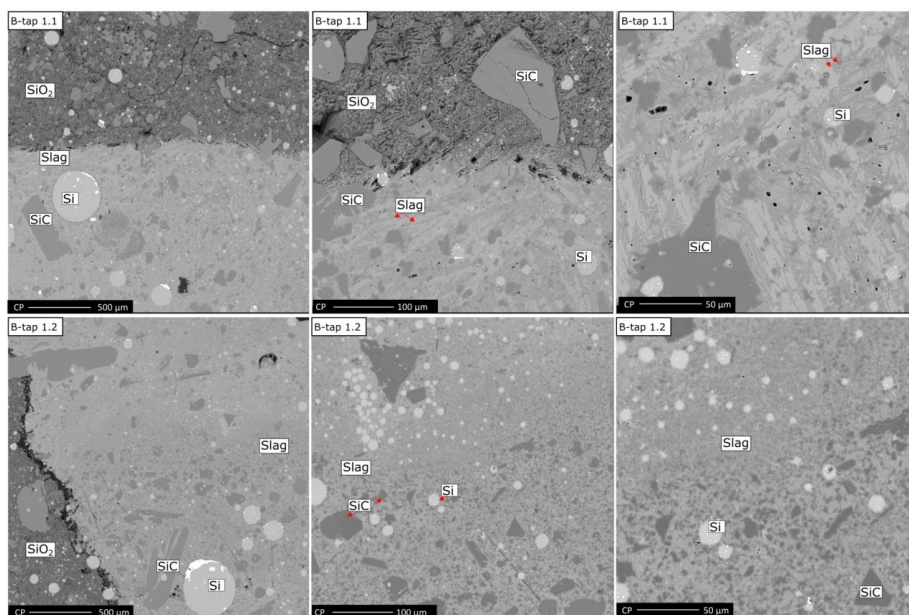


Figure 191 EPMA images of sample B-tap 1.1 and 1.2 with three different magnifications; 40X, 200X and 400X. B-tap 1.1 and 1.2 are mainly SiO<sub>2</sub>-CaO-Al<sub>2</sub>O<sub>3</sub> slag and SiC, and some Si and areas with SiO<sub>2</sub>.

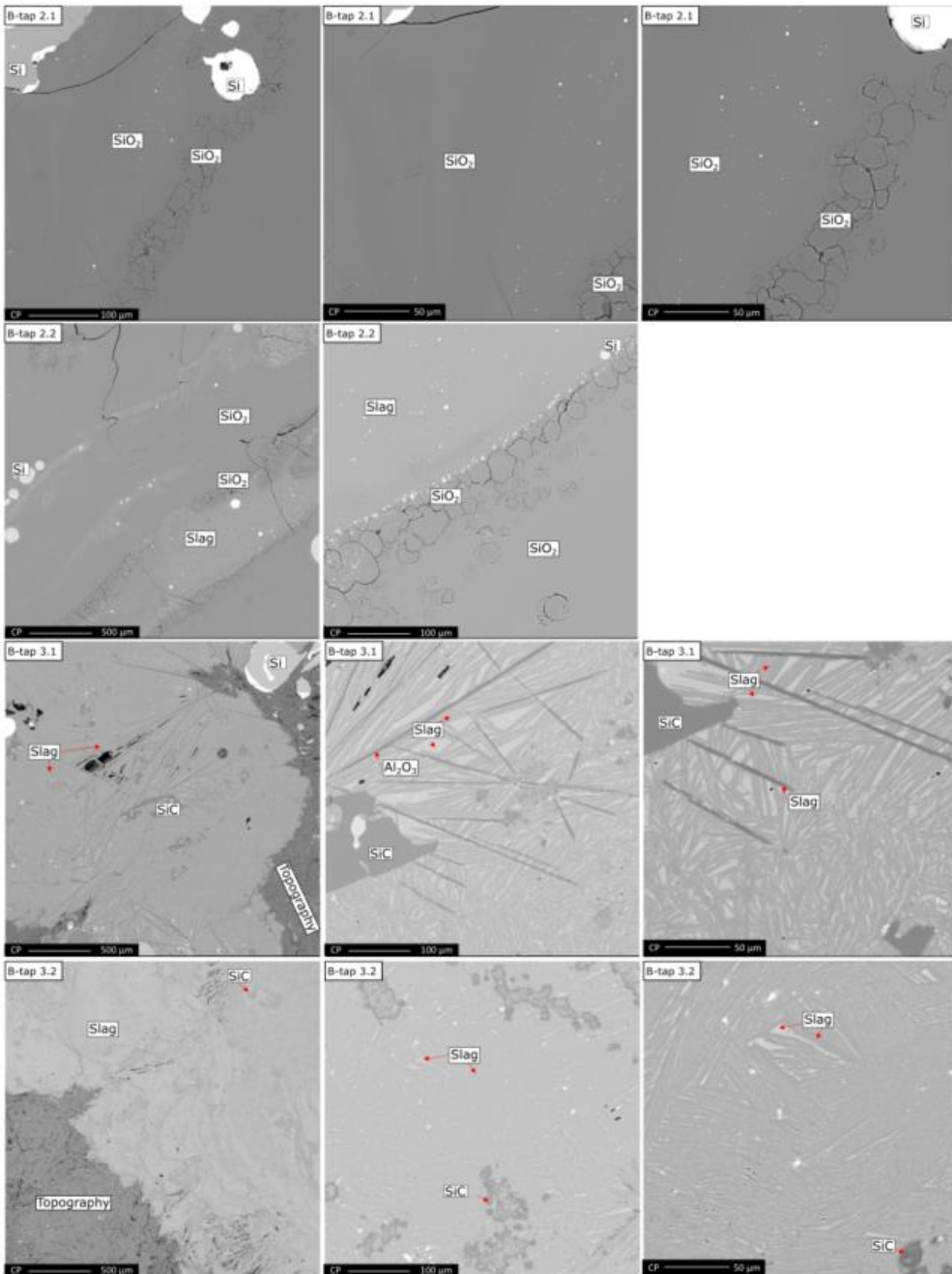


Figure 192 EPMA images of sample B-tap 2.1, 2.2, 3.1 and 3.2 with three different magnifications; 40X, 200X and 400X. B-tap 2.1 and 2.2 are SiO<sub>2</sub>. B-tap 2.2 has a small area with SiO<sub>2</sub> rich slag. The small white circles are SiO<sub>2</sub>, which indicates that this is condensate. Both B-tap 3.1 and 3.2 are mainly SiO<sub>2</sub>-CaO-Al<sub>2</sub>O<sub>3</sub> slag and some SiC. Sample B-tap 3.2 also have some Al<sub>2</sub>O<sub>3</sub>.

## A.2 Slag samples from five previous Norwegian excavations

Slag samples from five earlier Norwegian silicon and ferrosilicon furnace excavations were found from the archive and analyzed. Elkem Thamshavn furnace no. 2, Wacker Chemicals Holla no.4 and no.1, Elkem Salten and Finnfjord AS. The full WDS analysis are given in Table 52.

Figure 193 shows the EPMA images from the higher parts of the furnace. S-37 consists of SiO<sub>2</sub>-CaO-Al<sub>2</sub>O<sub>3</sub> slag, SiC and SiO<sub>2</sub>. F-75 consists of SiO<sub>2</sub>-CaO-Al<sub>2</sub>O<sub>3</sub> slag, SiC, FeSi and Al<sub>2</sub>O<sub>3</sub>. W<sub>4</sub>-5 consists of SiO<sub>2</sub>-CaO-Al<sub>2</sub>O<sub>3</sub> slag, Si and SiO<sub>2</sub>, and W<sub>1</sub>-33 of SiC, SiO<sub>2</sub>-CaO-Al<sub>2</sub>O<sub>3</sub> slag and some Si. The EPMA images from the lower parts of the furnace are shown in Figure 194.

Four slag samples were collected from the lower parts of the furnace, F-36, T-2, W<sub>4</sub>-12 and W<sub>4</sub>-20. F-36 and T-2 are mostly slag with smaller SiC particles. F-36 also has FeSi. In W<sub>4</sub>-12, W<sub>4</sub>-20, and S-43, most of the sample is SiC. There were only small areas with slag and for W<sub>4</sub>-12 some SiO<sub>2</sub>.

Two samples from Wacker Chemicals furnace no. 1 were collected from the zone right next to the Si tapping channel and S-46 from Elkem Salten was collected from the outer edge of a taphole. W<sub>1</sub>-115 consists of slag and SiC similar as in the green zone in Furnace B. W<sub>1</sub>-114 is mostly SiO<sub>2</sub> with slag in between grain boundaries and cracks, and some SiC particles. S-46 consist of mainly SiC and SiO<sub>2</sub>. Here only a small area with slag is found.

Table 52 Full WDS results for the slag in the earlier excavation samples. The first letter in the sample ID refers to the first letter in the furnace they are collected from; Elkem Salten, Finnfjord AS, Wacker Chemicals and Elkem Thamshavn. The oxide compositions are given in wt%.

Sample	Distribution	SiO <sub>2</sub>	Na <sub>2</sub> O	K <sub>2</sub> O	MnO	MgO	CaO	FeO	Al <sub>2</sub> O <sub>3</sub>	TiO <sub>2</sub>	BaO	Total
S-37		67.5	0	1.8	0	1.1	19.9	0	11.7	0	0.04	101.9
F-75		44.8	0	0.1	0	0.04	20.4	0.01	34.9	0	0	100.5
W <sub>4</sub> -5		69.5	0	1.2	0	1.8	2.8	8.0	15.2	0	0.04	98.5
S-43		69.5	0	0.05	0	0.01	19.2	0.01	12.3	0	0.1	101.3
F-36		33.7	0	0.1	0	0.7	27.9	0.01	37.4	0	1.0	100.9
T-2	Bright, 50%	32.6	0.01	0.03	0.01	0.3	38.0	0.1	28.5	0	0.02	99.7
	Dark, 50%	44.4	0.02	0.1	0	0.1	21.5	0.2	34.9	0.1	0.6	101.9
W <sub>1</sub> -33	Bright, 80%	26.4	0	0.01	0	0.04	42.4	0.02	33.2	0	0.02	102.2
	Dark, 20%	45.3	0	0.04	0	0.02	20.4	0	35.1	0	0.1	100.9
W <sub>4</sub> -12	Bright	44.1	0.02	0	0	0.1	33.6	0.03	24.2	0	0.1	102.1
	Grey	74.4	0.1	2.0	0.02	0.5	14.5	0	9.4	0.02	0.01	100.9
W <sub>4</sub> -20		57.0	0	0.1	0	0.2	25.9	0.01	18.4	0	0.03	101.6
S-46		51.5	0	0.01	0	15.8	19.8	8.5	2.5	0	0.02	98.2
W <sub>1</sub> -114		63.4	0	0.7	0	0.2	18.6	0.02	17.4	0	0.1	100.4
W <sub>1</sub> -115	Grey, 50%	50.2	0	0.1	0	0.04	19.1	0	31.9	0	0.02	101.2
	Dark, 50%	76.9	0	0.8	0	0.3	11.7	0.01	11.6	0	0.4	101.7

## Higher parts of Si and FeSi furnaces

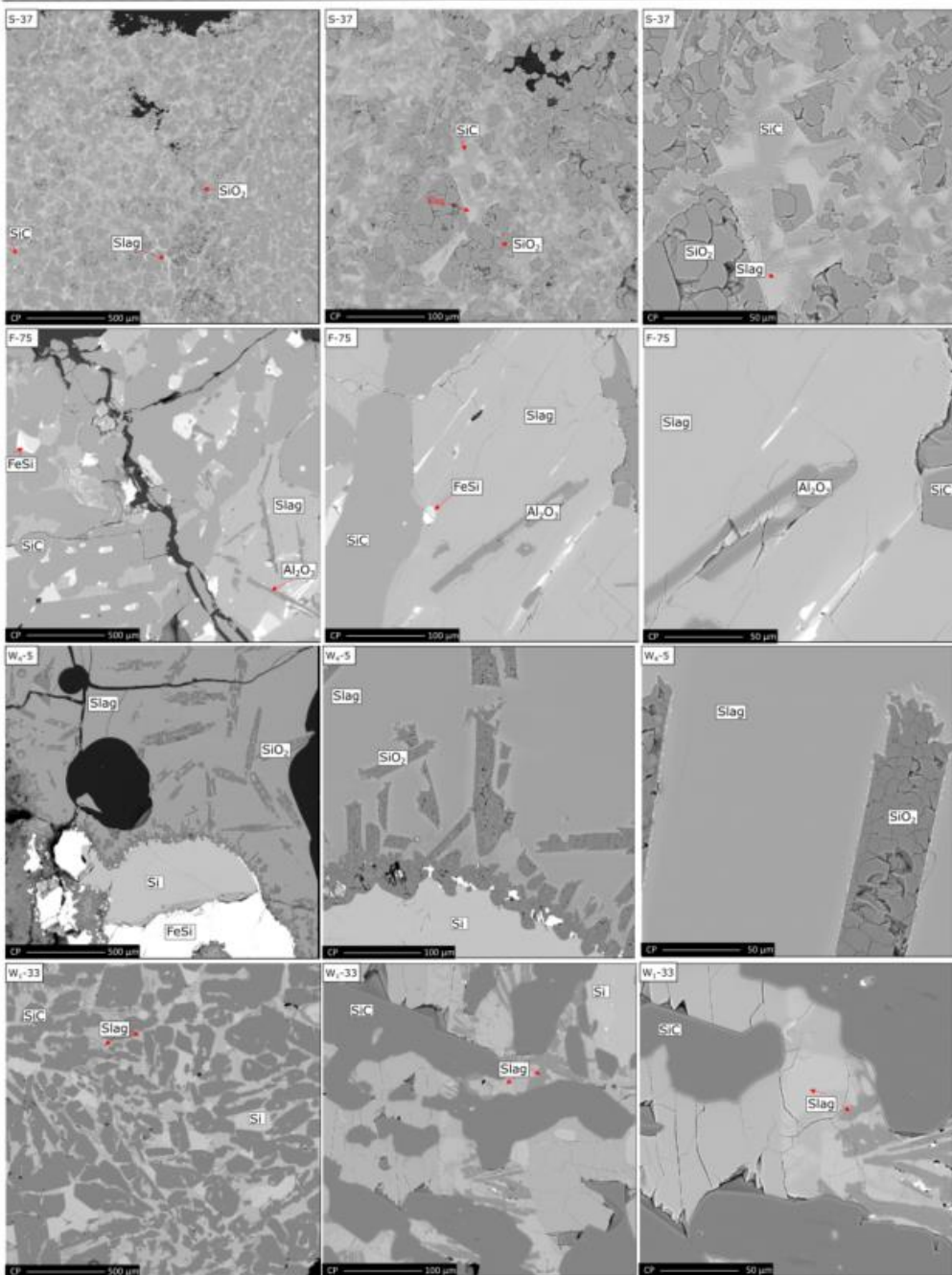


Figure 193 EPMA images of samples from the higher parts of the furnace, S-37, F-75, W<sub>4</sub>-5 and W<sub>1</sub>-33 with three different magnifications; 40X, 200X and 400X. S-37 consists of SiO<sub>2</sub>-CaO-Al<sub>2</sub>O<sub>3</sub> slag, SiC and SiO<sub>2</sub>. F-75 consists of SiO<sub>2</sub>-CaO-Al<sub>2</sub>O<sub>3</sub> slag, SiC, FeSi and Al<sub>2</sub>O<sub>3</sub>. W<sub>4</sub>-5 consists of SiO<sub>2</sub>-CaO-Al<sub>2</sub>O<sub>3</sub> slag, Si and SiO<sub>2</sub>, and W<sub>1</sub>-33 of SiC, SiO<sub>2</sub>-CaO-Al<sub>2</sub>O<sub>3</sub> slag and some Si.



## Lower parts of Si and FeSi furnaces

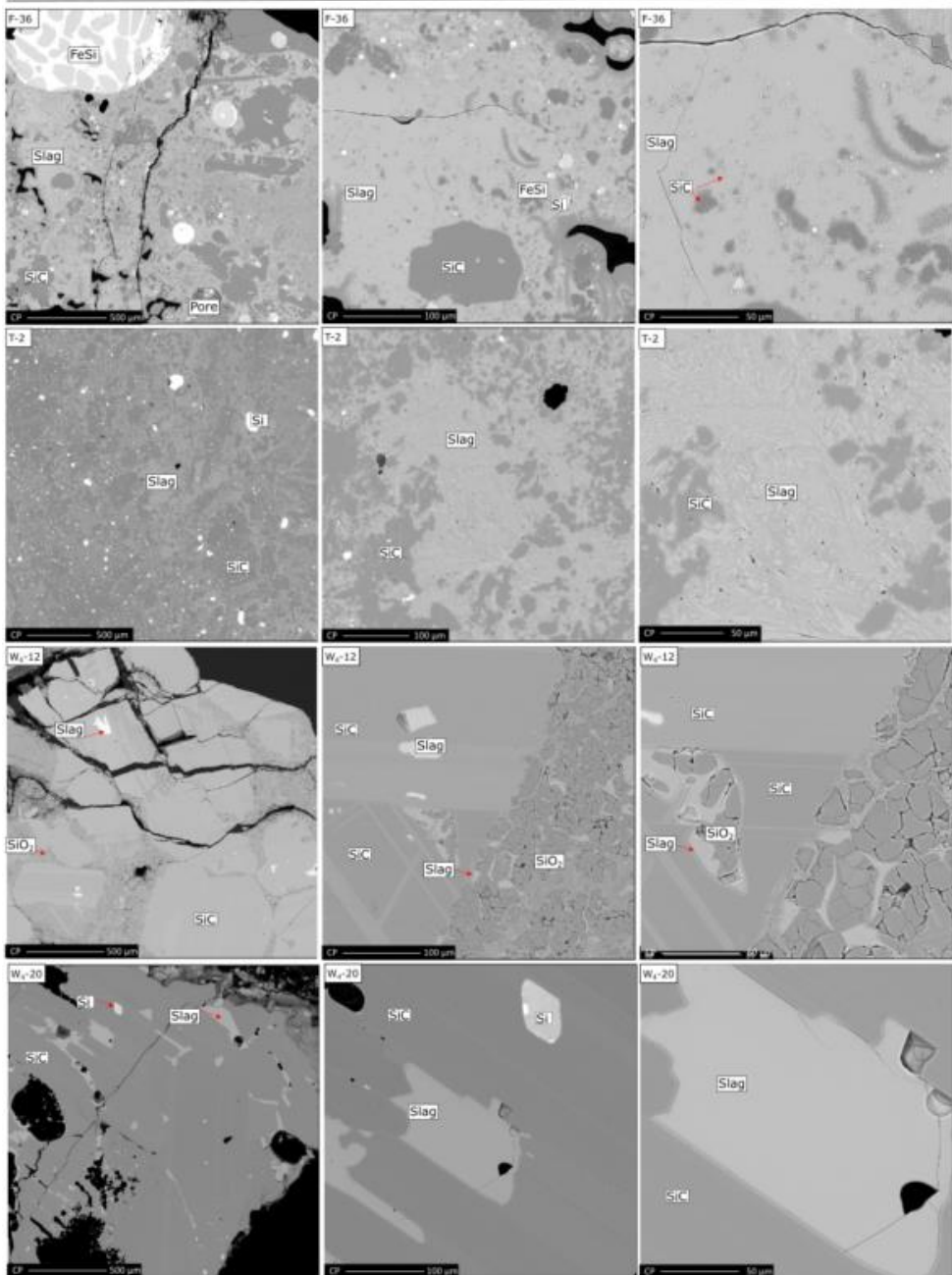


Figure 194 EPMA images of samples from the lower parts of the furnace, F-36, T-2, W<sub>4</sub>-12 and W<sub>4</sub>-20 with three different magnifications; 40X, 200X and 400X. F-36 and T-2 consist of SiO<sub>2</sub>-CaO-Al<sub>2</sub>O<sub>3</sub> slag and SiC. F-36 also has some FeSi. W<sub>4</sub>-12 and W<sub>4</sub>-20 consist of mostly SiC and some SiO<sub>2</sub>-CaO-Al<sub>2</sub>O<sub>3</sub> slag. W<sub>4</sub>-12 also has some SiO<sub>2</sub>.

## Zones next to tapping canal of Si furnaces

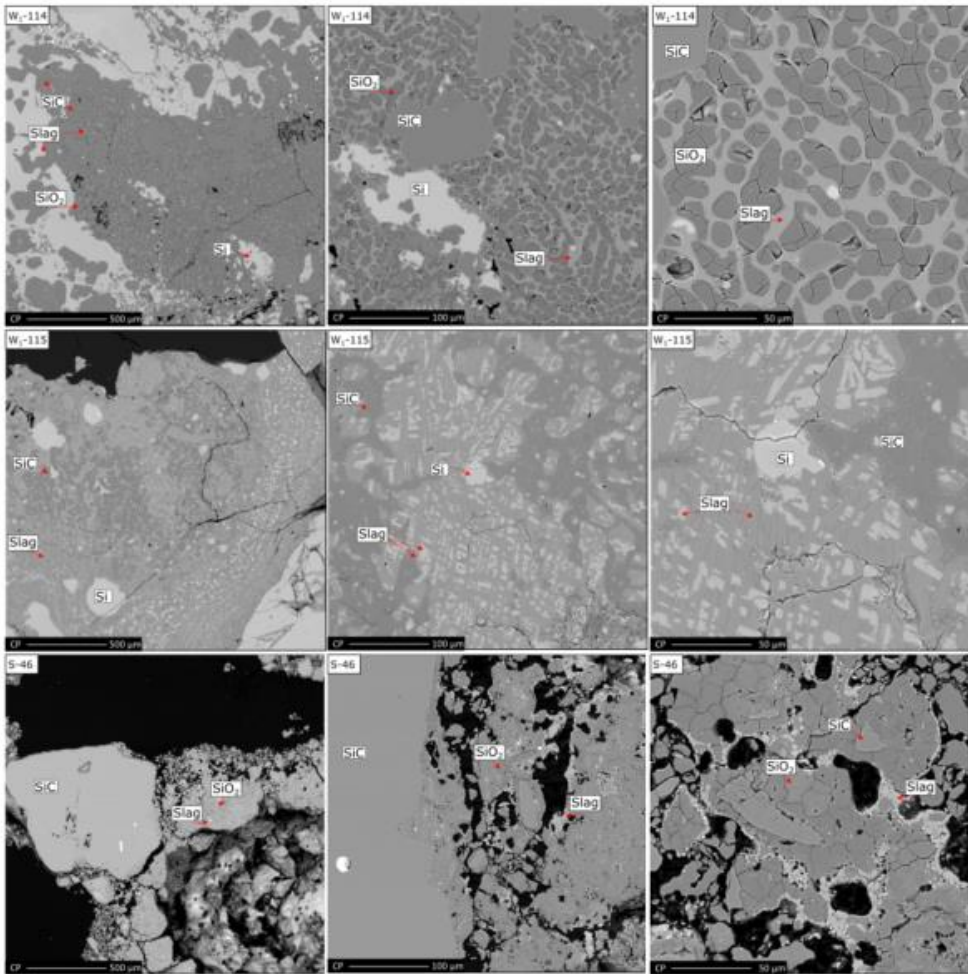


Figure 195 EPMA images of samples from the zone next to the tapping channel, W<sub>1</sub>-114 and -115 with three different magnifications; 40X, 200X and 400X. Both samples consist of SiO<sub>2</sub>-CaO-Al<sub>2</sub>O<sub>3</sub> slag, SiC and some Si. W<sub>1</sub>-114 also has some SiO<sub>2</sub>. S-46 consists of mostly SiC and some SiO<sub>2</sub> and slag of SiO<sub>2</sub>, MgO, CaO, FeO and Al<sub>2</sub>O<sub>3</sub>.

### A.3.Tapped slag

In addition to Si and FeSi, slag is also tapped from the tap-hole. Slag samples from three different furnaces have been collected and analyzed in this study. Elkem Thamshavn from May 2019 to May 2020, Furnace B in June 2020 and Furnace O and R, at Finnjord AS from September 2020 to March 2022. Table 53, Table 54 and Table 55 list the original WDS oxide analysis for all the slag samples.

Table 53 Original WDS results for the analyzed slag for the tapped samples collected from Elkem Thamshavn, furnace no. 2. Oxide analysis are given in mass percent.

Sample		SiO <sub>2</sub>	Na <sub>2</sub> O	K <sub>2</sub> O	MnO	MgO	CaO	FeO	Al <sub>2</sub> O <sub>3</sub>	TiO <sub>2</sub>	BaO	Total
19.05.24	1	67.2	2.6	0.2	0	0.8	20.7	0.2	8.9	0.1	0.1	100.8
	2	52.7	0.8	0.04	0	0.1	26.9	0.01	20.6	0.04	0.2	101.5
19.06.05	1	39.6	0.05	0.01	0.01	0.1	34.6	0.03	28.0	0.03	0.03	102.8
	2	46.6	0.4	0.02	0.01	0.1	31.7	0.03	23.4	0.02	0.3	102.6
19.08.18	1	46.8	0.03	0.01	0.01	0.2	42.5	0.04	12.9	0.01	0.1	102.6
	2	47.2	0.2	0	0	0.2	33.0	0.04	21.9	0.1	0.2	102.7
19.10.26	1	53.2	0.03	0.1	0.01	0.1	29.1	0	17.2	0.04	0.1	100.0
	2	63.1	0.04	0.1	0.01	0.2	25.5	0.03	12.4	0.0	0.1	101.4
19.12.03	1	52.8	0.01	0.01	0.02	0.2	25.7	0.03	20.3	0.03	0.2	99.3
	2	51.1	1.0	0.02	0.01	0.5	24.3	0.1	22.5	0.02	0.2	99.8
19.12.04	1	59.0	0.03	0.01	0.03	0.2	24.9	0	16.2	0.01	0.1	100.4
	2	57.7	0.03	0.02	0.01	0.2	26.4	0.04	15.1	0.1	0.3	99.9
19.12.07	1	56.3	1.2	0.5	0.1	1.3	26.8	1.1	13.1	0.3	0.1	100.9
	2	49.9	0.3	0	0.02	0.2	29.4	0.01	19.5	0.01	0.2	99.5
19.12.09	1	54.1	1.0	0.02	0	0.4	25.8	0.03	18.6	0	0.2	100.2
	2	55.1	5.1	0.2	0	0.9	22.3	0.5	16.4	0.1	0.2	100.7
20.01.10	1	40.6	0.2	0.03	0.01	1.4	35.1	0.8	22.1	0.02	0.3	100.6
	2	68.7	0.5	0.1	0.03	2.6	15	1.2	12.7	0.03	0.2	101.2
20.02.07	1	52.2	0.3	0.01	0	0.4	31.3	0.2	16.2	0.02	0.3	100.9
	2	46.8	0.2	0.01	0.02	0.2	26.6	1.2	22.5	0.04	0.2	97.7
20.05.05	1	45.5	2.8	0.02	0.02	0.20	23	0.12	29	0.02	0.23	100.0
	2	55.4	6.8	0.13	0.02	0.23	20.5	0.11	18.8	0.01	0.21	102.2

Table 54 Original WDS results for the analyzed slag for the tapped samples collected from Furnace B. Oxide analysis are given in mass percent.

Sample		SiO <sub>2</sub>	Na <sub>2</sub> O	K <sub>2</sub> O	MnO	MgO	CaO	FeO	Al <sub>2</sub> O <sub>3</sub>	TiO <sub>2</sub>	BaO	Total
20.06.09	1	39.8	2.9	0.1	0.1	0.3	22.3	0.3	34.8	0.03	0.2	100.6
	2	49.2	0.1	0	0	0.3	18.6	0.04	31.0	0	0.2	99.4
20.06.18	1	29.2	0.01	0.1	0.1	0.3	26.3	0.01	43.1	0.01	0.3	99.3
	2	31.1	0.01	0.1	0.01	0.4	25.7	0.01	42.4	0.01	0.3	100.1
20.06.19	1	45.7	0.1	0.01	0.02	0.6	19.1	0.01	33.1	0.03	0.3	98.8
	2	33.3	0.03	0.1	0	0.5	24.6	0.04	40.5	0.03	0.3	99.4

Table 55 Original WDS results for the analyzed slag for the tapped samples collected from Finnford AS. Oxide analysis are given in mass percent.

Sample	SiO <sub>2</sub>	Na <sub>2</sub> O	K <sub>2</sub> O	MnO	MgO	CaO	FeO	Al <sub>2</sub> O <sub>3</sub>	TiO <sub>2</sub>	BaO	Total
TPR170920a	32.1	0.03	0.07	0	0.5	27.4	0.01	37.0	0.08	1.3	98.5
TPR180920a	36.0	0	0.1	0.02	0.5	26.0	0	34.2	0.1	1.2	98.1
TPR180920c	34.7	0.04	0.1	0.01	0.7	23.1	0.03	38.4	0.1	1.2	98.2
TPR190920a	35.6	0.02	0.02	0.01	0.4	29.7	0.01	31.8	0.1	1.2	98.8
TPR220920a	36.7	0.03	0.02	0.01	0.5	27.0	0.03	35.4	0.02	0.4	100.0
TPR230920a	36.3	0.03	0.1	0.03	0.8	23.9	0.01	36.5	0.1	1.1	98.8
TPR230920b	36.4	0.02	0.1	0	0.8	24.9	0.01	35.4	0.1	1.1	98.8
TPR221020a	34.3	0.03	0.1	0	0.9	24.8	0.01	38.2	0.02	1.1	99.4
TPR271020	33.5	0.02	0.01	0	0.5	33.3	0	30.1	0.03	1.1	98.6
TPR281020	36.3	0.03	0.03	0.01	0.8	27.9	0.02	32.2	0.01	1.2	98.4
TPR041120	39.0	0.01	0.03	0.01	1.1	28.5	0.03	30.8	0.01	1.2	100.6
TPR131120	36.3	0.03	0.04	0	0.9	27.9	0	33.3	0.02	1.2	99.7
TPO220920	35.6	0.01	0.01	0.01	0.2	28.8	0.02	34.8	0.05	0.5	100.0
TPO221020a	42.5	0.14	0.6	0.01	1.2	22.7	0.03	32.0	0	1.0	100.3
TPO131120	35.1	0.01	0.01	0.02	0.5	29.8	0.03	32.5	0.02	1.3	99.3
TPO231120.1	69.6	0.05	0.2	0.1	0.5	7.6	0.7	20.1	0.01	0.3	99.2
TPO231120.2	55.4	0.03	0.2	0.02	0.7	12.0	0.1	30.0	0.01	0.6	99.0
TPO170121a	35.0					31.5		32.7			99.3
TPO170121b	34.8					32.7		32.6			100.1
TPO170121c	35.1					32.1	0.03	32.3			99.5
TPO260121	36.6					31.1	0.01	32.0			99.6
TPO230221	55.1					17.3		26.7			99.1
TPR310121	35.7					28.2		36.3			100.2
TPR010221.T3	41.2					22.6		34.9			98.8
TPR010221.T5	63.2					10.3	9.1	16.0			98.7
TPR120221	34.9					29.4		34.8			99.1
TPR140221	31.7					32.0		35.1			98.9
TPR180221	37.3					28.4		32.2			97.9
TPR090321	34.4					27.8		36.1			98.2
TPR170321N	39.1	0.02	0.1	0	0.5	28.3	0.01	30.4	0	0	98.5
TPR27421	34.7					28.9		34.7			98.1
TPR261121	32.3					35.1		29.8			97.7
TPX2022	64.2					11.7	2.1	19.8			97.5
TPR030122	37.3					26.9		35.7			97.4
TPO030322.1	71.9					0.9	21.5	2.7			97.7
TPO030322.2	77.1					1.0	15.8	3.0			97.2

#### A.4 Samples from the charge surface at Finnford AS

From Finnford furnace O and R, there were also collected six large samples from the charge surface from September 2020 to March 2021. These furnaces have a maximum power of 42 MW and 45 MW, respectively. The sampling was done in a period of 6 months. The following figures shows pictures of the samples taken at the plant and EPMA images. When examining the samples in the microscope, it could be seen that many visually different samples contained the same components.

### A.4.1 Sample CPR1809

The 18<sup>th</sup> of September 2020, three samples were collected from the charge top by the stoking car. CPR1809 a, b and c, which are from different locations at the charge top. The position of CPR1809a is unknown. Picture and EPMA images are shown in Figure 196. The sample consist of mostly SiO<sub>2</sub> and slag and some FeSi. CPR1809a.1 also has some Al<sub>2</sub>O<sub>3</sub>.

CPR1809b were described as viscous matter which were located just between two electrodes. This sample is mostly brown condensate on carbon, as can be seen in Figure 197.

Sample CPR1809c was taken around 0.5m from the edge of the crust. At this sampling time, the charge had stopped being viscous. Both parallels of sample c are SiO<sub>2</sub> and some SiO<sub>2</sub> rich slag. In between the SiO<sub>2</sub> is also a white slag phase.

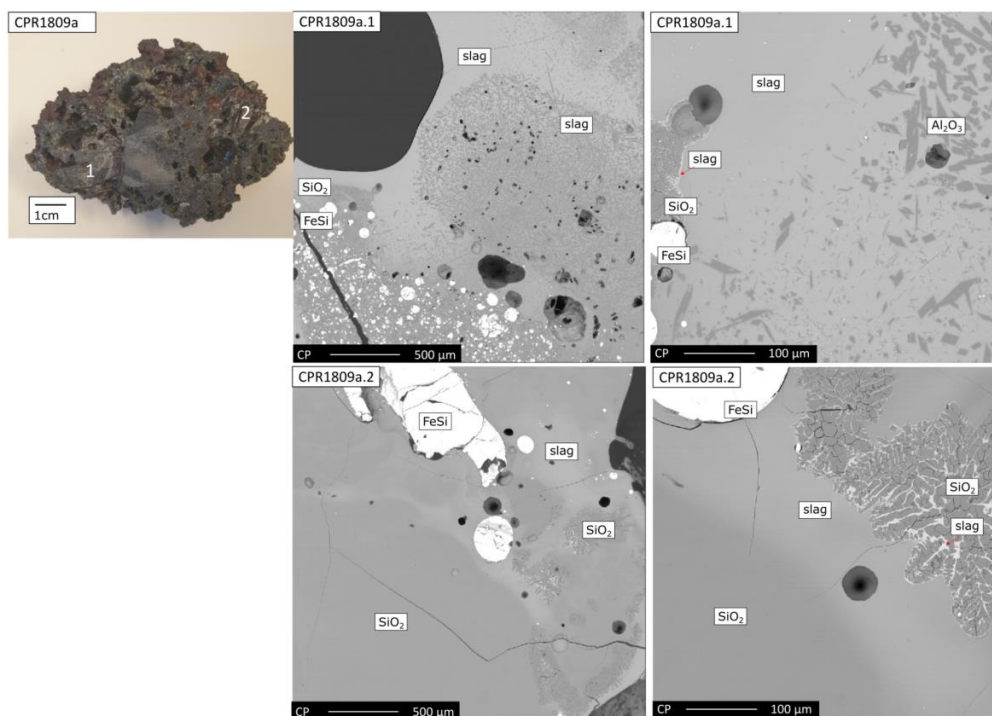


Figure 196 Sample CPR1809a.1 and a.2 with two different magnifications; 40X and 200X. The samples are mostly SiO<sub>2</sub>, slag and some FeSi. CPR1809a also has some Al<sub>2</sub>O<sub>3</sub>. The top left picture is taken at the plant and marked with 1 and 2, which corresponds to a.1 and a.2.

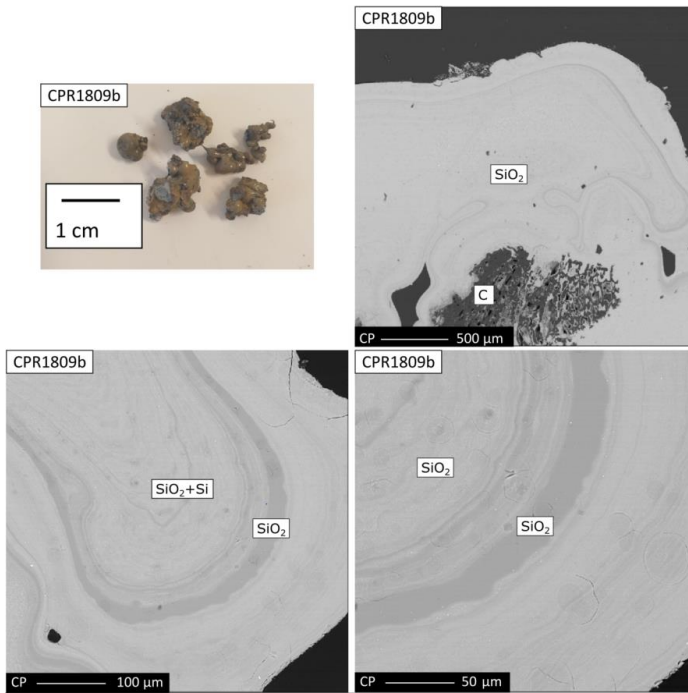


Figure 197 Sample CPR1809b with three different magnifications; 40X, 200X and 400X. The sample is brown condensate, as can be seen in the top left picture taken at the plant.

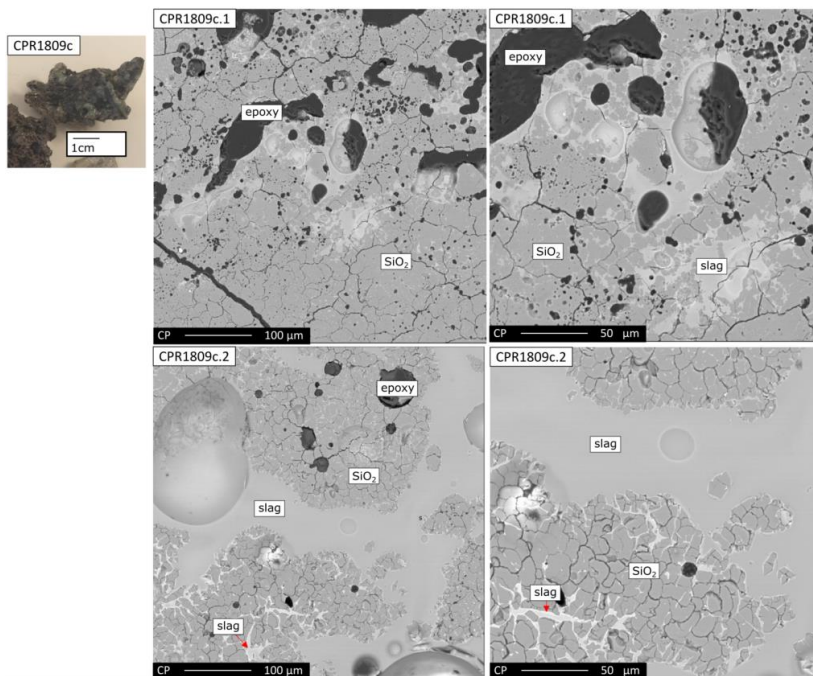


Figure 198 Sample CPR1809c.1 and c.2 with two different magnifications; 200X and 400X. Both samples are SiO<sub>2</sub> and slag.

## A.4.2 Sample CPR0211

The sample CPR0211 was taken from an area with viscous matter, between two electrodes. Three visually different samples marked in the top left picture in Figure 199 were analyzed. The first is from the brown colored area which is brown condensate of  $\text{SiO}_2$  and Si covering quartz. The second sample is more green/white/brown and is  $\text{SiO}_2$  with some  $\text{SiO}_2+\text{Si}$  in between the grain boundaries and cracks. The last sample is from the red and dark grey area. The overview EPMA image to the bottom left is divided in two areas to highlight the contrasts. Area 1 is a mix of slag,  $\text{SiO}_2$  and FeSi. The slag is both next to the  $\text{SiO}_2$  and in between the grain boundaries and cracks. Area 2 is carbon and slag. The dark grey areas on the EPMA image are some epoxy left from the sample preparation.

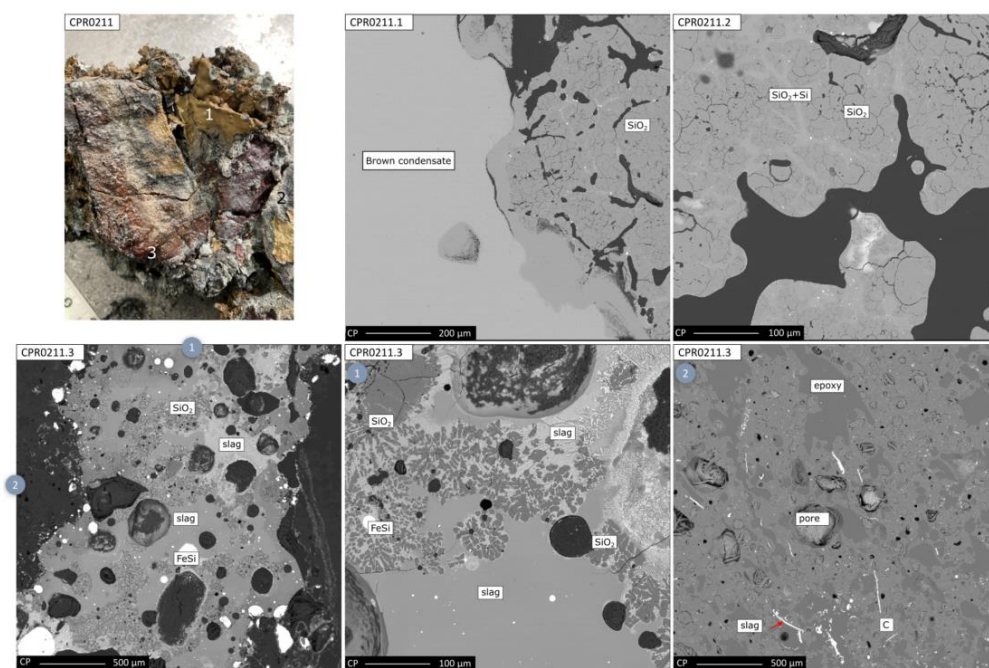


Figure 199 Sample CPR0211 1, 2 and 3 with three different magnifications; 40X, 100X and 200X. The top left picture is the whole sample taken from the furnace with marked position of sample 1, 2 and 3. CPR0211.1 is brown condensate of  $\text{SiO}_2$  and Si covering quartz and CPR0211.2 is  $\text{SiO}_2$  with some  $\text{SiO}_2+\text{Si}$  in between the grain boundaries and cracks. CPR0211.3 is divided in two areas, marked in the bottom left image. Area 1 is a mix of slag,  $\text{SiO}_2$  and FeSi and Area 2 is carbon and slag. The dark grey areas on the EPMA image are some epoxy left from the sample preparation.

## A.4.3 Sample CPO1101

Sample CPO1101 was collected from Furnace O at the charge surface and is a large sample of around 0.5m. It was reported from the operators that the charge was viscous at sampling

time and that the area around the sample was hard. The sample is divided into several smaller samples which are named after what they were believed to be.

CPO1101.S was believed to be slag with some brown condensate and the analysis S.1 and S.2 can be seen in Figure 200. It was observed several areas on the main sample which were hard and appeared as solidified slag. The EPMA images shows that both analysis samples from this area is SiO<sub>2</sub> rich slag and brown condensate of SiO<sub>2</sub> and Si.

CPO1101.BK is brown condensate which were also observed in several areas on the main sample. Pictures taken at the plant and EPMA images of the two analysis samples can be seen in Figure 201. In some areas there were also layer by layer with brown condensate of SiO<sub>2</sub>+Si and white condensate of SiO<sub>2</sub>+SiC, which can be observed in the right image of BK.2 in the figure.

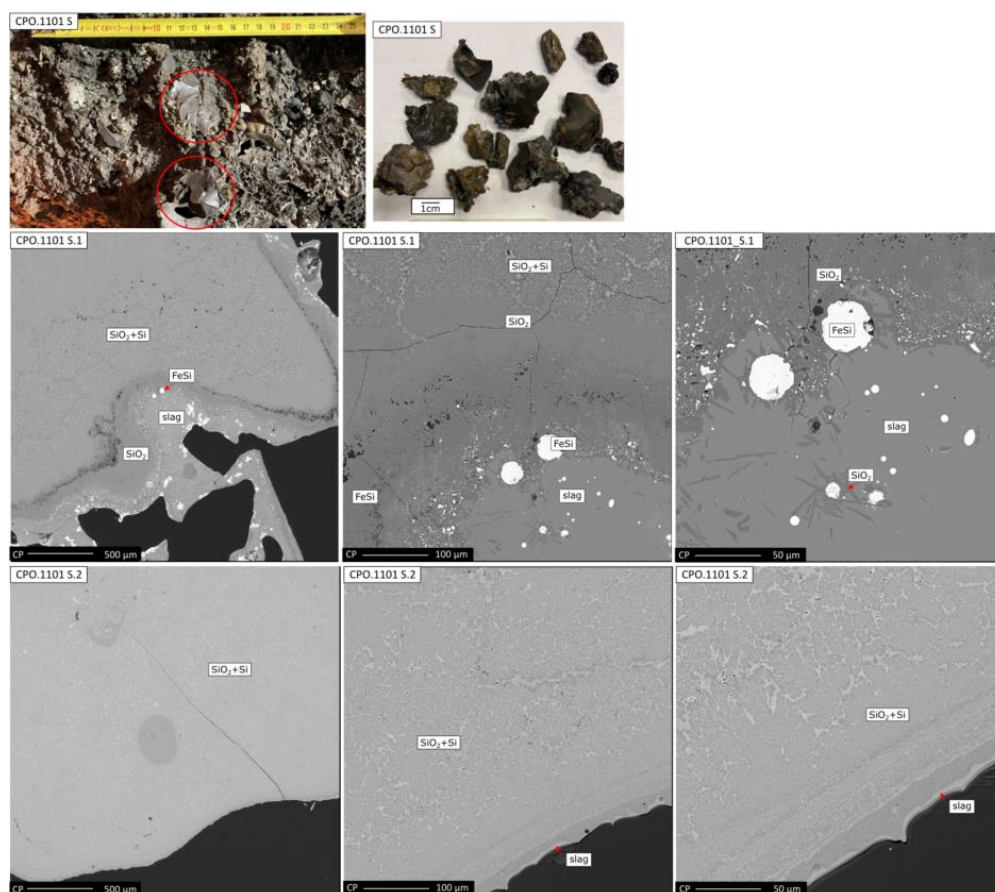


Figure 200 Sample CPO1101.S.1 and S.2 with three different magnifications; 40X, 200X and 400X. Both analysis samples from this area is SiO<sub>2</sub> rich slag and brown condensate of SiO<sub>2</sub> and Si.



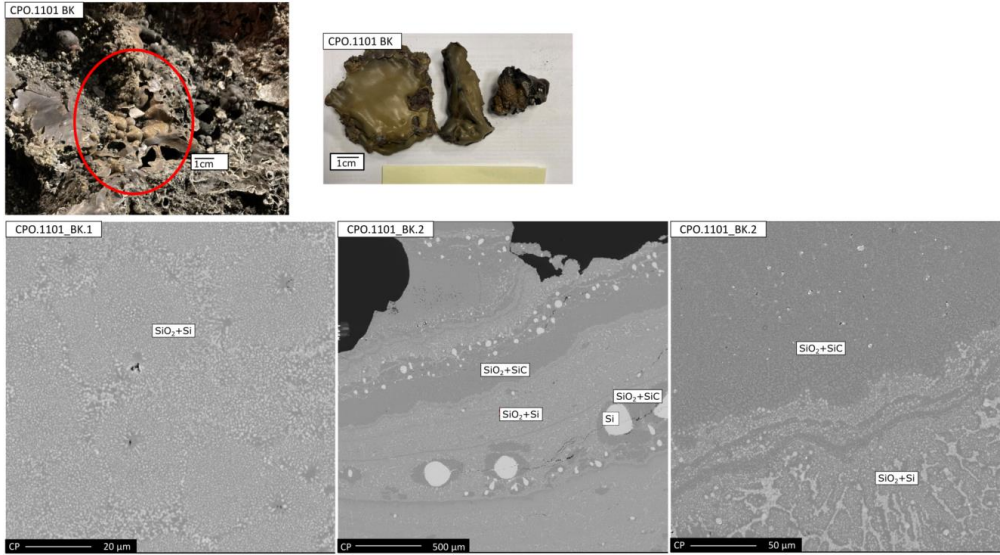


Figure 201 Sample CPO1101 BK.1 with magnification 1000X and BK.2 with magnifications 40X and 400X. Both samples are brown condensate of  $\text{SiO}_2$  and Si. BK.2 have several layers with brown and white condensate. The white condensate is  $\text{SiO}_2$  and SiC.

Further inside the main sample it was observed what appeared to be gas channels where SiO and CO gas have found its way through the hard and compact charge, seen in Figure 202. From deeper in the furnace, four visually different samples were collected.



Figure 202 Picture of sample CPO1101 and what appeared to be gas channels where SiO and CO gas have found its way through the hard and compact charge.

CPO1101 M was observed to have what was called “a metallic glance” and was believed to contain some FeSi. The two analyzed samples M.1 and M.2 are shown in Figure 203. Some FeSi were found, as can be seen in M.1, but most of the samples were SiO<sub>2</sub>, both with grain boundaries and partly melted, and SiO<sub>2</sub> rich slag. Some brown condensates of SiO<sub>2</sub> and Si were found in M.2.

The main sample was compact, but some parts also contained some porous areas. CPO1101 K was collected from here and was believed to be the raw material quartz. This was confirmed by the two analyzed samples K.1 and K.2 shown in Figure 204. Both samples also contain impurities in the SiO<sub>2</sub> and K.2 also have some Fe.

Sample CPO1101 P was also from the porous area with white and green colors. The two analyzed samples P.1 and P.2 can be seen in Figure 205. P.1 is white and is SiO<sub>2</sub> and some initial formation of slag. The sample also have some small particles of FeSi. The second analyzed sample P.2 is brown and white condensate in layer.

Sample CPO1101 U can be seen in Figure 206. This is a dark grey sample with a thin red layer outside, which is found to be FeO. The sample is mainly SiO<sub>2</sub> and SiO<sub>2</sub> rich slag. Also, some particles with FeSi were observed.

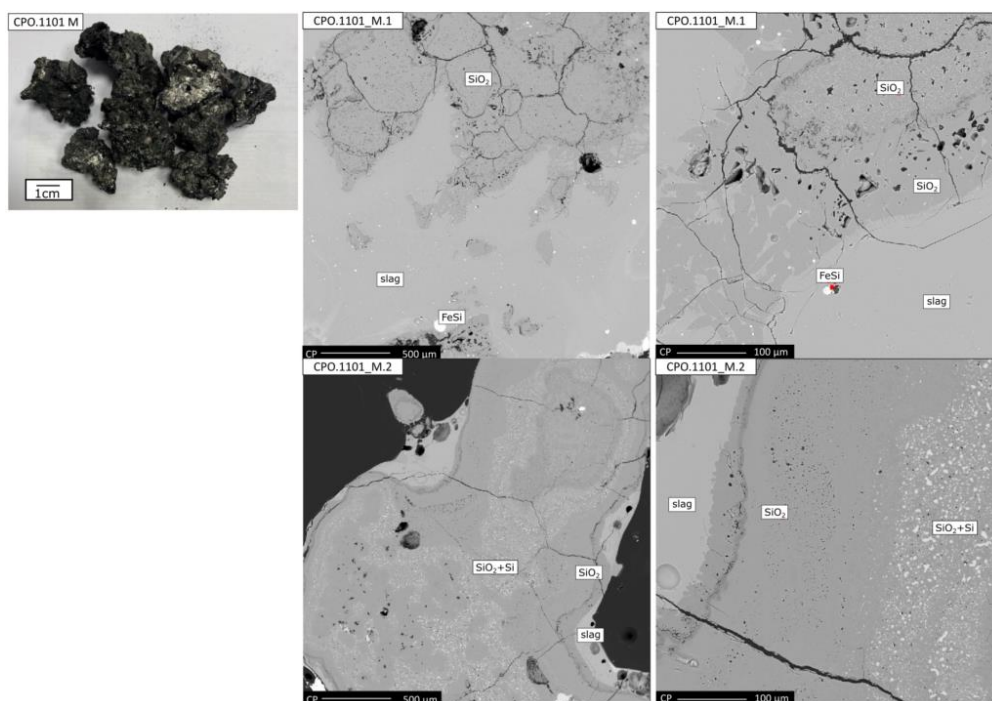


Figure 203 Sample CPO1101 M.1 and M.2 with two different magnifications; 40X and 200X. Both samples are mostly SiO<sub>2</sub> and SiO<sub>2</sub> rich slag. Some FeSi was found in M.1, and some brown condensate were found in M.2.

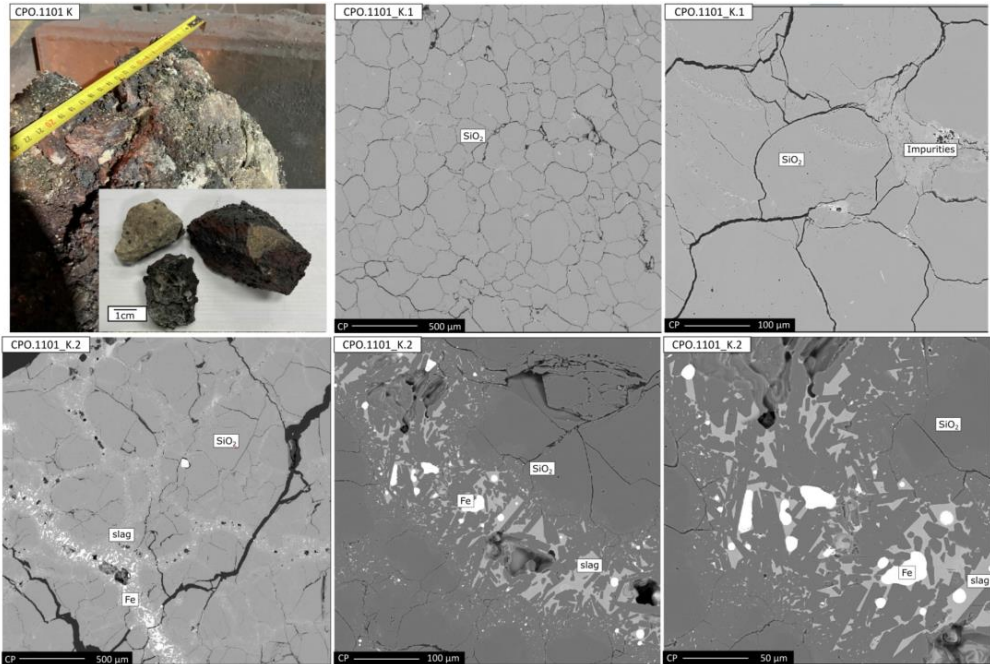


Figure 204 Sample CPO1101 K.1 and K2 with three different magnifications; 40X, 200X and 400X. The top left pictures are taken at the plant. Both samples consist of  $\text{SiO}_2$  and its impurities. Some Fe is also found in K.2.

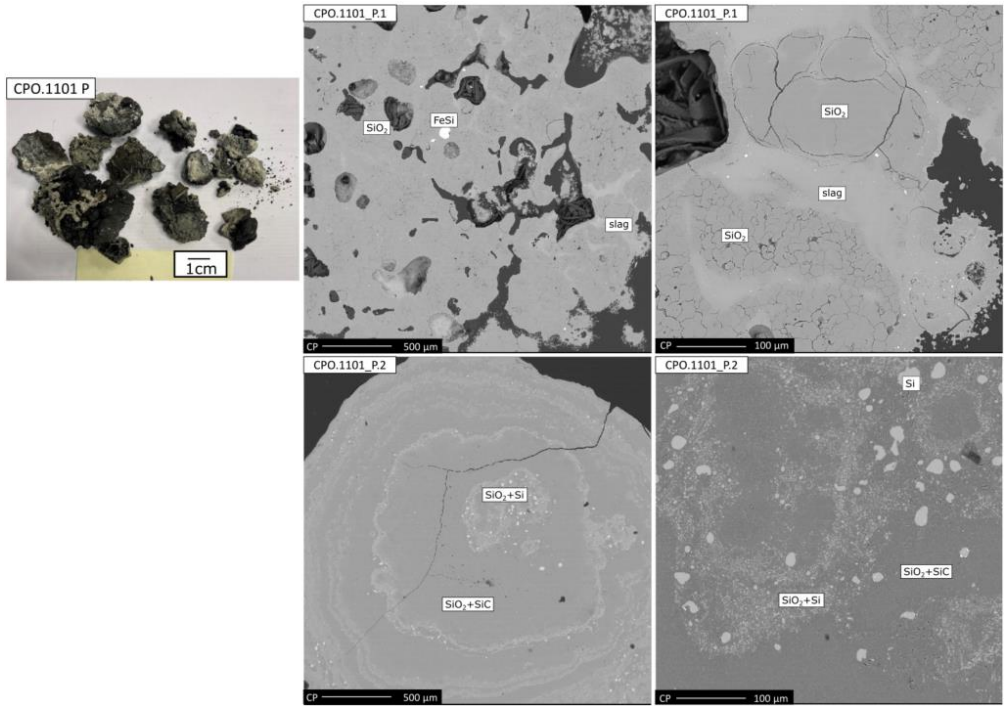


Figure 205 Sample CPO1101 P.1 and P.2 with two different magnifications; 40X and 200X. The top left image is picture of the sample taken at the plant. Sample P.1 is mainly  $\text{SiO}_2$  and initial formation of slag. P.2 is layered by brown and white condensate of  $\text{SiO}_2+\text{Si}$  and  $\text{SiO}_2+\text{SiC}$ , respectively.

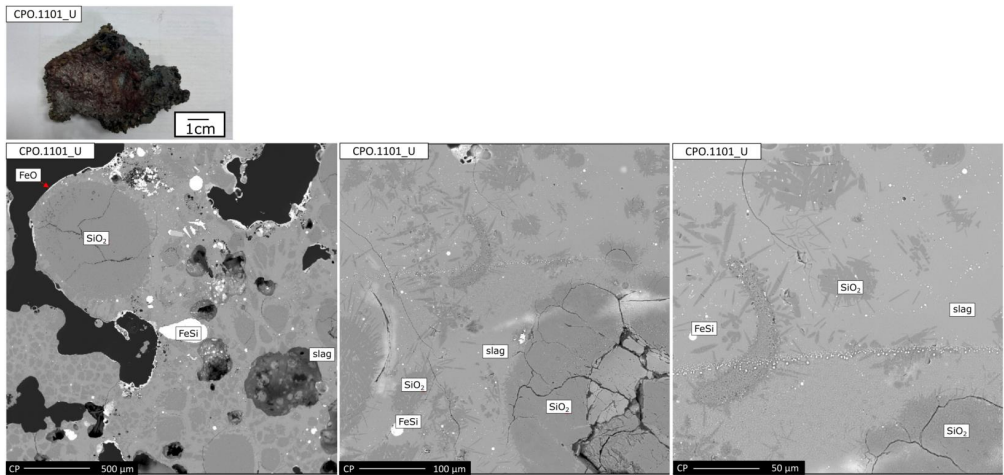


Figure 206 Sample CPO1101\_U with three different magnifications; 40X, 200X and 400X. The sample consists of mainly  $\text{SiO}_2$ , a  $\text{SiO}_2$  rich slag, and some  $\text{FeSi}$  particles. A thin layer of  $\text{FeO}$  is covering the sample.

#### A.4.4 Sample GR1602

Sample GR1602 was taken from the charge surface during challenging conditions and was described as matter melted together. The sample analyzed is covered with a thin red layer which is found to be FeO. In the sample is mainly SiO<sub>2</sub>, and in between the grain boundaries is slag. It is also found particles of FeSi in the sample.

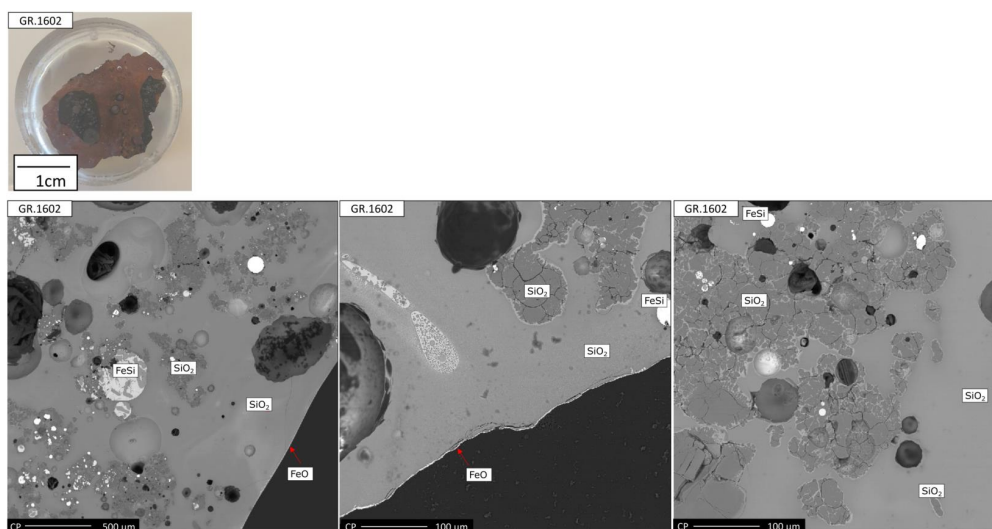


Figure 207 Sample GR1602 with three different magnifications; 40X, 200X and 400X. The sample consists of mainly SiO<sub>2</sub> and has a thin layer of FeO surrounding the sample. In the sample is also particles of FeSi.

#### A.4.5 Sample CPR2502

Sample CPR2502 from Furnace R was a large, heterogenous sample, as can be seen in Figure 208. It was reported several large and viscous pieces at the charge top during sampling time. The sample is divided into five smaller samples and some of them are named after what they were believed to be.

Sample CPR2502k was believed to be SiO<sub>2</sub>, and this was confirmed as shown in Figure 209. In between the grain boundaries were some impurity oxides.

CPR2502m was named based on its “metallic glance”. The analyzed sample is shown in Figure 210. For the sample analyzed it was found several smaller and larger areas with FeSi. Most of the sample were carbon and smaller SiC particles covering either SiO<sub>2</sub> or SiO<sub>2</sub>-CaO-Al<sub>2</sub>O<sub>3</sub> slag.

CPR2502y is taken from the outer edge of the sample. It has a black color on the outside, but also areas of white when it was crushed in smaller pieces. Figure 211 shows the

analyzed sample and it can be seen that the sample is  $\text{SiO}_2$  and some areas with small Si particles in the  $\text{SiO}_2$ .

Both sample CPR2502a and CPR2502b are from an unknown position and has a dark color. Two samples were analyzed from sample a and one for b, and these are shown in Figure 212 and Figure 213, respectively. All three samples consist of  $\text{SiO}_2$  and a  $\text{SiO}_2$  rich slag phase, in addition to some particles of FeSi.



Figure 208 The left picture is the whole sample CPR2502, while the picture in the middle and to the right shows different parts of the sample.

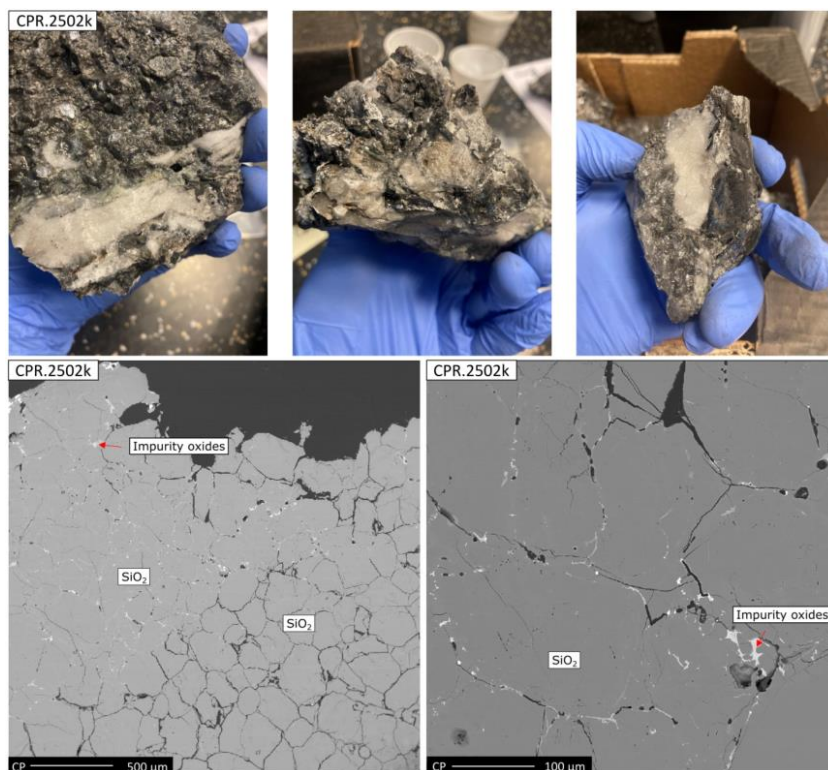


Figure 209 Sample CPR2502k with two different magnifications; 40X and 200X. This was confirmed to be  $\text{SiO}_2$ . Some impurity oxides were found in between the grain boundaries and cracks.

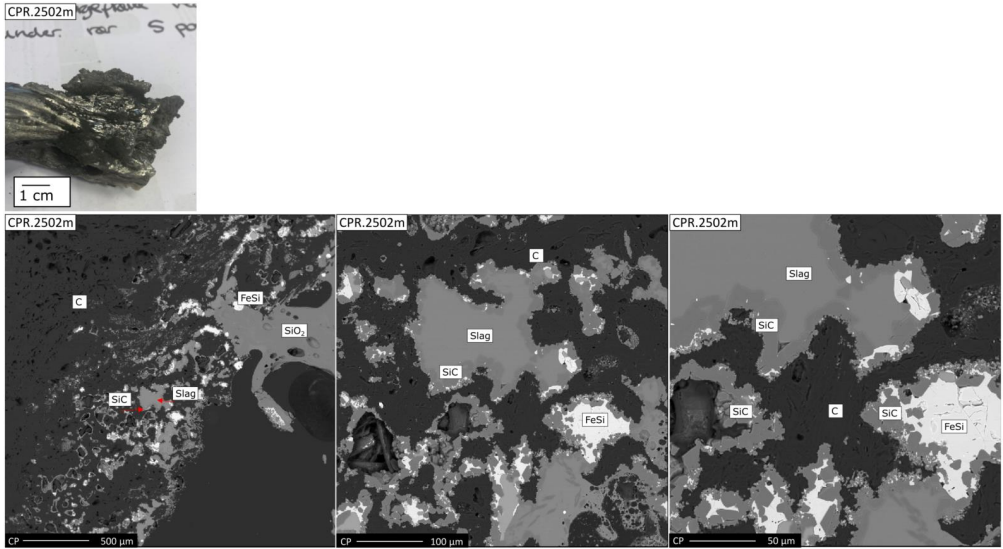


Figure 210 Sample CPR2502m with three different magnifications; 40X, 200X and 1000X. In the sample was mostly carbon, but also several smaller and larger FeSi areas. Small SiC particles were covering either slag or SiO<sub>2</sub>.

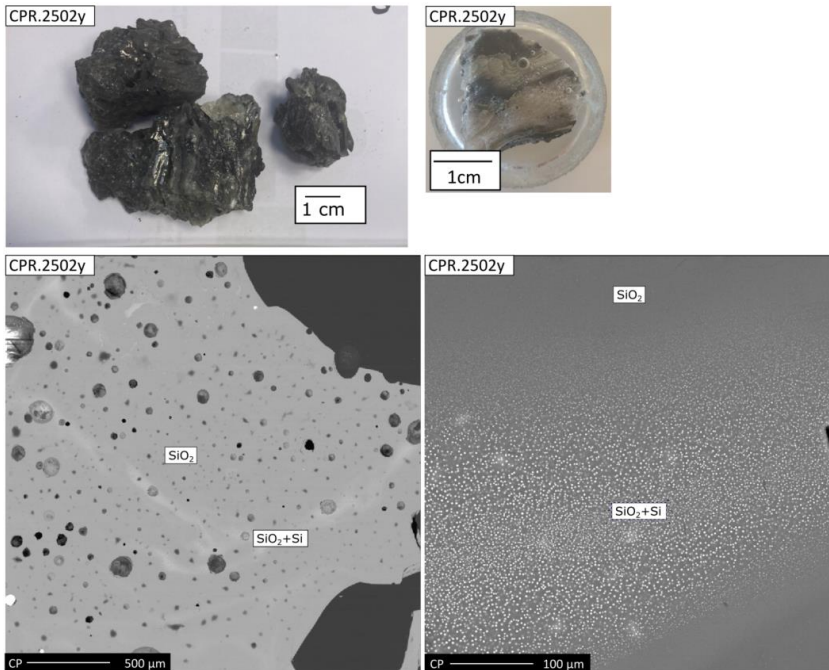


Figure 211 Sample CPR2502y with two different magnifications; 40X and 200X. The sample is mostly SiO<sub>2</sub> and areas with small Si particles in the SiO<sub>2</sub>.

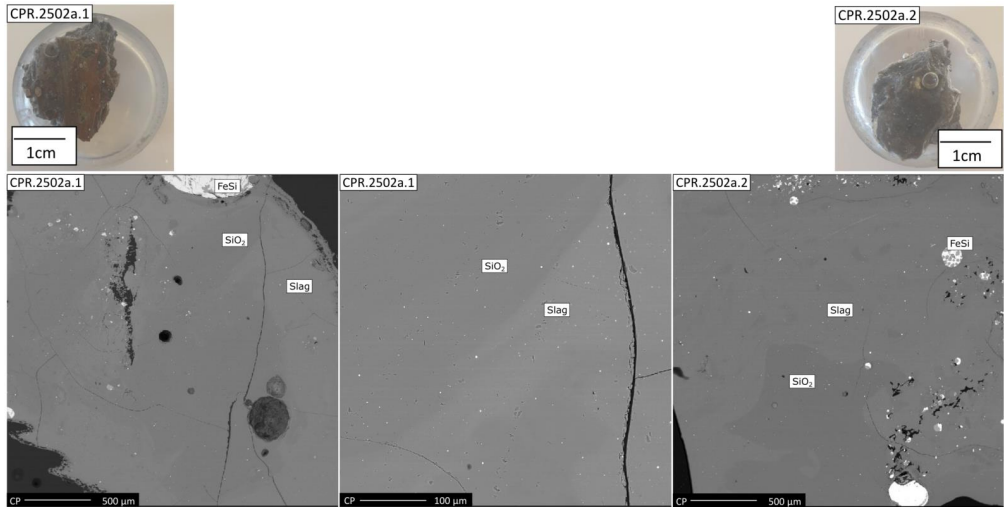


Figure 212 Sample CPR2502 a.1 with two different magnifications; 40X and 200X and a.2 with magnification 40X. Both samples consist of  $\text{SiO}_2$  and a  $\text{SiO}_2$  rich slag phase, in addition to some particles of FeSi.

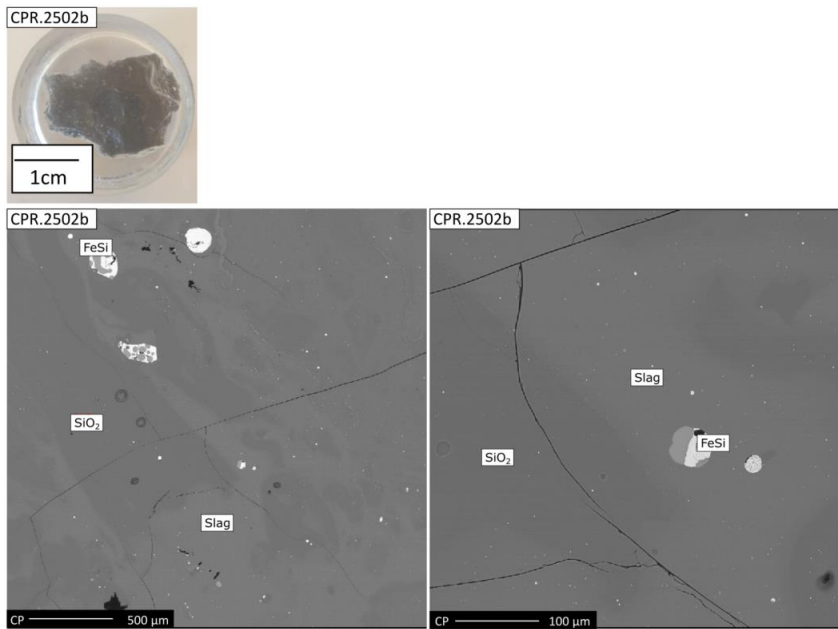


Figure 213 Sample CPR2502b with two different magnifications; 40X and 200X. The sample consists of  $\text{SiO}_2$  and a  $\text{SiO}_2$  rich slag phase, in addition to some particles of FeSi.



#### A.4.6 Sample CPR1903

For sample CPR1903 it was not given any information about the furnace condition at sampling time. One representative sample was chosen for analysis. Covering the main sample is a layer with brown condensate of  $\text{SiO}_2$  and Si. The analyzed sample consists of a 96%  $\text{SiO}_2$  phase with traces of mainly  $\text{Al}_2\text{O}_3$ ,  $\text{CaO}$  and  $\text{K}_2\text{O}$ . In the sample is also particles of FeSi.

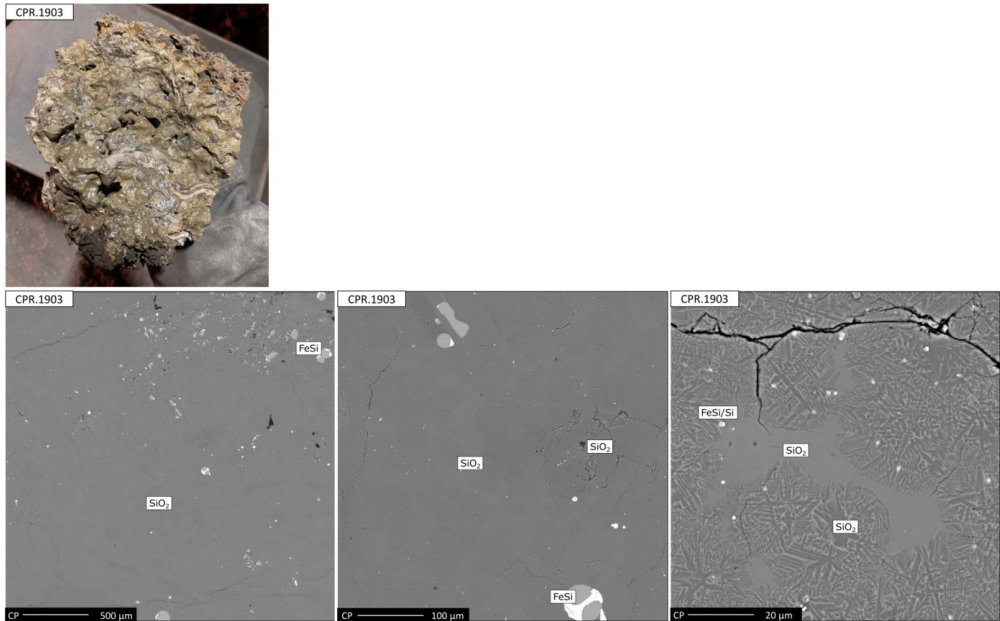


Figure 214 Sample CPR1903 with three different magnifications; 40X, 200X and 1000X. The sample consists of  $\text{SiO}_2$  with some particles of FeSi. It is found that the matrix is ~96%  $\text{SiO}_2$  with traces of mainly  $\text{Al}_2\text{O}_3$ ,  $\text{CaO}$  and  $\text{K}_2\text{O}$ .



## Appendix B: Changes in quartz during heating

Six different quartz types were used for the quartz experiments in this study: A, B, C, D, F and G. The pseudonym for quartz type A, D, F and G are the same quartz as used in Jusnes [9] doctoral thesis. Quartz B and C are Qz8 and Qz35, respectively.

### B.1 Trace element behaviour

The original data for the WDS analysis performed on the impurities found in the Quartz C, D and F samples, presented in Table 56, Table 57 and Table 58, respectively.

Table 56 The original WDS results for the impurities found in the quartz C samples.

Quartz type C	SiO <sub>2</sub>	Na <sub>2</sub> O	K <sub>2</sub> O	MnO	MgO	CaO	FeO	Al <sub>2</sub> O <sub>3</sub>	TiO <sub>2</sub>	BaO	Total
Initial Area1	49.0	0.4	10.0	0.01	1.2	0.02	2.1	34.9	0.2	0.1	97.9
Area2	51.0	0.2	9.6	0.02	1.4	0.1	1.4	32.5	2.4	0.01	97.1
1600°C Dark, 20% (1)	56.3	0.4	4.6	0	0.8	0.1	1.0	37.6	0.01	0	100.8
Bright, 80% (2)	72.1	0.7	7.0	0.02	0.9	0.1	0.9	18.9	0	0.03	100.6
1600°C (2)	65.5	0.3	9.5	0.3	0.9	0.2	0.4	22.9	0.01	0.1	100.2
1800°C (1)	-	-	-	-	-	-	-	-	-	-	-
1800°C (2)	86.0	0.1	1.7	2.0	1.3	0.04	0.8	7.2	0.6	0.03	99.7

Table 57 The original WDS results for the impurities found in the quartz D samples.

Quartz type D	SiO <sub>2</sub>	Na <sub>2</sub> O	K <sub>2</sub> O	MnO	MgO	CaO	FeO	Al <sub>2</sub> O <sub>3</sub>	TiO <sub>2</sub>	BaO	Total
Initial	21.7	0.2	3.6	0.04	0.2	0.4	57.4	13.4	1.1	0.1	98.1
1600°C (1)	88.4	0.02	0.9	0	0.05	0.02	3.4	4.5	0.1	0	97.4
1600°C White slag (2)	61.3	0.03	2.3	0.5	0.2	0.04	23.2	13.9	0.5	0.03	102.0
Grey slag	82.1	0.03	2.1	0.02	0.1	0.02	4.8	9.5	0.2	0.01	98.8
1800°C (1)	92.7	0.01	0.2	0.05	0.2	0	2.9	1.6	2.2	0.03	99.9
1800°C (2)	93.2	0.02	0.2	0.4	0.01	0.02	1.3	2.4	1.3	0.04	98.9

Table 58 The original WDS results for the impurities found in the quartz F samples.

Quartz type F	SiO <sub>2</sub>	Na <sub>2</sub> O	K <sub>2</sub> O	MnO	MgO	CaO	FeO	Al <sub>2</sub> O <sub>3</sub>	TiO <sub>2</sub>	BaO	Total
Initial	54.7	0.1	8.6	0	0.8	0.02	2.2	30.2	0.3	0.4	97.4
1600°C (1)	98.4	0	0.01	0	0	0.01	0	0.02	0	0	98.4
1600°C (2)	98.0	0.02	0.01	0	0	0.01	0	0.02	0	0	98.1
1800°C (1)	99.3	0.1	0	0.01	0	0.02	0	0	0	0	99.3
1800°C (2)	99.3	0.03	0.01	0.03	0	0.1	0	0	0	0.04	99.5



# Appendix C: CaO dissolution into SiO<sub>2</sub>-CaO-Al<sub>2</sub>O<sub>3</sub> slag

## C.1 X-ray diffraction

X-ray diffractions with Si, Al and Ca elemental mapping were done after dissolution experiments with CaO and 56% SiO<sub>2</sub> – 15% CaO – 29% Al<sub>2</sub>O<sub>3</sub> to see the spatial distribution of the different oxides in the slag. The results are shown in Figure 1-12.

### C.1.1 Heating rate 50 °C/min to 1200 °C and 25 °C/min to 1600 °C

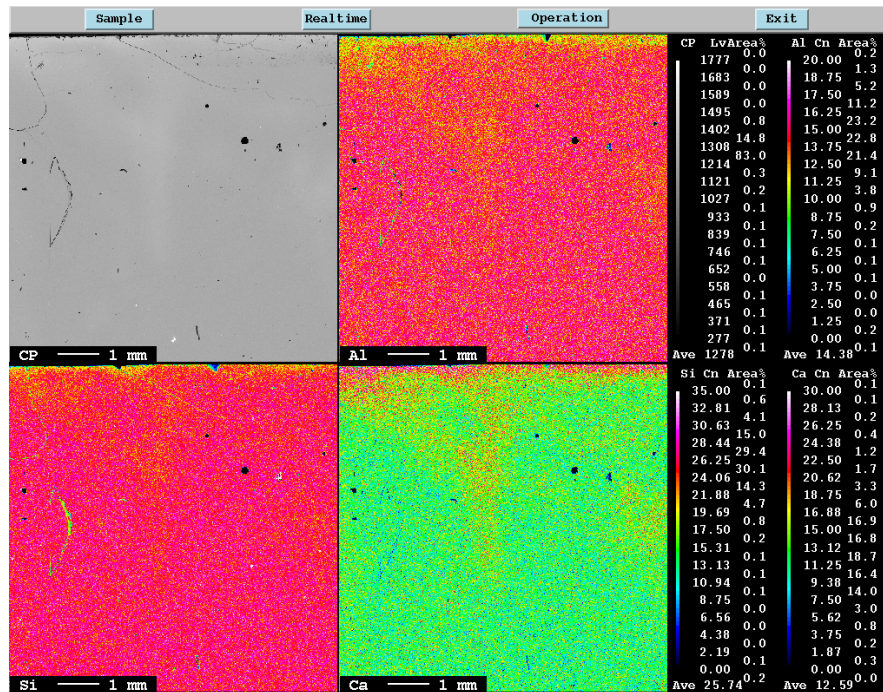


Figure 215 Si, Al and Ca elemental mapping on the sample 50.0.1, which is heated with 50 °C/min up to 1200 °C and 25 °C/min to 1600 °C with 0 minutes holding time.

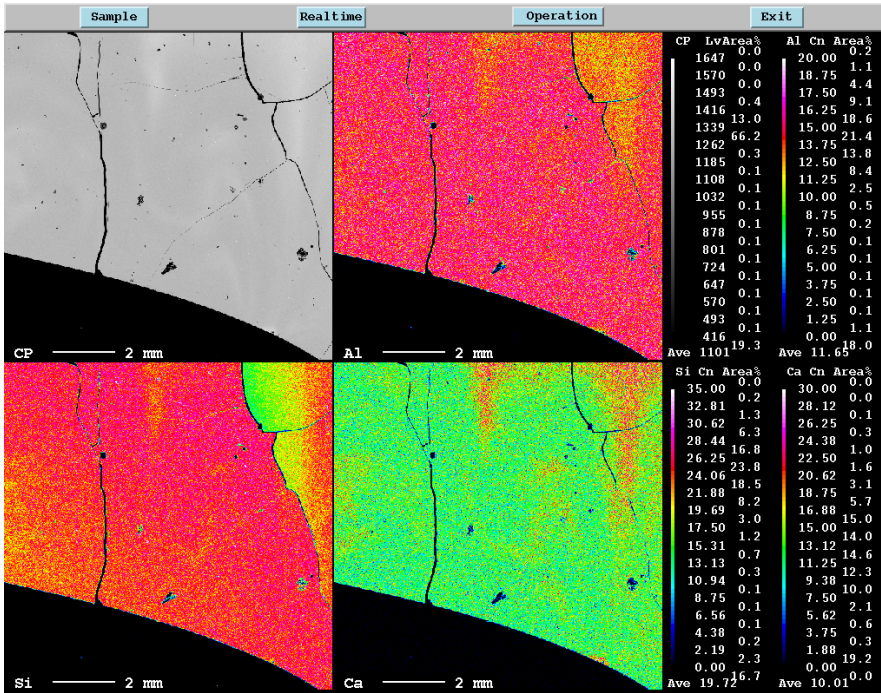


Figure 216 Si, Al and Ca elemental mapping on the sample 50.0.2, which is heated with 50 °C/min up to 1200 °C and 25 °C/min to 1600 °C with 0 minutes holding time.

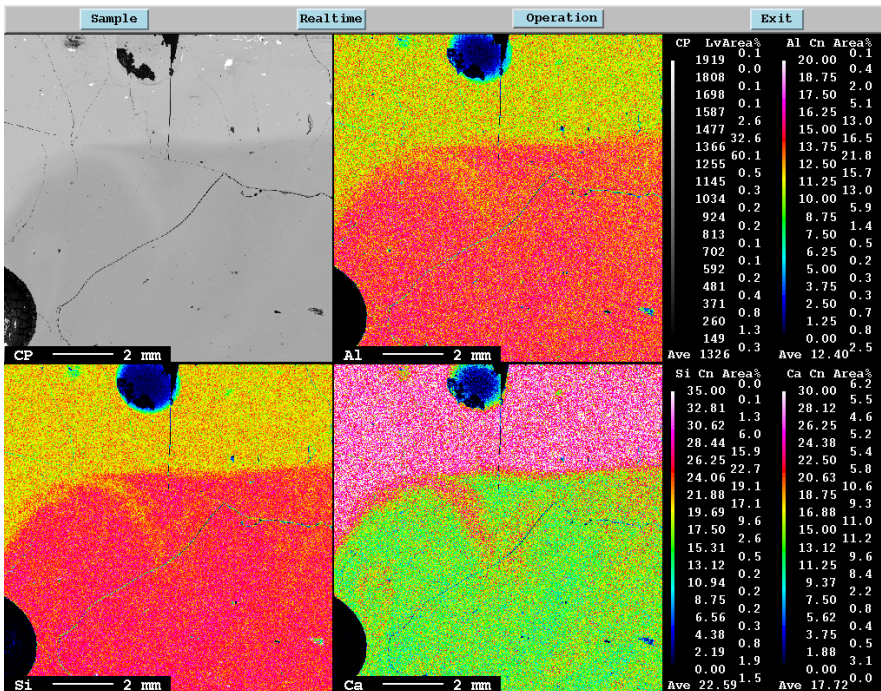


Figure 217 Si, Al and Ca elemental mapping on the sample 50.10, which is heated with 50 °C/min up to 1200 °C and 25 °C/min to 1600 °C with 10 minutes holding time.

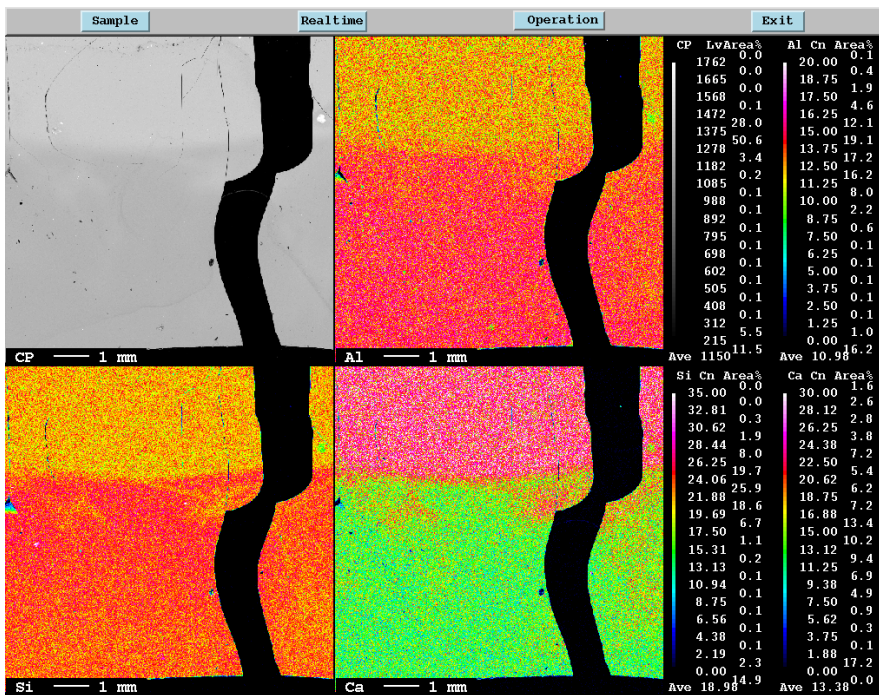


Figure 218 Si, Al and Ca elemental mapping on the sample 50.20, which is heated with 50 °C/min up to 1200 °C and 25 °C/min to 1600 °C with 20 minutes holding time.

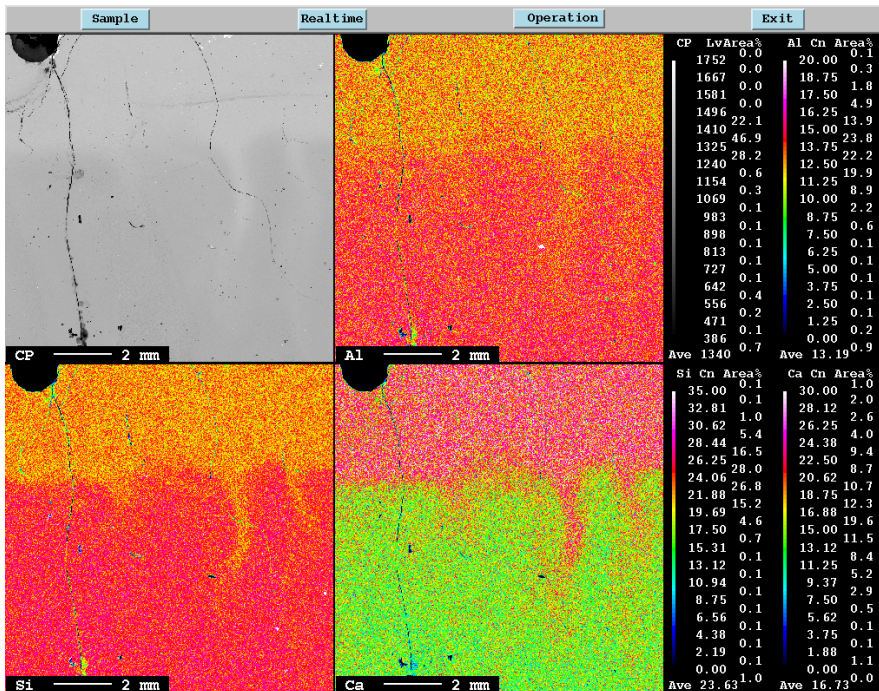


Figure 219 Si, Al and Ca elemental mapping on the sample 50.30, which is heated with 50 °C/min up to 1200 °C and 25 °C/min to 1600 °C with 30 minutes holding time.

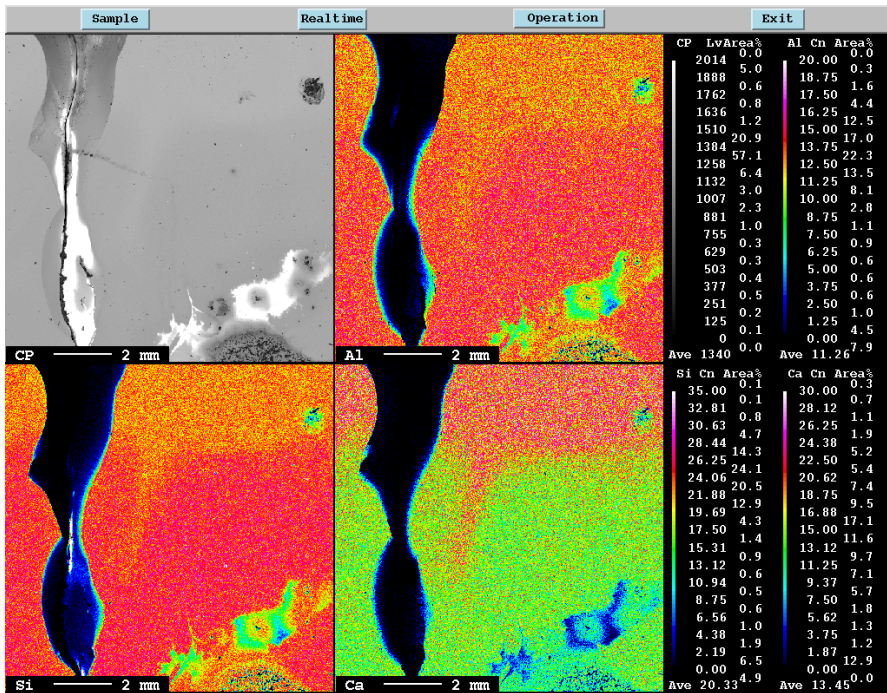


Figure 220 Si, Al and Ca elemental mapping on the sample 50.40, which is heated with 50 °C/min up to 1200 °C and 25 °C/min to 1600 °C with 40 minutes holding time.

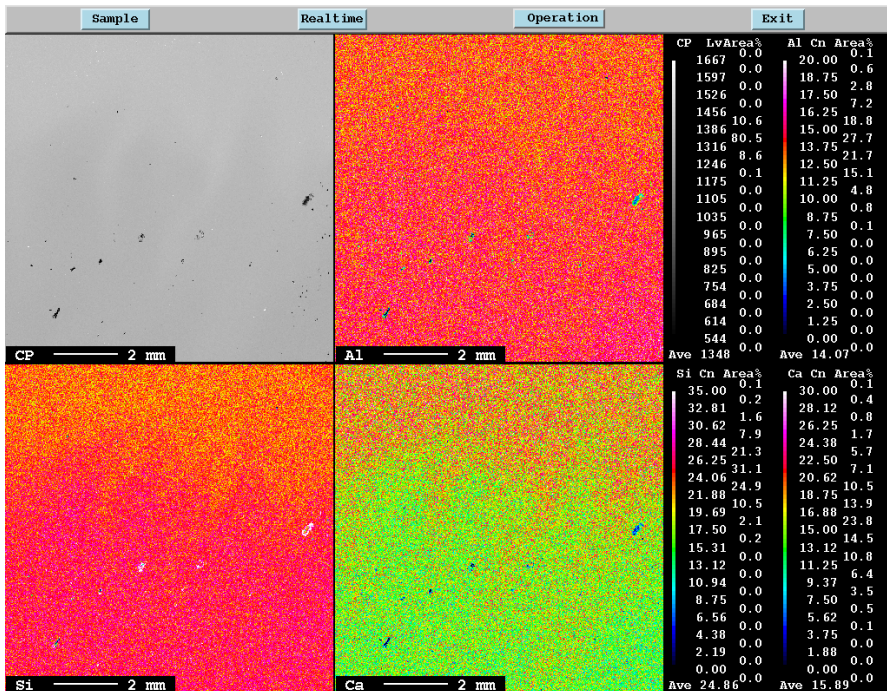


Figure 221 Si, Al and Ca elemental mapping on the sample 50.60.1, which is heated with 50 °C/min up to 1200 °C and 25 °C/min to 1600 °C with 60 minutes holding time.



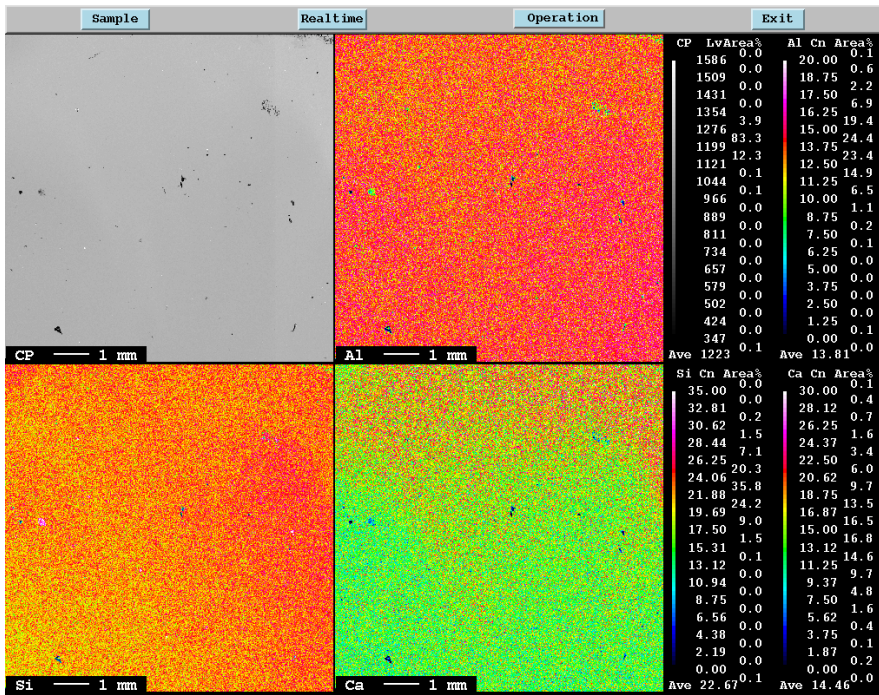


Figure 222 Si, Al and Ca elemental mapping on the sample 50.60.2, which is heated with 50 °C/min up to 1200 °C and 25 °C/min to 1600 °C with 60 minutes holding time.

C.1.2 Heating rate 25 °C/min to 1200 °C and 15 °C/min to 1600 °C

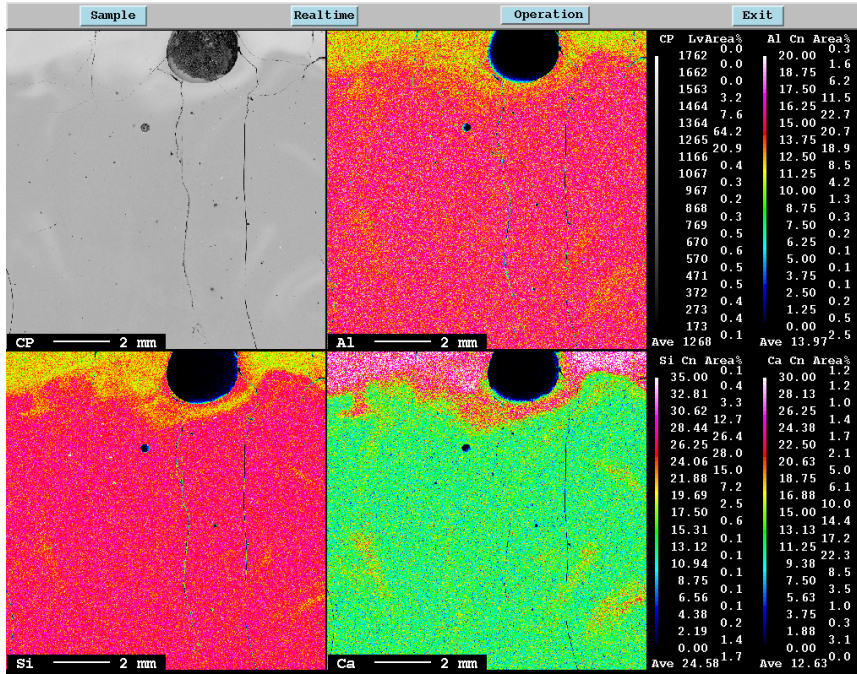


Figure 223 Si, Al and Ca elemental mapping on the sample 25.0, which is heated with 25 °C/min up to 1200 °C and 15 °C/min to 1600 °C with 0 minutes holding time.

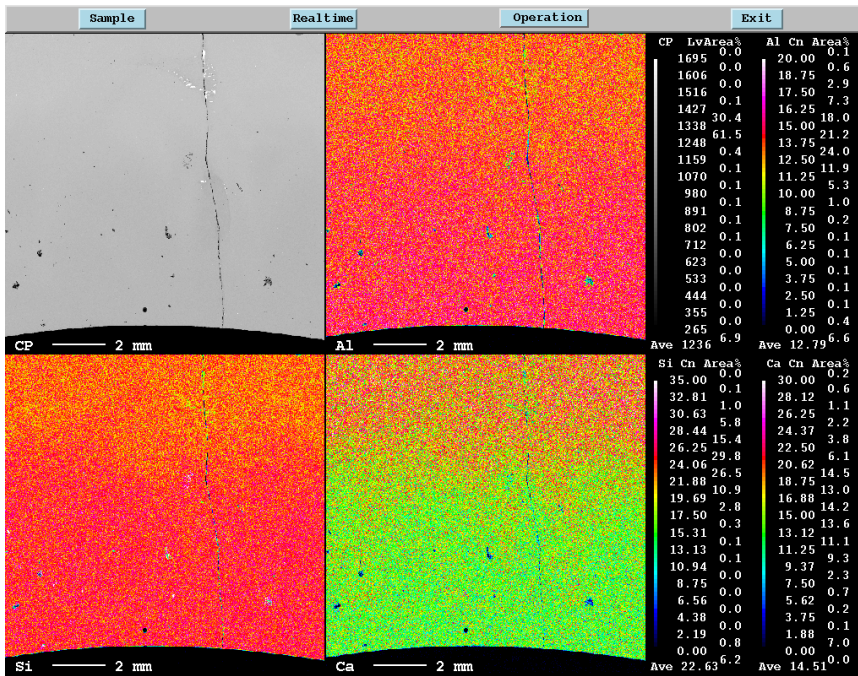


Figure 224 Si, Al and Ca elemental mapping on the sample 25.40, which is heated with 25 °C/min up to 1200 °C and 15 °C/min to 1600 °C with 40 minutes holding time.

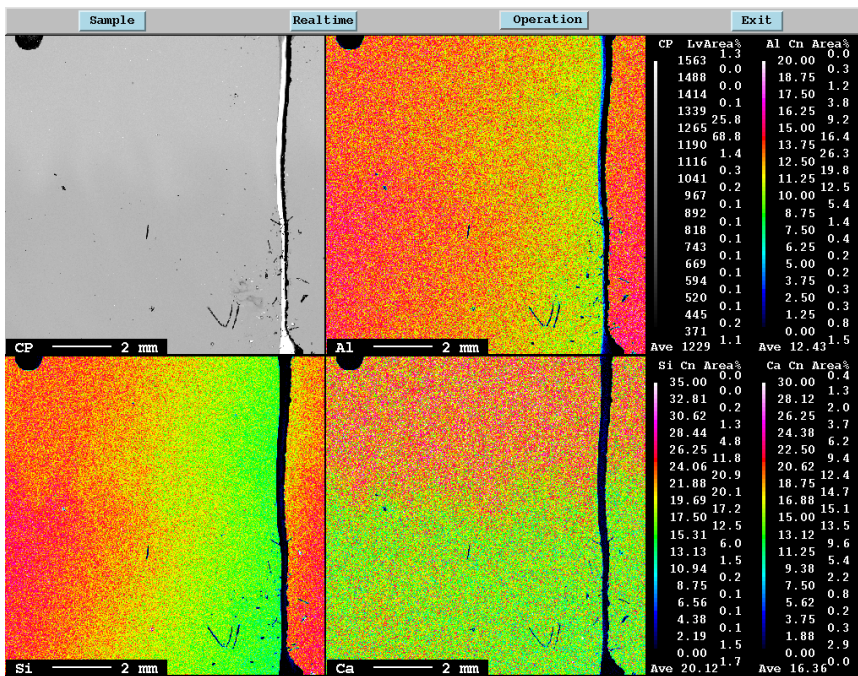


Figure 225 Si, Al and Ca elemental mapping on the sample 25.60, which is heated with 25 °C/min up to 1200 °C and 15 °C/min to 1600 °C with 60 minutes holding time.

### C.1.3 Heating rate 25 °C/min to 1200 °C and 15 °C/min to 1600 °C

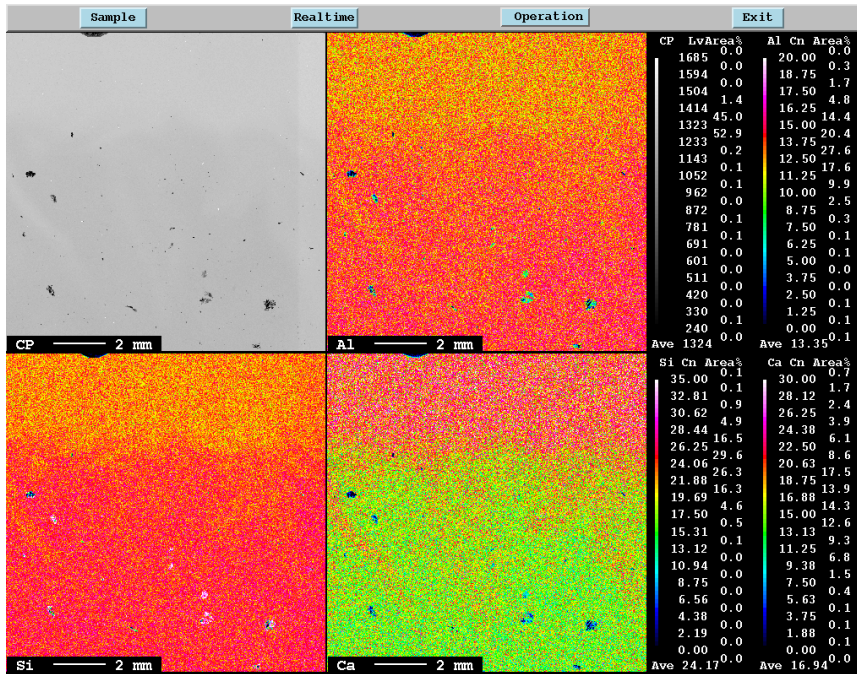


Figure 226 Si, Al and Ca elemental mapping on the sample 15.40, which is heated with 15 °C/min up to 1200 °C and 10 °C/min to 1600 °C with 40 minutes holding time.

## C.2 Dissolution experiments in the sessile drop furnace

Small-scale experiments with CaO and three different compositions of SiO<sub>2</sub>-CaO-Al<sub>2</sub>O<sub>3</sub> slag were done in a sessile drop furnace. The figures below show images of all the experiments during heating and the EPMA images taken of a vertical cross section after the experiments for the experiments that is not shown in the Results chapter in section 4.3.3.

### C.2.1 Slag 1: 56% SiO<sub>2</sub> – 15% CaO – 29% Al<sub>2</sub>O<sub>3</sub>

Figure 227, Figure 228 and Figure 229 show the results from CaO and slag 1 heated to 1500 °C with 10 minutes (second parallel), 20 minutes and 30 minutes holding time.

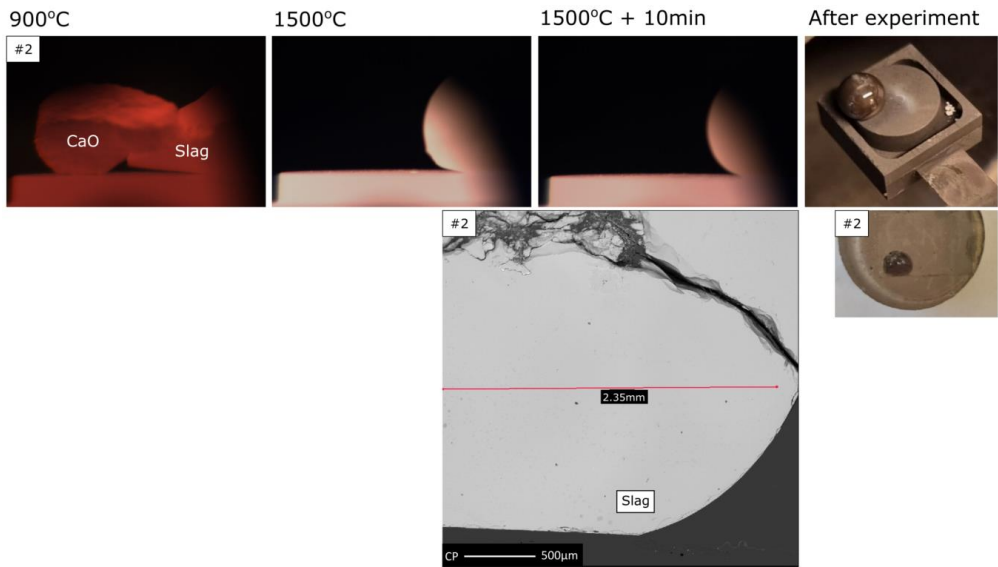


Figure 227 At the top are the images taken during and after experiments for the second parallel of CaO and 56% SiO<sub>2</sub>-15% CaO-29% Al<sub>2</sub>O<sub>3</sub> slag heated to 1500 °C and with 10 minutes holding time. Below are the cross-section image and the EPMA image after experiment. The initial CaO/slag were 0.36.

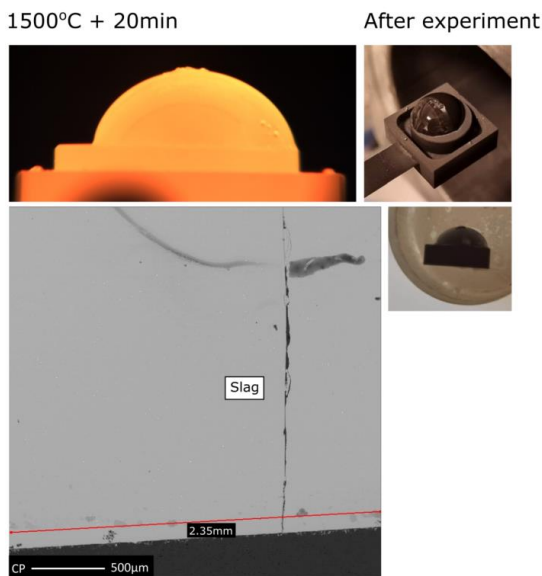


Figure 228 At the top are the images taken during and after experiment for the sample of CaO and 56% SiO<sub>2</sub>-15% CaO-29% Al<sub>2</sub>O<sub>3</sub> slag heated to 1500 °C and with 20 minutes holding time. Below are the cross-section image and the EPMA image after experiment. The initial CaO/slag were 0.30. The camera on the furnace did not work until the end of the experiment and it is therefore not obtained the images during the experiment at 900 °C and right after reached 1500 °C.

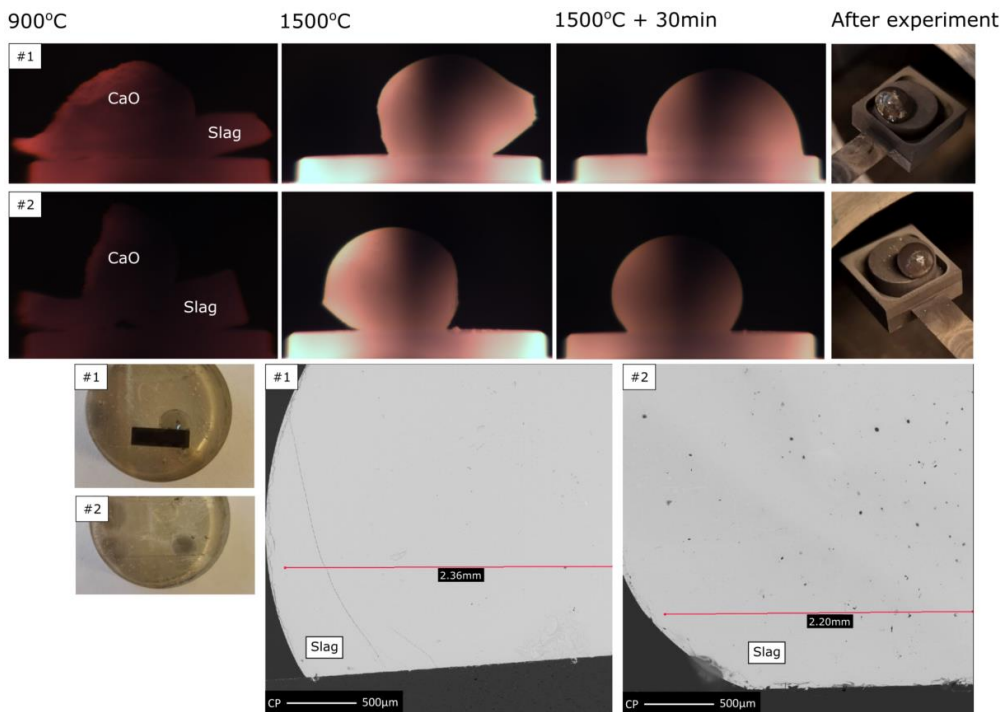


Figure 229 At the top are the images taken during and after experiments for the first and second parallel of CaO and 56% SiO<sub>2</sub>- 15% CaO-29% Al<sub>2</sub>O<sub>3</sub> slag heated to 1500 °C and with 30 minutes holding time. Below are the cross-section images and the EPMA images taken after experiment. The initial CaO/slag were 0.46 and 0.38 for the first and second parallel, respectively.

It was attempted to do experiments with excess of CaO to see the effect on the dissolution rate. However, because CaO decomposes in room atmosphere it was not possible to do any analysis of the materials after the materials were cooled down. This can be seen in Figure 230.

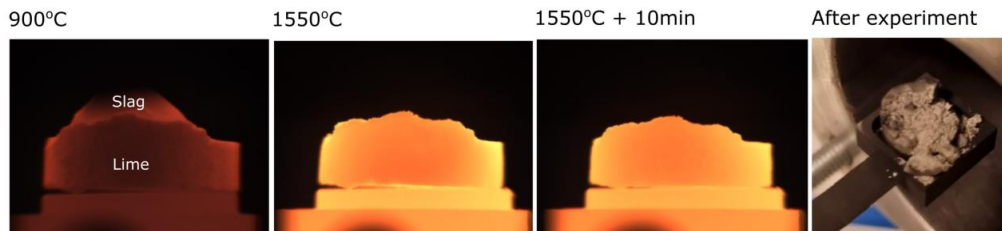


Figure 230 Images taken during and after experiment for the experiment run with slag on a lime substrate. The sample was heated to 1550 °C and held there for 10 minutes.

## C.2.2 Slag 2: 38% SiO<sub>2</sub> – 20% CaO – 42% Al<sub>2</sub>O<sub>3</sub>

Figure 231 shows the results from CaO and slag 2 heated to 1500 °C with 20 minutes holding time.

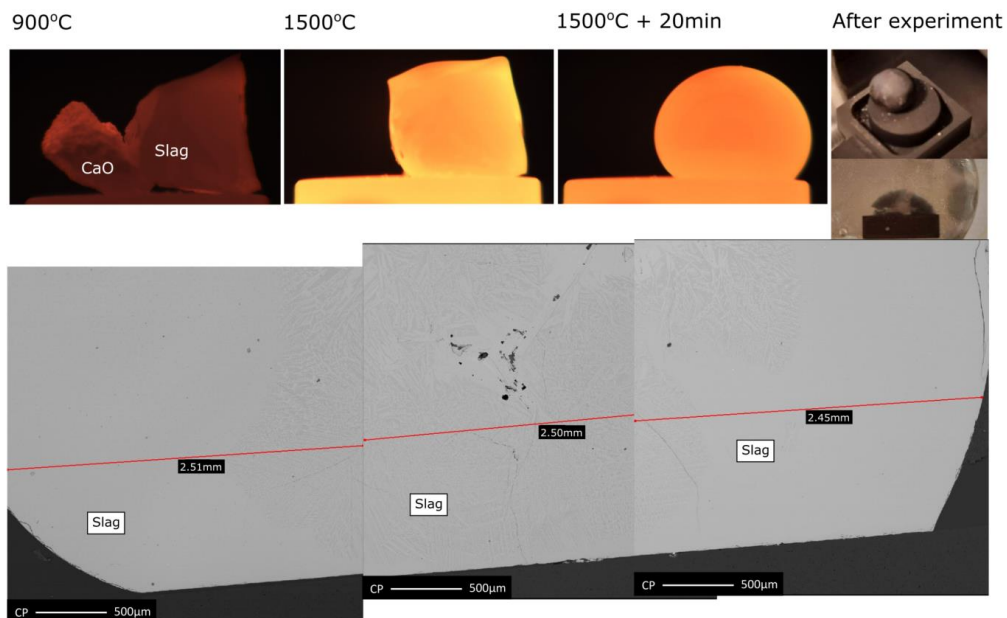


Figure 231 At the top are the images taken during and after experiment for the sample of CaO and 38% SiO<sub>2</sub>- 20% CaO- 42% Al<sub>2</sub>O<sub>3</sub> slag heated to 1500 °C and with 20 minutes holding time. Below are the cross-section image and the EPMA images after experiment. The initial CaO/slag were 0.17.

### C.2.3 Slag 3: 56% SiO<sub>2</sub> – 21% CaO – 23% Al<sub>2</sub>O<sub>3</sub>

Figure 232 shows the results from CaO and slag 2 heated to 1500 °C with 20 minutes holding time.

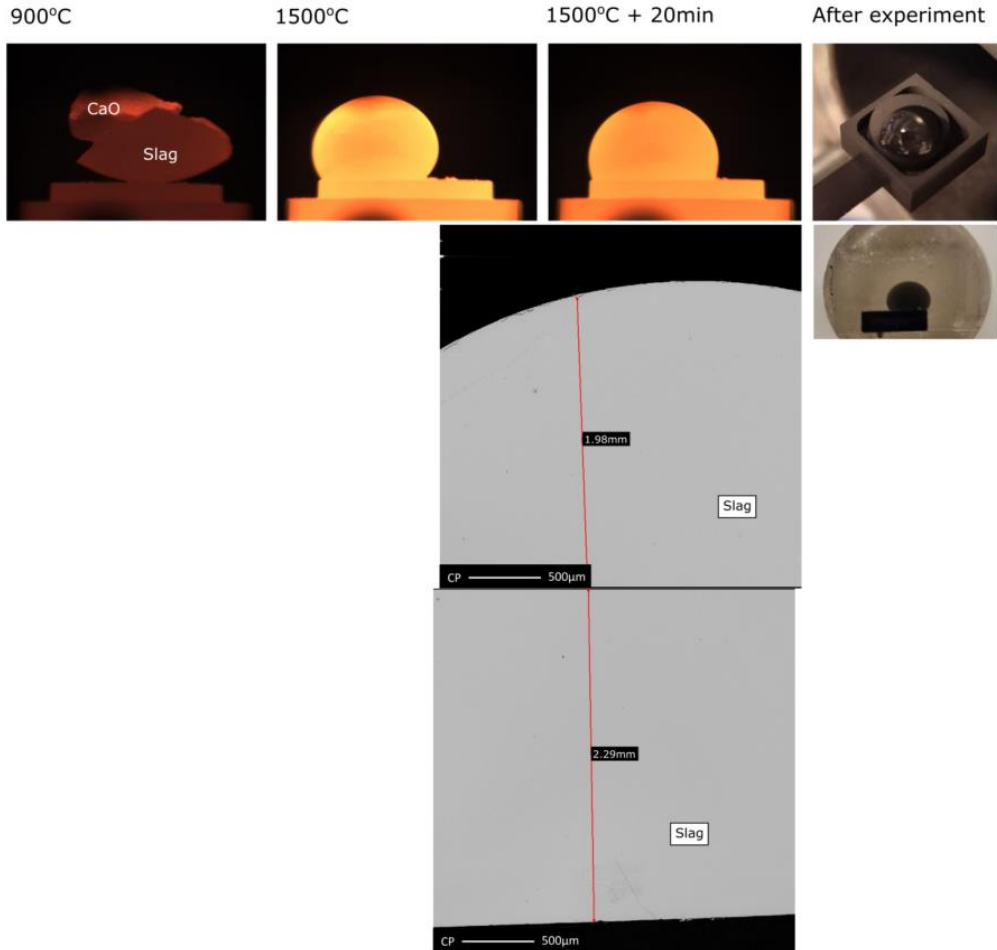


Figure 232 At the top are the images taken during and after experiment for the sample of CaO and 56% SiO<sub>2</sub>- 21% CaO- 23% Al<sub>2</sub>O<sub>3</sub> slag heated to 1500 °C and with 20 minutes holding time. Below are the cross-section image and the EPMA images after experiment. The initial CaO/slag were 0.28.



ISBN 978-82-326-7334-6 (printed ver.)  
ISBN 978-82-326-7333-9 (electronic ver.)  
ISSN 1503-8181 (printed ver.)  
ISSN 2703-8084 (online ver.)



**NTNU**

Norwegian University of  
Science and Technology